

# NASA Technical Memorandum 88784

NASA-TM-88784-VOL-1  
19860018569

## Advances in Planetary Geology

*Volume 1*

LIBRARY COPY

LANGLEY RESEARCH CENTER  
LIBRARY, NASA  
HAMPTON, VIRGINIA

JULY 1986

NOT FOR PUBLICATION

DO NOT TO BE TAKEN FROM THIS ROOM

**NASA**





NASA Technical Memorandum 88784

# Advances in Planetary Geology

*Volume 1*

*NASA Office of Space Science and Applications  
Washington, D.C.*



National Aeronautics  
and Space Administration

Scientific and Technical  
Information Branch

1986



## FOREWORD

This document is a compilation of reports from Principal Investigators and their Associates of NASA's Office of Space Science and Applications, Solar System Exploration Division, Planetary Geology and Geophysics Program. The reports present research that adds to our knowledge of the origin and evolution of the solar system and to our understanding of the earth as a planet. Advances in Planetary Geology was established as a complement to the abstract document "Reports of the Planetary Geology and Geophysics Program" and to professional journals. This document provides a method of publishing research results which are in a form that would not normally be published elsewhere. The research reports may be in the form of lengthy research reports, progress reports, Ph.D. dissertations, or master's theses.

Joseph M. Boyce  
Discipline Scientist  
Planetary Geosciences Program  
Office of Space Science and Applications

To Contributors:

A wider variety of manuscripts can be accommodated by Advances in Planetary Geology than by most journals. Particularly appropriate are completed theses, dissertations, and research reports reliant on extensive presentations of supporting data. All contributions must be of direct interest to planetary geologists and must be of high scientific quality. Manuscripts must be typed, preferably single spaced, in a camera-ready format. Inquiries concerning contributions as well as submissions of contributions should be made to:

Dr. Alex Woronow  
Geosciences Department  
University of Houston, University Park  
Houston, TX 77004

## Contents

A Harmonic and Statistical Analysis of the Topography of the Earth, Moon and Mars.....1 Bruce Gordon Bills	
Geologic Interpretation of Remote Sensing Data for the Martian Volcano Ascraeus Mons.....271 James Ray Zimbelman	



A HARMONIC AND STATISTICAL ANALYSIS OF THE  
TOPOGRAPHY OF THE EARTH, MOON AND MARS

Thesis by

Bruce Gordon Bills

In Partial Fulfillment of the Requirements  
for the Degree of  
Doctor of Philosophy

California Institute of Technology  
Pasadena, California

1978

(Submitted October 11, 1977)

## ACKNOWLEDGMENTS

Many people have contributed to the research reported in this thesis. I am particularly indebted to Dr. Alfred J. Ferrari for his continued support and encouragement during the course of this investigation. Indeed, the first three chapters of this thesis report the results of work on which we have collaborated for the better part of the last three years. I would also like to express appreciation to Prof. Duane O. Muhleman and Dr. Roger J. Phillips of the Jet Propulsion Laboratory (J.P.L.) for support and valuable discussion during various phases of this investigation.

L.A. Schirmerman of the Defense Mapping Agency and E.J. Christensen of J.P.L. provided us with magnetic tapes of lunar and martian topographic data, respectively. R.W. Wimberly, also of J.P.L., assisted in adapting these data to our computational facilities.

I have benefitted from discussions with Professors H.J. Melosh, R.P. Sharp and E.M. Shoemaker concerning geological implications of this research. S.S.C. Wu of the U.S. Geological Survey and M.E. Davies of the Rand Corporation were helpful in the early phases of the martian data analysis. E.C. Posner of J.P.L. improved my understanding of stochastic processes.

I have also enjoyed lively discussions and debates with my fellow students Dave Diner, John Dvorak, Bill McKinnon and particularly Tony Dobrovolskis.



I would like to thank Kay Campbell and Brenda Parson for their help in the preparation of several early drafts and the final manuscript of this thesis.

The first two chapters of this thesis have been previously published in Icarus <sup>31</sup>, 244-259 (1977) and Journal of Geophysical Research <sup>82</sup>, 1306-1314 (1977), respectively. I thank Academic Press and the American Geophysical Union for permission to include them here. Figure 4.3 is adapted from T.H. Bell's paper in Deep-Sea Research <sup>22</sup>, 883-891 (1975). I am grateful to Pergamon Press for permission to use this material.

This research was performed at both the California Institute of Technology and the Jet Propulsion Laboratory under NASA contract NAS 7-100.

## ABSTRACT

In chapter I a global lunar topographic map is derived from Earth-based and orbital observations supplemented in areas without data by a linear autocovariance predictor. Of 2592 bins, each  $5^\circ$  square, 1380 (64.7% by area) contain at least one measurement. A spherical harmonic analysis to degree 12 yields a mean radius of  $(1737.53 \pm 0.03)$  km (formal standard error) and an offset of the center of figure of  $(1.98 \pm 0.06)$  km toward  $(19 \pm 2)^\circ\text{S}$ ,  $(194 \pm 1)^\circ\text{E}$ . A Bouguer gravity map is also presented. It is confirmed that the low-degree gravity harmonics are caused primarily by surface height variations and only secondarily by lateral density variations.

In chapter II a series of models of the lunar interior are derived from topographic, gravitational, librational and seismic data. The moon departs from isostasy, even for the low-degree harmonics, with a maximum superisostatic stress of 200 bars under the major mascon basins. The mean crustal thicknesses under different physiographic regions are: mascons, 30-35 km; irregular maria, 50-60 km; and highlands, 90-110 km. A significant correlation between lunar surface chemistry and crustal thickness suggests that regions of thicker crust are more highly differentiated. A possible mean composition consistent with our model is an anorthositic crust, underlain by a predominantly forsterite upper mantle which grades into a refractory rich lower mantle surrounding a pyrrhotite core.

In chapter III a model of martian global topography is obtained by fitting a spherical harmonic series of degree 16 to occultation, radar, spectral and photogrammetric measurements. The existing observations are supplemented in areas without data by empirical elevation estimates based on photographic data. The mean radius is  $(3389.92 \pm 0.04)$  km. The corresponding mean density is  $(3.933 \pm 0.002)$  g cm<sup>-3</sup>. The center of figure is displaced from the center of mass by  $(2.50 \pm 0.07)$  km towards  $(62 \pm 3)^\circ\text{S}$ ,  $(272 \pm 3)^\circ\text{W}$ . The geometric flattening  $[f_g = (6.12 \pm 0.04) 10^{-3}]$  is too great and the dynamic flattening  $[f_d = (5.22 \pm 0.03) 10^{-3}]$  is too small for Mars to be homogeneous and hydrostatic. It is confirmed that, similar to the Moon, the martian low-degree gravity harmonics are produced primarily by surface height variations and only secondarily by lateral density variations. Maps of the global topography and Bouguer gravity are presented. These are interpreted in terms of a crustal thickness map which is consistent with gravity, topography and recent preliminary Viking seismic results. Using plausible density contrasts and an assumed zero crustal thickness at Hellas, the inferred minimum mean crustal thickness is  $(28 \pm 4)$  km.

In chapter IV it is shown that the topographic variance spectra of the Earth, Moon, Mars and Venus are all very similar. The variance per harmonic degree  $V(H;n)$  decreases roughly as the inverse square of the degree, or more precisely  $V(H;n) \doteq V(H;0)/(n)(n+1)$ . On the Earth and Moon this relationship has been confirmed down to scale lengths as

small as  $L \approx 100$  m. At the other end of the spectrum, the variance appears to be deficient relative to this model for scale lengths greater than  $L \approx 2000$  km. The most satisfactory explanation for this phenomenon appears to be a simple equilibrium between constructional or "tectonic" processes which tend to roughen the surface uniformly at all scales, and destructional or erosive processes which tend to smooth the surface preferentially at small scales. The deficiency in the low-degree variances is attributable to visco-elastic deformation.

# CONTENTS

<u>Section</u>	<u>Page</u>
PREFACE . . . . .	13
I A HARMONIC ANALYSIS OF LUNAR TOPOGRAPHY . . . . .	14
A Introduction . . . . .	14
B Data . . . . .	14
C Analysis . . . . .	19
D Results . . . . .	23
References . . . . .	42
II A LUNAR DENSITY MODEL . . . . .	47
A Introduction . . . . .	47
B Data . . . . .	47
C Theory . . . . .	50
D Models . . . . .	54
E Summary . . . . .	72
References . . . . .	73
III A HARMONIC ANALYSIS OF MARTIAN TOPOGRAPHY . . . . .	76
A Introduction . . . . .	76
B Data . . . . .	77
C Analysis . . . . .	81
D Results . . . . .	86
1 Low degree harmonics . . . . .	86
2 High degree harmonics . . . . .	105
References . . . . .	124

## CONTENTS (Continued)

<u>Section</u>	<u>Page</u>
IV TOPOGRAPHIC VARIANCE SPECTRA OF THE EARTH, MOON AND MARS:	
AN EQUILIBRIUM MODEL . . . . .	130
A Introduction . . . . .	130
B Observations . . . . .	134
1 Variance spectra . . . . .	134
a Earth . . . . .	134
b Moon . . . . .	139
c Mars . . . . .	144
d Venus . . . . .	147
2 Isotropy . . . . .	152
3 Simulation . . . . .	153
4 Summary . . . . .	158
C Analysis . . . . .	164
1 Convection . . . . .	165
2 Geometry . . . . .	167
3 Energy Redistribution . . . . .	170
a Elastic energy reduction . . . . .	170
b Two dimensional fluid flow . . . . .	171
4 Random Pulse Model . . . . .	173
a Energy equipartitioning . . . . .	178
b Slope stability . . . . .	179
c Impact cratering . . . . .	180

# CONTENTS (Continued)

<u>Section</u>	<u>Page</u>
5 Equilibrium . . . . .	184
a Historical background . . . . .	184
b Dynamic model . . . . .	186
c Visco-elastic relaxation . . . . .	190
d Maximum entropy conjecture . . . . .	194
D Implications . . . . .	197
E Summary . . . . .	202
References . . . . .	204
V APPENDICES . . . . .	215
A Spherical Harmonics . . . . .	215
B Probability Densities . . . . .	226
C Stochastic Processes . . . . .	233
1 Poisson . . . . .	234
2 Weiner . . . . .	234
3 Ornstein-Uhlenbeck . . . . .	238
D Covariance Functions . . . . .	239
E Visco-elastic Deformation . . . . .	246
F Potential Energy . . . . .	252
1 Elastic . . . . .	252
2 Gravitational . . . . .	256
G Slopes . . . . .	260
1 Isotropy . . . . .	262
2 Stability . . . . .	264
References . . . . .	268

## ILLUSTRATIONS

<u>Figure</u>		<u>Page</u>
1.1	Lunar Data Distribution . . . . .	17
1.2	Comparison of Laser Altimetry Data and Harmonic Model . .	27
1.3	Lunar Topography Map . . . . .	30
1.4	Lunar Topographic Error Map . . . . .	32
1.5	Lunar Bouguer Gravity Map . . . . .	37
2.1	Envelope of Plausible Lunar Density Profiles . . . . .	56
2.2	Lunar Seismic Travel Times . . . . .	65
2.3	Lunar Crustal Thickness Variation	
	A. Nearside . . . . .	67
	B. Farside . . . . .	67
3.1	Martian Data Distribution	
	A. Mid-latitudes . . . . .	78
	B. Polar Regions . . . . .	79
3.2	Martian Topography and Error Variance . . . . .	107
3.3	Correlation Coefficients: Present and Previous Models . .	110
3.4	Martian Topography Map	
	A. Mid-latitudes . . . . .	112
	B. Polar Regions . . . . .	112
3.5	Correlation Coefficients: Gravity and Topography . . . .	115
3.6	Martian Bouguer Gravity Map . . . . .	118
3.7	Martian Crustal Thickness Variation . . . . .	121
4.1	Simulated Topographic Variance Spectrum . . . . .	132
4.2	Earth: Spherical Topographic Variance Spectrum . . . . .	136
4.3	Earth: Composite Topographic Variance Spectrum . . . . .	136



## ILLUSTRATIONS (Continued)

<u>Figure</u>	<u>Page</u>
4.4 Moon: Spherical Topographic Variance Spectrum . . . . .	141
4.5 Moon: Circular Topographic Variance Spectrum . . . . .	141
4.6 Moon: Slope Analysis . . . . .	145
4.7 Mars: Spherical Topographic Variance Spectrum . . . . .	148
4.8 Venus: Circular Topographic Variance Spectrum . . . . .	150
4.9 Isotropy Spectra	
A. Random Simulation . . . . .	154
B. Earth . . . . .	155
C. Mars . . . . .	156
D. Moon . . . . .	157
4.10 Topographic Contour Maps	
A. Moon . . . . .	159
B. Mars . . . . .	159
C. Earth . . . . .	159
D. Random Simulation . . . . .	159

# TABLES

<u>Table</u>		<u>Page</u>
1.1	Lunar Topographic Data Sources . . . . .	16
1.2	Normalized Lunar Topography Harmonics . . . . .	24
1.3	Lunar Topography and Error Variances . . . . .	34
2.1	Lunar Gravitational, Topographic and Librational Data . . .	49
2.2	Two-layered Lunar Density Model . . . . .	59
2.3	Lunar Interior Structure Model . . . . .	63
2.4	Moments of Lunar Density Distribution . . . . .	64
3.1	Normalized Martian Topography Harmonics . . . . .	87
3.2	Martian Dynamic Flattening . . . . .	101
3.3	Martian Geometric Flattening . . . . .	102

## PREFACE

The surface topography of a planet is one of its most important characteristics, since it reflects the complex history of interaction between exogenic and endogenic processes which have formed and subsequently modified the planet. Topographic data can also be used in conjunction with gravity observations to estimate the lateral variation of subsurface density and the stress distribution which maintains the gravity anomalies.

The initial objective of this investigation was to obtain spherical harmonic representations of lunar and martian topography of sufficient resolution and fidelity to be of use in performing global Bouguer analyses and in internal density modeling. The results of these efforts are reported in the first three chapters.

In the course of this research it was discovered that the topographic variance spectra of the Moon and Mars are very similar to the Earth's. The statistical similarity of these surfaces which have been subjected to vastly different formative processes seems to require some explanation. In the fourth chapter we investigate this phenomenon and find a simple explanation in terms of equilibrium between constructional and erosive activity. The statistical aspects of the resultant surface are largely independent of the details of the processes producing it.

## I. A HARMONIC ANALYSIS OF LUNAR TOPOGRAPHY

### A. INTRODUCTION

The objective of this investigation has been to obtain a lunar topography model that resolves basin-sized features, and can be used with a gravity model of equivalent resolution to perform global Bouguer analyses. A variety of elevation data types have been used to derive a spherical harmonic representation of the lunar figure. Previous analyses of lunar topography (Goudas, 1971; Jones, 1973; Chuikova, 1976) have suffered from inadequate data coverage and insufficient model resolution.

This chapter presents a discussion of the data used in the analysis, its selenographic distribution, and associated errors. A development is also presented of the analysis technique used to compensate for the irregular data distribution.

Maps of the global topography and its formal uncertainty are presented, along with a Bouguer anomaly map. The implications of some of the low-degree harmonics are considered separately.

### B. DATA

The determination of the figure of the Moon has had a long and interesting history (see, e.g., Kopal and Carder, 1974). The measurements have been referred to several similar, but fundamentally different, coordinate systems. All measures are of the basic form  $R(\theta, \varphi)$ , where  $R$  is the radial distance from the origin,  $\theta$  is the latitude, and  $\varphi$  is the (east) longitude. The angles are measured from the mean sub-Earth point.

The basic difference between the various reference systems used is in the location of their respective coordinate origins. For analytical purposes, the most convenient coordinate origin is the lunar center of mass. Before combining the various data types used in this analysis, we will refer them to this selenodetic coordinate system.

The data used which are already selenodetically referenced consist of Apollo laser altimetry (Roberson and Kaula, 1972; Wollenhaupt and Sjogren, 1972; Wollenhaupt et al., 1974; Kaula et al., 1972, 1973, 1974), vertical and oblique metric photogrammetry (Schirmerman, 1975, personal communication), and landmark tracking data (Wollenhaupt et al., 1972).

The data which were not initially in a selenodetic coordinate system consists of Watts' (1963) limb profiles (sampled at 2.5 intervals in the libration frame) and ground-based stereoscopic photogrammetry (Hopmann, 1967; Mills and Sudbury, 1968; Arthur and Bates, 1968). These limb and photogrammetric data were referred to the selenodetic system by means of transformations determined by Van Flandern (1970) and Schirmerman et al. (1973), respectively.

Other recent data which we have examined but have not used (either because of redundancy with the above data or because of ambiguity in the associated coordinate systems) include more ground-based photogrammetry (Baldwin, 1963), Zond-6 limb profiles (Rodionov et al., 1971), lunar orbiter photogrammetry (Jones, 1973), radar

interferometry (Zisk, 1972), and Apollo radar altimetry (Brown et al., 1974).

Table 1.1 is a summary of the various data types used, the number of points measured, and their estimated accuracies. Figure 1.1 indicates the approximate distribution of the data, summarized according to  $5^\circ \times 5^\circ$  bins. The most important aspect of this distribution is the complete lack of data for large regions on the far side. This situation considerably complicates our analysis.

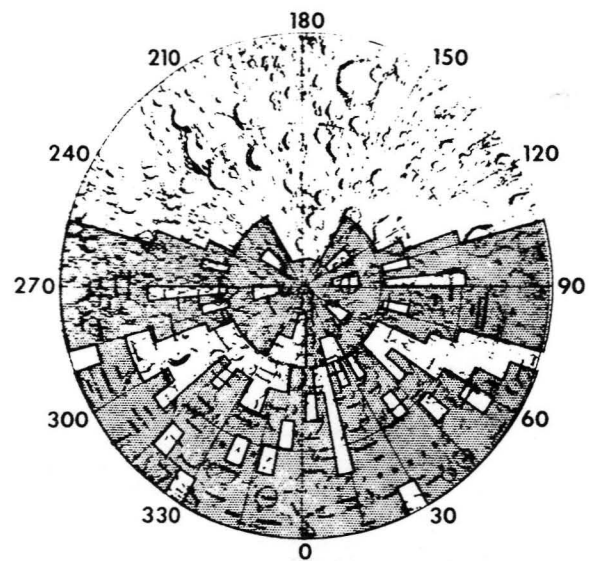
TABLE 1.1  
DATA SOURCES

Data type	Number of points	Error (km)
Inertial		
Laser altimeter		
Apollo 15	919	0.30
Apollo 16	1 353	0.30
Apollo 17	3 359	0.30
Orbital photogrammetry	12 432	0.30
Landmark tracking	31	0.50
Noninertial		
Earth-based photogrammetry		
Hopmann	1 049	0.80
Mills and Sudbury	906	0.40 <sup>a</sup>
Arthur and Bates	1 356	0.90 <sup>a</sup>
Limb profile	483	0.38

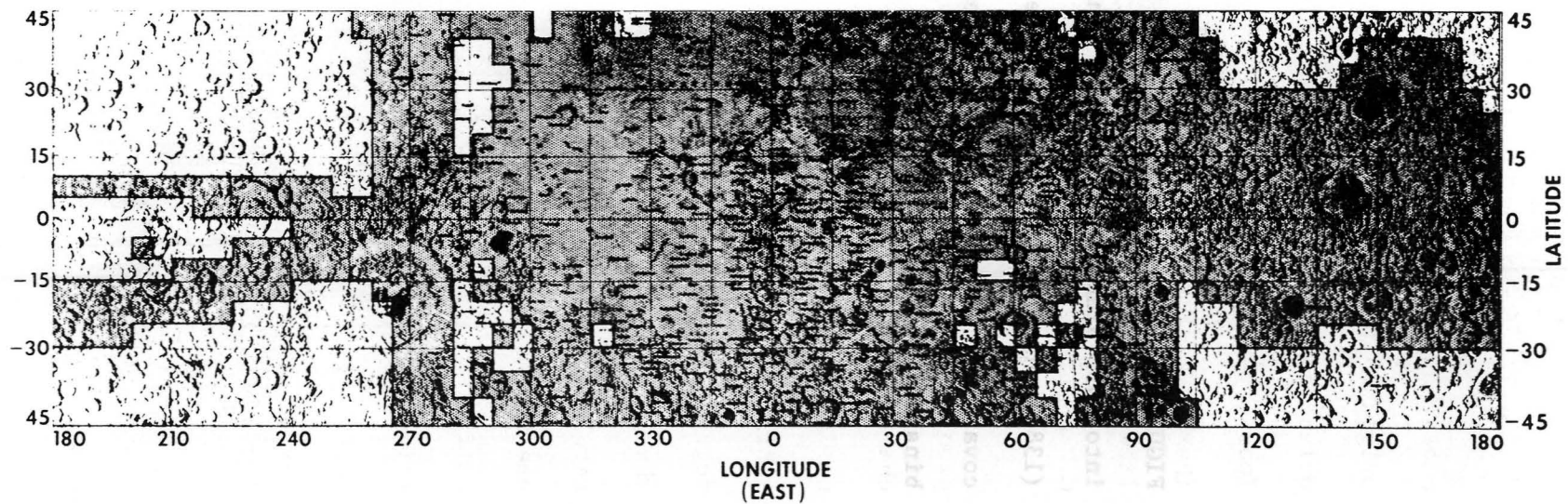
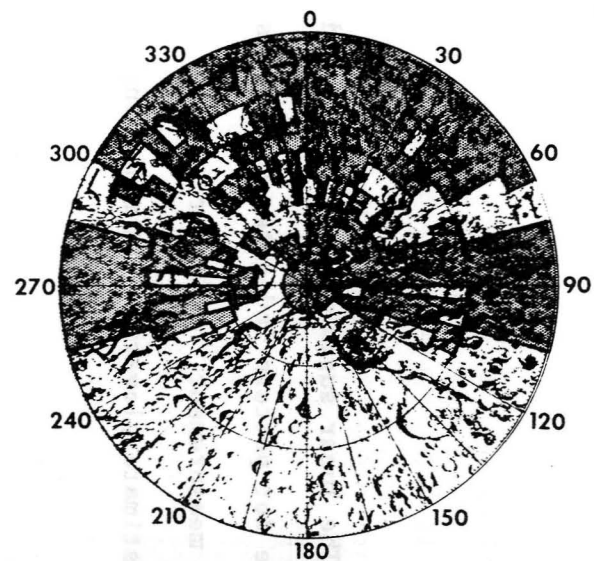
<sup>a</sup> Errors are estimated for each point separately. Number quoted is the mean of the individual errors.

FIGURE 1.1 - Data Distribution. The lunar surface is shown divided into 2592 bins, each  $5^\circ \times 5^\circ$ . The dot pattern indicates those bins (1380) which contain at least one measurement. A linear autocovariance analysis was used to estimate elevations in remaining bins.

NORTH POLAR REGION



SOUTH POLAR REGION





In addition to the spherical coordinates  $(R, \theta, \varphi)$ , we will have occasion to use a Cartesian coordinate system  $(X_1, X_2, X_3)$ , with its origin at the lunar center of mass. This system is right-handed and oriented such that the  $X_1$  axis lies along the mean Earth-Moon line (positive toward Earth), the  $X_2$  axis points east along the orbit (positive away from direction of orbital motion), and the  $X_3$  axis lies along the rotation axis (positive toward north).

### C. ANALYSIS

Given the data discussed in the previous section, we now have the problem of how best to estimate a set of harmonic coefficients which characterize the shape of the lunar surface. We will be interested not only in the complete ensemble of harmonics and the global lunar configuration which they represent, but also in some of the low-degree harmonics, considered separately. Therefore, it is imperative that we obtain harmonic coefficient estimates which not only accurately represent the data, but are also optimally uncorrelated with one another, consistent with the uneven data distribution. An intimately related problem is that we desire to avoid unreasonable values for our harmonic model in regions containing no direct measurements. We will now formulate this problem more rigorously and present our solution thereto.

Given a collection of topographic data  $F$ , with standard deviation  $\sigma$ , distributed on a sphere

$$R(\theta_i, \varphi_i) = F_i \pm \sigma_i \quad (1.1)$$

we desire optimally uncorrelated estimates of the harmonic coefficients  $H_{nm}$  through degree and order N.

Our basic model is of the form

$$R(\theta, \varphi) = R_o \left[ 1 + \sum_{n=1}^{12} \sum_{m=0}^n H_{nm}^T \Lambda_{nm}(\theta, \varphi) \right] \quad (1.2)$$

where

$$H_{nm} = \begin{bmatrix} H_{nm1} \\ H_{nm2} \end{bmatrix} = \begin{bmatrix} \bar{C}_{nm} \\ \bar{S}_{nm} \end{bmatrix}$$

$$\Lambda_{nm}(\theta, \varphi) = \bar{P}_{nm}[\sin(\theta)] \begin{bmatrix} \cos(m\varphi) \\ \sin(m\varphi) \end{bmatrix}$$

are the normalized harmonic coefficients and surface spherical harmonic functions, respectively. These functions are defined and discussed at some length in Appendix A.

A 12-degree model was chosen since it is capable of resolving the major lunar basins. This facilitates comparison with recent gravity studies. A higher-degree model was not utilized because of the adverse effect of data gaps. For the ensemble of observations, (1.2) can be written as

$$F_i = (\partial F_i / \partial Z_j) Z_j = A_{ij} Z_j \quad (1.3)$$

where  $Z_j$  is the vector of  $H_{nm}$ . In this notation, the weighted least-squares estimator is (see, e.g., Lawson and Hanson, 1974)

$$\hat{Z} = [A^T B A]^{-1} [A^T B F] \quad (1.4)$$

where the weighting matrix B is the inverse of the data noise

covariance matrix (assumed, in this analysis, to be diagonal).

To obtain uncorrelated estimates of the parameters  $Z_j$ , we must diagonalize the solution covariance matrix

$$E(ZZ^T) = [A^TBA]^{-1} \quad (1.5)$$

where  $E(\cdot)$  is the expectation operator. Since we are assuming that  $B$  is diagonal, the problem thus reduces to the diagonalization of

$$[A^TA]_{ij} = \int_0^{2\pi} \int_{-1}^1 \Lambda_i \Lambda_j d\mu d\varphi \quad (1.6)$$

where  $\mu = \sin(\theta)$ . The problem then is the optimal approximation of an integral by a finite sum. If we had data of uniform accuracy, evenly distributed over the sphere, the evaluation of this integral could be performed by any standard quadrature formula. However, the very uneven distribution of the data necessitates further analysis (Carlson and Helmsen, 1969).

The approach we have taken is to determine the weighted mean and standard deviation of all the data within each of 2592  $5^\circ \times 5^\circ$  bins. Actually, only 1380 of the bins, representing 64.7% of the lunar surface, contain data (see Fig. 1.1). In the remaining bins, we have used a linear autocovariance technique (see, e.g., Kaula, 1967; Heiskanen and Moritz, 1967) to estimate the most probable elevations and associated errors, consistent with the known statistical characteristics of the available data. Chapman and Pollack (1975) have applied a linear cross-covariance predictor to a very similar problem in terrestrial heat flow measurements.

In much of what follows, it will be useful to regard the surface of the Moon as a realization of a homogeneous stochastic process on a sphere (see Appendix C). A process is said to be homogeneous if its first and second moments are invariant under the group of rotations of the sphere. This is equivalent (Roy, 1973) to stationarity, i.e., constancy of the mean  $E[F(\theta, \varphi)]$ , and isotropy of the covariance function

$$C(\gamma) = E[F(\Omega)F(\Omega + \gamma)] \quad (1.7)$$

where  $\Omega = (\theta, \varphi)$ , i.e.  $C(\gamma)$  depends only on the angular separation  $\gamma$  between the points  $(\theta, \varphi)$  and  $(\theta + \Delta\theta, \varphi + \Delta\varphi)$ . This separation is given by

$$\begin{aligned} 2 \cos(\gamma) &= (\cos(\Delta\varphi) + 1) \cos(\Delta\theta) \\ &+ (\cos(\Delta\varphi) - 1) \cos(\Sigma\theta) \end{aligned} \quad (1.8)$$

The predicted radii  $\hat{R}$  and associated variances  $\hat{\sigma}^2$  are calculated from the covariance function and the known radii  $F_i$  as follows:

$$\begin{aligned} \hat{R} &= Q^T S^{-1} F \\ \hat{\sigma}^2 &= C(0) - Q^T S^{-1} Q \end{aligned} \quad (1.9)$$

where

$$S = E(F^T F) \quad \text{and} \quad Q = E(F^T R)$$

the known-known and known-unknown covariance matrices, respectively, are obtained from  $C(\gamma)$ .

In a further effort to compensate for the extremely uneven distribution of the data, a lower bound of 0.05 km was imposed on the bin standard deviation. This measure prevents those regions in which the data are most densely concentrated from completely

dominating the solution, at the expense of other regions. This censoring affected 220 bins, representing 12.9% of the lunar surface.

Finally, the weighted least-squares estimate of the harmonic coefficients was obtained by applying (1.4) to the averaged data, augmented by the predicted radii in the unsurveyed areas. The weighting of each point was proportional to the area of its bin and inversely proportional to the variance of the measurement or prediction:

$$B_{ij} = 2 \sin(\Delta\theta/2) \cos(\theta_i) \Delta\varphi \delta_{ij} / \sigma_i^2 \quad (1.10)$$

The estimates of the normalized harmonic coefficients and their formal uncertainties are presented in Table 1.2.

Solutions were also obtained in which the predicted elevations were weakly weighted ( $\sigma = 5, 10$  km). These solutions were characterized by unrealistically large estimates for the high-degree coefficients and large height excursions in the regions containing no data.

#### D. RESULTS

Figure 1.2 shows a comparison between raw laser altimeter data and the harmonic model evaluated along the ground tracks of representative orbits of Apollo missions 15, 16, and 17. The amount of high-frequency information contained in the data is indicated, as well as the fidelity of the harmonic model to the global and regional shape of the Moon. The variance of the 21 888 unaveraged data is  $4.22 \text{ km}^2$ , whereas the model variance is

TABLE 1.2  
NORMALIZED LUNAR TOPOGRAPHY HARMONICS ( $\times 10^6$ )

n	m	$\bar{C}_{nm}$	$\bar{S}_{nm}$	$\sigma(\bar{C}_{nm})$	$\sigma(\bar{S}_{nm})$
1	0	-212.3		25.7	
1	1	-605.8	147.4	17.5	13.6
2	0	-135.9		22.1	
2	1	-149.8	-23.6	26.5	19.3
2	2	11.5	-167.1	11.5	14.5
3	0	62.2		20.5	
3	1	102.1	-53.1	28.0	18.2
3	2	47.2	-51.9	18.1	22.7
3	3	250.1	-28.9	11.1	11.4
4	0	104.2		20.5	
4	1	30.9	-57.3	26.7	17.0
4	2	-115.5	25.6	20.7	24.2
4	3	-13.1	41.0	18.0	18.5
4	4	-92.1	-20.9	9.6	10.1
5	0	0.6		20.3	
5	1	-50.6	79.2	25.4	16.2
5	2	5.5	-35.9	21.4	23.5
5	3	-48.2	-51.7	20.3	21.2
5	4	-2.0	6.6	16.0	16.0
5	5	86.9	10.5	8.2	8.7
6	0	-56.4		19.8	
6	1	-27.6	44.5	24.6	15.4
6	2	-3.5	-15.3	21.1	21.8
6	3	-1.9	-32.2	21.0	22.0
6	4	-62.6	44.2	19.3	18.5
6	5	-70.5	62.0	13.8	14.5
6	6	-30.9	-54.6	7.3	7.3

TABLE 1.2 (Cont'd)

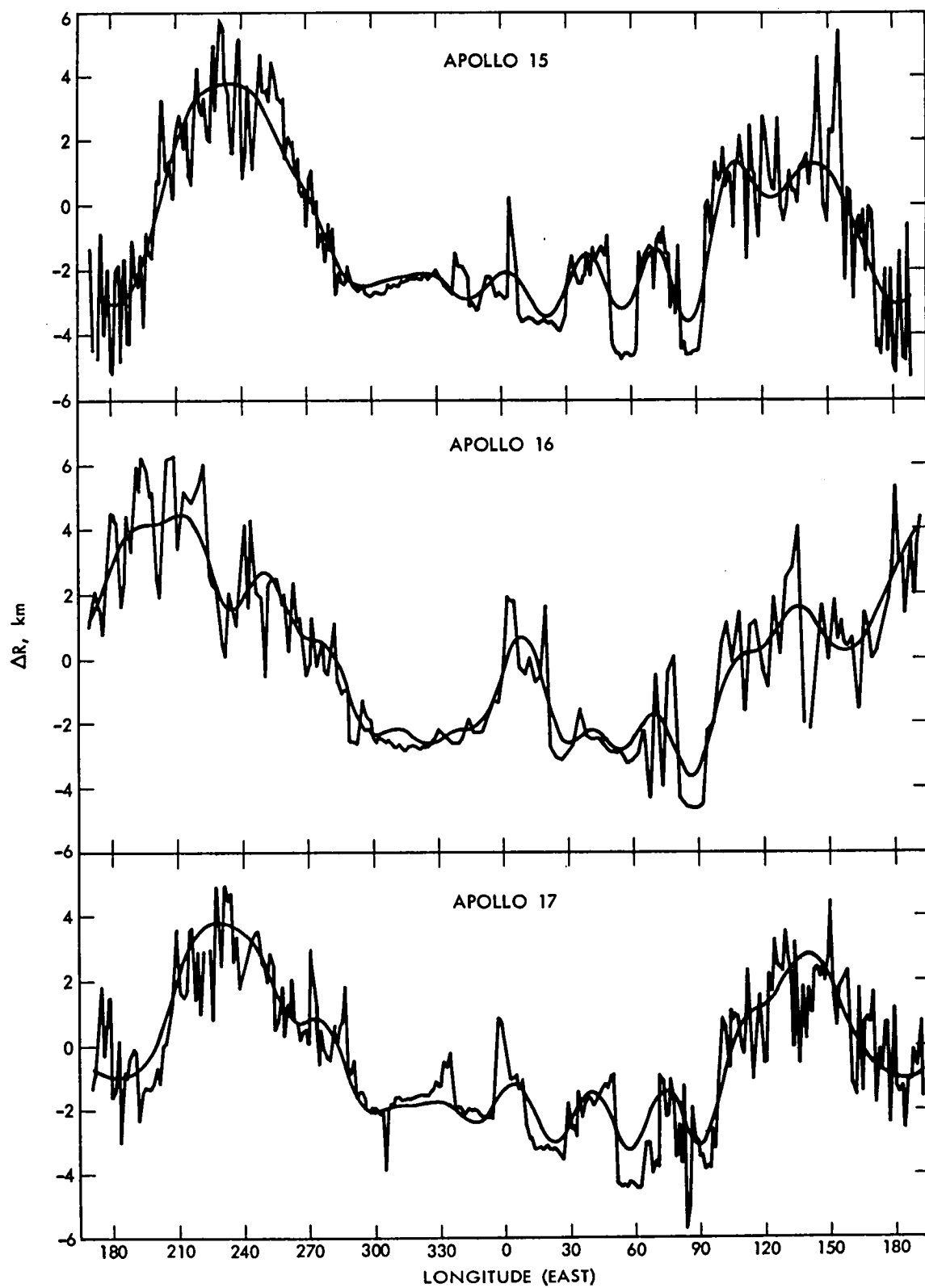
n	m	$\bar{C}_{nm}$	$\bar{S}_{nm}$	$\sigma(\bar{C}_{nm})$	$\sigma(\bar{S}_{nm})$
7	0	-60.4		18.5	
7	1	219.4	-18.2	22.8	15.2
7	2	107.1	23.6	20.0	20.2
7	3	-76.9	12.7	20.3	21.4
7	4	-14.9	-14.0	20.1	19.3
7	5	107.5	20.2	16.4	16.8
7	6	54.0	2.2	12.2	12.3
7	7	4.1	-29.2	6.2	6.2
8	0	85.6		18.0	
8	1	-0.4	35.7	21.2	14.3
8	2	-134.3	-54.6	18.9	19.2
8	3	-23.8	-8.2	19.0	20.0
8	4	69.9	-64.9	19.8	19.6
8	5	45.6	-0.1	17.2	17.6
8	6	-156.3	0.8	14.4	14.3
8	7	-12.5	52.5	10.1	10.3
8	8	31.0	-41.5	5.1	5.1
9	0	9.8		16.9	
9	1	64.4	-28.0	19.7	13.5
9	2	13.2	56.6	17.6	16.9
9	3	-63.0	3.8	17.6	18.3
9	4	-67.3	13.9	18.2	17.9
9	5	53.4	115.6	17.4	17.7
9	6	39.5	-36.0	14.8	15.0
9	7	25.1	-14.2	12.3	12.1
9	8	48.0	-45.7	8.5	8.0
9	9	-1.2	16.8	4.0	4.0
10	0	95.0		14.2	
10	1	33.0	12.3	15.9	12.5
10	2	-55.2	6.9	14.7	14.0
10	3	-1.6	-31.3	14.9	14.7
10	4	34.5	-32.8	15.2	15.1
10	5	25.8	34.2	14.8	14.8
10	6	-75.5	-44.3	13.4	14.1
10	7	2.4	48.5	11.4	11.3
10	8	16.8	-6.0	9.4	9.5
10	9	8.5	59.6	6.5	6.4
10	10	54.9	-27.3	3.6	3.6

TABLE 1.2 (Cont'd)

n	m	$\bar{C}_{nm}$	$\bar{S}_{nm}$	$\sigma(\bar{C}_{nm})$	$\sigma(\bar{S}_{nm})$
11	0	41.2		11.9	
11	1	-99.0	-52.6	13.4	10.8
11	2	35.3	-33.6	11.4	12.2
11	3	-69.0	-98.1	12.0	12.3
11	4	-30.9	63.7	11.7	12.0
11	5	57.5	-71.8	11.6	12.0
11	6	-29.2	-63.6	10.8	11.1
11	7	43.4	-38.2	9.4	9.5
11	8	35.0	-91.5	7.5	7.2
11	9	11.9	53.6	6.5	6.4
11	10	8.6	-31.7	4.1	4.2
11	11	-17.1	-54.2	3.0	3.0
12	0	-38.8		9.5	
12	1	-33.6	8.3	10.2	8.8
12	2	15.2	2.1	9.5	9.4
12	3	-109.2	29.3	9.2	9.4
12	4	13.9	20.5	9.4	9.1
12	5	-15.8	0.6	8.8	9.1
12	6	-11.1	-10.3	8.6	9.0
12	7	9.2	9.6	8.0	8.0
12	8	-76.3	40.0	6.9	7.1
12	9	32.9	33.6	5.6	5.8
12	10	-20.0	-70.9	5.0	5.0
12	11	43.0	15.8	3.6	3.6
12	12	-35.1	-41.7	2.6	2.7



FIGURE 1.2 - Comparison of laser data and harmonic model. Elevations relative to 1738.0 km sphere. Indicates amount of high frequency information in data and general fidelity of model to global and regional scale features.



$$\begin{aligned}
C(0) &= R_o^2 \sum_{n=1}^{12} \sum_{m=0}^n H_{nm}^T H_{nm} \\
&= 3.08 \text{ km}^2
\end{aligned} \tag{1.11}$$

Figures 1.3 and 1.4 are maps of lunar topography, as given by our model, and the associated formal uncertainties, respectively. These are derived from the relationships (Graybill, 1961)

$$\begin{aligned}
R(\theta, \varphi) &= A^T(\theta, \varphi) Z \\
\sigma^2(\theta, \varphi) &= A^T(\theta, \varphi) [A^T B A]^{-1} A(\theta, \varphi)
\end{aligned} \tag{1.12}$$

The error map reflects the distribution of the data, showing quite clearly the regions where we have no direct data. Since the model duplicates 73.0% of the original data variance, this computed error map should be a good first-order approximation to the actual error distribution. The topographic map, with heights relative to the lunar mean radius, resolves most major features within the areas of data coverage. This was a major objective in the construction of the model and permits comparison with equivalent-resolution gravity models for the purpose of determining the lunar internal density distribution.

Dimensionless degree variances  $V(H;n)$  of lunar topography and the associated error variances  $W(H;n)$  are listed in Table 1.3. These variances are given by:

FIGURE 1.3 - Lunar topography. Twelfth degree model. Elevations relative to 1737.53 km mean sphere. Contour interval is 1 km (solid line). Selected  $\frac{1}{2}$  km contours indicated (dashed line).

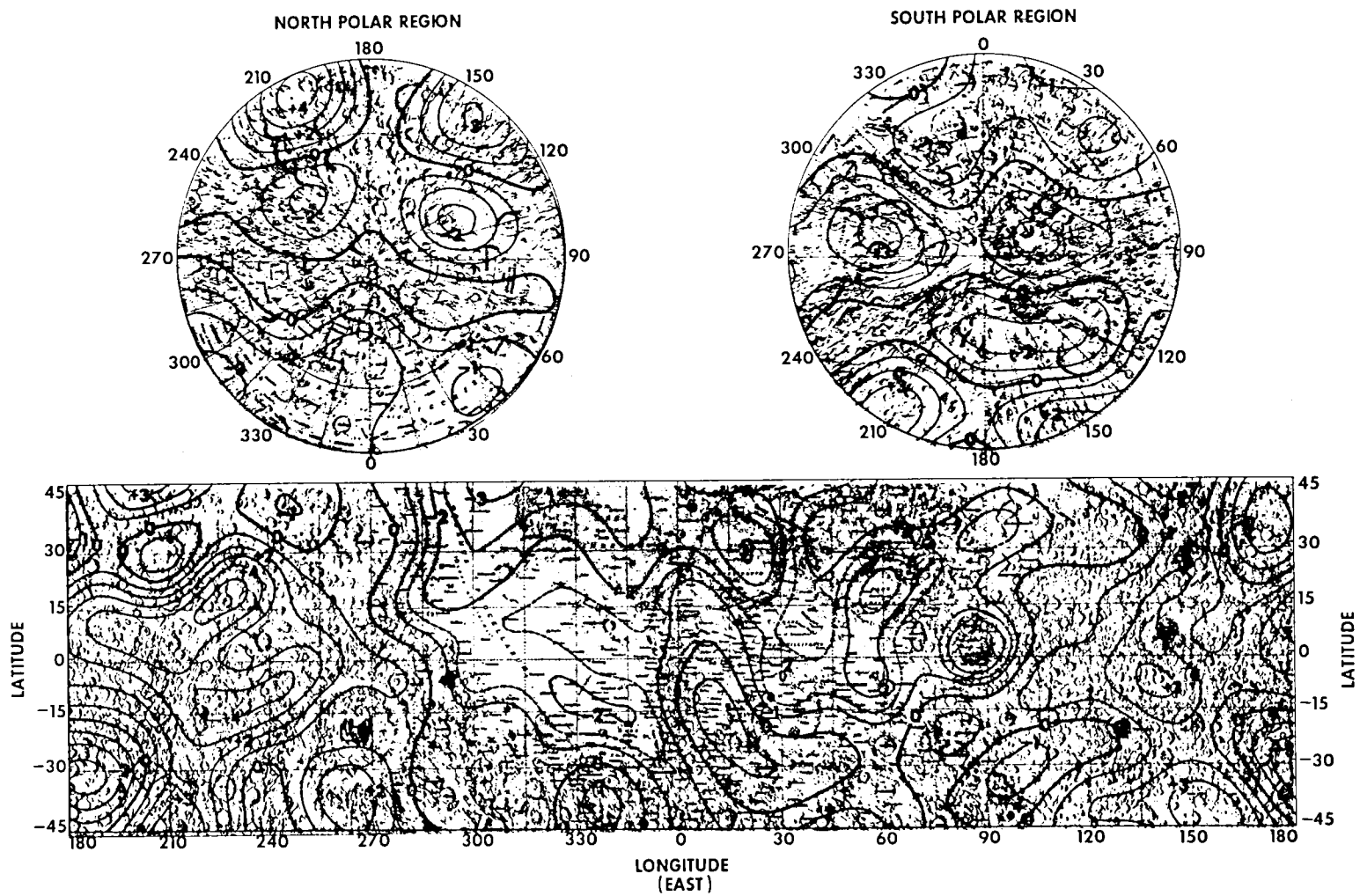


FIGURE 1.4 - Lunar topography error. Formal standard error computed from equation (1.12). Actual error can be somewhat larger. Contour interval is 0.2 km.

NORTH POLAR REGION

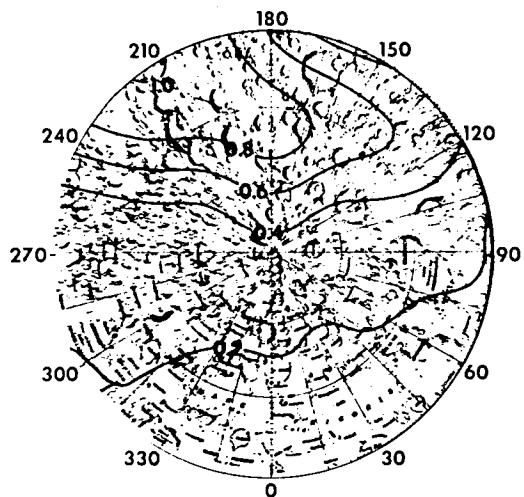


TABLE 1.3

LUNAR TOPOGRAPHY AND ERROR VARIANCES ( $\times 10^8$ )

Degree n	Topography $V(H;n)$	Error $W(H;n)$
1	43.38	0.12
2	6.95	0.19
3	8.54	0.26
4	3.99	0.33
5	2.29	0.38
6	2.58	0.43
7	8.64	0.45
8	7.15	0.45
9	4.17	0.43
10	3.62	0.33
11	6.97	0.23
12	3.71	0.15



$$\begin{aligned}
V(H;n) &= \sum_{m=0}^n H_{nm}^T H_{nm} \\
W(H;n) &= \sum_{m=0}^n \sigma^T(H_{nm}) \sigma(H_{nm})
\end{aligned} \tag{1.13}$$

where  $\sigma^2(H_{nm})$ , the variance of the error in  $H_{nm}$ , is obtained from the solution covariance matrix  $[A^TBA]^{-1}$ . We note that the topographic degree variances decrease in magnitude with increasing harmonic degree approximately as

$$V(H;n) \doteq \frac{V(H,0)}{(n)(n+1)} \tag{1.14}$$

We will discuss the significance of this spectral behavior at considerable length in Chapter IV. We also note that in the case of uniformly accurate data, i.e.,  $\sigma[R(\theta,\varphi)] = \sigma_o$ , the degree error variances are (Heiskanen and Moritz, 1967)

$$W(H;n) = \frac{2n+1}{4\pi} \left( \frac{\sigma_o}{R_o} \right)^2 \tag{1.15}$$

The small departures of our error variances from this simple form are due to the irregular data distribution.

The observed gravity of a planet may be considered as the sum of contributions due to internal lateral density variations and surface topography. The topography of a planet characterized by harmonics  $H_{nm}$ , gives rise to gravitational potential perturbations  $\Delta G_{nm}$ , where (MacRobert, 1967)

$$\left(\frac{2n+1}{3}\right) \bar{\rho} \Delta G_{nm} = \rho(R_o) H_{nm} \quad (1.16)$$

and  $\rho(R_o)$  and  $\bar{\rho}$  are the surface and mean mass densities, respectively, of the planet. The difference between the observed gravity and the topographic correction, known as the Bouguer anomaly, is thus a measure of the extent of lateral density variation.

Figure 1.5 is a map of lunar Bouguer gravity, evaluated at an elevation of 100 km above the mean lunar radius. This is calculated as the radial component of the gradient of the 12th degree Bouguer anomaly potential

$$\Delta \Phi_B(R, \theta, \varphi) = \frac{GM}{R_o} \sum_{n=1}^{12} \left(\frac{R_o}{R}\right)^{n+1} \sum_{m=0}^n B_{nm} \Lambda_{nm}(\theta, \varphi) \quad (1.17)$$

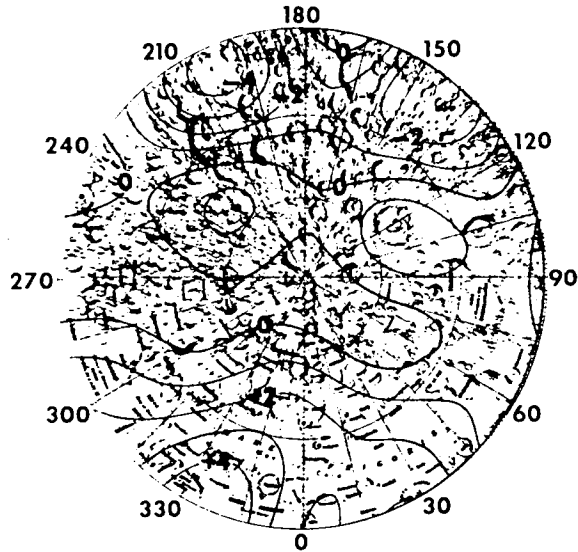
with

$$B_{nm} = G_{nm} - \Delta G_{nm}$$

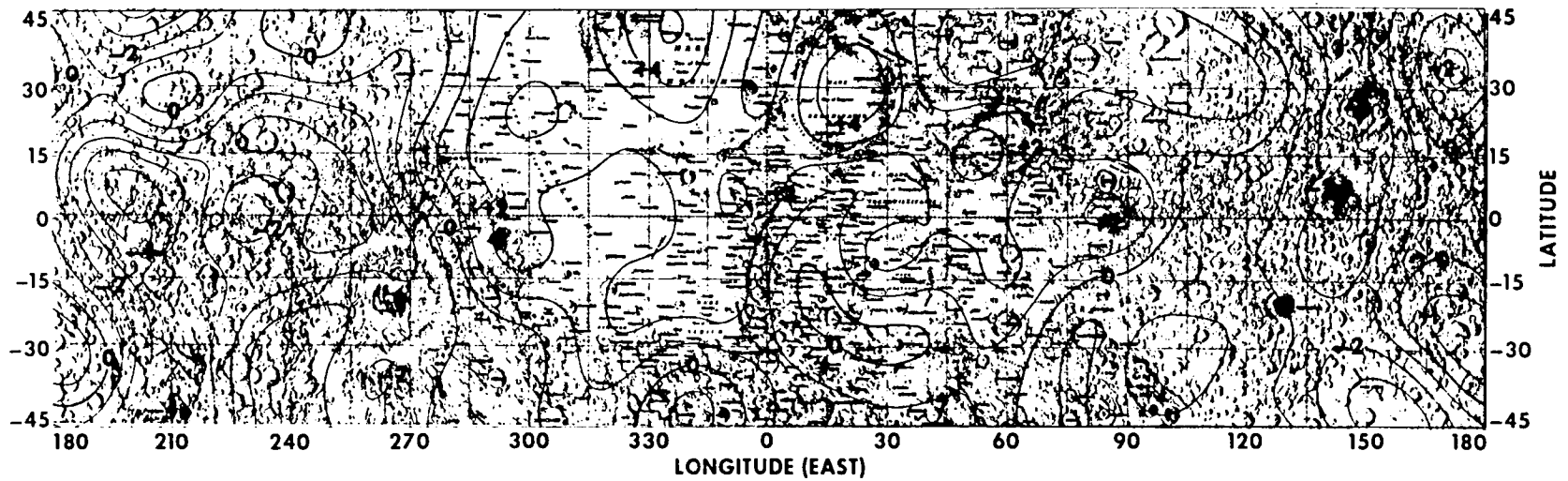
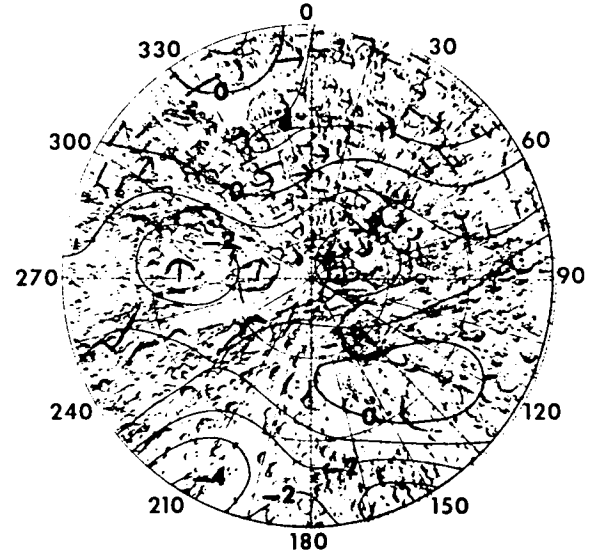
where  $G$  is the gravitational constant,  $M$  is the planetary mass,  $G_{nm}$  is a harmonic coefficient of the observed gravitational field (Ferrari, 1977), and we have assumed a surface density  $\rho(R_o) = 2.7 \text{ g cm}^{-3}$ . We find that the low-degree harmonics of the gravitational field are determined primarily by surface height variations and only secondarily by lateral density variations. The most striking feature of this map is the association of large positive anomalies with the mascons (Muller and Sjogren, 1968). It is also interesting to note that large regions of the farside highlands are associated with strong negative anomalies. This map, along with other data types such as librational and seismic observations, can be used to infer

FIGURE 1.5 - Lunar Bouguer gravity anomaly. Twelfth degree model.  
Evaluated 100 km above mean sphere. Contour interval 100 mGal =  
0.1 cm sec<sup>-2</sup>. Free-air gravity from Ferrari (1977). Assumed crustal  
density is 2.7 gm cm<sup>-3</sup>.

NORTH POLAR REGION



SOUTH POLAR REGION



lunar crustal and upper mantle structure, an effort which we discuss in the next chapter (see also, Bills and Ferrari, 1977). In that analysis a mean crustal thickness of 70 km is estimated by matching the gravimetrically derived local crustal thickness with the seismic results (Toksöz et al., 1974) from Mare Cognitum.

We now turn our attention to the harmonics of degrees 0, 1, and 2. These represent the mean radius, center of figure displacement, and triaxial figure, respectively.

The estimated lunar radius is  $(1737.53 \pm 0.03)$  km. This, in conjunction with estimates of  $GM = (4902.796 \pm 0.003) \text{ km}^3 \text{ sec}^{-2}$  (Sinclair et al., 1976) and  $G = (667.32 \pm 0.31 \times 10^{-25}) \text{ km}^3 \text{ g}^{-1} \text{ sec}^{-2}$  (Heyl and Chrzanowski, 1942), yields an estimate for the mean density of  $\bar{\rho} = (3.3437 \pm 0.0016) \text{ g cm}^{-3}$ . Most of this error comes from the error in G. The mean density, in conjunction with the mean inertial moment, places important constraints on models of lunar internal composition and structure (Gast and Giuli, 1972; Bills and Ferrari, 1977).

We now consider the first-degree terms in the topography. They represent a displacement of the center of figure (C.F.) from the center of mass (C.M.). In terms of rectangular coordinates, and un-normalized harmonics, the location of the C.F. is

$$\begin{bmatrix} \Delta X_1 \\ \Delta X_2 \\ \Delta X_3 \end{bmatrix} = R_0 \begin{bmatrix} C_{1,1} \\ S_{1,1} \\ C_{1,0} \end{bmatrix} = \begin{bmatrix} -1.823 \pm 0.053 \\ -0.444 \pm 0.041 \\ -0.639 \pm 0.077 \end{bmatrix} \text{ km} \quad (1.18)$$

or in terms of spherical coordinates,

$$\begin{bmatrix} R \\ \theta \\ \varphi \end{bmatrix} = \begin{bmatrix} (1.982 \pm 0.057) \text{ km} \\ (18^\circ.8 \pm 2^\circ.1) \text{ S} \\ (193^\circ.7 \pm 1^\circ.1) \text{ E} \end{bmatrix}$$

where, as before, the origin is at the C.M.

This offset, by definition, implies a departure from spherical symmetry in the internal density distribution. Attempts have been made to explain this asymmetry in terms of two-layered models, with either an offset between the centers of the spheres comprising the model (Ransford and Sjogren, 1972; Kaula et al., 1972) or an outer layer of randomly varying thickness (Kobrick, 1976). Large-scale internal convection (Lingenfelter and Schubert, 1973) and asymmetric bombardment (Wood, 1973) have been suggested as possible mechanisms for the preferential thinning of the crust of the earthward hemisphere and concomitant thickening in the opposite hemisphere.

We now consider the shape and orientation of the triaxial figure represented by the second-degree harmonics. The principal axes of this figure are

$$\begin{aligned} X'_1 &= (1738.43 \text{ km}, 13^\circ.58 \text{ S}, 38^\circ.40 \text{ E}) \\ X'_2 &= (1737.50 \text{ km}, 32^\circ.70 \text{ N}, 119^\circ.48 \text{ E}) \\ X'_3 &= (1736.66 \text{ km}, 53^\circ.91 \text{ N}, 327^\circ.76 \text{ E}) \end{aligned} \tag{1.19}$$

This misalignment between these axes and the principal inertial axes implies that, if all lateral density variation occurs as undulations on the crust-mantle interface, the principal axes of the triaxial

mantle must be skewed in the opposite direction. According to this simplified model, the region of minimum crustal thickness is in southern Procellarum. Many deep-focus moonquakes occur along two great circle arcs which intersect in this same area (Lammlein et al., 1974; Lammlein, 1977). Thus, the stresses induced by near surface mass anomalies may control the release of seismic energy at depth.

## REFERENCES

- Arthur, D.W.G., and Bates, P. (1968). The Tucson selenodetic triangulation. Commun. Lunar Planet. Lab. 7, 313-361.
- Baldwin, R.B. (1963). The Measure of the Moon. Univ. of Chicago Press, Chicago.
- Bills, B.G., and Ferrari, A.J. (1977). A lunar density model consistent with topographic, gravitational, librational and seismic data. J. Geophys. Res. 82 1306-1314.
- Brown, W.E., Jr., Adams, G.F., Eggleton, R.E., Jackson, P., Jordan, R., Kobrick, M., Peeples, W.J., Phillips, R.J., Porcello, L.J., Schaber, G., Sill, W.R., Thompson, T.W., Ward, S.H., and Zelenka, J.S. (1974). Elevation profiles of the Moon. Proc. Fifth Lunar Sci. Conf. 3, 3037-3048.
- Carlson, A.E., and Helmsen, M. (1969). Validity of topography represented by truncated series of surface harmonics. Icarus 10, 57-65.
- Chapman, D.S., and Pollack, H.N. (1975). Global heat flow: A new look. Earth Planet. Sci. Lett. 28, 23-31.
- Chuikova, N.A. (1976). The geometrical figure of the Moon represented in the form of an expansion in spherical and sampling functions. Sov. Astron. 19, 764-771.
- Ferrari, A.J. (1977). Lunar gravity: A harmonic analysis. J. Geophys. Res. 82, 3065-3084.



- Gast, P.W., and Giuli, R.T. (1972). Density of the lunar interior. Earth Planet. Sci. Lett. 16, 299-305.
- Goudas, C.L. (1971). Geometrical and dynamical properties of the Moon. In Physics and Astronomy of the Moon (Z. Kopal, Ed.), pp. 101-152. Academic Press, New York.
- Graybill, F.A. (1961). An Introduction to Linear Statistical Models, Vol. I. McGraw-Hill, New York.
- Heiskanen, W.A., and Moritz, H. (1967). Physical Geodesy. Freeman, San Francisco.
- Heyl, P.R., and Chrzanowski, P. (1942). A new determination of the constant of gravitation. J. Res. Nat. Bur. Standards 29, 1-31.
- Hopmann, J. (1967). General-Katalog absoluter Höhen auf dem Mond. Ann. Univ. Sternw. Wien 26, 7 Heft.
- Jones, R.H. (1963). Stochastic processes on a sphere. Ann. Math. Statist. 34, 213-218.
- Jones, R.L. (1973). Estimates of the Moon's geometry using lunar orbiter imagery and Apollo laser altimeter data. NASA TR R-407.
- Kaula, W.M. (1967). Theory of statistical analysis of data distribution over a sphere. Rev. Geophys. 5, 83-107.
- Kaula, W.M., Lingenfelter, R.E., Schubert, G. Sjogren, W.L., and Wollenhaupt, W.R. (1972). Analysis and interpretation of lunar laser altimetry. Proc. Third Lunar Sci. Conf. 3, 2189-2204.
- Kaula, W.M., Lingenfelter, R.E., Schubert, G., Sjogren, W.L. and Wollenhaupt, W.R. (1973). Lunar topography from Apollo 15 and 16 laser altimetry. Proc. Fourth Lunar Sci. Conf. 3, 2811-2819.

- Kaula, W.M., Lingenfelter, R.E., Schubert, G., Sjogren, W.L., and Wollenhaupt, W.R. (1974). Apollo laser altimetry and inference as to lunar structure. Proc. Fifth Lunar Sci. Conf. 3, 3049-3058.
- Kobrick, M. (1976). Random processes as a cause of the lunar asymmetry. The Moon 15, 83-89.
- Kopal, Z., and Carder, R.W. (1974). Mapping of the Moon. Reidel, Dordrecht.
- Lammlein, D.R., Latham, G.V., Dorman, J., Nakamura, Y., and Ewing, M. (1974). Lunar seismicity, structure and tectonics. Rev. Geophys. Space Phys. 12, 1-21.
- Lammlein, D.R. (1977). Lunar seismicity and tectonics, Phys. Earth Planet. Int. 14, 224-273.
- Lawson, C.L., and Hanson, R.J. (1974). Solving Least Squares Problems. Prentice-Hall, Englewood Cliffs, N.J.
- Lingenfelter, R.E., and Schubert, G., (1973). Evidence for convection in planetary interiors from first-order topography. The Moon 7, 172-180.
- MacRobert, T.M. (1967). Spherical Harmonics. Pergamon Press, New York.
- Mills, G.A., and Sudbury, P.V. (1968). Absolute coordinates of lunar features. Icarus 9, 538-561.
- Muller, P.M., and Sjogren, W.L. (1968). Mascons: Lunar mass concentrations. Science 161, 680-684.
- Ransford, G., and Sjogren, W.L. (1972). Moon model - An offset core. Nature 238, 260-262.

- Roberson, F.I., and Kaula, W.M. (1972). Apollo 15 laser altimeter.  
In Apollo 15 Preliminary Science Report, pp. 25:48-50. NASA  
SP-239.
- Rodionov, B.N., Isavnina, I.V., Avdeev, Yu.F., Blagov, V.D., Dorofeev,  
A.S., Dunaev, B.S., Ziman, Ya.L., Kiselev, V.V., Krasikov, V.A.,  
Lebedev, O.N., Mikhailovskii, A.B., Tishchenko, A.P., Nepoklonov,  
B.V., Samoilov, V.K., Truskov, F.M., Chesnokov, Yu.M., and  
Fivenskiĭ, Yu.I. (1971). New data on the Moon's figure and  
relief based on results from the reduction of Zond-6 photographs.  
Cosmic Res. 9, 410-417.
- Roy, R. (1973). Estimation of the covariance function of a homo-  
geneous process on the sphere. Ann. Statist. 1, 780-785.
- Schirmerman, L.A., Cannel, W.D., and Meyer, D. (1973). Relationship of  
spacecraft and earth-based selenodetic systems. Paper presented  
at the 15th General Assembly of the International Astronomical  
Union, Sidney, Australia.
- Sinclair, W.S., Sjogren, W.L., Williams, J.G., and Ferrari, A.J. (1976).  
The lunar moment of inertia derived from combined doppler  
and laser ranging data. In Lunar Science VII, p. 817. Lunar  
Science Institute, Houston.
- Toksöz, M.N., Dainty, A.M., Solomon, S.C., and Anderson, K.R. (1974).  
Structure of the Moon. Rev. Geophys. Space Phys. 12, 539-567.
- Van Flandern, T.C. (1970). Some notes on the use of the Watts limb-  
correction charts. Astron. J. 75, 744-746.

- Watts, C.B. (1963). The marginal zone of the Moon. Astron. Papers  
Amer. Ephemer. Naut. Almanac 17.  
~~~~~
- Wollenhaupt, W.R., Osburn, R.K., and Ransford, G.A. (1972). Comments  
on the figure of the Moon from Apollo landmark tracking.  
The Moon 5, 149-157.  
~
- Wollenhaupt, W.R., and Sjogren, W.L. (1972). Apollo 16 laser altimeter.  
In Apollo 16 Preliminary Science Report, pp. 30:1-5. NASA SP-315.
- Wollenhaupt, W.R., Sjogren, W.L., Lingrenfelter, R.E., Schubert, G.,  
and Kaula, W.M. (1974). Apollo 17 laser altimeter. In Apollo 17  
Preliminary Science Report, pp. 33 : 41 - 42.. NASA SP-330.
- Wood, J.A. (1973). Bombardment as a cause of the lunar asymmetry.  
The Moon 8, 73-103  
~
- Zisk, S.H. (1972). Lunar topography: First radar-interferometer  
measurements of the Alphonsus-Ptolemaeus-Arzachel region.  
Science 178, 977-980.  
~~~~~

## II. A LUNAR DENSITY MODEL

### A. INTRODUCTION

Lunar interior models of increasing complexity are derived from topographic, gravitational, librational, and seismic data. A series of models, rather than only the final one, is presented in an effort to demonstrate the unique contribution of each data type and its effect on determining model parameters for the lunar density structure.

The various data types and their errors are discussed, and these data are cast into a form most convenient for internal model determination. The basic theory for this analysis is developed, and a series of lunar interior models are derived from the different data. Discussions are presented at each level of modeling, showing which data are satisfied and presenting the geophysical significance of that stage of the model development. Ultimately, a six-layered model is determined which satisfies all the data. The innovative aspects of this investigation are discussed in light of previous work, and the compositional implications of this lunar interior model are analyzed.

### B. DATA

The topography of the Moon will be represented in this analysis by the harmonic model developed in the preceding chapter (see also Bills and Ferrari, 1977). However, in the present chapter, it will be more convenient to use the un-normalized harmonics (see Appendix A).

As a representation of lunar gravity, we will use Ferrari's (1975) model truncated to degree twelve for consistency with the topography model.

The physical librations of the Moon are dependent upon both the low-degree gravity harmonics and the parameters  $(\alpha, \beta, \gamma)$ , which are defined in terms of the principal inertial moments  $A < B < C$  as

$$\alpha = \frac{C - B}{A} \quad \beta = \frac{C - A}{B} \quad \gamma = \frac{B - A}{C} \quad (2.1)$$

Sinclair et al. (1976) have estimated the low-degree gravity harmonics and librational parameters from a combination of Doppler and laser-ranging data. Table 2.1 presents these estimates, the low-degree topography harmonics (Bills and Ferrari, 1977), and an estimate of the gravitational constant  $G$  (Heyl and Chrzanowski, 1942).

The resulting estimates for the lunar mean density and moments are

$$\begin{aligned} \bar{\rho} &= 3.3437 \pm 0.0016 \text{ g cm}^{-3} \\ C &= (4C_{22}^g/\gamma)MR_0^2 = (0.3933 \pm 0.0021)MR_0^2 \\ I &= \frac{A + B + C}{3} = \left[ \frac{3 + \beta + \gamma - \beta\gamma}{3(1 + \beta)} \right] C = (0.3931 \pm 0.0021)MR_0^2. \end{aligned} \quad (2.2)$$

The moments  $M_n$  of the radial density distribution are

$$M_n \equiv (n+1) \int_0^1 \rho(\xi) \xi^n d\xi \quad (2.3)$$

where  $\xi = r/R_0$ . On the basis of the values listed in (2.2), the second

TABLE 2.1

## LUNAR GRAVITATIONAL, TOPOGRAPHIC AND LIBRATIONAL DATA

$$\begin{aligned}
 G &= (667.32 \pm 0.31) \times 10^{-10} \text{ cm}^3 \text{ sec}^{-2} \text{ gm}^{-1} \\
 GM &= (4902.796 \pm 0.003) \times 10^{15} \text{ cm}^3 \text{ sec}^{-2} \\
 R_o &= (1737.59 \pm 0.24) \times 10^5 \text{ cm} \\
 \beta &= (631.68 \pm 0.13) \times 10^{-6} \\
 \gamma &= (227.82 \pm 0.08) \times 10^{-6}
 \end{aligned}$$

TOPOGRAPHY				GRAVITY	
n	m	$C_{nm}^t \times 10^6$	$S_{nm}^t \times 10^6$	$C_{nm}^g \times 10^6$	$S_{nm}^g \times 10^6$
0	0	$10^6$	---	$10^6$	---
1	0	$-367.7 \pm 44.6$	---	---	---
1	1	$-1049.3 \pm 30.3$	$-255.4 \pm 23.6$	---	---
2	0	$-303.9 \pm 49.5$	---	$-203.62 \pm 1.09$	---
2	1	$-193.4 \pm 34.2$	$30.4 \pm 24.9$	---	---
2	2	$7.4 \pm 7.4$	$107.8 \pm 9.4$	$22.40 \pm 0.12$	---

NOTE: --- indicates zero by definition.

and fourth moments are

$$\begin{aligned} M_2 &= \bar{\rho} = 3.3437 \pm 0.0016 \\ M_4 &= 5\bar{\rho}I/2MR_0^2 = 3.286 \pm 0.018 \end{aligned} \quad (2.4)$$

This form will prove useful for comparison with models to be derived later.

The seismic data used consist of (1) the inferred crustal structure in the region of the Apollo seismic array including discontinuities at depths of ~20 and 50-60 km (Toksöz et al., 1974), and (2) the travel time as a function of epicentral distance for P and S waves (Nakamura et al., 1974).

### C. THEORY

We will be mainly concerned with models consisting of nearly concentric nearly spherical shells of uniform density material. Each shell  $\ell$  will be characterized by the normalized radius of its outer surface,  $\xi_\ell = R_\ell/R_0$ ; a density contrast from the immediately overlying layer,  $\Delta\rho_\ell = \rho_\ell - \rho_{\ell-1}$ ; and a set of spherical harmonic coefficients  $H_{nm}^\ell$  which represent the shape of the outer surface of the layer. Thus the interface has the form

$$R(\theta, \varphi) = R_0 \xi_\ell \sum_{n=0}^{12} \sum_{m=0}^n (H_{nm}^\ell)^T \Lambda_{nm}(\theta, \varphi) \quad (2.5)$$

The mean density and mean inertial moment of such a model are expressed by



$$M_2 = \bar{\rho} = \sum_{\ell} \Delta \rho_{\ell} \xi_{\ell}^3, \quad M_4 = \frac{5\bar{\rho}I}{2MR_0^2} = \sum_{\ell} \Delta \rho_{\ell} \xi_{\ell}^5 \quad (2.6)$$

The complete inertia tensor of such a configuration is given by

$$I_{ij} = \frac{8\pi R_0^5}{15} \sum_{\ell} \Delta \rho_{\ell} (\xi_{\ell})^5 L_{ij}^{\ell} \quad (2.7)$$

where, in terms of un-normalized shape harmonics,

$$\begin{aligned} L_{11}^{\ell} &= 1 + \frac{5}{2} \left[ (S_{11}^{\ell})^2 + (C_{10}^{\ell})^2 \right] + \frac{C_{20}^{\ell}}{2} - 3C_{22}^{\ell} \\ L_{22}^{\ell} &= 1 + \frac{5}{2} \left[ (C_{11}^{\ell})^2 + (C_{10}^{\ell})^2 \right] + \frac{C_{20}^{\ell}}{2} + 3C_{22}^{\ell} \\ L_{33}^{\ell} &= 1 + \frac{5}{2} \left[ (C_{11}^{\ell})^2 + (S_{11}^{\ell})^2 \right] - C_{20}^{\ell} \\ L_{12}^{\ell} &= L_{21}^{\ell} = -\frac{5}{2} (C_{11}^{\ell} S_{11}^{\ell}) - 3S_{22}^{\ell} \\ L_{13}^{\ell} &= L_{31}^{\ell} = -\frac{5}{2} (C_{11}^{\ell} C_{10}^{\ell}) - \frac{3}{2} C_{21}^{\ell} \\ L_{23}^{\ell} &= L_{32}^{\ell} = -\frac{5}{2} (S_{11}^{\ell} C_{10}^{\ell}) - \frac{3}{2} S_{21}^{\ell} \end{aligned}$$

The gravitational harmonics of the configuration are given by

$$\left( \frac{2n+1}{3} \right) \bar{\rho} G_{nm} = \sum_{\ell} \Delta \rho_{\ell} \xi_{\ell}^{n+3} H_{nm}^{\ell} \quad (2.8)$$

to first order in the  $H_{nm}^{\ell}$ . From the relation between the inertia tensor and the un-normalized gravity harmonics

$$\begin{aligned}
C_{20}^{g_{MR_0^2}} &= (I_{11} + I_{22} - 2I_{33})/2 \\
C_{21}^{g_{MR_0^2}} &= I_{13} = I_{31} \\
S_{21}^{g_{MR_0^2}} &= I_{23} + I_{32} \\
C_{22}^{g_{MR_0^2}} &= (I_{22} - I_{11})/4 \\
S_{22}^{g_{MR_0^2}} &= I_{12}/2 = I_{21}/2
\end{aligned} \tag{2.9}$$

we note that for  $n = 2$ , (2.8) is merely the linear approximation to (2.7). We will thus use (2.7) in place of (2.8) for  $n = 2$ .

We will also be interested in the extent to which our models depart from isostatic equilibrium. This will be measured in terms of the variations about the mean of the hydrostatic pressure at the crust-mantle interface. The mean pressure at this level is approximately,

$$\bar{P} = (4\pi GR_0^2/3) \rho_0 \bar{\rho} (1 - \xi_1) \tag{2.10}$$

and the pressure deviations are

$$\Delta P(\theta, \varphi) = \frac{4\pi GR_0^2}{3} \rho_0 \bar{\rho} \sum_{n=1}^{12} \sum_{m=0}^n J_{nm}^T \Lambda_{nm}(\theta, \varphi) \tag{2.11}$$

where

$$J_{nm} = H_{nm}^0 + \left( \frac{\Delta \rho_1}{\rho_0} \right) \left( \frac{\bar{\rho}_1}{\bar{\rho}} \right) \xi_1^2 H_{nm}^1$$

and  $\bar{\rho}_1$  is the mean density of the Moon beneath the crust.

In order to use seismic data as a constraint on lunar internal structure, we will need to specify compressional and shear wave velocities  $V_p$  and  $V_s$  at each layer. These two velocities are

determined by

$$v_p^2 = (K + 4\mu/3)/\rho \quad v_s^2 = \mu/\rho \quad (2.12)$$

where

$$K \equiv \rho(\partial P/\partial \rho)_S$$

is the adiabatic bulk modulus and  $\mu$  is the shear modulus or rigidity. These in turn are functions of temperature and pressure for any given material. We will assume a linear dependence on temperature and pressure:

$$\begin{aligned} \rho(T,P) &= \rho_{STP} + (\partial \rho/\partial T)\Delta T + (\partial \rho/\partial P)\Delta P \\ K(T,P) &= K_{STP} + (\partial K/\partial T)\Delta T + (\partial K/\partial P)\Delta P \\ \mu(T,P) &= \mu_{STP} + (\partial \mu/\partial T)\Delta T + (\partial \mu/\partial P)\Delta P \end{aligned} \quad (2.13)$$

A number of estimates of the lunar internal temperature distribution are available (e.g., Toksöz and Solomon, 1973). All such models are characterized by a steep gradient near the surface and a more gradual gradient at depth. We will assume a temperature profile of the form (Nakamura and Latham, 1969)

$$T(\xi) = T(0) + \Delta T \xi^n \quad (2.14)$$

with the parameters chosen to match the near-surface gradient and deep interior temperatures. A more complex model is not justified in light of the lack of constraints on the problem.

The pressure at each level is obtained by numerically integrating the equation of hydrostatic equilibrium. The pressure and temperature are then used to estimate the ambient density and elastic moduli from

their assumed STP values.

The seismic travel times  $T$  and epicentral angles  $\Delta$  are calculated from the velocity profile  $V(\xi)$  for a given ray path by (Bullen, 1963)

$$T = 2R_0 \int_{\xi_m}^1 [\eta^2 - \eta_m^2]^{-1/2} \frac{\eta^2 d\xi}{\xi} \quad (2.15)$$

$$\Delta = 2\eta_m \int_{\xi_m}^1 [\eta^2 - \eta_m^2]^{-1/2} \frac{d\xi}{\xi}$$

where  $\eta = \xi/V(\xi)$  and  $\eta_m$  is the value of  $\eta$  at the midpoint of the ray path, where it reaches its minimum radius  $\xi_m$ .

#### D. MODELS

The simplest model considered has a uniform density of  $\bar{\rho} = 3.3437$  g cm<sup>-3</sup> and the outer surface is characterized by the topography harmonics  $H_{nm}^0$ . An interesting aspect of this model is that its librational parameters are

$$\beta = (5.28 + 485.39) \times 10^{-6} = 490.67 \times 10^{-6}$$

$$\gamma = (5.65 + 45.29) \times 10^{-6} = 50.94 \times 10^{-6}$$

where the parenthetical terms are the first- and second-degree contributions, respectively. We thus conclude that the first-degree harmonics are of little consequence dynamically in comparison to the second-degree harmonics. Comparing these estimates with the values in Table 2.1, we note that the assumption of uniform density, coupled with the actual topography, gives, at least qualitatively, reasonable estimates of  $\beta$  and  $\gamma$ , whereas Kopal (1969) has shown that the

rotational and tidal distortions of a hydrostatic moon would yield

$$\beta_H = 37.39 \times 10^{-6} \qquad \gamma_H = 27.97 \times 10^{-6}$$

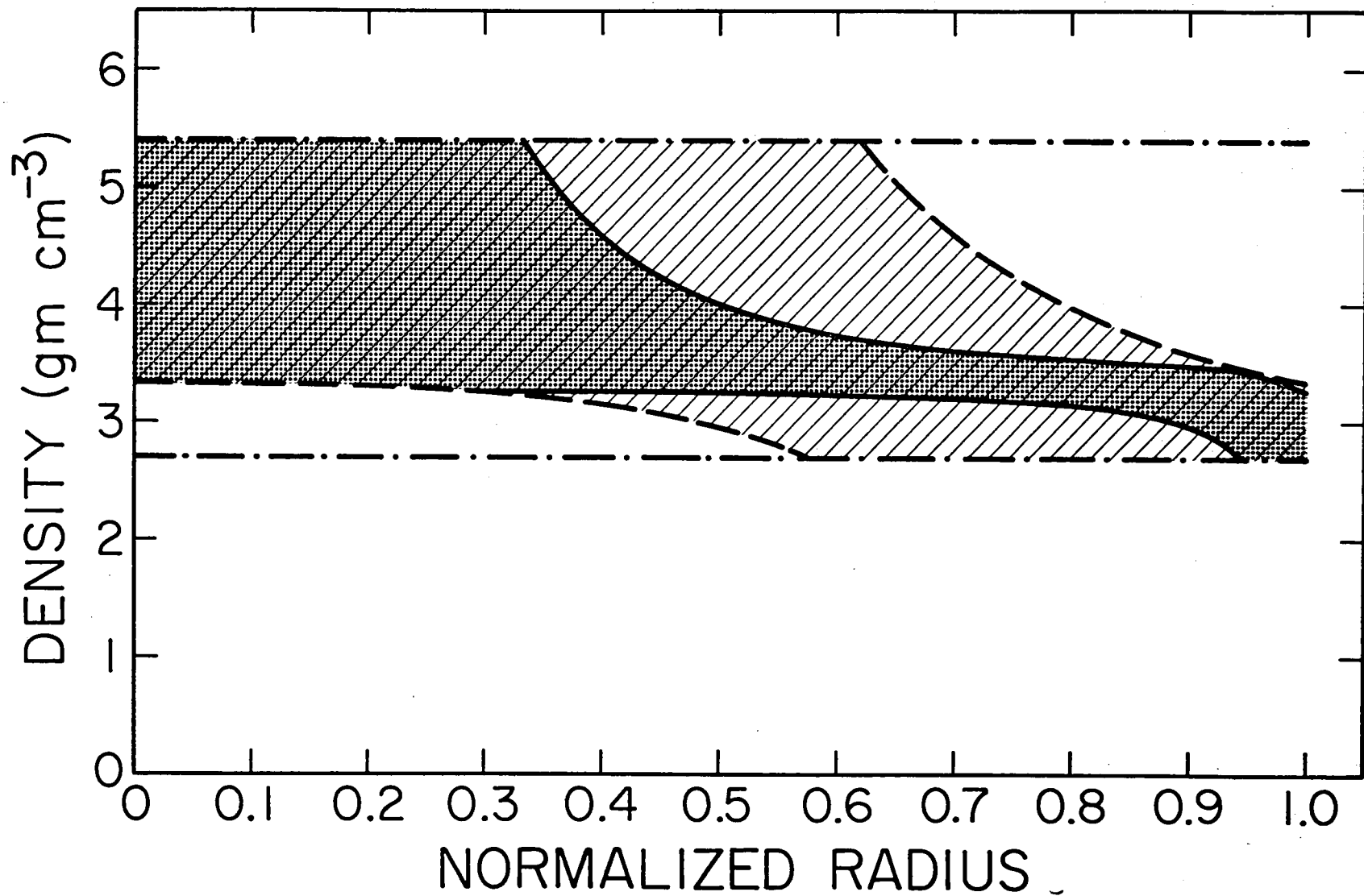
Two basic conclusions are obtained from this comparison: first, the orientation and rotational dynamics of the Moon are intrinsically determined primarily by surface height variations and only secondarily by lateral density variations, and second, the Moon is not well approximated by a hydrostatic model (Kopal, 1969).

We now turn our attention to models with a radial density variation. The simplest such model considered consists of two concentric spherical shells having a density  $\rho_0$  in the outer shell and a density contrast  $\Delta\rho_1$  across the interface at a normalized radius of  $R_1/R_0 = \xi_1$ . A weak compositional constraint is imposed in that we assume

$$2.7 \leq \rho(\xi) \leq 5.4 \text{ g cm}^{-3}$$

where the lower bound corresponds roughly to anorthosite and the upper bound to an Fe-FeS eutectic composition (Brett, 1973) at the lunar central pressure (~50 kbar) and room temperature. These bounds are shown by the dot-dash lines Figure 2.1. If in addition, the model is constrained to have the observed mean density and density inversions with depth are not allowed, the envelope of acceptable density profiles is given by the dashed lines in Figure 2.1. When the model is subjected to the additional constraint that it have the correct mean moment of inertia, the resulting density bounds are those given by the solid lines in Figure 2.1.

FIGURE 2.1 - Envelope of plausible lunar density profiles. Successively applied model constraints: 1)  $2.7 \leq \rho \leq 5.4$  (dot-dash lines); 2) observed mean density  $\bar{\rho} = 3.344 \pm 0.002$  (dashed lines); 3) observed mean inertial moment  $I/MR_0^2 = 0.393 \pm 0.002$  (solid lines).



These lower and upper bounds for the mean moment of inertia are simply the solutions for  $\rho_0(\xi)$  and  $\rho_0(\xi) + \Delta\rho_1(\xi)$ , respectively, subject to

$$2.7 \leq \rho_0 \leq \rho_0 + \Delta\rho_1 \leq 5.4$$

$$\rho_0 + \Delta\rho_1 \xi_1^3 = M_2 = 3.3437 \quad \rho_0 + \Delta\rho_1 \xi_1^5 = M_4 = 3.286$$

They represent the envelope of all possible monotonic density distributions subject to the above constraints. However, not all models falling within these bounds are allowed. In particular, a uniform density model is inconsistent with these constraints. Although these bounds are not tight enough to be of real value in determining the composition of the lunar interior, they do exclude such extreme cases as either a uniform density or an Fe-Ni core with a radius of 380 km or greater. These bounds are also useful in conjunction with other data types.

The next step in complexity is to allow the model to depart from spherical symmetry in order to match not only the actual topography, as was done before, but also the gravitational potential to degree and order 12 and the entire inertia tensor, three moments and three products of inertia, rather than just the mean moment. To do this, we start by including the first- and second-degree harmonics  $H_{nm}^{\ell}$  ( $\ell = 0, 1; n = 1, 2$ ) describing the shape of the outer surface and the crust-mantle interface. The eight harmonics  $H_{nm}^0$  (three first degree and five second degree) of the outer layer are known from the observed topography (Bills and Ferrari, 1977)



TABLE 2.2  
TWO-LAYERED LUNAR DENSITY MODEL  
REPRESENTATIVE SOLUTIONS

parameter	a priori	a posteriori	a posteriori
		$R_c = 0$	$R_c = 400 \text{ km}$ $\rho_c = 5.4 \text{ gm cm}^{-3}$
$\rho_o (\text{gm cm}^{-3})$	$2.90 \pm 0.20$	$2.72 \pm 0.07$	$2.75 \pm 0.06$
$\Delta \rho (\text{gm cm}^{-3})$	$0.50 \pm 0.20$	$0.74 \pm 0.08$	$0.64 \pm 0.07$
$T_c (\text{km})$	$69.5 \pm 17.4$	$95.7 \pm 15.6$	$73.2 \pm 15.8$
$\Delta x_1 (\text{km})$	$0.00 \pm 1.64$	$8.33 \pm 1.20$	$9.40 \pm 1.30$
$\Delta x_2 "$	" "	$2.53 \pm 0.56$	$2.86 \pm 0.40$
$\Delta x_3 "$	" "	$1.40 \pm 0.20$	$1.57 \pm 0.22$
$C_{20}^1 (10^{-4})$	$0.00 \pm 10.00$	$-7.98 \pm 0.63$	$-8.40 \pm 0.66$
$C_{21}^1 "$	" "	$10.45 \pm 1.51$	$11.43 \pm 1.59$
$S_{21}^1 "$	" "	$-0.25 \pm 0.04$	$-0.27 \pm 0.04$
$C_{22}^1 "$	" "	$0.45 \pm 0.004$	$0.44 \pm 0.01$
$S_{22}^1 "$	" "	$-5.71 \pm 0.84$	$-6.26 \pm 0.89$

(see Table 2.1), but the crustal density  $\rho_0$  and the eight harmonics of the crust-mantle interface  $H_{nm}^1$ , as well as the density contrast  $\Delta\rho_1$  and the normalized radius  $\xi_1 = R_1/R_0$ , are unknown and must be determined from (2.7) and (2.8) by constraining the inertia tensor of the model to the observed values. Equation (2.8) applied to the first-degree harmonics ensures that the center of figure of the mantle is offset in such a way as to counterbalance the center of figure displacement of the outer layer.

Such a model has 11 unknown parameters [ $H_{nm}^1$  (eight),  $\rho_0$ ,  $\Delta\rho_1$ , and  $\xi_1$ ], but only 10 constraints [ $G_{nm}$  (three),  $I_{ij}$  (six), and  $\bar{\rho}$ ]. However, we have some a priori knowledge about each of the parameters, and since this makes the system effectively overdetermined, we can perform a weighted least squares inversion. See Table 2.2 for some representative results. Therein are presented the a priori and a posteriori estimates and uncertainties for each of the 11 parameters for both the nominal solution and a solution with a core of radius  $R_c = 400$  km and density  $\rho_c = 5.4 \text{ g cm}^{-3}$ . The first-degree harmonics are presented in terms of the corresponding center of figure displacement

$$\Delta X = R_0 \xi_1 (C_{11}^1, S_{11}^1, C_{10}^1)$$

and the crustal thickness is  $T_c = R_0(1 - \xi_1)$ .

We discover two important facts from this model. First, in the case with no core the mean crustal thickness is significantly greater than that inferred from the locally derived seismic value,

even though the densities are quite reasonable. This conflict can be removed by inclusion of a region of higher density at depth. Although the core model presented ( $R_c = 400$  km and  $\rho_c = 5.4 \text{ g cm}^{-3}$ ) is by no means unique, the amount of density increase required is greater than can be accounted for by self-compression of a homogeneous moon for any reasonable elastic moduli and temperature profile.

Second, this model may be shown to depart from isostatic equilibrium, even for the low-degree harmonics. We shall have more to say about isostasy later.

Having established the inadequacy of a two layered model, we will now present a more detailed model in which the density, elastic moduli, and temperature are all allowed to vary more or less continuously with depth. Our analyses have shown that a three-layered model satisfies the constraints imposed by the gravitational, topographic, and librational data. However, current seismic studies (e.g., Nakamura et al., 1974) suggest a more complex internal structure. The model that we have chosen has six distinct regions. The approximate depths to the boundary interfaces are: upper and lower crust, 20 and 70 km; upper, middle, and lower mantle, 300, 800, and 1400 km. The core has a radius of 340 km. The crustal and upper mantle interfaces correspond to seismic discontinuities (Toksöz et al., 1974; Nakamura et al., 1974). The middle and lower mantle and core are inferred from deep seismic events (Nakamura et al., 1974), electrical conductivity profiles (Dyal et al.,

1976), and thermal and compositional constraints (Brett, 1973).

For modeling purposes the normalized radii of the interfaces are taken to be  $\xi_\ell = 1.00, 0.99, 0.96, 0.83, 0.54$ , and  $0.20$ .

Within each region the STP density and elastic moduli are assumed to vary linearly with depth between the values specified at the upper and lower boundaries. The ambient density and elastic moduli at each layer are then calculated from the STP values and the ambient temperature and pressure.

The assumed temperature and pressure derivatives of the density and elastic moduli correspond in the crust to anorthosite (Baldrige and Simmons, 1971), in the mantle to forsterite, and in the core to pyrite (Skinner, 1966; Birch, 1966). The STP density and bulk modulus of the core are those estimated for an Fe-FeS eutectic composition (Brett, 1973; Brett and Bell, 1969; King and Ahrens, 1973). The crustal density profile is from Gast and Giuli (1972), and the elastic moduli were chosen to duplicate a suitable average of the crustal velocity profile as given by Toksöz et al., (1974).

The lunar temperature profile is imprecisely known, particularly in the deep interior (e.g., Toksöz and Solomon, 1973). We have assumed surface and central temperatures of  $250^\circ$  and  $1900^\circ\text{K}$ , respectively, and have treated the actual temperature distribution with depth as a variable determined by the parameter  $n$  in (2.14). The value ultimately used was  $n = 4.0$ .

A family of models was generated by varying the density and elastic moduli at the mantle region interfaces ( $\xi = 0.96, 0.83, 0.54$ ,

TABLE 2.3  
LUNAR INTERIOR STRUCTURE MODEL

$\xi$	Depth, km	Temperature, °K	Pressure, kbar	$\rho$ , g cm <sup>-3</sup>	K, Mbar	$\sigma$	$v_p$ , km s <sup>-1</sup>	$v_s$ , km s <sup>-1</sup>
<u>Upper Crust</u>								
1.00	0	250	0.00	2.703	0.410	0.250	5.22	3.02
0.99	20	315	0.76	2.703	0.410	0.250	5.22	3.02
<u>Lower Crust</u>								
0.99	20	315	0.76	2.852	0.651	0.293	6.12	3.31
0.96	70	499	3.19	2.950	0.769	0.296	6.52	3.51
<u>Upper Mantle</u>								
0.96	70	499	3.19	3.371*	1.222*	0.246*	8.11	4.71
0.83	300	1117	14.57	3.382*	1.234*	0.275*	7.89	4.39
<u>Middle Mantle</u>								
0.83	300	1117	14.57	3.408*	1.234*	0.275*	7.89	4.39
0.54	800	1760	34.36	3.397*	1.691*	0.420*	7.80	2.89
<u>Lower Mantle</u>								
0.54	800	1760	34.36	3.399*	1.691*	0.420*	7.80	2.89
0.20	1400	1897	48.13	3.424*	1.745*	0.443*	7.68	2.46
<u>Core</u>								
0.20	1400	1897	48.13	5.209	1.400	0.500	5.18	0.00
0.00	1740	1900	52.95	5.223	1.423	0.500	5.22	0.00

\*Parameter which was varied in search for acceptable model.

and 0.20) subject to the constraints that (1) the STP values of  $\rho$ ,  $K$ , and Poisson's ratio  $\sigma = (3K - 2\mu)/(6K + 2\mu)$  are all nondecreasing with depth and (2)  $K$  and  $\sigma$  are continuous across the interfaces at  $\xi = 0.83$  and  $0.54$ . The STP values of  $\rho$ ,  $K$ , and  $\sigma$  at intermediate points are found by linear interpolation, and the ambient values of these parameters are found, as they were before, from the ambient temperature and pressure. These perturbations are performed until a model is found which has the desired mean density and moment as well as P and S wave travel times. The resultant temperature, pressure, density, bulk modulus, Poisson ratio, and seismic velocity profiles of such a model are given in Table 2.3. Table 2.4 gives the moments of the density distribution  $M_n$  ( $n = 0, 1, \dots, 8$ ). The seismic travel time as a function of epicentral distance for the model is compared with observed teleseismic data (Nakamura et al., 1974) in Figure 2.2. The seismic phases shown are identified according to the nomenclature usually applied to the earth (Jeffreys, 1959).

TABLE 2.4  
MOMENTS OF DENSITY DISTRIBUTION  $M_n$

$n$	$M_n$	$n$	$M_n$	$n$	$M_n$
0	3.7409	3	3.3101	6	3.2496
1	3.4247	4	3.2875	7	3.2322
2	3.3433	5	3.2679	8	3.2156

Observed values are  $M_2 = 3.3437 \pm 0.0016$  and  $M_4 = 3.2858 \pm 0.0211$ .

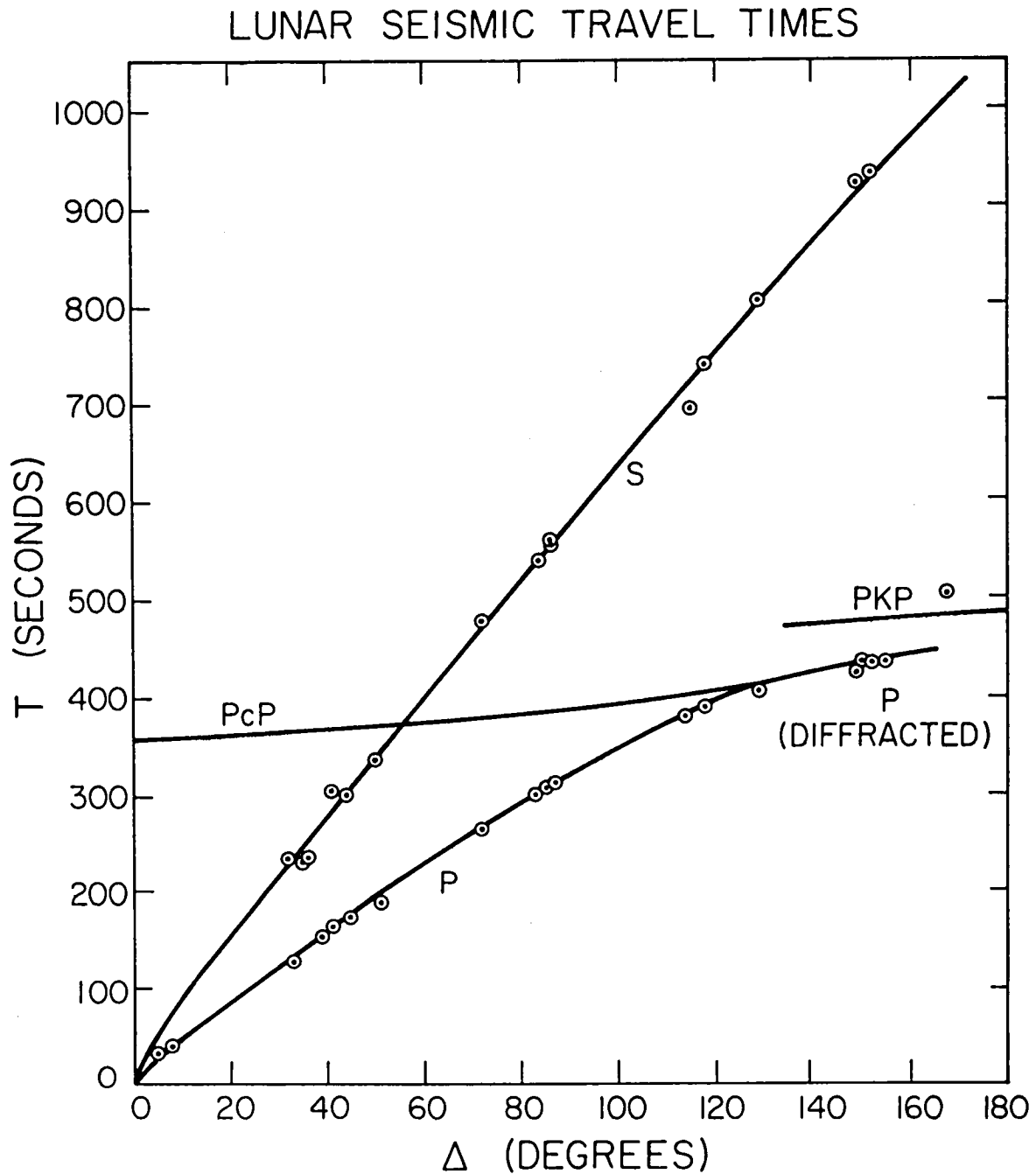


FIGURE 2.2 - Lunar seismic travel times. Curves represent model calculations; circles represent data (Nakamura *et al.*, 1974).

We tentatively interpret the P wave arrivals near  $\Delta = 150^\circ$  as rays diffracted around the core and the weak arrival at  $\Delta = 168^\circ$  as a PKP<sub>2</sub> phase (not shown in the figure) due to a rapid decrease in seismic velocity at the mantle-core interface.

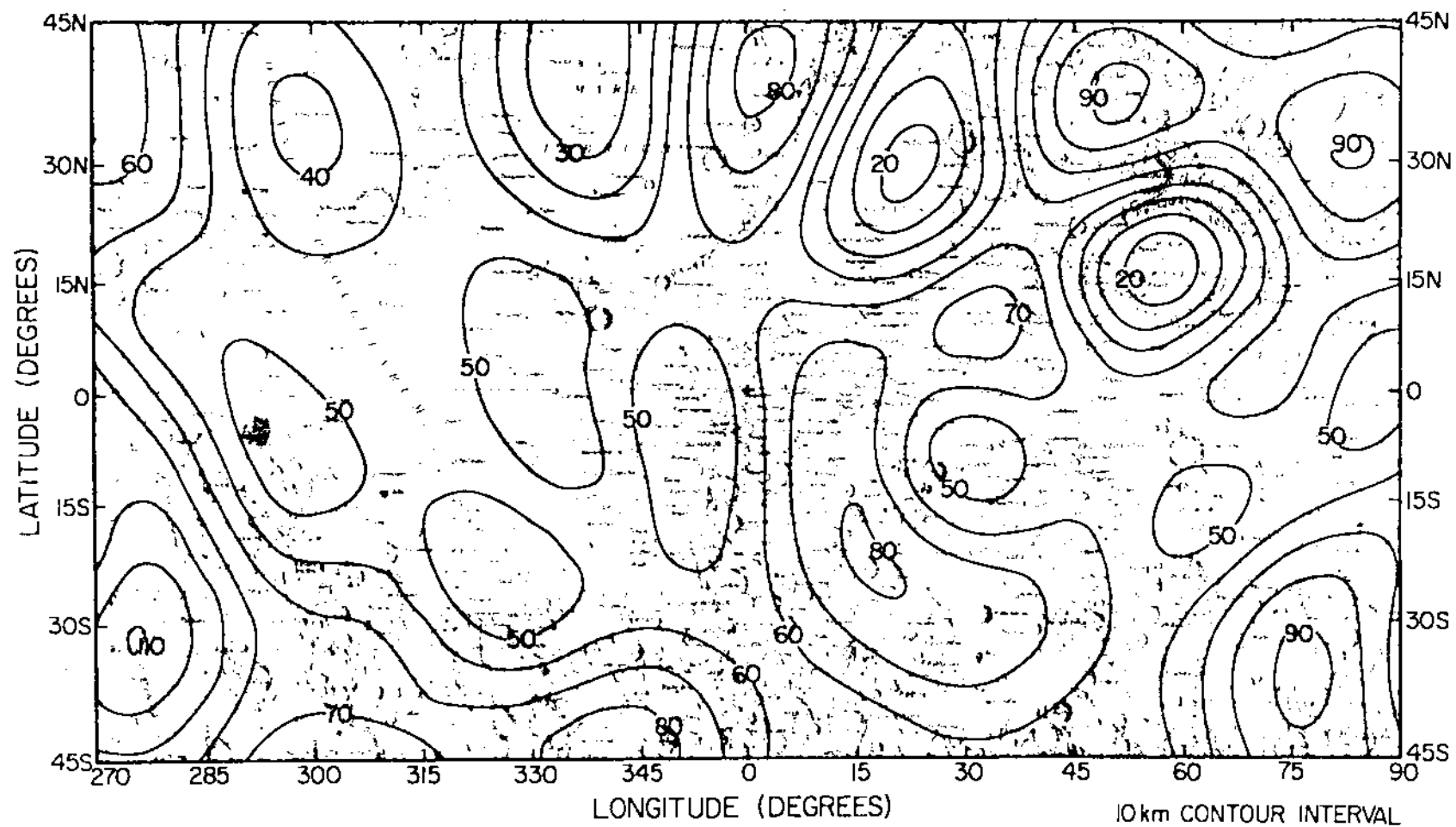
A comparison of the STP density and elastic moduli with those of olivine and pyroxene (Chung, 1970; Nakamura et al., 1974) reveals that a mineral assemblage consisting largely of olivine (80-85% forsterite) and some pyroxene is consistent with the upper mantle model. The increase in density and bulk modulus with depth is consistent with an increase in CaO, TiO<sub>2</sub>, and/or Al<sub>2</sub>O<sub>3</sub> (Simmons and Wang, 1971; Anderson, 1975).

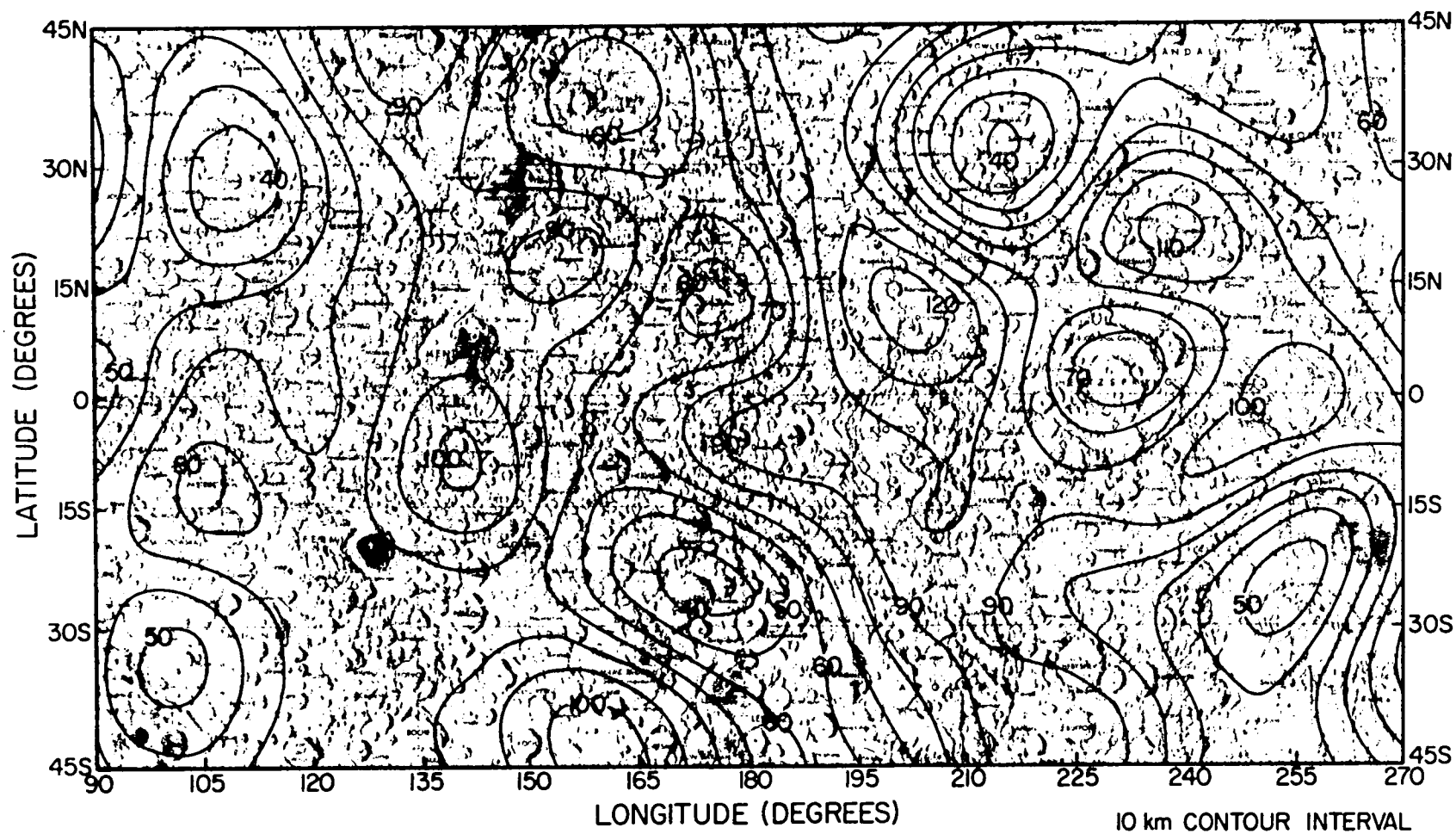
Given values for the mean crustal thickness and density and the density contrast with the mantle, we can include the higher harmonics of topography and gravity in our model, solving for  $H_{nm}^1$  from  $H_{nm}^0$  and  $G_{nm}$  by (2.7) and (2.8). We are thus able to estimate the variation of crustal thickness over the planet on the assumption that all lateral density variations occur as undulations on the mantle-crust interface, which is at a depth of 50-60 km in the area of the Apollo seismic array. For the densities in our model, a mean crustal thickness of 70 km is required to match the seismic values. The resultant crustal thickness map is presented in Figures 2.3a and 2.3b. Wood (1973) has presented a similar analysis based on a more restricted data set. He inferred crustal thicknesses which are systematically less than our estimates.



FIGURE 2.3a - Crustal thickness variations. Lunar nearside. Twelfth degree model. Gravity from Ferrari (1975). Assumed mean crustal density is  $2.9 \text{ gm cm}^{-3}$  crust-mantle density contrast is  $0.4 \text{ gm cm}^{-3}$  and mean crustal thickness is 70 km.

FIGURE 2.3b - Crustal thickness variations. Lunar farside. See caption of Figure 2.3a.





The crustal thickness indicated in the mascon basins is somewhat of an underestimate, since the effect of a surface layer of basalt is ignored. Bowin et al. (1975) estimate that such a surface fill accounts for roughly 20% of the observed gravity anomaly. They estimate a mantle uplift in Mare Serenitatis of 12 km, compared to our estimate of roughly 50 km. However, there is a factor of 2 discrepancy between the free-air anomaly estimates used, and the fact that Bowin et al. are modeling only free-air gravity, whereas we are modeling Bouguer gravity; accounts for an additional factor of 2.

The mean crustal thicknesses under different physiographic regions are: mascons, 30-35 km; irregular maria, 50-60 km; and highlands, 90-110 km.

Schonfeld (1977) has recently shown significant correlations between lunar surface chemistry and the above crustal thickness model. From Al/Si and Mg/Si ratios determined by x-ray fluorescence measurements and Mg and Fe concentrations as determined by gamma ray spectroscopy, he has determined that, in the non-mare regions, total  $\text{Al}_2\text{O}_3$  shows a positive correlation, whereas both total FeO and the MgO/FeO ratio are negatively correlated with crustal thickness. Though these quantities show the same type of correlation with surface elevation alone, their correlation with crustal thickness is much better.

The mere existence of compositional and thickness variations in the crust suggests that the processes of crustal formation and

differentiation did not completely homogenize the surface material. The additional fact that these variations are mutually correlated requires further explanation. Recalling that magmatic differentiation leads to enrichment in Al and depletion in Fe, as well as lowering of the Mg/Fe ratio in the surface layers (Schonfeld, 1977), we see that a possible model for the observed correlations involves the simple assumption that regions of thicker crust are more highly differentiated.

As was previously mentioned, this crustal thickness model is not in isostatic equilibrium; i.e., the pressure at the crust-mantle interface varies with position about its mean value of 3.2 kbar. The maximum superisostatic stress, as calculated from (2.11), is a value, slightly in excess of 200 bars, associated with the major mascon basins Imbrium, Serenitatis, and Crisium. Other regions have smaller stresses, and the global rms stress variation is 64 bars.

It should be noted that it is possible to produce a model which satisfies both topographic and gravitational data and is also isostatically compensated at depth. However, when such models were attempted, the depth of compensation of the low-degree harmonics approached that of the presently proposed mantle-core interface. Since the superisostatic stresses implied by the above model are close to the stresses found in the Earth, it appears more reasonable to accept a nonisostatic Moon.

## E. SUMMARY

We have presented a series of lunar models culminating in a six-layered model with undulations on the outer surface and at the crust-mantle interface. This model is consistent with all available topographic, gravitational, librational, and seismic data.

We have concluded that the librational parameters of the Moon are determined primarily by surface height variations and only secondarily by lateral density variations and that the surface topography is not isostatically supported, nor is it predominated by a fossil tidal or rotational bulge. The largest pressure departures from isostasy are approximately 200 bars under the major mascon basins. The crustal thickness varies from 30-35 km under mascon basins to 90-110 km under the highlands, with the irregular maria intermediate at 50-60 km.

All of the data considered are consistent with an anorthositic crust extending to a mean depth of 70 km underlain by a predominantly forsterite upper mantle grading into a refractory-rich lower mantle surrounding a pyrrhotite core. Such a composition is consistent with, but not uniquely specified by, our model calculations.

We note that a smaller estimate of the mean inertial moment would be consistent with a larger core, which in turn would simplify the interpretation of the P wave arrival times near  $\Delta = 150$  and at 168 deg, which are presently interpreted as diffracted P and PKP<sub>2</sub>, respectively.

## REFERENCES

- Anderson, D.L. (1975). On the composition of the lunar interior.  
J. Geophys. Res. 80, 1555-1557.
- Baldrige, W.S., and Simmons G. (1971). Thermal expansion of lunar rocks. Proc. Lunar Sci. Conf. 3rd, 2317-2321.
- Bills, B.G., and Ferrari, A.J. (1977). A harmonic analysis of lunar topography. Icarus 31, 244-259.
- Birch, F. (1966). Compressibility; Elastic constants, Handbook of Physical Constants, Geol. Soc. Amer. Mem., Sect. 7, 97-173.
- Bowin, C., Simon, B., and Wollenhaupt, W.R. (1975). Mascons: A two-body solution. J. Geophys. Res. 80, 4947-4955.
- Brett, R. (1973). A lunar core of Fe-Ni-S. Geochim. Cosmochim. Acta 37, 165-170.
- Brett, R., and Bell, P.M. (1969). Melting relations in the Fe-rich portion of the system Fe-FeS at 30 kb pressure. Earth Planet. Sci. Lett. 6, 479-482.
- Bullen, K.E. (1963). An Introduction to the Theory of Seismology. Cambridge University Press, New York, pp. 109-113.
- Chung, D.H. (1970). Effects of Fe/Mg ratio on  $V_p$  and  $V_s$  in olivine. J. Geophys. Res. 75, 7353-7361.
- Dyal, P., Parkin, C.W., and Daily, W.D. (1976). Structure of the lunar interior from magnetic field measurements (abstract). In Lunar Science VII, Lunar Science Institute, Houston, pp. 224-226.

- Ferrari, A.J., (1975). Lunar gravity: The first farside map.  
Science 188, 1297-1300.
- Gast, P.W., and Giuli, R.T. (1972). Density of the lunar interior.  
Earth Planet. Sci. Lett. 16, 299-305.
- Heyl, P.R., and Chrzanowski, P. (1942). A new determination of the  
 constant of gravitation. Radio Sci. 29, 1-31.
- Jeffreys, H. (1959). The Earth, Cambridge University Press, New  
 York, pp. 87-93.
- King, D.A., and Ahrens, T.J. (1973). Shock compression of FeS.  
Nature Lond. Phys. Sci. 243, 82-83.
- Kopal, Z. (1969). The Moon, D. Reidel, Dordrecht, Netherlands,  
 pp. 77-90.
- Nakamura, Y., and Latham, G.V. (1969). Internal constitution of the  
 moon. J. Geophys. Res. 74, 3771-3780.
- Nakamura, Y., Latham, G., Lammlein, D., Ewing, M., Duennebier, F.,  
 and Dorman J. (1974). Deep lunar interior inferred from recent  
 seismic data. Geophys. Res. Lett. 1, 137-140.
- Phillips, R.J., and Saunders, R.S. (1975). The isostatic state of  
 Martian topography. J. Geophys. Res. 80, 2893-2898.
- Schonfeld, S. (1977). Comparison of orbital chemistry with crustal  
 thickness and lunar sample chemistry. Proc. Lunar Sci. Conf.  
 8th, in press.
- Simmons, G., and Wang, H. (1971). Single Crystal Elastic Constants  
 and Calculated Aggregate Properties: A Handbook, 2nd ed.,  
 MIT Press, Cambridge, Mass., 370 pp.



Sinclair, W.S., Sjogren, W.L., Williams, J.G., and Ferrari, A.J. (1976)

The lunar moment of inertia derived from combined Doppler and  
laser ranging data (abstract). In Lunar Science VII, Lunar  
Science Institute, Houston, Tex, p. 817.

Skinner, B.J. (1966). Thermal expansion, Handbook of Physical  
Constants. Geol. Soc. Amer. Mem. Sect. 6 97, 75-96.

Toksöz, M.N., and Solomon, S.C. (1973). Thermal history and evolution  
of the moon. Moon 7, 251-278.

Toksöz, M.N., Dainty, A.M., Solomon, S.C., and Anderson, K.R. (1974).  
Structure of the moon. Rev. Geophys. Space Phys. 12, 539-567.

Wood, J.A. (1973). Bombardment as a cause of the lunar asymmetry.  
Moon 8, 73-103.

### III. A HARMONIC ANALYSIS OF MARTIAN TOPOGRAPHY

#### A. INTRODUCTION

The primary objective of this investigation was to obtain a spherical harmonic representation of Martian topography of sufficient resolution and fidelity to be of use in performing global Bouguer gravity analyses. Previous harmonic analyses (Pettengill et al., 1969; Cain et al., 1972; Christensen, 1975) have suffered from inadequate data coverage and insufficient model resolution. An improved model of Martian global topography has been obtained by fitting a sixteenth degree harmonic series to occultation, radar, spectral and photogrammetric measurements. The data are described by Christensen (1975) and Wu (1975). Our analysis differs from Christensen's mainly in that we have attempted to compensate for the very uneven distribution of the data by a process of interpolation similar to that used in our analysis of lunar topography in Chapter I (see also Bills and Ferrari, 1977a).

This chapter presents a brief discussion of the data used in the analysis, its spatial distribution and associated errors. The technique used to compensate for the irregular data distribution is then elaborated. The resulting harmonic estimates are presented and compared with previous analyses. Some of the low degree harmonics and their geophysical implications are discussed separately. The center-of-figure displacement and the excess topographic oblateness receive particular attention.

Maps of the global topography and the Bouguer gravity anomaly are presented, followed by a crustal thickness map consistent with gravity, topography and recent preliminary Viking seismic results.

## B. DATA

The basic data used in this analysis are identical to those used by Christensen (1975). They consist of occultation and spectral measurements from Mariner 9, and Earth-based radar data. The occultation measurements yield absolute distances of surface points from the center of mass. All the other data are only relative. Christensen (1975) solved for and partially eliminated the biases between the various reference surfaces, and thus produced a more unified data set. Figure 3.1 indicates the approximate distribution of these data, summarized according to  $5^\circ \times 5^\circ$  bins. An important aspect of this distribution is its uneven character. Only 1381 of the 2592 bins, representing 68.5% of the total surface area, contain any data. Even among these, the number and quality of measurements varies widely, from only one measurement per bin in some high latitude regions, to over a hundred measurements per bin in the low southern latitudes.

Carlson and Helmsen (1969) have shown that it is the unevenness, rather than the sparsity, of the data distribution which causes the greatest difficulty in obtaining reliable estimates of harmonic coefficients. It is primarily in our treatment of this problem that our analysis differs from Christensen's.

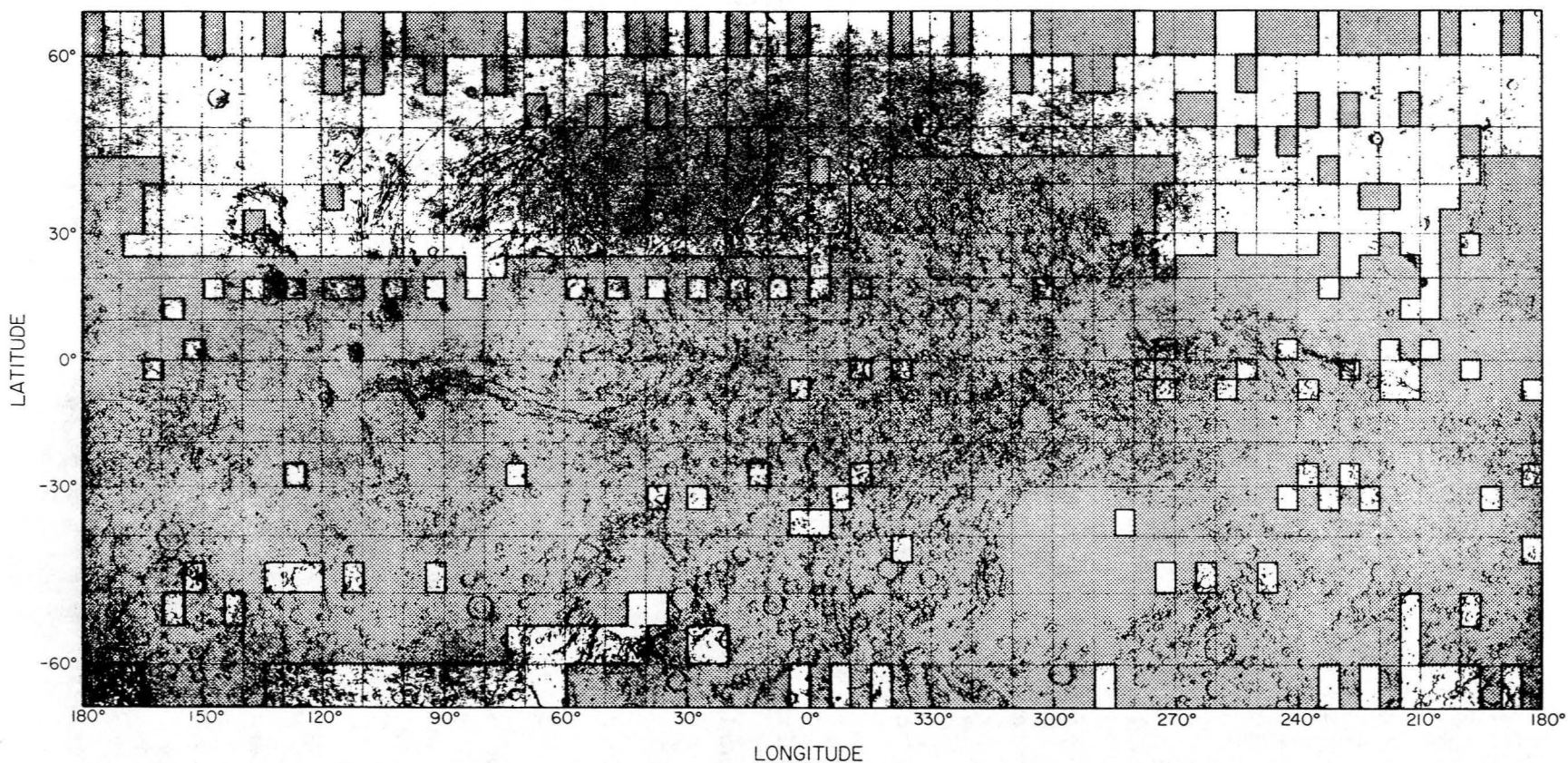


FIGURE 3.1a - Data distribution. Mid-latitudes. The Martian surface is shown divided into 2592 bins, each  $5^\circ \times 5^\circ$ . Shading indicates those bins (1381) which contain at least one measurement. Photographic data were used to estimate elevations in the remaining bins.

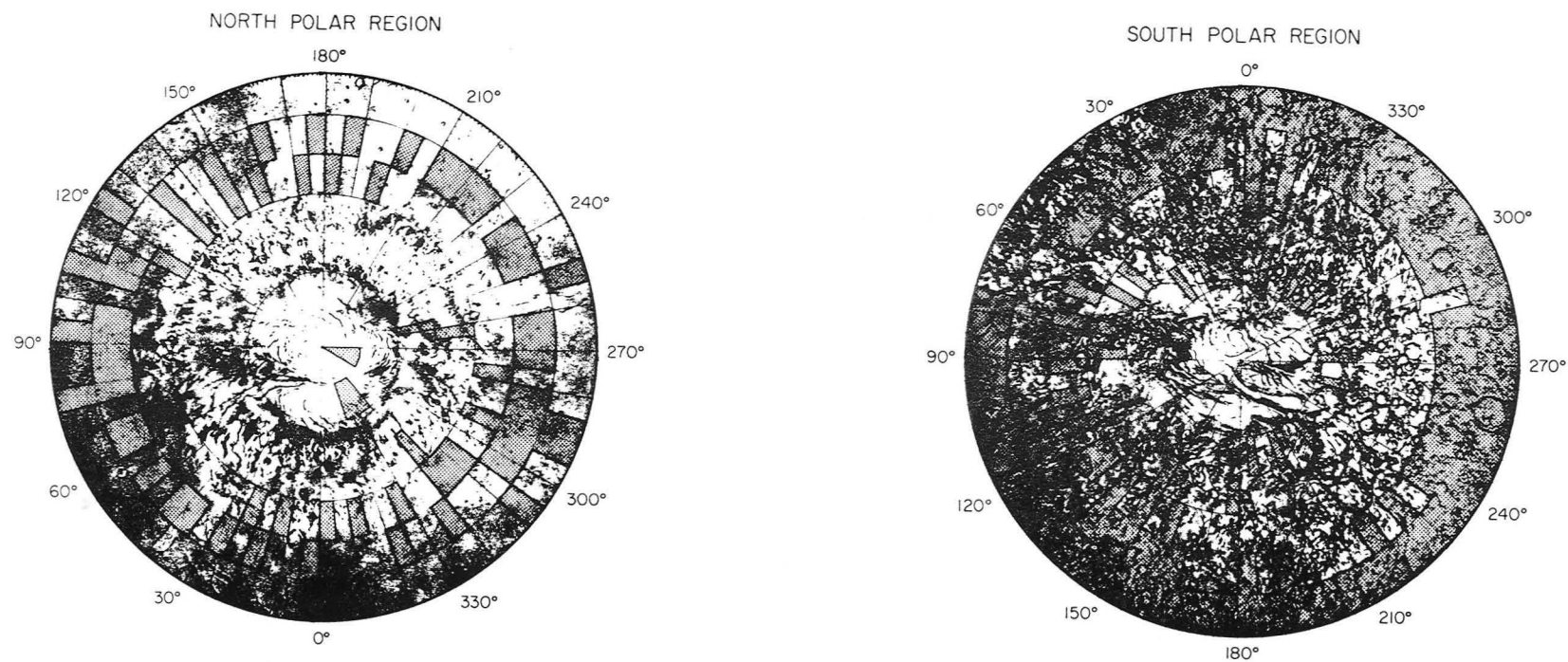


FIGURE 3.1b - Data distribution. Polar regions. See caption of Figure 3.1a.

In a similar analysis of lunar topography in Chapter I, we relied on a linear auto-regressive interpolation scheme to obtain estimates, in the regions without data, of the most probable elevations and associated errors, consistent with the known statistical characteristics of the available data. This process minimizes the expected mean square error of the estimates, but, unfortunately, it totally ignores the actual topography in the unmeasured regions. Fortunately, in the case of Mars, we can do better.

Wu (1975) has used essentially this same data set, in conjunction with photographic interpretation, to produce a topographic contour map of Mars. In the regions without direct measurements, the contours have been interpolated by photogrammetric and interpretive techniques. Presumably this interpolation procedure gives a faithful representation of the high frequency components of the topography, but may suffer from low frequency distortion or bias errors.

Our complete data set thus consists of Christensen's (1975) data, where available, augmented by a bias corrected version of Wu's interpolation in the regions without direct measures. This is preferable to leaving large voids in the data distribution.

All data are of the basic form  $R(\theta, \varphi)$ , where  $R$  is the radial distance from the origin,  $\theta$  is the latitude, and  $\varphi$  is the (west) longitude. In addition to the spherical coordinates  $(R, \theta, \varphi)$ , we will have occasion to use a Cartesian coordinate system  $(X_1, X_2, X_3)$  with its origin at the center of mass. This system is right-handed

and oriented such that the  $X_1$  and  $X_2$  axes are in the equator plane with the positive  $X_1$  axis on the  $\varphi = 0^\circ$  meridian and the positive  $X_2$  axis on the  $\varphi = 270^\circ$  meridian. The  $X_3$  axis lies along the rotation axis (positive towards north).

1

### C. ANALYSIS

As discussed in the previous section, the greatest problem we face in the analysis of the data is compensating for their irregular spatial distribution. We will be interested, not only in the complete ensemble of harmonics which characterize the Martian surface, but also in some of the low degree harmonics considered separately. Therefore we require harmonic coefficients which not only accurately represent the data, but which are also optimally uncorrelated with one another, consistent with the uneven data distribution.

Given a collection of topographic data  $F_i$  with associated standard deviation  $\sigma_i$  distributed on a sphere,

$$R(\theta_i, \varphi_i) = F_i \pm \sigma_i \quad (3.1)$$

we desire optimally uncorrelated estimates of the harmonic coefficients  $H_{nm}$  through degree and order  $N$ .

Our basic model is of the form

$$R(\theta, \varphi) = R_o \left[ 1 + \sum_{n=1}^{16} \sum_{m=0}^n H_{nm}^T \Lambda_{nm}(\theta, \varphi) \right] \quad (3.2)$$

where, as before

$$H_{nm} = \begin{bmatrix} H_{nm1} \\ H_{nm2} \end{bmatrix} = \begin{bmatrix} \bar{C}_{nm} \\ \bar{S}_{nm} \end{bmatrix}$$

$$\Lambda_{nm}(\theta, \varphi) = \bar{P}_{nm}[\sin(\theta)] \begin{bmatrix} \cos(m\varphi) \\ \sin(m\varphi) \end{bmatrix}$$

are the normalized harmonic coefficients and surface harmonic functions, respectively. A sixteenth degree model was chosen as a compromise between resolution and credibility, since, as the sphere is tessellated into a finer mesh of bins, the proportion of bins containing data decreases. This model resolves many of the major physiographic features, and in fact exceeds the resolution of any presently available Martian gravity model. A higher degree model was not utilized because of the adverse effect of the data gaps.

For the ensemble of observations, equation (3.2) can be written as

$$F_i = \left( \frac{\partial F_i}{\partial Z_j} \right) Z_j = A_{ij} Z_j \quad (3.3)$$

where  $Z_j$  is the vector of harmonic coefficients  $H_{nm}$ . In this notation, the weighted least-squares estimator is (see e.g., Lawson and Hanson, 1974)

$$\hat{Z} = [A^T B A]^{-1} A^T B F \quad (3.4)$$

where the weighting matrix B is the inverse of the data noise covariance matrix (assumed, in this analysis, to be diagonal), and superscript T denotes transposition.



To obtain uncorrelated estimates of the parameters  $Z_j$ , we must diagonalize the solution covariance matrix

$$E(ZZ^T) = [A^TBA]^{-1} \quad (3.5)$$

where  $E(\bullet)$  is the expectation operator. Since we are assuming that  $B$  is diagonal, the problem thus reduces to the optimization of the uniformity of the effective data distribution. If we had data of uniform accuracy, evenly distributed over the sphere, we would be assured of uncorrelated estimates. However, the very uneven distribution of the data necessitates further analysis.

The approach we have taken is to represent the surface of Mars, in each bin which contains data, by an average of those data, and, in the bins lacking direct measures, by elevations from Wu's (1975) map corrected for low frequency biases. The first step was to determine the weighted mean of all the data within each of the  $1381 \ 5^\circ \times 5^\circ$  bins which contain data. We then sampled Wu's map at the midpoint of each of the  $2592 \ 5^\circ \times 5^\circ$  data bins. The map elevations are referenced to the equipotential surface of Jordan and Lorell's (1975) gravity model with mean radius  $R = 3382.946$  km. This approximately corresponds to the 6.1 mb equipressure level. Absolute radii were thus constructed by adding the map elevations to the radii of the corresponding points on the equipotential. These radii were then expanded in a harmonic series of degree sixteen, with coefficients  $H'_{nm}$ .

To determine the bias, if any, between the averaged data  $\bar{R}$  and the map radii  $R$ , we define the difference function

$$\Delta H(\theta, \varphi) = \begin{cases} \bar{R}(\theta, \varphi) - R(\theta, \varphi) & \text{if } (\theta, \varphi) \in D \\ 0 & \text{otherwise} \end{cases} \quad (3.6)$$

where  $D$  is the set of points  $(\theta, \varphi)$  enclosed in the 1381 bins which contain data. This difference function can be represented as

$$\Delta H = b \cdot w \quad (3.7)$$

the product of the true bias  $b(\theta, \varphi)$  times a sampling window function

$$w(\theta, \varphi) = \begin{cases} 1 & \text{if } (\theta, \varphi) \in D \\ 0 & \text{otherwise.} \end{cases} \quad (3.8)$$

Therefore, in a harmonic series expansion of  $\Delta H(\theta, \varphi)$ , the coefficients

$$\Delta H_{nm} = b_{nm} * w_{nm} \quad (3.9)$$

are convolutions of the bias function coefficients with the window function coefficients.

We are unable to perform a direct deconvolution. However, since the detrimental effect of this convolution is greatest in the high degree harmonics, and since our a priori expectation is that most of the actual bias introduced by Wu's (1975) interpolation is of a low degree nature, we desire a low-pass filtered version of the difference function to use as our estimate of the actual bias. A candidate low-pass filter is realized by truncating the harmonic expansion at some low degree  $N$ . However, this filter is rather too abrupt for the present purpose, and the choice of cutoff degree is somewhat arbitrary. Therefore, we have chosen to convolve the difference function with a Gaussian function of angular distance  $\gamma$  (Roberts and Ursell, 1960)

$$G(\gamma) = \sum_{n=1}^{\infty} \frac{(2n+1)}{4\pi} e^{-(n)(n+1)\Theta/4} P_n(\cos(\gamma)) \quad (3.10)$$

with angular variance

$$\Theta = \frac{4\pi}{(N)(N+1)}, \quad N = 16$$

equivalent to the resolution of a sixteenth degree harmonic series.

According to the addition theorem of spherical harmonics (see Appendix A)

$$P_n(\cos(\gamma)) = \frac{1}{2n+1} \sum_{m=0}^n \Lambda_{nm}^T(\theta, \varphi) \Lambda_{nm}(\theta', \varphi') \quad (3.11)$$

where

$$\gamma = \cos^{-1} \left[ \frac{\cos(\Delta\varphi) + 1}{2} \cos(\Delta\theta) + \frac{\cos(\Delta\varphi) - 1}{2} \cos(\Sigma\theta) \right]$$

is the angular separation between points  $(\theta, \varphi)$  and  $(\theta', \varphi') = (\theta + \Delta\theta, \varphi + \Delta\varphi)$ . Therefore, the result of convolving the difference function with the specified Gaussian function and expanding the convolution in a harmonic series is

$$\Delta H'_{nm} = \Delta H_{nm} e^{-(n)(n+1)\Theta/4} \quad (3.12)$$

where  $\Delta H_{nm}$  is a harmonic coefficient of the difference function.

Our final bias corrected harmonic coefficient estimate is thus

$$H_{nm} = H'_{nm} + \Delta H'_{nm} \quad (3.13)$$

where  $H'_{nm}$  is a harmonic coefficient of the elevations from Wu's (1975) map.

In performing these harmonic expansions, we have used the weighted least-squares algorithm [equation (3.4)]. The weighting of each point was proportional to the area of its bin and inversely proportional to the variance of the measurement or interpolation:

$$B_{ij} = 2 \sin(\Delta\theta/2) \cos(\theta_i) \Delta\varphi \delta_{ij} / \sigma_i^2 \quad (3.14)$$

The presumed errors were  $\sigma = 0.3$  km for the actual data and  $\sigma = 1.0$  km for the interpolation.

The estimates of the normalized harmonic coefficients and their formal uncertainties are presented in Table 3.1.

#### D. RESULTS

##### 1. Low Degree Harmonics

We will now consider the harmonics of degree zero, one and two. These represent the mean radius, center of figure displacement, and tri-axial figure, respectively.

The estimated mean Martian radius is  $R_0 = (3389.92 \pm 0.04)$  km. This, in conjunction with estimates of  $GM = (42828.1 \pm 0.5) \text{ km}^3 \text{ sec}^{-2}$  (Born, 1974) and  $G = (667.32 \pm 0.31) \times 10^{-25} \text{ km}^3 \text{ sec}^{-2} \text{ gm}^{-1}$  (Heyl and Chrzanowski, 1942) yields an estimate for the mean density of  $\bar{\rho} = (3.9331 \pm 0.0018) \text{ gm cm}^{-3}$ . Most of this error comes from the error in  $G$ . The mean density, in combination with the mean inertial moment, places important constraints on models of Martian internal structure and composition (see e.g., Johnston et al., 1974).

We now turn our attention to the first degree harmonics. They represent a displacement of the center of figure (C.F.) from the

TABLE 3.1

Normalized Martian Topography Harmonics (  $\times 10^6$  )

$$R_o = 3389.916 \pm 0.038 \text{ km}$$

n	m	$\bar{C}_{nm}$	$\bar{S}_{nm}$	$\sigma(\bar{C}_{nm})$	$\sigma(\bar{S}_{nm})$
1	0	-376.0		12.7	
1	1	-8.1	-199.8	10.3	10.6
2	0	-1823.9		12.2	
2	1	71.7	103.0	11.6	11.8
2	2	-288.1	214.5	10.1	10.1
3	0	73.4		12.5	
3	1	-27.7	23.4	11.5	11.4
3	2	-37.9	68.1	11.3	11.3
3	3	111.5	250.7	9.9	10.0
4	0	19.6		12.6	
4	1	3.0	14.3	11.3	11.3
4	2	121.9	-63.2	11.3	11.3
4	3	-109.3	-4.2	10.9	11.1
4	4	-15.1	-61.0	9.8	9.8
5	0	-1.2		12.1	
5	1	7.8	16.2	11.5	11.7
5	2	-60.1	19.9	11.0	10.9
5	3	-5.9	45.4	11.1	11.3
5	4	-14.7	-95.2	10.7	10.7
5	5	-47.3	17.0	9.8	9.8
6	0	51.7		11.8	
6	1	-3.1	-64.7	11.4	11.6
6	2	-66.1	47.3	11.1	11.0
6	3	-22.3	-22.5	10.8	10.9
6	4	27.6	52.7	11.0	11.0
6	5	59.0	12.1	10.5	10.5
6	6	60.3	4.4	9.9	9.9

TABLE 3.1 (Cont'd)

n	m	$\bar{C}_{nm}$	$\bar{S}_{nm}$	$\sigma(\bar{C}_{nm})$	$\sigma(\bar{S}_{nm})$
7	0	98.2		11.4	
7	1	-8.2	29.3	11.3	11.4
7	2	48.0	-15.4	10.9	11.0
7	3	17.7	-24.4	10.8	10.8
7	4	14.9	5.0	10.8	10.7
7	5	25.7	13.2	10.9	10.8
7	6	22.6	3.6	10.4	10.4
7	7	35.1	-43.5	10.0	10.0
8	0	29.8		11.1	
8	1	-9.1	35.7	11.2	11.2
8	2	9.2	15.0	10.8	10.9
8	3	15.1	16.6	10.7	10.7
8	4	-0.6	32.6	10.7	10.6
8	5	37.4	20.5	10.7	10.7
8	6	-38.7	-15.2	10.7	10.7
8	7	33.6	7.3	10.4	10.3
8	8	-28.6	5.3	10.1	10.1
9	0	34.8		10.9	
9	1	30.6	-10.6	10.9	10.9
9	2	2.9	5.8	10.8	10.8
9	3	-9.7	-0.5	10.5	10.6
9	4	4.2	15.4	10.6	10.6
9	5	-23.8	8.1	10.6	10.6
9	6	2.9	5.6	10.6	10.6
9	7	14.2	-14.0	10.6	10.5
9	8	-33.1	-11.1	10.3	10.3
9	9	-30.2	12.2	10.2	10.2
10	0	13.6		10.8	
10	1	20.5	-1.0	10.7	10.7
10	2	9.9	-21.7	10.7	10.7
10	3	25.9	9.1	10.5	10.5
10	4	2.3	-21.0	10.5	10.5
10	5	-18.0	3.0	10.6	10.6
10	6	1.9	-14.3	10.5	10.5
10	7	-12.2	-12.9	10.6	10.5
10	8	-8.1	-9.3	10.5	10.5
10	9	-25.6	-12.7	10.3	10.3
10	10	6.7	13.5	10.3	10.3

TABLE 3.1 (Cont'd)

n	m	$\bar{C}_{nm}$	$\bar{S}_{nm}$	$\sigma(\bar{C}_{nm})$	$\sigma(\bar{S}_{nm})$
11	0	-2.7		10.6	
11	1	1.6	-8.6	10.6	10.6
11	2	-2.4	-8.9	10.6	10.6
11	3	-2.5	-14.3	10.5	10.5
11	4	-1.3	-9.3	10.5	10.5
11	5	3.3	-8.6	10.5	10.5
11	6	11.0	10.8	10.5	10.5
11	7	1.5	-1.4	10.5	10.5
11	8	0.2	11.4	10.5	10.5
11	9	-12.3	-4.4	10.4	10.5
11	10	12.1	14.6	10.4	10.4
11	11	6.9	-8.7	10.3	10.3
12	0	23.3		10.6	
12	1	2.5	-13.8	10.5	10.5
12	2	8.9	-6.0	10.5	10.5
12	3	-18.1	-0.8	10.5	10.5
12	4	-6.6	-7.7	10.5	10.5
12	5	5.7	0.5	10.4	10.4
12	6	0.7	-11.3	10.5	10.5
12	7	2.9	11.7	10.5	10.5
12	8	0.8	-10.2	10.5	10.5
12	9	3.8	2.5	10.5	10.5
12	10	15.9	17.7	10.4	10.4
12	11	-8.7	-3.6	10.4	10.4
12	12	5.3	-6.1	10.4	10.4
13	0	-5.2		10.5	
13	1	2.2	19.1	10.5	10.5
13	2	-2.9	-3.3	10.5	10.5
13	3	10.0	10.8	10.5	10.5
13	4	4.4	1.1	10.5	10.4
13	5	7.8	3.4	10.4	10.4
13	6	-2.9	3.4	10.4	10.4
13	7	-3.2	-8.4	10.4	10.4
13	8	-2.7	-8.1	10.4	10.4
13	9	0.6	2.9	10.4	10.4
13	10	8.7	0.8	10.4	10.4
13	11	-1.0	-9.3	10.4	10.4
13	12	-3.6	3.1	10.4	10.4
13	13	-21.5	-4.6	10.4	10.4

TABLE 3.1 (Cont'd)

n	m	$\bar{C}_{nm}$	$\bar{S}_{nm}$	$\sigma(\bar{C}_{nm})$	$\sigma(\bar{S}_{nm})$
14	0	4.7		10.5	
14	1	-4.0	8.8	10.5	10.5
14	2	-10.1	5.2	10.5	10.5
14	3	5.8	-3.2	10.5	10.5
14	4	3.1	5.1	10.4	10.4
14	5	3.1	-3.4	10.4	10.4
14	6	1.4	7.2	10.4	10.4
14	7	-10.1	-2.0	10.4	10.4
14	8	0.7	7.4	10.4	10.4
14	9	0.3	1.7	10.4	10.4
14	10	-1.4	-4.0	10.4	10.4
14	11	-18.3	-11.7	10.4	10.4
14	12	4.6	2.4	10.4	10.4
14	13	5.9	1.8	10.4	10.4
14	14	-1.7	10.2	10.4	10.4
15	0	-4.6		10.4	
15	1	-3.3	-12.2	10.4	10.4
15	2	-3.3	4.8	10.4	10.4
15	3	-10.6	-10.6	10.4	10.4
15	4	-2.5	4.7	10.4	10.4
15	5	-3.3	-6.2	10.4	10.4
15	6	-0.2	-1.1	10.4	10.4
15	7	-2.6	-0.5	10.4	10.4
15	8	1.0	0.4	10.4	10.4
15	9	-6.0	12.3	10.4	10.4
15	10	-4.4	-0.3	10.4	10.4
15	11	-8.0	4.0	10.4	10.4
15	12	5.5	7.0	10.4	10.4
15	13	1.9	1.6	10.4	10.4
15	14	-3.6	-6.3	10.4	10.4
15	15	5.0	5.8	10.4	10.4



TABLE 3.1 (Cont'd.)

n	m	$\bar{C}_{nm}$	$\bar{S}_{nm}$	$\sigma(\bar{C}_{nm})$	$\sigma(\bar{S}_{nm})$
16	0	15.1		10.4	
16	1	10.0	1.5	10.4	10.4
16	2	11.0	-5.0	10.4	10.4
16	3	5.8	-6.6	10.4	10.4
16	4	-0.0	-6.4	10.4	10.4
16	5	1.6	0.1	10.4	10.4
16	6	-11.1	-10.8	10.4	10.4
16	7	0.9	5.5	10.4	10.4
16	8	1.5	-7.2	10.4	10.4
16	9	4.9	8.8	10.4	10.4
16	10	0.7	9.6	10.4	10.4
16	11	2.1	-9.2	10.4	10.4
16	12	-10.7	11.0	10.4	10.4
16	13	4.4	10.8	10.4	10.4
16	14	-5.9	-10.6	10.4	10.4
16	15	1.2	18.1	10.4	10.4
16	16	-5.3	-6.7	10.4	10.4

center of mass (C.M.). In terms of rectangular coordinates, the location of the C.F. is

$$\begin{bmatrix} \Delta X_1 \\ \Delta X_2 \\ \Delta X_3 \end{bmatrix} = R_0 \begin{bmatrix} C_{1,1} \\ -S_{1,1} \\ C_{1,0} \end{bmatrix} = \begin{bmatrix} -0.047 \pm 0.061 \\ 1.173 \pm 0.062 \\ -2.208 \pm 0.075 \end{bmatrix} \text{ km} \quad (3.15)$$

or in terms of spherical coordinates

$$\begin{bmatrix} R \\ \theta \\ \varphi \end{bmatrix} = \begin{bmatrix} (2.501 \pm 0.073) \text{ km} \\ (62^\circ.0 \pm 3^\circ.7) \text{ S} \\ (272^\circ.3 \pm 3^\circ.0) \text{ W} \end{bmatrix}$$

where, as before, the origin is at the C.M. This offset, by definition, implies a departure from spherical symmetry in the internal density distribution.

Love (1911) investigated the problem of gravitational instabilities in an initially homogeneous planet. He found that if the rigidity is sufficiently small, the initial homogeneous configuration will be unstable, and the mass will redistribute itself into a more stable state. Any such displacement of mass can be expressed as a sum of spherical harmonics. The critical rigidity for the onset of instability is a decreasing function of harmonic degree. Thus, as a planet is heated during accretion, or subsequently by radiogenic processes, and the rigidity decreases, the first mode to become unstable is that of degree zero which is characterized by purely radial disturbances. In an extreme case, this may involve radial differentiation into a core, mantle and crust. The next

mode to become unstable is the first degree, which represents hemispherical disturbances. Thus, it is not surprising that all known differentiated terrestrial planets have sizable C.F. offsets. Lingenfelter and Shubert (1973) have discussed large scale thermally driven convection as a possible mechanism for the production of these offsets.

Both the Earth and Mars display a dichotomy in physiography as well as topography. Balmino et al., (1973) have determined the distribution of oceanic and continental regions, as well as the global topography of the Earth. The Earth's C.F. offset is toward ( $41.6^{\circ}$  N,  $34.7^{\circ}$  E), whereas the center of the continental province is ( $46^{\circ}$  N,  $27^{\circ}$  E). In a coordinate system centered at the latter point, much of the boundary between continental plates and oceanic plates occurs between colatitudes of  $90^{\circ}$  and  $110^{\circ}$ . Much of the volcanic and seismic activity of the Earth occurs in this transition zone, with an additional clustering near the pole.

The surface of Mars can also be divided into two broad physiographic regions: a high, heavily cratered southern region and a low, northern region which contains smooth plains as well as the Tharsis and Elysium volcanic provinces. The direction of the C.F. offset ( $62^{\circ}$  S,  $272^{\circ}$  W) is fairly close ( $\gamma \pm 30^{\circ}$ ) to the center of the southern, heavily cratered region ( $55^{\circ}$  S,  $335^{\circ}$  W) as determined by Mutch and Saunders (1976). In a coordinate system centered at the latter position, the boundary between cratered uplands and smooth lowland

plains approximately follows the equator. There is also a concentration of volcanoes in the colatitude band between  $120^\circ$  and  $150^\circ$ , with another grouping near the pole. In this regard, Mars is obviously very similar to the Earth.

Mutch and Saunders (1976) have suggested that this distribution may be due to convective motions under the control of rotational forces. In fact, they argued that the axis of this shifted coordinate system may have coincided with the rotation axis prior to the structural uplift in the Tharsis region. Though global scale convection may well have been responsible for the physiographic and tectonic dichotomy of Mars, and the symmetry axis may have temporarily coincided with the rotation axis, it appears doubtful that there was any causal connection between these events. The argument is as follows:

The influence of rotation on the pattern of convection in the Earth's mantle has received considerable attention (see e.g., Knopoff, 1964; McKenzie, 1968) and is known to be negligible at present. In general the effect of rotation can be estimated in terms of the Taylor number (Roberts, 1968)

$$\mathcal{T} = \left( \frac{2\Omega R_0^2}{\nu} \right)^2 \quad (3.16)$$

where  $R_0$  is the mean radius (cm),  $\Omega$  is the rotational angular velocity ( $\text{sec}^{-1}$ ) and  $\nu$  is the kinematic viscosity (stoke =  $\text{cm}^2 \text{sec}^{-1}$ ). This is essentially the square of the ratio of Coriolis to viscous forces. For rotational effects to be significant, the Taylor number must exceed unity. For the Earth and Mars, the values are  $3.6 \times 10^{27}/\nu^2$  and  $2.6 \times 10^{26}/\nu^2$ , respectively. Weertman (1970) has estimated the effective viscosity (at a constant strain rate) as a function of depth for the present-day Earth and Mars. In both planets, the viscosity initially decreases with depth, due to increasing temperature, goes through a minimum ( $\nu \doteq 2 \times 10^{20}$  stokes) and then increases due to increasing pressure. Even during initial planetary differentiation, the effective viscosity was likely no less than  $10^{18}$  stokes (Tozer, 1972). This minimum viscosity is still great enough to preclude the rotation from influencing the pattern of convection.

Furthermore, in situations where Coriolis forces do dominate convective motion, the induced flow is often highly inclined to the rotation axis (Roberts, 1968). The motion invoked by Mutch and Saunders (1976) is parallel to their purported rotation axis.

We now consider the shape and orientation of the tri-axial figure represented by the second degree harmonics. The principal axes of this figure are:

$$\begin{aligned}
X'_1 &= (3394.5 \pm 0.3 \text{ km}, \quad 0^\circ.7 \pm 0^\circ.2\text{N}, \quad 18^\circ.5 \pm 0^\circ.8\text{W}) \\
X'_2 &= (3399.2 \pm 0.3 \text{ km}, \quad 2^\circ.0 \pm 0^\circ.2\text{S}, \quad 108^\circ.4 \pm 0^\circ.8\text{W}) \\
X'_3 &= (3376.1 \pm 0.4 \text{ km}, \quad 87^\circ.9 \pm 0^\circ.2\text{N}, \quad 128^\circ.8 \pm 6^\circ.3\text{W})
\end{aligned} \tag{3.17}$$

These differ somewhat in orientation from the principal inertial axes, as determined from the second degree gravity harmonics (Sjogren et al., 1975):

$$\begin{aligned}
X''_1 &= (0^\circ.0\text{N}, \quad 15^\circ.7 \pm 1^\circ.0\text{W}) \\
X''_2 &= (0^\circ.0\text{N}, \quad 105^\circ.7 \pm 1^\circ.0\text{W}) \\
X''_3 &= (90^\circ.0\text{N})
\end{aligned} \tag{3.18}$$

This misalignment, if confirmed by subsequent analysis, implies some lateral density variation. If such variation occurs as undulations on the crust-mantle interface, the principal axes of the tri-axial mantle must be skewed in the opposite direction. We shall pursue this idea further in a subsequent section. First, we will consider the problem of Mars' excessive oblateness.

When subjected to a disturbing potential characterized by harmonic coefficients  $\Phi_{nm}$ , an elastic sphere suffers a surface distortion

$$H'_{nm} = h_n \Phi_{nm} \tag{3.19}$$

and this redistribution of mass gives rise to a further disturbance of the potential

$$G'_{nm} = k_n \Phi_{nm} \tag{3.20}$$

The Love numbers  $h_n$  and  $k_n$ , for a homogeneous, incompressible elastic sphere are given by (Munk and MacDonald, 1960)

$$\begin{aligned}
k_n &= \frac{3}{2(n-1)} \left( \frac{1}{1 + N(n)\mu/P_c} \right) \\
h_n &= \left( \frac{2n+1}{3} \right) k_n
\end{aligned} \tag{3.21}$$

where

$$\begin{aligned}
N(n) &= \frac{2(n+1)^2 + 1}{2n} \\
P_c &= \frac{3GM^2}{8\pi R_o^4}
\end{aligned}$$

is the hydrostatic pressure at the center of the sphere and  $\mu$  is the elastic rigidity. See Appendix E for a more complete discussion of these matters.

The disturbing potential induced by rotation is, in terms of un-normalized harmonics,

$$\Phi_{2,0}(\Omega) = \frac{-\Omega^2 R_o^3}{3GM} = -\frac{m}{3} \tag{3.22}$$

where  $\Omega$  is again the rotational angular velocity and  $m$  is the ratio of centrifugal to gravitational accelerations on the equator. We shall use the usual geodetic terminology and denote by "gravitation"

the attraction due to the mass of a planet and by "gravity" the combined effect of gravitation and rotation. Thus the rotational contributions to the surface topography and to the shape of the gravity equipotential are

$$H'_{2,0} = \frac{5}{2} \left( \frac{1}{1+19\mu/4P_c} \right) \left[ - \frac{\Omega^2 R_0^3}{3GM} \right] = - \frac{2f_g}{3}$$

and

(3.23)

$$\begin{aligned} \Phi_{2,0}(\Omega) + G'_{2,0} &= \left[ 1 + \frac{3}{2} \left( \frac{1}{1+19\mu/4P_c} \right) \right] \\ &\quad \left[ - \frac{\Omega^2 R_0^3}{3GM} \right] = - \frac{2f_d}{3} \end{aligned}$$

respectively. Here  $f_g$  and  $f_d$  are the geometric and dynamic flattenings. They are defined as the fractional difference between equatorial and polar radii of the actual topography and the gravity equipotential surfaces, respectively.

If the rotation of Mars has been essentially uniform for a period longer than its second degree visco-elastic relaxation time  $\tau'_2$ , where (Darwin, 1879)

$$\tau'_n = \left[ \frac{N(n)}{P_c} + \frac{1}{\mu} \right] \eta$$

and  $\eta = \rho\nu$  is the dynamic viscosity (poise = g cm<sup>-1</sup> sec<sup>-1</sup>), we should expect the topography to conform to an equipotential surface. Since



$\Phi_{2,0}(\Omega) = -1.523 \times 10^{-3}$ , we would expect for a homogeneous, incompressible fluid Mars:

$$\begin{aligned} H'_{2,0} &= -3.808 \times 10^{-3} \\ G'_{2,0} &= -2.285 \times 10^{-3} \end{aligned} \quad (3.24)$$

However, we find

$$H_{2,0} = (-4.078 \pm 0.027) \times 10^{-3}$$

and Sjogren et al. (1975) have found

$$G_{2,0} = (-1.958 \pm 0.021) \times 10^{-3}$$

Thus the topographic oblateness is too great, and the gravitational oblateness is too small for Mars to be homogeneous and hydrostatic.

The radial variation of density inside Mars is easily incorporated into the hydrostatic theory. In the traditional notation, the flattening of a hydrostatic configuration is (Darwin, 1900)

$$f_g = f_d = \frac{5m/2}{1 + \left[ \frac{5}{2} \left( 1 - \frac{3C}{2MR_0^2} \right) \right]^2} \quad (3.25)$$

where  $C$  is the polar moment of inertia. The homogeneous case we previously considered corresponds to  $C = 2MR_0^2/5$  and therefore

$$f_g = f_d = \frac{5m}{4} \quad (3.26)$$

Since the rate of precession of Mars' rotation axis is not known, all present estimates of the moment of inertia are obtained from

the dynamic flattening according to the hydrostatic theory. The discrepancy between dynamic and geometric flattening makes this approach rather suspect. This problem has a long and interesting history. We will digress now to a brief discussion of the principal points.

The earliest determination of the dynamic flattening of Mars appears to be that of Struve (1895), who analyzed the precession of the orbits of Phobos and Deimos. His result was  $f_d = 5.210 \times 10^{-3}$  ( $G_{2,0} = -1.951 \times 10^{-3}$ ). Subsequent analyses (Table 3.2) of the motions of both natural and artificial satellites have essentially confirmed this result. The situation is very different regarding the geometric flattening (Table 3.3). Though the early estimates varied widely, they tended to be large. Darwin (1877) pointed out that the best estimates available to him exceeded even the flattening predicted for a homogeneous fluid planet. A summary of the best Earth-based telescopic determinations is given by de Vaucouleurs (1964). The mean of 32 polar radius determinations spanning the period 1890-1958 yields  $3378 \pm 3.6$  km. The mean of 68 measurements of the equatorial radius from the period 1879-1958 is equivalent to  $3414.2 \pm 3.6$  km. The corresponding flattening is  $f_g = (10.6 \pm 0.5) \times 10^{-3}$ . It is interesting that these early polar radius estimates essentially agree with present estimates whereas the equatorial radius was consistently overestimated. It has been suggested (de Vaucouleurs, 1964) that the excess apparent equatorial radius

TABLE 3.2

## Mars Dynamic Flattening

Source		$f_d \times 10^3$	$G_{2,0} \times 10^3$
Struve	(1895)	5.210	-1.951
Woolard	(1944)	5.215	-1.955
Wilkins	(1967)	$5.208 \pm 0.030$	$-1.950 \pm 0.020$
Sinclair	(1972)	$5.232 \pm 0.005$	$-1.966 \pm 0.003$
Lorell et al.	(1973)	$5.223 \pm 0.015$	$-1.960 \pm 0.010$
Born	(1974)	$5.223 \pm 0.027$	$-1.960 \pm 0.018$
Sjogren et al.	(1975)	$5.220 \pm 0.032$	$-1.958 \pm 0.021$
Reasenberget al.	(1975)	5.216	-1.955

TABLE 3.3

## Mars Geometric Flattening

Source		$f_g \times 10^3$		$H_{2,0} \times 10^3$	
Schur	(1896)	21.5	$\pm 1.7$	-14.3	$\pm 1.1$
Hartwig	(1899)	8.6	$\pm 1.5$	-5.7	$\pm 1.0$
Trumpler	(1924)	10.4	$\pm 0.6$	-7.1	$\pm 0.4$
Camichel	(1954)	12.0	$\pm 4.7$	-8.0	$\pm 3.1$
Dollfus	(1972)	7.9	$\pm 1.5$	-5.3	$\pm 1.0$
Cain et al.	(1972)	5.39	$\pm 0.15$	-3.59	$\pm 0.10$
Christensen	(1975)	5.90		-3.93	
Present work		6.117 $\pm$ 0.041		-4.078 $\pm$ 0.027	

may be an atmospheric effect. In any event, it gave rise to a number of interesting theories which attempt to explain an actual excess oblateness. Darwin (1877) considered, but discarded, the idea that Mars is in hydrostatic equilibrium, but has a density which decreases with depth. Urey (1950) hypothesized an equatorial belt of isostatically supported mountains. Lamar (1962) proposed instead that the elevation of the surface increases gradually from the poles to the equator, and that this increase is isostatically compensated by variation in the crustal thickness. Runcorn (1967) suggested that second order convection cells might produce the excess flattening. This unexplained oblateness was one of the greatest Martian geophysical problems prior to spacecraft exploration (Loomis, 1965).

More recent radar (Pettengill et al., 1969; Downs et al., 1975) and spacecraft (Cain et al., 1972; Fjeldbo et al., 1972) observations have confirmed a smaller mean equatorial radius, and the problem of excess topographic oblateness has fallen into relative obscurity. The prime geophysical problem has become the support, isostatic or otherwise, of the Tharsis ridge and associated volcanic constructs (Carr, 1973). Phillips and Saunders (1975) investigated the isostatic support of three low degree harmonics ( $H_{2,2}$ ,  $H_{3,2}$  and  $H_{3,3}$ ) which contribute significantly to the Tharsis uplift. They conclude that the Tharsis plateau and the adjacent Chryse and Amazonis lowlands are geologically young and only partially compensated, whereas the isostatic support of other, older areas is essentially complete. Recently, Reasenber (1977) has attempted to estimate the influence

of the Tharsis region on the topographic and gravitational oblateness. His basic premise is that, prior to the uplift of Tharsis, Mars was in hydrostatic equilibrium ( $f_g = f_d$ ). By excising Tharsis and the adjacent lowlands, he obtains an estimate of the equilibrium gravitational oblateness  $G_{2,0}(E) = (-1.829 \pm 0.012) \times 10^{-3}$  [ $f_d = (5.027 \pm 0.018) \times 10^{-3}$ ]. He then argues (but not convincingly) that the minor (rather than the mean) equatorial radius should be used in computing the topographic flattening of the pre-Tharsis Mars. Thus, based on Christensen's (1975) topography model, he finds  $H_{2,0}(E) = 3.418 \times 10^{-3}$  [ $f_g = 5.127 \times 10^{-3}$ ]. When calculated this way, the topographic and dynamic flattenings are nearly equal. If this result is correct, it is profound not only in the historical context of showing that the solution to the older excess oblateness problem is to be found in studying Tharsis, but also because this hydrostatic flattening estimate gives a substantially reduced estimate for the moment of inertia of Mars. Previous estimates of  $G_{2,0} = (-1.966 \pm 0.003) \times 10^{-3}$  (Sinclair, 1972) yield  $C/MR_0^2 = 0.3768 \pm 0.0003$ , whereas Reasenberg's estimate yields  $C/MR_0^2 = 0.3660 \pm 0.0010$ . This has important implications for the internal structure of Mars. Most internal models (Jeffreys, 1937; Bullen, 1949; MacDonald, 1962; Anderson, 1972; Johnston et al., 1974) have found a high density mantle and a small core. This new estimate for the moment of inertia would imply a lower mantle density and a larger core. This would appear to be consistent with a more extensively differentiated interior than has previously been supposed.

Another effect which could contribute to the discrepancy between the geometric and dynamic flattenings is a possible secular decrease in the rotation rate of Mars. Hartmann et al. (1975) have discussed possible rotation histories for Mars and suggest on dynamical grounds that it rotated more rapidly in the past. Binder and McCarthy (1972) have suggested a despinning of Mars based on tectonic arguments.

The influx of debris from the asteroid belt could have slowed Mars' rotation at a rate which could be significant over geologic time. In order to account for the entire excess flattening as a fossil bulge left over from a period when Mars rotated more rapidly, the ancient rotation period would be 82050 sec ( $22^{\text{h}} 44^{\text{m}} 30^{\text{s}}$ ) as opposed to the present period of 88642.67 sec ( $24^{\text{h}} 37^{\text{m}} 22.67^{\text{s}}$ ). The slowing of Mars to its present rotation rate by accretion of asteroidal debris would have involved the accumulation of a debris mantle some tens of kilometers thick. This would presumably tend to mask any excess oblateness due to former spin states. However, some degree of despinning by this or other mechanisms may have occurred.

## 2. High Degree Harmonics

In common with the Earth (Balmino et al., 1973) and the Moon (Bills and Ferrari, 1977a), the topography of Mars is dominated by the low degree harmonics. Furthermore, the rate at which the total topographic variance per degree decreases with increasing degree is similar for all three planets. Dimensionless degree variances  $V(H^*;n)$ , of equipotentially referenced Martian topography and the

associated error variances  $W(H;n)$  are displayed in Figure 3.2.

These variances are given by:

$$V(H^*;n) = \sum_{m=0}^n H_{nm}^{*T} H_{nm}^* \quad (3.27)$$

$$W(H;n) = \sum_{m=0}^n \sigma^T(H_{nm}) \sigma(H_{nm})$$

where  $H_{nm}^* = H_{nm} - G_{nm}$ . We note that the topographic variances decrease approximately as

$$V(H^*;n) \doteq \frac{V(H^*;0)}{(n)(n+1)}$$

We further discuss this relationship and its implications in the next chapter. We also note that, in the case of uniformly accurate data, i.e.,  $\sigma[R(\theta, \varphi)] = \sigma_0$ , the degree error variances are (Heiskanen and Moritz, 1967):

$$W(H;n) = \frac{2n+1}{4\pi} \left( \frac{\sigma_0}{R_0} \right)^2 \quad (3.28)$$

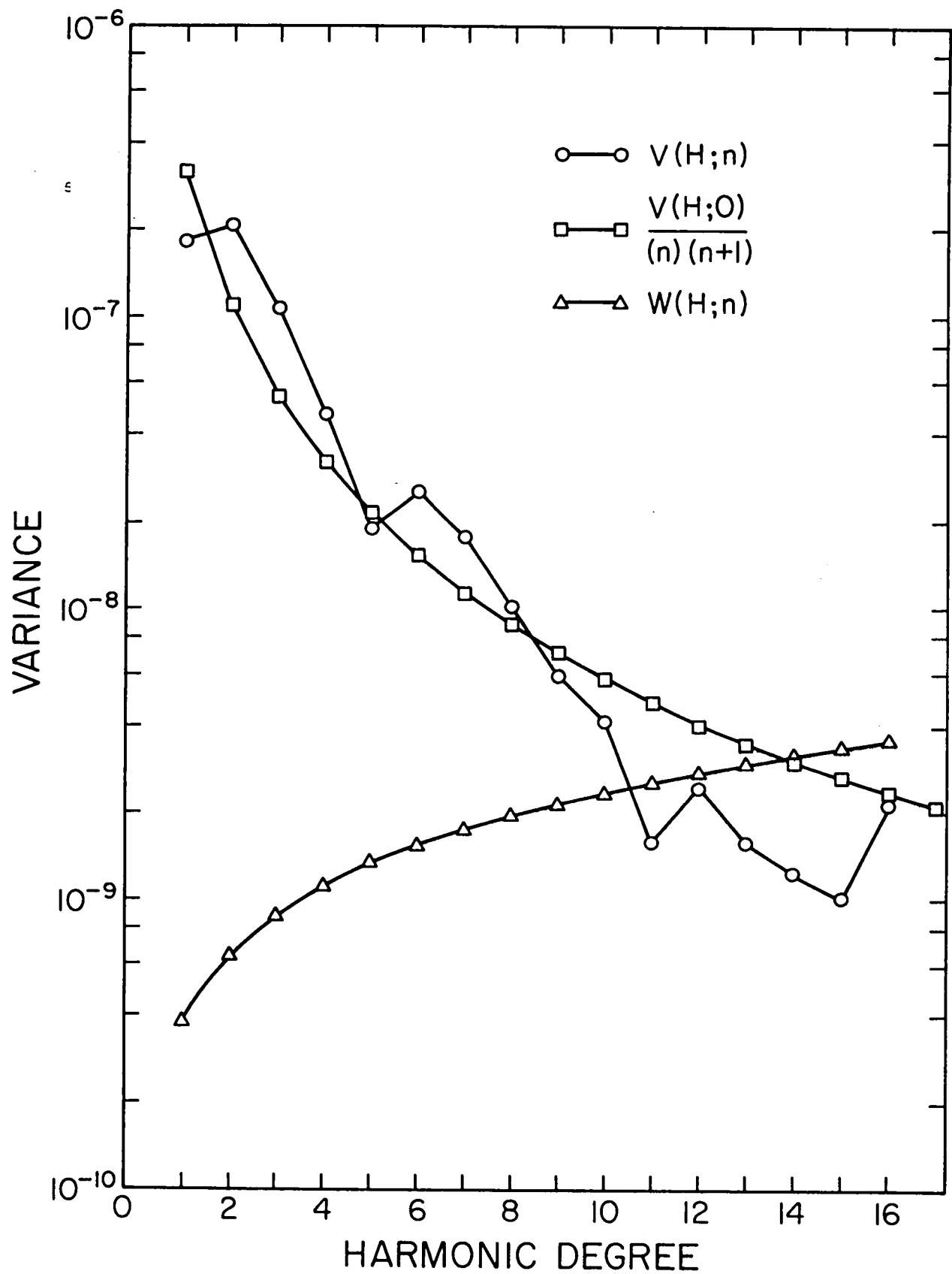
The small departures of our calculated error variances from this simple form are due to the irregular data distribution.

In order to compare our results  $H_{nm}$ , with those of Christensen (1975)  $H'_{nm}$ , we have calculated the degree correlation coefficients (Kaula, 1967)

$$\beta_n(H, H') = \frac{V(H, H'; n)}{[V(H; n) V(H'; n)]^{1/2}} \quad (3.29)$$



FIGURE 3.2 - Martian topographic variance spectrum. The actual dimensionless variances,  $V(H;n)$ , of the equipotentially referenced topography follow quite well the relationship  $V(H;n) = V(H;0)/(n)(n+1)$ . The error variances,  $W(H;n)$ , are approximated by  $4\pi W(H;n) = (2n+1)(\sigma_0/R_0)^2$ .



In Figure 3.3, we present these correlation coefficients and the critical values for various confidence levels. The correlation is seen to be very good. In computing the correlation, we have corrected two typographical errors in Christensen's original paper. The correct values for  $C_{4,1}$  and  $C_{4,2}$  are ten times the values listed (E.J. Christensen, personal communication, 1977).

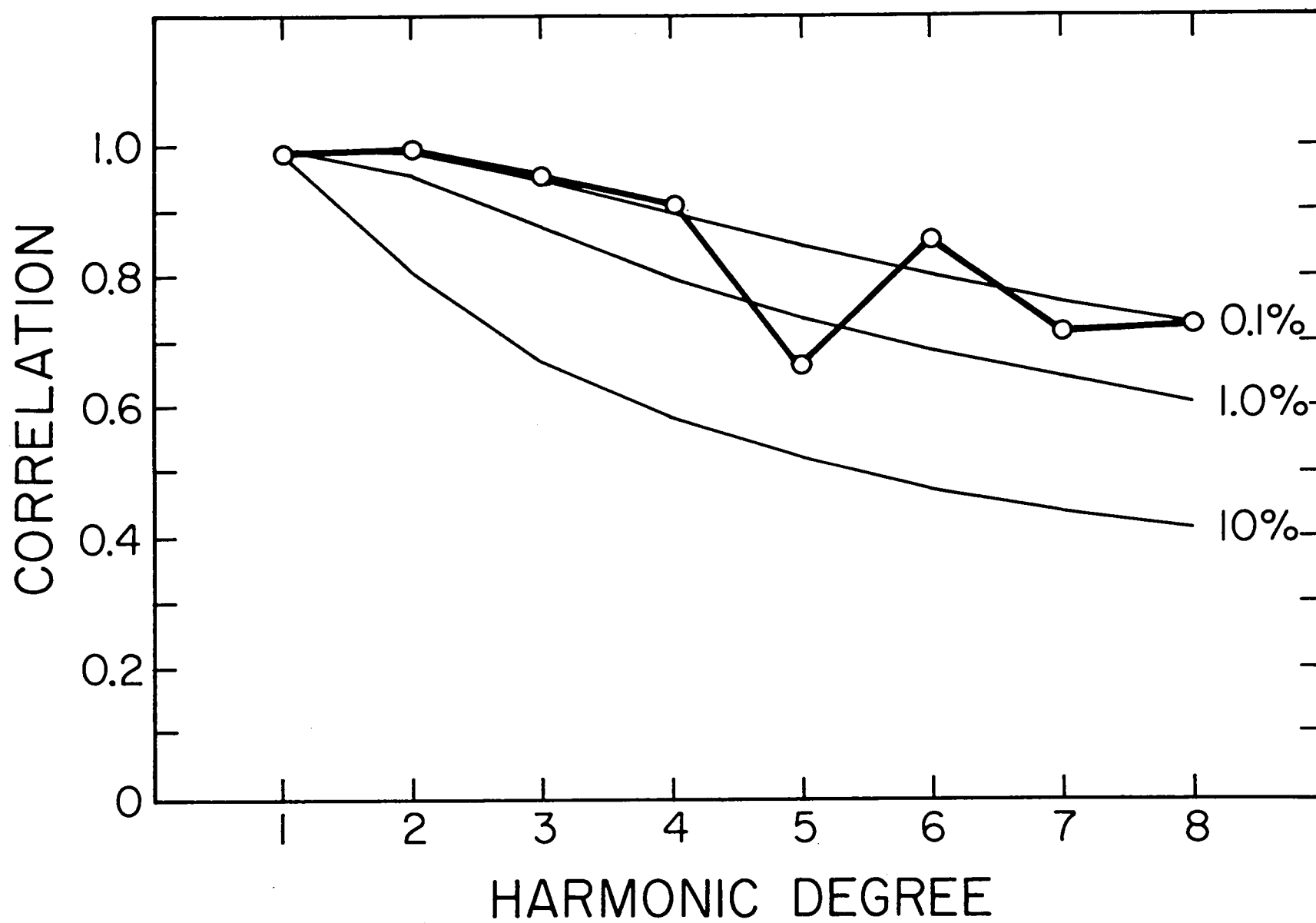
Figure 3.4 is a map of Martian topography derived from our harmonic model. The map elevations are referenced to the 6.1 mb equipressure surface. This surface will be referred to as the reference equipotential or areoid. It is approximated by

$$R'(\theta, \varphi) = R'_0 \left[ 1 + \frac{m}{2} \cos^2(\theta) + \sum_{n=2}^4 \sum_{m=0}^n G_{nm}^T \Lambda_{nm}(\theta, \varphi) \right] \quad (3.30)$$

where  $R'_0 = 3382.946$  km (Wu, 1975) and  $G_{nm}$  are the coefficients of Jordan and Lorell's (1975) gravity model. The rotational contribution can be expressed as an increase in the reference oblateness,  $G'_{2,0} = G_{2,0} - m/3$ , and an increase in the reference mean radius,  $R''_0 = R'_0(1 + m/3) = 3388.099$  km. The heights are thus  $H(\theta, \varphi) = R(\theta, \varphi) - R'(\theta, \varphi)$ , where  $R$  and  $R'$  are given by equations (3.2) and (3.30) respectively.

As expected, we find a considerable increase in resolution over Christensen's (1975) eighth degree model. In fact, our model resolves most major features within areas of adequate data coverage. This was a major objective in the construction of the model and permits comparison with equivalent resolution gravity models for the purpose

FIGURE 3.3 - Correlation coefficients: topography with topography.  
Comparison of present model with Christensen's (1975) model. Confidence levels indicate probability of specified correlation between Gaussian random variables.



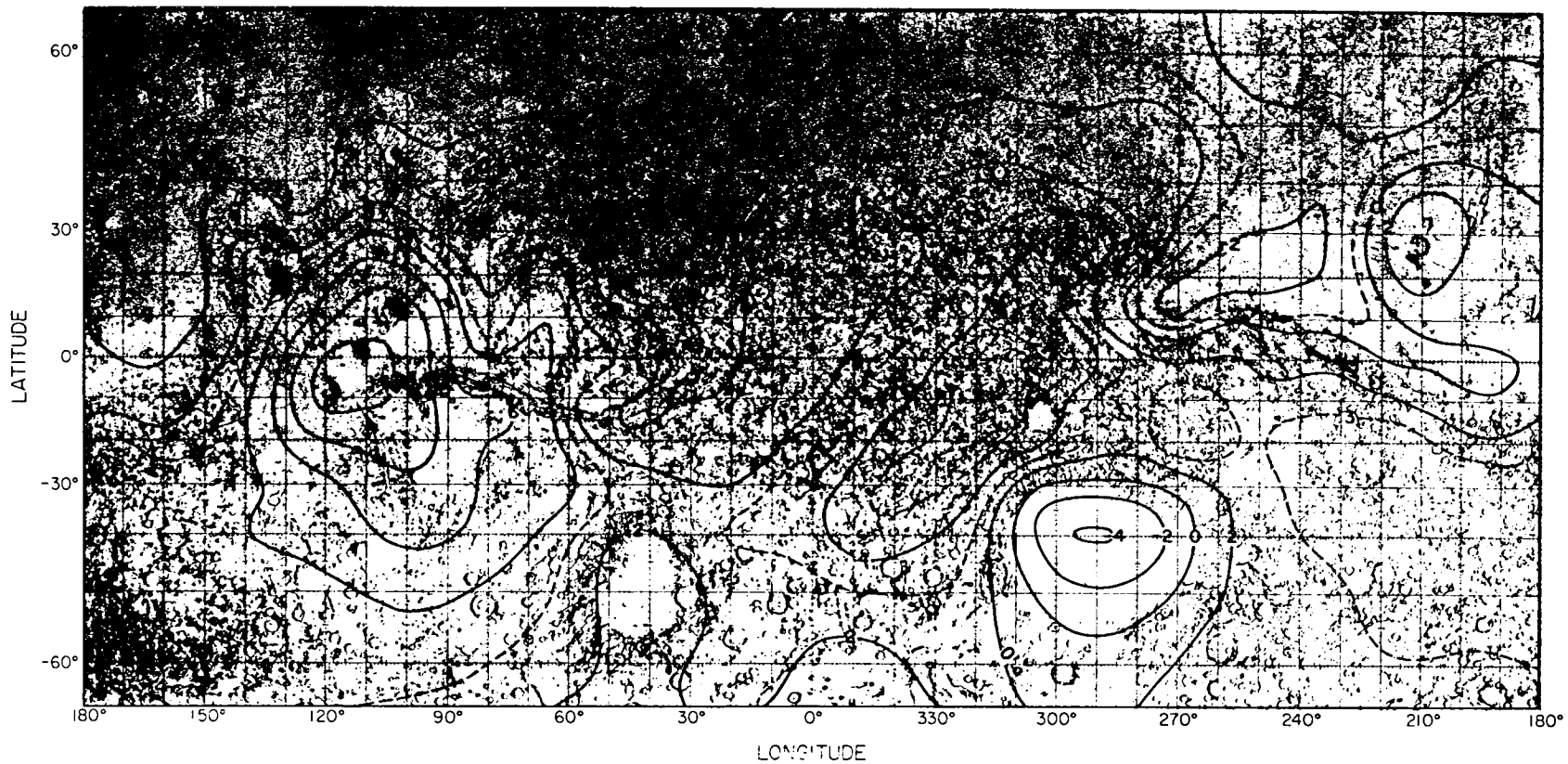


FIGURE 3.4a - Martian topography. Mid-latitudes. Sixteenth degree model. Elevations relative to the 6.1 mb areoid. Main contour interval is 2 km (solid line). Selected 1 km contours indicated (dashed line).

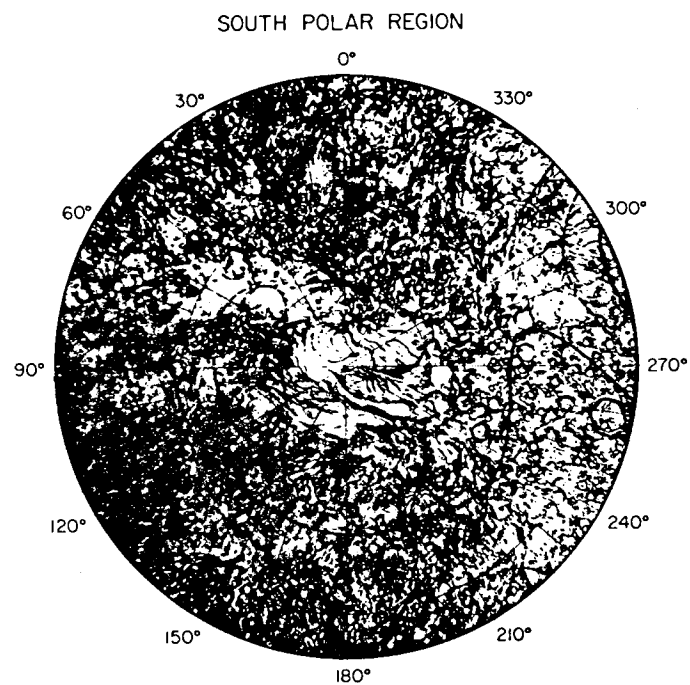
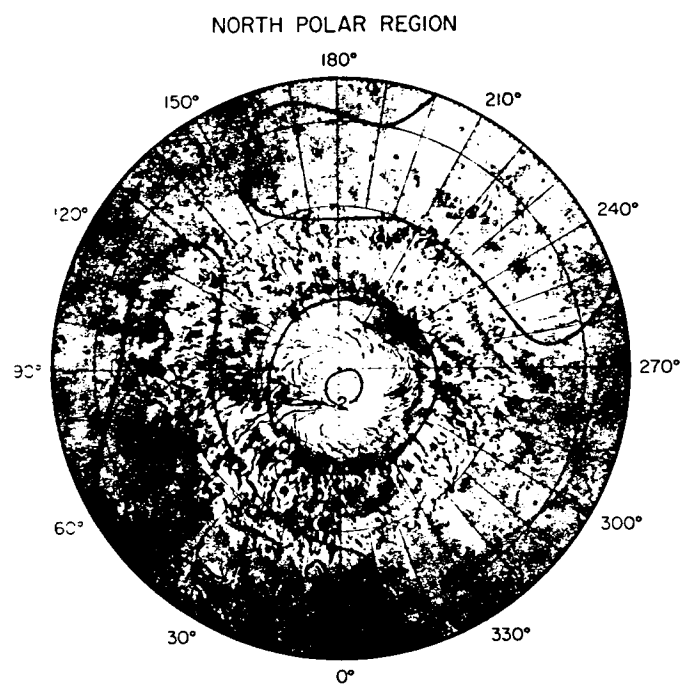


FIGURE 3.4b - Martian topography. Polar regions. See caption of Figure 3.4a.

of determining the internal density. We will now attempt to do just that.

As a first step, we wish to know what correlation, if any, exists between the topography and gravity of Mars. For that purpose, we have calculated degree correlation coefficients  $\beta_n(H,G)$  for  $n \leq 10$  of our topography model with the gravity models of Sjogren et al. (1975) and Laing (1977, private communication). These are presented in Figure 3.5. It is seen that the low degree correlations are significant. Thus, the low degree gravity harmonics appear to be primarily due to surface height variations and only secondarily due to density anomalies. The decrease in correlation of the higher degree harmonics is presumably due to the relatively poor determination of the relevant coefficients, but may reflect an actual property of the planet.

The observed gravitational anomalies may be ascribed to contributions from both lateral density variations and surface topography. The topography of a planet with crustal density  $\rho_o$  and mean density  $\bar{\rho}$  gives rise to gravitational potential perturbations (MacRobert, 1967):

$$\Delta\Phi(R,\theta,\varphi) = \frac{GM}{R_o} \sum_{n=1}^{\infty} \sum_{m=0}^n \left[ \frac{R_o}{R} \right]^{n+1} \Delta G_{nm}^T \Lambda_{nm}(\theta,\varphi) \quad (3.31)$$

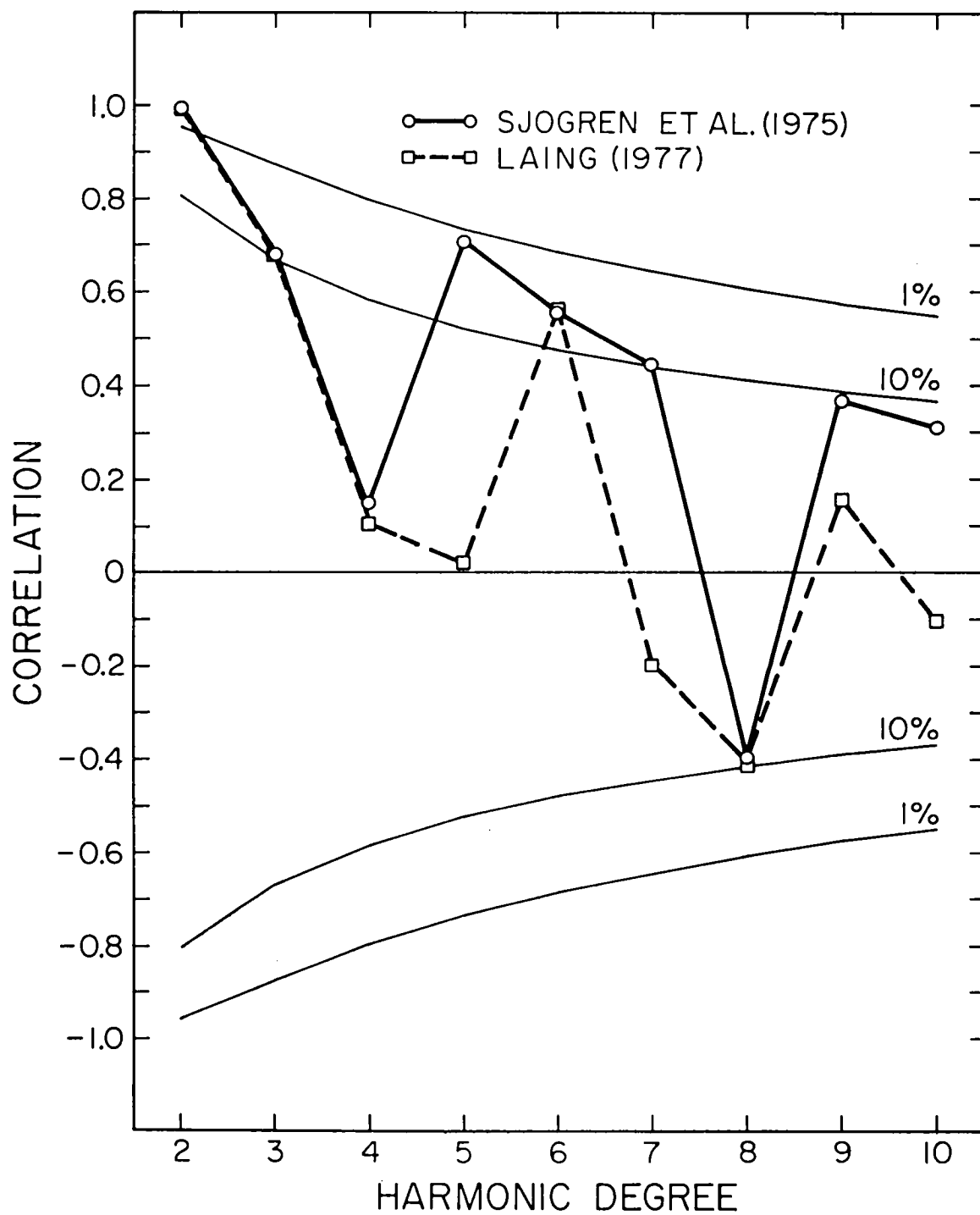
where

$$\left( \frac{2n+1}{3} \right) \bar{\rho} \Delta G_{nm} = \rho_o H_{nm}$$

The difference between the observed gravity and the topographic



FIGURE 3.5 - Correlation coefficients: topography with gravity.  
Comparison of present topography model with gravity models of  
Sjogren et al. (1975) and P.A. Laing (1977, personal communication).  
The low degree harmonics are significantly correlated.



correction, known as the Bouguer anomaly, is thus a measure of the extent of lateral density variation.

Figure 3.6 is a map of the Martian Bouguer anomaly evaluated on the areoid. This is calculated as the vertical component of the gradient of the Bouguer anomalous potential on the reference surface (Heiskanen and Moritz, 1967)

$$\Delta g_B(R, \theta, \varphi) = \frac{GM}{R_o^2} \sum_{n=1}^{10} \sum_{m=0}^n \left[ \frac{R_o}{R} \right]^n (n-1) B_{nm}^T \Lambda_{nm}(\theta, \varphi) \quad (3.32)$$

where

$$B_{nm} = G_{nm} - \Delta G_{nm}$$

and we have assumed a surface density  $\rho_o = 2.9 \text{ gm cm}^{-3}$ . The series is truncated to tenth degree because of limitations of the gravity model (Sjogren et al., 1975).

As was anticipated in our discussion of the correlation coefficients, the low degree harmonics of the gravitational field are produced primarily by surface height variations, and only secondarily by lateral density variations. However, it is interesting to note the large negative anomalies associated with Phlegra Montes (35°N, 200°W), near the Elysium volcanics, and with Tharsis Montes (5°N, 110°W) another high volcanic province. This latter feature is flanked by prominent positive anomalies in Amazonis Planitia (5°N, 160°W) and Chryse Planitia (20°N, 40°W). Other significant positive anomalies are in the low regions of Hellas Planitia (35°S, 290°W)

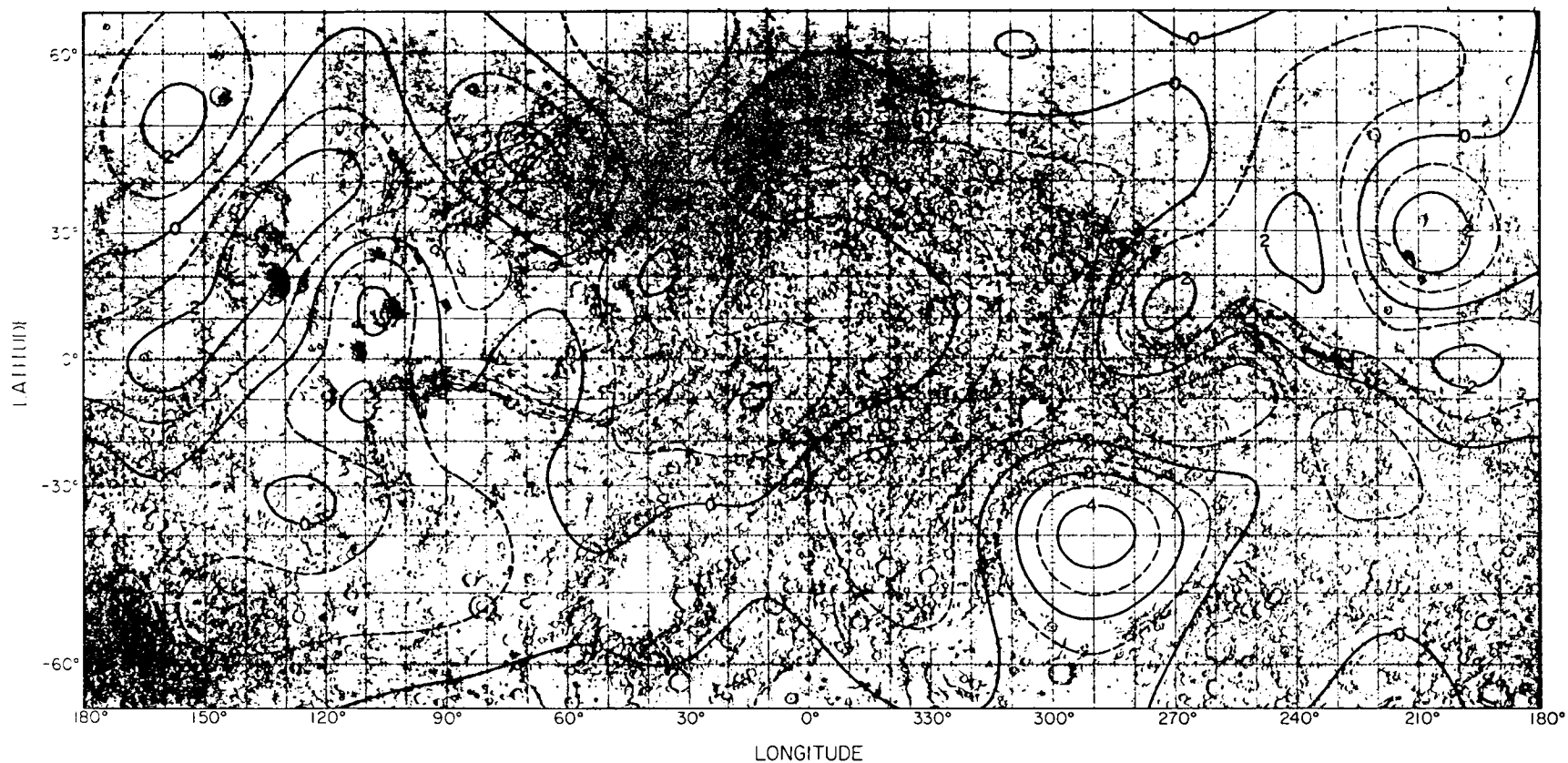


FIGURE 3.6 - Martian Bouguer gravity anomaly. Tenth degree model.  
 Evaluated on areoid. Contour interval is 100 mGal =  $0.1 \text{ cm sec}^{-2}$ .  
 Free-air gravity from Sjogren et al. (1975).

and Isidis Planitia (15°N, 270°W). Most of the prominent negative anomalies are associated with topographic highs, and conversely. This implies some degree of isostatic compensation. To ascertain the degree of compensation, we need to know how the crustal thickness varies with elevation and location on the surface of Mars.

Recent seismic results (Anderson et al., 1977), although tentative, can be interpreted as indicative of a crustal thickness of 15 km in the vicinity of the second Viking landing site (47°89N, 225°86W). We can estimate the variation of crustal thickness implied by the Bouguer anomaly map on the assumption that all lateral density variations occur as undulations on the crust-mantle interface (Khan, 1977; Bills and Ferrari, 1977b). These undulations are determined from the relation

$$\left(\frac{2n+1}{3}\right) \bar{\rho}_G = \rho_o H_{nm}^{(o)} + \Delta\rho \xi^{n+3} H_{nm}^{(1)} \quad (3.33)$$

where  $H_{nm}^{(o)}$  and  $H_{nm}^{(1)}$  define the shape of the surface topography and crust-mantle interface, respectively. The mean normalized radius of the interface is  $\xi = R/R_o$ . The crustal density and density contrast across the interface are  $\rho_o$  and  $\Delta\rho$ , respectively. These latter three parameters are unknown.

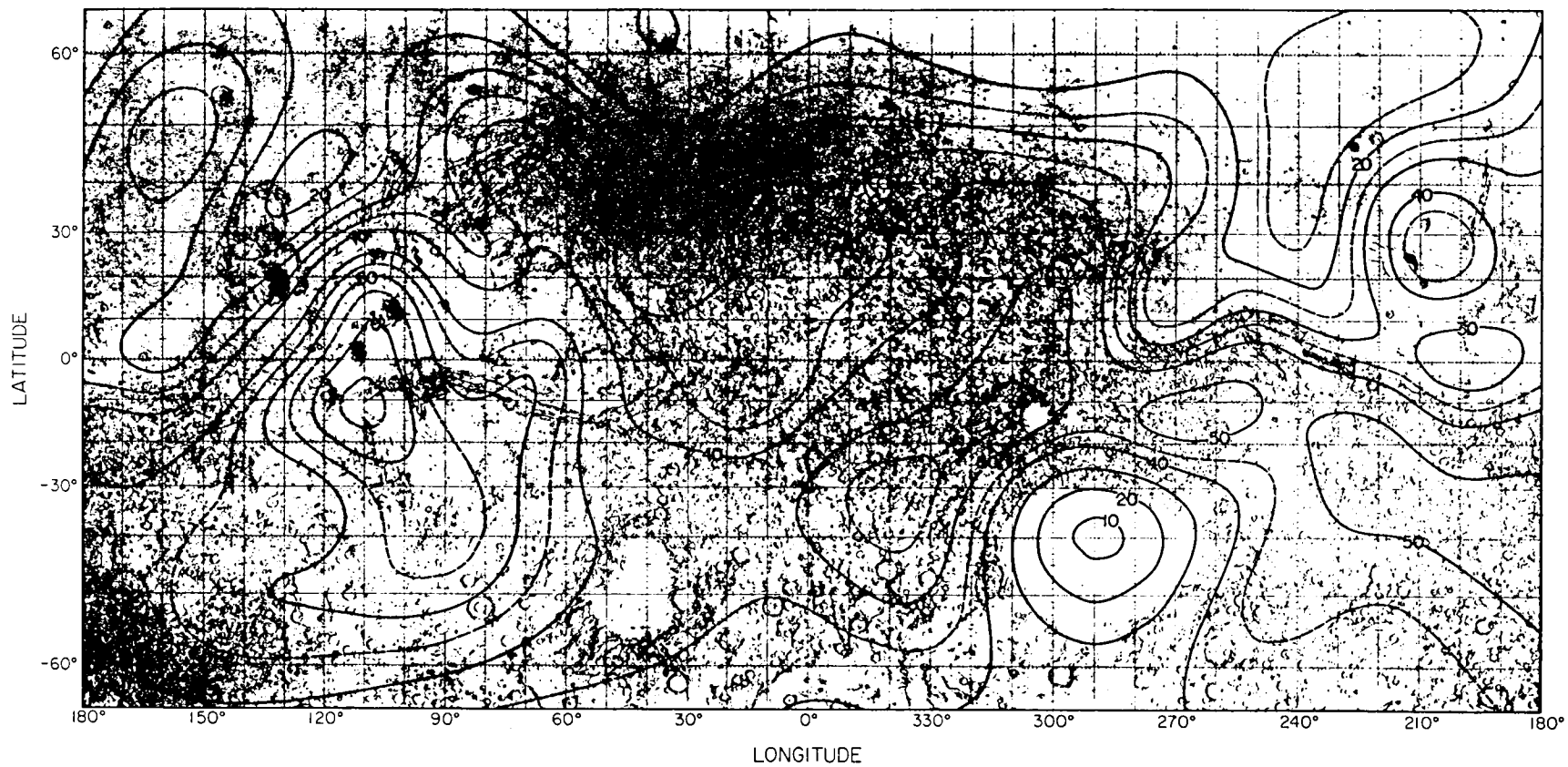
We have examined a number of cases and will discuss three of them in particular. For this discussion, we have assumed an upper mantle density of  $\rho_o + \Delta\rho = 3.5 \text{ gm cm}^{-3}$  (Anderson, 1972). We then consider the three cases  $\rho_o = 2.7, 2.8$  and  $2.9 \text{ gm cm}^{-3}$ , which span the

range of probable crustal densities. The mean crustal thickness was varied in each case until a 15 km thickness was obtained at the Viking landing site. The values obtained are 34, 36 and 40 km respectively. The resulting map for the high crustal density case ( $\rho_0 = 2.9 \text{ gm cm}^{-3}$ ) is shown in Figure 3.7. The maps corresponding to the other cases are qualitatively very similar. However, when the crustal density is low and the crust-mantle density contrast is accordingly high, smaller amplitude undulations on the crust-mantle interface are required to produce the observed Bouguer anomalies. For example, the maximum crustal thickness was obtained in all cases under Tharsis. These maxima were 61, 67, and 77 km, respectively. Likewise, all three models exhibited a minimum crustal thickness under Hellas (10, 9 and 8 km).

Because the Viking crustal thickness estimate (Anderson et al., 1977) is based on a single anomalous event that cannot be proven to be of internal origin and may, in fact, be a wind event, we have also considered models based on the assumption of zero crustal thickness in Hellas. These yield minimum mean crustal thickness estimates for a given density regime. For the densities previously considered,  $\rho_0 = 2.7, 2.8$  and  $2.9 \text{ gm cm}^{-3}$ , the mean crustal thickness estimates are 23, 24 and 32 km, respectively. The corresponding crustal thickness estimates under Tharsis are 50, 58 and 68 km, and at the Viking landing site 5, 6 and 7 km, respectively.

None of these models is completely isostatic. However, it was found that the mean squared super-isostatic stress at the crust

FIGURE 3.7 - Martian crustal thickness. Tenth degree model. Gravity from Sjogren et al. (1975). Assumed crustal density is  $2.9 \text{ gm cm}^{-3}$ , crust-mantle density contrast is  $0.6 \text{ gm cm}^{-3}$  and mean crustal thickness is 40 km. Second Viking landing site ( $47^{\circ}89\text{N}$ ,  $225^{\circ}86\text{W}$ ) is indicated by dot. Crustal thickness at that location tentatively estimated from Viking seismic data (Anderson et al., 1977).





mantle interface was least for models with low crustal density, thin crust and high density contrast across the interface. The range of models we considered indicate that Tharsis is 60-65% compensated, whereas, Hellas is 95-105% compensated. A complete discussion of Martian isostasy is beyond the scope of this paper.

## REFERENCES

- Anderson, D.L. (1972). Internal constitution of Mars. J. Geophys. Res. 77, 789-795.
- Anderson, D.L., Miller, W.F., Latham, G.V., Nakamura, Y., Duennebier, F.K., Lazarewicz, A., Toksöz, M.N., Dainty, A., Kovach, R.L., and Knight, T.C.D. (1977). Seismology on Mars. Submitted to J. Geophys. Res.
- Balmino, G., Lambeck, K., and Kaula, W.M. (1973). A spherical harmonic analysis of the Earth's topography. J. Geophys. Res. 78, 478-481.
- Bills, B.G., and Ferrari, A.J. (1977a). A harmonic analysis of lunar topography. Icarus, 31, 244-259.
- Bills, B.G., and Ferrari, A.J. (1977b). A lunar density model consistent with topographic, gravitational, librational and seismic data. J. Geophys. Res. 82, 1306-1314.
- Binder, A.B., and McCarthy, D.W. (1972). Mars: The lineament systems. Science 176, 279-281.
- Born, G.H. (1974). Mars physical parameters as determined from Mariner 9 observations of the natural satellites and doppler tracking. J. Geophys. Res. 79, 4837-4844.
- Bullen, K.E. (1949). On the constitution of Mars. M. Not. Roy. Astr. Soc. 109, 688-692.
- Cain, D.L., Kliore, A.J., Seidel, B.L., and Sykes, M.J. (1972). The shape of Mars from the Mariner 9 occultations. Icarus 17, 517-524.

- Camichel, H. (1954). Determination photographique du pole de Mars,  
de son diamètre et des coordonnées areographiques. Bull. Astron.  
18, 83-191.
- Carlson, A.E., and Helmsen, M. (1969). Validity of topography  
represented by truncated series of surface harmonics. Icarus  
10, 57-65.
- Carr, M.H. (1973). Volcanism on Mars. J. Geophys. Res. 78, 4049-4062.
- Christensen, E.J. (1975). Martian topography derived from occultation,  
radar, spectral and optical measurements. J. Geophys. Res. 80,  
2909-2913.
- Darwin, G.H. (1877). On an oversight in the mécanique celeste and on  
the internal densities of the planets. M. Not. Roy. Astr. Soc.  
37, 77-89.
- Darwin, G.H. (1879). On the bodily tides of viscous and semi-elastic  
spheroids. Phil. Trans. Roy. Soc. 170, 1-35.
- Darwin, G.H. (1900). The theory of the figure of the Earth carried to  
the second order of small quantities. M. Not. Roy. Astr. Soc.  
60, 82-124.
- Dollfus, A. (1972). New optical measurements of planetary diameters -  
Part IV: Mars. Icarus 17, 525-539.
- Downs, G.S., Reichley, P.E., and Green, R.P. (1975). Radar measure-  
ments of Martian topography and surface properties: The 1971  
and 1973 oppositions. Icarus 26, 273-312.

- Fjeldbo, G., Kliore, A., and Seidel, B. (1972). Bistatic radar measurements of the surface of Mars with Mariner 1969. Icarus 16, 502-508.
- Hartmann, W.K., Davis, D.R., Chapman, C.R., Soter, S., and Greenberg, R. (1975). Mars: Satellite origin and angular momentum. Icarus 25, 588-594.
- Hartwig, E. (1899). Determination of the diameter and polar compression of the planet Mars. M. Not. Roy. Astr. Soc. 59, 488-491.
- Heiskanen, W.A., and Moritz, H. (1967). Physical Geodesy. W.H. Freeman, San Francisco.
- Heyl, P.R., and Chrzanowski, P. (1942). A new determination of the constant of gravitation. J. of Research of the Nat. Bur. of Standards 29, 1-31.
- Jeffreys, H. (1937). The density distribution in the inner planets. M. Not. Roy. Astr. Soc., Geophys. Suppl. 4, 62-71.
- Johnston, D.H., McGetchin, T.R., and Toksöz, M.N. (1974). The thermal state and internal structure of Mars. J. Geophys. Res. 79, 3959-3971.
- Jordan, J.F., and Lorell, J. (1975). Mariner 9, an instrument of dynamical science. Icarus 25, 146-165.
- Kaula, W.M. (1967). Theory of statistical analysis of data distributed over a sphere. Rev. Geophys. 5, 83-107.
- Khan, M.A. (1977). Depth of sources of gravity anomalies. Geophys. J. Roy. Astr. Soc. 48, 197-209.

- Knopoff, L. (1964). The convection current hypothesis. Rev. Geophys.  
2, 89-122.
- Lamar, D.L. (1962). Optical ellipticity and internal structure of  
Mars. Icarus 1, 258-265.
- Lawson, C.L., and Hanson, R.J. (1974). Solving Least Squares Problems.  
Prentice-Hall, Englewood Cliffs, N.J.
- Lingenfelter, R.E., and Schubert, G. (1973). Evidence for convection  
in planetary interiors from first-order topography. The Moon  
7, 172-180.
- Loomis, A.A. (1965). Some geologic problems of Mars. Geo. Soc. Am.  
Bull. 76, 1083-1104.
- Lorell, J., Born, G.H., Christensen, E.J., Esposito, P.B., Jordan, J.F.,  
Laing, P.A., Sjogren, W.L., Wong, S.K., Reasenberg, R.D., Shapiro,  
I.I., and Slater, G.L. (1973). Gravity field of Mars from  
Mariner 9 Tracking Data. Icarus 18, 304-316.
- Love, A.E.H. (1911). Some Problems of Geodynamics. pp. 111-125,  
Dover Publications Inc., New York.
- MacDonald, G.J.F. (1962). On the internal constitution of the inner  
planets. J. Geophys. Res. 67, 2945-2974.
- MacRobert, T.M. (1967). Spherical Harmonics. Pergamon Press,  
New York.
- McKenzie, D.P. (1968). The influence of the boundary conditions  
and rotation on convection in the Earth's mantle. Geophys. J.  
Roy. Astr. Soc. 15, 457-500.

- Munk, W.H., and MacDonald, G.J.F. (1960). The Rotation of the Earth.  
Cambridge Univ. Press, London.
- Mutch, T.A., and Saunders, R.S. (1976). The geologic development of  
Mars: A review. Space Sci. Rev. 19, 3-57.
- Pettengill, G.H., Counselman, C.C., Rainville, L.P., and Shapiro, I.I.  
(1969). Radar measurement of Martian topography. Astron. J.  
74, 461-482.
- Phillips, R.J., and Saunders, R.S. (1975). The isostatic state of  
Martian topography. J. Geophys. Res. 80, 2893-2898.
- Reasenber, R.D. (1977). The moment of inertia and isostasy of Mars.  
J. Geophys. Res. 82, 369-375.
- Reasenber, R.D., Shapiro, I.I., and White, R.D. (1975). The gravity  
field of Mars. Geophys. Res. Lett. 2, 89-92.
- Roberts, P.H. (1968). On the thermal instability of a rotating  
fluid sphere containing heat sources. Phil. Trans. Roy. Soc.  
London A263, 93-117.
- Roberts, P.H., and Ursell, H.D. (1960). Random walk on a sphere and  
on a Riemannian manifold. Phil. Trans. Roy. Soc. London A252,  
317-356.
- Runcorn, S.K. (1967). The problem of the figure of Mars. In Mantles  
of the Earth and Terrestrial Planets (S.K. Runcorn, Ed.).  
pp. 425-430. Wiley, London.
- Schur, W. (1897). Determination of the diameter and compression of  
the planet Mars. M. Not. Roy. Astr. Soc. 57, 150-154.

- Sinclair, A.J. (1972). The motion of the satellites of Mars. M. Not. Roy. Astr. Soc. 155, 249-274.
- Sjogren, W.L., Lorell, J., Wong, L., and Downs, W. (1975). Mars gravity field based on a short-arc technique. J. Geophys. Res. 80, 2899-2908.
- Struve, H. (1895). A determination of the oblateness and equator of Mars. Astron. Nachr. 138, 217-228.
- Tozer, D.C. (1972). The present thermal state of the terrestrial planets. Phys. Earth Planet. Interiors 6, 182-197.
- Trumpler, R.J. (1927). Observations of Mars at the opposition of 1924. Lick Obs. Bull. 13, 19-45.
- Urey, H.C. (1950). The structure and chemical composition of Mars. Phys. Rev. 80, 295-302.
- de Vaucouleurs, G. (1964). Geometric and photometric parameters of the terrestrial planets. Icarus 3, 187-235.
- Weertman, J. (1970). The creep strength of the Earth's mantle. Rev. Geophys. Space Phys. 8, 145-168.
- Wilkins, G.A. (1967). The determination of the mass and oblateness of Mars from the orbits of its satellites. In Mantles of the Earth and Terrestrial Planets (S.K. Runcorn, Ed.). pp. 77-84. Wiley, London.
- Woolard, E.W. (1944). The secular perturbations of the satellites of Mars. Astron. J. 51, 33-36.
- Wu, S.S.C. (1975). Topographic mapping of Mars. U.S. Geol. Survey Interagency Report 63.

#### IV. TOPOGRAPHIC VARIANCE SPECTRA OF THE EARTH, MOON AND MARS: AN EQUILIBRIUM MODEL

##### A. INTRODUCTION

The surface topography of a solid planet or satellite may be thought of as the superposition of two components; one deterministic, the other stochastic. The nature of the deterministic component (due to influences such as rotational and tidal deformation) has been extensively studied and is rather well understood (see e.g., Kopal, 1960; Chandrasekhar, 1969). In such analyses, the solid planets are usually modeled as fluids in equilibrium with simple deformational forces possessing axial or radial symmetry. The attention this deterministic approach has received is well deserved, since for most planets and satellites, the basic spherical shape, as well as the principal departures from sphericity, are adequately understood in this paradigm. However, on a local or even regional scale, the topography is dominated by its stochastic component. Though the individual constituent features of this topography (ridges, mountains, craters, etc.) have received attention previously and are fairly well understood in isolation, it is the random superposition of many such features, each basically deterministic, which produces the stochastic nature of the topography.

A general lack of understanding and appreciation for this aspect of the problem is well illustrated by the statement of Cook (1973) that "the shape of the solid surface of the Earth is very irregular and of no scientific interest."



The principal objective of this chapter is to isolate the stochastic components in the topography of the Earth, Moon and Mars (with brief reference to Venus) and gain a better understanding of their properties. We will find interesting statistical similarities among these rather diverse surfaces. In particular, we will consider the hypothesis that the variance spectra of all solid planets have the form

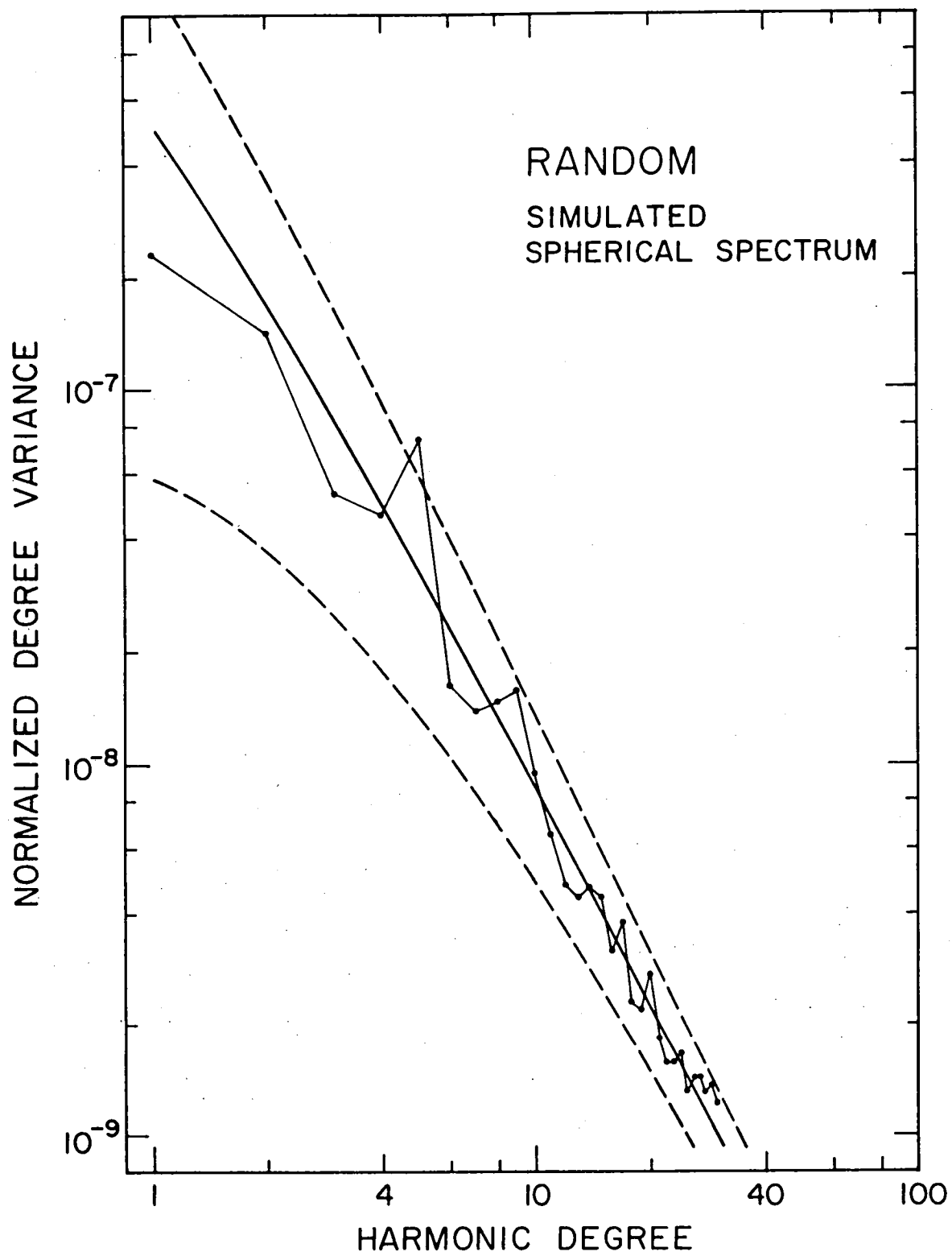
$$V(H;n) = \frac{V(H;0)}{(n)(n+1)} \quad (4.1)$$

for all  $n$  such that  $R_0/n \leq 2000$  km, and that furthermore, the individual harmonic coefficients  $H_{nmi}$  are Gaussian random variables  $N(0, \sigma_n^2)$  with mean  $\mu = 0$  and variance

$$\sigma_n^2 = \frac{V(H;n)}{2n+1} \quad (4.2)$$

For comparison with later observations, in figure 4.1 we present a topographic variance spectrum constructed according to this hypothesis. For each harmonic degree  $n$ :  $1 \leq n \leq 30$ , the  $2n+1$  harmonic coefficients  $H_{nmi}$  were assigned values drawn from a population of Gaussian  $N(0, \sigma_n^2)$  random variables. The fluctuations of the resultant sample variances relative to the population variances are distributed as  $\chi^2/(2n+1)$ , i.e., chi-square over degrees of freedom with  $2n+1$  degrees of freedom (see Appendix B). The critical values for the 90% confidence level are indicated. There is thus a 10% chance that the sample variance will fall outside these limits if the population variance is as specified by the model. The value of  $V(H;0) = 10^{-6}$  was chosen to be representative of actual planetary values.

4.1 Simulated spherical topographic variance spectrum. Harmonic coefficients are  $N(0, \sigma_n^2)$  Gaussian random variables with  $\sigma_n^2 = 10^{-6}/(n)(n+1)$ . Points are sample variances. Solid line is theoretical variance. Dotted lines indicate critical values for 90% confidence level.



In the remainder of the chapter, we will discuss some observations relevant to this hypothesis, and then examine a number of possible explanations for this peculiar behavior. Lastly, we will consider some of its implications and point out some directions for future research.

## B. OBSERVATIONS

### 1. Variance Spectra

#### Earth

Vening-Meinesz (1951) was apparently the first to call attention to the fact that the Earth's topographic variance spectrum, as obtained from Prey's (1922) harmonic analysis, is approximated by equation (4.1) at least for harmonic degrees  $n$ :  $1 \leq n \leq 16$ . We shall therefore refer to this ideal form as the Vening-Meinesz spectrum. In a later paper (Vening-Meinesz, 1962), he showed that an unpublished harmonic analysis by G.J. Bruins, with  $n \leq 31$ , further supports and extends the observed range of validity of his initial observation. Balmino et al. (1973) have performed a harmonic analysis complete through degree and order 36. In Figure 4.2, we present the degree variances from this analysis compared with the Vening-Meinesz spectrum. The value of  $V(H;0)$  was adjusted to optimize the match with the actual spectrum.

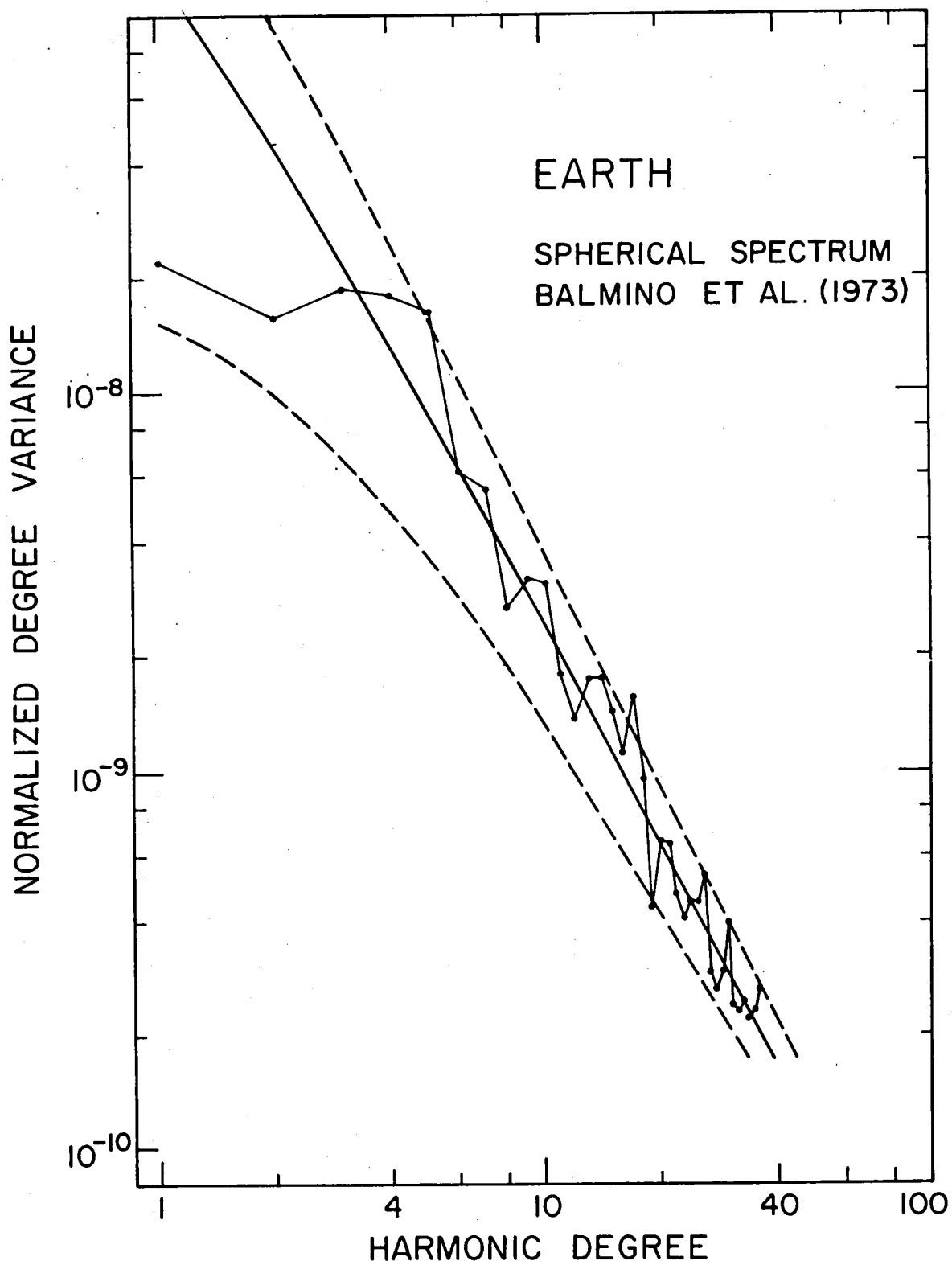
We will often loosely refer to  $V(H;0)$  as the total variance. However, this is only strictly true for the pure Vening-Meinesz spectrum. In most cases,  $C(H;0) \leq R_0^2 V(H;0)$  (see Appendix D).

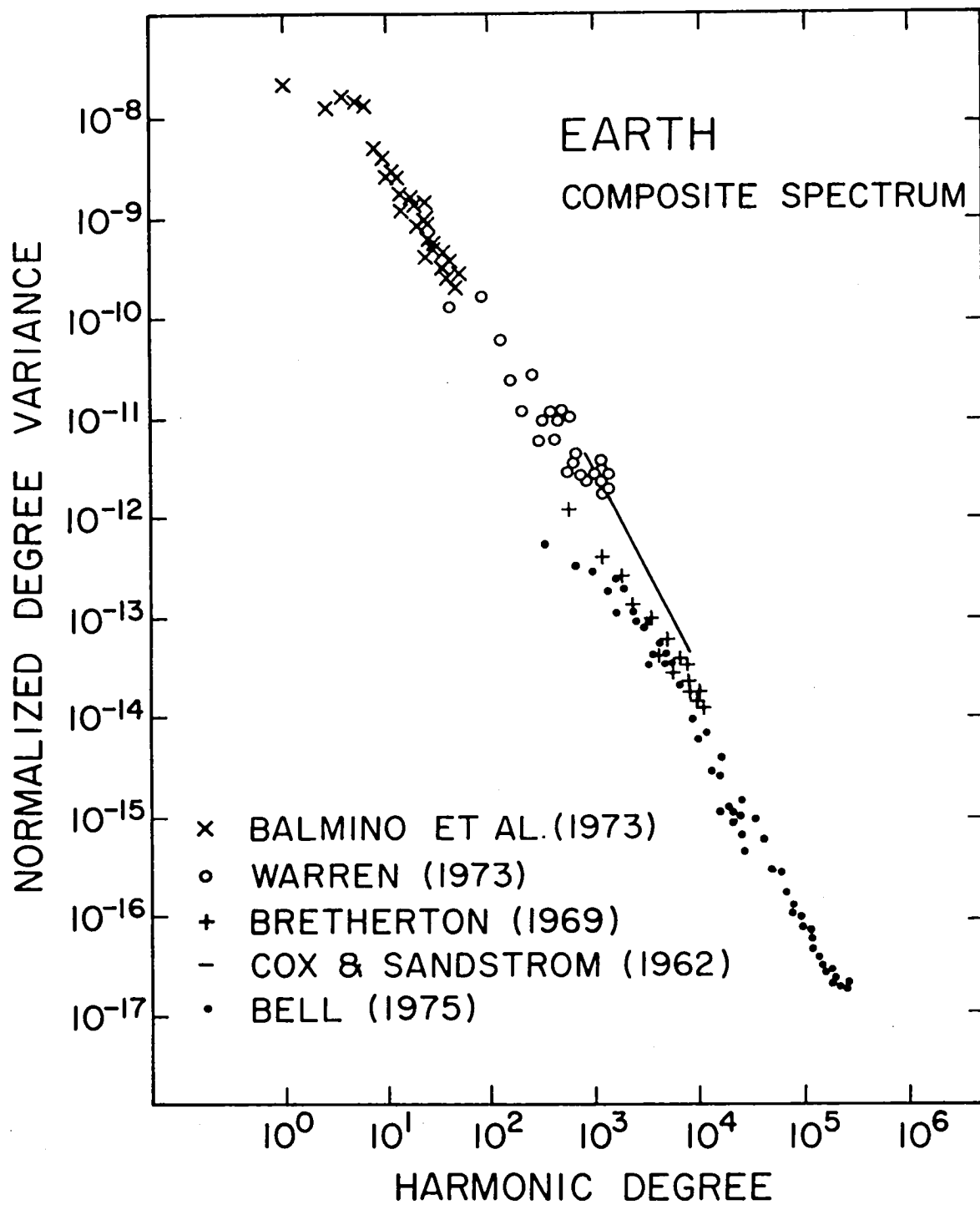
It is easily seen that the largest departures from the Vening-Meinesz spectral form are for the first few harmonic degrees. Though the confidence limits for the low degree harmonics are quite wide, it still seems significant that for the Earth, Mars and Venus, the low degree variances are consistently deficient relative to our expectations. We shall return to this point later. First, we want to find out what happens at the high frequency end of the spectrum.

For sufficiently high spatial frequencies, spherical harmonic analysis becomes computationally impractical. For small enough areas, the curvature of the earth may be neglected and a simple planar Fourier analysis is quite adequate. Several such analyses have been performed over a wide spectral range (see e.g., Cox and Sandstrom, 1962; Krause and Menard, 1965; Bretherton, 1969; Warren, 1973; Pike and Rozema, 1975). Recently, Bell (1975) has compiled the results of several previous analyses and, in conjunction with his own analysis of the oceanic abyssal hills province, has shown a rather impressive agreement between various spectral estimates over a cumulative spatial frequency range corresponding to harmonic degrees  $n$ :  $1 \leq n \leq 300,000$ . Even more impressive is the fact that these spectral estimates approximate the Vening-Meinesz spectrum over essentially the entire range (see Figure 4.3).

Since the topography of the Earth is dominated by the continent-ocean dichotomy, particularly in the low degree harmonics, it is possible to investigate the history of the Earth's topography spectrum from reconstructions of previous continental configurations

- 4.2 Earth - Spherical topographic variance spectrum. Harmonic coefficients are from Balmino et al. (1973). Points are computed degree variances. Solid line is Vening-Meinesz spectrum:  $V(H;n) = 2.6 \times 10^{-7} / (n)(n+1)$ . Dotted lines indicate critical values for 90% confidence level.
- 4.3 Earth - Composite topographic variance spectrum. Adapted from Bell (1975). Used by permission. The smallest scale features (harmonic degree  $n \doteq 3 \times 10^5$ ) have dimensions  $L = 2\pi R_o / n \doteq 120$  m.







(Dietz and Holden, 1970). A preliminary analysis of this sort indicates a shift of spectral energy from the lowest degrees ( $1 \leq n \leq 3$ ) to the higher harmonics as the continents have dispersed. This may be relevant to the previously mentioned fact that low degree variances are deficient relative to the higher harmonics.

#### Moon

Due to the paucity and uneven distribution of lunar topographic data, the variance spectrum calculated from harmonic coefficient estimates is not as representative of the true variance spectrum as was the case for the Earth. Nevertheless, recent harmonic analyses (Goudas, 1971; Chuikova, 1976; Bills and Ferrari, 1977a) indicate that lunar topography is also dominated by the low degree harmonics, and even suggest that the spectrum may approximate the Vening-Meinesz form. See Figure 4.4 for a comparison of the spectrum from Bills and Ferrari (1977a) with the Vening-Meinesz theoretical spectrum. Though the agreement is not outstanding, we should not reject the hypothesis that the Moon has a topographic variance spectrum similar to the Earth's until we examine some further evidence, particularly considering the amount of spectral distortion induced by the irregular data distribution - in spite of the efforts described in Chapter I to compensate for this effect.

As an independent estimation of the variance spectrum and to extend it to higher harmonic degree, a simple one-dimensional Fourier analysis has been performed on complete orbital segments of laser

altimetry data from Apollo missions 15, 16 and 17 (Kaula et al. 1972, 1973, 1974). The resultant spectra were then averaged and are displayed in Figure 4.5. This technique of averaging raw spectra provides statistical stability at low harmonic degree, and is equivalent to smoothing the spectra with a Bartlett window (Jenkins and Watts, 1968). Since the effective domain of these data is a circle rather than a sphere, the appropriate comparison spectrum is

$$V(H;n) = \frac{V(H;0)}{n^2} \quad (4.3)$$

rather than equation (4.1) (see Appendix A). It can be seen that, at least in the range  $1 \leq n \leq 32$ , the variance spectrum of the Moon conforms to the Vening-Meinesz pattern.

A further, more stringent test of the applicability of the Vening-Meinesz spectrum to the Moon at high harmonic degrees involves comparison of r.m.s. slopes at various slope lengths with model values. As is shown in Appendix G, the mean square slope between points a distance  $L = R_0 \gamma$  apart on a planet characterized by a Vening-Meinesz spectrum is

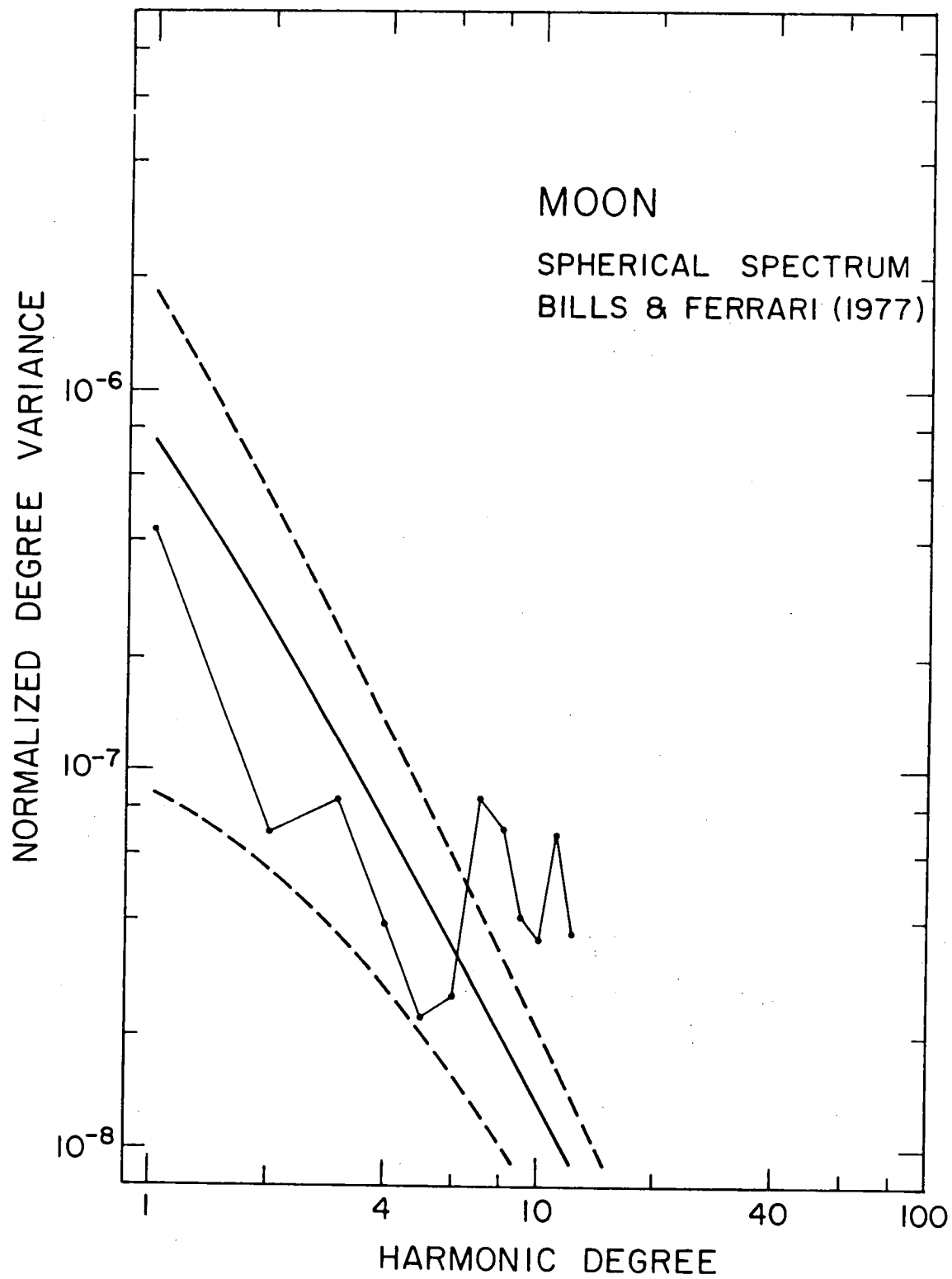
$$S^2(\gamma) = 4 V(H;0) \ln [1 + \sin(\gamma/2)] / \gamma^2 \quad (4.4)$$

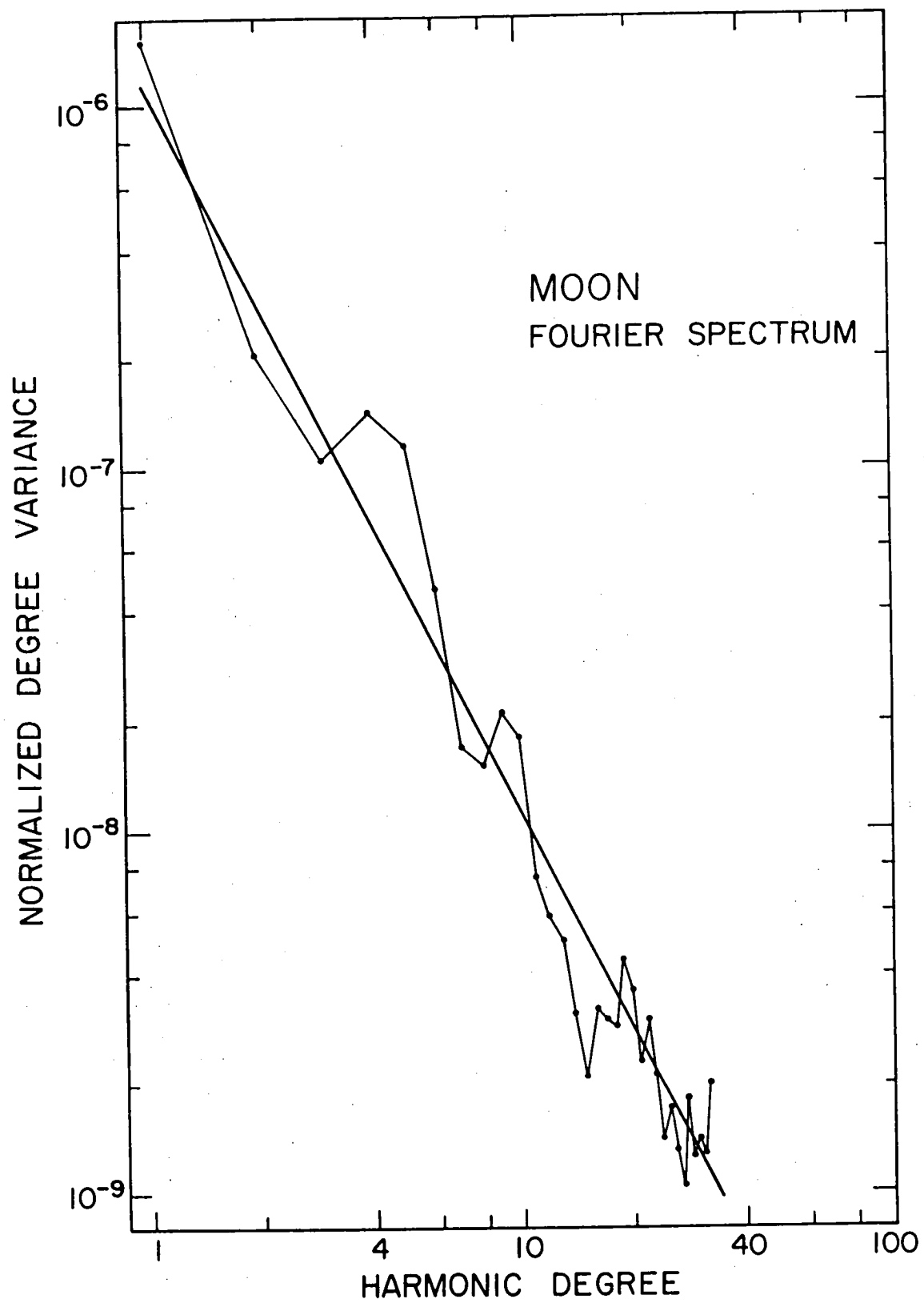
which for  $\gamma \ll 1$ , reduces to

$$S^2(\gamma) \doteq 2V(H;0)/\gamma \quad (4.5)$$

Thus, given an estimate for  $V(H;0)$ , we can estimate values for the r.m.s. slope angle

- 4.4 Moon - Spherical topographic variance spectrum. Harmonic coefficients are from Bills and Ferrari (1977a). Points are computed degree variances. Solid line is Vening-Meinesz spectrum:  $V(H;n) = 1.5 \times 10^{-6} / (n)(n+1)$ . Dotted lines indicate critical values for 90% confidence level.
- 4.5 Moon - Circular topographic variance spectrum. Points are averaged degree variances from Fourier analysis of Apollo laser altimetry data. Solid line is model variance spectrum:  $V(H;n) = 1.5 \times 10^{-6} / (n)^2$ . This is the circular analog of the Vening-Meinesz spectrum.





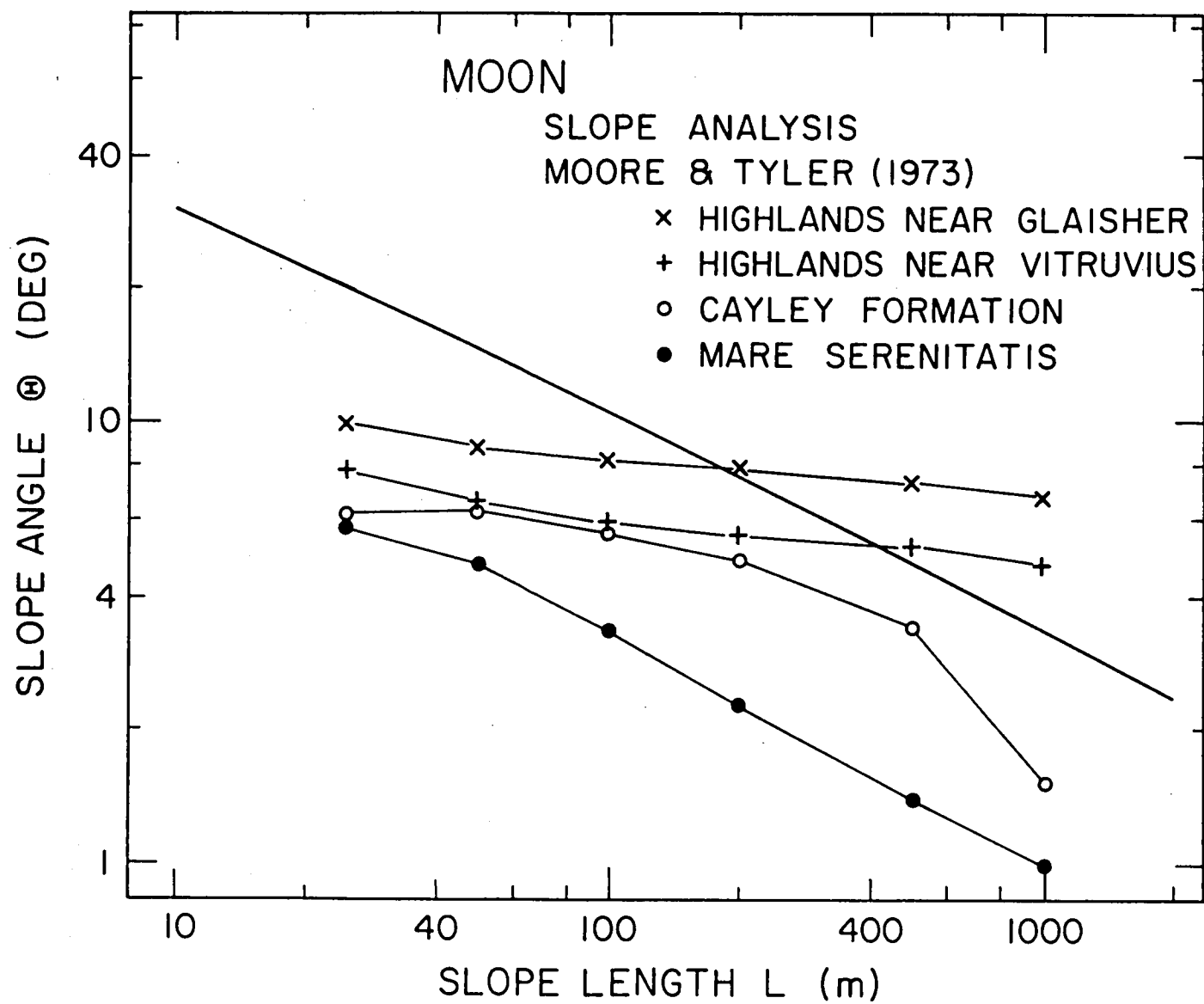
$$\Theta(L) = \tan^{-1} [S(L/R_0)] \quad (4.6)$$

at any linear separation  $L$ . In Figure 4.6, we compare this estimate with photogrammetrically determined r.m.s. slopes for typical highland and mare regions of the Moon over the range  $25 \text{ m} \leq L \leq 1000 \text{ m}$  (Moore and Tyler, 1973). The agreement with these observations could be made much better by reducing the value of  $V(H;0)$ , however, we have used the value estimated from the spectrum in Figure 4.5. Thus, we are extrapolating from  $n \leq 32$  to  $n = 2\pi R_0/L = 40,000$  ( $L = 250 \text{ m}$ ). We note that our predicted slopes are intermediate between the highland and mare values and actually parallel the mare values. The highlands, though rougher than the maria at all slope lengths considered, exhibit weaker dependence of slope angle on slope length. This agreement between observed and predicted slopes is a strong confirmation of the validity of the Vening-Meinesz spectrum as applied to the Moon.

#### Mars

The earliest topographic spectral estimates for Mars appear to be those of Pettengill et al. (1969), who performed a Fourier analysis of elevations along the  $22^\circ \text{ N}$  latitude parallel as determined from radar observations. They first argued from terrestrial topography data that "the Fourier spectrum of the topographic variation around any great circle (e.g., the equator), or near-equatorial parallel of latitude, will tend to approximate the spherical harmonic spectrum." They then showed that their estimated topographic

4.6 Moon - Slope analysis. Points are photogrammetrically determined r.m.s. slopes on different lunar terrain types from Moore and Tyler (1973). The solid line indicates theoretical slope angles given by equations (4.5) and (4.6) using the value  $V(H;0) = 1.5 \times 10^{-6}$  determined from Figure 4.5. A representative slope length ( $L = 250$  m) corresponds to a harmonic degree of  $n = 2\pi R_0/L \doteq 40,000$ .





variance spectrum for Mars, which covered the range  $1 \leq n \leq 16$ , is quite similar to the Earth's.

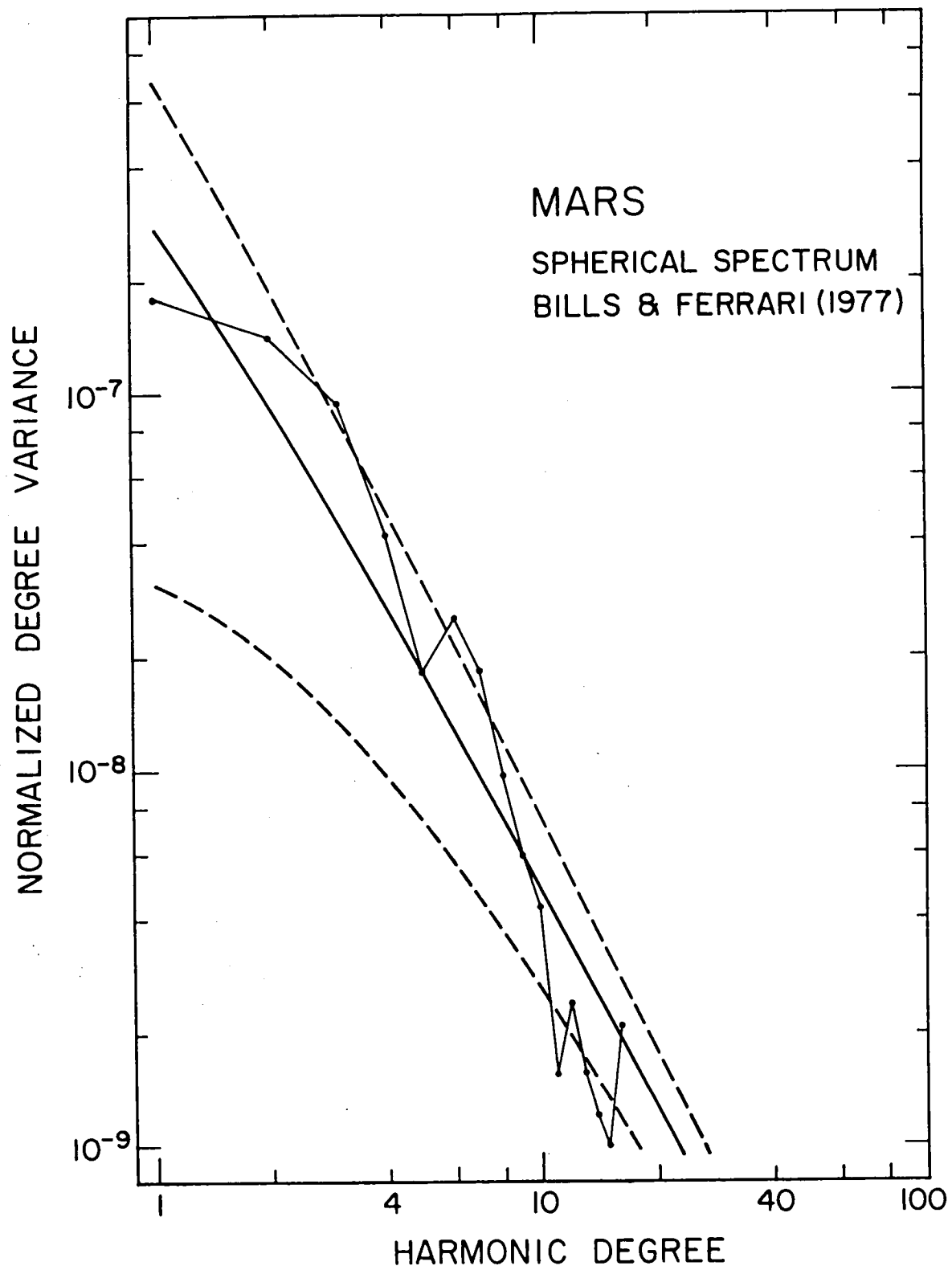
As was true of the lunar spectrum, the Martian variance spectrum as computed from spherical harmonics (Figure 4.7) is somewhat corrupted by the irregular data distribution, in spite of efforts such as those described in the last chapter. Nevertheless, harmonic analyses by Christensen (1975), with  $1 \leq n \leq 8$ , and by Bills and Ferrari (1977c), with  $1 \leq n \leq 16$  (see Chapter III), have confirmed that the spectral behavior discovered by Pettengill et al. (1969) is indeed a feature of the entire planet rather than merely characteristic of a single latitude band.

As of this writing, r.m.s. slope determinations from Viking photogrammetry are still unavailable (H. Masursky, personal communication) for comparison with predicted slopes, as was done for the Moon.

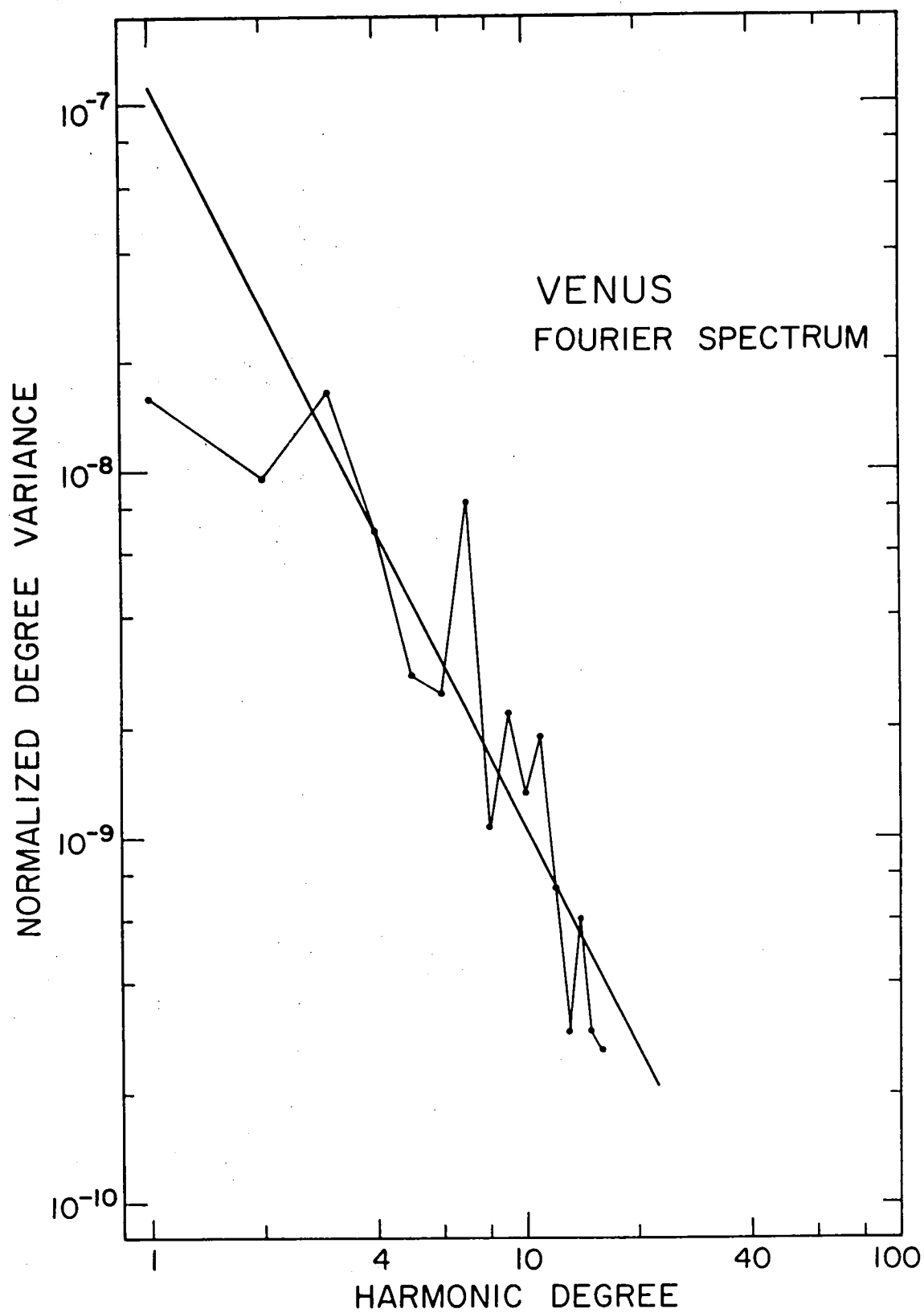
#### Venus

The only topographic data presently available for Venus come from radar observations (Smith et al., 1970; Campbell et al., 1972; Shapiro et al., 1973) and are essentially restricted to the sub-Earth points. A preliminary Fourier analysis ( $1 \leq n \leq 16$ ) of the data from Shapiro et al. (1973), which have complete longitude coverage but are severely limited in latitudinal extent, shows a distinct tendency toward decreasing variance with increasing degree (Figure 4.8). Though the spectrum is somewhat "noisy", the general trend is surprisingly consistent with the Vening-Meinesz model.

4.7 Mars - Spherical topographic variance spectrum. Harmonic coefficients are from Bills and Ferrari (1977c). Points are computed degree variances. Solid line is Vening-Meinesz spectrum:  $V(H;n) = 5.5 \times 10^{-7} / (n)(n+1)$ . Dotted lines indicate critical values for 90% confidence level.



4.8 Venus - Circular topographic variance spectrum. Points are degree variances from Fourier analysis of near equatorial radar altimetry data of Shapiro et al. (1973). Solid line is model variance spectrum:  $V(H;n) = 1.1 \times 10^{-7}/n^2$ . This is the circular analog of the Vening-Meinesz spectrum.



## 2. Isotropy

Another aspect of our original hypothesis was that, apart from rotational and tidal effects, the topography should be essentially random. A convenient and informative way to check this conjecture is to measure the isotropy of the surface. As is developed in Appendix G, a necessary condition for isotropy is that the mean square east-west slope at zero slope length

$$s_{\theta}^2(0) = \sum_{n=1}^{\infty} T_{\theta}(n) \quad (4.7)$$

equals the mean square north-south slope at zero slope length

$$s_{\varphi}^2(0) = \sum_{n=1}^{\infty} T_{\varphi}(n) \quad (4.8)$$

where the degree tilts are

$$T_{\theta}(n) = \sum_{m=0}^n \left[ \frac{(2n+1)(m)}{2} \right] H_{nm}^T H_{nm} \quad (4.9)$$

$$T_{\varphi}(n) = \sum_{m=0}^n \left[ (n)(n+1) - \frac{(2n+1)(m)}{2} \right] H_{nm}^T H_{nm}$$

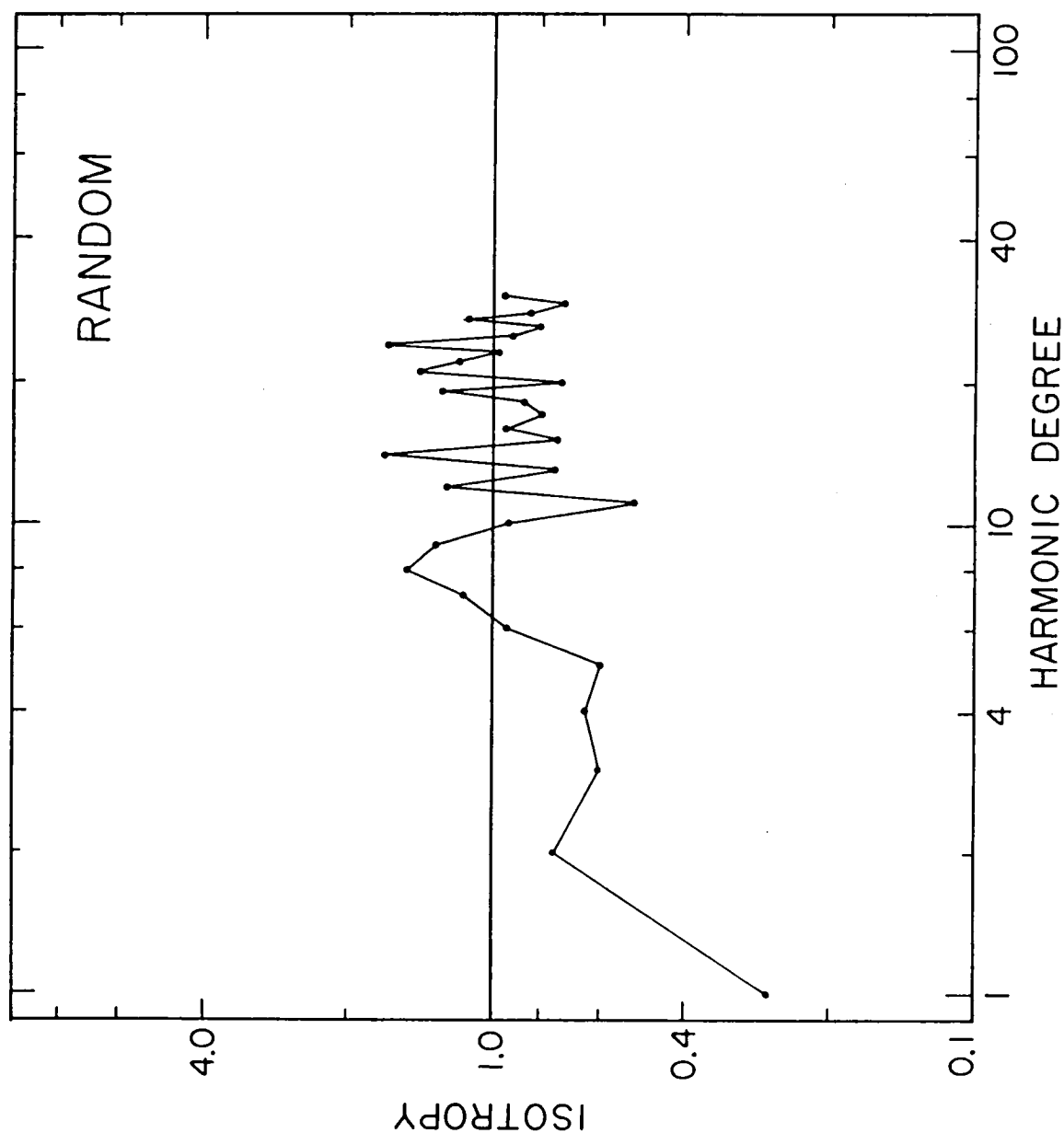
A sufficient condition for mean square isotropy is the equality of the degree tilts for each harmonic degree. We thus define a degree isotropy parameter

$$\alpha_n \equiv T_{\theta}(n)/T_{\varphi}(n) \quad (4.10)$$

In Figure 4.9a, we present the isotropy spectrum for the random harmonic model previously discussed. Figures 4.9b-d are isotropy spectra calculated from spherical harmonic models of the topography of the Earth (Balmino et al., 1973), Mars (Bills and Ferrari, 1977c) and the Moon (Bills and Ferrari, 1977a), respectively. For the Earth, the topography was measured relative to the geoid, and thus the primary effect of rotation has been removed. For Mars and the Moon, the original harmonic analyses are for spherically referenced elevations, but for this analysis, the second degree terms have been corrected for rotational effects. For all three planets, we find quite consistent isotropy, with the largest departures for the low degrees.

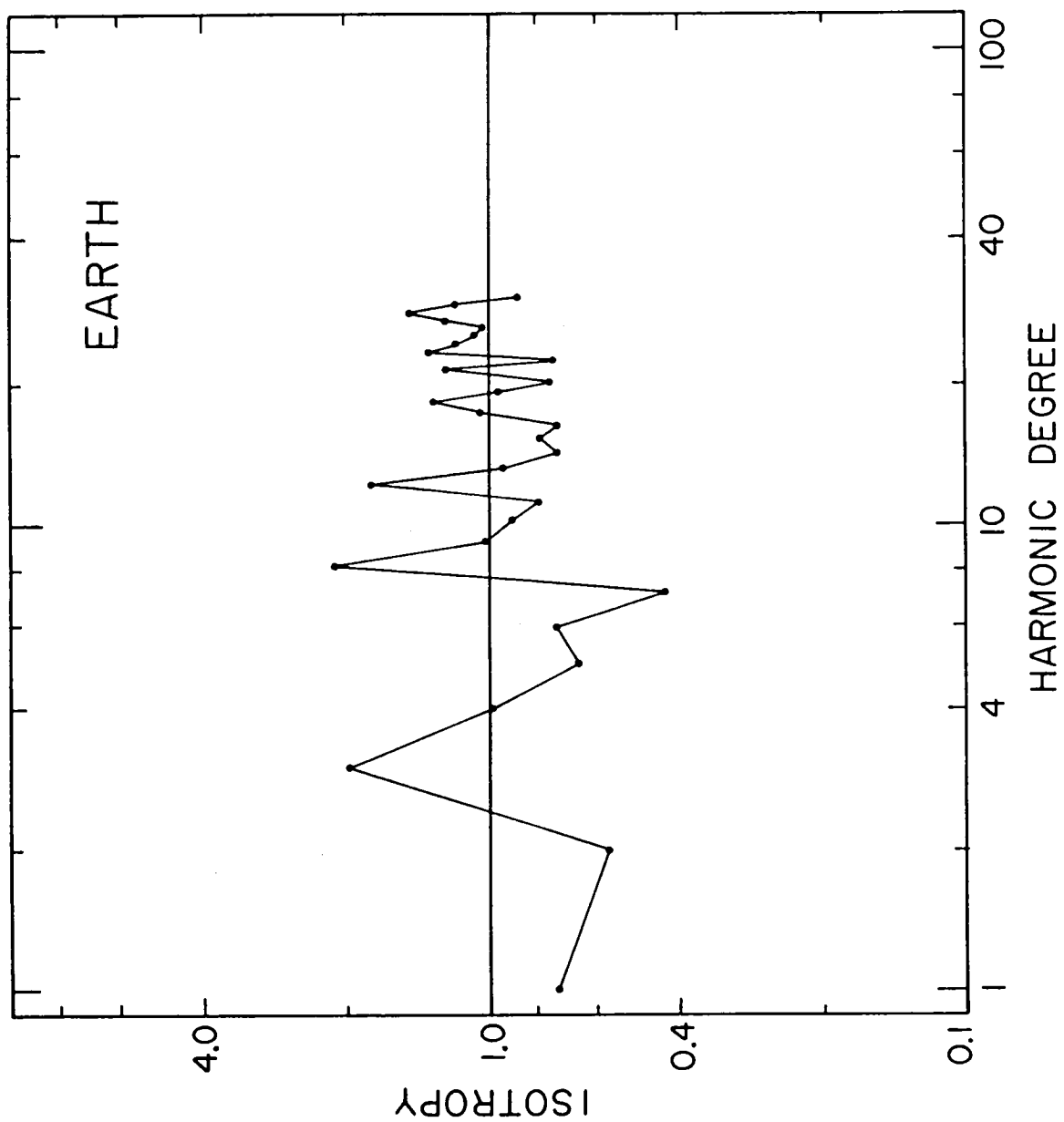
### 3. Simulation

As a further, somewhat subjective criterion for judging the validity of our primary hypothesis that the topography of a solid planet or satellite is well modeled by zero-mean Gaussian random harmonic coefficients with a Vening-Meinesz variance spectrum, we would expect that a contour map produced from these coefficients would appear qualitatively similar to equivalent resolution maps of actual planetary surfaces. Figures 4.10a-c are topographic maps generated from harmonic representations of the Moon, Mars and Earth, all truncated at degree  $n = 12$ . For comparison, Figure 4.10d is a map of the random topography represented by the harmonic coefficients used in producing Figures 4.1 and 4.9a, also truncated

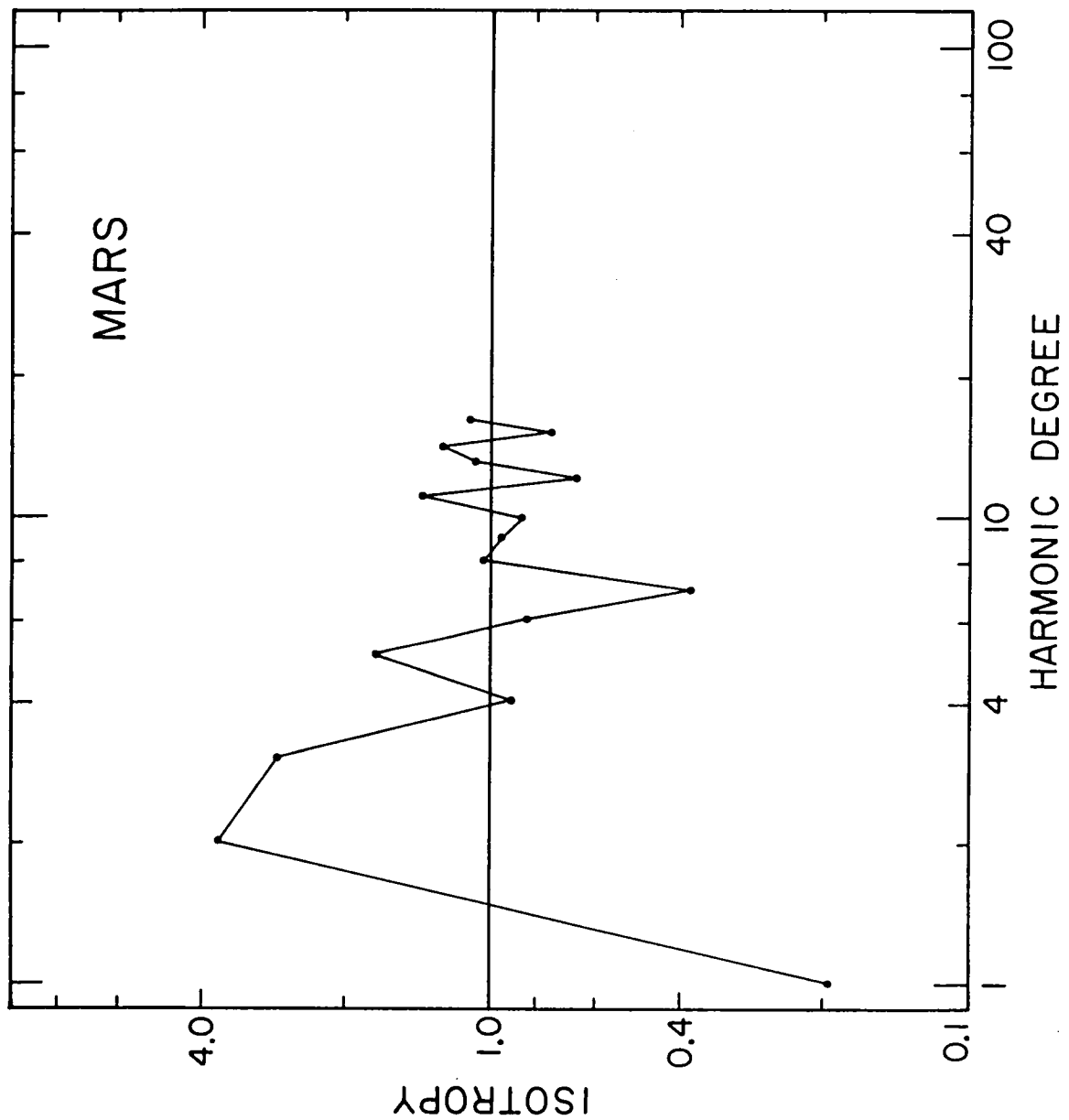


4.9a Simulated isotropy spectrum. Points are ratios  $\alpha_n = T_\theta(n)/T_\varphi(n)$  of east-west degree tilts  $T_\theta(n)$  to north-south degree tilts  $T_\varphi(n)$  as defined in equation 4.9. Harmonic coefficients are the same random variables used in generating Figure 4.1. Solid line represents perfect isotropy  $\alpha_n = 1.0$ .

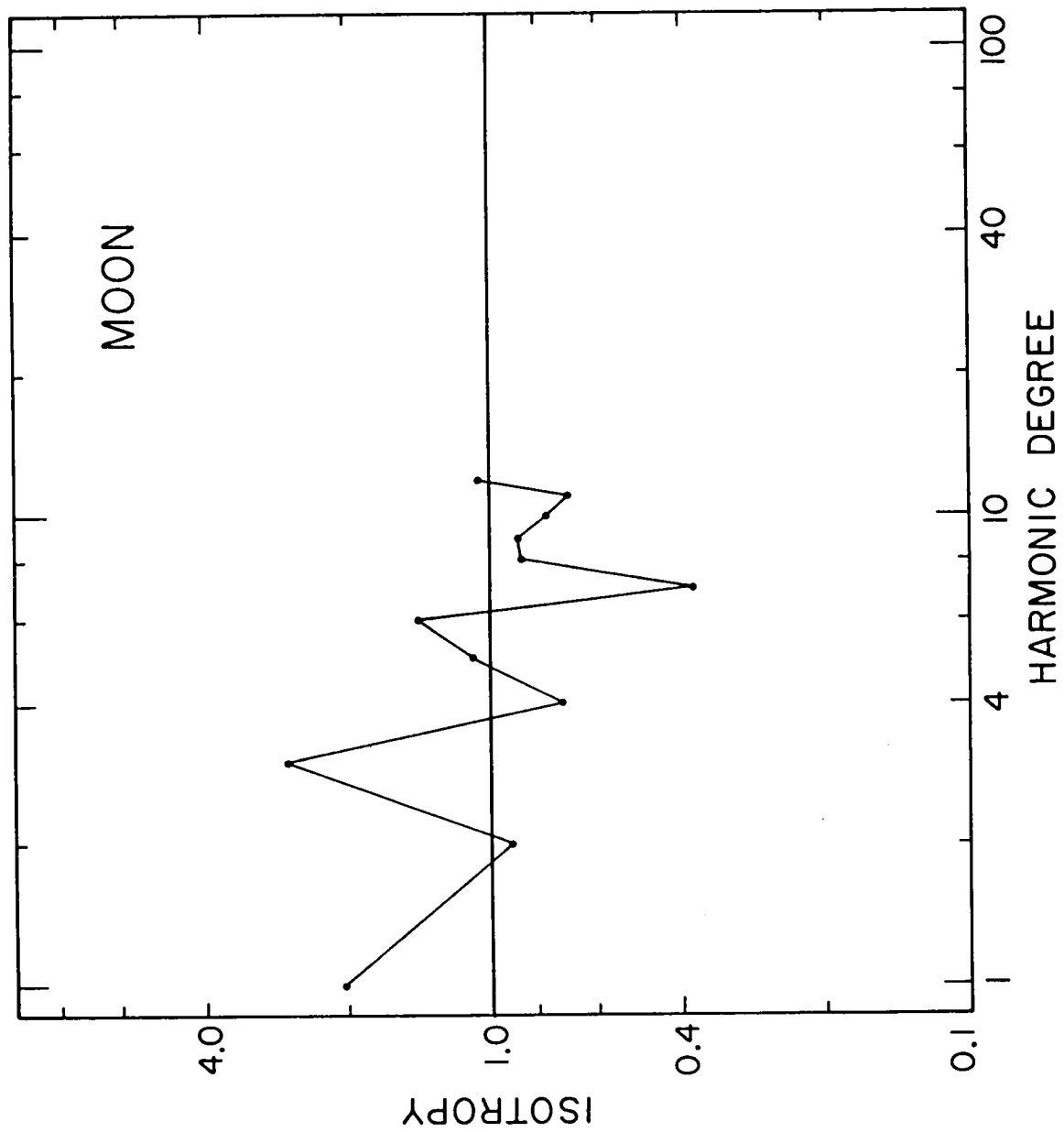




4.9b Earth - Isotropy spectrum. Harmonic coefficients are from Balmino et al. (1973). See caption to Figure 4.9a.



4.9c Mars - Isotropy spectrum. Harmonic coefficients are from Bills and Ferrari (1977c). See caption to Figure 4.9a.



4.9d Moon - Isotropy spectrum. Harmonic coefficients are from Bills and Ferrari (1977a). See caption to Figure 4.9a.

at  $n = 12$ . All of these figures are Mercator projections and cover the latitude range  $-75^\circ \leq \theta \leq +75^\circ$ . The contour interval in each case is 1.0 km. The mean radius of the random planet was arbitrarily taken to be  $R_0 = 3000$  km. This, in conjunction with the assumption that  $V(H;0) = 10^{-6}$ , determines the physical variance of the surface. A decision as to the adequacy of this simulation, being rather subjective, will be left to the judgment of the reader.

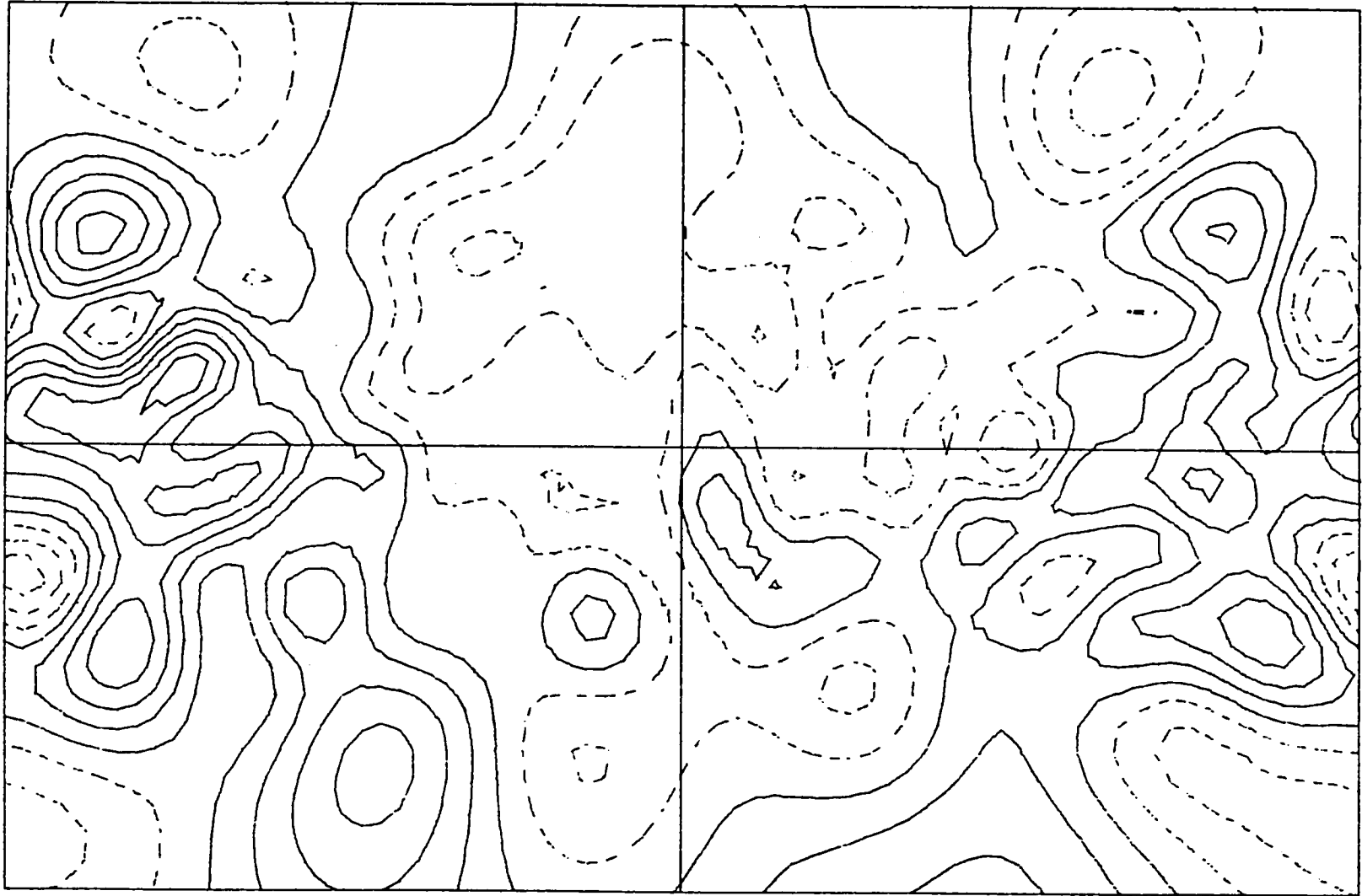
#### 4. Summary

In summary, we find that on all planets for which we have sufficient data to check our hypothesis the stochastic component of the topography is very nearly isotropic and the degree variances decrease with increasing harmonic degree consistent with the Vening-Meinesz spectrum (equation 4.1). Furthermore, we find that the largest reliably determined departures from this basic model are for the low degree harmonics. In fact, the point of incipient departure appears to correspond roughly to a scale length  $L = R_0/n$  of 1700-2100 km (Earth:  $L = 6380/3$ , Venus:  $L=6050/3$ , Mars:  $L = 3390/2$ , Moon:  $L = 1740/1$  ).

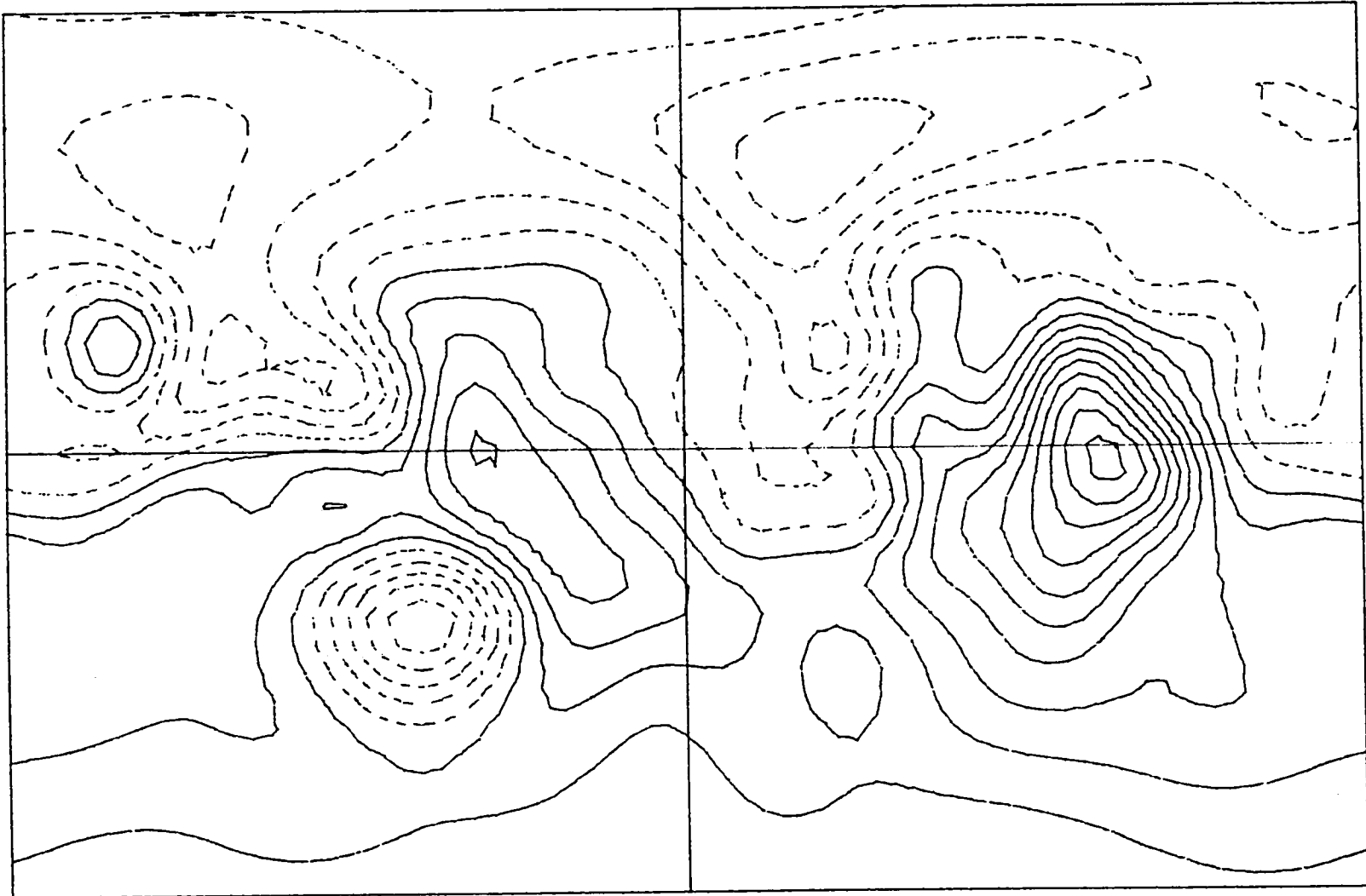
Since this Vening-Meinesz spectral form is applicable over such a wide range of feature sizes and on planets subject to widely differing geomorphic processes, it appears to reflect some fundamental property of the terrestrial planets. We will now attempt to gain a better theoretical understanding of this spectrum in hopes of being able to explain its ubiquity.

- 4.10a Moon - Topographic contour map. From harmonic coefficients of Bills and Ferrari (1977a) truncated at degree  $N = 12$ . Mean radius  $R_0 = 1737.5$  km. Contour interval  $\Delta H = 1.0$  km. Solid lines are above reference level, dashed lines are below it. Mercator projection with latitude range  $-75^\circ \leq \theta \leq 75^\circ$ .
- 4.10b Mars - Topographic contour map. From harmonic coefficients of Bills and Ferrari (1977c) truncated at degree  $N = 12$ . Mean radius  $R_0 = 3389.9$  km. Heights are referenced to 6.1 millibar level. See caption to Figure 4.10a
- 4.10c Earth - Topographic contour map. From harmonic coefficients of Balmino et al. (1973) truncated at degree  $N = 12$ . Mean radius = 6371.0 km. Heights are referenced to geoid. See caption to Figure 4.10a
- 4.10d Simulated topographic contour map. From harmonic coefficients used in figures 4.1 and 4.9 truncated at degree  $N = 12$ . Assumed mean radius  $R_0 = 3000$  km. See caption to Figure 4.10a

# MOON



# MARS

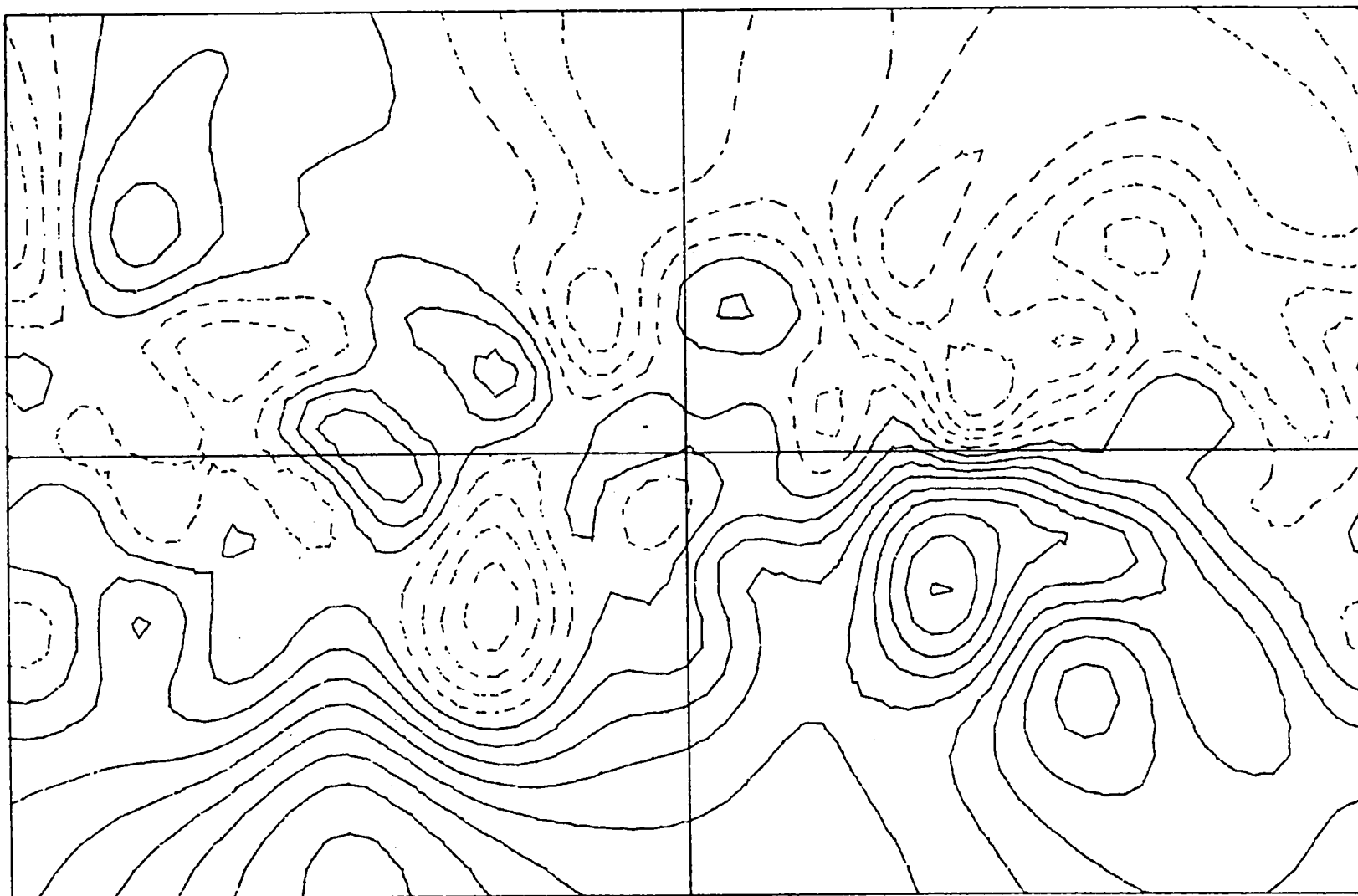


# EARTH





RANDOM



### C. ANALYSIS

In this section, we will attempt to understand why planetary surfaces are characterized by the Vening-Meinesz spectral form (equ. 4.1). We will first consider (and subsequently reject) a specific physical mechanism championed by Vening-Meinesz himself - thermal convection. We will then examine some of the geometrical implications of this spectral form. This will lead to a completely equivalent reformulation of the problem in terms of a particular stochastic process rather than the variance spectrum. We then turn our attention to a number of physical systems which have analogous spectral forms to see how energy is transferred from one spectral component to another. Next, we will consider a fairly specific model for the topography which involves superposition of random pulses. We will see that the size-frequency distribution of pulses largely determines the spectral form of the resulting surface. Finally, we will consider a model which supposes only that there is a degree of equilibrium between erosive and constructional processes acting on the surface. In terms of simplicity of assumptions and verisimilitude of results, we consider this the most satisfactory explanation of the Vening-Meinesz spectral form. We close the section with a conjectured characterization of planetary surfaces in terms of continuity, fixed variance and maximal entropy.

## 1. Convection

Vening-Meinesz (1951) not only provided the earliest reference to the shape of the Earth's topographic variance spectrum, but also offered the earliest explanation. He argued that both the general pattern given by equation 4.1 and the principal departures therefrom are related to thermally driven convection in the mantle. The increased variance at degrees 5, 10 and 15, as best seen in the slope variance spectrum

$$V(S;n) = (n)(n+1)V(H;n) \quad (4.11)$$

were taken to be manifestations of a predominantly fifth degree convection pattern.

Walzer (1971, 1972a,b) has invoked a complex pattern of convective cells to explain the Earth's topographic variance spectrum over the range  $1 \leq n \leq 31$ . Convective models have also been proposed for the Moon (Runcorn, 1967) and Mars (Wells, 1971).

Coode (1966, 1967) showed that in a harmonic analysis of the locations of active and passive oceanic ridges and continental rift zones, the aseismic ridges have a major spectral peak at degree 4 and a secondary peak at degree 9, whereas the active seismic ridges have major and secondary spectral peaks at degrees 5 and 10 respectively. He interpreted this as evidence of a change in the dominant mode of mantle convection from degree 4 to 5. Runcorn (1965) further extended this notion in claiming that the core of the Earth has been steadily growing and that, as it has grown, the stable mode of

mantle convection has been increasing. In particular, he claims that the most recent change of mode (from 4 to 5) occurred in the Permian (200 My. ago) and initiated the present era of continental drift.

Convection may very well influence the topography of the Earth and other planets. In fact, McKenzie et al. (1973) have found both positive relief features and positive gravity anomalies associated with rising convective flows in their numerical simulations. However, to infer the modes of convection in a planet from wiggles in its topographic or gravitational variance spectrum seems unjustified. Furthermore, even if convection could explain part of the spectrum, if a single explanation is sought for the form of the variance spectrum on all planets and over the entire observed spectral range, then convection is clearly inadequate.

## 2. Geometry

There are several interesting geometrical aspects of planetary topography which relate directly to the variance spectrum. A brief consideration of the geometry will give us better insight into the significance of the Vening-Meinesz spectral form; and, in fact, will enable us to reformulate our basic problem in different, but equivalent terms. We will be better able to say what the topography is like, but not necessarily better able to say why.

A common observation is that even those landscapes which appear quite smooth when viewed from afar, are often quite rough at a small scale. If we suppose this behavior to continue to arbitrarily small scale, we could characterize the surface as continuous but not differentiable. Based on the analyses of Beers and Dragt (1970) and of Beers (1972), we show in appendix A that a function on a sphere which is continuous, but not differentiable, has a variance spectrum which is asymptotically proportional to  $1/(n)(n+1)$ . Thus, if we could explain why planetary surfaces appear to be continuous, but not differentiable, we would at least understand the asymptotic behavior of the variance spectrum. However, we would still have the problem of why the low degree harmonics behave this way.

Another simple model is obtained by assuming that the surface is random and that the slope at any point is uncorrelated with the slope at any other point. In this case, the slope covariance is a delta

function (Yaglom, 1962; Parzen, 1962) (see Appendix D)

$$C(S;\gamma) = S_o \delta(\gamma) \quad (4.12)$$

and the slope variance spectrum is constant

$$V(S;n) = S_o \quad (4.13)$$

Using the relationship between topographic variance and slope variance in equation (4.11), we see that this implies

$$V(H;n) = \frac{S_o}{(n)(n+1)} \quad (4.14)$$

The spherical Wiener process (see Appendix C) is the only stochastic process with continuous realizations which has these properties. We may, in fact, reformulate the main problem of this section. We may now ask: why are the surfaces of planets and satellites realizations of a spherical Wiener stochastic process? We will return to this notion later.

Vening-Meinesz (1951) made another interesting observation concerning the variance spectrum. He claimed that it is a result of the topography being composed of "features with elevations roughly proportional to their horizontal dimensions." As we shall see later when we consider a random pulse model for the topography, this direct proportionality is a sufficient, but not necessary, condition for the desired spectral form. However, the idea was a good one and can be developed further.

The increments

$$\Delta F(g, g + \gamma) \equiv F(g + \gamma) - F(g) \quad (4.15)$$

of a random function  $F: G \rightarrow R$  are said to be self-similar with

with parameter  $\beta$  if, for any  $\gamma > 0$  and any  $g \in G$

$$\Delta F(g, g + \gamma) = \gamma^{-\beta} \Delta F(g, g + \beta\gamma) \quad (4.16)$$

where the indicated equality means that the two random variables are identically distributed. The traditional Wiener process has self-similar increments with parameter  $\beta = 0.5$ . Mandelbrot (1967, 1975b, 1977) has introduced the concept of fractional Wiener processes  $W_\beta$  which have self-similar increments with  $0 \leq \beta \leq 1$ . He also claims, on the basis of various landscape simulations, that the topography of the Earth is a realization of a fractional Wiener process with  $\beta \doteq 0.65$ . However, we note that the variance spectrum of  $W_\beta$  on a circle is proportional to  $n^{-(2\beta+1)}$ , and the observed variance spectrum of the Earth (Figure 4.3) is closer to  $n^{-1.9}$  ( $\beta = 0.45$ ) than to  $n^{-2.3}$  ( $\beta = 0.65$ ) and within probable errors is consistent with  $n^{-2.0}$  ( $\beta = 0.5$ ).

Another interesting aspect of the Wiener and fractional Wiener processes is the extreme irregularity of their realizations. Generalizing a result of Mandelbrot (1975a) (see Appendix C), we suggest that if  $D[G]$  is the dimension of its parameter set, the dimension of a realization of  $W_\beta(g)$  satisfies

$$D[W_\beta(g)] = D[G] + \beta \quad (4.17)$$

Since for our topography model  $D[G] = 2$  (the surface of a sphere), we conclude that the dimension of the surface of the Earth is  $2 + \beta \doteq 2.5$ . It is thus intermediate between a traditional surface ( $D = 2$ ) and a solid ( $D = 3$ ).

### 3. Energy Redistribution

There are a number of physical systems which might serve as models for various aspects of the process or processes responsible for the observed topographic variance spectra of the terrestrial planets. A common feature of the systems we will consider is that energy is typically fed into the system over some characteristic range of spatial wavenumbers and, through non-linear interactions, this energy is redistributed across the spectrum - typically to high wavenumbers where it is dissipated.

#### Elastic Energy Reduction

Shaham and coworkers (Pines and Shaham, 1973; Au and Shaham, 1974) have suggested an elastic energy reduction principle for planets according to which "the direction of irreversible crustal motions must always be such as to reduce the overall elastic energy." They further suggest that an important source of elastic energy, at least for the Earth, is excess oblateness due to tidal despinning. As is shown in Appendix F, if we suppose that the total topographic variance is fixed, a shift of variance across the spectrum to higher wavenumber will in fact result in a decrease in both elastic and gravitational energy. However, at this point we have no reason to suppose that variance is conserved.



### Two Dimensional Fluid Flow

There is a system in which analogs of both topographic variance and slope variance are conserved. Non-divergent two dimensional inviscid fluid flow on a sphere may be characterized by a stream function  $\psi$  in terms of which velocity  $v$  and vorticity  $w$  are

$$v = \nabla\psi \quad (4.18)$$

$$w = \nabla^2\psi \quad (4.19)$$

If the vorticity is expanded in a harmonic series

$$w(\theta, \varphi) = \sum_{n=1}^{\infty} \sum_{m=0}^n w_{nm}^T \Lambda_{nm}(\theta, \varphi) \quad (4.20)$$

then the kinetic energy  $E$  and enstrophy  $F$  (mean square vorticity) may be expressed as (Baines, 1976),

$$E = \frac{1}{2} \int_S (\nabla\psi)^2 dS = \pi \sum_{n=1}^{\infty} E_n \quad (4.21)$$

$$F = \frac{1}{2} \int_S (\nabla^2\psi)^2 dS = \pi \sum_{n=1}^{\infty} F_n \quad (4.22)$$

where

$$E_n = \frac{F_n}{(n)(n+1)} \quad (4.23)$$

and

$$F_n = \sum_{m=0}^n w_{nm}^T w_{nm} \quad (4.24)$$

These quantities are clearly analogous to topographic variance and slope variance, respectively.

Fjortoft (1953) has shown that for a system in which both energy and enstrophy are conserved, any energy transfer across the spectrum must take place between components with (at least) three different values of  $n$ . Also if one of three components is a source or sink for both of the other two, its  $n$  value must be between those of the latter. The net redistribution of energy across the spectrum in such a case is rather limited.

However, in a turbulent two dimensional flow, enstrophy systematically cascades to very small scales, at which it is dissipated (Bretherton and Haidvogel, 1976). The kinetic energy, on the other hand, remains at large scales and the total kinetic energy is constant. In fact, there is an inverse energy cascade. Since the total energy

$$E = \pi \sum_{n=1}^{\infty} E_n \quad (4.25)$$

remains constant while the enstrophy

$$F = \pi \sum_{n=1}^{\infty} (n)(n+1) E_n \quad (4.26)$$

decreases, the energy must become more concentrated at low  $n$ .

The obvious analogy is to a system in which we maintain a fixed topographic variance while reducing the mean square slope. In such a system there will be an inverse topographic variance cascade,

the slope spectrum will become flatter and the topography spectrum will approach the Vening-Meinesz form. We shall return to this notion later. Incidentally, turbulence in three dimensional flows is more complicated (Hinze, 1959; Mandelbrot, 1975a).

#### 4. Random Pulse Model

We have seen that the spherical Wiener process is an excellent model for planetary surface topography. We now hope to gain some further insight into this situation by considering representations of random processes by superposition of random pulses. The general theory of such phenomenological models for random processes is discussed by Middleton (1951).

Halford (1968) has shown that processes with variance spectra proportional to  $n^{-\alpha}$  over an arbitrarily large range of frequencies can be generated from a physically realizable class of pulses only if  $0 \leq \alpha \leq 2$ . Bell (1974) has recently considered the inverse problem of inferring the pulse size-frequency distribution from the variance spectrum of the process and an assumed pulse shape. We shall only be directly concerned with the forward problem.

As a model for a broad class of stochastic processes on the sphere, we may consider the superposition of a collection of zero-sum binary pulses  $A_k Z(\gamma, \gamma_k)$  with random amplitudes, widths and locations. These pulses represent individual topographic features and the conservation of mass requires that

$$\int_{-1}^1 Z(\mu, \mu_k) d\mu = 0 \quad (4.27)$$

where  $\gamma$  is angular distance and  $\mu = \cos(\gamma)$ . See Appendix A for more about these pulses and Appendices A and D for discussion of several theorems mentioned in the following.

To facilitate the calculation of the covariance function and variance spectrum of this model, we will first consider two simpler scenarios. This will enable us to obtain valuable intermediate results. The first configuration is a Poisson distribution of unit delta functions with an average of  $\alpha$  impulses per unit area:

$$F(\theta, \varphi) = \sum_k \delta(\theta - \theta_k, \varphi - \varphi_k) \quad (4.28)$$

where  $(\theta_k, \varphi_k)$  is the location of the  $k$ -th impulse. By a simple application of Campbell's theorem, equation (D.23), we find that the covariance function is

$$C(F; \gamma) = \alpha \delta(\gamma) \quad (4.29)$$

and therefore the variance spectrum is

$$\begin{aligned} V(F; n) &= \int_{-1}^1 C(F; \mu) P_n(\mu) d\mu \\ &= \alpha \end{aligned} \quad (4.30)$$

Obviously, this is not a very good model for topography, since the spectrum is flat.

The next model we consider consists of a Poisson distribution of zero-sum pulses with amplitude  $A$ , width  $\gamma_0$  and an average density of  $\alpha$  pulses per unit area. We use the relocation property of convolution with a delta function to express this configuration as:

$$G(\theta, \varphi) = \sum_k A_0 Z(\gamma, \gamma_0) * \delta(\theta - \theta_k, \varphi - \varphi_k) \quad (4.31)$$

The variance spectrum is, by the convolution theorem, equation (D.25),

$$\begin{aligned} V(G; n) &= [A_0 Z_n(\mu_0)]^2 V(F; n) \\ &= 4 \alpha A_0^2 (1 - \mu_0)^2 \left[ \frac{P'_n(\mu_0)}{(n)(n+1)} \right]^2 \end{aligned} \quad (4.32)$$

This is a better model in that the variance spectrum does generally decrease with increasing degree, but it is still unsatisfactory since the spectrum is quite irregular. Superimposed on the overall decrease, there are nearly periodic variations which correspond to fluctuations in  $P'_n(\mu_0)$  with varying  $n$ . For  $\gamma_0 = 0$ , the spectrum is still flat. However, as the pulse width increases the spectrum begins to fall off more rapidly and the fluctuations get closer together and generally more pronounced. Finally when  $\gamma_0 = \pi/2$ , all the even degree harmonics are identically zero.

Finally, we consider the case where the amplitudes and widths of the pulses are also random:

$$H(\theta, \varphi) = \sum_k A_k Z(\gamma, \gamma_k) * \delta(\theta - \theta_k, \varphi - \varphi_k) \quad (4.33)$$

This will maintain the overall spectral decrease, but smooths out the

the fluctuations. If  $p(A, \mu_o)$  is the joint probability density of pulse amplitudes and widths, then we can write the variance spectrum as

$$V(H;n) = \alpha \int_0^{\infty} \int_{-1}^1 p(A, \mu_o) [A Z_n(\mu_o)]^2 d\mu_o dA \quad (4.34)$$

We can simplify this somewhat by noting that

$$\int_0^{\infty} p(A, \mu_o) A^2 dA = p(\mu_o) A^2(\mu_o) \quad (4.35)$$

where  $p(\mu_o)$  is the marginal probability density of pulse widths and  $A^2(\mu_o)$  is the mean square amplitude of pulses of width  $\gamma_o = \cos^{-1}(\mu_o)$ .

We thus find

$$\begin{aligned} V(H;n) &= \alpha \int_{-1}^1 p(\mu_o) [A(\mu_o) Z_n(\mu_o)]^2 d\mu_o \\ &= \frac{4\alpha}{[(n)(n+1)]^2} \int_{-1}^1 p(\mu_o) [A(\mu_o)(1 - \mu_o) P'_n(\mu_o)]^2 d\mu_o \end{aligned} \quad (4.36)$$

In order to make further progress with this integral, we will need to make some assumptions concerning the distribution of pulse sizes. A particularly interesting distribution results from the assumption that the product

$$p(\mu_o) A^2(\mu_o) \frac{1 - \mu_o}{1 + \mu_o} = \beta \quad (4.37)$$

is a constant. The resulting variance spectrum is

$$\begin{aligned}
V(H;n) &= \frac{4\alpha\beta}{[(n)(n+1)]^2} \int_{-1}^1 (1 - \mu_o^2) [P'_n(\mu_o)]^2 d\mu_o \\
&= \frac{8\alpha\beta}{(n)(n+1)}
\end{aligned} \tag{4.38}$$

since

$$\int_{-1}^1 (1 - \mu_o^2) [P'_n(\mu_o)]^2 d\mu_o = 2(n)(n+1) \tag{4.39}$$

If we now increase the average density of pulses  $\alpha$  and decrease the average pulse size in such a way that the product  $\alpha\beta$  remains constant, we obtain a good approximation to a spherical Weiner process. The covariance function and total variance are:

$$\begin{aligned}
C(H;\gamma) &= \sum_{n=1}^{\infty} V(H;n) P_n[\cos(\gamma)] \\
&= 8\alpha\beta \sum_{n=1}^{\infty} \frac{P_n[\cos(\gamma)]}{(n)(n+1)} \\
&= 8\alpha\beta \left( 1 - 2 \ln[1 + \sin(\gamma/2)] \right) \\
C(H;0) &= 8\alpha\beta
\end{aligned} \tag{4.40}$$

In the next few paragraphs, we will attempt to justify the assumed pulse size-frequency distribution used in the above derivation. Perhaps the strongest justification comes simply from the fact that it produces the observed variance spectrum, and, within the context of this random pulse model, it is the only way to do so. However, we should try to find out more about why it works. Paraphrasing Halford

(1968), "the crucial problem is to find the physical circumstances which cause the product  $p(\mu_o) A^2(\mu_o)$  to vary approximately as  $(1+\mu_o)/(1-\mu_o)$ ; the shape of the perturbation is probably irrelevant." We will therefore consider both  $A^2(\mu_o)$ , the relation between mean square pulse amplitude and width or horizontal extent, and  $p(\mu_o)$ , the pulse width-frequency distribution, in a number of different contexts.

### Energy Equipartitioning

Bell (1975) has presented an interesting model which essentially argues for constancy of the product

$$\beta = p(\mu_o) A^2(\mu_o) \left( \frac{1 - \mu_o}{1 + \mu_o} \right) \quad (4.41)$$

based on putative equipartitioning of gravitational potential energy amongst various hill sizes. His analysis was set on a line rather than a sphere, and thus ignores both the curvature and two-dimensional nature of the domain; however, neither of these are serious problems. In essence, he claims that the potential energy of a binary pulse with amplitude  $A$  and width  $\gamma_o = \cos^{-1}(\mu_o)$  is proportional to  $A^2(1-\mu_o)/(1+\mu_o)$  and that  $p(\mu_o)$  is the relative frequency of these pulses. He then claims that "the observed shape of the spectrum implies an equilibrium state of maximum disorder in which energy of formation is distributed uniformly over all hill sizes... The smaller hills may require less energy of formation, but are sufficiently more numerous than the larger hills so as to insure this equipartition of energy."



Though this argument has a certain appeal, some of which accrues from analogies with thermodynamic concepts such as entropy maximization, energy equipartitioning and statistical equilibrium, which we shall mention again later, it has at least two serious flaws. First, as is shown in Appendix F, the potential energy perturbation of a cylindrical mass on the surface of a sphere is not simply proportional to the basal area times the squared height. To assume so is to neglect the self-potential of the added mass which significantly alters the potential energy spectrum. Secondly, there is no obvious physical reason why energy should be equally partitioned among hill sizes. The thermodynamic analogy invoked would appear to be valid only for energy distribution among the normal modes of the system (Kampé de Fériet, 1962).

#### Slope Stability

The height of a topographic feature may be limited simply by the strength of its constituent materials. Hartmann (1972) and Johnson and McGetchin (1973) have attempted to explain the scale of planetary topographic features in this way. As shown in Appendix G, a simple slope stability analysis (Culmann, 1866) indicates that, neglecting internal friction, the maximum stable height of a slope of length  $L$  in material characterized by density  $\rho$  and cohesion  $c$  on a planet with surface gravity  $g$  is given by

$$H^2(L) = \frac{8cL}{\rho g} \left(1 + \frac{L_0}{L}\right) \quad (4.42)$$

where

$$L_o = \frac{2c}{\rho g}$$

has a value of meters to possibly tens of meters in typical terrestrial or lunar soils. Thus, at the scales in which we are interested  $L \gg L_o$ , and we have approximately

$$H^2(L) = \frac{8c}{\rho g} L \quad (4.43)$$

Thus, we might expect the mean square height of topographic features to be directly proportional to their horizontal extent. We shall find, in fact, that this is a reasonable approximation in several important situations.

A further implication of the above analysis is that the mean square slope between points a distance  $L = R_o \gamma$  apart should be approximately

$$S^2(\gamma) = \frac{H^2(R_o \gamma)}{(R_o \gamma)^2} = \frac{8c}{\rho g R_o \gamma} \quad (4.44)$$

Comparing this result with equation 4.5, we see that our slope stability analysis has yielded not only the correct functional dependence on  $\gamma$ , but also an estimate of the total topographic variance

$$V(H;0) = \frac{4c}{\rho g R_o} \quad (4.45)$$

#### Impact Cratering

Impact cratering has been an important process on essentially all planetary surfaces. Malin and Dzurisin (1977) summarize morphology and depth/diameter relationships for craters on the Moon, Mars

and Mercury. They find that the relationship between depth  $d$  and diameter  $D$  for morphologically fresh craters is adequately represented by a two part power law:

$$d = d_o (D/D_o)^b \quad (4.46)$$

for craters with  $D \leq 10$  km the exponent is approximately  $b = 1.0$ , whereas for  $D > 10$  km, the exponent decreases to 0.25-0.45 depending upon the data set analyzed. Our slope stability analysis in the previous paragraphs would imply  $b = 0.5$ . If both fresh and degraded craters are considered together, there is an increased scatter, but a single power law is quite adequate to describe the entire range of crater sizes and the corresponding exponent is approximately  $b = 0.6$  on all three planets.

Another important aspect of impact cratering is the resultant distribution of crater sizes. We may imagine an initially uncratered surface upon which craters are being produced at random. We further suppose that the relative frequency of craters larger than  $D$  being produced is

$$N = N_o (D/D_o)^{-c} \quad (4.47)$$

As the first few craters are formed, there will be little obliteration of pre-existing craters and the size-density distribution of the surface will reflect the production distribution. As more craters are formed, older craters will be destroyed, and the size-density distribution will tend more to reflect the details of the obliteration

process rather than the production size distribution. Eventually a point may be reached where the size-density distribution no longer changes with the formation of additional craters. If the crater-destroying process is simply geometrical overlap, the surface will be said to have attained saturation. If, in addition to crater overlap, crater destruction occurs by processes of erosion and filling, the surface will be said to have attained equilibrium. Woronow (1977) notes that "saturation results from purely geometrical and statistical considerations, valid for any hypothetical surface anywhere, whereas equilibrium results from the interaction of the crater population with its physical environment.... The difference between the crater densities at saturation and at equilibrium on any planetary body indicates the vitality of the degradational processes present there."

The equilibrium and saturation size-density distributions have been studied through stochastic models of formation and survival of craters (Marcus, 1964, 1966, 1967, 1970b; Neukum and Dietzel, 1971) and Monte-Carlo simulations (Woronow, 1977). An interesting result is that a production distribution with  $c > 2$  leads to a saturation population with  $c = 2$ , whereas production distributions with  $1.5 \leq c \leq 2$  lead to saturation populations with  $c$  approaching 1.0. Furthermore, it is found that equilibrium populations always have  $c \leq 2$ , with equality only as equilibrium degenerates to saturation. Observed size-density distributions tend to have  $c \approx 1.7$  for craters larger than a kilometer (Soderblom, 1970).

We will now compare these observations with Halford's (1968) one dimensional pulse criterion for an  $n^{-a}$  spectrum. The requirement is that

$$p(D) A^2(D) = p_0 A_0^2 (D/D_0)^{-a+1} \quad (4.48)$$

The probability distribution  $p(D)$  corresponding to a cumulative size-frequency distribution of the form (4.47)

$$p(D) = p_0 (D/D_0)^{-c-1} \quad (4.49)$$

and the mean-square amplitude distribution corresponding to the depth-diameter relation (4.46) is

$$A^2(D) = A_0^2 (D/D_0)^{2b} \quad (4.50)$$

In this case, Halford's criterion reduces to

$$a = 2 - 2b + c \quad (4.51)$$

For the observed mean values of  $c = 1.7$  and  $b = 0.6$ , we find  $a = 2.4$ .

On the other hand, if we consider a surface saturated with small ( $D \leq 10$  km) craters for which  $c = 2.0$  and  $b = 1.0$ , we do obtain  $a = 2.0$ , as desired.

Though this agreement (or lack thereof) is instructive, it is not as definitive as we might hope, since the actual shape of the craters changes as a function of size, contrary to the assumption of Halford's (1968) model. Thus, depth and diameter measurements and counts of craters do not suffice to directly estimate the spectrum of a planetary surface.

## 5. Equilibrium

### Historical Background

At least since the work of Gilbert (1877), it has been widely recognized that most terrestrial landforms are in a state of dynamic equilibrium between the erosional and constructional processes to which they are subjected. Most of the quantitative applications of this concept have dealt with single landform elements. For example, Kirkby (1971) states that in the development of a hillslope "the influence of the initial form of the slope can be shown to decrease rapidly with time, while the slope forms tend closer and closer towards a 'characteristic form,' in which the elevation of each point continues to decline with time, but is independent of the initial form." He further notes that this equilibrium form "depends solely on the nature and relative rates of the formative process and not at all on the initial profile of the hillslope." This relationship between form and process is further developed by Carson and Kirkby (1972), again in relation to hillslopes.

Leopold and Langbein (1962) have attempted to apply the equilibrium approach to the more general problem of evolution of an entire landscape. They claim that, for example, "the most probable condition exists when energy in a river system is as uniformly distributed as may be permitted by physical constraints." An analogy is drawn with closed thermodynamic systems in which entropy is maximized at equilibrium and topographic elevation is identified as the corresponding analog of temperature. Though the analogy is

enlightening, they do not rigorously justify it, and furthermore they fail to produce any quantitative results for general landscapes. However, they do examine a "most probable" river profile in which the downstream rate of entropy production is constant.

Culling (1960, 1963, 1965), in developing an analytical theory of erosion, states that "slope erosion is subject to a minimal law; that factor, whether the rate of transport or the rate of weathering, which is relatively the least efficient, controls the general course of denudation. On soil covered slopes the rate of transport is the dominant denudational control, soil creep being the responsible agency." He further concludes that the mass movement of weathered material on a hillside slope takes place at a rate proportional to the surface gradient. This leads to a diffusivity-type equation for elevation change

$$\beta' \frac{\partial H}{\partial t} = \nabla^2 H \quad (4.52)$$

This model is not only consistent with a microscopic analysis of motions of individual soil particles, but also, on a macroscopic level, it predicts slope forms actually observed on soil covered slopes. Soderblom (1970) has considered a similar model for erosion due to impact cratering.

Scheidegger and Chaudhari (1964) have examined these thermodynamic analogies in some detail. They conclude that "whenever a system is a linear combination of a large number of fluctuating systems, and in the 'large' system a certain quantity is a constant

of the motion to which the component systems contribute positive-definite amounts, then, under equilibrium conditions, that quantity is canonically distributed in the component systems and, under nonequilibrium conditions, assuming linear regression of the fluctuations and microscopic reversibility, the quantity in question is subject to a diffusivity equation with symmetric diffusivity tensor." Scheidegger (1967) then attempted to develop a complete thermodynamic analogy for landscape evolution in which the conserved quantity is mass or equivalently mean topographic elevation. Local elevation is then analogous to temperature. Though the complete analogy is interesting and even extends to Carnot cycles and the like, it is not clear that anything additional of real relevance to the topographic variance spectrum emerges from this analysis. Another criticism of the model is that topographic elevation can be either positive or negative, and thus is not a suitable temperature analog. Perhaps in addition to conserving mass (mean elevation), we should consider a model in which topographic variance (mean square elevation) is conserved (Chung and Scheidegger, 1968). We shall return to this notion in our final attempt to explain the Vening-Meinesz spectrum.

#### Dynamic Model

Up to this point, we have paid little explicit attention to the time variation of surface topography. However, we now have all the necessary background information for our penultimate model in which we consider the dynamics of planetary surfaces. We simply



suppose that the observed surface is formed by two opposing processes, erosion and uplift. We model the erosion by the diffusivity equation (Culling, 1960, 1963, 1965)

$$\beta' \frac{\partial H}{\partial t} = \nabla^2 H \quad (4.53)$$

where  $\beta'$ , a measure of the intensity of the erosion, is assumed constant. We further suppose that linearly additive constructional or "tectonic" events occur essentially instantaneously relative to the erosive time scale and that they occur at random times and places. The times of occurrence have a Poisson distribution with an average of  $\alpha'$  events per unit time. A typical event has the form

$$f(\theta, \varphi) = R_0 \sum_{n=1}^{\infty} \sum_{m=0}^n f_{nm}^T \Lambda_{nm}(\theta, \varphi) \quad (4.54)$$

where  $f_{nm}$  are zero-mean Gaussian random variables  $N(0, \sigma_n^2)$ , where

$$\sigma_n^2 = \frac{V(f; n)}{2n+1} \quad (4.55)$$

and the degree variances of the process are

$$V(f; n) = \sum_{m=0}^n f_{nm}^T f_{nm} \quad (4.56)$$

We will now determine what form the variance spectrum of the constructional process must take in order to produce the Vening-Meinesz topographic spectral form.

The spatial covariance of the topography initially produced by a single event is

$$C(f; \gamma) = R_0^2 \sum_{n=1}^{\infty} V(f; n) P_n [\cos(\gamma)] \quad (4.57)$$

However, erosion reduces the effect at time  $t$  of a single tectonic event which occurred at an earlier time  $t - \tau$  to

$$f'(\theta, \varphi; \tau) = R_0 \sum_{n=1}^{\infty} \sum_{m=0}^n f_{nm}^T \Lambda_{nm}(\theta, \varphi) \mathcal{C}_n(\tau) \quad (4.58)$$

where

$$\mathcal{C}_n(\tau) = e^{-(n)(n+1)\tau/\beta'} \quad (4.59)$$

(see Appendix A). Therefore, the spatial and temporal covariance function of the equilibrium surface produced by these processes is, by the convolution theorem,

$$\begin{aligned} C(H; \gamma, \tau) &\equiv E [H(\Omega, t) H(\Omega + \gamma, t + \tau)] \\ &= \alpha' R_0^2 \int_{-\infty}^t \sum_{n=1}^{\infty} V(f; n) P_n[\cos(\gamma)] \\ &\quad \cdot \mathcal{C}_n(t-s) \mathcal{C}_n(t+\tau-s) ds \end{aligned} \quad (4.60)$$

We can simplify this by taking terms with no time dependence outside the integral and noting that

$$\begin{aligned} &\int_{-\infty}^t \mathcal{C}_n(t-s) \mathcal{C}_n(t+\tau-s) ds \\ &= \mathcal{C}_n(2t+\tau) \int_{-\infty}^t \mathcal{C}_n(-2s) ds \\ &= \frac{\beta' \mathcal{C}_n(\tau)}{2(n)(n+1)} \end{aligned} \quad (4.61)$$

Therefore, we obtain

$$C(H; \gamma, \tau) = \frac{\alpha' \beta'}{2} R_o^2 \sum_{n=1}^{\infty} \frac{V(f; n)}{(n)(n+1)} P_n[\cos(\gamma)] \mathcal{C}_n(\tau) \quad (4.62)$$

The resulting purely spatial ( $\tau = 0$ ) and purely temporal ( $\gamma = 0$ ) covariance functions are

$$C(H; \gamma) = \frac{\alpha' \beta'}{2} R_o^2 \sum_{n=1}^{\infty} \frac{V(f; n)}{(n)(n+1)} P_n[\cos(\gamma)] \quad (4.63)$$

and

$$C(H; \tau) = \frac{\alpha' \beta'}{2} R_o^2 \sum_{n=1}^{\infty} \frac{V(f; n)}{(n)(n+1)} \mathcal{C}_n(\tau) \quad (4.64)$$

respectively, since  $P_n[\cos(0)] = \mathcal{C}_n(0) = 1$ . Generalizing a result of Grenander (1975), we assert that for a model of this type, given the heights at a time  $t$

$$H(\theta, \varphi; t) = R_o \sum_{n=1}^{\infty} \sum_{m=0}^n H_{nm}^T \Lambda_{nm}(\theta, \varphi) \quad (4.65)$$

the optimal estimate (in the sense of least-square error) of heights at an earlier or later time  $t \pm \tau$  is given by

$$\hat{H}(\theta, \varphi; t \pm \tau) = R_o \sum_{n=1}^{\infty} \sum_{m=0}^n H_{nm}^T \Lambda_{nm}(\theta, \varphi) \mathcal{C}_n(\tau) \quad (4.66)$$

The mean square error of the estimate is

$$\begin{aligned} & E \left[ \left| \hat{H}(\Omega, t \pm \tau) - H(\Omega, t \pm \tau) \right|^2 \right] \\ &= R_o^2 \sum_{n=1}^{\infty} V(H; n) \left[ 1 - \mathcal{C}_n(2\tau) \right] \end{aligned} \quad (4.67)$$

Unfortunately, unless we have independent estimates of  $\alpha' V(f; n)$  or  $\beta'$ , we cannot evaluate  $\mathcal{C}_n(\tau)$ , since all that is observable at one time is

$$V(H;n) = \frac{\alpha' \beta'}{2} \frac{V(f;n)}{(n)(n+1)} \quad (4.68)$$

In order to duplicate the Vening-Meinesz spectrum, we simply require that

$$V(f;n) = \frac{2}{\alpha' \beta'} V(H;0) \quad (4.69)$$

i.e. the variance spectrum of the constructional process must be constant. This has the interesting interpretation that there is no preferred scale at which tectonic or constructional processes occur.

In order to match the observed low degree variances as well, we must either allow for a decrease in constructional activity at scale lengths greater than  $L \doteq 2000$  km, or assume more erosive or attenuative activity at that scale than the diffusivity model predicts. Note that, whereas diffusive erosion is essentially a low pass filter, visco-elastic deformation acts as a high pass filter and would selectively attenuate the low degree harmonics. We will now consider this in more detail.

#### Visco-Elastic Deformation

Darwin (1879) determined that a homogeneous Maxwell sphere (see Appendix E) subjected to a surface load of height  $f(\theta, \varphi)$  at time  $t$  will deform in such a way that, at a later time  $t + \tau$ , the load height will be reduced to

$$f'(\theta, \varphi; \tau) = R_0 \sum_{n=1}^{\infty} \sum_{m=0}^n f_{nm}^T \Lambda_{nm}(\theta, \varphi) e^{-\tau/\tau'_n} \quad (4.70)$$

If the sphere of radius  $R_0$  has density  $\rho$ , viscosity  $\eta$  and rigidity  $\mu$ , then the relaxation time will be

$$\tau'_n = \eta \left[ \frac{N(n)}{P_c} + \frac{1}{\mu} \right] \quad (4.71)$$

where

$$P_c = 2\pi G \rho^2 R_o^2 / 3 \quad (4.72)$$

is the hydrostatic pressure at the center of the sphere and

$$N(n) = \frac{2(n+1)^2 + 1}{2n} \quad (4.73)$$

is a geometrical factor determined by the spherical boundary conditions. This can be rewritten as

$$\tau'_n = \tau_n + \tau_M \quad (4.74)$$

where  $\tau_n = \eta N(n)/P_c$  is the corresponding relaxation time for a purely viscous sphere and  $\tau_M = \eta/\mu$  is the Maxwell relaxation time of the material. For times  $\tau < \tau_M$ , the behavior is predominantly elastic, whereas for  $\tau > \tau_M$ , viscous behavior predominates.

If the topography of a Maxwell sphere is then subjected to erosion, the attenuating factor for the harmonics of degree  $n$  will be

$$\mathcal{C}'_n(\tau) = e^{-[(n)(n+1)\tau/\beta' + \tau/\tau'_n]} \quad (4.75)$$

rather than (4.59). If we now carry through the same covariance analysis as before, substituting  $\mathcal{C}'_n$  for  $\mathcal{C}_n$ , we find that the resultant topographic variance spectrum is

$$V(H;n) = \frac{\alpha'\beta'}{2} \frac{V(f;n)}{(n)(n+1)} A(n) \quad (4.76)$$

where

$$A(n) = \left[ 1 + \frac{\beta'}{(n)(n+1)\tau'_n} \right]^{-1} \quad (4.77)$$

If we neglect the elastic component, this is approximately

$$A(n) \doteq \left[ 1 + \frac{2P_c \beta' / \eta}{(n+1)(2(n+1)^2 + 1)} \right]^{-1} \quad (4.78)$$

This model succeeds in predicting attenuation of the low degree variances. Furthermore, because of the strong dependence of  $P_c$  on  $R_0$ , it also predicts relatively more attenuation on large planets than on small planets with the same material properties. A value of  $P_c \beta' / \eta \doteq 70$  yields a spectrum very similar in shape to those of the Earth and Venus.

A possible criticism of the above model is that it assumes the planets to be homogeneous. However, more sophisticated analyses of the viscous relaxation time spectrum  $\tau_n$  of the Earth (e.g., Anderson and O'Connell, 1967) have shown it to be qualitatively similar to the homogeneous case. The important point is that  $\tau_n$  is a rapidly increasing function of harmonic degree.

The success of this model in duplicating the entire topographic variance spectrum on all planets for which we have observations increases our confidence in the model and strengthens our earlier conclusion that there is no preferred scale of constructional activity on the planets.

In addition to duplicating the Vening-Meinesz spectral form, the models we have considered have given us three separate estimates of the total dimensionless variance. From slope stability considerations, we find

$$V(H;0) = \frac{4c}{\rho g R_0} \quad (4.79)$$

from the random pulse model, we have

$$\begin{aligned} V(H;0) &= 8\alpha p(\mu_0) A^2(\mu_0) \left[ \frac{1 - \mu_0}{1 + \mu_0} \right] \\ &= 8\alpha\beta \end{aligned} \quad (4.80)$$

and from the equilibrium model, we obtain

$$V(H;0) = \frac{\alpha'\beta'}{2} V(f;0) \quad (4.81)$$

We would like to use these model variances to predict the actual variance on planetary surfaces which have not yet been measured. However, the only one of these formulas with any real predictive value is the first, since we have no good a priori estimates of the parameters in the other two. The greatest uncertainty in equation (4.79) is the mean cohesion  $c$ . It turns out that a value of  $c$  between 0.2-0.8 bar gives the correct variance on all four planets we have considered. These values roughly correspond to a loosely consolidated soil.

A still better prediction comes from the observation that the physical variance  $C(H;0)$  of the four planets we have studied all fall in the range 4.0-6.5 km<sup>2</sup> (Moon, 4.5; Mars, 6.4; Venus, 4.0; Earth 5.6). This is perhaps suggestive of a plastic rather than visco-elastic rheology. However, we shall not pursue this matter further.

### Maximum Entropy Conjecture

Our final attempt at explaining the topography of the planets focuses on the fact that planetary surfaces resemble realizations of the spherical Wiener stochastic process. First, we are going to make two conjectures concerning the Wiener process: neither of them will be proven, but we will give plausibility arguments for both. We will then discuss how this relates to planetary surfaces.

As background for our first conjecture, we note that the process which we have glibly referred to as the spherical Wiener process differs from the usual Wiener process  $W(\varphi)$  in several fundamental aspects. The domain  $\Phi$  of  $W(\varphi)$  is usually taken to be either the real line  $R$  or some Euclidean space  $R^n$  (Levy, 1948), and on those domains  $W(\varphi)$  is not stationary. However, Levy (1954) has shown that a process defined as

$$h(\varphi) = \sum_{m=1}^{\infty} \xi_m^T \Lambda_m(\varphi) \quad (4.82)$$

where

$$\Lambda_m(\varphi) = \begin{bmatrix} \cos(m\varphi) \\ \sin(m\varphi) \end{bmatrix} \quad (4.83)$$

and

$$\xi_m = \begin{bmatrix} \xi_{m1} \\ \xi_{m2} \end{bmatrix} \quad (4.84)$$

is equivalent to

$$h(\varphi) = W(\varphi) - \frac{\varphi}{2\pi} W(2\pi) \quad (4.85)$$

and is stationary, if  $\xi_{mi}$  are Gaussian random variables  $N(0, \sigma_m^2)$  with



$$\sigma_m^2 = \frac{V(h;0)}{2m^2} \quad (4.86)$$

Of course, this is nothing more than a great circle slice of what we have been calling a spherical Wiener process. Another stationary process which otherwise resembles the Wiener process is the Ornstein-Uhlenbeck process (see Appendix C). It is obtained from a random walk subjected to a restoring force in the limit as the step size goes to zero. Our first conjecture then is that, when the domain of the process is a sphere (or circle), the Wiener and Ornstein - Uhlenbeck processes are identical. Since these are both Gaussian processes, all that is required for the proof is a demonstration that their covariance functions are identical. Though this appears likely, we have not rigorously shown it to be so. In our discussion, we have assumed that the conjecture is true and simply refer to the process in question as a spherical (or circular) Wiener process.

Our second conjecture is that for a given variance, the spherical (or circular) Wiener process is the unique maximal entropy spherical (circular) process with continuous realizations and infinite bandwidth. As an argument for the plausibility of this conjecture, consider our random pulse model. The positions of the pulses are governed by a Poisson distribution which has the maximum entropy rate of any point process for a given intensity  $\alpha$  (McFadden, 1965). As we let the average variance per pulse  $\beta$  decrease while increasing  $\alpha$  so as to maintain a constant total variance  $\alpha\beta$ , the central limit theorem assures us that the distribution of heights tends to a

Gaussian, which is the maximal entropy distribution for a fixed mean and variance. This argument is suggestive only and not conclusive, since our conjecture concerns the entire process describing the surface and not merely the distribution of heights. The fact that the spherical (circular) Wiener process is a Gaussian process is probably a necessary condition, but is definitely not sufficient for our conjecture.

A proof might be developed as follows. For simplicity, we consider Levy's (1954) construction of the circular Wiener process (4.79). The system has two degrees of freedom for each harmonic degree  $m$ . The variance and entropy per degree of freedom are (Shannon, 1948)

$$v(h) = \sigma_m^2 \quad (4.87)$$

$$e(h) = \frac{1}{2} \left[ 1 + \ln(2\pi\sigma_m^2) \right] \quad (4.88)$$

Therefore, the total variance and entropy are

$$V(h) = \sum_{m=1}^{\infty} 2\sigma_m^2 \quad (4.89)$$

$$E(h) = \sum_{m=1}^{\infty} \left[ 1 + \ln(2\pi\sigma_m^2) \right] \quad (4.90)$$

The requirement of continuous realizations for the process is essentially assured by maintaining finite total variance. This, in conjunction with the requirement of infinite bandwidth, requires

$$\sigma_m^2 = \mathcal{O}(m^{-2}) \quad (4.91)$$

Our conjecture is that the extremal value of E subject to these constraints is obtained when

$$\sigma_m^2 = \frac{3 V(h)}{(\pi m)^2} \quad (4.92)$$

since

$$\sum_{m=1}^{\infty} \frac{1}{m^2} = \frac{\pi^2}{6} \quad (4.93)$$

The application of this conjecture to planetary topographic variance spectra is very simple, and is akin to the thermodynamic analogies of Scheidegger (1967) with the additional constraint of fixed variance. Our final model for the Vening-Meinesz spectrum merely supposes that the surface of a planet is as random or chaotic as it can be subject to the constraints of continuity and finite variance.

#### D. IMPLICATIONS

The simplest application of this study is to predict the form of the topographic variance spectra of other planets and satellites. Therefore, we make the following

---

##### Prediction:

The topographic variance spectra of the surfaces of all solid planets and satellites have the form

$$V(H;n) = \begin{cases} V(H;n_0) & n \leq n_0 \\ \frac{V(H;0)}{(n)(n+1)} & n \geq n_0 \end{cases} \quad (4.94)$$

where  $L_o = 2\pi R_o / n_o \approx 2000$  km.

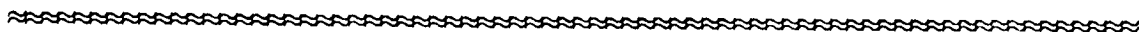
Furthermore, the total physical variance is

$$C(H;0) \equiv R_o^2 \sum_{n=1}^{\infty} V(H;n) \quad (4.95)$$

$$\approx 5 \pm 2 \text{ km}^2$$

independent of the size of the body, for all

$$R_o \geq 10 \text{ km}$$



We note that recent observations of Phobos ( $R_o = 11.2$  km) and Deimos ( $R_o = 6.3$  km) indicate rough, heavily cratered surfaces with variances of  $2-3 \text{ km}^2$  about the best fitting tri-axial ellipsoids (Duxbury, 1974, 1976).

Our observations concerning topographic variance spectra may contribute to another problem of current interest: determining the depth of sources of planetary gravity anomalies. The main difficulty is the inherent non-uniqueness of the density distribution

$$\rho(R, \theta, \varphi) = \bar{\rho} \left[ 1 + \sum_{n=1}^{\infty} \sum_{m=0}^n \rho_{nm}^T(R) \Lambda_{nm}(\theta, \varphi) \right] \quad (4.96)$$

associated with a given external potential

$$\Phi(R, \theta, \varphi) = \frac{GM}{R_o} \left[ \frac{R_o}{R} + \sum_{n=1}^{\infty} \sum_{m=0}^n \left( \frac{R_o}{R} \right)^{n+1} G_{nm}^T \Lambda_{nm}(\theta, \varphi) \right] \quad (4.97)$$

This non-uniqueness is evident in the relationship

$$\frac{2n+1}{3} G_{nm} = \int_0^1 \rho_{nm}(\xi) \xi^{n+2} d\xi \quad (4.98)$$

where  $\xi = R/R_0$ , since these integral constraints can be satisfied by an infinite class of density distributions. However, if we have additional information or are willing to make some plausible assumptions, we can make some progress. It is also possible to characterize the class of admissible density distributions in terms of various extremal properties such as greatest lower bound on density contrast or least upper bound on the depth of burial of an anomalous mass (Parker, 1974,1975).

Another approach is to assume that the density anomalies are due to undulations of an interface across which there is a density contrast  $\Delta\rho$ . If the mean radius of the interface is  $R = \xi R_0$  and the height of the undulations is

$$h(\theta, \varphi) = R \sum_{n=1}^{\infty} \sum_{m=0}^n h_{nm}^T \Lambda_{nm}(\theta, \varphi) \quad (4.99)$$

then the potential coefficients are

$$\frac{2n+1}{3} \bar{\rho} G_{nm} = \Delta\rho \xi^{n+3} h_{nm} \quad (4.100)$$

This approach was used to model lunar and Martian crustal thickness variations in chapters II and III respectively (Bills and Ferrari, 1977, b,c). It has also been applied to terrestrial data by Bott (1971) who attributed the gravity anomalies to undulations in the mantle phase transition boundaries, and by Hide and Horai (1968) who placed the topography on the core-mantle interface. As can be seen from equation (4.97), an increase in the depth of the interface requires an increase in either the density contrast or the amplitude of the

undulations. This effect is more pronounced for high degree harmonics.

With that fact in mind, Higbie and Stacey (1970) have sought the depth at which the stresses required to support the density anomalies would be most nearly equal across the spectrum. After considering a number of different gravity models, they concluded that the most likely location of the anomalous masses is in the upper mantle.

The method which has received the most attention, though, "rests only on the assumption that the gravity anomalies arise from many independent density variations and that correlation between the density variations at different points falls to zero as the distance between the points increases" (Allan, 1972). This assumption is actually implemented through the use of a flat spectrum for the density anomalies or interface undulations. It has been widely used (Guier and Newton, 1965; Kaula, 1967; Allan, 1972; Lambeck, 1976; McQueen and Stacey, 1976; and Khan, 1977), and its practitioners consistently find two separate source depths: the low degree harmonics ( $n \leq 5$ ) derive from depths of 800-1500 km whereas the higher harmonics have a shallower source (200-400 km). However, this result is highly suspect because of both the neglected surface topographic effect and the assumed source spectrum. Obviously, the correct spectrum to examine in seeking the depth of the source mass anomalies is the Bouguer spectrum and not the

free-air spectrum. Yet every one of the above studies used the free-air spectrum. The assumed spectral behavior of the source warrants further discussion.

The models which incorporate a flat source spectrum are informative, since they yield a maximum source depth for a given potential spectrum (Naidu, 1968). Furthermore, McQueen and Stacey (1976) have argued that "the superposition of sharp features on an otherwise spherically symmetrical distribution of any kind can be represented by a white spatial spectrum, that is by a sum of spherical harmonic terms of equal amplitudes. Thus if phase boundary undulations are highly localized relative to the wavelengths corresponding to the highest available harmonic terms, their spatial spectra will be white." On the other hand it might be more reasonable to suppose that all equi-density surfaces in a planet have roughly the same spectral form as the external surface topography. The resulting model potential variance for a single interface at a depth  $D = R_0$  (1 -  $\xi$ ) is

$$\hat{V}(G;n) = \frac{9\alpha V(h;0)}{(n)(n+1)(2n+1)^2} \xi^{2n+6} \quad (4.101)$$

where  $\alpha = (\Delta\rho/\bar{\rho})^2$ . This model is still lacking in realism though, since it seems unlikely that all of the density anomalies would be concentrated at one depth.

The last approach we consider makes a less restrictive assumption about the source behavior. We simply assume that the density anomalies satisfy

$$\nabla^2 [R^k \rho(R, \theta, \varphi)] = 0 \quad (4.102)$$

where  $k$  is an integer. In this case Tscherning (1976) has shown that the variance spectrum and covariance of the density anomalies which are consistent with the potential variances  $V(G;n)$  have the form

$$V(\rho;n) = \left(\frac{2n+1}{3}\right)^2 (2n+3-k)^2 V(G;n) \quad (4.103)$$

$$C(\rho_i, \rho_j) = \bar{\rho}^2 \sum_{n=1}^{\infty} V(\rho;n) (\xi_i \xi_j)^{n-k} P_n(\cos(\gamma_{ij})) \quad (4.104)$$

It may be shown that the potential covariance is the convolution of the covariances of the density anomalies and the Green's function (Kautzleben et al., 1977). We note also that the case of  $k = 0$  corresponds to the density distribution of minimum variance which will produce the observed spectrum.

#### E. SUMMARY

In this chapter we have seen that the topographic variance spectra of the Earth, Moon, Mars and Venus are all very close to the Vening-Meinesz spectral form (4.1), in spite of vast differences in the geomorphic processes acting on these surfaces. This observation has prompted the conjecture that the solid surfaces of all planets and satellites are similarly characterized by this spectral form. Equivalently, these surfaces are conjectured to be realizations of a spherical Wiener stochastic process.



In examining a number of possible explanations for this behavior, we have found the most promising model to involve a simple equilibrium between constructional or "tectonic" processes which tend to roughen the surface uniformly at all scales, and destructional or erosive processes which tend to smooth the surface preferentially at small scales. This balance is maintained in such a way that the resultant surface is continuous almost everywhere but is differentiable almost nowhere.

This improved insight into the topographic variance spectrum may ultimately lead to a better understanding of the gravitational variance spectrum and the distribution of anomalous source masses. Another possible area for future research involves the connection between plate tectonics, elastic energy reduction and the resultant topographic variance spectrum.

## REFERENCES

- Allan, R.R. (1972). Depth of sources of gravity anomalies.  
Nature Phys. Sci. 236, 22-23.
- Anderson, D.L. and O'Connell, R. (1967). Viscosity of the Earth.  
Geophys. J. R. Astr. Soc. 14, 287-295.
- Au, C.K. and Shaham, J. (1971). Elastic energy and plate tectonics.  
Nature 250, 211-213.
- Baines, P.G. (1976). The stability of planetary waves on a sphere.  
J. Fluid Mech. 73, 193-213.
- Balmino, G., Lambeck, K. and Kaula, W.M. (1973). A spherical harmonic  
analysis of the Earth's topography. J. Geophys. Res. 78, 478-481.
- Beers, B.L. (1972). Harmonic analysis of analytic functions on  
hyperspheres. J. Math. Phys. 13, 950-955.
- Beers, B.L. and Dragt, A.J. (1970). New theorems about spherical  
harmonic expansions. J. Math. Phys. 11, 2313-2328.
- Bell, T.H. (1974). Representation of random noise by random pulses.  
J. Appl. Phys. 45, 1902-1904.
- Bell, T.H. (1975). Statistical features of sea floor topography.  
Deep Sea Research 22, 883.
- Bills, B.G. and Ferrari, A.J. (1977a). A harmonic analysis of lunar  
topography. Icarus 31, 244-251.
- Bills, B.G. and Ferrari, A.J. (1977b). A lunar density model  
consistent with topographic, gravitational, librational and  
seismic data. J. Geophys. Res. 82, 1306-1314.

- Bills, B.G. and Ferrari, A.J. (1977c). Mars topography harmonics and geophysical implications. Submitted to J. Geophys. Res.
- Bott, M.H.P. (1971). The mantle transition zone as possible source of global gravity anomalies. Earth Planet. Sci. Lett. 11, 28-34.   
 \*\*\*\*
- Bretherton, F.P. (1969). Momentum transport by gravity waves. Q.J. Roy. Meteor. Soc. 95, 213-243.   
 \*\*\*\*
- Bretherton, F.P. and Haidvogel D.B. (1976). Two-dimensional turbulence above topography. J. Fluid Mech. 78, 192-154.   
 \*\*\*\*
- Campbell, D.B., Dyce, R.B., Ingalls, R.P., Pettengill, G.H., and Shapiro, I.I. (1972). Venus: topography revealed by radar data. Science 175, 514-516.   
 \*\*\*\*
- Carson, M.A. and Kirkby, M.J. (1972). Hillslope Form and Process. Cambridge University Press, 467 pp.
- Chandrasekhar, S. (1969). Ellipsoidal Figures of Equilibrium. Yale University Press, New Haven, 247 pp.
- Christensen, E.J. (1975). Martian topography derived from occultation, radar, spectral and optical measurements. J. Geophys. Res. 80, 2909-2913.   
 \*\*\*\*
- Chuikova, N.A. (1976). The geometrical figure of the Moon represented in the form of an expansion in spherical and sampling functions. Sov. Astron. 19, 764-771.   
 \*\*\*\*
- Chung, C.L. and Scheidegger, A.E. (1968). A thermodynamic analogy for transport processes involving a non-positive definite transported quantity. Bull. Int. Asso. Sci. Hyd. 13, 88-94.   
 \*\*\*\*

- Coode, A.M. (1966). An analysis of major tectonic features. Geophys. J. Roy. Astr. Soc. 12, 55-66.
- Coode, A.M. (1967). The spherical harmonic analysis of major tectonic features. In (S.K. Runcorn, ed.) Mantles of the Earth and Terrestrial Planets, Interscience, London, pp 489-498.
- Cook, A.H. (1963). Sources of harmonics of low order in the external gravity field of the Earth. Nature 198, 1186.
- Cook, A.H. (1973). Physics of the Earth and Planets. John Wiley, New York, 316 pp.
- Cox, C. and Sandstrom, H. (1962). Coupling of internal and surface waves in water of variable depth. J. Ocean. Soc. Japan 20, 499-513.
- Culling, W.E.H. (1960). Analytical theory of erosion. J. Geol. 68, 336-344.
- Culling, W.E.H. (1963). Soil creep and the development of hillside slopes. J. Geol. 71, 127-161.
- Culling, W.E.H. (1965). Theory of erosion on soil-covered slopes. J. Geol. 73, 230-254.
- Dietz, R.S. and Holden, J.C. (1970). Reconstruction of Pangaea: breakup and dispersion of continents, Permian to present. J. Geophys. Res. 75, 4939-4956.
- Duxbury, T.C. (1974). Phobos: control network analysis. Icarus 23, 290-299.

- Duxbury, T.C. (1976). Phobos and Deimos: geodesy. In Planetary Satellites (J.A. Burns, Ed.) University Arizona Press, Tucson, Arizona, pp. 346-362.
- Fjortoft, R. (1953). On changes in the spectral distribution of kinetic energy in two dimensional non-divergent flow. Tellus 5, 225-230.
- Gilbert, G.K. (1877) Report on the Geology of the Henry Mountains U.S. Geogr. Geol. Survey, 173pp.
- Goudas, C.L. (1971). Geometrical and dynamical properties of the Moon. In Physics and Astronomy of the Moon (Z. Kopal, Ed.) pp. 101-152. Academic Press, New York.
- Grafarend, E.W. (1976). Geodetic applications of stochastic processes. Phys. Earth Planet. Inter. 12, 151-179.
- Grenander, U. (1975). Dynamic models of geomorphological patterns. Mathematical Geology 7, 267-278.
- Guier, W.H. and Newton, R.R. (1965). The Earth's gravity field as deduced from the Doppler tracking of five satellites. J. Geophys. Res. 70, 4613-4626.
- Halford, D. (1968). A general mechanical model for  $f^\alpha$  spectral density noise. Proc. I.E.E.E. 56, 251-258.
- Hartmann, W.K. (1972). Interplanet variations in scale of crater morphology - Earth, Mars, Moon. Icarus 17, 707-713.
- Hide, R. and Horai, K. (1968). On the topography of the core-mantle interface. Phys. Earth Planet. Inter. 1, 305-308.

- Higbie, J. and Stacey, F.D. (1970). Depth of density variations responsible for features of the satellite geoid. Phys. Earth Planet. Inter. 4, 145-148.
- Hinze, J.O. (1959). Turbulence. McGraw-Hill, 586 pp.
- Jenkins, G.M. and Watts, D.G. (1968). Spectral Analysis and Its Application. Holden-Day, 525 pp.
- Johnson, T.V. and McGetchin, T.R. (1973). Topography on satellite surfaces and the shape of asteroids. Icarus 18, 612-620.
- Kampé de Fériet, J. (1962). Statistical mechanics of continuous media. Proc. Symp. Appl. Math. 13, 165-198.
- Kaula, W.M. (1967). Geophysical implications of satellite determinations of the Earth's gravitational field. Space Sci. Rev. 7, 769-794.
- Kaula, W.M., Lingenfelter, R.E., Schugert, G. Sjogren, W.L. and Wollenhaupt, W.P. (1972). Analysis and interpretation of lunar laser altimetry. Proc. Lunar Sci. Conf. 3rd 3, 2189-2204.
- Kaula, W.M., Lingenfelter, R.E., Schubert, G., Sjogren, W.L., and Wollenhaupt, W.R. (1973). Lunar topography from Apollo 15 and 16 laser altimetry. Proc. Lunar Sci. Conf. 4th 3, 2811-2819.
- Kaula, W.M., Lingenfelter, R.E., Schubert, G., Sjogren, W.L. and Wollenhaupt, W.R. (1974). Apollo laser altimetry and inference as to lunar structure. Proc. Lunar Sci. Conf. 5th. 3, 2049-3058.
- Kautzleben, H., Harnisch, M. and Schwahn, W. (1977). The statistical description and interpretation of geophysical potential fields using covariance functions. J. Geophys. 43, 163-177.

- Khan, M.A. (1977). Depth of sources of gravity anomalies. Geophys. J. R. Astr. Soc. 48, 197-209.
- Kirkby, M.J. (1971). Hillslope process-response models based on the continuity equation in slopes: Form and process. Inst. Brit. Geographers Special Pub. 3, pp. 15-30.
- Kopal, Z. (1960). Figures of Equilibrium of Celestial Bodies. Univ. Wisconsin Press, Madison, 135 pp.
- Krause, D.C. and Menard, H.W. (1965). Depth distribution and bathymetric classification of some sea-floor profiles. Marine Geology 3, 169-193.
- Lambeck, K. (1976). Lateral density anomalies in the upper mantle. J. Geophys. Res. 81, 6333-6340.
- Lauritzen, S.L. (1975). Random orthogonal set functions and stochastic models for the gravity potential of the Earth. Stoch. Proc. Appl. 3, 65-72.
- Leopold, L.B. and Langbein, W.B. (1962). The concept of entropy in landscape evolution. U.S. Geol. Survey Prof. Paper 500-A.
- Levy, P. (1948). Processus Stochastiques et Mouvement Brownien. Gauthier-Villars, Paris, 365pp.
- Levy, P. (1954). Le mouvement brownien. Mem. Sci. Math. 126, 1-84.
- Malin, M.C. and Dzurisin, D. (1977). Landform degradation on Mercury, the Moon, and Mars: Evidence from crater depth/diameter relationships. J. Geophys. Res. 82, 376-388.
- Mandelbrot, B.B. (1967). How long is the coast of Britain? Statistical self-similarity and fractional dimension. Science 156, 636-638.

- Mandelbrot, B.B. (1975a). Stochastic models for the Earth's relief, the shape and fractal dimension of coastlines, and the number - area rule for islands. Proc. Nat. Acad. Sci. 72, 3825.
- Mandelbrot, B.B. (1975b). On the geometry of homogeneous turbulence with stress on the fractal dimension of the iso-surfaces of scalars. J. Fluid Mech. 72, 401-416.
- Mandelbrot, B.B. (1977). Fractals: Form, Chance and Dimension. W.H. Freeman, San Francisco.
- Mandelbrot, B.B. and VanNess J.W. (1968). Fractional Brownian motions, fractional noises and applications. SIAM Review 10, 422-437.
- Marcus, A.H. (1964). A stochastic model of the formation and survival of lunar craters. I. Distribution of diameter of clean craters. Icarus 3, 460-472.
- Marcus, A.H. (1966). A stochastic model of the formation and survival of lunar craters. II. Approximate distribution of diameter of all observable craters. Icarus 5, 165-177.
- Marcus, A.H. (1967). Statistical theories of lunar and Martian craters. In Mantles of the Earth and Terrestrial Planets (S.K. Runcorn, Ed.) John-Wiley, New York, pp. 417-424.
- Marcus, A.H. (1969). Distribution of slopes on a cratered planetary surface: Theory and preliminary applications. J. Geophys. Res. 74, 5253-5267.
- Marcus, A.H. (1970a). Distribution and covariance function of elevations on a cratered planetary surface. The Moon 1, 297-337.



- Marcus, A.H. (1970b). Comparison of equilibrium size distributions for lunar craters. J. Geophys. Res. 75, 4977-4984.
- McFadden, J.A. (1965). The entropy of a point process. J. Soc. Indust. Appl. Math. 13, 988-994.
- McKenzie, D., Roberts, J., and Weiss, N. (1973). Numerical models of convection in the Earth's mantle. Tectonophysics 19, 89-103.
- McQueen, H.W.S. and Stacey, F.D. (1976). Interpretation of low degree components of gravitational field in terms of undulations of mantle phase boundaries. Tectonophysics 34, T1-T8.
- Middleton, D. (1951). On the theory of random noise: Phenomenological models. J. Appl. Physics 22, 1143-1163.
- Moore, H.J. and Tyler, G.L. (1973). Comparison between photogrammetric and bistatic-radar slope-frequency distributions. Apollo 17 Preliminary Science Report 33: 17-26, NASA SP-330.
- Naidu, P. (1968). Spectrum of the potential field due to randomly distributed sources. Geophysics 33, 337-345.
- Neukum, G. and Dietzel, H. (1971). On the development of the crater population on the Moon with time under meteorite and solar wind bombardment. Earth Planet. Sci. Lett. 12, 59-66.
- Parker, R.L. (1974). Best bounds on density and depth from gravity data. Geophysics 39, 644-649.
- Parker, R.L. (1975). The theory of ideal bodies for gravity interpretation. Geophys. J.R. Astr. Soc. 42, 315-334.
- Parzen, E. (1962). Stochastic Processes. Holden-Day, San Francisco 324 pp.

- Pettengill, G.H., Counselman, C.C., Rainville, L.P. and Shapiro, I.I.  
(1969). Radar measurements of Martian topography. Astron. J.  
74, 461-482.
- Pike, R.J. and Rozema, W.J. (1975). Spectral analysis of landforms.  
Ann. Asso. Amer. Geogr. 65, 499-516.
- Pines, D. and Shaham, J. (1973). Quadrupolar analysis of storage and  
release of elastic energy in the Earth. Nature Phys. Sci. 243,  
122-127.
- Prey, A. (1922). Darstellung der höhen und tiefenverhältnisse der  
erde. Abh. Ges. Wiss. Göttingen 11, 1-35.
- Runcorn, S.K. (1965). Changes in the convection pattern in the Earth's  
mantle and continental drift. Phil. Trans. Roy. Soc. A258,  
228-251.
- Runcorn, S.K. (1967). Convection in the Moon and the existence of a  
lunar core. Proc. Roy. Soc. Lond. A296, 270-384.
- Scheidegger, A.E. (1967). A complete thermodynamic analogy for  
landscape evolution. Bull. Int. Asso. Sci. Hydrology 12, 57-62
- Scheidegger, A.E. and Chaudhari, N.M. (1964). Some statistical pro-  
perties of certain geophysical transport equations. Pure Appl.  
Geophys. 59, 45-57.
- Shannon, C.E. (1948). A mathematical theory of communication. Bell  
System Tech. J. 27, 379-423.

- Shapiro, I.I., Pettengill, G.H., Sherman, G.N., Rogers, A.E.E., and  
Ingalls, R.P. (1973). Venus: Radar determination of gravity  
potential. Science 179, 473-476.
- Smith, W.B., Ingalls, R.P., Shapiro, I.I. and Ash, M.E. (1970).  
Surface-height variations on Venus and Mercury. Radio Science  
5, 411-423.
- Soderblom, L.A. (1970). A model for small-impact erosion applied  
to the lunar surface. J. Geophys. Res. 75, 2655-2661.
- Tscherning, C.C. (1976). A mass covariance function consistent with  
the covariance function of the anomalous potential. Bollettino di  
Geodesia e Scienze Affini 35, 161-172.
- Tyler, G.L., Simpson, R.A. and Moore, H.J. (1971). Lunar slope  
distributions: Comparison of bistatic-radar and photographic  
results. J. Geophys. Res. 76, 2790-2795.
- Vening-Meinesz, F.A. (1951). A remarkable feature of the Earth's  
topography. Proc. Kon. Ned. Akad. V. Wet. B54, 212-228.
- Vening-Meinesz, F.A. (1962). Thermal convection in the Earth's mantle.  
In Continental Drift (S.K. Runcorn, Ed.), Academic Press pp 145-  
176.
- Walzer, U. (1971). Convection currents in the Earth's mantle and the  
spherical harmonic development of the topography of the Earth.  
Pure Appl. Geophys. 87, 73-92.
- Walzer, U. (1973a). A quantitative kinematic theory of convective  
currents in the Earth's mantle. Pure Appl. Geophys. 105, 669-695.

- Walzer, U. (1973b). Discussion of the new kinematic mantle convection theory. Pure Appl. Geophys. 105, 696-712.  
 theory. Pure Appl. Geophys. 105, 696-712.  
 theory. Pure Appl. Geophys. 105, 696-712.
- Warren, B.A. (1973). Transpacific hydrographic sections at lats. 43°S and 28°S. Deep-sea Res. 20, 9-38.
- Wells, R.A. (1971). Martian surface harmonics and continental drift. Phys. Earth Planet. Int. 4, 273-285.
- Woronow, A. (1977). Crater saturation and equilibrium: A Monte-Carlo simulation. J. Geophys. Res. 82, 2447-2356.
- Yaglom, A.M. (1962). Stationary Random Functions. Dover, New York, 235 pp.

## V. APPENDICES

### A. SPHERICAL HARMONICS

We will mainly be concerned with functions whose domain of definition is the surface of a sphere. Points on the sphere will usually be identified by their latitude ( $\theta$ ) and longitude ( $\varphi$ ) relative to some coordinate system. Angular distance between points is better expressed in terms of colatitude ( $\gamma$ ) or direction cosine ( $\mu = \cos(\gamma)$ ) of one point relative to the other. We will occasionally interchange the coordinate pairs  $(\theta, \varphi)$  and  $(\mu, \varphi)$ , where now  $\mu = \sin(\theta)$ , as the argument of a function while retaining the same symbol for the function, e.g.,  $F(\theta, \varphi) = F(\mu, \varphi)$ . This should cause no confusion.

The family of functions on the sphere which are continuous almost everywhere (i.e., except on a set of measure zero) may be converted into a Hilbert space by introduction of a scalar product

$$\langle F, G \rangle = \frac{1}{4\pi} \int_0^{2\pi} \int_{-1}^1 F(\mu, \varphi) G(\mu, \varphi) d\mu d\varphi \quad A.1$$

The associated norm is given by

$$\|F\| = \langle F, F \rangle^{1/2} \quad A.2$$

Any function for which  $\|F\| < \infty$  will be said to be square integrable.

It will often prove convenient to express a function defined over the surface of a sphere as a product of a dimensional scale factor times a non-dimensional sum of orthogonal functions - the

surface spherical harmonics. This summation, sometimes referred to as a Fourier-Legendre series, is the analogue on the sphere  $S^2$  of a simple Fourier series on the circle  $S^1$ , and shares many of its properties. For example, the topography of a planet with mean radius  $R_0$  might be represented as

$$\begin{aligned}
 F(\mu, \varphi) &= R_0 \left( 1 + \sum_{n=1}^{\infty} \sum_{m=0}^n \bar{P}_{nm}(\mu) [C_{nm} \cos(m\varphi) + S_{nm} \sin(m\varphi)] \right) \\
 &= R_0 \sum_{n=0}^{\infty} \sum_{m=0}^n F_{nm}^T \Lambda_{nm}(\mu, \varphi)
 \end{aligned}
 \tag{A.3}$$

where

$$F_{nm} = \begin{pmatrix} F_{nm1} \\ F_{nm2} \end{pmatrix} = \begin{pmatrix} C_{nm} \\ S_{nm} \end{pmatrix} = \frac{1}{R_0} \langle F, \Lambda_{nm} \rangle$$

is the vector of harmonic coefficients or Fourier-Legendre transforms, of degree  $n$  and order  $m$ . The superscript  $T$  (as in  $F_{nm}^T$ ) denotes transposition and

$$\Lambda_{nm}(\mu, \varphi) = \begin{pmatrix} \Lambda_{nm1}(\mu, \varphi) \\ \Lambda_{nm2}(\mu, \varphi) \end{pmatrix} = \bar{P}_{nm}(\mu) \begin{pmatrix} \cos(m\varphi) \\ \sin(m\varphi) \end{pmatrix}$$

the vector of normalized surface harmonic functions, is the product of a normalized Legendre function in latitude times a trigonometric (Fourier) vector in longitude. The Legendre polynomials  $P_n(\mu)$  and associated Legendre functions  $P_{nm}(\mu)$  are solutions of the differential equation (see e.g., MacRobert, 1967)

$$\frac{d}{d\mu} \left[ (1 - \mu^2) \frac{dP_{nm}}{d\mu} \right] + \left[ (n)(n+1) - \frac{m^2}{1 - \mu^2} \right] P_{nm} = 0 \quad A.4$$

In the un-normalized form, they satisfy the initial condition

$$P_{nm}(1) = \begin{cases} 1 & m = 0 \\ 0 & n \neq 0 \end{cases} \quad A.5$$

and are given by

$$\begin{aligned} P_{nm}(\mu) &= (1 - \mu^2)^{m/2} \frac{d^m P_n}{d\mu^m}(\mu) \\ &= (1 - \mu^2)^{m/2} \frac{d^{n+m}(\mu^2 - 1)^n}{d\mu^{n+m}} \end{aligned} \quad A.6$$

The normalized form is denoted by a bar  $\bar{P}_{nm}(\mu)$  and is given by

$$\bar{P}_{nm}(\mu) = N_{nm} P_{nm}(\mu) \quad A.7$$

where the normalization factor

$$N_{nm}^2 = (2 - \delta_{m0})(2n+1) \frac{(n-m)!}{(n+m)!}$$

is chosen so as to make the harmonics orthonormal over the sphere i.e.

$$\langle \Lambda_{nmi}, \Lambda_{n'm'j} \rangle = \delta_{nn'} \delta_{mm'} \delta_{ij} \quad A.8$$

The rate of convergence of a Fourier-Legendre series depends on the smoothness of the function  $F$  being represented, i.e., smooth functions have rapidly convergent series representations. The individual harmonic coefficients  $F_{nm}$  depend, not only on the function  $F$ , but also on the particular orientation of the coordinate system. However, the sum of the squares of all the coefficients of a given

degree

$$V(F;n) = \sum_{m=0}^n F_{nm}^T F_{nm} \quad A.9$$

is invariant under rotation (Kaula, 1967) and is thus better suited to discussions of convergence. Using the facts that

$$\begin{aligned} \nabla^2 \Lambda_{nm} + (n)(n+1) \Lambda_{nm} &= 0 \\ \|\Lambda_{nmi}\|^2 &= 1 \\ \|\nabla \Lambda_{nmi}\|^2 &= (n)(n+1) \end{aligned} \quad A.10$$

where  $\nabla$  and  $\nabla^2$  are the gradient and Laplacian differential operators, respectively, it may be shown (Beers and Dragt, 1970) that if the  $p$ -th derivative of  $F$  exists and is square integrable, i.e., if

$$\|\nabla^p F\| < \infty$$

then

$$V(F;n) = \mathcal{O}\left(\frac{1}{[(n)(n+1)]^{p+1}}\right) \quad A.11$$

A more general result (Beers, 1972) is that, for a function  $F$  defined on the hypersphere  $S^k$  ( $S^1$  is a circle,  $S^2$  is a sphere, etc.) with a square integrable  $p$ -th derivative,

$$V(F;n) = \mathcal{O}\left(\frac{1}{[(n)(n+k-1)]^{p+1}}\right) \quad A.12$$

where now  $V(F;n)$  is the sum of the squares of all

$$M(n,k) = (2n+k-1) \frac{(n+k-2)!}{(n)!(k-1)!}$$

hyperspherical harmonic coefficients of degree  $n$ , and  $(n)(n+k-1)$



is an eigenvalue of the Laplacian on  $S^k$ . Thus, for functions with bounded variation, but which are not differentiable almost everywhere, we have

$$V(F;n) = O\left(\frac{1}{n^2}\right) \quad F: S^1 \rightarrow R \quad A.13$$

$$V(F;n) = O\left(\frac{1}{(n)(n+1)}\right) \quad F: S^2 \rightarrow R$$

on circles and spheres, respectively. On the other hand, infinitely differentiable functions give rise to harmonic coefficients which fall off faster than any inverse power of  $n$ , i.e., they decrease exponentially

$$V(F;n) = O\left(e^{-\alpha(n)(n+k-1)}\right), \quad F: S^k \rightarrow R \quad A.14$$

for some  $\alpha > 0$ .

Functions whose domain of definition extends beyond the surface of a sphere to include its interior and exterior may be expressed as a sum of solid spherical harmonics. For example, the gravitational potential exterior to a planet might be represented as

$$\Phi(R, \theta, \varphi) = \frac{GM}{R_o} \left[ \frac{R_o}{R} + \sum_{n=1}^{\infty} \left(\frac{R_o}{R}\right)^{n+1} \sum_{m=0}^n G_{nm}^T \Lambda_{nm}(\theta, \varphi) \right], \quad R \geq R_o \quad A.15$$

whereas, the potential interior to a homogeneous planet would be

$$\Phi(R, \theta, \varphi) = \frac{GM}{R_o} \left[ \frac{3 - (R/R_o)^2}{2} + \sum_{n=1}^{\infty} \left(\frac{R}{R_o}\right)^n \sum_{m=0}^n G_{nm}^T \Lambda_{nm}(\theta, \varphi) \right], \quad R \leq R_o \quad A.16$$

where  $G$  is the gravitational constant and  $M$  is the planetary mass.

In many applications, we will be more concerned with the angular distance

$$\mu = \cos(\gamma) = \left( \frac{\cos(\Delta\varphi) + 1}{2} \right) \cos(\Delta\theta) + \left( \frac{\cos(\Delta\varphi) - 1}{2} \right) \cos(2\theta + \Delta\theta) \quad A.17$$

between the points  $(\theta, \varphi)$  and  $(\theta', \varphi') = (\theta + \Delta\theta, \varphi + \Delta\varphi)$ , than with the specific location of the points. In such situations, we will invoke the so-called addition theorem of spherical harmonics (see e.g., Heiskanen and Moritz, 1967) which states that:

$$P_n(\mu) = \frac{1}{2n+1} \sum_{m=0}^n \Lambda_{nm}^T(\theta', \varphi') \Lambda_{nm}(\theta, \varphi) \quad A.18$$

We will also have occasion to use the convolution theorem, which states that convolution in the spatial domain is equivalent to multiplication in the transform domain, and conversely. Thus, if

$$\begin{aligned} F(\theta, \varphi) &= A(\theta, \varphi) * B(\theta, \varphi) \\ &\equiv \frac{1}{4\pi} \int_0^{2\pi} \int_{-\pi/2}^{\pi/2} A(\theta', \varphi') B(\theta - \theta', \varphi - \varphi') \cos(\theta') \\ &\quad \cdot d\theta' d\varphi' \end{aligned} \quad A.19$$

then

$$F_{nm} = A_{nmi} B_{nmj} \delta_{ij} \quad A.20$$

A simplification occurs if  $B$  has no azimuthal variation, i.e.,

$$B(\theta - \theta', \varphi - \varphi') = B(\gamma) = \sum_{n=0}^{\infty} (2n+1) B_n P_n(\cos(\gamma)) \quad A.21$$

where now

$$B_n = \frac{1}{4\pi} \int_0^{2\pi} \int_{-1}^1 B(\mu) P_n(\mu) d\mu d\varphi = \frac{1}{2} \int_{-1}^1 B(\mu) P_n(\mu) d\mu \quad A.22$$

is the Legendre transform of  $B$ . In that case,

$$F_{nm} = A_{nm} B_n \quad A.23$$

We will now consider some particularly useful examples of such azimuthally symmetric functions. Our first example is a delta function of magnitude  $M$

$$B(\gamma) = M \delta(\gamma) \quad A.24$$

for which

$$B_n = \frac{M}{2}$$

The result of convolving a function of  $(\theta', \varphi')$  with a unit delta function located at  $(\theta, \varphi)$  is simply,

$$\begin{aligned} & \frac{1}{4\pi} \int_0^{2\pi} \int_{-\pi/2}^{\pi/2} A(\theta', \varphi') \delta(\theta - \theta', \varphi - \varphi') \cos(\theta') d\theta' d\varphi' \\ & = A(\theta, \varphi) \end{aligned} \quad A.25$$

the original function evaluated at  $(\theta, \varphi)$ . This relocation property of delta functions under convolution will prove quite useful in the sequel.

A rather wide class of azimuthally symmetric spherical functions can be obtained as solutions of the diffusion equation

$$\frac{\partial F}{\partial t} + \alpha^2 \nabla^2 F = 0 \quad A.26$$

and the wave equation

$$\frac{\partial^2 F}{\partial t^2} + \beta^2 \nabla^2 F = 0 \quad \text{A.27}$$

by suppressing the radial and azimuthal dependence of the Laplacian differential operator so that it has the form

$$\nabla^2 = \frac{\partial}{\partial \mu} \left[ (1 - \mu^2) \frac{\partial}{\partial \mu} \right] \quad \text{A.28}$$

We first consider the diffusion equation

$$\frac{\partial F(\mu, t)}{\partial t} + \alpha^2 \nabla^2 F(\mu, t) = 0 \quad \text{A.29}$$

subject to the initial condition

$$F(\mu, 0) = A(\mu)$$

Taking Legendre transforms of these equations, we obtain:

$$\frac{\partial F_n(t)}{\partial t} + \alpha^2 (n)(n+1) F_n(t) = 0 \quad \text{A.30}$$

$$F_n(0) = A_n$$

The solution of this transformed system is

$$F_n(t) = A_n e^{-(n)(n+1)\alpha^2 t} \quad \text{A.31}$$

so that the solution of the original system is

$$F(\mu, t) = \sum_{n=1}^{\infty} A_n e^{-(n)(n+1)\alpha^2 t} (2n+1) P_n(\mu) \quad \text{A.32}$$

The process of diffusion is seen to act as a low-pass filter, since it attenuates the high degree harmonics of the initial condition.

In the important case where the initial condition corresponds to a unit delta function, we find

$$F_n(t) = \frac{1}{2} e^{-(n)(n+1)\alpha^2 t} \quad A.33$$

This is the spherical analogue of the normal or Gaussian probability density of variance  $\sigma^2 = 4\alpha^2 t$  (Roberts and Ursell, 1960). Obviously, when  $\sigma^2 = 0$ , this reduces to the original unit delta function.

We now consider the wave equation

$$\frac{\partial^2 F(\mu, t)}{\partial t^2} + \beta^2 \nabla^2 F(\mu, t) = 0 \quad A.34$$

subject to the initial conditions

$$F(\mu, 0) = A(\mu)$$

$$\frac{\partial F(\mu, 0)}{\partial t} = B(\mu)$$

Transforming these equations, we obtain the system

$$\frac{\partial^2 F_n(t)}{\partial t^2} + \beta^2 (n)(n+1) F_n(t) = 0 \quad A.35$$

$$F_n(0) = A_n$$

$$\frac{\partial F_n(0)}{\partial t} = B_n$$

whose solution is

$$F_n(t) = \begin{cases} A_0 + B_0 t & n = 0 \\ A_n \cos(\omega t) + B_n \frac{\sin(\omega t)}{\omega} & n \neq 0 \end{cases} \quad A.36$$

where  $\omega^2 = \beta^2 (n)(n+1)$ . In a time averaged sense, the displacement field of such a wave preserves the spectral character of its displacement initial condition  $[A(\mu)]$ , but is smoother than its velocity

initial condition  $[B(\mu)]$ , since it attenuates the high degree harmonics.

Another important class of azimuthally symmetric functions is represented by the binary pulse

$$B(\gamma, \gamma_0) = \begin{cases} 1 & \gamma \leq \gamma_0 \\ 0 & \gamma > \gamma_0 \end{cases} \quad \text{A.37}$$

This will alternatively be denoted  $B(\mu, \mu_0)$ , where  $\mu = \cos(\gamma)$  and  $\mu_0 = \cos(\gamma_0)$ .

In the evaluation of the Legendre transform of this and similar functions, we will use the relation (Erdelyi, 1953, p. 170)

$$\int_{\alpha}^{\beta} P_n P_m d\mu = \frac{(1 - \mu^2) [P_n P'_m - P'_n P_m]}{(n - m)(n + m + 1)} \Big|_{\alpha}^{\beta} \quad \text{A.38}$$

where the prime denotes differentiation. Applying this formula, we find that the Legendre transform of the unit impulse is

$$\begin{aligned} B_n(\mu_0) &= 2\pi \int_{-1}^1 B(\mu, \mu_0) P_n(\mu) d\mu = 2\pi \int_{\mu_0}^1 P_n(\mu) d\mu \\ &= \frac{2\pi(1 - \mu_0^2) P'_n(\mu_0)}{(n)(n + 1)} \end{aligned} \quad \text{A.39}$$

In some applications, it will be more convenient to use a simple binary pulse  $Z$  with the added property that

$$\int_{-1}^1 Z(\mu, \mu_0) d\mu = 0 \quad \text{A.40}$$

The functional form of this zero-sum pulse is

$$Z(\gamma; \gamma_o) = \begin{cases} 1 & \gamma \leq \gamma_o \\ -\left[ \frac{1 - \mu_o}{1 + \mu_o} \right] & \gamma > \gamma_o \end{cases} \quad \text{A.41}$$

and its Legendre transform is

$$\begin{aligned} Z_n(\mu_o) &= 2\pi \int_{-1}^1 Z(\mu, \mu_o) P_n(\mu) d\mu \\ &= 2\pi \left[ \int_{\mu_o}^1 P_n(\mu) d\mu - \left( \frac{1 - \mu_o}{1 + \mu_o} \right) \int_{-1}^{\mu_o} P_n(\mu) d\mu \right] \quad \text{A.42} \\ &= \frac{4\pi(1 - \mu_o) P'_n(\mu_o)}{(n)(n+1)} \end{aligned}$$

## B. PROBABILITY DENSITIES

In much of our analysis, we will be concerned with probabilistic arguments. Therefore, in this section we briefly introduce some of the basic notions and terminology which will be employed elsewhere. Most of this material is quite well known and unless otherwise noted can be found in standard texts (e.g., Gallager, 1968; Middleton, 1960; Thomasian, 1969).

A probability density is a real-valued function  $p: \Omega \rightarrow \mathbb{R}$ , defined on some set  $\Omega$  and satisfying the conditions:

$$p(\omega) \geq 0, \quad \text{for all } \omega \in \Omega \quad \text{B.1}$$

$$\int_{\Omega} p(\omega) d\omega = 1 \quad \text{B.2}$$

The set  $\Omega$  is called the sample space, an element  $\omega$  of  $\Omega$  is called a sample point, and each subset of  $\Omega$  is called an event. The probability of an event  $A$

$$P(A) \equiv \int_A p(\omega) d\omega \quad \text{B.3}$$

is thus a real-valued function whose domain is the class of events in  $\Omega$ . The function  $P$  and the ordered pair  $(\Omega, P)$  are called the probability measure and the probability space, respectively, corresponding to the probability density  $p: \Omega \rightarrow \mathbb{R}$ . A random variable with associated probability space  $(\Omega, P)$  is any real-valued function  $F: \Omega \rightarrow \mathbb{R}$ .

If  $A$  and  $B$  are events in  $\Omega$ , with  $P(A) > 0$ , then the conditional probability of  $A$ , given  $B$ , is defined



$$P(A|B) = P(AB)/P(A) \quad B.4$$

The events A and B are said to be independent, if and only if

$$P(AB) = P(A) P(B) \quad B.5$$

The n-th moment of a density is defined as

$$M_n(p) \equiv \int_{\Omega} \omega^n p(\omega) d\omega \quad B.6$$

All densities are normalized so that  $M_0 = 1$ . We will be concerned mainly with the mean (first moment)

$$E(\omega) = \int_{\Omega} \omega p(\omega) d\omega = M_1 = \mu_{\omega} \quad B.7$$

where  $E(\cdot)$  is the expectation operator, and the variance (second moment about the mean)

$$V(\omega) = E(\omega - \mu_{\omega})^2 = M_2 - M_1^2 = \sigma_{\omega}^2 \quad B.8$$

In predicting the value of a random variable, a highly concentrated probability distribution conveys more information than a relatively uniform distribution. To quantify this notion, we introduce the self-information

$$I(\omega) = -\log [p(\omega)] \quad B.9$$

and the average information or entropy

$$H(\omega) = E[I(\omega)] = - \int_{\Omega} \log [p(\omega)] p(\omega) d\omega \quad B.10$$

The entropy, thus defined, depends not only on the probability distribution, but also on the coordinate system used. If we have

a joint probability distribution  $p(X)$  for the variables  $X = (x_1, x_2, \dots, x_n)$  and then change variables to  $Y = (y_1, y_2, \dots, y_n)$ , the new distribution is

$$q(Y) = p(X) \left| \frac{\partial Y}{\partial X} \right| \quad \text{B.11}$$

where

$$\left| \frac{\partial Y}{\partial X} \right| = \left| \frac{\partial y_i}{\partial x_j} \right|$$

is the Jacobian determinant of the transformation, and therefore

$$H(Y) = H(X) - \int \ln \left| \frac{\partial Y}{\partial X} \right| p(X) dX \quad \text{B.12}$$

In spite of this dependence on the coordinate system, entropy is a useful way to characterize probability distributions, since we will be mostly interested in relative entropies. In fact, many of the distributions we will encounter can be obtained by seeking the distribution with maximum entropy subject to constraints such as fixed mean or variance. This approach ensures that the distribution so obtained incorporates all of our prior knowledge about the system of interest, but no more.

In the remainder of this section, we will introduce the one dimensional forms (i.e.,  $\Omega = \mathbb{R}$ ) of some elementary probability densities which we will need later.

The simplest form we consider is the uniform density, which is the maximum entropy solution subject only to the constraints that

$$\int_{-\infty}^{\infty} p(X) dX = 1 \quad \text{B.13}$$

$$p(X) = 0 \quad \text{unless} \quad \alpha \leq X \leq \beta \quad \text{B.14}$$

It thus arises in the situation where a random variable is certain to lie in the interval  $(\alpha, \beta)$ , but nothing is known further about its location. The functional form of the uniform density is

$$p(X) = \begin{cases} (\beta - \alpha)^{-1} & \alpha \leq X \leq \beta \\ 0 & \text{otherwise} \end{cases} \quad \text{B.15}$$

and its moments and entropy are

$$\begin{aligned} M_1 &= \frac{\alpha + \beta}{2} & M_2 &= \frac{\alpha^2 + \alpha\beta + \beta^2}{3} \\ V &= \frac{(\beta - \alpha)^2}{12} & H(X) &= \ln(\beta - \alpha) \end{aligned} \quad \text{B.16}$$

The normal or Gaussian density arises in the analysis of the sums of independent random variables. In fact, the central limit theorem asserts that under quite general conditions, the standardized sum of independent random variables has an approximately normal distribution. The normal density with the two parameters,  $\mu$  and  $\sigma^2$  has the form

$$p(X) = \left[ 2\pi\sigma^2 e^{\left(\frac{X-\mu}{\sigma}\right)^2} \right]^{-1/2} \quad -\infty \leq X \leq \infty \quad \text{B.17}$$

and its moments and entropy are

$$\begin{aligned} M_1 &= \mu & M_2 &= \mu^2 + \sigma^2 \\ V &= \sigma^2 & H(X) &= \frac{1}{2} \left[ 1 + \ln 2\pi\sigma^2 \right] \end{aligned}$$

The normal distribution has the maximum entropy of any distribution with the same mean and variance. We will occasionally use the symbol

$N(\mu, \sigma^2)$  to indicate that a random variable is normal with mean  $\mu$  and variance  $\sigma^2$ .

The Rayleigh distribution characterizes the fluctuations in amplitude of the sum of independent random variables. Thus, if

$$A \cos (m\varphi) + B \sin (m\varphi) = J \cos (m\varphi + \Delta\varphi) \quad \text{B.19}$$

where  $A$  and  $B$  are independent  $N(0, \beta^2)$  random variables, then  $J$  and  $\Delta\varphi$  are independent random variables,  $\Delta\varphi$  is uniformly distributed on the interval  $(0, 2\pi)$  and  $J$  is Rayleigh distributed with probability density

$$p(X) = \begin{cases} \frac{X}{\beta^2} e^{-1/2\left(\frac{X}{\beta}\right)^2} & X \geq 0 \\ 0 & X < 0 \end{cases} \quad \text{B.20}$$

The Rayleigh distribution has a single parameter  $\beta$ , and its moments are

$$\begin{aligned} M_1 &= \left(\frac{\pi}{2}\right)^{1/2} \beta & M_2 &= 2\beta^2 \\ V &= \left(\frac{4-\pi}{2}\right) \beta^2 \end{aligned} \quad \text{B.21}$$

If  $\{X_i: i = 1, 2, \dots, 2n\}$  are independent  $N(0, \sigma^2)$  random variables, then

$$X_{2n}^2 = \sum_{i=1}^{2n} \left(\frac{X_i}{\sigma}\right)^2$$

has a chi-square density with  $2n$  degrees of freedom. The functional form of the density is:

$$p(X) = \begin{cases} [2\Gamma(n)]^{-1} (X/2)^{n-1} e^{-X/2} & X \geq 0 \\ 0 & X < 0 \end{cases} \quad \text{B.23}$$

where the gamma function takes the values

$$\Gamma(n) = \begin{cases} (n-1)! & 2n = 2, 4, 6, \dots \\ \left(\frac{\pi}{4^{2n-1}}\right)^{1/2} \frac{(2n-1)!}{\left(\frac{2n-1}{2}\right)!} & 2n = 1, 3, 5, \dots \end{cases} \quad \text{B.24}$$

The chi-square distribution has a single parameter,  $2n$  and its moments are

$$\begin{aligned} M_1 &= 2n & M_2 &= 4n(n+1) \\ V &= 4n \end{aligned} \quad \text{B.25}$$

If independent random events occur at a constant mean rate  $X$ , the probability that  $k$  events occur in an interval of length  $X$  is Poisson distributed with discrete density

$$p(k) = \begin{cases} \frac{e^{-\alpha x} (\alpha x)^k}{(k)!} & k = 0, 1, 2, \dots \\ 0 & \text{otherwise} \end{cases} \quad \text{B.26}$$

Since this is a discrete density, its moments are defined in terms of sums rather than integrals:

$$M_n \equiv \sum_{k=0}^{\infty} k^n p(k) \quad \text{B.27}$$

The Poisson distribution has a single parameter,  $\alpha x$ , and its first two moments, variance and entropy are

$$M_1 = \alpha x$$

$$M_2 = \alpha x + (\alpha x)^2$$

$$V = \alpha x$$

$$H(X) = \alpha x [1 - \ln(\alpha)]$$

B.28

Of all point processes with intensity  $\alpha$ , the Poisson process has the maximum entropy rate  $dH(x)/dx$  (McFadden, 1965).

### C. STOCHASTIC PROCESSES

A stochastic process is, roughly speaking, an ensemble of random functions, all governed by the same probability law. More precisely (Parzen, 1962; Thomasian, 1969), a stochastic process consists of a probability space  $(\Omega, P)$ , a non-empty set  $G$ , called the parameter set, and a random variable,  $F_g: \Omega \rightarrow R$ , assigned to each  $g \in G$ . The only parameter sets we will explicitly consider are the real line  $R$ , the positive reals  $R^+$ , the circle  $S^1$ , and the sphere  $S^2$ .

For any  $\omega \in \Omega$ , the function  $H_\omega: G \rightarrow R$ , defined by

$$H_\omega(g) = F_g(\omega) \quad \text{for all } g \in G \quad \text{C.1}$$

is called a realization, or sample function, of the stochastic process. For any  $(g, h) \in G \times G$ , the function  $\Delta F_{g,h}: G \times G \rightarrow R$ , defined by

$$\Delta F_{g,h} = F_h - F_g \quad \text{C.2}$$

is called the increment of  $F$  from  $g$  to  $h$ .

A very important class of processes are those with stationary and independent increments. The increments of a process are said to be stationary if the distribution of  $\Delta F_{g,h}$  depends on  $g$  and  $h$  only through their difference  $|h - g|$ . If the parameter set  $G$  is a sphere, this difference is just the angular distance  $\gamma$  between the points  $g = (\theta, \varphi)$  and  $h = (\theta + \Delta\theta, \varphi + \Delta\varphi)$ . The increments of a process are independent if the random variables  $\Delta F_{g,h}$  and  $\Delta F_{g',h'}$  are independent whenever the intervals  $(g, h)$  and  $(g', h')$  are disjoint. The only processes we will actually encounter in this analysis are

the Poisson and Wiener processes and some of their generalizations. All of these processes have stationary and independent increments.

### 1. Poisson Process

The Poisson process is basically a counting process. We define a counting function as any non-decreasing function  $N$  whose range is restricted to the non-negative integers  $\{0,1,2,\dots\}$  and which assumes every value in its range less than  $N_0$ , if it assumes the value  $N_0$ . We then define a Poisson process  $N_g$  with parameter  $\alpha$  as any process with stationary independent increments such that the random variable  $N_g$  induces a Poisson density with mean  $\alpha g$ , and every realization of the process is a counting function.

A process  $X_g$  is said to be a filtered Poisson process if it can be represented by

$$X_g = \sum_{n=1}^{N_g} B(g, h_n, A_n) \quad \text{C.3}$$

where  $N_g$  is a Poisson process with intensity  $\alpha$ ,  $\{A_n\}$  is a sequence of identically distributed random variables, independent of one another and of  $N_g$ , and  $B(g, h, A): G^2 \times R \rightarrow R$  is the response function. We may interpret  $B(g, h, A)$  as the value at  $g$  of a response of magnitude  $A$  to an impulse at  $h$ .  $X_g$  is thus the value at  $g$  of  $N_g$  such responses.

### 2. Weiner Process

The Wiener process is obtained as the limit of a random walk as the step size decreases to zero. Specifically, a Wiener process  $W(g)$  with parameter  $\sigma^2$  is any stationary independent increment process



such that the random variable  $W(g)$  induces a normal  $N(0, \sigma^2)$  density, and every realization of the process is a continuous function. Thus, if  $\gamma = |h - g|$  is the length of the interval  $(g, h)$  in the parameter set  $G$ , then the increment  $\Delta W(g, h; \omega)$  is normally distributed as  $N(0, \gamma \sigma^2)$ . Although realizations of a Wiener process are continuous, they are almost nowhere differentiable, i.e., for any  $g \in G$ , the set of realizations which have a derivative at  $g$  has probability zero.

The Wiener process has a number of other interesting properties. For example, it might be supposed that in a typical interval, the fraction  $(X)$  of the interval over which the process is positive, would be normally distributed about its mean 0.5. However, as first shown by Levy (1948, pg. 216) the probability density is minimum at its mean and is concentrated toward the extremes 0 and 1. In fact, the density is

$$p(X) = \frac{1}{\pi} \frac{1}{\sqrt{X(1-X)}} \quad \text{C.4}$$

and therefore the probability

$$\begin{aligned} P[X \leq u^2] &= \frac{1}{\pi} \int_0^{u^2} \frac{dx}{\sqrt{X(1-X)}} \\ &= \frac{2}{\pi} \sin^{-1}(u) \quad 0 \leq u \leq 1 \end{aligned} \quad \text{C.5}$$

This arc-sine law obviously also gives the distribution of the fraction  $(1-X)$  of the interval over which the process is negative.

The points at which the process assumes its mean value are also of interest. Let  $\gamma_k$  be the length of the k-th interval between consecutive returns to the mean. Short intervals are more frequent than long ones. In particular, when the parameter set is the real line or the positive reals,  $G \in \{R, R^+\}$ , the probability distribution of  $\gamma_k$  is

$$P[\gamma_k = u] = \left(\frac{8}{\pi}\right)^{1/2} u^{-3/2}$$

This distribution is approximately the same when the parameter set is the circle or sphere,  $G \in \{S^1, S^2\}$ , if the intervals considered are sufficiently short, i.e.,  $\gamma \ll 2\pi$ . This is also true of a number of the other properties we will consider below.

We now consider a generalization of the Wiener process whose increments are a moving average of the increments of the standard Wiener process. Following Mandelbrot and Van Ness (1968), we define a fractional Wiener process  $W_\beta(g)$  with parameters  $\beta$  and  $\sigma^2$  ( $0 \leq \beta \leq 1$ ,  $0 \leq \sigma^2$ ) as any stationary increment process such that all the realizations of the process are continuous and the increments  $\Delta W_\beta(g, h)$  are normally distributed as  $N(0, \sigma^2 \gamma^{2\beta})$ , where  $\gamma = |h - g|$  is the distance between the points  $g$  and  $h$  in the parameter set. The increments of  $W_\beta(g)$  are independent if, and only if,  $\beta = \frac{1}{2}$ . In that case, we merely obtain the traditional Wiener process,  $W_{1/2}(g) = W(g)$ . The fractional process is similar to the traditional process in that, although all its realizations are continuous, they are nowhere differentiable.

The realizations of a fractional Wiener process have a degree of invariance with respect to changes of scale. To quantify this notion, we introduce the concept of self-similarity. The increments of a random function  $F(g)$  are said to be self-similar with parameter  $Q$  if for any  $\gamma > 0$ , and any  $g \in G$ ,

$$\Delta F(g, g + \gamma) = \gamma^{-Q} \Delta F(g, g + \gamma Q) \quad C.6$$

where the indicated equality means that the two random variables are indentially distributed. If the parameter set  $G \in \{R, R^+\}$  then the fractional Wiener process  $W_\beta(g)$  has self-similar increments with parameter  $\beta$ . If  $G \in \{S^1, S^2\}$ , then  $W_\beta(g)$  is asymptotically self-similar for small  $\gamma$ .

The realizations of  $W_\beta(g)$  are also characterized by their extreme irregularity. This is, of course, suggested by their lack of differentiability. However, when we consider the realizations of a process with  $G \in \{R, R^+\}$ , we find that in their degree of convolution and intricacy they are, in fact intermediate between a smooth rectifiable curve and a Peano curve, which passes through every point of a two dimensional region. This, in conjunction with a self-similarity parameter  $0 \leq \beta \leq 1$ , suggests a dimensionality  $D$  for these realizations with  $1 \leq D \leq 2$ . In fact, generalizing a result of Mandelbrot (1975), we suggest that if  $D[G]$  is the dimension of its parameter set, the dimension of a realization of  $W_\beta(g)$  satisfies

$$D[W_\beta(g)] = D[G] + \beta \quad C.7$$

Thus, for example, if  $G = S^1$  or  $S^2$ , then  $D[W_\beta(g)] = 1 + \beta$  or  $2 + \beta$  respectively.

### 3. Ornstein-Uhlenbeck Process

We now consider another extension of the Wiener process. If  $W(g)$  is a standard Wiener process, then

$$U(g) = e^{-\beta g} W(\alpha e^{2\beta g}) \quad \text{C.8}$$

is called the Ornstein-Uhlenbeck process (Uhlenbeck and Ornstein, 1930; Doob, 1942) with parameters  $\alpha > 0$  and  $\beta > 0$ . It is a stationary normal process with zero mean and covariance

$$C(U; \gamma) = \alpha e^{-\beta \gamma} \quad \text{C.9}$$

Whereas the Wiener process is obtained from a random walk in the limit as the step length goes to zero, the Ornstein-Uhlenbeck process is derived by a similar limiting procedure from a random walk subjected to a restoring force. Thus, the Ornstein-Uhlenbeck process is stationary, whereas the Wiener process is not.

#### D. COVARIANCE FUNCTIONS

In much of what follows, it will be useful to consider functions on the sphere  $F(\theta, \varphi)$  which are realizations of homogeneous stochastic processes. A process is said to be homogeneous if its first and second moments are invariant under the group of rotations of the sphere. This is equivalent (Roy, 1973) to stationarity, i.e., constancy of the mean  $E[F(\theta, \varphi)]$  and isotropy of the covariance function  $E[F(\theta, \varphi)F(\theta', \varphi')]$ , i.e., the covariance depends only on the angular separation  $\gamma$ , between the points  $(\theta, \varphi)$  and  $(\theta', \varphi')$ .

If we now consider two functions  $A(\theta, \varphi)$  and  $B(\theta, \varphi)$ , we may calculate the expected value of the product  $A(\Gamma) \cdot B(\Gamma + \gamma)$ , where  $\Gamma = (\theta, \varphi)$  and  $\Gamma + \gamma = (\theta', \varphi')$  are any two points on the sphere which are an angular distance  $\gamma$  apart. This mean product is known as the cross-correlation of  $A$  and  $B$  (Middleton, 1960). In the case where  $E(A) = E(B) = 0$ , it is known as the cross-covariance and is designated

$$C(A, B; \gamma) = E[A(\Gamma) \cdot B(\Gamma + \gamma)] \quad D.1$$

The requirement that  $E(A) = E(B) = 0$  is easily met by defining new functions,  $A' = A - E(A)$  and  $B' = B - E(B)$ . This is equivalent to the vanishing of the harmonic coefficients of degree zero;  $A_{0,0} = B_{0,0} = 0$ . For example, instead of topographic radius  $R(\theta, \varphi)$ , we will use topographic height;  $H(\theta, \varphi) = R(\theta, \varphi) - R_0$ .

The covariance of a function with itself is known as the auto-covariance, or simply the covariance, and is denoted variously as

$$C(A, A; \gamma) = C(A; \gamma) = C(\gamma) = E[A(\Gamma) A(\Gamma + \gamma)] \quad D.2$$

The (cross-) covariance of the functions A and B at separation  $\gamma$  has a convenient representation in terms of Legendre polynomials in  $\mu = \cos(\gamma)$ , and the harmonic coefficients  $A_{nm}$  and  $B_{nm}$ . Applying the addition theorem

$$P_n(\cos(\gamma)) = \frac{1}{2n+1} \sum_{m=0}^n \Lambda_{nm}^T(\theta, \varphi) \Lambda_{nm}(\theta', \varphi') \quad D.3$$

where  $\gamma$  is again the angular distance between  $(\theta, \varphi)$  and  $(\theta', \varphi')$ , we find (Heiskanen and Moritz, 1967; Kaula, 1967)

$$C(A, B; \gamma) = R_0^2 \sum_{n=1}^{\infty} V(A, B; n) P_n[\cos(\gamma)] \quad D.4$$

where

$$V(A, B; n) = \sum_{m=0}^n A_{nm}^T B_{nm}$$

is the (cross-) variance spectrum of A with B. For a given n,  $V(A, B; n)$  will be referred to as the degree (cross-) variance. For further discussion of spectral analysis of random processes on the sphere, see Jones (1963) and Roy (1976).

The (cross-) covariance at zero separation is known as the (cross-) variance and has the form

$$C(A, B; 0) = R_0^2 \sum_{n=1}^{\infty} V(A, B; n) \quad D.5$$

since

$$P_n[\cos(0)] = 1.$$

If a random variable  $X$  has mean  $E(X) = \mu_x$  and variance  $E(X - \mu_x)^2 = \sigma_x^2$ , then (Thomasian, 1969; pp. 202-208)

$$X^* = \frac{X - \mu_x}{\sigma_x} \quad D.6$$

is called the standardized random variable corresponding to  $X$ , and has zero mean and unit variance:

$$\begin{aligned} E(X^*) &= 0 \\ E(X^*)^2 &= 1 \end{aligned} \quad D.7,$$

If  $X$  and  $Y$  have finite, nonzero variances, then the covariance between their standardizations is called their correlation coefficient and is denoted by

$$(X, Y) = C(X^*, Y^*) = \frac{C(X, Y)}{\sigma_x \sigma_y} \quad D.8$$

For random variables on the sphere, we also define the degree correlation coefficient

$$\rho(X, Y; n) = V(X^*, Y^*; n) = \frac{V(X, Y; n)}{[V(X; n) V(Y; n)]^{1/2}} \quad D.9$$

Clearly,  $-1 \leq \rho_{xy} = \rho_{yx} \leq 1$ , and  $\rho_{xy} = 1$  ( $-1$ ) iff  $X$  and  $Y$  are perfectly (anti-) correlated, whereas  $\rho_{xy} = 0$  means that  $X$  and  $Y$  are uncorrelated. Thus,  $\rho_{xy}$  is a standardized measure of the degree of statistical dependence between  $X$  and  $Y$ .

If we desire to predict the value of a random variable  $Y$  based on observations of another random variable  $X$ , we may seek the numbers  $\alpha$  and  $\beta$  which minimize the error variance

$$E [Y - (\alpha X + \beta)]^2$$

In terms of standardized variables, the solution is

$$\alpha = \rho_{xy} \quad \beta = 0 \quad \text{D.10}$$

and the error variance is

$$E (Y^* - \rho_{xy} X^*)^2 = 1 - \rho_{xy}^2 \quad \text{D.11}$$

In terms of nonstandardized variables, the so called regression line and error variance are:

$$Y = \mu_y + \sigma_y \rho_{xy} \left( \frac{X - \mu_x}{\sigma_x} \right) \quad \text{D.12}$$

$$E [Y - (\alpha X + \beta)]^2 = \sigma_y^2 (1 - \rho_{xy}^2) \quad \text{D.13}$$

The Wiener-Khintchine theorem (Middleton, 1960; pp. 141-144) states that under quite general conditions the (cross-) covariance function and the (cross-) variance spectrum are related by a pair of integral (or series) transforms. In the case of spherical geometry, we have a Legendre transform relationship:

$$C(\mu) = R_0^2 \sum_{n=1}^{\infty} V(n) P_n(\mu)$$

$$R_0^2 V(n) = \frac{2n+1}{2} \int_{-1}^1 C(\mu) P_n(\mu) d\mu \quad \text{D.14}$$

Thus we can deal with whichever quantity is more convenient or gives greater insight into a problem. A case of particular interest is the spherical Wiener process, which is representative of the stochastic



component of the topography of the terrestrial planets:

$$V(H;n) = \frac{V(H;0)}{(n)(n+1)} \quad D.15$$

The covariance in this case is

$$C(H;\gamma) = R_0^2 V(H;0) \sum_{n=1}^{\infty} \frac{P_n[\cos(\gamma)]}{(n)(n+1)} \quad D.16$$

We can obtain a closed-form expression for this series by noting that

$$\frac{1}{(n)(n+1)} = \frac{1}{n} - \frac{1}{n+1} \quad D.17$$

and (Wheelon, 1968; pg. 53)

$$\sum_{n=1}^{\infty} \frac{P_n[\cos(\gamma)]}{n} = -(\ell_n[\sin(\gamma/2)] + \ell_n[1 + \sin(\gamma/2)]) \quad D.18$$

$$\sum_{n=1}^{\infty} \frac{P_n[\cos(\gamma)]}{n+1} = -(1 + \ell_n[\sin(\gamma/2)] - \ell_n[1 + \sin(\gamma/2)]) \quad D.19$$

Therefore, we find that:

$$\begin{aligned} C(H;\gamma) &= R_0^2 V(H;0) \left[ \sum_{n=1}^{\infty} \frac{P_n[\cos(\gamma)]}{n} - \sum_{n=1}^{\infty} \frac{P_n[\cos(\gamma)]}{n+1} \right] \\ &= R_0^2 V(H;0) (1 - 2\ell_n[1 + \sin(\gamma/2)]) \end{aligned} \quad D.20$$

When  $\gamma = 0$ , this has the form

$$C(H;0) = R_0^2 V(H;0) \quad D.21$$

since

$$P_n[\cos(0)] = 1$$

and

$$\sum_{n=1}^{\infty} \frac{1}{(n)(n+1)} = 1$$

Similarly, for a fractional Wiener process  $W_{\beta}$  on a circle, the variance spectrum is

$$V(W_{\beta};n) = V(W_{\beta};0) n^{-(2\beta+1)} \quad D.22$$

Campbell's theorem (Rice, 1944) gives convenient expressions for the mean and covariance function of those filtered Poisson processes which can be expressed as

$$X(g) = \sum_{n=1}^N A_n B(g - h_n) \quad D.23$$

where  $N$  is a Poisson process of intensity  $\alpha$ ,  $A_n$  is the amplitude of the  $n$ -th pulse, and  $B(g - h_n)$  is the response at  $g$  to a unit pulse at  $h_n$ . If the parameter set of the process is  $G$ , then

$$E(X) = \alpha E(A) \int_G B(g) dg \quad D.24$$

$$C(X;\gamma) = \alpha E(A)^2 \int_G B(g) B(g + \gamma) dg$$

As the intensity  $\alpha$  is increased, the process  $X(g)$  approaches a normal distribution with mean  $E(X)$  and variance  $C(X;0)$ , as given above.

As an application of the convolution theorem to the calculation of variance spectra and covariance functions, we note that, if the function  $F$  is a convolution of  $A$  and  $B$ ,

$$F(\theta, \varphi) = \frac{1}{4\pi} \int_0^{2\pi} \int_{-\pi/2}^{\pi/2} A(\theta', \varphi') B(\theta - \theta', \varphi - \varphi') \cos(\theta') d\theta' d\varphi' \quad D.25$$

and if B has no azimuthal variation, then the variance spectrum of F is simply

$$V(F; n) = B_n^2 V(A; n) \quad D.26$$

and the covariance function is

$$C(F; \gamma) = R_0^2 \sum_{n=1}^{\infty} B_n^2 V(A; n) P_n[\cos(\gamma)] \quad D.27$$

## E. VISCO-ELASTIC DEFORMATION

The response of a planet to applied stress depends on the size and composition of the planet as well as the spatial and temporal distribution of the stresses. We will restrict our attention here to planets composed of homogeneous, incompressible, linear visco-elastic materials. This considerably simplifies the analysis while retaining many of the behavioral features of a more complex substance. A planet will thus be characterized by its radius  $R_0$  [cm], either mass  $M$  [gm] or density [ $\text{gm cm}^{-3}$ ], rigidity  $\mu$  [ $\text{dyne cm}^{-2}$ ] and either kinematic viscosity  $\nu$  [ $\text{stoke} = \text{cm}^2 \text{sec}^{-1}$ ] or dynamic viscosity  $\eta = \rho\nu$  [ $\text{poise} = \text{gm cm}^{-1} \text{sec}^{-1}$ ].

The relationship between applied stress  $\sigma$  [ $\text{dyne cm}^{-2}$ ] and consequent deformation, as expressed in terms of either strain  $\epsilon$  [dimensionless] or strain rate  $\dot{\epsilon} \equiv d\epsilon/dt$  [ $\text{sec}^{-1}$ ], depends on the material being deformed. For linear elastic, linear viscous and Maxwell visco-elastic materials, the relations are:

$$\epsilon = \sigma/\mu \quad (\text{elastic}) \quad \text{E.1}$$

$$\dot{\epsilon} = \sigma/\eta \quad (\text{viscous}) \quad \text{E.2}$$

$$\dot{\epsilon} = \dot{\sigma}/\mu + \sigma/\eta \quad (\text{visco-elastic}) \quad \text{E.3}$$

This latter form is only one of many possible models for linear visco-elastic behavior, but we focus on it because of historical precedent (Maxwell, 1868; Darwin, 1879) and analytical simplicity. Furthermore, it is apparently a reasonable model in many situations of geophysical interest (McKenzie, 1967).

A Maxwell material subjected to a constant stress  $\sigma$ , initially undergoes an elastic deformation  $\epsilon = \sigma/\mu$ , but also commences creeping at a rate  $\dot{\epsilon} = \sigma/\eta$ . After a time  $t = \tau_M$ , known as the Maxwell relaxation time, the viscous deformation  $\epsilon = \sigma t/\eta$  exceeds the initial elastic deformation. Thus, for short time periods ( $t < \tau_M$ ) the material is essentially elastic, whereas, for long time periods ( $t > \tau_M$ ), the behavior is predominantly viscous.

We will now examine the short time or elastic limit in the behavior of visco-elastic planets under stress. When subjected to a disturbing potential

$$\Phi(R, \theta, \varphi) = \frac{GM}{R_0} \sum_{n=1}^{\infty} \left(\frac{R_0}{R}\right)^{n+1} \sum_{m=0}^n \Phi_{nm}^T \Lambda_{nm}(\theta, \varphi) \quad E.4$$

an elastic sphere suffers a surface distortion proportional to the disturbing potential

$$U(\theta, \varphi) = R_0 \sum_{n=1}^{\infty} \sum_{m=0}^n \Phi_{nm}^T U_{nm}(\theta, \varphi) \quad E.5$$

where  $U_{nm}(\theta, \varphi)$  is a vector spherical harmonic whose components in the direction of the unit vectors  $(\hat{e}_R, \hat{e}_\theta, \hat{e}_\varphi)$  are:

$$\begin{aligned} \hat{e}_R \cdot U_{nm}(\theta, \varphi) &= h_n \Lambda_{nm}(\theta, \varphi) \\ \hat{e}_\theta \cdot U_{nm}(\theta, \varphi) &= \ell_n \frac{\partial}{\partial \theta} \Lambda_{nm}(\theta, \varphi) \\ \hat{e}_\varphi \cdot U_{nm}(\theta, \varphi) &= \frac{\ell_n}{\cos(\theta)} \frac{\partial}{\partial \varphi} \Lambda_{nm}(\theta, \varphi) \end{aligned} \quad E.6$$

This redistribution of mass gives rise to a further disturbance of the potential whose harmonic coefficients are

$$\Delta\Phi_{nm} = k_n \Phi_{nm} \quad \text{E.7}$$

These constants of proportionality  $L_n = (k_n, h_n, \ell_n)$  are known as Love numbers (Love, 1927, pp. 257-299; Munk and MacDonald, 1960, pp. 29-31), and their functional form depends on the nature of the disturbing potential. For a potential which does not load the surface, such as a rotational or tidal potential, acting on a homogeneous elastic sphere

$$\begin{aligned} k_n &= \frac{3}{2(n-1)} \left( \frac{1}{1+N(n)} \frac{\mu}{P_c} \right) \\ h_n &= \left( \frac{2n+1}{3} \right) k_n \\ \ell_n &= \left( \frac{1}{n} \right) k_n \end{aligned} \quad \text{E.8}$$

where

$$P_c = \frac{3GM^2}{8\pi R_0^4} \quad \text{E.9}$$

the hydrostatic pressure at the center of the planet, is a measure of the gravitational resistance to deformation,  $\mu$  is the elastic rigidity, and

$$N(n) = \frac{2(n+1)^2 + 1}{2n} \quad \text{E.10}$$

is a purely geometrical factor related to the boundary conditions for the sphere. In a fluid planet  $\mu = 0$ , and the restoring force is purely gravitational. Since  $N(n)$  is an increasing function of  $n$ , the elastic response is clearly more important for small features.

If the perturbing potential is due to a surface load of material of the same density as the rest of the planet, and the height of the surface load is

$$H(\theta, \varphi) = R_0 \sum_{n=1}^{\infty} \sum_{m=0}^n H'_{nm} \Lambda_{nm}(\theta, \varphi) \quad \text{E.11}$$

then the potential harmonics are

$$\left( \frac{2n+1}{3} \right) \Phi_{nm} = H'_{nm} \quad \text{E.12}$$

In this case, the deformation due to the normal stress applied by the load is opposed by the gravitational attraction of the planet by the load. The corresponding Love numbers are thus

$$L'_n = \left[ 1 - \frac{2n+1}{3} \right] L_n \quad \text{E.13}$$

where  $L_n$  are the Love numbers for a potential which does not load the surface. Thus, we have explicitly

$$\begin{aligned} k'_n &= \left( \frac{1}{1 + N(n) \mu/P_c} \right) \\ h'_n &= \left( \frac{2n+1}{3} \right) k'_n \\ \ell'_n &= \left( \frac{1}{n} \right) k'_n \end{aligned} \quad \text{E.14}$$

If a load of initial height  $H'_{nm}$  were placed on a sphere, the original surface would deform by  $h'_n \Phi_{nm}$ , and the final height of the load would be

$$H_{nm} = H'_{nm} + h'_n \Phi_{nm} \quad \text{E.15}$$

However, since

$$\begin{aligned} H'_{nm} &= \left( \frac{2n+1}{3} \right) \phi_{nm} \\ h'_n &= \left( \frac{2n+1}{3} \right) k'_n \end{aligned} \quad \text{E.16}$$

this can be rewritten as

$$H_{nm} = (1 + k'_n) H'_{nm} \quad \text{E.17}$$

Clearly, if the body were perfectly fluid, so that  $\mu = 0$ , then we would have  $k'_n = -1$  and thus  $H_{nm} = 0$

The Love numbers have the following asymptotic behavior in the limit of small wavelength features:

$$\lim_{n \rightarrow \infty} \begin{bmatrix} nh_n \\ n^2 k_n \\ n^3 \ell_n \end{bmatrix} = \frac{P_c}{\mu} \begin{bmatrix} 1 \\ 3/2 \\ 3/2 \end{bmatrix} \quad \text{E.18}$$

$$\lim_{n \rightarrow \infty} \begin{bmatrix} h'_n \\ nk'_n \\ n^2 \ell'_n \end{bmatrix} = \frac{P_c}{\mu} \begin{bmatrix} 2/3 \\ 1 \\ 1 \end{bmatrix} \quad \text{E.19}$$

Darwin (1879) solved the problem of purely viscous deformation of a homogeneous sphere by a surface load. If the load has the same density as the sphere, and the initial height of the load is characterized by harmonic coefficients

$$H_{nm}(0) = A_{nm} \quad \text{E.20}$$

then, at a later time  $t$ , the load height harmonics will be attenuated to

$$H_{nm}(t) = A_{nm} e^{-t/\tau_n} \quad \text{E.21}$$



where the relaxation time for degree  $n$  is

$$\tau_n = \left[ \frac{N(n)}{P_c} \right] \eta \quad \text{E.22}$$

and  $\eta$  is the dynamic viscosity. Since  $\tau_n$  is an increasing function of  $n$ , the proportional attenuation of laterally extensive features is more rapid than for small features. This is just opposite the behavior of diffusion processes.

The deformation of a Maxwell sphere due to a surface load was also determined by Darwin (1879) and is essentially identical to the behavior of a purely viscous sphere. The only difference is that the relaxation times are uniformly increased to (McKenzie, 1967; Peltier, 1974)

$$\begin{aligned} \tau'_n &= \left[ \frac{N(n)}{P_c} + \frac{1}{\mu} \right] \eta \\ &= \tau_n + \tau_M \end{aligned} \quad \text{E.23}$$

where  $\tau_n$  is the viscous spherical relaxation time, and  $\tau_M$  is the Maxwell relaxation time of the material.

## F. POTENTIAL ENERGY

The configuration of lowest energy for an isolated mass of homogeneous material is a sphere. Any departure from sphericity thus represents an increase in potential energy, both elastic and gravitational. We will now estimate the energy corresponding to harmonic surface loads and use the constraint of finite total energy to place bounds on possible surface configurations. We will first consider elastic energy.

### 1. Elastic Energy

The elastic energy density, which is the work done per unit volume in elastically deforming the material, is given by

$$e = \frac{1}{2} \sum_{i=1}^3 \sum_{j=1}^3 \sigma_{ij} \epsilon_{ij} \quad \text{F.1}$$

where  $\sigma_{ij}$  and  $\epsilon_{ij}$  are the stress and strain tensors respectively. The constitutive relation between stress and strain for an incompressible material is

$$\sigma_{ij} = \mu \epsilon_{ij} \quad \text{F.2}$$

and thus the energy density simplifies to

$$e = \frac{\mu}{2} \sum_{i=1}^3 \sum_{j=1}^3 \epsilon_{ij} \epsilon_{ij} \quad \text{F.3}$$

In a system with coordinate axes  $X_i$ , the strain tensor is obtained from the displacement vector  $U_i$  by the formula

$$\epsilon_{ij} = \frac{1}{2} \left( \frac{\partial U_i}{\partial X_j} + \frac{\partial U_j}{\partial X_i} \right) \quad \text{F.4}$$

In spherical coordinates, the strain components are:

$$\begin{aligned}
\epsilon_{RR} &= \frac{\partial U_R}{\partial R} \\
\epsilon_{\theta\theta} &= \frac{1}{R} \left[ U_R + \frac{\partial U_\theta}{\partial \theta} \right] \\
\epsilon_{\varphi\varphi} &= \frac{1}{R} \left[ U_R + \tan(\theta) U_\theta + \frac{1}{\cos(\theta)} \frac{\partial U_\varphi}{\partial \varphi} \right] \\
\epsilon_{R\theta} = \epsilon_{\theta R} &= \frac{1}{2R} \left[ \frac{\partial U_R}{\partial \theta} + R \frac{\partial U_\theta}{\partial R} - U_\theta \right] \\
\epsilon_{R\varphi} = \epsilon_{\varphi R} &= \frac{1}{2R} \left[ \frac{1}{\cos(\theta)} \frac{\partial U_R}{\partial \varphi} + R \frac{\partial U_\varphi}{\partial R} - U_\varphi \right] \\
\epsilon_{\theta\varphi} = \epsilon_{\varphi\theta} &= \frac{1}{2R} \left[ \frac{1}{\cos(\theta)} \frac{\partial U_\theta}{\partial \varphi} + \frac{\partial U_\varphi}{\partial \theta} - \tan(\theta) U_\varphi \right]
\end{aligned} \tag{F.5}$$

Substituting the displacement due to a single harmonic disturbing potential

$$\Phi(R, \theta, \varphi) = \frac{GM}{R_0} \left( \frac{R}{R_0} \right)^n \Phi_{nm}^T \Lambda_{nm}(\theta, \varphi) \quad R \leq R_0 \tag{F.6}$$

into the above equations we obtain

$$\epsilon_{ij}(R, \theta, \varphi) = \left( \frac{R}{R_0} \right)^n \Phi_{nm}^T \epsilon'_{ij}(\theta, \varphi) \tag{F.7}$$

where

$$\begin{aligned}
\epsilon'_{RR} &= n h_n \Lambda_{nm} \\
\epsilon'_{\theta\theta} &= h_n \Lambda_{nm} + \ell_n \frac{\partial^2 \Lambda_{nm}}{\partial \theta^2} \\
\epsilon'_{\varphi\varphi} &= \left[ h_n - \frac{m^2 \ell_n}{\cos^2(\theta)} \right] \Lambda_{nm} + \ell_n \tan(\theta) \frac{\partial \Lambda_{nm}}{\partial \theta}
\end{aligned}$$

$$\begin{aligned}
2\epsilon'_{R\theta} &= \left[ h_n + (n-1) \ell_n \right] \frac{\partial \Lambda_{nm}}{\partial \theta} \\
2\epsilon'_{R\varphi} &= \left[ h_n + (n-1) \ell_n \right] \frac{1}{\cos(\theta)} \frac{\partial \Lambda_{nm}}{\partial \varphi} \\
2\epsilon'_{\theta\varphi} &= \frac{\ell_n}{\cos(\theta)} \frac{\partial}{\partial \varphi} \left[ 2 \frac{\partial \Lambda_{nm}}{\partial \theta} - \tan(\theta) \Lambda_{nm} \right]
\end{aligned}$$

where the form of the Love numbers depends on the nature of the disturbing potential, i.e., whether it loads the surface or not.

As our principal interest is in the asymptotic behavior of the energy density for large  $n$ , we can neglect the terms in  $\ell_n$ , since

$$\ell_n = \left( \frac{3}{2n+1} \right) \frac{h_n}{n} \quad \text{F.8}$$

Using the approximation  $\ell_n = 0$  and the facts

$$\frac{1}{4\pi} \int_S (\Lambda_{nm})^2 dS = 1 \quad \text{F.9}$$

$$\frac{1}{4\pi} \int_S \left( \frac{\partial \Lambda_{nm}}{\partial \theta} \right)^2 dS = (n)(n+1) - \frac{(2n+1)(m)}{2} \quad \text{F.10}$$

$$\frac{1}{4\pi} \int_S \frac{1}{\cos^2(\theta)} \left( \frac{\partial \Lambda_{nm}}{\partial \varphi} \right)^2 dS = \frac{(2n+1)(m)}{2} \quad \text{F.11}$$

(Lowes, 1966), we find that

$$\begin{aligned}
\frac{1}{4\pi} \int_S \sum_{i=1}^3 \sum_{j=1}^3 \epsilon'_{ij} \epsilon'_{ij} dS &= \left[ n^2 + 2 + \frac{(n)(n+1)}{2} \right] h_n^2 \\
&= \left( \frac{3n^2 + n + 4}{2} \right) h_n^2
\end{aligned} \quad \text{F.12}$$

Therefore, the total elastic energy corresponding to the harmonic disturbance  $\Phi_{nm}$  is  $E_{nm} = 4\pi R_0^3 \epsilon_{nm}/3$ , or

$$\begin{aligned}
E_{nm} &= \frac{\mu}{2} \left( \frac{3n^2 + n + 4}{2} \right) h_n^2 \Phi_{nm}^2 \left( \frac{4\pi R_0}{3} \right)^3 \int_0^1 \xi^{2n+2} d\xi \\
&= \frac{\pi \mu R_0^3}{3} \left( \frac{3n^2 + n + 4}{2n + 3} \right) h_n^2 \Phi_{nm}^2
\end{aligned} \tag{F.13}$$

where  $\xi = R/R_0$ .

If we consider the surface topography of a planet

$$H(\theta, \varphi) = R_0 \sum_{n=1}^{\infty} \sum_{m=0}^n H_{nm}^T \Lambda_{nm}(\theta, \varphi) \tag{F.14}$$

to be the result of the emplacement of a surface load  $H'(\theta, \varphi)$  and the subsequent deformation of the original surface, we can calculate the total elastic energy stored during the deformation. In this case,

$$\left( \frac{2n+1}{3} \right) \Phi_{nm} = H'_{nm} = \frac{H_{nm}}{1 + k'_n} \tag{F.15}$$

so that a sum over all  $2n+1$  terms of degree  $n$  in the harmonic expansion of the surface load yields

$$E_n = 3\pi \mu R_0^3 \frac{3n^2 + n + 4}{(2n+3)(2n+1)^2} \left( \frac{h'_n}{1 + k'_n} \right)^2 V(H;n) \tag{F.16}$$

where

$$V(H;n) = \sum_{m=0}^n H_{nm}^T H_{nm}$$

is the topographic degree variance. The total elastic energy due to the topography is thus simply

$$E_{el} = \sum_{n=1}^{\infty} E_n = \frac{4\pi R_0^3}{3} \sum_{n=1}^{\infty} e_n \quad F.17$$

However, since

$$\lim_{n \rightarrow \infty} \left( \frac{h'_n}{1+k'_n} \right) = \frac{2P_0}{3\mu} \quad F.18$$

Therefore,

$$\lim_{n \rightarrow \infty} (2n+1) e_n = \frac{3P_0^2}{4\mu} V(H;n) \quad F.19$$

i.e., the elastic energy density per harmonic degree converges to zero more rapidly than the topographic degree variances. It would thus be possible to have infinite topographic variance and finite elastic energy.

## 2. Gravitational Energy

We now direct our attention to the gravitational energy associated with the surface topography of a planet. The gravitational energy density is just the work done per unit volume against the gravitational field in assembling the configuration from some reference state. It is calculated from

$$e = \frac{1}{2} \rho \Phi \quad F.20$$

where, as before,  $\rho$  is the mass density and  $\Phi$  is the gravitational potential. We have already seen that the potential of a homogeneous spheroid with mean radius  $R_0$  and mass  $M$  has the form

$$\Phi_1(R, \theta, \varphi) = \frac{GM}{R_0} \left[ \left( \frac{3 - (R/R_0)^2}{2} \right) + \sum_{n=1}^{\infty} \left( \frac{R_0}{R} \right)^{n+1} \sum_{m=0}^n \Phi_{nm}^T \Lambda_{nm}(\theta, \varphi) \right] \quad F.21$$

for interior points ( $R \leq R_0$ ), and

$$\Phi_e(R, \theta, \varphi) = \frac{GM}{R_0} \left[ \frac{R_0}{R} + \sum_{n=1}^{\infty} \left( \frac{R_0}{R} \right)^{n+1} \sum_{m=0}^n \Phi_{nm}^T \Lambda_{nm}(\theta, \varphi) \right] \quad F.22$$

for exterior points  $R \geq R_0$ , where

$$\left( \frac{2n+1}{3} \right) \Phi_{nm} = H_{nm}$$

and  $H_{nm}$  are the harmonic coefficients for the topographic heights..

If we denote the potential of a homogeneous sphere by  $\Phi_0(R)$ , then the gravitational energy of such a spherical configuration is

$$E_0 = \frac{1}{2} \int_0^{2\pi} \int_{-1}^1 \int_0^{\infty} \rho(R) \Phi_0(R) R^2 dR d\mu d\varphi \quad F.23$$

However, since  $\rho(R) = 0$  for  $R > 0$ , this can be written

$$\begin{aligned} E_0 &= \frac{GM}{2R_0} \int_0^{2\pi} \int_{-1}^1 \int_0^{R_0} \left[ \frac{3 - (R/R_0)^2}{2} \right] R^2 dR d\mu d\varphi \\ &= \frac{GM}{2R_0} \left[ \frac{3}{2} \left( \frac{4\pi R_0^3}{3} \right) - \frac{1}{2R_0} \left( \frac{4\pi R_0^5}{5} \right) \right] \\ &= \frac{3GM^2}{5R_0} \end{aligned} \quad F.24$$

The effect of surface topography  $H(\mu, \varphi)$ , is found from the integral

$$E = \frac{1}{2} \int_0^{2\pi} \int_{-1}^1 \int_0^{\infty} \rho(R) \Phi(R, \mu, \varphi) R^2 dR d\mu d\varphi \quad F.25$$

where now  $\Phi(R, \mu, \varphi)$  includes the topographic perturbations. We will evaluate this interval over three disjoint regions: 1) the interior of the sphere,  $R < R_0$ , 2) an infinitesimal shell at the surface  $R = R_0$ , where we let  $dR = H(\mu, \varphi)$ , and 3) the exterior of the sphere  $R > R_0$ , where  $\rho(R) = 0$ . The desired integral will be the sum of these three parts.

The first integral is

$$\begin{aligned}
 E' &= \frac{1}{2}\rho \int_0^{2\pi} \int_{-1}^1 \int_0^{R_0} \Phi_i(R) R^2 dR d\mu d\varphi \\
 &= E_0 + \frac{GM_0}{2R_0} \sum_{n=1}^{\infty} \left( \frac{R_0^3}{n+3} \right) \sum_{m=0}^n \Phi_{nm}^T \int_0^{2\pi} \int_{-1}^1 \Lambda_{nm}(\mu, \varphi) d\mu d\varphi
 \end{aligned} \tag{F.26}$$

but this last term is zero due to the orthogonality of  $\Lambda_{nm}$ . Thus,

$$E' = E_0 \tag{F.27}$$

The second part, or integral over the surface shell is

$$\begin{aligned}
 E'' &= \frac{1}{2}\rho \int_0^{2\pi} \int_{-1}^1 \Phi(R_0, \mu, \varphi) H(\mu, \varphi) R_0^2 d\mu d\varphi \\
 &= \frac{GM_0}{2R_0} \left[ 4\pi R_0^3 \sum_{n=1}^{\infty} \sum_{m=0}^n \Phi_{nm}^T H_{nm} \right] \\
 &= E_0 \frac{15}{2} \sum_{n=1}^{\infty} \sum_{m=0}^n \frac{H_{nm}^T H_{nm}}{2n+1}
 \end{aligned} \tag{F.28}$$



where we have used the relationship between  $\phi_{nm}$  and  $H_{nm}$  to simplify the last expression. The third integral is trivially  $E''' = 0$ , since  $\rho(R) = 0$  for  $R > R_0$ .

Thus, the effect of surface topography on a homogeneous planet is to increase the gravitational energy above the spherical value of  $E_0 = 3GM^2/5R_0$  to

$$E = E_0 \left[ 1 + \frac{15}{2} \sum_{n=1}^{\infty} \sum_{m=0}^n \frac{H_{nm}^T H_{nm}}{2n+1} \right] \quad \text{F.29}$$

where

$$E_n = \frac{15}{2} \sum_{m=0}^n \frac{H_{nm}^T H_{nm}}{2n+1}$$

is the contribution of harmonic degree  $n$  to the total. The gravitational energy is similar to the elastic energy in that their increments per degree both decrease with increasing degree more rapidly than the corresponding increments in topographic variance, and, in fact, the asymptotic convergence rates of the two energies are identical.

## G. SLOPES

Given a representation of the topographic heights on a planet  $H(\theta, \varphi)$ , we now desire a characterization of the slopes on the surface. We will first develop expressions for the mean square slope of given slope length, and criteria for the establishment of isotropy of the topography, and then we will consider the problem of mechanical stability of the slopes. In much of this analysis, we will consider the topography to be a realization of a homogeneous stochastic process.

The slope of the secant line between any two points a distance  $L = R_0 \gamma$  apart is

$$\frac{\Delta H}{L} = \frac{|H(\Gamma + \gamma) - H(\Gamma)|}{R_0 \gamma} \quad G.1$$

and the mean square slope with slope length  $L$  is

$$\begin{aligned} S^2(L) &\equiv E\left(\left[\frac{H(\Gamma + \gamma) - H(\Gamma)}{R_0 \gamma}\right]^2\right) \\ &= \frac{E[H^2(\Gamma + \gamma)] - 2E[H(\Gamma + \gamma)H(\Gamma)] + E[H^2(\Gamma)]}{(R_0 \gamma)^2} \end{aligned} \quad G.2$$

However, by the assumed stationarity of the topography

$$E[H^2(\Gamma + \gamma)] = E[H^2(\Gamma)] \quad G.3$$

and, we already have

$$E[H^2(\Gamma)] = C(H; 0) \quad G.4$$

and

$$E[H(\Gamma + \gamma) H(\Gamma)] = C(H; \gamma) \quad G.5$$

Therefore, the mean square slope of length  $L$  is

$$S^2(L) = \frac{2[C(H;0) - C(H;\gamma)]}{L^2}$$

$$= 2 \sum_{n=1}^{\infty} V(H;n) \left[ \frac{1 - P_n(\cos(\gamma))}{\gamma^2} \right]$$
G.6

As the slope length goes to zero and the secants defining the slope approach tangency (if the surface is, in fact, differentiable), we obtain

$$S^2(0) = \sum_{n=1}^{\infty} V(H;n) (n)(n+1)$$
G.7

since

$$\lim_{\gamma \rightarrow 0} \left[ \frac{1 - P_n(\cos(\gamma))}{\gamma^2} \right] = \frac{(n)(n+1)}{2}$$

In the important case where

$$V(H;n) = \frac{V(H;0)}{(n)(n+1)}$$
G.8

we obtain the closed form expression

$$S^2(L) = 2 V(H;0) \sum_{n=1}^{\infty} \left[ \frac{1 - P_n(\cos(\gamma))}{(n)(n+1)} \right]$$

$$4 V(H;0) \frac{2n[1 + \sin(\gamma/2)]}{\gamma^2}$$
G.9

(see Appendix D for more details). When the slope length is small, we have approximately

$$s^2(L) = 2 \frac{V(H;0)}{Y} \quad G.10$$

since

$$\sin(x) = x - \frac{x^3}{3!} + \frac{x^5}{5!} - \dots$$

$$\ln(1+x) = x - \frac{x^2}{2!} + \frac{x^3}{3!} - \dots$$

so that

$$\ln[1 + \sin(x/2)] = \frac{x}{2} - \frac{x^2}{8} + \frac{x^3}{48} - \dots$$

### 1. Isotropy of Slopes

Though we have assumed isotropy of covariance (and therefore of slopes) in modeling the topography as a realization of a homogeneous stochastic process, it is possible to check the validity of this assumption. We first recall that the differential arc length is given by

$$dL^2 = R_0^2 [d\theta^2 + \cos^2(\theta) d\varphi^2] = R_0^2 d\gamma^2 \quad G.11$$

We then calculate the mean square infinitesimal slopes facing east-west

$$s_{\theta}^2(0) = \frac{1}{4\pi} \int_A \left( \frac{\partial H}{\partial L} \right)_{\theta}^2 dA \quad G.12$$

and similarly for north-south facing slopes

$$s_{\varphi}^2(0) = \frac{1}{4\pi} \int_A \left( \frac{\partial H}{\partial L} \right)_{\varphi}^2 dA \quad G.13$$

where the subscript indicates which coordinate is held fixed and the integration is over the entire surface of the sphere. We note that

$$\left(\frac{\partial H}{\partial L}\right)_\theta = \left(\frac{\partial H}{\partial \varphi}\right)\left(\frac{\partial \varphi}{\partial L}\right) = \sum_{n=1}^{\infty} \sum_{m=0}^n \frac{H_{nm}^T}{\cos(\theta)} \frac{\partial \Lambda_{nm}(\theta, \varphi)}{\partial \varphi} \quad G.14$$

and

$$\left(\frac{\partial H}{\partial L}\right)_\varphi = \left(\frac{\partial H}{\partial \theta}\right)\left(\frac{\partial \theta}{\partial L}\right) = \sum_{n=1}^{\infty} \sum_{m=0}^n H_{nm}^T \frac{\partial \Lambda_{nm}(\theta, \varphi)}{\partial \theta} \quad G.15$$

The required integrals are (Lowes, 1966)

$$\frac{1}{4\pi} \int_A \frac{1}{\cos^2(\theta)} \left(\frac{\partial \Lambda_{nm}}{\partial \varphi}\right)^2 dA = \frac{(2n+1)(n)}{2} \quad G.16$$

and

$$\frac{1}{4\pi} \int_A \left(\frac{\partial \Lambda_{nm}}{\partial \theta}\right)^2 dA = (n)(n+1) - \frac{(2n+1)(n)}{2} \quad G.17$$

Therefore, the mean square east-west slope is

$$s_\theta^2(0) = \sum_{n=1}^{\infty} T_\theta(n) \quad G.18$$

and the mean square north-south slope is

$$s_\varphi^2(0) = \sum_{n=1}^{\infty} T_\varphi(n) \quad G.19$$

where the degree tilts are

$$T_\theta(n) = \sum_{m=0}^n \left[ \frac{(2n+1)(n)}{2} \right] H_{nm}^T H_{nm}$$

$$T_\varphi(n) = \sum_{m=0}^n \left[ (n)(n+1) - \frac{(2n+1)(n)}{2} \right] H_{nm}^T H_{nm} \quad G.20$$

The total mean square slope at zero slope length is simply

$$\begin{aligned} s^2(0) &= \sum_{n=1}^{\infty} T_{\theta}(n) + T_{\varphi}(n) \\ &= \sum_{n=1}^{\infty} (n)(n+1) V(H;n) \end{aligned} \quad \text{G.21}$$

as previously established.

Our desired criterion for mean square isotropy of a function  $H(\theta, \varphi)$  on a sphere is thus

$$T_{\theta}(n) = T_{\varphi}(n) \quad \text{G.22}$$

or equivalently

$$(2n+1) \sum_{m=0}^n (m) \left[ H_{nm}^T H_{nm} \right] = (n)(n+1) \sum_{m=0}^n H_{nm}^T H_{nm}$$

for all  $n$ . Here  $H_{nm}$  are the normalized Fourier-Legendre transforms of  $H(\theta, \varphi)$ .

## 2. Slope Stability

Physical slopes are limited in height by the strength of their constituent materials. The stability of a slope in soil is dependent upon characteristics of the soil [density ( $\rho$ ), cohesion ( $c$ ) and internal friction angle ( $\varphi$ )], characteristics of the slope [height ( $H$ ), length ( $L$ ) and inclination ( $i$ )] and a characteristic of the planetary surface on which the slope resides, [the local gravity ( $g$ )]. If a slope of constant inclination is extended in height, the shear stress ( $\tau$ ) will eventually exceed the shear resistance of the

material and the slope will fail. A common failure criterion is the Mohr-Coulomb relation

$$\tau = c + \sigma \tan(\varphi) \quad \text{G.23}$$

which expresses a linear increase in shear stress at failure with increasing normal stress ( $\sigma$ ). The general determination of slope stability is a difficult variational problem (Revilla and Castillo, 1977), but in the case of shallow slopes the failure surface is essentially planar and the analysis of Culmann (1866) is adequate (see e.g., Terzaghi, 1943). According to this analysis the maximum height attainable in a slope of length  $L$  is

$$H(L) = \frac{4c}{\rho g} \left[ \frac{\sin(i) \cos(\varphi)}{1 - \cos(i - \varphi)} \right] \quad \text{G.24}$$

In many situations the effects of internal friction are negligible, so we shall assume  $\varphi = 0$ , and

$$H(L) = \frac{4c}{\rho g} \left[ \frac{\sin(i)}{1 - \cos(i)} \right] \quad \text{G.25}$$

In a rectilinear slope segment, we also obviously have

$$H(L) = L \tan(i) \quad \text{G.26}$$

so that

$$\cos(i) = \left[ 1 + \frac{4c}{\rho g L} \right]^{-1} \quad \text{G.27}$$

Thus, the squared height is

$$H^2(L) = \frac{8cL}{\rho g} \left( 1 + \frac{L_o}{L} \right) \quad \text{G.28}$$

where

$$L_o = \frac{2c}{\rho g}$$

However, on the Moon, for example

$$\left. \begin{array}{l} c \doteq 0.1 \text{ bar} \\ \rho \doteq 3.0 \text{ gm cm}^{-3} \\ g \doteq 160 \text{ gal} \end{array} \right\} \Rightarrow L_o = 4\text{m} \quad \text{G.29}$$

Thus, to a good approximation

$$H^2(L) = \frac{8cL}{\rho g} \quad L \gg L_o \quad \text{G.30}$$

i.e., the squared height of a stability limited slope is proportional to the length of the slope.

It is interesting to note an analogous behavior exhibited by the Wiener process. If we consider the slope profile to be a realization of a Wiener process on the positive reals with parameter  $\sigma^2 = 3c/\rho g$  and  $W(0) = 0$  then

$$E[W^2(L)] = \sigma^2 L = \frac{8cL}{\rho g} \quad \text{G.31}$$

i.e., the variance of the process is proportional to the length of the slope.

The spherical Wiener process also exhibits this type of behavior for sufficiently short slopes ( $\gamma \ll 2\pi$ ). Since the covariance has the form

$$\begin{aligned} C(H; \gamma) &= C(H; 0) \sum_{n=1}^{\infty} \frac{P_n[\cos(\gamma)]}{(n)(n+1)} \\ &= C(H; 0) \left[ 1 - 2\mathcal{L}_n[1 + \sin(\gamma/2)] \right] \end{aligned} \quad \text{G.32}$$

the mean square range over a distance  $L = R_o \gamma$  is



$$\begin{aligned} E\left([H(\Gamma+\gamma) - H(\Gamma)]^2\right) &= 2[C(H;0) - C(H;\gamma)] & \text{G.33} \\ &= 4C(H;0) \ln [1 + \sin(\gamma/2)] \end{aligned}$$

For short distances, this reduces to

$$E\left([H(\Gamma+\gamma) - H(\Gamma)]^2\right) = 2C(H;0) \gamma \quad \gamma \ll 2\pi \quad \text{G.34}$$

i.e., the mean square slope height is proportional to slope length.

If we let  $C(H;0) = 4c R_0/\rho g$ , we recover the slope stability result exactly.

## REFERENCES

- Beers, B.L. (1972). Harmonic analysis of analytic functions on hyperspheres. J. Math. Phys. 13, 950-955.
- Beers, B.L. and Dragt, A.J. (1970). New theorems about spherical harmonic expansions. J. Math. Phys. 11, 2313-2328.
- Culmann, K. (1866). Die graphische static. In Theorie der Stütz und Futtermauern, Meyer and Zeller, Zürich, 564 pp.
- Darwin, G.H. (1879). On the bodily tides of viscous and semi-elastic spheroids. Phil. Trans. Roy. Soc. 170, 1-35
- Doob, J.L. (1942). The Brownian movements and stochastic equations. Ann. Math. 43, 351-369.
- Erdelyi, A. (1953). Higher Transcendental Functions, vol. I., McGraw-Hill, New York.
- Gallager, R.G. (1968). Information Theory and Reliable Communication. Wiley, New York, 588 pp.
- Heiskanen, W.A. and Moritz, H. (1967). Physical Geodesy. W.H. Freeman, San Francisco, 364 pp.
- Jones, R.H. (1963). Stochastic processes on a sphere. Ann. Math. Statist. 34, 213-218.
- Kaula, W.M. (1967). Theory of statistical analysis of data distributed over a sphere. Rev. Geophys. 5, 83-107.
- Levy, P. (1948). Processus Stochastiques et Mouvement Brownien. Gauthier-Villars, Paris, 365 pp.
- Love, A.E.H. (1927). A Treatise on the Mathematical Theory of Elasticity. Dover, New York, 643 pp.

- Lowes, F.J. (1966). Mean-square values of spherical harmonic vector fields. J. Geophys. Res. 71, 2179.
- MacRobert, T.M. (1967). Spherical Harmonics. Pergamon Press, New York, 345 pp.
- Mandelbrot, B.B. (1975). Stochastic models for the Earth's relief, the shape and fractal dimension of coastlines, and the number-area rule for islands. Proc. Nat. Acad. Sci. 72, 3825 - 3828.
- Mandelbrot, B.B. and Van Ness, J.W. (1968). Fractional Brownian motions, fractional noises and applications. SIAM Review 10, 422-437.
- Maxwell, J.C. (1868). On the dynamical theory of gases. Phil. Mag. 35, 129-145.
- McFadden, J.A. (1965). The entropy of a point process. J. Soc. Indust. Appl. Math. 13, 988-994.
- McKenzie, D.P. (1967). The viscosity of the mantle. Geophys. J. Roy. Astr. Soc. 14, 297-305.
- Middleton, D. (1960). An Introduction to Statistical Communication Theory. McGraw-Hill, New York, 1140 pp.
- Munk, W.H. and MacDonald G.J.F. (1960). The Rotation of the Earth. Cambridge Univ. Press, London, 323 pp.
- Parzen, E. (1962). Stochastic Processes. Holden-Day, San Francisco 324 pp.
- Peltier, W.R. (1974). The impulse response of a Maxwell Earth. Rev. Geophys. Space Phys. 12, 649-669.

- Revilla, J. and Castillo E. (1977). The calculus of variations applied to stability of slopes. Geotechnique 27, 1-11.
- Rice, S.O. (1944). Mathematical analysis of random noise. Bell System Tech. Jour. 23, 282-332.
- Roberts, P.H. and Ursell, H.D. (1960). Random walk on a sphere and on a Riemannian manifold. Phil. Trans. Roy. Soc. London A 252, 317-356.
- Roy, R. (1973). Estimation of the covariance function of a homogeneous process on the sphere. The Annals of Statistics 1, 780-785.
- Roy R. (1976). Spectral analysis for a random process on the sphere. Ann. Inst. Stat. Math. 28, 91-97.
- Terzaghi, K. (1943). Theoretical Soil Mechanics. John Wiley, New York, 510 pp.
- Thomasian, A.J. (1969). The Structure of Probability Theory with Applications. McGraw-Hill, New York, 746 pp.
- Uhlenbeck, G.E. and Ornstein, L.S. (1930). On the theory of the Brownian motion. Phys. Rev. 36, 823-841.
- Wheelon, A.D. (1968). A Short Table of Summable Series. Holden-Day, San Francisco, 86 pp.

GEOLOGIC INTERPRETATION OF  
REMOTE SENSING DATA FOR THE  
MARTIAN VOLCANO ASCRAEUS MONS

by

James Ray Zimbelman

A Dissertation Presented in Partial Fulfillment  
of the Requirements for the Degree  
Doctor of Philosophy

ARIZONA STATE UNIVERSITY

December 1984

## ABSTRACT

Photographs and other remote sensing data of Ascræus Mons were analyzed in order to relate the remotely determined surface properties to the geology of the volcano. Photogeologic analysis indicates that Ascræus Mons is similar to terrestrial basaltic shield volcanoes in both surface morphology and estimated rheologic properties. Lava flows are interpreted to include pahoehoe, aa, and toey pahoehoe. At elevations  $\leq 15$  km, features  $< 500$  m in scale are very subdued. This is interpreted to be the result of deposition of aeolian or pyroclastic materials on the surface. An aeolian origin is preferred because aeolian activity presently occurs on the volcano and there is no evidence of major pyroclastic eruptions on the volcano. The wavelength dependence of albedos on Ascræus Mons parallels the reflectance spectrum of classical high albedo regions (e.g. Arabia), which suggests that dust is present throughout the volcano summit area. High spatial resolution infrared sequences show no correlation between the thermal properties and surface terrains, including various lava flow terrains, consistent with dust deposits at least 2 cm thick on all terrains. Caldera walls have the highest thermal inertias on the volcano ( $I = 4.5 \times 10^{-3}$  cal cm<sup>-2</sup> sec<sup>1/2</sup> K<sup>-1</sup>) but bedrock exposures probably account for  $< 15\%$  of the observed area. Thermal inertias increase down the flanks of the volcano ( $I = 2$  to 4) while the areal

abundance of high thermal inertia materials ( $I = 30$ ) decreases; downslope sediment transportation and sorting could account for both of these trends. The properties of Ascræus Mons at visual and infrared wavelengths are dominated by surface materials that do not appear to be directly associated with the underlying terrains. Radar signals are strongly scattered by the volcano, indicating that features  $> 10$  cm but  $< 100$  m are not effectively obscured by the surface materials.

## ACKNOWLEDGEMENTS

Many people have provided valuable assistance during the course of this project. They are too numerous to give proper recognition to each, but some deserve special note.

The guidance of Dr. Ronald Greeley as my advisor was most instrumental in bringing this project to completion. Dr. Michael Malin provided numerous hours of consultation and stimulating discussion. Dr. Philip Christensen led me through the complexities of the computer programming involved in the infrared data processing. I am also indebted to Dr. Michael Sheridan, Dr. Susan Wyckoff, Dr. Carlton Moore, and Dr. Jonathan Fink for their input and advice.

The planetary geology group at ASU deserves mention for their encouragement and scientific interaction. Dan Ball and his assistants in the darkroom provided invaluable help in the photographic requirements of this work. The office personnel, particularly Terry Gautesen-Borg and Maureen Schmelzer, kept me from being inundated by paperwork. Eilene Theilig thoroughly reviewed the geologic maps in this work. I am grateful to my office partner, Dean Eppler, for valuable discussions and many good times.

The encouragement, prayers and support of friends and family cannot be overemphasized. I am particularly grateful to my wife, Cheryl, for countless hours of typing, drafting figures, proof-reading text, and uplifting my spirits.



Finally, my faith in God was the stabilizing force in my life throughout this project.

This work was supported through the Planetary Geology Program at Arizona State University under NASA grant 7548.

## TABLE OF CONTENTS

LIST OF TABLES . . . . .	280
LIST OF FIGURES . . . . .	281
LIST OF MAPS . . . . .	284
CHAPTER 1. INTRODUCTION . . . . .	285
CHAPTER 2. BACKGROUND AND PREVIOUS WORK . . . . .	289
Introduction . . . . .	289
Historical Summary . . . . .	290
Global Setting . . . . .	293
Regional Setting . . . . .	299
Photogeology . . . . .	303
Morphology . . . . .	303
Geologic history . . . . .	309
Surface Properties . . . . .	313
Surface-Atmosphere Interactions . . . . .	319
Martian Eruption Characteristics . . . . .	322
Summary . . . . .	325
Background . . . . .	325
Previous work . . . . .	326
CHAPTER 3. PHOTOGEOLOGY . . . . .	327
Introduction . . . . .	327
Stratigraphy . . . . .	328
Mountainous terrains . . . . .	334
Tharsis plains terrains . . . . .	339
Shield base terrains . . . . .	344
Shield summit terrains . . . . .	352

Caldera terrains . . . . .	355
Summary . . . . .	360
Cratering Record . . . . .	363
Structure . . . . .	376
Rheology Estimates . . . . .	385
Discussion . . . . .	395
Shield erosion . . . . .	395
Subdued base morphology . . . . .	399
Summary: Geologic History . . . . .	402
Pre-shield stage . . . . .	403
Shield-building stage . . . . .	403
Caldera stage . . . . .	404
Shield erosion stage . . . . .	405
Recent stage . . . . .	406
CHAPTER 4. SURFACE PROPERTIES . . . . .	407
Introduction . . . . .	407
Visual Reflectance . . . . .	409
Thermal Inertias . . . . .	421
High resolution data . . . . .	422
Terrain unit correlations . . . . .	429
Diurnal temperature amplitude . . . . .	440
"Block" abundances . . . . .	444
Moderate resolution data . . . . .	451
Summary . . . . .	455
Surface Roughness . . . . .	456
Atmospheric Water Vapor . . . . .	461

Discussion . . . . .	464
Summary: Geologic Implications . . . . .	470
Visual reflectance . . . . .	470
Thermal inertia . . . . .	471
Surface roughness . . . . .	472
Atmospheric water vapor . . . . .	472
CHAPTER 5. HAWAII-MARS COMPARISONS . . . . .	473
Introduction . . . . .	473
Hawaiian Lava Flows . . . . .	475
Mantling . . . . .	475
Surface roughness . . . . .	479
Hummocks . . . . .	481
Ridges . . . . .	483
Summary . . . . .	485
Porosity and Thermal Inertia . . . . .	487
Summary . . . . .	496
Hawaiian lava flows . . . . .	496
Porosity and thermal inertia . . . . .	497
CHAPTER 6. DISCUSSION AND CONCLUSIONS . . . . .	498
Discussion . . . . .	498
Geologic history . . . . .	498
Surface properties . . . . .	504
Global implications . . . . .	511
Conclusions . . . . .	517
Future work . . . . .	521
REFERENCES . . . . .	522

APPENDIX 1.	GEOLOGIC TERRAIN UNIT DESCRIPTIONS . . .	540
APPENDIX 2.	DATA DESCRIPTIONS . . . . .	552
APPENDIX 3.	ELEVATION-DEPENDENT CORRECTIONS FOR THERMAL INERTIAS ON MARS . . . . .	563

## LIST OF TABLES

2.1	Martian volcanoes . . . . .	297
2.2	X-ray fluorescence chemical analyses . . . . .	300
2.3	Ages of martian shield volcanoes . . . . .	311
3.1	Volumes, areas, and thicknesses of individual basalt flows . . . . .	343
3.2	Crater retention ages for Ascraeus Mons . . . . .	374
3.3	Symbols for Fig. 3.20 . . . . .	378
3.4	Maximum length of a thrust block (km) . . . . .	383
3.5	Yield strength estimates for six Ascraeus Mons flows . . . . .	388
3.6	Yield strength estimates for flows on the Earth, Moon, and Mars . . . . .	392
4.1	Albedo values for Ascraeus Mons . . . . .	415
5.1	Correlation coefficients for basalt properties . . . . .	490

## LIST OF FIGURES

2.1	Mars from Mariner 7 . . . . .	292
2.2	Shaded relief map of Mars . . . . .	295
2.3	Martian volcanoes on a Lambert equal-area projection . . . . .	296
2.4	Shaded relief and topographic map of the Tharsis region . . . . .	302
2.5	Topographic profiles of Olympus Mons, Ascraeus Mons and Mauna Loa, Hawaii . . . . .	305
2.6	Oblique view of Ascraeus Mons . . . . .	307
2.7	Thermal inertia as a function of particle size .	316
3.1	Regional geologic map of Ascraeus Mons . . . . .	330
3.2	Photomosaic of Ascraeus Mons . . . . .	331
3.3	Topography of Ascraeus Mons . . . . .	332
3.4	High resolution photographs of shield flank and caldera complex . . . . .	333
3.5	Northwestern flank of Ascraeus Mons . . . . .	335
3.6	Stereoscopic photomosaic of the western flank .	336
3.7	Plains south and southeast of Ascraeus Mons . .	341
3.8	Shield base terrains . . . . .	346
3.9	Smooth plains (s) on shield base . . . . .	347
3.10	Northwestern flank of Ascraeus Mons . . . . .	349
3.11	Summit area terrains east of the caldera complex	353
3.12	Caldera wall and floor terrains . . . . .	357
3.13	Caldera complex of Ascraeus Mons . . . . .	359
3.14	Stereoscopic photographs of the southern portion of the caldera complex . . . . .	361
3.15	Cumulative distributions of all craters for the odd-numbered frames . . . . .	364

3.16	Cumulative distributions of all craters visible in the 401B photographs . . . . .	365
3.17	Cumulative distributions for impact craters in the 401B photographs . . . . .	368
3.18	Cumulative distribution of all craters from Photographs 698A01-08 of the Tharsis plains . . .	371
3.19	Cumulative distributions for impact craters on caldera floor areas . . . . .	372
3.20	Structural map for Ascraeus Mons . . . . .	377
3.21	Location map of the summit area flows measured for rheology estimates . . . . .	386
3.22	Yield strength values calculated for the flows indicated in Fig. 3.21 . . . . .	389
3.23	Yield strength values calculated for flow E . . .	390
4.1	Color photograph of Ascraeus Mons . . . . .	410
4.2	Red/violet ratio of photographs used in Fig. 4.1	412
4.3	Ascraeus Mons albedos . . . . .	414
4.4	High resolution thermal inertias . . . . .	423
4.5	Corrected thermal inertias for summit caldera .	430
4.6	Corrected thermal inertias correlated with terrain types from Map 1 . . . . .	434
4.7	Southeast flank of Ascraeus Mons . . . . .	438
4.8	Diurnal temperature amplitude for the floor of the northeast caldera . . . . .	442
4.9	"Block" abundances for nighttime IRTM sequences	446
4.10	Temperature differences for different "block" abundances and thermal inertias . . . .	448
4.11	Corrected thermal inertias for Ascraeus Mons . .	452
4.12	Corrected thermal inertias for Ascraeus Mons . .	453



4.13	Depolarized component of radar data from the Tharsis region . . . . .	458
4.14	Atmospheric water vapor abundance . . . . .	462
5.1	Location map for photographs of Hawaiian lava flows . . . . .	474
5.2	Mantled surface of an aa flow near Mauna Iki . .	477
5.3	Grass-covered flows on the northwest flank of Mauna Kea . . . . .	478
5.4	Surface roughness on the 1823 flow of Kilauea .	480
5.5	Hummocky terrain near the summit of Mauna Loa .	482
5.6	Pahoehoe toes on a partially covered aa flow . .	484
5.7	Ridges on the Puu Waawaa trachyte flow . . . . .	486
5.8	Properties of Hawaiian basalts as a function of porosity . . . . .	489
5.9	Thermal inertias calculated for the Hawaiian basalts . . . . .	492
6.1	Topography of the equatorial region of Mars . .	512
6.2	Thermal inertias in the equatorial region . . .	513
6.3	Thermal inertias for the Tharsis and Elysium regions . . . . .	514

# LIST OF MAPS

1	Photogeology of Ascræus Mons . . . . .	571
2	Photogeology of Ascræus Mons, 401B01-24 photographs . . . . .	572

## CHAPTER 1. INTRODUCTION

How comfortless the winter season there!  
And cheerless, Ascra, is thy summer air.

Hesiod, 8th century B.C. Greek poet  
(from Cooke, 1976)

The planet Mars has been a subject of scientific interest for hundreds of years. Earth-based telescopic observations alone can provide very little information about the geologic history of the planet. During the past twenty years spacecraft have flown by, orbited, and landed on Mars, providing detailed information about the martian surface. Photographs from the Mariner and Viking spacecraft indicate that Mars has had a very complex and diverse geologic history. Spacecraft data are of sufficient spatial resolution to allow geologic problems to be addressed for specific surface features. This work presents a synthesis of photogeologic and remote sensing results for Ascraeus Mons, one of the large martian shield volcanoes.

The objective of this study is to relate the surface morphology and properties of Ascraeus Mons obtained from remote sensing data to the geologic history of the volcano. Until samples can be obtained from Mars, all information about the planet must be acquired through remote sensing techniques. A detailed investigation of both the geologic history and the remotely determined properties of Ascraeus

Mons provides a basis for evaluating the geologic significance of the remotely determined surface properties of Mars.

The approach adopted for this study involves addressing the following questions:

- 1) What is the geologic history of the Ascraeus Mons volcano?
- 2) What geologic processes are active on the surface of Ascraeus Mons?
- 3) How do the surface features of Ascraeus Mons compare with the surface features observed on similar terrestrial volcanoes?

The geologic history of the volcano provides the framework for identifying the processes that have produced its surface as it is observed today. The processes responsible for the present condition of the surface may be related to the development of the surface morphology. Examination of terrestrial volcanic features can aid in the interpretation of similar features on Mars, where surface features smaller than 10s of meters cannot be directly observed.

Geologic investigations of planetary surfaces rely primarily on terrain morphology and stratigraphic relationships between different terrains. The best photographs of Mars obtained from orbiting spacecraft have individual picture elements ("pixels") that correspond to 8 m on the surface (Snyder, 1979) but many aspects important

to the history of the surface occur at scales much smaller than this. Processes associated with the emplacement or modification of the surface usually involve transportation or redistribution of materials (e.g. volcanic, aeolian, fluvial, glacial processes). Remote sensing techniques provide a method of obtaining information about surface materials on the km to m scale, which could aid in evaluating the processes active on the surface. Unfortunately, these techniques typically have spatial resolutions inferior to the resolutions of the photographs and it is often difficult to relate the remote sensing results to surface features. In order to aid the geologic interpretation of the remote sensing results, this work presents analyses of several types of data for Ascraeus Mons with the best available spatial resolution. A fundamental limitation to a remote sensing analysis of Mars is the lack of in situ observations except at the locations of the two Viking landers. Geologic interpretations of martian volcanic terrains have been assisted by field investigations of terrestrial volcanoes (e.g. Hawaii) as analogs to the martian features (Carr and Greeley, 1980). The Hawaiian volcanoes serve as a useful analog to some of the features observed on Ascraeus Mons.

The thesis is organized around the questions presented above. Chapter 2 reviews background information concerning Ascraeus Mons and martian volcanic studies. Chapter 3

provides the photogeologic interpretation of geomorphic terrain units, contact relationships, and crater counts used in establishing the history of the volcano. Structural features and compositional constraints from flow morphologies are also included in this chapter. Chapter 4 presents the interpretation of remote sensing data at several wavelengths in terms of the geologic processes active on Ascræus Mons. Reflectance properties at three visual wavelengths, thermal infrared surface temperatures and thermal inertias, radar scattering properties of the volcano, and atmospheric water vapor abundances are discussed. Chapter 5 provides brief descriptions of surface conditions on selected lava flows on Hawaii for comparison with some features observed on Ascræus Mons. Laboratory measurements of the thermophysical properties of Hawaiian basalts provide indications of thermal inertia variations between Earth and Mars due to atmospheric pressure differences. Chapter 6 presents a synthesis of the results from the previous chapters and discusses their global implications. Each chapter is extensively summarized to aid in accessing the results and conclusions presented here. Appendices contain detailed descriptions of individual terrain units, the data used in this analysis, and the elevation correction procedure developed for the infrared data.

## CHAPTER 2. BACKGROUND AND PREVIOUS WORK

### Introduction

The discovery of volcanoes on Mars during the Mariner 9 mission was the first of many important advances in the study of martian geology. The great diversity and complexity of martian surface features have prompted many scientific investigations, resulting in an enormous volume of literature about the planet. Various texts provide detailed descriptions of the numerous results obtained from the study of Mars (e.g. Mutch et al., 1976; Carr, 1981). The discussion here concentrates on the results and interpretations for the martian volcanoes, with particular emphasis on Ascraeus Mons and the other large volcanoes in the Tharsis area of Mars.

This chapter begins with a brief historical summary of information related to Ascraeus Mons. The global setting of the Tharsis volcanoes is presented next, followed by a description of the regional setting for Ascraeus Mons. Published photogeologic results for the Tharsis volcanoes are summarized, along with the remotely determined surface properties of the volcanoes obtained prior to this study. Atmospheric phenomena such as clouds and aeolian interactions with the surface are discussed in relation to the Tharsis volcanoes. Characteristics related to martian

volcanic eruptions are briefly summarized, emphasizing their potential effect on observable properties. A summary of the results important to this study of Ascræus Mons concludes the chapter.

### Historical Summary

The name Ascræus Mons has its roots in the geography of ancient Greece. Schiaparelli (in 1888) named a low albedo (dark) feature near 20°N, 100°W Ascræus Lacus ("Lake of Ascræ") after the birthplace of the Greek poet Hesiod (Blunck, 1977). Following the discovery of the martian volcanoes in 1971, the one closest to Schiaparelli's dark feature was named Ascræus Mons (DeVaucouleurs et al., 1975). Hesiod's description of Ascræ (see Chapter 1) is not consistent with the present moderate climate of the Greek village (Wallace, 1974) but it is quite applicable to the harsh conditions on Ascræus Mons.

Telescopic observations reveal the Tharsis region to be a consistent center of cloud development, most notably the "W-cloud" which develops around local noon and persists through the afternoon (Hartmann and Raper, 1974). Polarization of the sunlight reflected by such clouds indicated the presence of ice crystals instead of liquid droplets (Dollfus, 1948), leading to their interpretation as water ice (Kuiper, 1952). These blue-white water ice



clouds are distinctly different from yellow dust clouds that typically originate in the southern hemisphere and can grow to obscure the entire planet (Slipher, 1962, p.31).

The Mariner 4 flyby in 1965 provided twenty-two photographs that first showed the cratered nature of the martian surface (Leighton et al., 1965). In 1969 Mariners 6 and 7 returned nearly 200 photographs of Mars, but the best photographs were all of the heavily cratered southern hemisphere (Leighton et al., 1969). Bright concentric rings in photographs taken during the approach to Mars were interpreted to be large craters (Collins, 1971 and Fig. 2.1) but they are now known to be associated with the Tharsis volcanoes (Mutch et al., 1976, p.182).

Mariner 9 provided the first direct evidence of volcanism on Mars. The spacecraft went into orbit around Mars in November 1971, nearly two months after a dust storm encompassed the whole planet. As the dust settled, four dark "spots" were observed in the Tharsis region. Ascraeus Mons ("north spot") became the first clearly identified martian volcanic structure as its complex summit caldera emerged from the settling dust (Masursky et al., 1972). Thousands of photographs and other data covering most of the planet were received from the Mariner 9 spacecraft.

In 1976 four Viking spacecraft arrived at Mars,

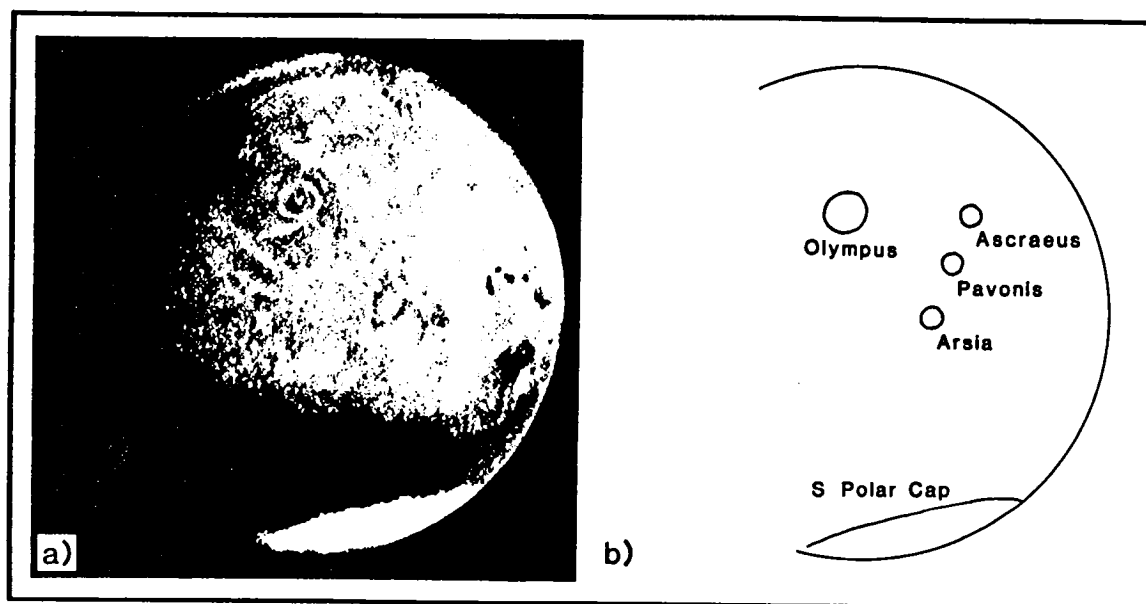


Figure 2.1. Mars from Mariner 7, showing the Tharsis region. a) Frame 7F74, range 435,307 km. b) Sketch identifying the Tharsis shield volcanoes in part a.

including two landers and two orbiters. The landers each had two cameras and a variety of other experiments (Soffen, 1977) and each orbiter had two cameras comprising the visual imaging system (VIS), twenty eight radiometers in the infrared thermal mapper (IRTM), and an infrared spectrometer in the Mars atmospheric water detector (MAWD) (Snyder, 1977). Four and a half years of operation by these spacecraft returned an immense volume of information, including the data for Ascreaus Mons discussed in the following chapters.

### Global Setting

The surface conditions on Mars are very different from those on the Earth. The tenuous martian atmosphere is more than 95% carbon dioxide with an average surface pressure of 7 mbar (millibars, where 1 bar corresponds to the average atmospheric pressure on Earth) that varies seasonally as CO<sub>2</sub> condenses at the poles in winter (Carr, 1981, p.25). The atmospheric pressure is too low to permit water to exist as a liquid on the surface of Mars under present climatic conditions (Carr, 1981, p.135). The red-brown color of Mars is attributed to iron oxides with strong absorption at wavelengths less than 0.75  $\mu\text{m}$  (McCord and Westphal, 1971; Singer, 1982). Surface albedos measured from 0.3 to 3.0  $\mu\text{m}$  range from .08 to .42 (1 = 100% reflection) throughout the equatorial latitudes (Pleskott and Miner,

1981). Telescopic observers gave classical names to the higher and lower albedo areas on Mars; the high albedo regions of Tharsis, Elysium, Arabia and Hellas, and the lower albedo region of Syrtis Major (Fig. 2.2) are of particular interest in subsequent chapters.

The surface of Mars is divided into two morphologically distinct hemispheres with plains in the north and densely cratered terrain in the south (Mutch et al., 1976, p.56 and Fig. 2.3). The martian volcanoes in the Tharsis and Elysium regions are located close to the boundary separating the two physiographically different hemispheres, and a third grouping of volcanoes occurs on the rim of the Hellas basin (Carr, 1973 and Fig. 2.3). Twenty-one volcanic features have been named in these locations according to the following nomenclature: "Mons" refers to the broad, shallow sloped volcanoes, "Tholus" refers to smaller, steeper sloped domes, and "Patera" refers to shallow complex craters with scalloped edges (DeVaucouleurs et al., 1975 and Table 2.1).

Topographic information obtained by several techniques were used to produce a global topographic map for Mars (Christensen, 1975; U.S.G.S., 1976). Recent Earth-based radar measurements of the northern hemisphere have revised some elevations downward by several km (Downs et al., 1982) but relative elevation differences are not greatly affected. The Tharsis volcanoes are located near

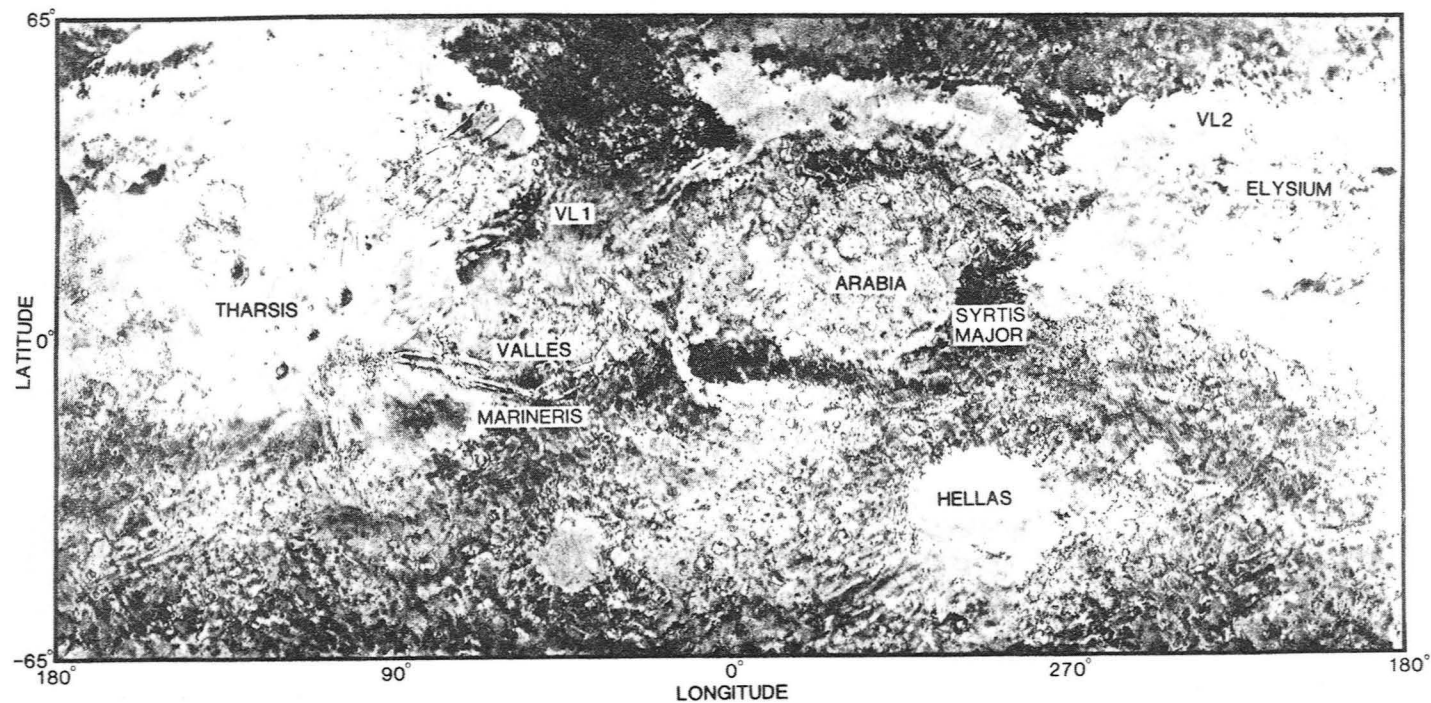


Figure 2.2. Shaded relief map of Mars, including albedo features (from U.S.G.S., 1976). Tharsis, Arabia, Hellas, Syrtis Major, and Elysium are classical names applied to bright or dark albedo areas. Valles Marineris is the equatorial system of canyons discovered during the Mariner 9 mission. VL1 and VL2 indicate the two Viking landing sites. Mercator projection.

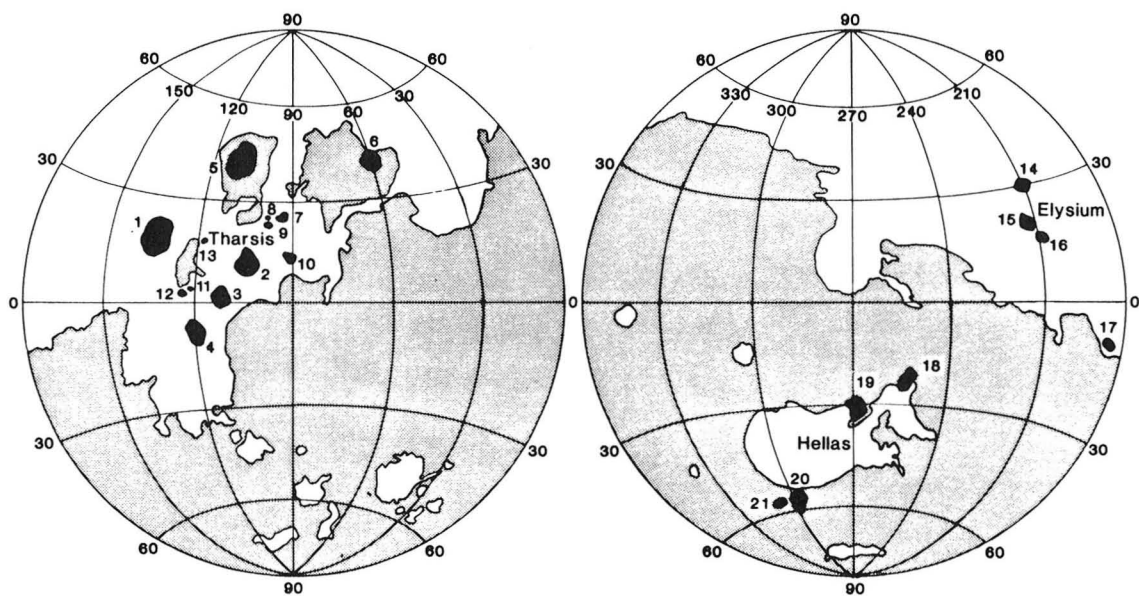


Figure 2.3. Martian volcanoes on a Lambert equal-area projection (after Mutch and Head, 1975). Volcanoes are shown in black and numbered according to Table 2.1. Moderately and densely cratered terrains concentrated in the southern hemisphere are shaded, volcanic and undivided plains in the northern hemisphere are not shaded, and polar units are not shown (geology from Carr *et al.*, 1973).

Table 2.1. Martian volcanoes.

	<u>Tharsis</u>	Lat	Long
1	Olympus Mons	28°N	133°W
2	Ascraeus Mons	11°N	104°W
3	Pavonis Mons	0°N	113°W
4	Arsia Mons	9°S	120°W
5	Alba Patera	40°N	110°W
6	Tempe Fossae	40°N	75°W
7	Uranus Patera	26°N	93°W
8	Uranus Tholus	26°N	98°W
9	Ceraunius Tholus	24°N	97°W
10	Tharsis Tholus	13°N	91°W
11	Ulysses Patera	3°N	122°W
12	Biblis Patera	2°N	124°W
13	Jovis Tholus	18°N	117°W
	<u>Elysium</u>		
14	Hecates Tholus	32°N	210°W
15	Elysium Mons	25°N	214°W
16	Albor Tholus	19°N	210°W
17	Apollinaris Patera	8°S	186°W
	<u>Hellas</u>		
18	Tyrhena Patera	22°S	253°W
19	Hadriaca Patera	30°S	266°W
20	Amphitrities Patera	59°S	299°W
21	Australis Patera	57°S	323°W

Numbers correspond to locations in Figure 2.3. Tempe Fossae includes several caldera-like features (Carr, 1973; Scott, 1982).

the crest of a 4000 km diameter bulge (the Tharsis Rise) elevated as much as 10 km above the surrounding surface (Carr, 1981, p.16). The Tharsis Rise corresponds to a large positive gravity anomaly ( $\geq 500$  mgals; Sjogren et al., 1975) indicative of a lack of complete isostatic compensation of the topography (Phillips and Saunders, 1975). Structural trends surrounding the Tharsis Rise, in conjunction with the gravity measurements, have been used to model the development of the Tharsis Rise either through isostasy and lithospheric loading (see Banerdt et al., 1982) or through volcanic construction (see Solomon and Head, 1982).

Tectonic features on Mars, including both fractures and ridges, are primarily concentrated around the Tharsis Rise. Valles Marineris, an equatorial system of canyons 4000 km long and up to 700 km wide (Fig. 2.2), is located on the eastern side of the Tharsis Rise and tectonic control appears to be the fundamental influence on the canyon form (Blasius et al., 1977). Several episodes of faulting are found in the vicinity of Tharsis, consistent with a NNE progression of the center of faulting (Plescia and Saunders, 1982).

Two Viking landers provide close-up views of the martian surface. Lander 1 (VL1) is located on volcanic plains in Chryse Planitia (Binder et al., 1977; Greeley et al., 1977 and Fig. 2.2) and Lander 2



(VL2) is located in Utopia Planitia on undulating terrain near Mie crater (Mutch et al., 1977). Both landing sites have cm- to m-sized blocks strewn across the surface. Within the few meters closest to the landers rocks > 3.5 cm cover 8% and 14% of the surface at VL1 and VL2, respectively (Moore et al., 1979). Rock abundances and types vary throughout both landing sites (Sharp and Malin, 1984). X-ray fluorescence spectrometry indicates that the soils at both landing sites are remarkably similar (Table 2.2). A mafic or ultramafic source is inferred for the soil components (Clark et al., 1982). No rock fragments were directly sampled; all pebbles broke apart during sieving and were interpreted to be indurated soil fragments (Clark et al., 1982). Both landing sites have aeolian features including drifts of particulate materials, drift tails by rocks, and possible ventifacts (Sagan et al., 1977). Lander cameras cannot resolve features smaller than 1 mm (Patterson et al., 1977), precluding photography of individual sand-sized particles; however, features at both landing sites have been interpreted to indicate the presence of sand (Sharp and Malin, 1984).

#### Regional Setting

Ascraeus Mons (centered at 11.3°N, 104.4°W) is the northernmost of three aligned volcanoes which comprise

Table 2.2. X-ray fluorescence chemical analyses.

	VL1 Chryse (%)	VL2 Utopia (%)
SiO <sub>2</sub>	44	43
Al <sub>2</sub> O <sub>3</sub>	7.3	7
Fe <sub>2</sub> O <sub>3</sub>	17.5	17.3
MgO	6	6
CaO	5.7	5.7
K <sub>2</sub> O	<0.5	<0.5
TiO <sub>2</sub>	0.62	0.62
SO <sub>3</sub>	6.7	7.9
Cl	0.8	0.4

After Clark et al. (1982, Table 3).

the Tharsis Montes (Fig. 2.4). Arsia Mons, Pavonis Mons, and Ascraeus Mons are each 350 to 400 km in diameter and spaced approximately 750 km apart. The Tharsis Montes are located near the crest of the Tharsis Rise, so that even their lower flanks are at elevations above much of the martian surface. Olympus Mons, 1700 km west of Ascraeus Mons, is nearly twice the diameter of any of the Tharsis Montes. Flank slopes are commonly 4° on all four volcanoes; total relief is 20 to 23 km for Olympus Mons (Blasius and Cutts, 1981) and generally 15 km for the Tharsis Montes, respectively (U.S.G.S., 1981a,b). These volcanoes are the tallest examples of centralized volcanic eruptions on Mars.

Volcanic plains surround the Tharsis Montes (Carr et al., 1973; Scott and Carr, 1978). The plains bury portions of both the Tharsis Montes and the smaller volcanoes located on the slopes of the Tharsis Rise (Fig. 2.3), perhaps to depths approaching 4 km (Whitford-Stark, 1982). Ceraunius Fossae, an area of widespread N-S faulting north of Ascraeus Mons, is embayed by the Tharsis plains; the Ceraunius Fossae materials are the oldest terrain exposed in the vicinity of Ascraeus Mons (Scott et al., 1981a).

Structural features near Ascraeus Mons are primarily related to tectonic events associated with the Tharsis Rise. Noctis Labyrinthus, a complex system of fault-

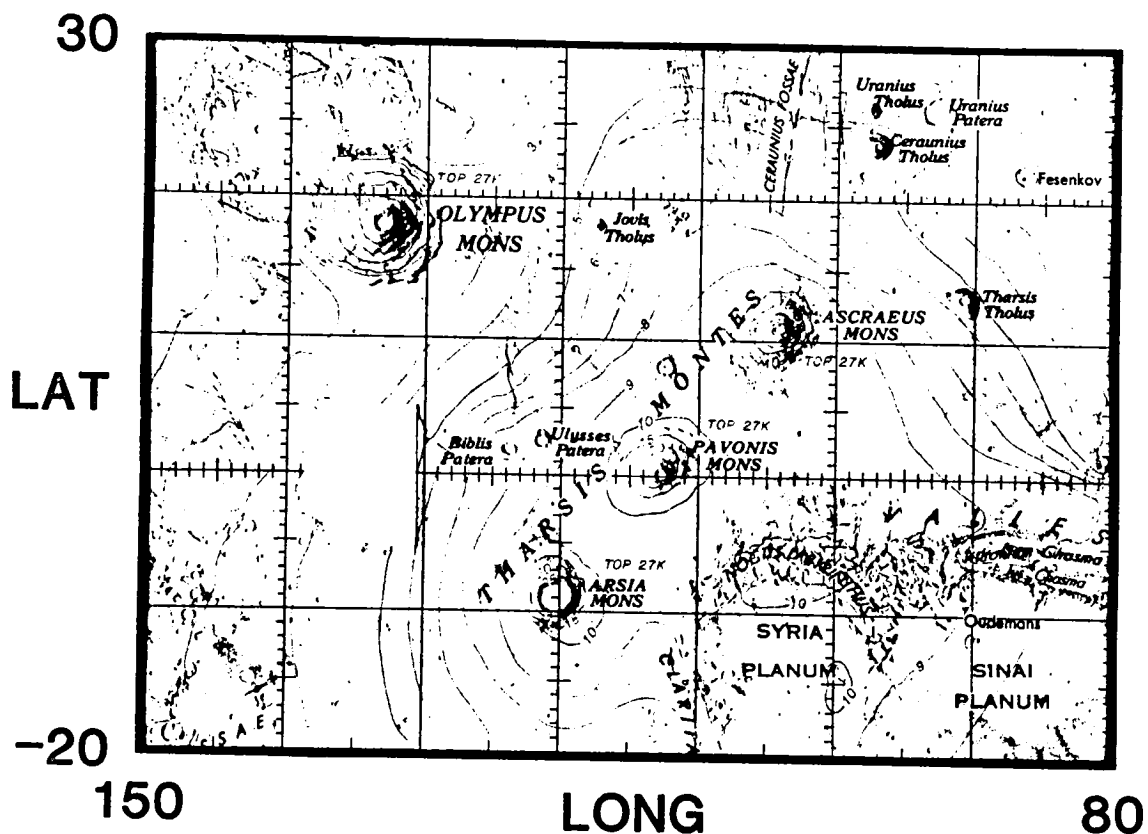


Figure 2.4. Shaded relief and topographic map of the Tharsis region of Mars. Contours indicate elevation as km above 6.1 mbar level. Area the size of Arizona is shown for scale. Mercator projection produces an apparent enlargement of features with increasing north or south latitude, relative to equatorial locations. Enlargement is a factor of 1.18 at 30° latitude.

controlled canyons, is located 1000 km south of Ascraeus Mons on the southeastern side of the Tharsis Rise and merges into the Valles Marineris canyons to the east. Grabens in both the Ceraunius Fossae and Claritas Fossae areas are radial to Syria Planum while the most recent faulting in the Tharsis area is centered on Pavonis Mons (Plescia and Saunders, 1982 and Fig. 2.4). Grabens northeast of Ascraeus Mons are part of the Pavonis Mons tectonic period.

#### Photogeology

Photographs of martian volcanoes from Mariner 9 and the Viking orbiters provide a basis for describing their geologic history. Volcanic landforms on Mars are very diverse in both scale and morphology; Greeley and Spudis (1981) provide a complete review of martian volcanism. Ascraeus Mons is quite similar to three other large volcanic mountains (Mons) in the Tharsis region. The morphology of the four volcanoes is described first, followed by a comparison with other martian volcanoes.

Morphology. On earth, eruption of fluid lava from a central vent produces a broad convex volcanic edifice called a shield volcano due to its resemblance to the rounded shields of early germanic warriors (Macdonald, 1972, p. 271). The Tharsis Montes and Olympus Mons are similar in general shape and appearance, but not in scale,

to terrestrial shield volcanoes (McCauley et al., 1972; Carr, 1973). The martian volcanoes are much larger than Mauna Loa in Hawaii, the largest shield volcano on Earth (Fig. 2.5). Ascraeus Mons is large enough to require a correction for the curvature of the martian surface in order to produce a realistic profile of the volcano (Fig. 2.5e). In spite of differences in scale, the Hawaiian shield volcanoes represent the most thoroughly studied terrestrial analogs for the martian shield volcanoes (Greeley, 1973, 1974; Carr and Greeley, 1980).

All four Tharsis shield volcanoes have surface features associated with lava effusion. A radial surface texture results from numerous flow lobes and leveed channels (Masursky et al., 1972; Carr et al., 1977). Leveed channels and collapsed lava tubes on Olympus Mons were interpreted to indicate aa and pahoehoe lavas, probably of basaltic composition (Greeley, 1973). Olympus Mons is surrounded by a basal scarp up to 6 km high but many flows extend across the scarp from the shield to the surrounding plains (Carr et al., 1977). The visible flows on the shield typically are much broader than they are high (Moore et al., 1978) and display few surface features other than leveed channels. Relatively fluid, most likely basaltic, lavas produced the individual flows and probably the bulk of each edifice (Masursky et al., 1972).

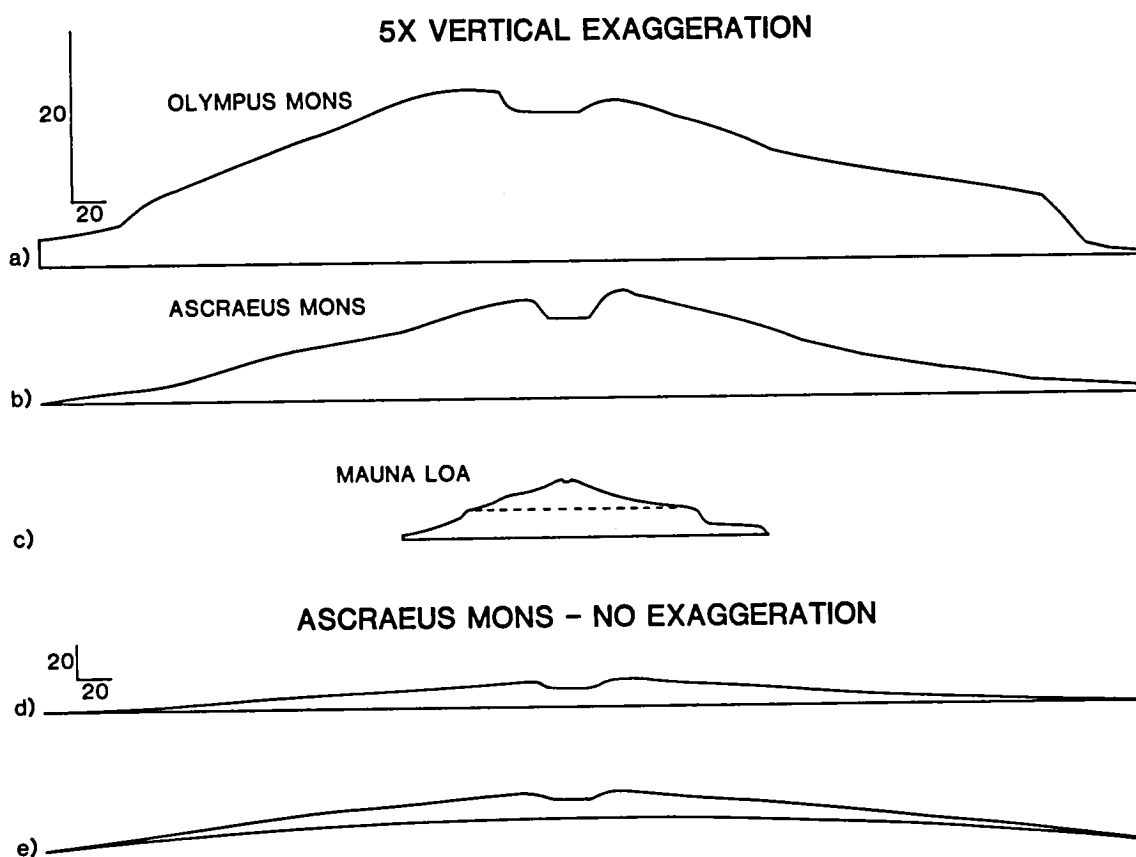


Figure 2.5. Topographic profiles of Olympus Mons, Ascræus Mons and Mauna Loa, Hawaii. Scale indicates 20 km. a) Olympus Mons along  $133.5^{\circ}\text{W}$  (U.S.G.S., 1981c). 5X vertical exaggeration. b) Ascræus Mons along  $\text{N}22^{\circ}\text{E}$  through the summit caldera (U.S.G.S., 1981a). 5X vertical exaggeration. c) Mauna Loa, Hawaii, from the summit caldera along  $\text{S}25^{\circ}\text{W}$  for the southwest rift zone and along  $\text{N}65^{\circ}\text{E}$  for the northeast rift zone (U.S.G.S., 1971). 5X vertical exaggeration. Dashed line indicates sea level. d) Ascræus Mons, no vertical exaggeration. e) Ascræus Mons, no vertical exaggeration, with planetary curvature included.

Enormous calderas are present near the summits of the Tharsis volcanoes. Arsia Mons has a shallow summit depression 110 km in diameter bounded by arcuate faults (Carr, 1973). Pavonis Mons has a steep-walled summit depression 40 km in diameter within a more subtle depression approximately the same size as the caldera on Arsia Mons (Crumpler and Aubele, 1978). Ascraeus Mons and Olympus Mons each have multiple calderas with cross-cutting relationships produced by collapse at different locations (Mouginis-Mark, 1981). The caldera complex on Ascraeus Mons is approximately 55 km in diameter (Fig. 2.6) while Olympus Mons has an elongate 80 by 50 km caldera. Each steep-walled caldera depression was partially refilled by plains-forming materials, although some floor areas were subsequently faulted and broken up by an adjacent collapse.

The shield flanks generally have prominent concentric features but there are variations among the volcanoes. Arcuate, concentric fractures and lines of pits are common on all three of the Tharsis Montes but these features are rare on Olympus Mons (Carr et al., 1977). Ascraeus Mons and Olympus Mons both have arcuate, convex-upward terraces 20 to 50 km across on their flanks but terraces are very subdued or absent on the other two shields (Carr, 1973; Carr et al., 1977). Flank terraces may represent the buildup of lava downslope of arcuate rift zones or escarpments resulting from outward slumping of the flanks (Carr et al., 1977).



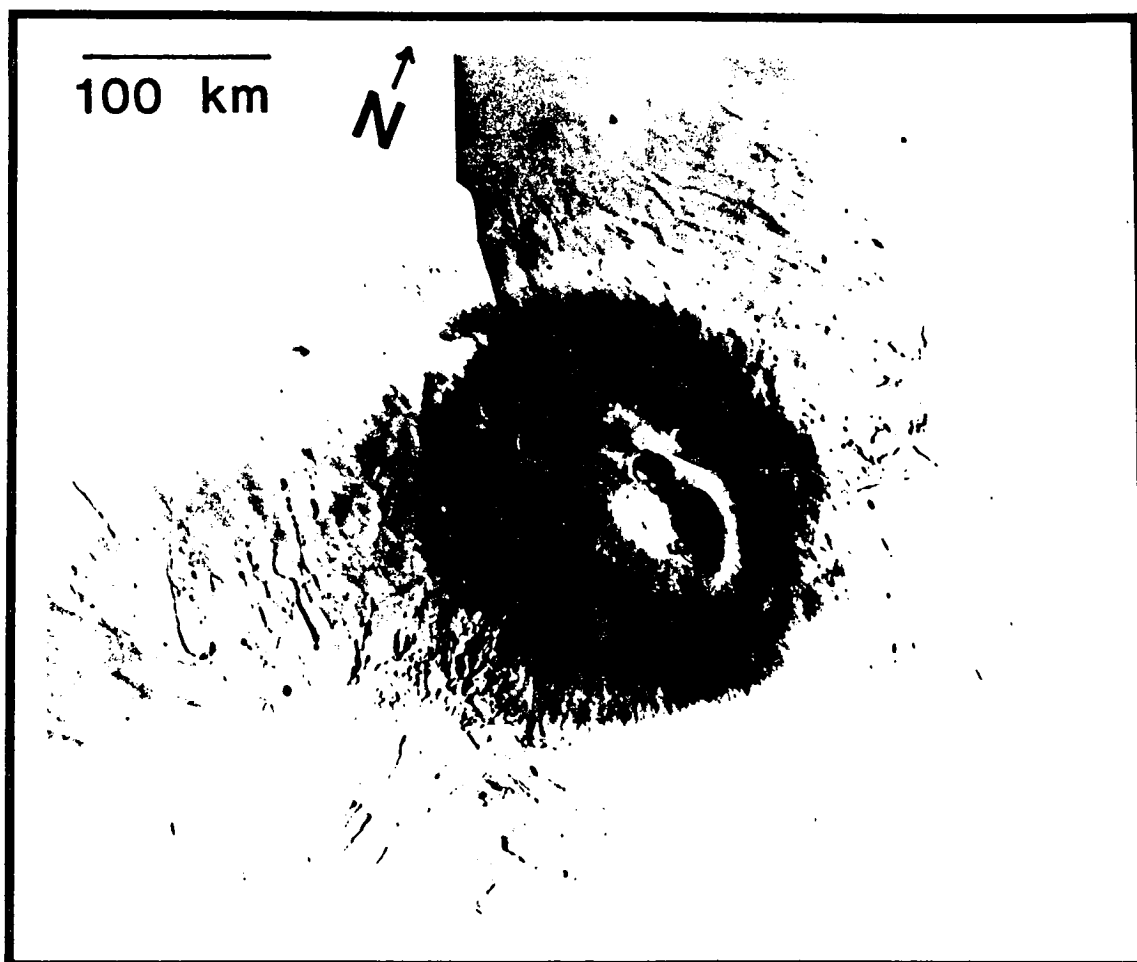


Figure 2.6. Oblique view of Ascræus Mons. Viking Orbiter photographs 643A75,77-78. Note the low albedo "collar" surrounding the summit area and the clouds over the northwest flank.

The Tharsis Montes all have prominent embayments or alcoves in their northeast and southwest flanks. The embayments are aligned with the N40°E trend of the Tharsis Montes and may be related to structural trends of the region (Crumpler and Aubele, 1978). Each embayment appears to have been the source of considerable lava, forming fan-shaped arrays of flows (Crumpler and Aubele, 1978). The flows southwest of Arsia Mons are particularly striking, extending up to 800 km from the shield (Carr et al., 1977). The embayments on Ascraeus Mons extend approximately one-third of the distance up the flank (Fig. 2.6) while the embayments on Arsia Mons breach the summit caldera. A line of low mounds on the caldera floor of Arsia Mons connects the flank embayments (Carr et al., 1977). Olympus Mons lacks any evidence of flank embayments.

The Tharsis shield volcanoes are quite distinct from other martian volcanoes. Alba Patera, 2000 km north of Ascraeus Mons, rivals Olympus Mons in areal extent but may be less than 6 km in height (Carr, 1976); this volcano appears to be a unique volcanic landform on Mars (Greeley and Spudis, 1981). Elysium Mons has steeper slopes (10°) than the Tharsis volcanoes, lacks the abundant flow features common on the shield flanks, and may represent a more chemically evolved magma than that of the shields (Malin, 1977). Patera and Tholi in both the

Tharsis and Elysium regions (Fig. 2.3 and Table 2.1) are smaller and steeper than the shield volcanoes, even allowing for burial by plains materials (Whitford-Stark, 1982). The volcanoes around the Hellas basin are greatly eroded and represent volcanism prior to the Tharsis volcanic activity (Greeley and Spudis, 1978, 1981). Numerous km-scale features on both the volcanic plains of the northern hemisphere (Frey et al., 1979; Plescia, 1981; Frey and Jarosewich, 1982) and the densely cratered terrain of the southern hemisphere (Scott, 1982) may be volcanic in origin but these small constructs contrast greatly with the enormous shield volcanoes.

Summary: Ascraeus Mons is similar to the other shield volcanoes in the Tharsis region. Differences in summit caldera size and complexity and in flank morphology make each shield unique. All four shield volcanoes are quite distinct from other martian volcanoes.

Geologic history. Without samples from Mars, the chronology of geologic events must be interpreted from terrain contact relationships and the impact cratering record of the martian surface. Crater counts on volcanic surfaces are complicated by the presence of endogenic craters (Greeley and Gault, 1971, 1979; Malin, 1977), however, exclusion of probable endogenic craters allows relative ages to be obtained for the volcanoes (Blasius, 1976; Plescia and Saunders, 1979; and Table 2.3). Crater

abundances can vary considerably on any one volcano (Neukum and Hiller, 1981) but this may be influenced by the location on the volcano of the areas counted, as discussed in Chapter 3. Absolute ages remain uncertain due to the lack of radiometric calibration for the proposed martian cratering fluxes (Neukum and Wise, 1977; Soderblom, 1977). However, in all models Tharsis is consistently the youngest region on Mars.

Differences in the structural features on the Tharsis Montes are interpreted to indicate different stages of shield development. The structural history of Arsia Mons suggests the following sequence of events (Crumpler and Aubele, 1978): 1) shield volcano construction from a central vent, 2) volcano-tectonic subsidence of the summit, possibly during the outbreak of parasitic eruptions on the northeast and southwest flanks, and 3) continued volcanism along a fissure or rift bisecting the main shield. Crumpler and Aubele indicate that the other Tharsis Montes follow the same sequence, with Pavonis Mons reaching the second phase and Ascraeus Mons the first phase; this is consistent with the sequence of ages in Table 2.3.

Olympus Mons and its environs has received most of the attention in photogeologic analyses of the Tharsis shield volcanoes. The scarp surrounding Olympus Mons led to speculations that the distal materials were nonwelded ash that easily eroded away (King and Riehle, 1974), the scarp

Table 2.3. Ages of martian shield volcanoes.  
(in millions of years)

	Neukum/Wise	Soderblom
Olympus Mons	120 $\pm$ 48	25 $\pm$ 10
Ascraeus Mons	480 $\pm$ 271	100 $\pm$ 58
Pavonis Mons	1530 $\pm$ 372	325 $\pm$ 79
Arsia Mons	3400 $\pm$ 590	730 $\pm$ 126
All others	3500 to 3700	925 to 3000

After Plescia and Saunders (1979, Table 3). Chronologies are from Neukum and Wise (1977) and Soderblom (1977).

was produced by vertical faulting through erosion of the pre-volcano substrate (Head et al., 1976), and a subglacial origin for the entire mountain (Hodges and Moore, 1979). The aureole deposits northwest of the volcano have been interpreted as lava flows (McCauley et al., 1972), the erosional remnants of an ancient volcano (Carr, 1973), landslide deposits from Olympus Mons (Lopes et al., 1980, 1982; Hiller et al., 1982), pyroclastic flows (Morris, 1982), and ice-lubricated gravity slides (Tanaka, 1984a,b). Olympus Mons volcanism is considered the source or triggering mechanism for aureole or scarp production in most of these analyses. Detailed geologic mapping of the Olympus Mons shield is currently in progress (K. Tanaka, personal communication, 1984).

Previous photogeologic mapping of Ascraeus Mons has occurred as part of regional or global analyses and is generally quite simplified. The first global (Carr et al., 1973) and regional (Carr, 1975) geologic maps including Ascraeus Mons only distinguished between the shield and the plains surrounding it. Subsequent maps based on Viking photographs distinguished volcanic plains originating at the southwestern flank embayment from the undivided Tharsis plains (Scott and Tanaka, 1981; Scott et al., 1981a,b). An arcuate-shaped unit with an irregular, knobby surface is located west of the Ascraeus

Mons shield; this terrain was interpreted both as mountainous terrain older than either Ascraeus Mons or the Tharsis plains (Carr, 1975) and as landslide and debris flow material younger than all other units in the Tharsis area (Scott et al., 1981b). The photogeologic analysis presented in Chapter 3 addresses this stratigraphic discrepancy as well as terrain variations on the shield surface.

Summary: Structural variations and impact crater densities on the shields suggest that the volcanoes generally increase in age from Arsia Mons to Pavonis Mons to Ascraeus Mons to Olympus Mons, although each volcano could include surfaces of different ages. Published geologic maps of Ascraeus Mons appear very simplified and are inconsistent at some locations.

### Surface Properties

Remote sensing techniques can be used to obtain information about the martian surface materials at the  $\mu\text{m}$  to m scale. Reflectance spectroscopy involves the examination of light reflected from the surface in order to evaluate compositional variations. Thermal infrared measurements provide information about the surface particle sizes or the compaction and induration of soil materials. Radar returns from Mars provide the surface elevation and the relative abundance of cm to m-scale features that

scatter the radar signal. These properties apply to features below the spatial resolution limit of orbital photographs and should complement the interpretations obtained from photogeologic analyses.

Telescopic reflectance spectroscopy has precise spectral resolution but the spatial resolution is greatly inferior to that available from spacecraft photographs. The spectral differences between the classical low and high albedo regions of Mars are consistent across the planet and indicate a variable abundance of oxidized iron (Singer et al., 1979; Singer, 1982) but it is not possible to relate these measurements directly to geologic features. During the V02 approach to Mars, global 3-filter color photographs were obtained with a spatial resolution of 30 km per line pair; the Tharsis shield volcanoes have a lower albedo than the rest of the Tharsis region and red/violet albedo ratios comparable to areas of densely cratered terrain (Soderblom et al., 1978). V02 spacecraft photographs, Earth-based spectra, and laboratory spectra have been combined to make compositional inferences for martian surface features (McCord et al., 1982). The Tharsis region was not included in the area examined by these investigators. In Chapter 4 the reflectance properties of Ascræus Mons are determined from a color photograph with a spatial resolution 15 times better than that of the V02 approach data.



Temperature measurements can be associated with the physical properties of surface materials through thermal inertia. Thermal inertia is defined as:

$$I = (\kappa \rho c)^{1/2} \quad (\text{Eq. 2.1})$$

where  $\kappa$  is thermal conductivity,  $\rho$  is density, and  $c$  is specific heat. Thermal inertia is related to the heat flux through the surface materials when the conduction equation is solved with a surface boundary condition that specifies heat sources and sinks (e.g. insolation, radiation from the surface, and conduction) throughout the day (Wesselink, 1948). For most geological materials density and specific heat vary much less than thermal conductivity, which ranges over several orders of magnitude (Kieffer et al., 1977). Laboratory measurements of the thermal conductivity of granulated materials (Wechsler and Glaser, 1965) allow thermal inertia (holding  $\rho c$  constant) to be interpreted as an "effective" particle diameter for an ideal surface composed entirely of the specified particle size (Kieffer et al., 1973 and Fig. 2.7). Natural surfaces have a wide range of particle sizes, so the effective particle diameter should only be considered as an averaged expression for all of the materials within the field of view of the instrument.

Temperatures have been obtained for most of the surface of Mars from the Infrared Thermal Mapper (IRTM). The IRTM measured the radiant flux from the planet in 28

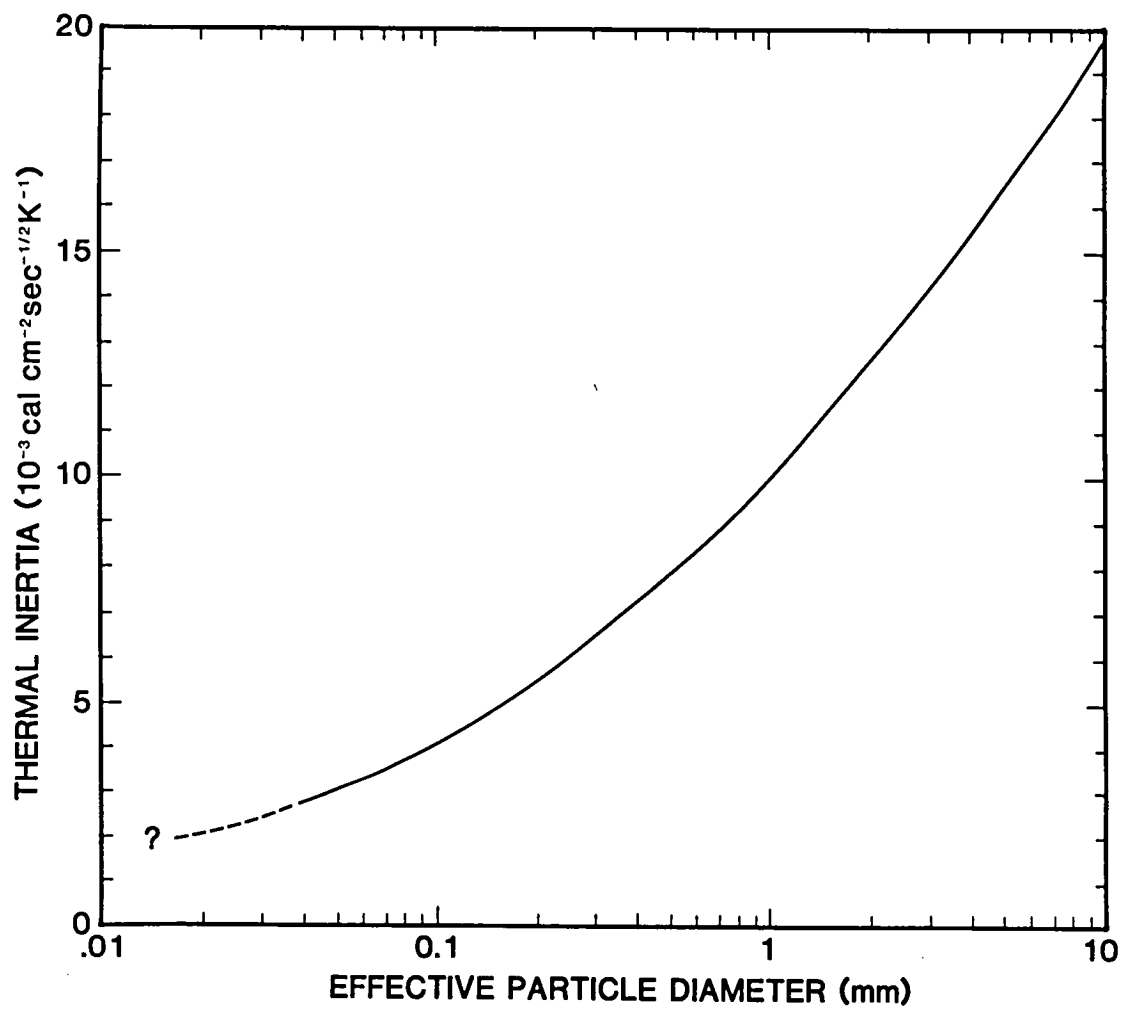


Figure 2.7. Thermal inertia as a function of particle size. Values correspond to a uniform surface composed of a single particle size, assuming  $\rho c = 0.3$  (after Kieffer et al., 1973, fig. 14).

detectors, including five thermal bands centered approximately at 7, 9, 11, 15, and 20  $\mu\text{m}$  and one albedo band that encompassed the visible portion of the spectrum (0.3 to 3.0  $\mu\text{m}$ ) (Chase et al., 1978; Kieffer et al., 1977). Calibration of the measured radiances provides brightness temperatures for each of the thermal bands, with an assumed surface emissivity of one. Albedos, pre-dawn temperatures, and thermal inertias have been mapped throughout the equatorial latitudes of Mars (Kieffer et al., 1977; Zimbelman and Kieffer, 1979; Palluconi and Kieffer, 1981; Pleskot and Miner, 1981). Differences between temperatures measured in the different thermal bands of the IRTM can be used to evaluate the relative abundances of particulate "fines" (generally < 1 mm) and high thermal inertia materials (Christensen, 1982). These high thermal inertia elements can include "blocks" (assumed to be > 10 cm) and bedrock (Christensen, 1982), and indurated fines (Ditteon, 1982). Surface emissivity variations can also be identified through the spectral dependence of surface temperatures (Christensen, 1982). Global maps of "block" abundance and emissivity are in preparation (Christensen, 1984a,c).

The Tharsis volcanoes have the lowest pre-dawn temperatures in the equatorial latitudes, implying the presence of very low thermal inertia materials (Kieffer et al., 1976, 1977; Zimbelman and Kieffer, 1979).

This led to the speculation that the Tharsis volcanoes are covered with extremely vesiculated materials ("reticulite") (Kieffer et al., 1976, 1977). Geologic problems are best addressed by using the highest spatial resolution IRTM data, which can separate thermal properties for individual terrain units (Zimbelman and Greeley, 1981, 1982). High resolution IRTM data for Ascraeus Mons are examined in Chapter 4 to evaluate their geologic implications for the volcano.

Earth-based radar provides information on the topography, dielectric properties, and surface "roughness" that tends to scatter the radar signal. Radar data from 1971 and 1973 are confined to 14° to 22°S but are available at all longitudes (Downs et al., 1973, 1975). These topographic data confirm the presence of a "parasitic" volcano 250 km S30°W of Arsia Mons aligned with the Tharsis Montes (Roth et al., 1980). Radar signal strength and shape (in Doppler-shifted frequencies) indicate that the entire Tharsis region is very rough on a scale of 0.1 to 100 m; this is attributed to the numerous flows visible throughout the region (Simpson et al., 1978a,b; Downs et al., 1982). Combination of radar and thermal data with Viking photographs suggests that the radar rough flows south and west of Arsia Mons have a recent aeolian mantle burying craters < 50 m in diameter (Schaber, 1980).

No radar signals have been reflected back to Earth from the Ascraeus Mons shield; this has been attributed to extreme roughness at the scale of the radar wavelength (12 cm, Downs et al., 1982). Depolarized (scattered) radar signals are very strong from the Tharsis region and the shield volcanoes may be areas of enhanced radar scattering (Harmon et al., 1982). These radar results are discussed in Chapter 4 in relation to other remote sensing and photogeology results for Ascraeus Mons.

Summary: Ascraeus Mons and the other Tharsis shield volcanoes are distinctly different from the surrounding Tharsis plains at visual to radar wavelengths. Prior analyses have not used data of sufficient resolution to relate the observed properties to geologic features on the volcano. This work represents the first use of both high resolution photographs and high resolution remote sensing data for Ascraeus Mons, providing a geologic context for the interpretation of the results.

#### Surface-Atmosphere Interactions

The atmosphere of Mars is very tenuous in comparison to the atmosphere of the Earth. However, it is substantial enough to affect both the modificational history and the remotely observed properties of the surface. Martian winds redistribute sediments across the surface of the volcanoes. Clouds comprised of volatiles and/or particulates are

common in the Tharsis region and they can influence both optical and infrared measurements of the surface. Atmospheric water vapor abundance is spatially and temporally variable across Mars and may reflect volatile transport to and from Tharsis. These topics are briefly evaluated here for their potential contribution to the investigation of Ascraeus Mons.

Aeolian features are present on all of the Tharsis shield volcanoes. The Tharsis Montes showed the only persistent aeolian activity documented during the Viking primary mission (Veeverka et al., 1977) and this activity persisted throughout a martian year (Lee et al., 1982; Lee, 1984). Each shield volcano has a dark albedo collar consisting of coalesced dark streaks that surrounds the summit area, typically located at altitudes between 10 and 20 km (Lee et al., 1982 and Fig. 2.6). Slope winds are predicted to develop over the flanks of the volcanoes (Sagan et al., 1974; Magalhaes and Gierasch, 1982) and the dark collar boundaries indicate a downslope wind flow (Sagan et al., 1974; Veeverka et al., 1977; Lee, 1984). The albedo patterns are interpreted to indicate downslope removal of a thin layer of bright dust from a darker substrate (Lee et al., 1982). These observations indicate that aeolian redistribution of sediments is presently occurring on Ascraeus Mons.

Clouds are often observed near the Tharsis volcanoes. Blue-white clouds develop daily in the Tharsis region, mainly during northern spring and summer (Slipher, 1962, p.36). Clouds regularly occur over the northwest slopes of the shield volcanoes during this season (Briggs et al., 1977). Infrared spectra of blue-white clouds in the Tharsis region indicate a water-ice composition (Curran et al., 1973). These clouds are probably orographic in origin (Leovy et al., 1973). Dust clouds can also occur in the Tharsis region, commonly as part of global dust storms (Briggs et al., 1979). Both dust and water-ice clouds influence the surface temperatures but spectral differences between IRTM thermal bands can be used to identify the presence of clouds (Martin et al., 1979; Hunt, 1979; Christensen and Zurek, 1984). Photographic and thermal data of Ascraeus Mons were selected to minimize the potential interference of surface measurements by either dust or water-ice clouds.

The MAWD instrument on the Viking orbiters provided the first opportunity to monitor the seasonal and spatial variations of atmospheric water vapor (Farmer et al., 1977). The atmosphere of Mars generally is saturated with water vapor on a daily basis, concentrated in the lowest several km of the atmosphere (Davies, 1979). The Tharsis volcanoes were observed to have very little water vapor over their summits during northern spring and

summer (Farmer et al., 1977), possibly because the vapor had condensed to form the visible clouds. There is an annual net transport of water vapor from the southern to the northern hemisphere during the period of Viking observations (Farmer and Doms, 1979; Jakosky, 1983a,b). Migration of absorbed water through the martian soil has been proposed as a possible mechanism for generating a high thermal inertia duricrust layer (Ditteon, 1982) and the increased abundance of water vapor at lower elevations on the volcanoes could potentially affect the surface properties there.

Summary: The atmosphere of Mars plays an important role in both the geologic history of the surface and the remotely determined surface properties. Aeolian activity is observed on the flanks of the Tharsis volcanoes, involving sediment transport on the surface. Remote sensing measurements of Ascraeus Mons have been selected to minimize the presence of clouds over the volcano. Atmospheric water vapor abundance varies across the volcanoes and this may influence surface properties.

#### Martian Eruption Characteristics

The eruptive processes associated with the growth and modification of volcanic surfaces are closely related to the geologic history of these surfaces. Explosive and effusive eruptions produce a great variety of surface



textures and morphologies on terrestrial volcanoes (Williams and McBirney, 1979, pp.101-114, 127-138) but most of these characteristics cannot be distinguished by remote sensing techniques. This section discusses a few eruptive characteristics that may have produced observable features on Ascræus Mons.

Explosive volcanism could produce distinctive deposits and surface features on martian volcanoes. Explosive eruption processes on Earth have been modeled extensively and some of these models can be applied to other planets. Extensive fragmentation of erupting magma is predicted to occur on Mars, producing plinian-style ash clouds and fallout (Wilson and Head, 1981; Mouginis-Mark et al., 1982b). An ash cloud deposit is interpreted to be present at the summit of Hecates Tholus based upon a reduced crater density within an elliptically shaped area (Mouginis-Mark et al., 1982). Hecates Tholus is morphologically very different from Ascræus Mons, so eruption styles for these volcanoes may also be different, however, ash deposits are considered in interpreting the results for Ascræus Mons. If cinder cones like those on Mt. Etna in Italy were present on Mars, they should have < 10 m of topographic relief (McGetchen et al., 1974). This would make cinder cone identification difficult from photographs alone but the cinders potentially may produce observable differences in other

data types, such as visual and radar reflectance and thermal inertias.

Effusive eruptions have played a major role in the development of the Tharsis shield volcanoes. Lava flow morphology can be related to the rheologic properties of the lava by considering the flow as a Bingham material with a finite yield strength (Hulme, 1974). Several geometric parameters, measurable from photographs, have been theoretically related to the flow yield strength  $Y$  (Moore et al., 1978):

$$Y = \rho g H \sin \theta \quad (\text{Eq. 2.2})$$

$$Y = \rho g H^2 / W \quad (\text{Eq. 2.3})$$

$$Y = 2 w \rho g \sin^2 \theta \quad (\text{Eq. 2.4})$$

where  $\sin \theta$  is the topographic gradient,  $H$  is the flow thickness,  $W$  is the flow width, and  $w$  is the horizontal width of the levees for a channelized flow. These equations were derived by modelling the lava flow with ideal material properties and very simplified emplacement processes. The assumptions of a Bingham rheology for the lava and of all flow morphology being the result of a finite yield strength require that great care must be used in inferring compositional information from these data. Application of Equations 2.2 to 2.4 to martian flows result in yield strengths of  $10^3$  to  $10^4 \text{ Nt m}^{-2}$  on Olympus Mons and Arsia Mons, generally consistent with the yield strengths of terrestrial basalts and andesites

(Hulme, 1976; Moore et al., 1978). In Chapter 3 lava flows on Ascraeus Mons are analyzed by this morphologic technique.

Summary: Detailed analysis of volcanic eruption processes is difficult to perform without extensive field and laboratory investigations. Remote sensing, however, can provide some broad constraints on the volcanic processes involved in the history of a volcanic edifice. Examination of the geologic history of Ascraeus Mons should provide additional evidence of the volcanic processes active on martian volcanoes.

#### Summary

Background. In 1971 Ascraeus Mons became the first clearly identified volcanic structure on Mars when its complex summit caldera became visible in Mariner 9 photographs. Ascraeus Mons is centered at 11.3°N, 104.4°W and is the northernmost of three aligned shield volcanoes comprising the Tharsis Montes. The three volcanoes are each 350 to 400 km in diameter with about 15 km of total relief, and they are spaced approximately 750 km apart. Olympus Mons, nearly twice the diameter of any of the Tharsis Montes, is 1700 km west of Ascraeus Mons. The Tharsis Montes are located near the crest of a crustal bulge (the Tharsis Rise) that influences the planet on a global scale. All four volcanoes have numerous lava flows

on their flanks, some with leveed channels. Each volcano has one or more calderas near its summit and the Tharsis Montes all have prominent embayments in their northeast and southwest flanks.

Previous work. Structural variations and impact crater densities on the shield surfaces suggest that the volcanoes generally increase in age from the southern end (Arsia Mons) to the northern end (Ascraeus Mons) of the Tharsis Montes but each volcano could include surfaces of different ages. Olympus Mons appears to be younger than any of the Tharsis Montes volcanoes. Published geologic maps of Ascraeus Mons distinguish the shield from the surrounding plains but terrain variations on the volcano surface have not been investigated in detail prior to this work. Surface properties for the Tharsis volcanoes are distinctive at visual to radar wavelengths but spatial resolution available prior to this work was not sufficient to relate the remote sensing measurements to geologic features on the volcano. Aeolian activity had been observed on the flanks of the Tharsis volcanoes, making transportation of surface sediments a likely contributor to the surface history of Ascraeus Mons. Remote sensing measurements could provide some constraints on the volcanic processes that have been active on Ascraeus Mons.

## CHAPTER 3. PHOTOGEOLOGY

### Introduction

Photogeologic analysis of the martian surface involves the interpretation of geologic features from spacecraft photographs. Viking photographs are used to delineate terrain units on and around Ascraeus Mons through morphologic and structural relationships. The terrain units identified through this procedure provide a basis for describing the geologic history of the volcano, and evaluating additional remote sensing data in a geological context. This chapter examines the geologic history of Ascraeus Mons; Chapter 4 relates the remote sensing properties of Ascraeus Mons to the history of the volcano.

Several geologic applications are available for the photographs of Ascraeus Mons. Moderate resolution photographs (where individual picture elements, or "pixels", correspond to scale lengths 30 or more meters across) give a regional view of Ascraeus Mons but do not always provide sufficient detail to interpret the surface history. High resolution photographs ( $\leq 30$  m per pixel) provide indications of the geologic processes responsible for the surface morphology; specific applications of these photographs include detailed morphologic terrain mapping, crater counts, and estimates of lava rheology from flow geometries. Appendix 1 provides

a complete description of the photographic data used in this chapter.

Stratigraphic relationships among the terrain units on Ascræus Mons are described first. The terrain units are discussed according to the five physiographic provinces identified during photogeologic mapping of Ascræus Mons. The cratering record on Ascræus Mons is complicated by the presence of both endogenic and exogenic (impact) craters; however, the physiographic provinces have distinctive cumulative distributions of craters. Structural features on the volcano are described in relation to the mapped terrains. Estimates of rheology are obtained for flows near the summit of Ascræus Mons from the flow dimensions visible in the high resolution photographs. The discussion section examines the implications of some distinctive surface features on the flanks of the volcano. The chapter concludes with a summary of the geologic history of Ascræus Mons.

### Stratigraphy

Stratigraphic relationships indicate the relative ordering of events in geologic terrains. The contact relationships between terrain units can be used to identify units that were superposed over other units. Surface morphology is related to the formation and modification of the geologic materials within each terrain unit;

morphologic features within a terrain unit aid in interpreting the history of that unit. These procedures provide the basis for identifying and interpreting the geologic history of Ascraeus Mons.

Two geologic terrain maps have been prepared for Ascraeus Mons. Moderate resolution photographs were used to create a regional map of features on and around Ascraeus Mons (Map 1 and Fig. 3.1). Published photomosaics (U.S.G.S., 1980a,b and Fig. 3.2) were used in compiling this map. A sequence of twenty four high resolution photographs crosses the Ascraeus Mons shield from the lower southwestern flanks to the summit caldera (Fig. 3.4); these photographs were used to produce a detailed map of terrain units on the volcano (Map 2). Both regional and local mapping were needed in order to evaluate the history of the terrains on Ascraeus Mons. Topography for Ascraeus Mons has been published in 1 km contour intervals with a relative uncertainty of about 200 m (U.S.G.S., 1981a,b and Fig. 3.3). Earth-based radar measurements indicate that these elevations are approximately 2.8 km too high (Downs et al., 1982); all elevations stated here include a 2.8 km reduction from the elevations in Fig. 3.3. Additional topographic discrepancies are included in the discussion of individual terrain units.

Five physiographic provinces are identified in the vicinity of Ascraeus Mons: 1) an arcuate region of

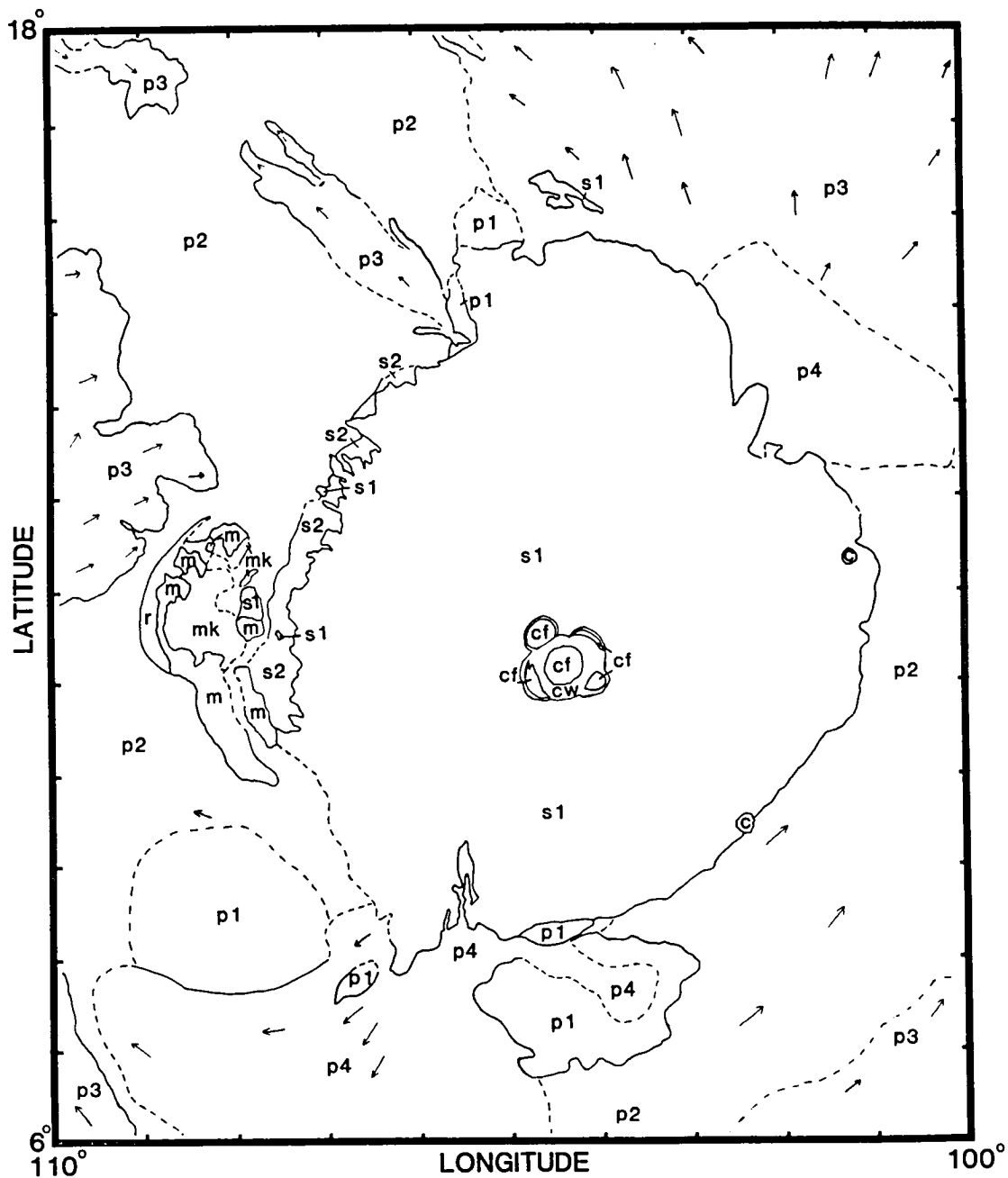


Figure 3.1. Regional geologic map of Ascræus Mons, from Map 1. Terrain units from Map 1 are shown for the area covered by Figs 3.2 and 3.3.



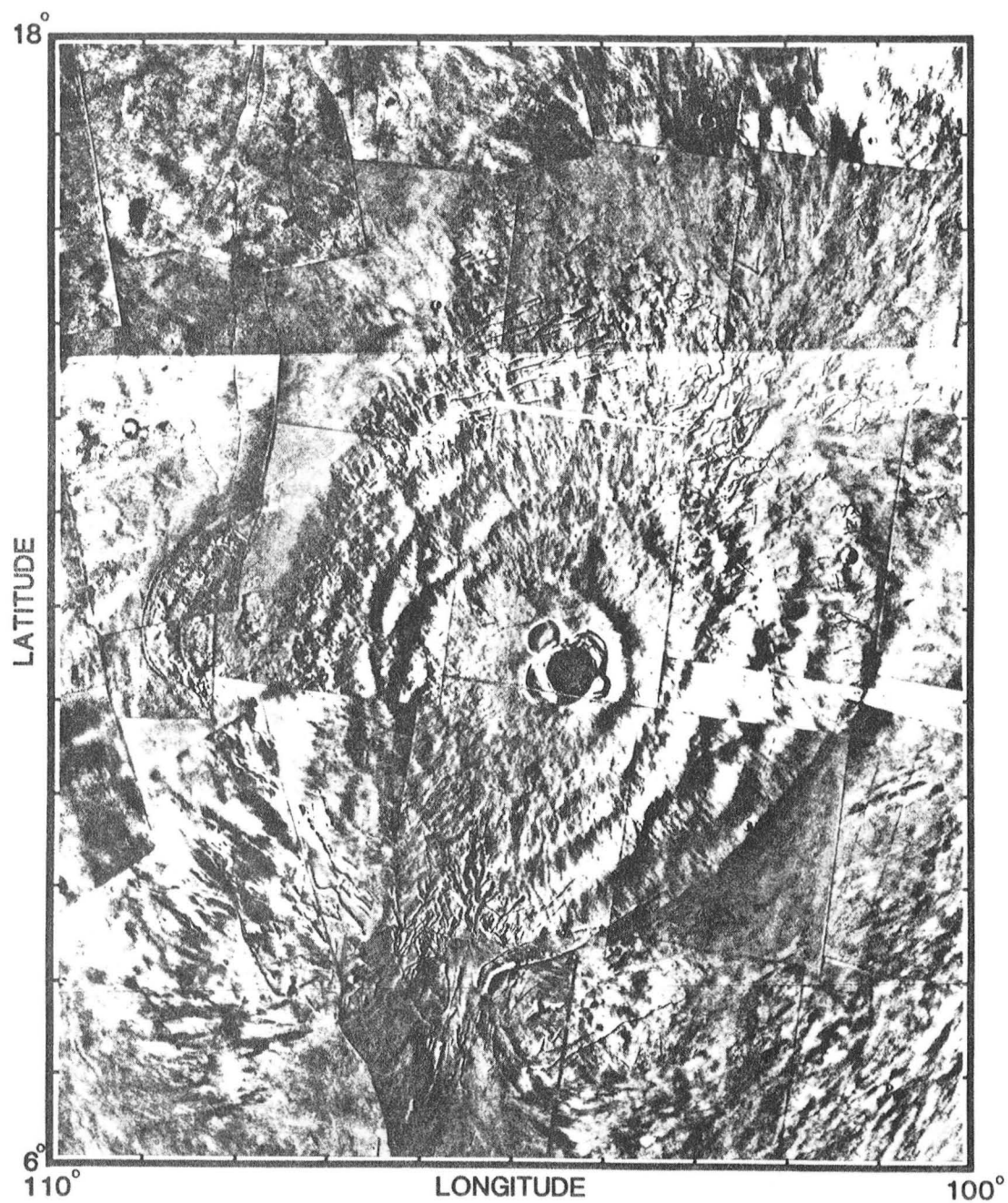


Figure 3.2. Photomosaic of Ascræus Mons and immediate surroundings (from U.S.G.S., 1980a,b).

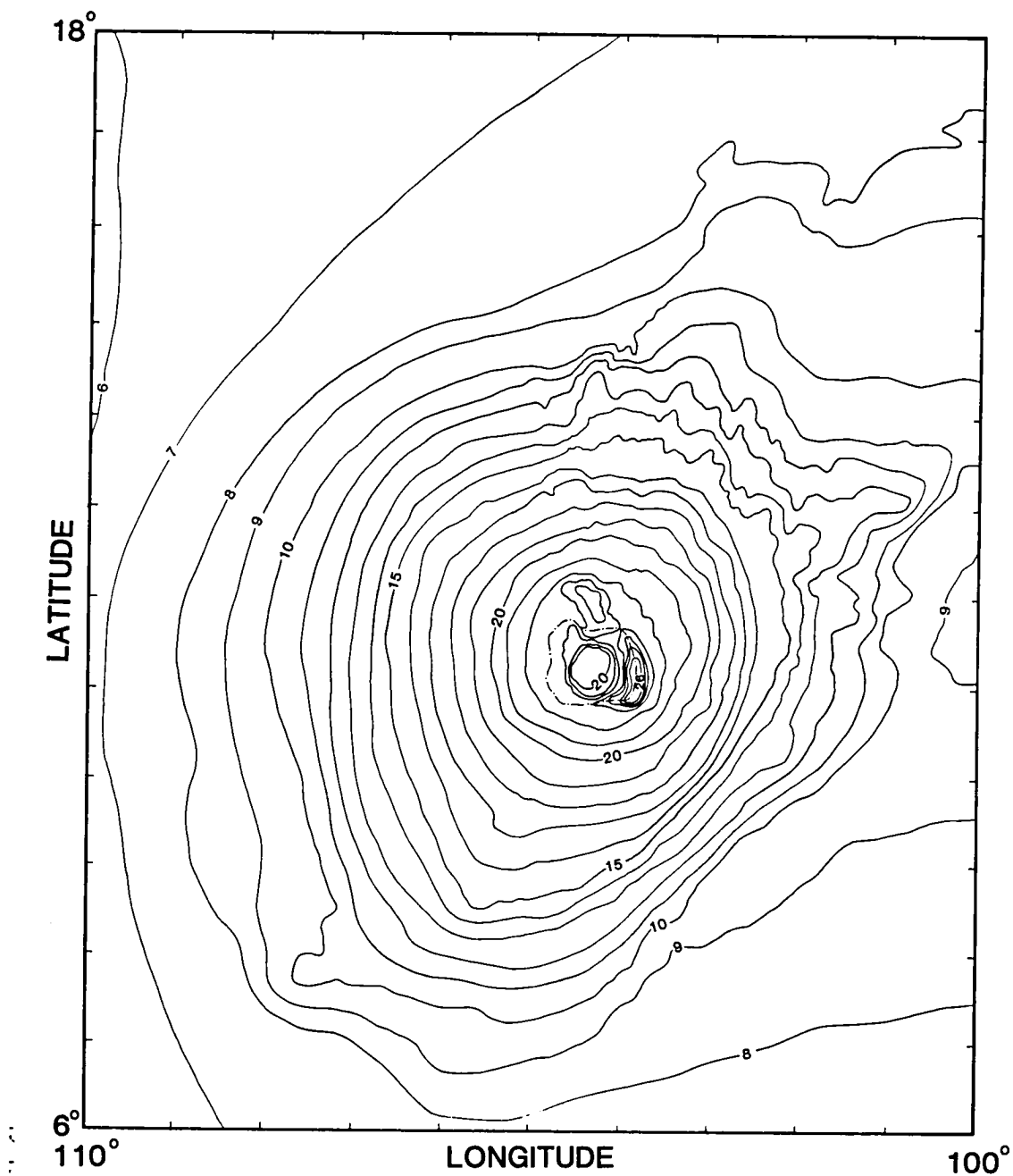


Figure 3.3. Topography of Ascræus Mons. Contours represent 1 km intervals above the 6.1 mbar Mars datum and were obtained from photogrammetric analysis of Viking Orbiter photographs (U.S.G.S., 1981a,b). Line with dots outlines the caldera complex. Recent Earth-based radar topography indicates these elevations should be reduced by an average of 2.8 km (Downs *et al.*, 1982).

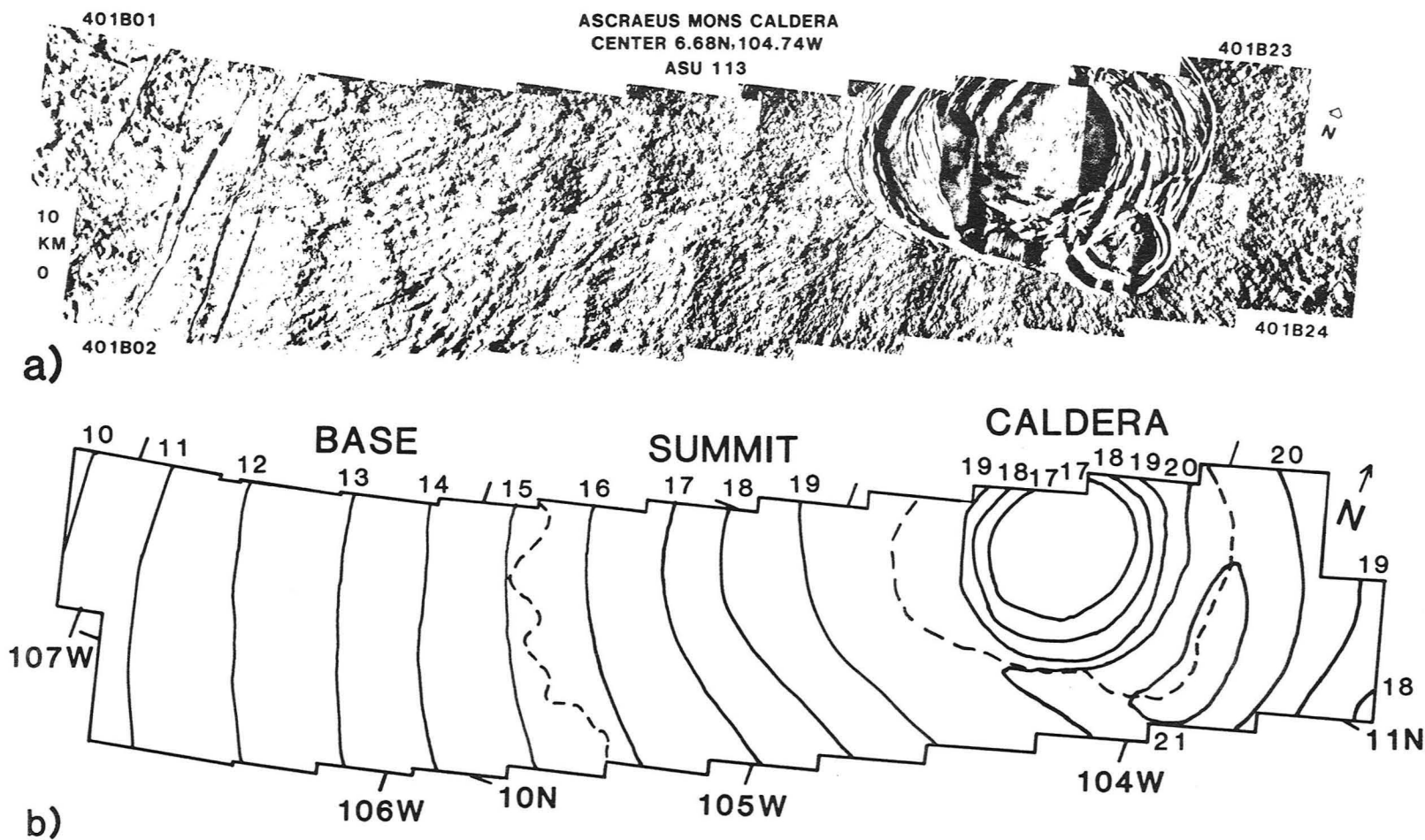


Figure 3.4. High resolution photographs of shield flank and caldera complex. a) Photomosaic of Viking Orbiter photographs 401B01-24, nongradient high pass filtered orthographic projection. b) Topography (1 km contours) corresponding to part a. Contours have been adjusted to agree with Earth-based radar.

mountainous terrain west of Ascræus Mons, 2) plains completely surrounding the volcano, 3) the flanks of Ascræus Mons below 16 km in elevation (shield base), 4) the flanks above 16 km in elevation (shield summit), and 5) the 55 km diameter caldera complex. The distinction between the base and summit portions of the shield is based on variations in morphology observed in high resolution photographs (Map 2). The surface relief and tonal contrast across distances of 100 m or more (4 or more pixels) is substantially subdued on the lower portion of the shield surface relative to the summit area. Thirty geologic terrain units were identified within these five regions. Appendix 2 provides detailed descriptions of each terrain unit in Maps 1 and 2. The terrain units within each of the five physiographic provinces are described next.

Mountainous terrains. A complex assemblage of faulted, km-sized mountains and hills (unit m) is present west of Ascræus Mons (Figs. 3.1 and 3.5). Flow fronts and scalloped escarpments separate the lower lying mountainous terrain from the surrounding plains at the northern end of the unit. The mountains-plains relief relationships change from north to south. Stereoscopic photographs show that the southernmost portions of the mountainous terrain is abruptly terminated at the contact with the surrounding (lower) plains (Fig. 3.6). Structural control is evident at the northern end of the mountainous terrain, where

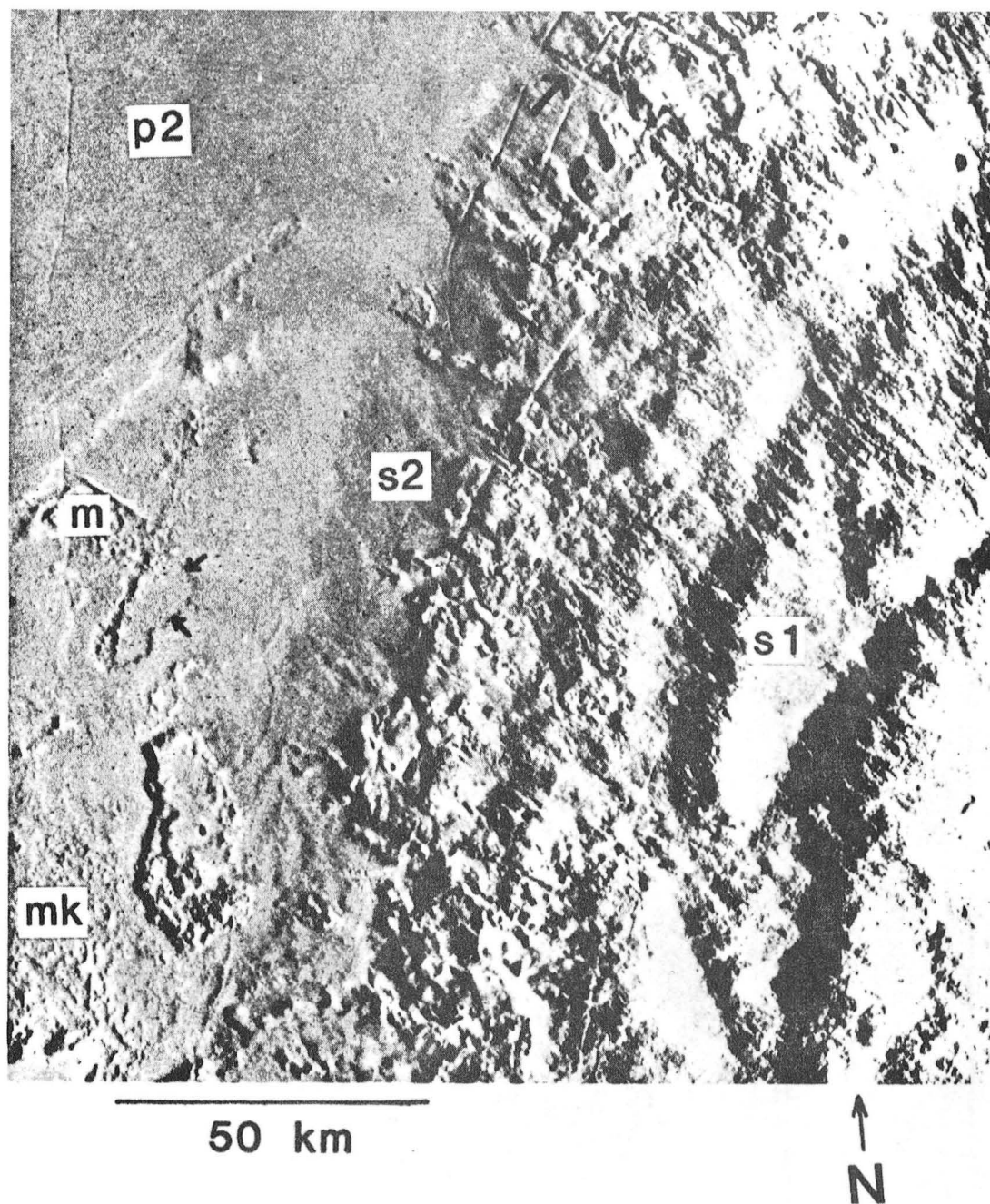


Figure 3.5. Northwestern flank of Ascræus Mons. Shield units include terraced s1 terrain and smooth-appearing s2 terrain. A sinuous channel (large arrow) originates on the s1 terrain and crosses the s2 terrain. The mountainous terrains (m,mk) are separated from the plains by irregular scarps or flow fronts (arrows). Photograph 892A09, nongradient high pass filtered orthographic projection. Center: 12.4°N, 107.1°W.



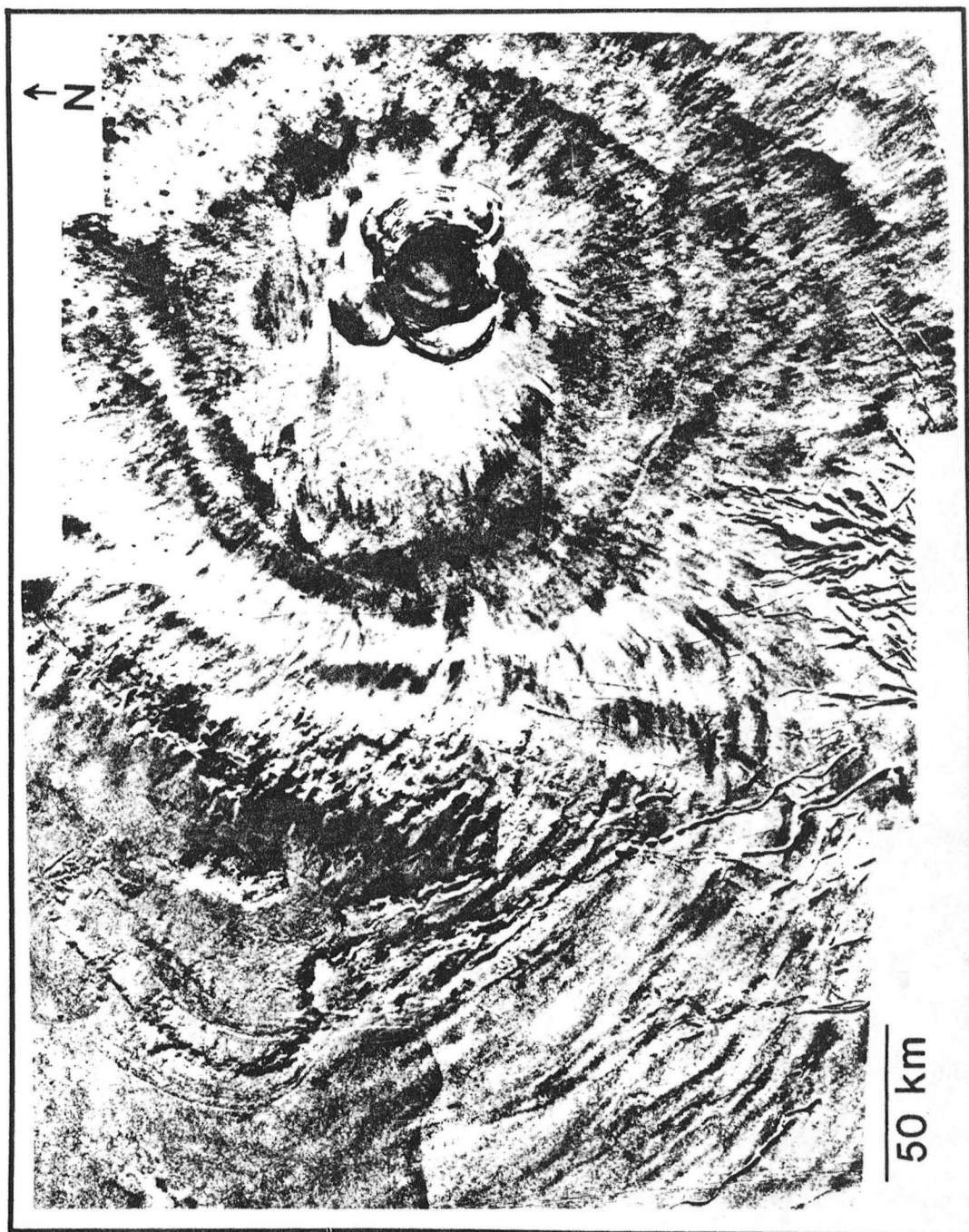


Figure 3.6. Stereoscopic photomosaic of the western flank of Ascræus Mons. (Right member of the stereoscopic pair, see Appendix 1 for the left member.) Photographs 223A10-16, nongradient high pass filtered orthographic projection. Center:  $10.7^{\circ}\text{N}$ ,  $106.2^{\circ}\text{W}$ .

downdropped blocks cause mountainous areas to be lower than the surrounding plains. The mountainous terrain is in contact with the Ascræus Mons shield at the southeastern margin of unit m; an escarpment hundreds of meters high separates the higher mountainous terrain from the shield units. The eastern margin of the mountainous terrain is surrounded by plains with numerous knobs protruding above the surface of the plains (unit mk). A crescent shaped area at the western margin of the mountainous terrain includes several curvilinear ridges that parallel its arcuate western margin (unit r). The mountainous terrain, the knobby plains, and the ridged terrain are quite distinct from either the surrounding plains or the shield units of Ascræus Mons.

The mountainous terrain has been interpreted both as material which predates the Ascræus Mons shield (Carr, 1975) and also as landslide or debris flow material younger than the shield (Scott and Tanaka, 1981). Truncated channels at the southeastern end of the mountainous terrain suggest an erosional origin for the escarpments that separate the elevated mountainous terrain from the plains and the shield, supporting the Carr (1975) stratigraphy. Channels within the mountainous terrain indicate that flowing materials (possibly lava, mud, or debris) were probably involved in their emplacement, consistent with the debris flow interpretation of Scott and Tanaka (1981).

However, there is no indication of a source on the shield flank for the mountainous terrain. A debris or lava flow origin remains likely for the mountainous terrain but these flows predate both the surrounding plains and the shield surface terrains.

The knobby plains appear to be directly associated with the mountainous terrain. The knobby plains occur on the eastern margin of the mountainous terrain but west of the base of Ascraeus Mons. Flows originating on Ascraeus Mons would have inundated the eastern margin of the mountainous terrain so that only the tallest knobs remained above the flow surface. No flow margins are identifiable in the knobby plains but a flooding by Ascraeus Mons flows seems preferable to either emplacement of the knobs through the plains or erosion of mountainous terrain resulting in knobby remnants above a uniform plain. An origin for the knobby plains involving flow that surrounded individual knobs of mountain material supports the origin for the mountainous terrain discussed above.

The ridged terrain on the western margin of the mountainous terrain may postdate both the plains and the mountainous terrain. The ridged terrain is similar in morphology to terrain west of Arsia Mons, interpreted to be landslide products from that volcano (Carr et al., 1977). The plains east of both the mountainous terrain and the ridged terrain are hundreds of meters lower than the



rest of the plains around the mountainous terrain (from stereoscopic viewing of Fig. 3.6). A tectonic origin for these lower plains (downdropped faulting) could provide the energy needed to initiate a landslide to the west (down slope) from the mountains. A tectonically induced landslide origin for the ridged terrain implies that this terrain postdates both the mountainous terrain and the plains. However, photographic resolution for the ridged terrain is insufficient to verify this interpretation.

Summary: The geologic history of the mountainous area west of Ascræus Mons began with the emplacement of the materials that comprise the mountainous terrain. Channels within this terrain suggest that flowing materials, probably lava or mud and debris, were involved in the mountainous terrain emplacement. Tectonic and/or erosional events truncated the southwestern margins of this terrain, perhaps coincident with the emplacement of the plains that now surround the mountainous terrain. Plains flows east of the mountainous terrain surrounded numerous individual knobs of mountain material, producing knobby plains. Tectonic events at the northern end of the mountainous terrain initiated landslides that resulted in the ridged terrain.

Tharsis plains terrains. The plains units are divided between flows associated with the embayments on the northeast and southwest shield flanks (p4), individual flows with well defined margins (p3), undivided Tharsis

flows with few flow features (p2), and patches of plains lacking flow features (p1). Many plains contacts are transitional or indistinct but some contacts suggest these units were emplaced sequentially from p1 to p4.

The p1 plains lack flow features but grabens and channels are abundant, commonly with orientations distinct from graben orientations on the adjacent plains (Fig. 3.7a). The p2 plains have few flow features and are superimposed over the shield materials (Fig. 3.7b). The increasing clarity of flow features in the plains units could result from degradation of surface morphology or changing eruption characteristics (effusion rates, flow volumes, lava viscosities, etc.); both processes probably contributed to the present surface morphology.

The p3 flow directions do not agree with the photogrammetrically derived topography (Fig.3.3) northwest and southeast of Ascræus Mons. The flows southeast of Ascræus Mons indicate a downward slope toward the northeast, parallel (not radial) to the base of the volcano. The flows northwest of Ascræus Mons all point toward grabens that parallel 108°W longitude. It would appear that the grabens are located within a topographic depression 200 km northwest of the volcano base. Similar depressions exist around Olympus Mons (Mouginis-Mark et al., 1982a; Hiller et al., 1982) and Hawaii (Macdonald and Abbott, 1970, p.280), interpreted to result

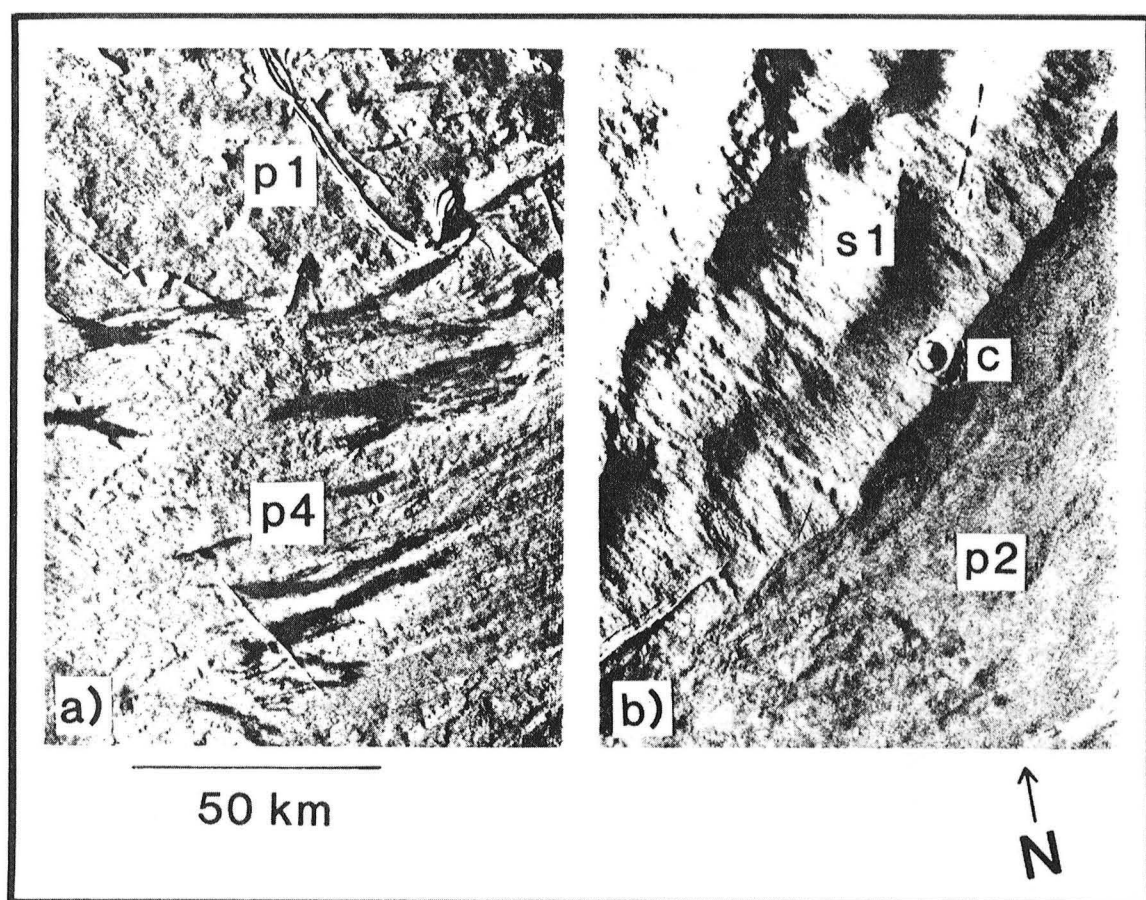


Figure 3.7. Plains south and southeast of Ascraeus Mons. a) The p4 plains from the southwestern embayment into the shield crosscut features of the p1 plains. Photograph 892A34, nongradient high pass filtered orthographic projection. Center: 7.3°N, 108.0°W. b) Southeastern margin of the shield with superposed p2 Tharsis plains. Crater ejecta (c) overlies both the shield and plains terrains. Photograph 892A29, nongradient high pass filtered orthographic projection. Center: 9.4°N, 102.7°W.

from crustal loading by the volcanoes. Alternatively, the flows could have been emplaced on slopes different from the present topography. However, this would contradict the correlation between flow direction and slope observed throughout most of the Tharsis area (Mouginis-Mark et al., 1982). Thus, the flow directions around Ascræus Mons suggest that the photogrammetrically derived topography for this area needs revision.

The p3 flows west of Ascræus Mons originate in the topographic "saddle" between Pavonis Mons and Ascræus Mons (Map 1). The easternmost flow lobe in this area can be traced for 480 km. If the average thickness of this flow is at least 30 m, consistent with the flow thicknesses for Ascræus Mons discussed below, it contains 220 km<sup>3</sup> of lava - a value orders of magnitude greater than the volume of most terrestrial flows but comparable to flood basalt volumes on the Moon and the Earth (Table 3.1). Shadows at the distal margins of the flow suggest a thickness > 100 m, so the volume estimate may only be a lower limit. Large volume eruptions played an important part in the production of the Tharsis plains on Mars.

The p4 plains originate at the channeled embayments in the northeastern and southwestern flanks of Ascræus Mons. Subtle ridges radiate from the southwestern embayment and are interpreted to represent local flow directions (Fig. 3.7a). The p4 materials clearly crosscut

Table 3.1. Volumes, areas, and thicknesses of individual basalt flows.

Location	Volume (km <sup>3</sup> )	Area (km <sup>2</sup> )	Average Thickness (m)	Ref
Hawaii	0.5	84	5	(1)
Iceland	12.3	565	22	(2)
Mars	220	7300	30	(3)
Moon	490	24500	20	(4)
Mars	2000	66600	30	(5)
Washington	2460	51200	48	(6)

References:

- 1) Macdonald and Abbott (1970, p.56-7). Mauna Loa, 1859 flow.
- 2) Thorarinsson (1970). Lakagigar, 1783 flow.
- 3) This work. Easternmost p3 flow lobe west of Ascræus Mons (Map 1).
- 4) Schaber (1973a,b). Mare Imbrium, Phase III flow.
- 5) This work. All p3 flows west of Ascræus Mons, originating between Ascræus Mons and Pavonis Mons (Map 1).
- 6) Mackin (1960). Columbia River plateau, Roza flow.

Average thicknesses for the flows on Earth were calculated from areas and volumes. Lunar flow areas were measured from maps in Schaber (1973a,b); the average thickness value is from Schaber *et al.* (1976). Martian flow areas are from Map 1 and flow thicknesses are assumed to be comparable to flows on Ascræus Mons.

features on the p1 plains south of Ascræus Mons but they gradually merge into the p2 and p3 plains downslope from the volcano. The plains emanating from the embayments into Ascræus Mons are interpreted to be the latest effusive activity from the lower flanks of Ascræus Mons, consistent with previous interpretations (Crumpler and Aubele, 1978; Scott and Tanaka, 1981).

Summary: The Tharsis plains surrounding Ascræus Mons are the result of numerous large volume eruptions. The flows west of Ascræus Mons indicate the presence of an unmapped depression northwest of the volcano, possibly related to loading of the surface by the volcano. The plains flows originated primarily but not exclusively at Ascræus Mons, with the latest effusive activity concentrated in the shield embayments.

Shield base terrains. Below 16 km in elevation the surface features on the Ascræus Mons shield display subdued relief and tonal variations compared to features at higher elevations on the volcano. The variation in surface morphology can be seen in high resolution photographs (Map 2) but at lower resolution the shield surface appears similar at all elevations, except for the lower northwestern flank (Map 1, unit s2). The subdued terrain units are discussed first, followed by descriptions of features present only at lower elevations on the volcano.

The shield base terrain units include five subdued

versions of units found at higher elevations (Map 2). Four flow-related units on the shield base (Fig. 3.8, ps, hs, fs, hks) are interpreted to be subdued counterparts to the summit region terrain units discussed below. Flow-related units are interpreted to be equivalent at all elevations but processes have modified the morphology of the base units to a greater extent than in the summit region. Impact craters (Fig. 3.9, c) are present on the shield base but surface detail is more subdued than on craters near the summit. Several sharp-rimmed craters are evident throughout the base region, indicating that atmospheric haze is not responsible for the subdued appearance of the photographs.

Low broad mounds are common in the shield base region, particularly between elevations of 12 and 15 km (Fig. 3.8, m). Some mounds are aligned with the downslope flow patterns in the surrounding terrains and all appear to be stratigraphically below the other base units. On Olympus Mons similar features are interpreted to be lava accumulations at the mouths of channels (Carr, 1981, p.97). However, channels are not visible immediately upslope of the mounds on Ascraeus Mons. The conical shape of some mounds (Fig. 3.8) suggests they may represent sites of localized lava effusion analogous to parasitic flank eruptive centers (Macdonald, 1972, p.201). The mounds are probably related to centralized eruption of small volumes

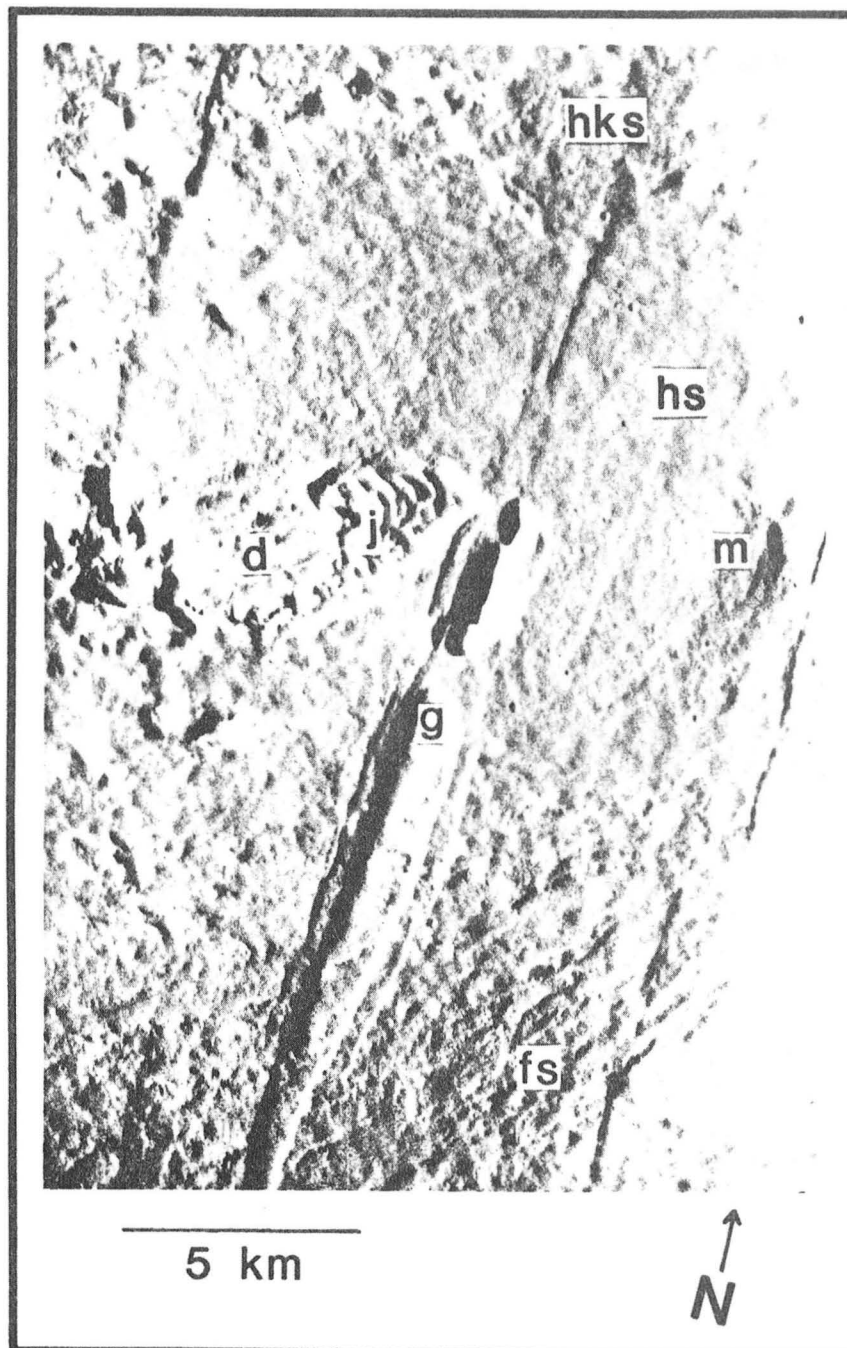


Figure 3.8. Shield base terrains. All units are subdued in morphology, relative to summit units. Hummocky and knobby plains (hk, hks) surround isolated mounds (m) and are covered by individual flows (fs). Linear grabens (g) and irregularly shaped depressions (d) crosscut surface features, with jumbled terrain (j) on the depression floors. Photograph 401B03, shading corrected rectilinear version. Center: 10.3°N, 106.6°W.



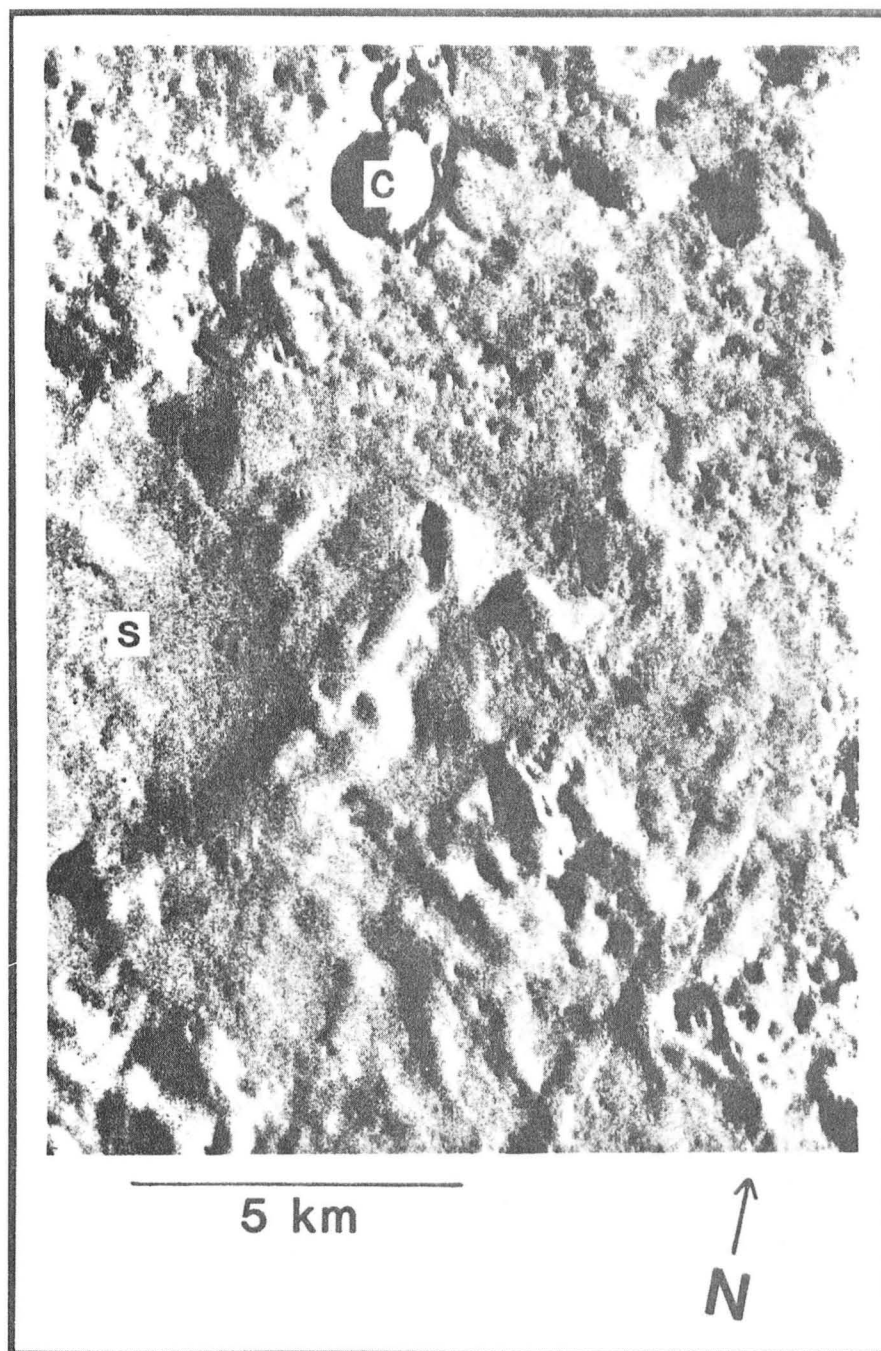


Figure 3.9. Smooth plains (s) on shield base. Reduced relief and tonal variations across unit s give this terrain a smooth-appearing surface. Crater (c) and ejecta blanket are subdued in morphology and partially foundered into the depression north of the crater. Photograph 401B01, nongradient high pass filtered orthographic projection. Center: 10.3°N, 107.0°W.

of lava on the lower flanks of Ascræus Mons.

Some planar areas lack surface features other than subtle depressions and grabens with subdued wall scarps, giving the unit a smooth appearance (Fig. 3.9, s). The smooth terrain stratigraphically overlies all other shield base units and probably represents an extreme example of the modificational processes affecting the entire base surface. Several processes could produce this morphology (e.g. aeolian, volcanic, fluvial) but surface features provide no compelling evidence to permit a choice between these processes. The discussion section includes an examination of the processes responsible for the subdued morphology of the shield base; aeolian or volcanic deposition seems to be the most likely explanation.

Three terrain units result from disruption of the shield surface. Grabens have downdropped central floors which may or may not retain surface features that were present before faulting occurred (Fig. 3.8, g). Depressions with irregular outlines are elongated up slope, with isolated groups of jumbled knobs on the floors of the depressions (Fig. 3.9, d, j and Fig. 3.10). The irregular depressions lack the straight walls of the fault-bounded grabens and appear to be the result of mass wasting through slope failure. Some jumbled knobs have lineations parallel to the depression walls, similar to rotated slump blocks. The depressions are most abundant on the western and

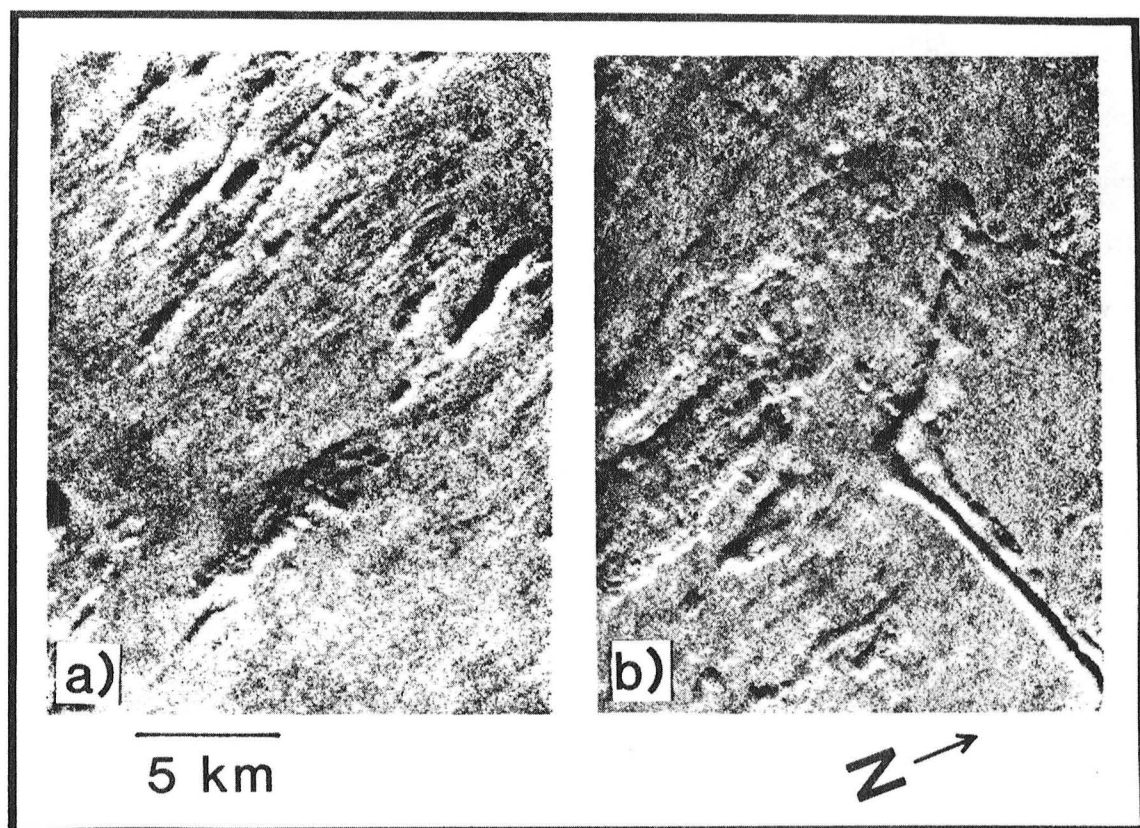


Figure 3.10. Northwestern flank of Ascraeus Mons. a) Linear to sinuous depressions, concentrated on the front face of a shield terrace. Photograph 698A16, nongradient high pass filtered orthographic projection. Center:  $13.5^{\circ}\text{N}$ ,  $105.5^{\circ}\text{W}$ . b) Irregular depressions with numerous rounded knobs on the depression floors. Photograph 698A13, nongradient high pass filtered orthographic projection. Center:  $14.1^{\circ}\text{N}$ ,  $105.9^{\circ}\text{W}$ .

northwestern flanks of the volcano. Both grabens and irregular depressions postdate all other terrain units except the smooth terrain.

The lower western and northwestern flanks are morphologically distinct from both the surrounding plains and the shield surface (Fig. 3.5, s2). Very subdued flow-like features extend downslope from a 400 to 800 meter scarp separating the s2 terrain from the rest of the shield. The scarp separating the s1 and s2 terrains may be the result of coalesced mass wasted depressions. Grabens are continuous through both the shield (s1) and s2 terrains, although the grabens are partially filled on the s2 terrain. A sinuous channel originating on the s1 shield unit crosses the s2 terrain and terminates at the s2-plains contact (Fig. 3.5, large arrow), indicating that the plains postdate both the s1 and s2 terrains. Flows from the Ascræus Mons flanks apparently traversed the s2 terrain during the emplacement of the p2 plains.

Linear to arcuate channels produce embayments into the southwestern and northeastern flanks of Ascræus Mons and are the sources of the p4 plains units (Figs. 3.1 and 3.2). The channels are 200 to 800 m deep and up to 25 km wide with blunt, circularly rimmed terminations at their headward (upslope) ends. Blunt terminations in channels are indicative of headwall undermining or sapping rather than downcutting from a liquid flowing on the surface

(Sharp, 1973). Channeling agents for the embayments are examined in the discussion section; lava erosion, ground ice sublimation, or debris flows (lahars) most likely contributed to the embayment formation. The alignment of the embayments with the Tharsis Montes suggests that volcanic processes initiated the channeling activity in the shield embayments, regardless of the channelization process.

Summary: The flanks of Ascraeus Mons display subdued relief and tonal variations below 16 km in elevation. Low mounds, probably the result of centralized eruptions, are stratigraphically below other shield units. Five flow-related terrain units on the shield base are similar to terrains in the summit region, except for the subdued morphology evident at the lower elevations. Smooth appearing terrain stratigraphically overlies the other base region terrains and has the most subdued surface morphology. Tectonic and mass wasting processes disrupted the shield surface after all flow-related terrains were emplaced but prior to the development of the smooth plains. The lower western and northwestern flanks are eroded and the plains surrounding the volcano postdate both the shield surface and the eroded terrain. Embayments into the southwestern and northeastern flanks are the sources for the most recent (p4) plains unit.

Shield summit terrains. The summit region of Ascræus Mons displays numerous flow features and surface variations at the smallest scale observable (22 to 24 m). The morphology of terrains both on the summit flanks and within the caldera is very distinct and detailed. There is no morphologic evidence on the flanks of late-stage pyroclastic activity potentially associated with the caldera collapse (Mouginis-Mark, 1981). The three terrain units containing flow features (p-plains, f-flows, h-hummocks; Fig. 3.11) are stratigraphically intermixed but commonly unit p is the lowest member and unit f is the highest member. This trend is similar to the surface features observed on terrestrial basalt flows as they move from the vent area, progressing from fluid pahoehoe nearer the vent to more viscous aa (Macdonald and Abbott, 1970, p.23; Carr and Greeley, 1980, p.137). The intermixed terrains probably result from flows overlapping at different distances from their sources. A fourth terrain unit (hk) is a variation of the hummocky terrain and is embayed or surrounded by the other terrain units.

Individual flows with distinct, rough appearing margins typically have a leveed central channel (Fig. 3.11, f). These flows have margins 15 to 45 m in height; smaller flows may also be present but they are not visible in the photographs. Some flows have a uniform tone on their upper surfaces, suggesting a lack of relief on these areas, but

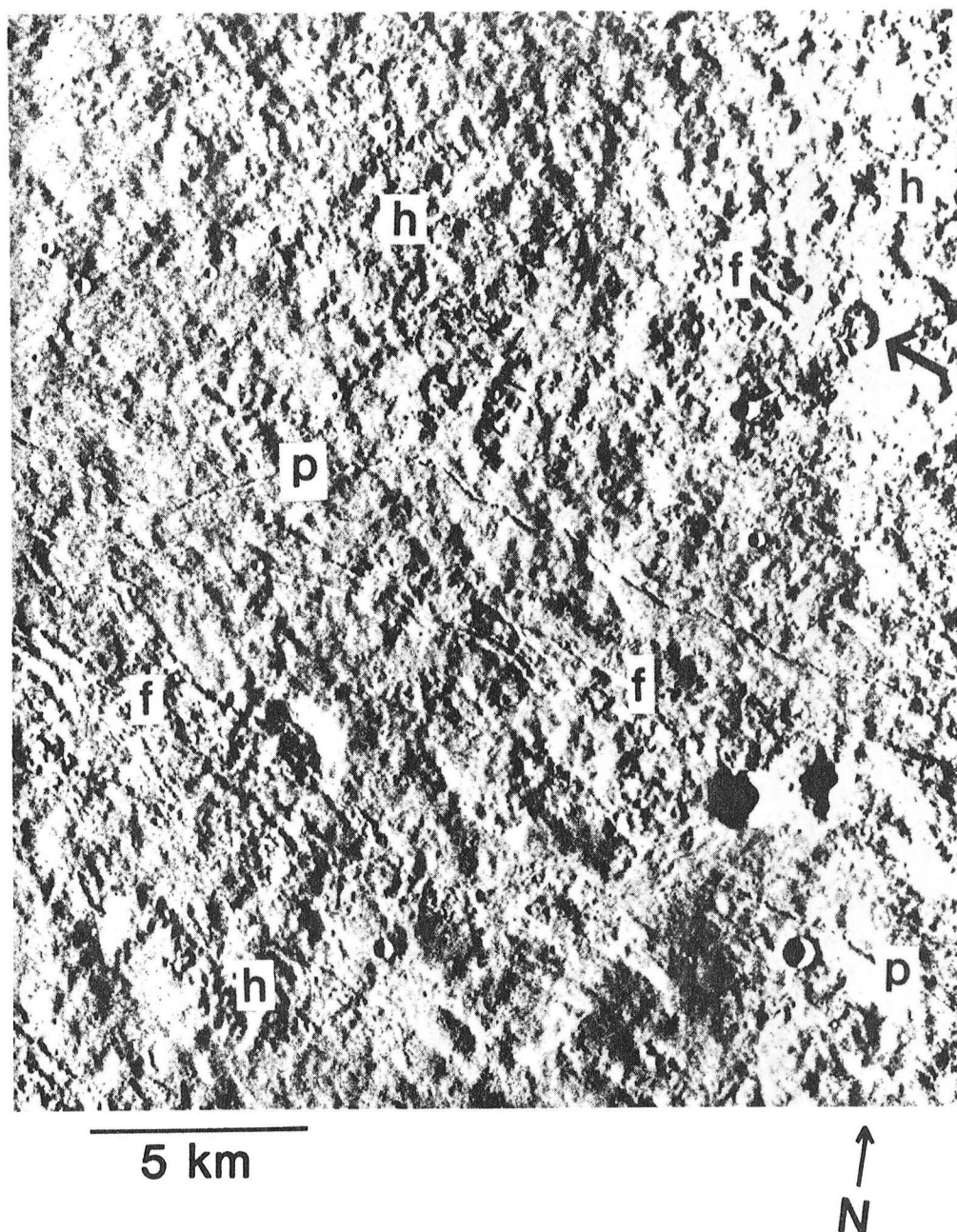


Figure 3.11. Summit area terrains east of the caldera complex. Flows with well defined margins and leveed central channels (f) are intermixed with plains (p) and hummocky terrain (h). One leveed flow (large arrow) has several ridges perpendicular to the flow direction. Elongate flow margins extend perpendicular to sinuous channels at some locations (arrows). Photograph 401B24, nongradient high pass filtered orthographic projection. Center: 11.3°N, 103.6°W.

the margins are always distinct. Caldera collapse truncated some flows, similar to Mauna Loa in Hawaii (Carr and Greeley, 1980, p.28; Mouginis-Mark, 1981). Comparison with shield volcanoes on Earth suggests that the f unit flow morphology corresponds to an aa surface texture consisting of broken and jumbled lava clinkers or blocks.

Planar areas typically have sinuous channels that are 100 to 200 m wide and up to 50 km long (Fig. 3.11, p). Tonal variations indicate the surface surrounding the channels has gentle undulations. Elongate toes extend radially from the sinuous channels at one location (Fig. 3.11, arrows) and tonal variations suggest that the sinuous channels run along the crest of a gently sloping ridge. Comparison with shield volcanoes on Earth suggests that these flows have a pahoehoe texture indicative of more fluid lava emplacement than flows of unit f. Similar interpretations of both aa and pahoehoe flows have been made for Olympus Mons (Greeley, 1973).

The rest of the summit area is composed of "hummocky" terrain (units h, hk) consisting of complex undulations on the scale of 100 to 1000 m. Undulations on a km scale are more common in the summit area east of the caldera while west of the caldera the undulations are 200 to 500 m apart. This terrain includes some sections of individual flow fronts or leveed channels but the flow segments are only traceable a few kilometers; some hummocky areas may be the



source of unit f flows (Fig. 3.11, large arrow). Numerous multiple or simultaneous extrusions appear to be involved in generating the intermixed patterns of this terrain. Some locations consist of individual knobs with a relatively uniform 200 to 300 m spacing (unit hk); this terrain is embayed or surrounded by the other summit materials. Similar terrain on Mauna Loa consists almost exclusively of toey pahoehoe extruded from numerous tumuli on hummocks 15 m high (M. Malin, personal communication, 1983 and Fig. 5.5). The numerous separate toes intermingle throughout the pahoehoe surface, burying individual aa and pahoehoe flows in the area.

Summary: Terrain units in the summit region of Ascræus Mons display numerous flow features. Individual flows with leveed central channels and prominent margins are interpreted to be aa flows. Planar areas with sinuous channels and gentle undulations are interpreted to be pahoehoe flows. Hummocky terrain with isolated portions of pahoehoe and aa flows may primarily consist of toey pahoehoe. All three terrain units are stratigraphically intermixed; however, the overlapping relationships generally follow the terrestrial trend of less fluid lavas further from the vent area. A variation of the hummocky terrain is embayed by the other terrain units.

Caldera terrains. The summit caldera complex consists of roughly circular collapse features centered at

different locations. The caldera walls include features related to mass wasting of the shield due to the caldera collapse events. Planar floors occur within each caldera and crosscutting of the floors indicates at least nine collapse events occurred in the caldera complex.

The caldera wall materials are distinctly segregated according to their location along the wall slope. The upper portion of many wall segments consists of alternating ridges and grooves that produce a fluted appearance (Fig. 3.12a, cwg). Some grooves are associated with grabens that intersect the caldera rim, indicating local fault or joint control. This terrain could potentially include a large proportion of exposed bedrock. Below the fluted zone the walls are featureless except at very low solar incidence angles, where subtle downslope ridges and depressions are visible (Fig. 3.12a, cw). The low illumination angles limit the relief of these features to less than 10 m. The cw terrain is interpreted to be talus accumulations produced by mass wasting and downslope transport. The bases of several walls include mounds of wall material (elongate parallel to the walls) that slumped off the caldera rim and were partly covered by the floor material (Fig. 3.12a, cws). If the caldera rim and the central floor are both assumed to be horizontal, then the southern caldera wall (Fig. 3.12a) has 2.9 kilometers of vertical relief with an average slope of 26°. The caldera wall

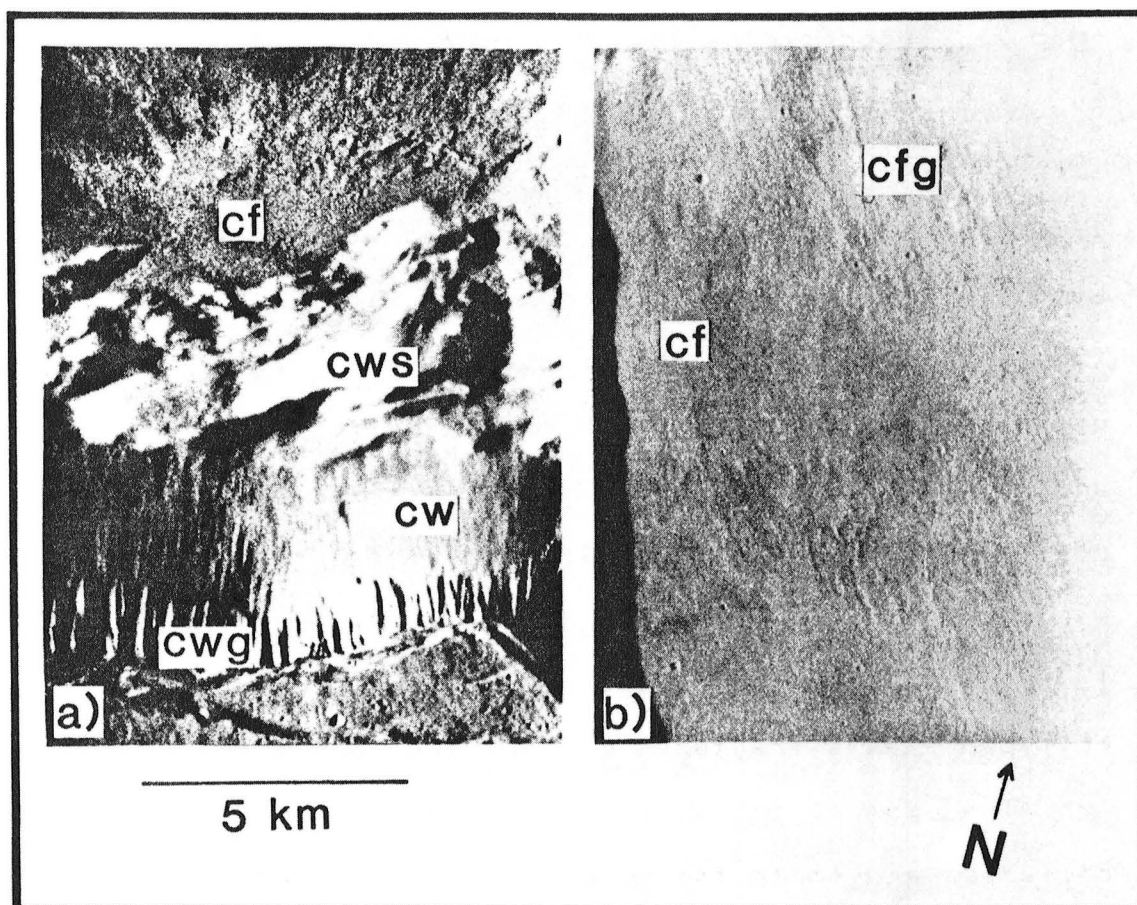


Figure 3.12. Caldera wall and floor terrains. a) Southern wall of the central caldera. Wall units include slump blocks at the wall base (cws), wall slopes (cw), and grooved terrain (cwg). Caldera floor terrain (cf) embay the wall terrains. Photograph 401B20, shading corrected rectilinear version. Center: 10.8°N, 104.4°W. b) Floor terrain (cf) and grooved floor terrain (cfg) of the central caldera. Photograph 401B19, shading corrected rectilinear version. Center: 11.2°N, 104.5°W.

terrains are products of mass wasting which accompanied or followed the caldera collapse events.

The caldera floors postdate the depressions in which they are located. Planar floors partly fill each caldera and are superposed on the caldera wall materials (Fig. 3.12, cf). Flow fronts are evident on two caldera floors (Map 2), supporting a lava flooding interpretation suggested from comparison with shield calderas on Earth (Carr, 1973; Carr and Greeley, 1980; Greeley and Spudis, 1981). The central caldera floor includes areas with slightly arcuate ridges and grooves (Fig. 3.12b, cfg); cf terrain flows overlies the grooved floor terrain. The eastern side of the caldera consists of extensively faulted and fractured blocks (cfs). Many of these blocks have planar upper surfaces that form terraces on the eastern caldera wall (Fig. 3.13a). The caldera floors result from lava flooding after caldera collapse but subsequent collapse events fractured most of the floors.

The central collapse cross-cuts the floors of earlier collapses and forms the deepest depression of the caldera complex, with the surrounding floor units exposed at various levels above the central floor (Fig. 3.13a). Following Mouginis-Mark (1981), the collapse events have been identified from the oldest (1) to the youngest (8), based on crosscutting of the caldera floors (Fig. 3.13b). This results in a consistent decrease in age of the floors

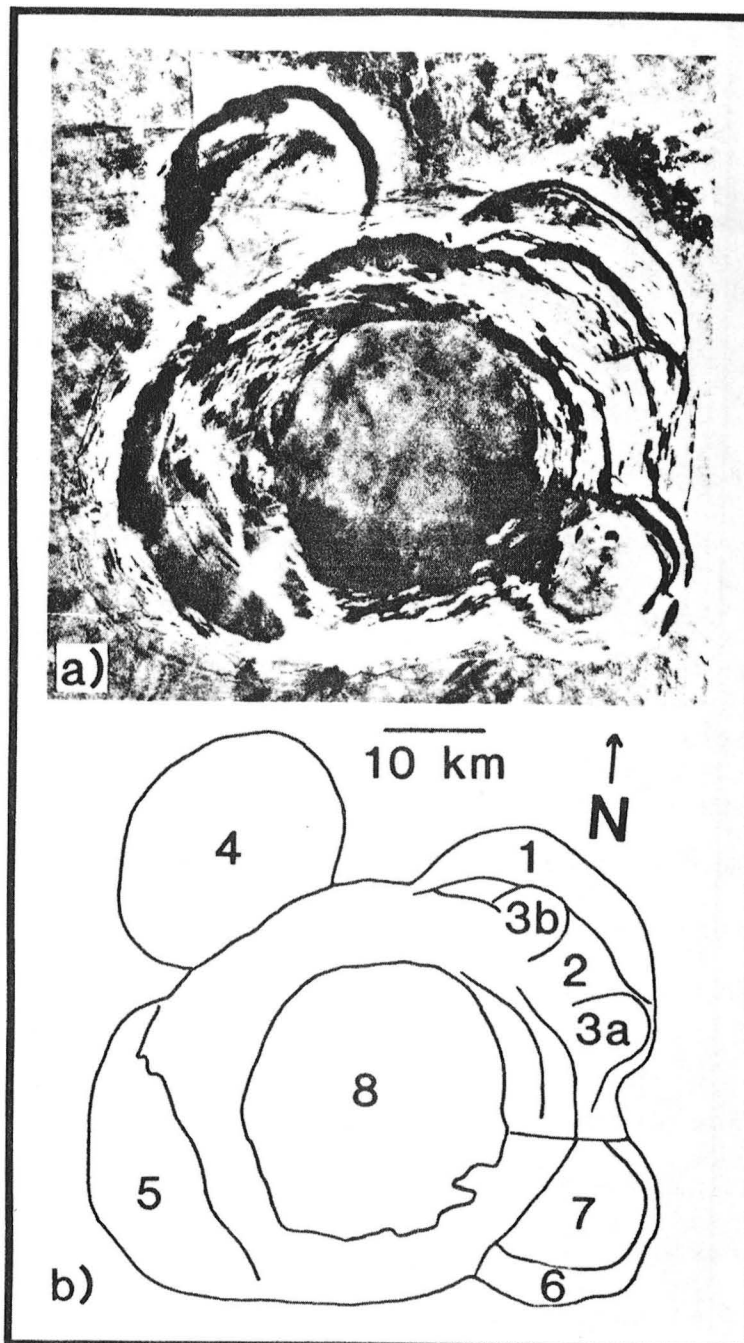


Figure 3.13. Caldera complex of Ascraeus Mons. a) Photomosaic of multiple collapse features within the summit caldera complex. Photographs 90A50 and 52, nongradient high pass filtered orthographic projection. Center:  $11.3^{\circ}\text{N}$ ,  $104.4^{\circ}\text{W}$ . b) Caldera collapse centers, numbered from oldest (1) to youngest (8) by crosscutting relationships and relative elevations (see text).

with decreasing elevation. Relative elevations (Fig. 3.6) suggest that floor segment 4 is older than both segments 5 and 6 even though no contacts exist between these floors. These relationships are illustrated in stereoscopic photos of the caldera complex (Figs. 3.6 and 3.14).

Summary: The summit area of Ascraeus Mons has undergone collapse at least nine times, followed by lava flooding within the collapse depressions. Each caldera collapse was accompanied by mass wasting and slumping of rim materials and subsequent partial flooding by fluid lavas. Crosscutting of floors indicates a progressive decrease in caldera age with decreasing elevation above the unfaulted central floor.

Summary. The stratigraphic relationships for the Ascraeus Mons terrain units are illustrated on Maps 1 and 2. The mountainous terrains west of Ascraeus Mons were emplaced prior to either the shield terrains or the surrounding plains. The Tharsis plains around Ascraeus Mons include areas with numerous visible flows, relatively few visible flows, and no visible flow features. All plains units in contact with the shield are either superposed on the shield terrain (p1, p2, p3) or embayed into the shield flank (p4). Some p3 flows originated in the topographic "saddle" between Ascraeus Mons and Pavonis Mons, with flow volumes comparable to flood basalts on the Moon and the Earth. In high resolution photographs the

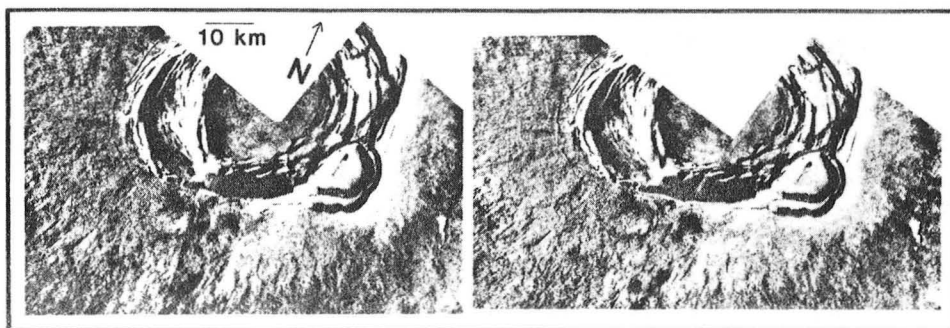


Figure 3.14. Stereoscopic photographs of the southern portion of the caldera complex. Relief is vertically exaggerated. Photographs 210A12,14 (left) and 62,64 (right), nongradient high pass filtered orthographic projection. Center:  $10.8^{\circ}\text{N}$ ,  $104.5^{\circ}\text{W}$ .

base area of Ascraeus Mons (below 16 km elevation) has subdued relief and tonal variations relative to the summit area. Flow-related terrains are interpreted to be the same in both the base and summit regions but modificational processes (most likely aeolian or volcanic deposition, possibly accompanied by chemical and physical weathering) have subdued the base area morphology. Tectonic and mass wasting features disrupt all base area terrains except the smooth plains, stratigraphically the youngest terrain on the volcano flanks. Channelized embayments into the southwestern and northeastern flanks are the sources of the most recent (p4) plains unit. Summit area terrains include individual flows with prominent margins and gently undulating plains with sinuous channels, interpreted to be aa and pahoehoe flows, respectively. The rest of the summit area consists of hummocky terrain that could include toey pahoehoe. All three flow-related terrains are stratigraphically intermixed but the terrain overlapping is generally consistent with less fluid lavas further from the flow vent areas. The caldera complex truncates all flank terrains in the summit area. At least nine collapse events occurred within the caldera complex, followed by lava flooding of the depressions. There is a decrease in caldera age with decreasing elevation above the central caldera floor.



### Cratering Record

The record of impact craters on planetary surfaces provides a method for comparing the relative ages of surface units. On volcanic terrains, however, endogenic craters occur along with the impact craters and increase the observed crater abundance. The cratering record on Ascraeus Mons is presented here both for all observed craters and for impact craters after probable endogenic craters have been eliminated. This provides some indications of how the endogenic craters influence the cratering results and where the endogenic craters are most abundant.

The flanks of Ascraeus Mons have systematic variations in the areal density and size frequency distribution of all craters (Fig. 3.15). The areal abundance of craters decreases with decreasing elevation, particularly for small craters ( $D < 200$  m or  $\log D < 2.3$ ). A distinctive distribution results for each of the physiographic regions on the shield (Fig. 3.16). The shield base is deficient in all craters  $< 1000$  m, relative to the summit area while the caldera has an excess of craters  $> 400$  m as compared to the flanks of the volcano. Cumulative distributions for the individual terrain units correspond to the average distribution of the physiographic region in which they occur. Variations in cratering may indicate differing ages, crater production processes (endogenic or exogenic)

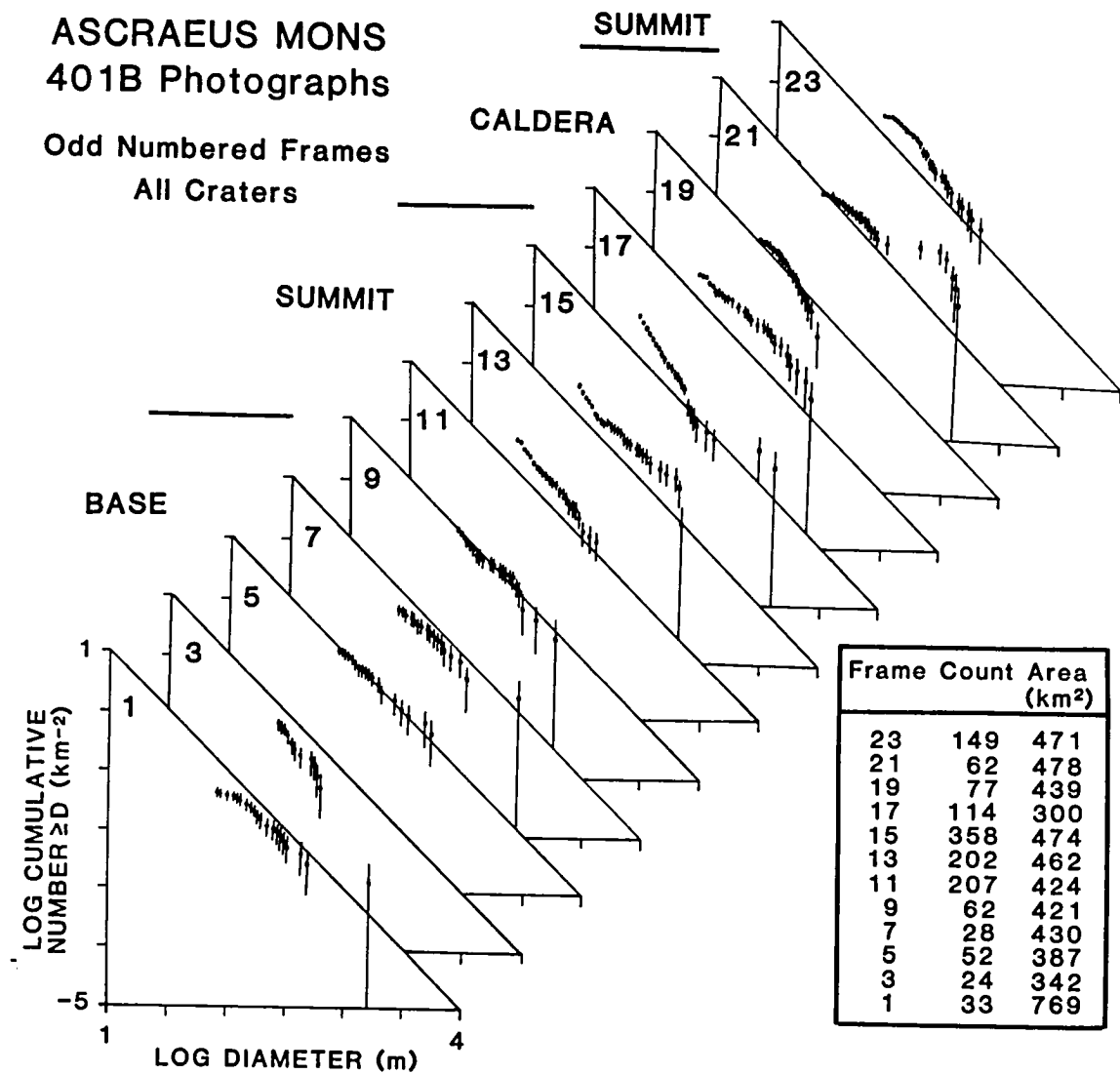


Figure 3.15. Cumulative distributions of all craters for the odd-numbered frames of the 401B photographs. Error bars represent  $\pm\sqrt{N}$ , where  $N$  is the measured number of craters within each diameter bin. Numbers to the left of each plot indicate the frame number.

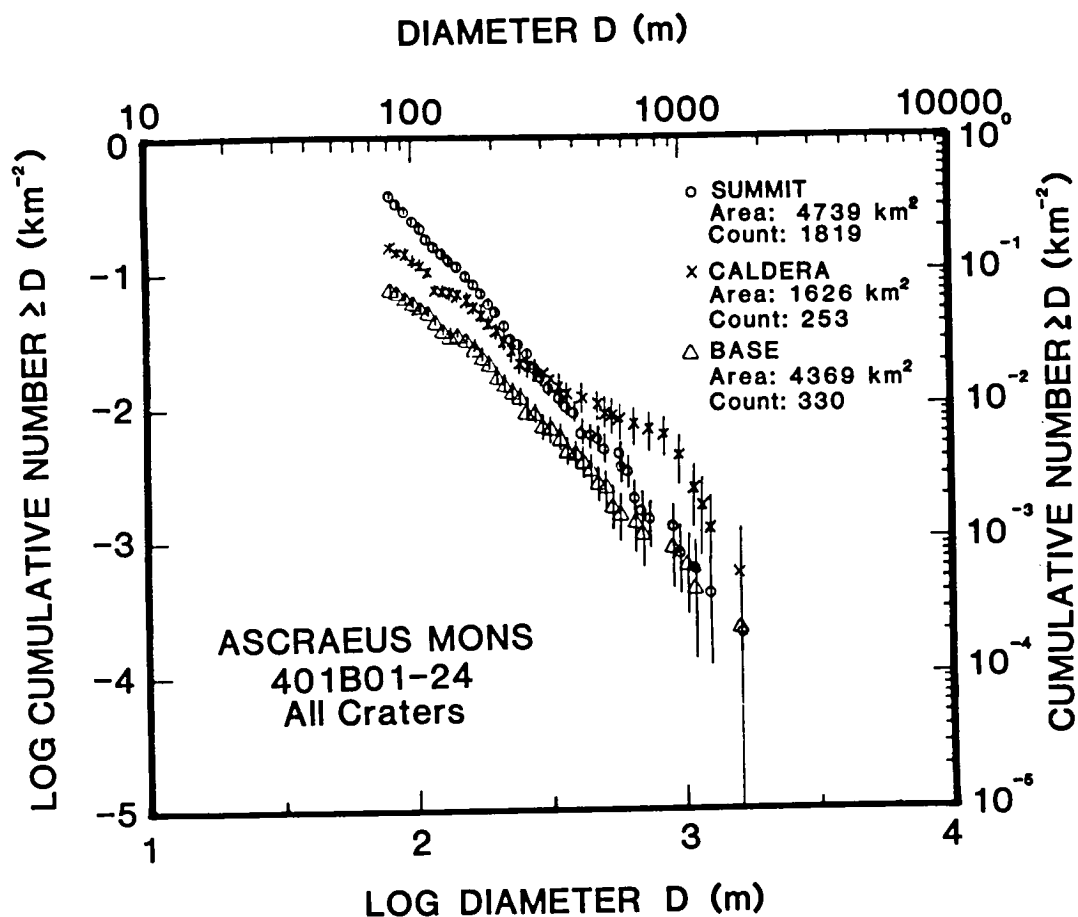


Figure 3.16. Cumulative distributions of all craters visible in the 401B photographs (see Fig. 3.4). Error bars represent  $\pm\sqrt{N}$ , where  $N$  is the measured number of craters within each diameter bin. Separation of the crater counts between the summit, base, and caldera regions is based upon the photogeologic terrain unit designation of the surface area counted.

or surface histories for each region on the volcano. The identification of potential endogenic craters, discussed next, aids in interpreting the cratering record on Ascræus Mons.

Relative age dating from crater counts on volcanic surfaces is complicated by the inclusion of volcanic and tectonic craters with the impact craters (Greeley and Gault, 1971; Blasius, 1976; Malin, 1977; Greeley and Gault, 1979, 1981). Although these endogenic craters cannot all be identified, some simple criteria help to identify the most obvious nonimpact craters. Blasius (1976) employed the following criteria for identifying craters of probable endogenic origin: elongate crater shape, crater chains along strike of structural trends, craters lacking positive relief rims, and craters lacking discernible ejecta blankets. Blasius (1976) reported that with these criteria less than 3% of the craters in nonvolcanic regions would be excluded from the counts. Very few craters on Ascræus Mons have either raised rims or ejecta blankets but the elongate shape and structural alignment criteria indicated that about 10% of the Ascræus Mons craters were probably of endogenic origin. Groups of small ( $< 300$  m in diameter) craters with areal densities substantially higher than the local average accounted for an additional 10% of the total crater abundance. These crater clusters could represent locally increased endogenic activity or secondary

craters generated by ejecta from large impacts or volcanic explosions. All endogenic craters on Ascraeus Mons may not be identified by the criteria discussed above but elimination of the probable endogenic craters from the crater counts aids in interpreting the impact cratering record for the volcano.

Figure 3.17 shows the cumulative crater frequency distributions for the three physiographic regions of the shield when probable endogenic craters are removed. In contrast to the results for all craters (Fig. 3.16), the summit and base cumulative distributions now agree for craters  $> 270$  m. Relative age differences on the volcano flanks are not distinguishable from the cratering record for craters  $> 270$  m. The selection criteria reduced but did not eliminate the excess of craters  $> 400$  m for the caldera (relative to the flank distributions). The cumulative distributions of all three regions are statistically separable only for craters  $< 200$  m.

Comparison of Figs. 3.16 and 3.17 indicates that probable endogenic craters are more abundant in the summit and caldera regions than in the base region. The selection criteria eliminated 328 probable endogenic craters from the summit distribution but only 10 from the base distribution. The subdued morphology of the base region may be partly responsible for this result by making it more difficult to identify elongate or aligned craters. The excess of

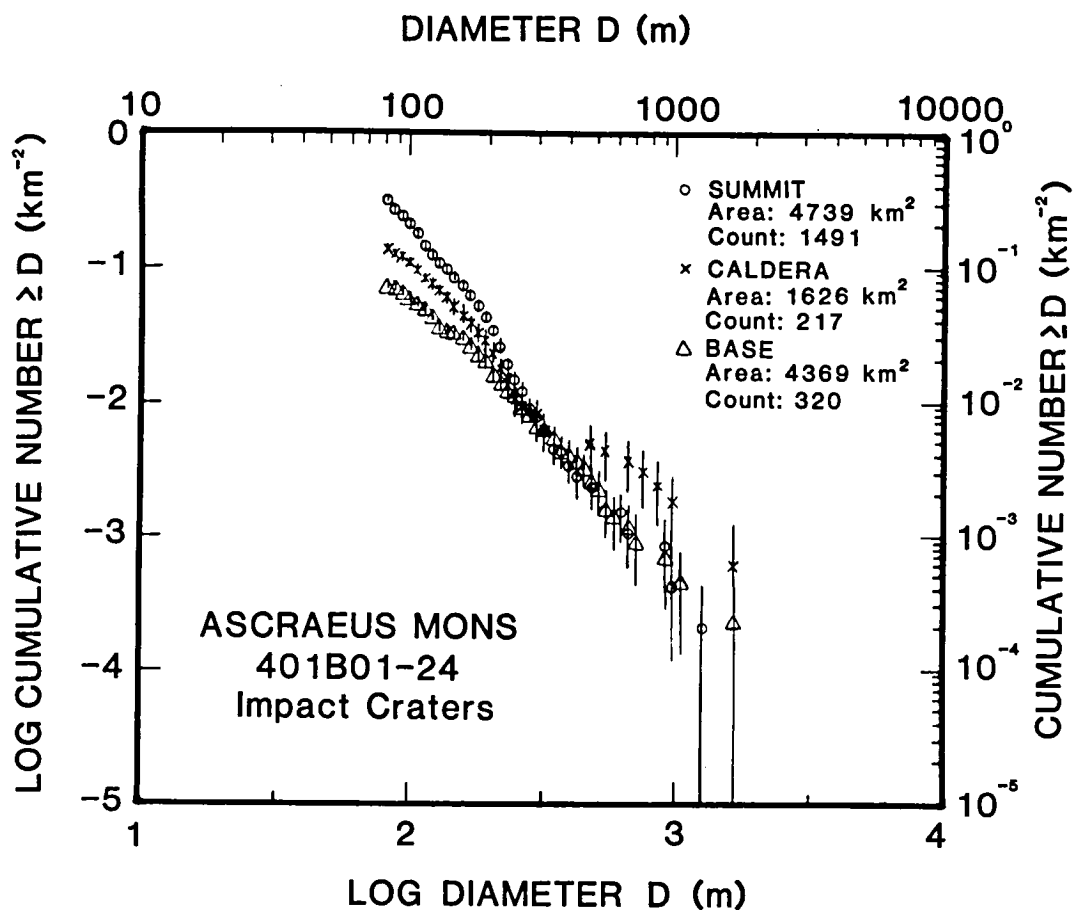


Figure 3.17. Cumulative distributions for impact craters visible in the 401B photographs. Probable endogenic craters, including clustered craters, have been removed from the distributions shown in Fig. 3.16 through criteria discussed in the text. Error bars represent  $\pm\sqrt{N}$ , where  $N$  is the measured number of craters within each diameter bin.

craters > 400 m across in the caldera region is most pronounced for the faulted eastern portion of the caldera (see Fig. 3.15, Frame 21); caldera collapse may lead to increased crater generation through collapse or explosion. None of the caldera craters have dark albedo halos, proposed as an indicator of explosive craters on the Moon (see McGetchin and Head, 1973), so that an endogenic origin through collapse may be more probable. Fine-grained materials are present on the entire volcano (Chapter 4), including the caldera units, and could have buried albedo variations related to explosion craters. Aligned craters ranging from 230 to 600 m across account for most of the probable endogenic craters on the summit flanks, perhaps related to collapse of large buried lava tubes or an alignment of explosive vents. Increased abundance of endogenic craters on the summit flanks of Ascraeus Mons relative to the base flanks is consistent with the interpretation that most volcanic vents on Olympus Mons are located on the upper flanks (Carr et al., 1977).

The surface history also can influence the observed crater distributions. The reduced areal abundance of small craters in the base region could result from reduced production of craters either endogenic or exogenic in origin. The present atmosphere of Mars is not dense enough to produce elevation-dependent variations in impact craters > 20 m (Dycus, 1969). Alternatively, the subdued

morphology of the base terrains may indicate that surface processes have eroded or buried small craters on the lower flanks. The presence of both subdued and sharp-rimmed small craters in the base region but exclusively sharp-rimmed small craters in the summit region supports a resurfacing interpretation for the shield base.

The regional cumulative distributions for small craters ( $< 200$  m in diameter, or about 9 pixels in the 401B photographs) are not significantly changed by application of the crater selection criteria (Figs. 3.16 and 3.17). This may indicate the limit for the 401B photographs of accurately identifying noncircular or aligned craters, and it is possible that many of the small craters are endogenic in origin. The areal abundance of small craters would suggest that the summit flanks are older than both the caldera terrains and the base flanks. Truncation of summit flows by the caldera rim indicates the caldera postdates the summit flanks but craters  $> 270$  m indicate the summit and base flanks have the same impact cratering age. Extrapolation of cumulative distributions that include craters below the limit of identifying endogenic craters could result in erroneous relative age interpretations on volcanic surfaces.

Cumulative crater distributions were also obtained for the Tharsis plains northwest of Ascraeus Mons (Fig. 3.18) and four caldera floors (Fig. 3.19, numbered according to



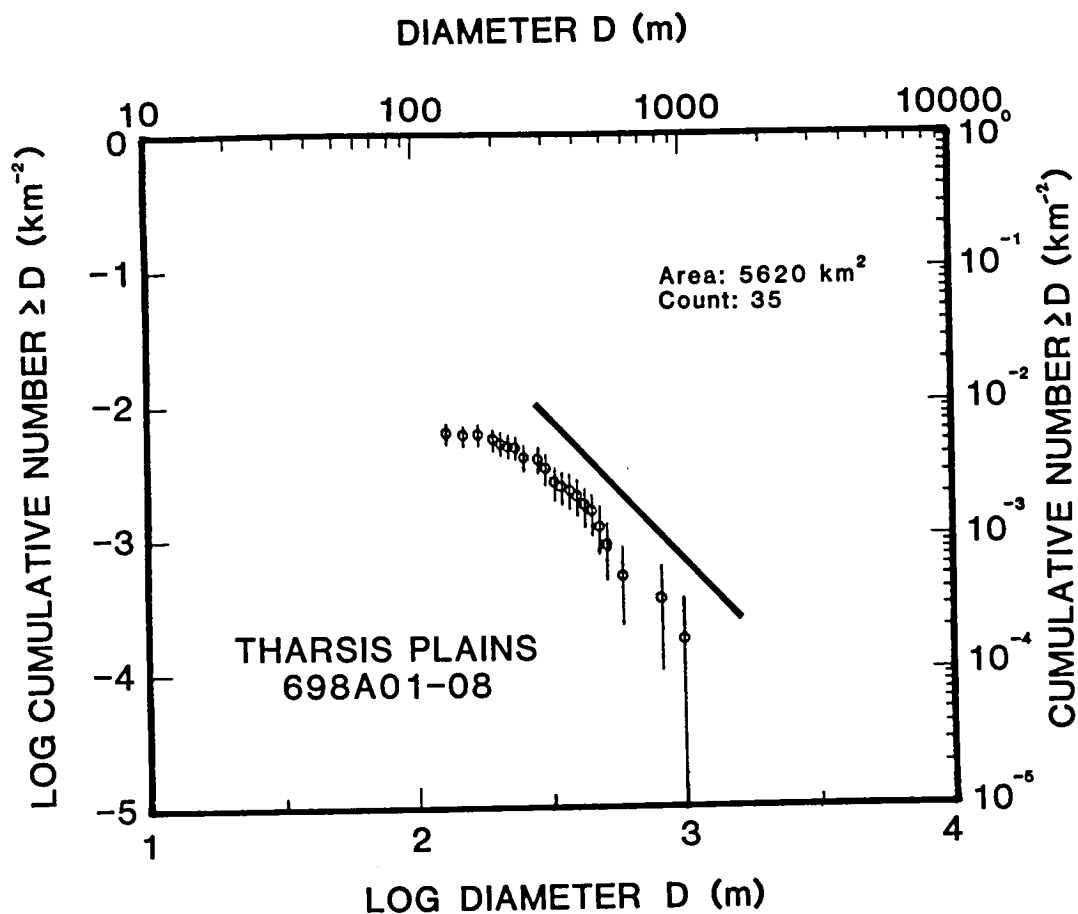


Figure 3.18. Cumulative distribution of all craters from Photographs 698A01-08 of the Tharsis plains northwest of Ascræus Mons (see Appendix 1 for location). Selection criteria for probable endogenic craters eliminated no craters. Center: 14.6°N, 107.5°W. Error bars represent  $\pm\sqrt{N}$ , where  $N$  is the measured number of craters within each diameter bin. Heavy line represents the shield distribution for craters >270 m in diameter, from Fig. 3.20.

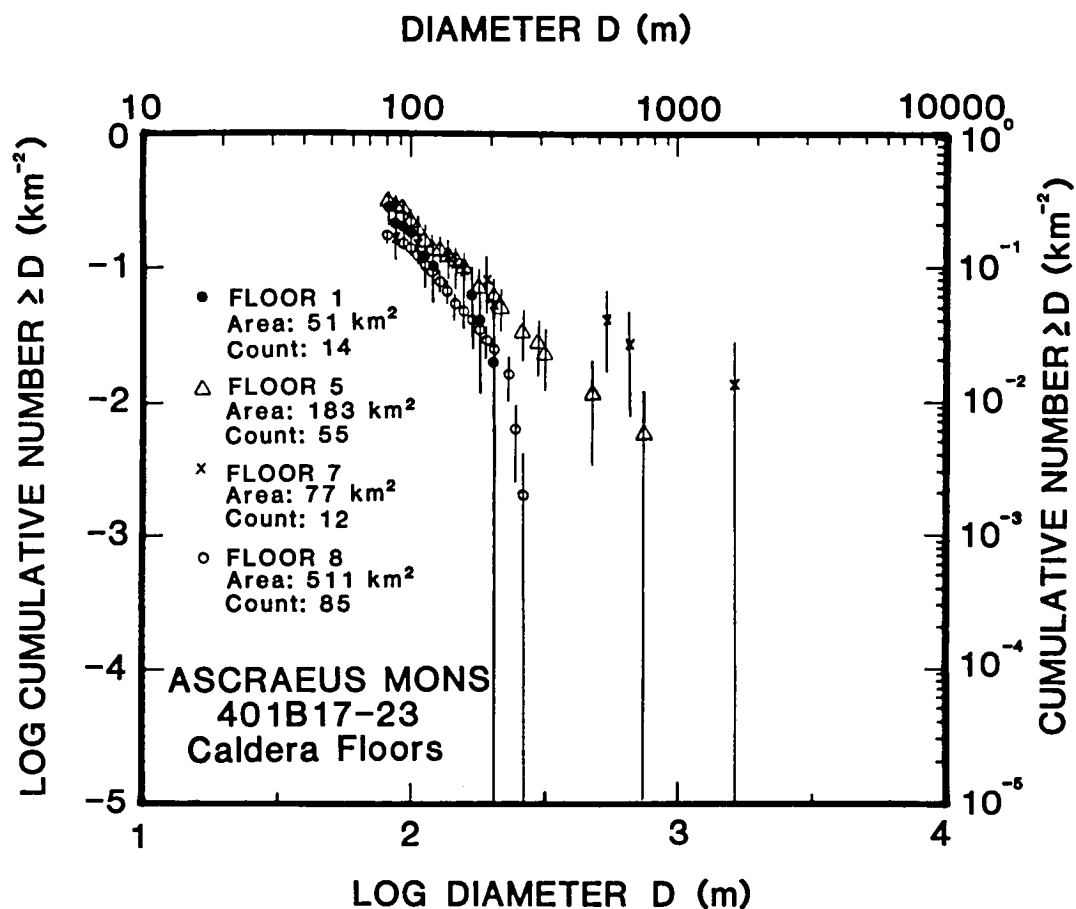


Figure 3.19. Cumulative distributions for impact craters on caldera floor areas included in the 401B photographs. Selection criteria for probable endogenic craters eliminated some craters on each floor. Floor areas are numbered according to Fig. 3.13. Error bars represent  $\pm\sqrt{N}$ , where  $N$  is the measured number of craters within each diameter bin.

Fig. 3.13). The areal abundance of craters on the plains is considerably less than the crater abundance on the shield flanks (represented by the solid line in Fig. 3.18), consistent with a younger relative age for the plains. Few endogenic craters were identified on the caldera floors, probably because most craters are < 250 m. The central caldera floor (Floor 8) has the only cumulative distribution statistically distinguishable from the other cumulative distributions. The central caldera floor has the lowest areal abundance of craters, consistent with its being the youngest caldera unit.

Cumulative crater distribution results for Ascraeus Mons from different investigators can be compared using crater retention ages, the cumulative crater frequency values at a specified diameter and area (Neukum and Hiller, 1981 and Table 3.2). The results for the flanks are consistent, except for the low value of Plescia and Saunders (1979). This may represent a discrepancy in counting procedures because both Crumpler and Aubele (1978) and Plescia and Saunders (1979) used the same photographs but they obtained quite different results. Neukum and Hiller (1981) used only the 401B photographs near the summit of Ascraeus Mons and projected the crater retention ages from the cumulative distribution for craters 100 to 600 m in diameter. The flank crater retention age obtained from Fig. 3.17) does not include craters < 270 m in

Table 3.2. Crater retention ages for Ascræus Mons.

Location	Cumulative number of craters ≥ 1 km per 10 <sup>6</sup> km <sup>2</sup>	Age in millions of years Neukum and Wise (1976)	Soderblom (1977)	Ref
<u>Ascræus Mons</u>				
Flanks	680 ± 270	2960 ± 1180	640 ± 250	(1)
	550 ± 320	2390 ± 1390	520 ± 300	(2)
	290 ± 500	1260 ± 2180	270 ± 470	(3)
	110 ± 62	480 ± 270	100 ± 60	(4)
Caldera (Central floor)	460 ± 950	2000 ± 800	430 ± 170	(5)
	120 ± 480	520 ± 2090	110 ± 390	(3)
<u>Tharsis Plains</u>				
Around Tharsis Montes	390 ± 22	1700 ± 100	360 ± 20	(6)
NW of Ascræus Mons	170 ± 170	740 ± 740	160 ± 160	(7)

Note: All ages rounded to the nearest 10 million years.

References:

- 1) This work (Fig. 3.17).
- 2) Crumpler and Aubele (1978, Fig. 11).
- 3) Neukum and Hiller (1981, Table 2).
- 4) Plescia and Saunders (1979, Table 2).
- 5) This work (Fig. 3.19).
- 6) Scott and Tanaka (1981, Table 1).
- 7) This work (Fig. 3.18).

diameter because of their excess abundance in the summit region; the Neukum and Hiller (1981) value is low because they included all small craters. Some of the variations in crater retention ages reported for the Tharsis volcanoes (Neukum and Hiller, 1981) may be due to the particular portion of the cumulative distribution that is used.

The crater retention ages for the shield flanks, the caldera floor, and the Tharsis plains agree with the stratigraphic relationships observed for these regions. The caldera floor results are highly uncertain because relatively few craters are present within the caldera complex, however, the results are consistent with the caldera postdating the shield flanks. The plains surrounding Ascraeus Mons are superposed over the shield terrain, consistent with the crater retention ages in Table 3.2. Cratering statistics are not sufficient to compare the relative ages of the plains and the caldera floor.

Summary: The areal density and total abundance of craters on the flanks of Ascraeus Mons decreases with decreasing elevation, particularly for craters  $< 200$  m in diameter. Elimination of probable endogenic craters results in equivalent cumulative crater frequency distributions in the summit and base regions for craters  $> 270$  m in diameter (Fig. 3.17); there is no observable relative age difference on the flanks for these craters. More craters of probable endogenic origin were identified

in the summit region than in the base region, consistent with results obtained from Olympus Mons (Carr et al., 1977). Resurfacing contributes to the lower crater abundances of the base region, indicated by the presence of both subdued and sharp-rimmed craters. Calculated crater retention ages that include craters smaller than the effective limit for identifying probable endogenic craters (for the 401B photographs this limit is approximately 9 pixels, or 200 m) may be biased toward values lower than those indicated by larger craters.

### Structure

Structural control is important for many of the features mapped on Ascræus Mons (Fig. 3.20 and Table 3.3). Grabens and faults are present throughout the vicinity of Ascræus Mons, some of which postdate both the shield and plains. Some features, such as the channels associated with the shield embayments, may not be the result of tectonic forces but the channels sometimes parallel adjacent grabens and possibly some channels followed grabens present before the embayment development.

Structural features in the plains surrounding Ascræus Mons include faults and linear to arcuate grabens. Several grabens extend south from Ceraunius Fossae between 106° and 108°W longitude (Map 1 and Fig. 3.20). Individual grabens in this area typically are 10 to 100 km long, < 2

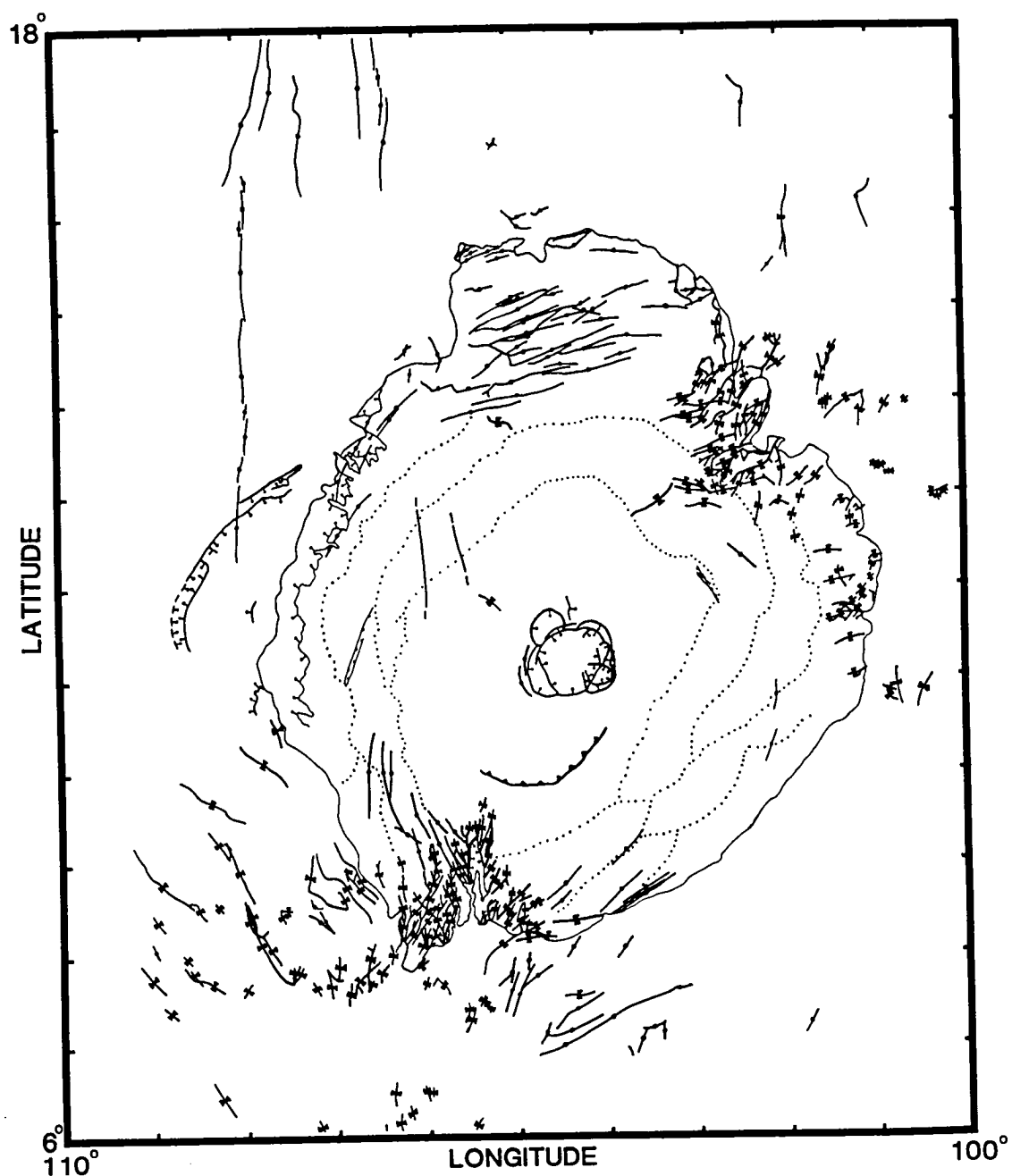













Figure 3.20. Structural map for Ascræus Mons, from Map 1. Symbols are defined in Table 3.4. Channel features have been included here because some channels merge into structurally controlled grabens. The shield-plains contact and the caldera rim are included for reference to Figs. 3.1 and 3.2.

Table 3.3. Symbols for Fig. 3.20.

(All symbols dashed where inferred)

	Contact
	Crater rim
	Graben, balls on downdropped side
	Fault, ball on downdropped side
	Thrust fault, sawteeth on upper plate
	Ridge, following crest
	Aligned pits
	Base of terrace
	Channel, at shield embayments
	Sinuuous channel
	Flow margin, hachures point down front



Km wide, and are oriented N-S. At 20°N, 104°W, one 10 km-wide graben crosscuts several p3 flows as well as the p2 plains north of Ascræus Mons. Arcuate grabens concentric to Ascræus Mons are located south and southwest of the shield, primarily within the p1 plains. Several of these grabens merge into channel features that emerge from the embayment on the southwestern flank of the volcano. An arcuate 10 km wide by 80 km long fault-bounded depression is present in the mountainous terrain west of Ascræus Mons. The western fault of this depression continues 60 km into the p2 plains as a scarp several hundred m high (Fig. 3.5). This feature is generally aligned with the shield margin and could represent a volcanotectonic depression associated with nearby flank eruptions.

The northwestern flank of Ascræus Mons has two linear faults that roughly parallel each other along a N5°W orientation (Fig. 3.20). Both faults are aligned with grabens in the plains northwest of the shield. The tectonism responsible for the N-S oriented grabens probably also produced the linear faults on the northwest flank. This tectonic activity corresponds to the most recent faulting in the Tharsis, centered on Pavonis Mons (Plescia and Saunders, 1982).

The shield flank is interrupted by arcuate terraces that are roughly concentric to the summit but elongated parallel to the N40°E trend of the Tharsis Montes (Fig.

3.20). Individual terraces are 30 to 50 km wide, with a convex profile at the lower terrace margin. The terraces crosscut and terminate each other on the northwestern and southeastern flanks but they are parallel on the other flanks. Terraces on Olympus Mons are interpreted to be the result of faulting concentric about a magma chamber (Carr et al., 1977). Applying this interpretation to Ascræus Mons would suggest that it had an elongate magma chamber or one that migrated along the Tharsis Montes trend. Alternatively, regional stresses could have contributed to the stress field on the volcano (see Carr, 1974a), resulting in terrace faults further from the summit of the volcano along the trend of the Tharsis Montes.

Linear to slightly arcuate grabens are common on the lower portions of the shield (Fig. 3.20). The embayment channels may have modified (through erosion) any grabens that were present on the southwestern and northeastern flanks prior to the development of the embayments. Grabens on the southwestern and southern margins of the shield are concentric to an area approximately 50 km southwest of the central caldera floor. The western and eastern flanks have relatively few grabens but they are concentric to the volcano summit. The northern base of the shield has many E-W oriented grabens that merge into coalescing depressions. These northern grabens are concentric to an area roughly 50 km northeast of the central caldera floor.

The graben orientations around the shield may be influenced by magma chamber locations or, more likely, regional stress patterns as discussed above in relation to the terraces.

An arcuate feature south of the summit is > 130 km long and is delineated by a sinuous ridge. Carr (1975) mapped this feature as a fault and Crumpler and Aubele (1978) mapped it only as a ridge. Stereoscopic photographs (387A06,16) indicate this ridge has a convex profile, with a rounded front on the downslope side but a gradual transition into the shield materials on the upslope side. The ridge relief is typically twice that of overlying flows, suggesting 30 to 90 m of relief for the ridge. On the Moon, ridges similar to the Ascræus Mons ridge have been interpreted both as flow fronts (Hodges, 1973; Scott, 1973) and as thrust faults (Howard and Muehlberger, 1973). No flow features appear to be directly associated with the Ascræus Mons ridge, favoring a thrust fault interpretation for this feature.

Thrust faulting results from near horizontal compressional stresses that exceed the strength of the surface rocks. The maximum length of a block that can be pushed downslope is limited by the crushing strength of the material and the shear stress exerted on the block (Hubbert and Rubey, 1959):

$$x = \frac{1}{(1 - \lambda) \tan \phi - \tan \theta} \cdot \left[ \frac{a}{\rho g \cos \theta} + \frac{b + (1-b)\lambda z}{2} \right] \quad (\text{Eq. 3.1})$$

$$a = 2 \tau_0 \sqrt{b}$$

$$b = (1 + \sin \phi) / (1 - \sin \phi)$$

where  $x$  is the maximum block length,  $\lambda$  is the pore pressure to the stress (normal to the surface) base of the block,  $\phi$  is the angle of internal friction,  $\theta$  is the slope,  $z$  is the block thickness,  $a$  is the crushing strength,  $b$  is the ratio between the maximum and minimum stresses, and  $\tau_0$  is the cohesion. A value of  $x$  longer than the value obtained above would be characteristic of a reverse fault because the crushing strength is greater (Hubbert and Rubey, 1959).

The maximum length of a thrust block under dry conditions was calculated from Eq. 3.1 for non-volcanic and igneous materials (Table 3.4). The pore pressure on Mars is likely at or near zero; pore pressures ( $\tau_0 < .1$ ) do not significantly affect block size limitation. The ridge associated with Ascræus Mons fault suggests that the thickness of the shield material involved in the thrust sheet is of the order of the precise value of the thickness is not certain. Individual segments of the ridge are typically 10 km wide and 5 to 15 km long, occupying a zone about 100 km wide. These values exceed the maximum block length for unconsolidated tuff (Table 3.4), indicating that comminuted materials do not comprise the major part of the shield materials. If the tuff became well

Table 3.4. Maximum length of a thrust block (km).

Pore Pres. $\lambda$	Block Thickness (m)			
	10	100	300	1000
<u>Basalt</u> ( $\tau_0 = 380$ bars, $\phi = 49^\circ$ )				
0.0	20.2	20.5	21.2	23.6
0.1	22.7	23.0	23.7	26.1
0.4	35.7	36.0	36.8	39.5
<u>Andesite</u> ( $\tau_0 = 285$ bars, $\phi = 45^\circ$ )				
0.0	16.0	16.3	16.9	19.1
0.1	17.9	18.2	18.9	21.2
0.4	28.4	28.8	29.5	32.2
<u>Granite</u> ( $\tau_0 = 185$ bars, $\phi = 57^\circ$ )				
0.0	9.1	9.5	10.3	13.0
0.1	10.2	10.6	11.4	14.2
0.4	15.8	16.2	17.1	20.1
<u>Unconsolidated Tuff</u> ( $\tau_0 = 5$ bars, $\phi = 42^\circ$ )				
0.0	0.5	0.8	1.4	3.6
0.1	0.6	0.9	1.5	3.8
0.4	0.9	1.3	2.0	4.7

Results were obtained with Eq. 3.1. Cohesion and internal friction values are averaged from Handin (1966, p.273). Density was taken to be  $2.5 \text{ gm cm}^{-3}$  for the basalt, andesite, and granite and  $1.5 \text{ gm cm}^{-3}$  for the unconsolidated (nonwelded) tuff. Slope was  $5^\circ$  for all cases.

crushing strength may increase sufficiently to accommodate the observed fault dimensions. No compositional information can be inferred from the martian thrust fault but the great length of the fault should be more easily attained from the longer thrust blocks permissible in basalt.

Summary: The plains surrounding Ascraeus Mons include grabens concentric to the volcano and N-S oriented grabens (northwest of the volcano) resulting from the most recent faulting in Tharsis (Plescia and Saunders, 1982). The shield flank is interrupted by arcuate terraces that may represent faulting concentric to a magma chamber, as proposed for Olympus Mons terraces (Carr et al., 1977). Both the terraces and the arcuate grabens on the shield flanks are elongated along the N40°E trend of the Tharsis Montes, suggesting that regional stresses may have contributed to the orientations of some faulting on the volcano. An arcuate feature south of the summit caldera is interpreted to be a thrust fault. The width of the zone affected by the thrust fault is greater than the theoretical maximum length of a thrust block composed of unconsolidated tuff, indicating that comminuted materials do not comprise the major portion of the flank materials.

### Rheology Estimates

Physical properties such as viscosity and yield strength directly influence the morphology of a lava flow. In the absence of samples from martian lava flows, these properties can only be estimated from the flow dimensions. The relationships between various physical properties and the flow dimensions were derived through the adaptation of several simplifying assumptions in order to utilize measurements obtained from photographs. The complexity and variety of mechanisms involved in the generation of lava flow morphology (see Sparks et al., 1976; Moore et al., 1978) indicate that these models do not incorporate many processes observed on terrestrial lava flows. However, the rheology estimates should allow some general comparisons to be made between lava flows on Ascraeus Mons and other volcanoes.

Geometric parameters were measured for six well-defined flows in the summit area of Ascraeus Mons (Fig. 3.21). Relative heights were obtained using shadow lengths and the local solar incidence angle. The darkest flow margins are assumed to be the result of a shadow and not a photometrically darkened but still illuminated surface. This assumption is valid if all of the flow margins measured have fronts with slopes  $> 24^\circ$ , which should be the case if these fronts are near the angle of repose. Measurements were made at different locations along each

## Flows Measured For Rheology Estimates

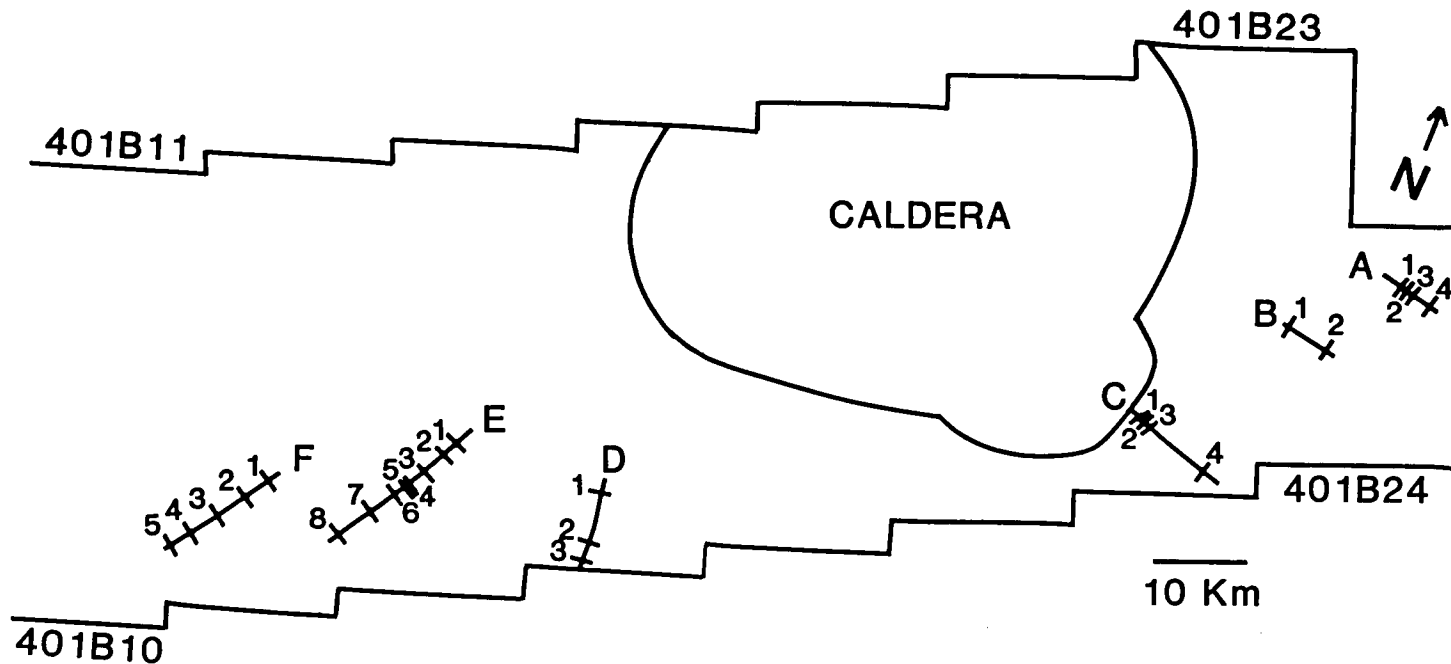


Figure 3.21. Location map of the summit area flows measured for rheology estimates. Photomosaic outline corresponds to the eastern portion of the 401B photographs (Fig. 3.4). Numbers identify the locations where flow dimensions were measured (perpendicular to the flow direction) on each of the six flows. Yield strength estimates for each location are given in Table 3.6 and Fig. 3.22.



flow in order to assess the down-flow variability of the parameters. Table 3.5 lists the values for the flow locations shown in Fig. 3.21 and the resulting yield strengths obtained from Eqs. 2.2 through 2.4.

The yield strength estimates range from 3400 to 84000  $\text{Nt m}^{-2}$ , with an average value of 21000. Fig. 3.22 illustrates the variation in yield strengths with position along the flows; no consistent trend is seen. Three of the flows (A, E, F) have distinct terminations, indicating the estimates apply to the distal portion of these flows, but the other three flows (B, C, D) could include distal, proximal, or both portions of the flows. Subtle variations down slope on flow E (Fig. 3.23) may be related to individual flow segments resulting from changes in flow direction through local topographic control (Borgia et al., 1983).

There are systematic differences in the yield strengths obtained from Eqs. 2.2 to 2.4. The results related to flow thickness and slope ( $Y_1$ , Eq. 2.2) show the least variation between the six flows as well as the greatest consistency downflow. The results related to flow thickness and width ( $Y_2$ , Eq. 2.3) are consistently lower than the  $Y_1$  values at the same location while the results related to levee width and slope ( $Y_3$ , Eq. 2.4) are consistently higher than the  $Y_1$  values. It is possible that the higher  $Y_3$  values result from processes that modify

Table 3.5. Yield strength estimates for six Ascræus Mons flows.

Flow	H (m)	W (m)	w (m)	$\theta$ (deg)	Y1	Y2 (Nt m <sup>-2</sup> )	Y3
A 1	30	1170	410	6.0	3.0E4	7.3E3	7.9E4
2	30	980	410	6.0	3.0E4	8.7E3	5.9E4
3	30	1040	410	6.0	3.0E4	8.2E3	6.5E4
3	40	1310	500	6.0	3.9E4	1.2E4	8.4E4
B 1	20	680	-	6.0	2.0E4	5.6E3	-
2	30	1000	-	6.0	3.0E4	8.6E3	-
C 1	20	630	300	5.0	1.7E4	6.0E3	2.4E4
2	20	660	360	5.0	1.7E4	5.8E3	2.2E4
3	15	530	220	5.0	1.2E4	4.0E3	2.2E4
4	25	1710	-	5.0	2.1E4	3.5E3	-
D 1	20	510	330	5.0	1.7E4	7.5E3	1.3E4
2	25	570	260	5.0	2.1E4	1.0E4	2.2E4
3	30	480	250	5.0	2.5E4	1.8E4	1.7E4
E 1	45	880	-	5.0	3.7E4	2.2E4	-
2	35	630	430	5.0	2.9E4	1.8E4	1.4E4
3	25	960	210	5.0	2.1E4	6.2E3	5.4E4
4	30	1230	580	5.0	2.5E4	7.0E3	4.7E4
5	25	1340	470	5.0	2.1E4	4.4E3	6.3E4
6	25	1370	-	5.0	2.1E4	4.3E3	-
7	40	1220	-	3.5	2.3E4	1.2E4	-
8	30	1350	-	3.5	1.7E4	6.3E3	-
F 1	25	1770	-	3.5	1.4E4	3.4E3	-
2	25	1380	-	3.5	1.4E4	4.3E3	-
3	30	2040	-	3.5	1.7E4	4.2E3	-
4	30	800	-	3.5	1.7E4	1.1E4	-
5	30	570	-	3.5	1.7E4	1.5E4	-

Averages: 2.2E4 8.6E3 4.2E4  
Cumulative average: 2.1 ( $\pm 1.8$ ) E4

Flow identification corresponds to locations shown in Fig. 3.21. Heights were determined from shadow lengths and local solar incidence angle, rounded to the nearest 5 m. Widths were measured directly from photographs, rounded to the nearest 10 m. Slopes were interpolated from the nearest 1 km contours (see Fig. 3.4b). Yield strength values for Y1, Y2, and Y3 were obtained from Eqs. 2.2, 2.3, and 2.4, respectively. Value in parentheses for the cumulative average is the standard deviation of the calculated values.

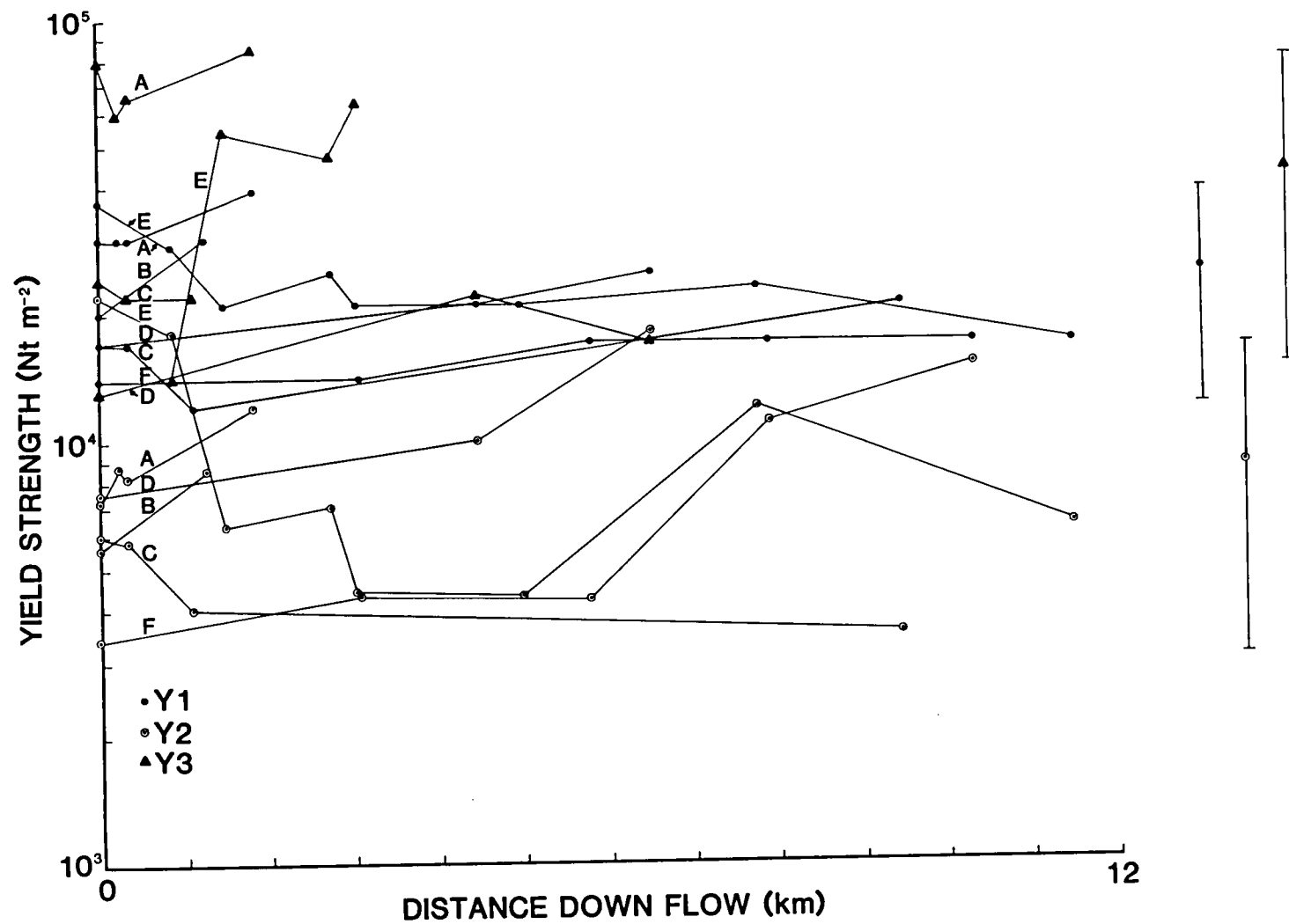


Figure 3.22. Yield strength values calculated for Ascræus Mons flows.

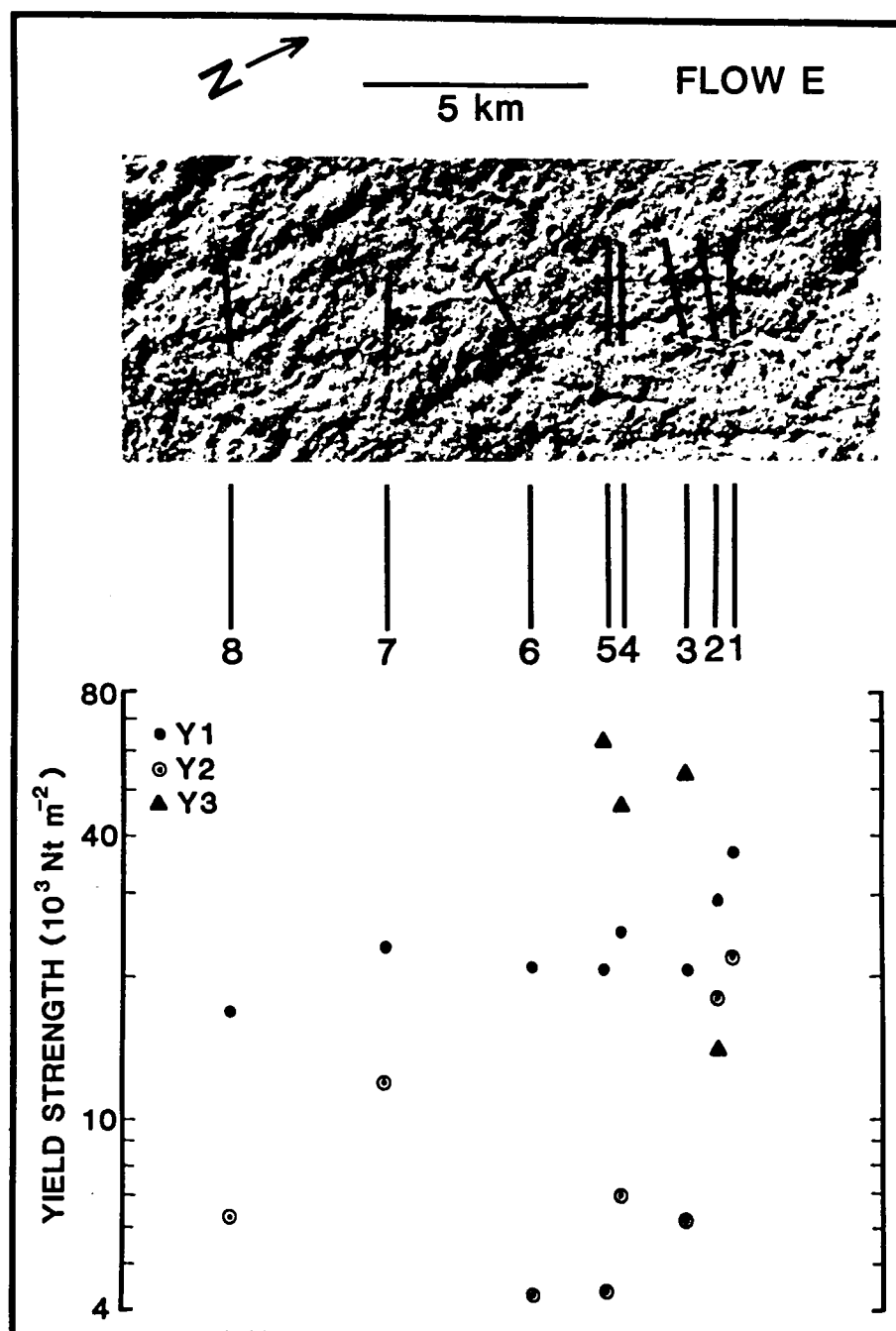


Figure 3.23. Yield strength values calculated for flow E of Fig. 3.21. Values correspond to the eight locations indicated along the flow profile. Equations 2.2 through 2.4 were used to obtain yield strength values Y1 through Y3, respectively. Photograph 401B14, nongradient high pass filtered orthographic projection. Center:  $10.4^\circ\text{N}$ ,  $105.1^\circ\text{W}$ .

or enlarge the levees during flow emplacement while the lower Y2 values may represent the most fluid portions of the lava that achieved the greatest lateral extent.

Yield strength estimates have been obtained for flows on the Earth, Moon, and Mars through this procedure (Table 3.6). The Ascraeus Mons values are similar to the values for both Olympus Mons and Mauna Loa and they are only slightly larger than the values for Kilauea and Arsia Mons. These "shield" values (for basalt flows on the terrestrial shields) are distinctly separated from both the higher Mount St. Helens value (for dacite flows) and the lower Mare Imbrium value (for very fluid flood basalts). These results, in addition to the flow morphologies, suggest that most Ascraeus Mons lavas are probably basaltic in composition and generally similar to lava flows on terrestrial shield volcanoes.

One of the flows (A in Figs. 3.21 and 3.22) has several regularly spaced ridges near its distal end (Fig. 3.11, large arrow). The ridges are perpendicular to the flow direction and extend beyond the leveed central channel at some locations. Fink (1980) related the dominant fold wavelength on a flow surface to the viscosity contrast between the surface and interior of the flow:

$$\eta_0 > \rho g h / 0.08 E_{xx} \ln R \quad (\text{Eq. 3.4})$$

$$R = \eta_0 / \eta_i > \exp (28 h / \lambda) \quad (\text{Eq. 3.5})$$

where  $\eta_0$  is the surface viscosity,  $h$  is the ridge

Table 3.6. Yield strength estimates for flows on the Earth, Moon, and Mars.

	Nt m <sup>-2</sup>	References
Mt. St. Helens, Wash.	1.5 (±0.8) E5	Moore <u>et al.</u> (1978)
Olympus Mons, Mars	3.1 (±1.2) E4	Moore <u>et al.</u> (1978)
Ascraeus Mons, Mars	2.1 (±1.8) E4	This work
Olympus Mons, Mars	2.0 (±0.3) E4	Hulme, 1976
Mauna Loa, Hawaii	1.3 (±1.1) E4	Moore <u>et al.</u> (1978)
Kilauea, Hawaii	3.8 (±3.1) E3	Moore <u>et al.</u> (1978)
Arsia Mons, Mars	1.0 (±0.8) E3	Moore <u>et al.</u> (1978)
Mare Imbrium, Moon	1.5 (±0.5) E2	Moore and Schaber (1975)

Mt. St. Helens value applies to dacite flows (Moore et al. (1978). Values in parentheses are standard deviations of the calculated values, not formal error limits (after Moore et al., 1978).

height (assumed to approximate the thickness over which the viscosity increases),  $E_{xx}$  is the compressive strain rate,  $R$  is the ratio of surface to interior viscosities,  $\eta_i$  is the interior viscosity, and  $\lambda$  is the arc length of the ridge folds (roughly equivalent to the ridge spacing). The compressive strain rate is related to the ridge growth time; this cannot be directly obtained from the photographs but can be approximately constrained.

The ridges on flow A are 15 m high (obtained from shadow lengths), with an average spacing of 120 m. Substituting these values into Eqs. 3.4 and 3.5 results in interior viscosities of  $1.3 \times 10^9$  to  $2.2 \times 10^{11}$  poise for ridge growth times of 1 hour to 1 week, respectively. These values are orders of magnitude larger than typical basalt viscosities ( $10^3$  to  $10^5$  poise); instead they are closer to dacite or rhyolite viscosities ( $10^{11-12}$  poise) (Macdonald, 1972, p.64). Flow A has the highest yield strength estimates among the Ascræus Mons flows (Fig. 3.22), consistent with a more evolved magma. The morphology of the martian flow is less similar to terrestrial rhyolite flows than to andesite or dacite flows, however, a trachyte flow on Hualalai, Hawaii, has ridges similar to the martian flow and a calculated viscosity only a factor of two higher than the calculated martian value (see Chapter 5). The Hawaiian trachyte flow represents extreme differentiation of alkali basalt magma

that probably became isolated from the main magma chamber of the volcano (Macdonald and Abbott, 1970, p.305); a similar origin is possible for the ridged martian flow.

Effusion rates have also been estimated for flows from geometric measurements (Hulme, 1976; Wilson and Head, 1983). The effusion rate is a function of yield strength and channel width, both parameters having large exponents (Wilson and Head, 1983). This causes the calculated values to be highly sensitive to measurement errors. The calculated effusion rates for all of the Ascræus Mons flows are  $< 100 \text{ m}^3 \text{ sec}^{-1}$ , so that more than 100 days was required to generate the observed flows. An Olympus Mons flow (computed effusion rate =  $470 \text{ m}^3 \text{ sec}^{-1}$ ) had an estimated 85 day eruption duration (Hulme, 1976). These results are consistent with the 5 to  $1000 \text{ m}^3 \text{ sec}^{-1}$  effusion rates and  $< 1$  to 400 day eruption durations observed for Hawaiian (Malin, 1980) and Icelandic (Williams and McBirney, 1979, p.101) basaltic eruptions.

Summary: Yield strengths estimated from the dimensions of six flows near the summit of Ascræus Mons averaged  $21000 \text{ Nt m}^{-2}$ . This value is similar to yield strengths calculated for other martian and terrestrial shield volcanoes but an order of magnitude less than the value for dacite flows on Mt. St. Helens, Washington, and two orders of magnitude greater than the value for lunar flood



basalts. Ridge dimensions on one Ascræus Mons flow provide a calculated interior viscosity orders of magnitude greater than basaltic viscosities but similar to the calculated interior viscosity of a trachyte flow on Hawaii; isolated pockets of magma may be responsible for individual flows of differentiated lavas. Calculated effusion rates and eruption durations for the Ascræus Mons flows are consistent with observations of Hawaiian and Icelandic basaltic eruptions.

#### Discussion

Most of the features identified on Ascræus Mons are consistent with observations of other shield volcanoes both on the Earth (Carr and Greeley, 1980) and Mars (Greeley and Spudis, 1981). Two aspects of the base region (lower flank) morphology of Ascræus Mons are particularly noteworthy: 1) the erosional features that postdate the shield flows, and 2) the subdued morphology of all base region terrains in high resolution photographs.

Shield erosion. Irregularly shaped depressions on Ascræus Mons appear to be the result of mass wasting. They are prevalent on the western and northwestern flanks of the volcano. It is possible that the lower portions of the eastern flank were similarly eroded and have subsequently been covered by the plains (Fig. 3.6a), however, the depressions on the western flank occur at high

enough elevations that they should have remained uncovered by the plains if they were present elsewhere on the volcano. This suggests that conditions on the western and northwestern flanks were particularly favorable for the mass wasting process. Morning and early afternoon clouds develop daily over the western and northwestern slopes of all of the Tharsis volcanoes during northern hemisphere spring and summer (Briggs et al., 1977). Although there is no evidence of fluvial activity on Ascraeus Mons, it is possible that condensation and evaporation of volatiles was concentrated on this part of the volcano. This suggests that the mass wasting process could involve the removal of volatiles stored in the surface, such as the sublimation of ground ice (Lopes et al., 1982). The cratering record on Ascraeus Mons suggests that the volcano is probably old enough to accommodate the subsurface accumulation of volatiles required by this erosional process. Additional processes, discussed next for the embayment channels, may also be involved in the mass wasting features.

The embayments into the southwestern and northeastern flanks consist of coalescing channels with blunt headward (upslope) terminations. Headwall undermining, or sapping, through groundwater seepage or dry mass wasting after ground ice sublimation has been proposed as the erosional process responsible for the bluntly terminated martian features

(Sharp, 1973; Sharp and Malin, 1975). Permafrost has been proposed as a contributing factor in a mass movement origin of the Olympus Mons aureole (Lopes et al., 1980, 1982), suggesting that ground ice may be present within martian volcanoes. Other proposed channeling agents include lava (Carr, 1974b), water (Milton, 1973), faulting (Schumm, 1974), wind (Cutts and Blasius, 1979), lahars (Christiansen and Greeley, 1981), and liquid hydrocarbons (Yung and Pinto, 1978). The embayment channel morphology is not consistent with the wind, water, faulting, and hydrocarbon mechanisms but lava and debris flows (lahars) cannot be ruled out. The embayments are sources for the p4 plains, supporting the possible role of lava in channel formation. However, the lack of flow fronts on the p4 plains could result from burial of the volcanic surface by debris flows. Lava erosion, ground ice sublimation, and debris flow generation are all viable alternatives for the embayment channeling process.

Both the irregularly shaped depressions and the embayment channels are typically < 1 km deep, so both features represent erosion to roughly the same depth. This may indicate that erosion on Ascræus Mons only proceeds to a certain depth. A uniform depth of erosion could be due to a level of more competent materials, such as dense (nonvesicular) basalt; terrestrial shield volcanoes tend to be built of numerous superposed lava flows (Macdonald,

1972, pp.272-275) without volcano-wide competent layers. Alternatively, the erosional process may only be effective to some critical depth. If sublimation of ground ice is responsible for the erosion, the erosional features on Ascraeus Mons would suggest the ground ice is present only to a depth  $< 1$  km, perhaps due to internal heating that would not allow ice to collect below some depth. If liquid water collected below this depth, it could potentially produce debris flows. Finally, the uniform depth could also be due to lava resurfacing that partially filled the floor of the erosional scars.

The irregular or straight outlines of these features would suggest that some process may be predominant for each feature (e.g. ground ice sublimation for the irregular depressions and the fluid flow processes for the channels). Volcanic processes and the release of volatiles, either water or ground ice, probably both contribute to the flank erosion on Ascraeus Mons.

Summary: Irregularly shaped depressions appear to be the result of mass wasting and the embayment morphology suggests that a sapping process produced the channels. Both features may be the result of lava erosion, ground ice sublimation, and debris flow generation; none of these processes can be excluded based on the data available. The different outlines of both features (irregular and straight) may indicate that ground ice sublimation is more

likely for the irregular depressions while fluid flow is more likely in the channels.

Subdued base morphology. The subdued terrains on the basal portion of the Ascraeus Mons shield indicate a different environment or surface history from that of the summit region. Possible explanations for the production of the subdued morphology can be broadly categorized as: 1) erosion of the surface, 2) deposition of material on the surface, and 3) chemical alteration of the surface. Both the erosional and depositional mechanisms could include fluvial, glacial, mass movement, aeolian, and volcanic processes while alteration would involve chemical reactions potentially influenced by the surface processes. None of the Ascraeus Mons photographs contain morphologic features indicative of fluvial activity. Glacial processes have been proposed for several locations on Mars (Luchitta, 1982), including Olympus Mons (Hodges and Moore, 1979), but again there is no other evidence of glacial activity on Ascraeus Mons. Tectonically induced mass movements on Ascraeus Mons are identifiable only as fault-associated features; it would seem unlikely that the entire base region was extensively modified through mass movement. Aeolian and volcanic processes are considered to be the most likely physical methods for modifying the base terrains.

The surface morphology would be expected to vary

considerably depending on whether erosion, deposition, or alteration were the dominant mechanism. Aeolian erosion could produce streamlined yardangs (Ward, 1979) and complex exhumation relationships among surfaces of differing age (Greeley et al., 1979) while volcanic erosion might be evidenced by channels radial to the vent area (Reimers and Komar, 1979). None of these erosional features (aeolian or volcanic) are observed in the base area.

Aeolian deposition could produce a variety of dune forms, depending upon the wind regime (Bagnold, 1941) while deposition of particles (dust) out of suspension would blanket the preexisting topography, as in loess deposits on Earth (Flint, 1971, pp.251-266). Pyroclastic deposits might take the form of localized pyroclastic flows, areally extensive ignimbrite sheets, or airfall deposits (Macdonald, 1972, pp.122-170). Explosive eruptions may produce distinctive bedforms near the vent area (Wohletz, 1980) while airfall deposits would mantle the preexisting topography (Macdonald, 1972, pp.135-139). No dunes are evident in the base region of the shield, although these features could be present on a scale below the resolution limit (22 m per pixel) of the photographs. Deposition out of suspension appears to be the most likely physical mechanism for producing the subdued morphology, although dunes < 50 m in horizontal scale could be present but unidentifiable.

There would be no readily distinguishable morphologic difference between deposits of either volcanic or aeolian origin produced by particles that settled out of suspension. Both types of deposits should generally increase in thickness toward the source area (e.g. vent or source area for loess) (Macdonald, 1972, p.137-8; Flint, 1971, p.255-6) and the increasingly subdued morphology with decreasing elevation would suggest a source external to the volcano. Individual flow margins are visible throughout the base region except in the smooth terrain; if these flows are comparable in height to the summit region flows (15 to 45 m) then the materials deposited on the surface are probably < 15 m thick over most of the base region but > 45 m thick on the smooth terrain. These thickness variations may indicate changes in the local efficiency of the deposition or repeated depositional events.

Chemical alteration of surface materials could potentially modify surface morphology through the redistribution of the weathered products. Earth-based spectral analyses suggest that weathered basaltic glass is a good candidate for the source material of martian dust (Allen et al., 1981; Singer, 1982). Volcanic heat sources could provide localized areas of substantially increased alteration. The volcano is sufficiently old to allow ample time for weathering to have progressed to the point of influencing surface morphology on the scale of 10s

of m, however, redistribution of the weathering products is needed in order to continue exposing unaltered materials to weathering. Once again both volcanic and aeolian processes could be involved, along with considerable mass movement. The surface morphology provides no constraint on the chemical weathering of the surface but physical processes would still need to be associated with the surface modification.

Summary: The subdued morphology of the shield base terrains is most likely the result of deposition of dust-sized particles out of suspension, either from aeolian or volcanic processes. Deposit thicknesses are probably < 15 m except on the smooth terrain, where it could be > 45 m. Chemical weathering could contribute to a breakdown of surface features but redistribution of the weathering products by surface processes would still be required. Photographic resolution is not sufficient to eliminate the possibility that dunes, representing collections of sand-sized particles, may also be present on the shield if their horizontal scale is < 50 m.

#### Summary: Geologic History

The geologic history of Ascræus Mons can be broadly divided into five stages: 1) activity prior to construction of the shield, 2) shield construction, 3) caldera collapse at the summit, 4) shield erosion and flank



eruptions associated with the Tharsis plains, and 5) recent surface modification.

Pre-shield stage. Very little of the surface that pre-dated the commencement of Tharsis Montes volcanism remains exposed in the vicinity of Ascraeus Mons. The Ceraunius Fossae surface underwent considerable N-S oriented faulting prior to emplacement of the Tharsis plains. The immense Tharsis Rise may be the result of either isostasy and lithospheric loading (Banerdt et al., 1982) or constructional volcanism (Solomon and Head, 1982) but either process involved voluminous outpourings of lava that buried the pre-Tharsis Rise surface. The eruptions became localized at the crest of the Tharsis Rise, leading to construction of the Tharsis Montes shield volcanoes. The Tharsis Montes eruptive activity generally migrated northeast from Arsia Mons to Ascraeus Mons.

Shield-building stage. Eruption of fluid lavas (most likely basalts) became centralized at 11°N, 104°W, building a broad, shallow-sloped (5°) volcanic construct. The hills and knobs of the mountainous terrain west of the shield were emplaced prior to the flows on the shield. Individual shield flows included gently undulating plains surrounding sinuous channels (interpreted to be pahoehoe flows), lobate flows with 15 to 45 m high margins and leveed channels (interpreted to be aa or block flows),

and hummocks 200 to 1000 m apart (interpreted to be toey pahoehoe flows). Thrust faulting disrupted the southern flank and all of the lower flanks became terraced (either through faulting or localized volcanism), however, all of these features were crossed by subsequent shield flows. The width of the thrust fault indicates that unconsolidated materials (such as nonwelded tuff) do not comprise the major portion of the shield flank. Flow dimensions suggest that the yield strength, effusion rate, and eruption duration of the Ascraeus Mons lavas are similar to the basaltic lavas on terrestrial shield volcanoes. Viscosity estimates for one ridged flow are orders of magnitude larger than basalt viscosities; it is possible that magma bodies separated from the main magma chamber of the volcano may have resulted in isolated flows of differentiated lavas. The cratering record indicates that the flanks of Ascraeus Mons are probably at least 600 million years old (Table 3.2).

Caldera stage. Repeated collapse of the summit area produced a caldera complex with at least nine distinct centers of collapse, most of which are not coincident. Lava lakes occurred within each caldera depression, only to be disrupted by subsequent collapse events. No flows go into the calderas from the summit flanks; caldera development postdated all effusive activity on the uppermost flanks. Caldera and summit area morphology do

not indicate the occurrence of late-stage pyroclastic activity associated with caldera collapse (Mouginis-Mark, 1981). Crosscutting of caldera floors and walls by subsequent caldera collapses indicates a decreasing elevation of lava flooding with time, perhaps related to diminishing hydrostatic magma pressure near the end of summit area volcanism. The most recent caldera floor is probably at least 400 million years old (Table 3.2).

Shield erosion stage. Portions of the shield surface were eroded by mass wasting, particularly on the western and northwestern lower flanks. The plains surrounding Ascræus Mons were emplaced by flank eruptions that may have either accompanied or postdated the flank erosion. Voluminous flows erupted from centers between Ascræus Mons and Pavonis Mons and northeast of Ascræus Mons; these flows have distinct margins, and are much larger than the individual flows on Ascræus Mons. Channelized erosion embayed the southwestern and northeastern flanks (aligned with the Tharsis Montes trend), which became the sources of the latest plains emplaced around Ascræus Mons. Grabens disrupted both the shield and the plains surfaces. Most grabens are approximately concentric to the summit of the volcano, however, those northwest of the shield are oriented N-S and are located within a topographic depression identified from lava flow directions. These N-S grabens are associated

with the latest tectonic events recorded throughout the Tharsis region (Plescia and Saunders, 1982). The plains northwest of Ascraeus Mons are probably at least 150 million years old (Table 3.2).

Recent stage. The shield base includes smooth-appearing terrain that postdates all other terrain units and structural features on the volcano. The smooth terrain is an extreme example of the subdued surface morphology evident on all shield base terrains. The subdued appearance of all surface features increases with decreasing elevation from the summit area, coincident with a decreasing abundance of small (< 200 m diameter) craters. The surface of the volcano has been modified by processes that result in an elevation-dependent variation in morphology; aeolian, volcanic, and weathering processes appear to be the most likely agents for the surface modification. Variations in albedo provide evidence that aeolian movement of materials is presently occurring on the Tharsis volcanoes (Lee, 1984).

## CHAPTER 4. SURFACE PROPERTIES

### Introduction

Most remote sensing analyses of Mars have concentrated on data of moderate or low spatial resolution to establish global and regional trends in properties such as albedo and thermal inertia. In order to address geologic questions for specific features the remote sensing data should be of sufficient resolution to distinguish terrain types within the study area. Ascræus Mons has a good combination of high and moderate resolution data collected at visual to radar wavelengths.

Remote sensing measurements of Ascræus Mons are variable in coverage and resolution but they are sufficiently diverse to complement the description of the surface materials obtained strictly from photographs (Chapter 3). Appendix 1 includes a description of quality, resolution, and coverage for the data discussed in this chapter. Photographs of Ascræus Mons taken through red, green, and violet filters ( $\lambda = 0.4$  to  $0.7 \mu\text{m}$ ) were combined to provide a color view of the volcano and to quantify the reflectance properties of the volcano surface at visible wavelengths. Infrared measurements ( $\lambda = 7$  to  $24 \mu\text{m}$ ) provide surface temperatures, and the variation of the surface temperature throughout the day (quantified as thermal inertia) can be related to the

particle size and porosity in the uppermost several cm of the surface materials. Radar data ( $\lambda = 3$  to 13 cm) provide the elevation of the surface while the strength and spectral shape of the reflected signal can be related to the roughness of the surface on the scale of 10 cm to 100 m. The water vapor abundance of the atmosphere was determined from infrared measurements of absorption bands due to water. These data cover a range of scales from that of the atoms comprising the surface materials to features approaching the resolution limit of the best photographs.

This chapter begins with the reflectance properties obtained from the color photographs of Ascræus Mons, along with their relationship to the spectrally superior but spatially inferior Earth-based measurements. Thermal inertias obtained from high resolution thermal sequences are correlated with the terrain units on the volcano (from Chapter 3), and moderate resolution sequences are used to expand the spatial and temporal coverage of the thermal results. Previously published data on the surface roughness of the volcano at radar wavelengths and the abundance of atmospheric water vapor above the volcano are discussed in relation to the results obtained here. The discussion section presents a synthesis of the properties observed at different wavelengths. A summary of the geologic implications of the remotely determined surface properties of Ascræus Mons concludes the chapter.

### Visual Reflectance

Sunlight reflected from planetary surfaces provides compositional information through the location and intensity of absorption features; the red color of Mars results from a strong  $\text{Fe}^{3+}$  absorption in the ultraviolet (Singer et al., 1979). Earth-based spectral data cannot spatially resolve the individual shield volcanoes from the surrounding Tharsis plains. However, Viking color photographs provide visual reflectance values at three wavelengths that can be compared to the Earth-based spectra. Measurements at only three wavelengths cannot constrain spectral features other than the dominant Fe absorption but spatial variations in visual reflectance can be investigated.

A color photograph of Ascraeus Mons (Fig. 4.1) was produced by combining Viking Orbiter photographs taken through violet, green, and red filters (centered at 0.45, 0.53, and 0.59  $\mu\text{m}$  wavelengths, respectively). No corrections for a surface photometric function have been applied to this photograph. A diffuse haze obscures the surface below an elevation of approximately 13 km and wispy patches of clouds are present northwest of the volcano. These clouds and haze are similar to features observed around Ascraeus Mons early in the Viking mission (Briggs et al., 1977).

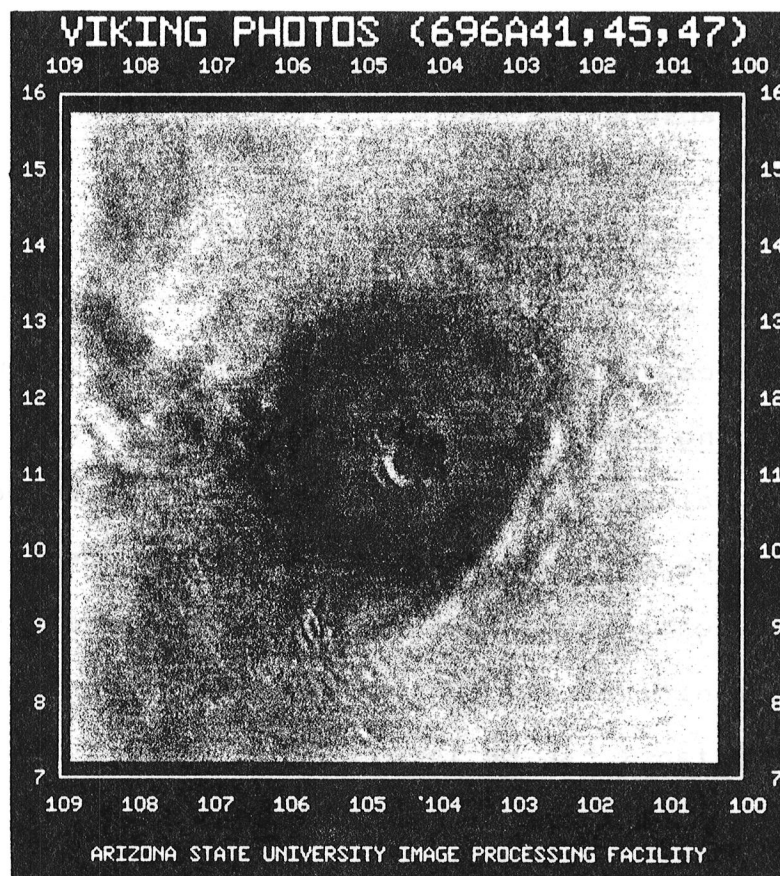


Figure 4.1. Color photograph of Ascræus Mons in early morning. Photographs taken through red, green, and violet filters were uniformly stretched so that the maximum brightness corresponds to an albedo of 0.137. The area shown here corresponds to the areas in Figs. 4.2, 4.4, 4.11, and 4.12. Appendix 1 provides information about the photographs.



The resolution of the color photograph (822 m per pixel) allows only large-scale features on the volcano to be identified. The southwestern and northeastern embayments into the shield base are both visible but they are partially obscured by the haze. The caldera complex is clearly outlined by shadows and highlights on the walls. The flank terraces on the eastern flank have strong highlights on the terrace faces.

The color patterns in the summit area of Ascraeus Mons are approximately symmetric around the caldera complex. The caldera complex and the summit area within 50 km of the caldera rim are a relatively uniform orange-brown. Below the summit area is a distinct ring of lower albedo; this "dark collar" is similar to low albedo rings observed on all of the Tharsis shield volcanoes (Veeverka et al., 1977; Lee et al., 1982). The lower margin of the dark collar is not clearly delineated because of the obscuring haze.

Soderblom et al. (1978) found that the Tharsis shield volcanoes have some of the highest red/violet ratios ( $\approx 3$ ) in the equatorial region of Mars, along with the oldest materials in the cratered southern hemisphere. The Ascraeus Mons red/violet ratio is  $< 2$  for the clouds and haze but  $> 3$  in the summit area (Fig. 4.2). The higher red/violet values on the western side of the volcano are due to the slope of the volcano surface, as discussed

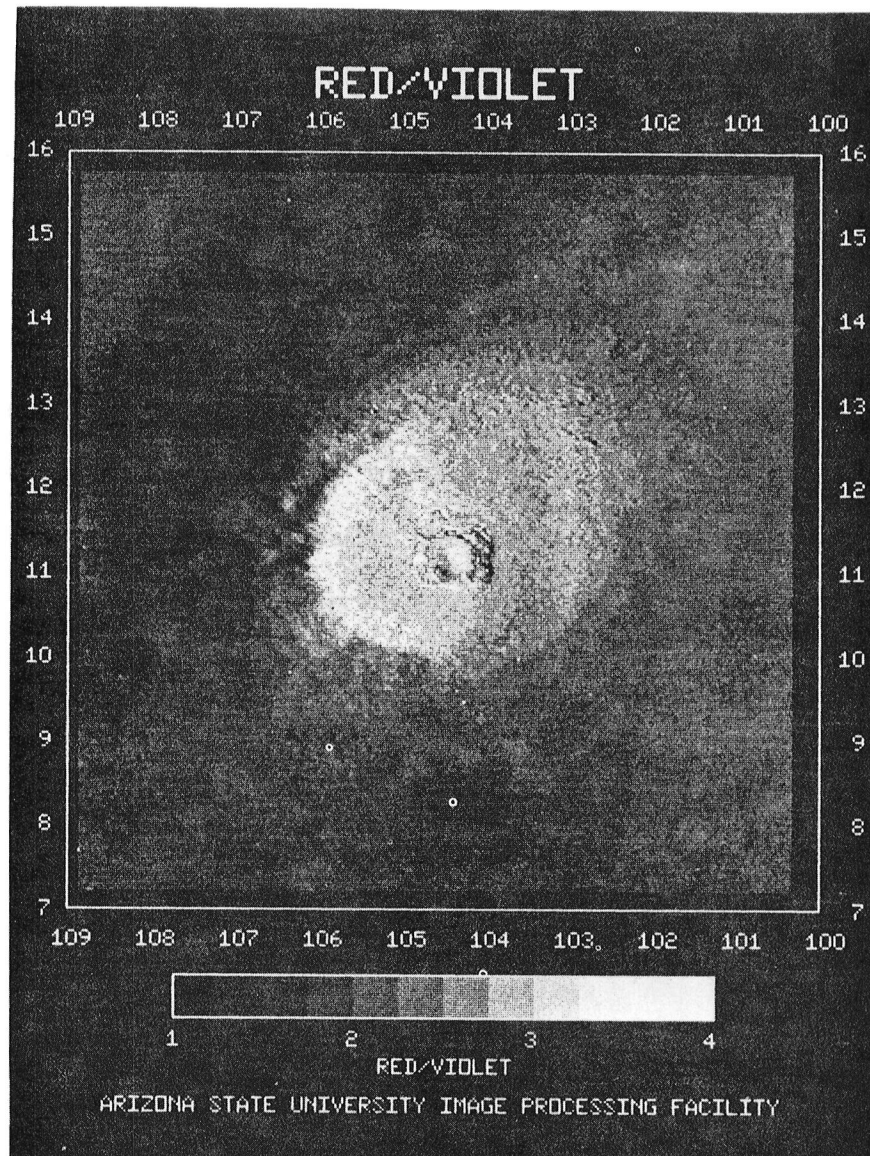


Figure 4.2. Red/violet ratio of photographs used in Fig. 4.1. Note the asymmetry associated with the illumination direction (from north of east).

below. The classical high albedo areas of the planet (e.g. Arabia, Tharsis) also have red/violet ratios  $> 3$  but they are twice as bright as the volcanoes and the southern hemisphere cratered terrain at visible wavelengths (Soderblom et al., 1978; McCord et al., 1982; Arvidson et al., 1982). Broadband albedos measured by the IRTM (0.3 to 3.0  $\mu\text{m}$ ) do not show the Tharsis volcanoes to be significantly darker than the high albedo Tharsis materials surrounding them (Pleskot and Miner, 1981), so the albedo difference between the volcanoes and the Tharsis plains could be confined to the visible wavelengths.

Nine locations from the color photograph were selected for quantitative evaluation of the reflectance properties (Fig. 4.3). Four locations sample the summit and dark collar materials, three locations sample one of the highlighted terrace faces on the eastern flank, and two locations sample the condensate haze and clouds. Table 4.1 lists the intensities at the three filter wavelengths, averaged from nine pixels that covered a total of 14.4  $\text{km}^2$  at each location.

Corrections for the surface photometric function provide the normal (zero incidence angle) albedo of the surface materials. Photometric variations on a surface assumed to be an ideal diffuse scatterer are described by the Lambert photometric equation (Short, 1975, p.61):

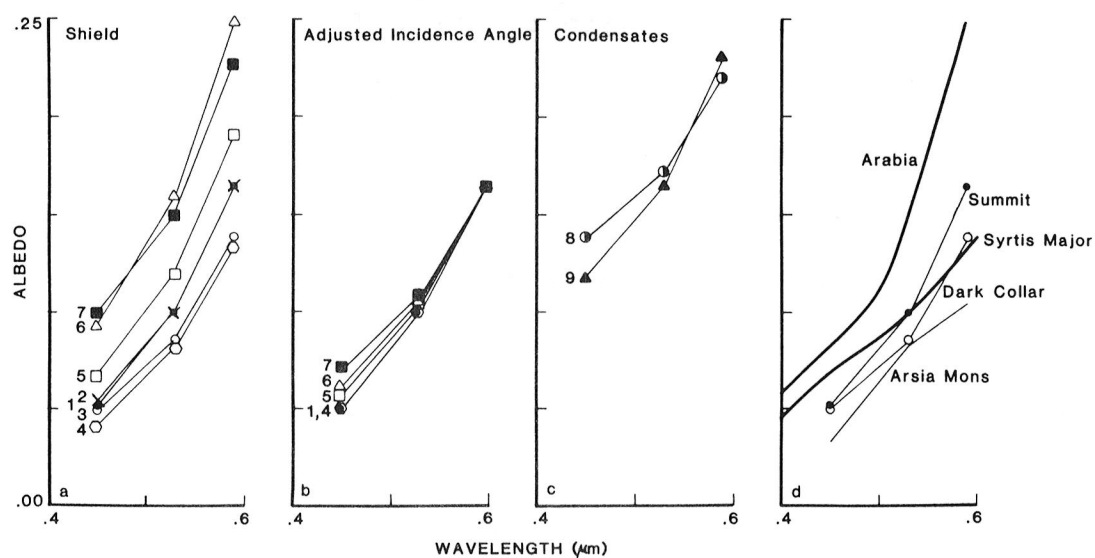
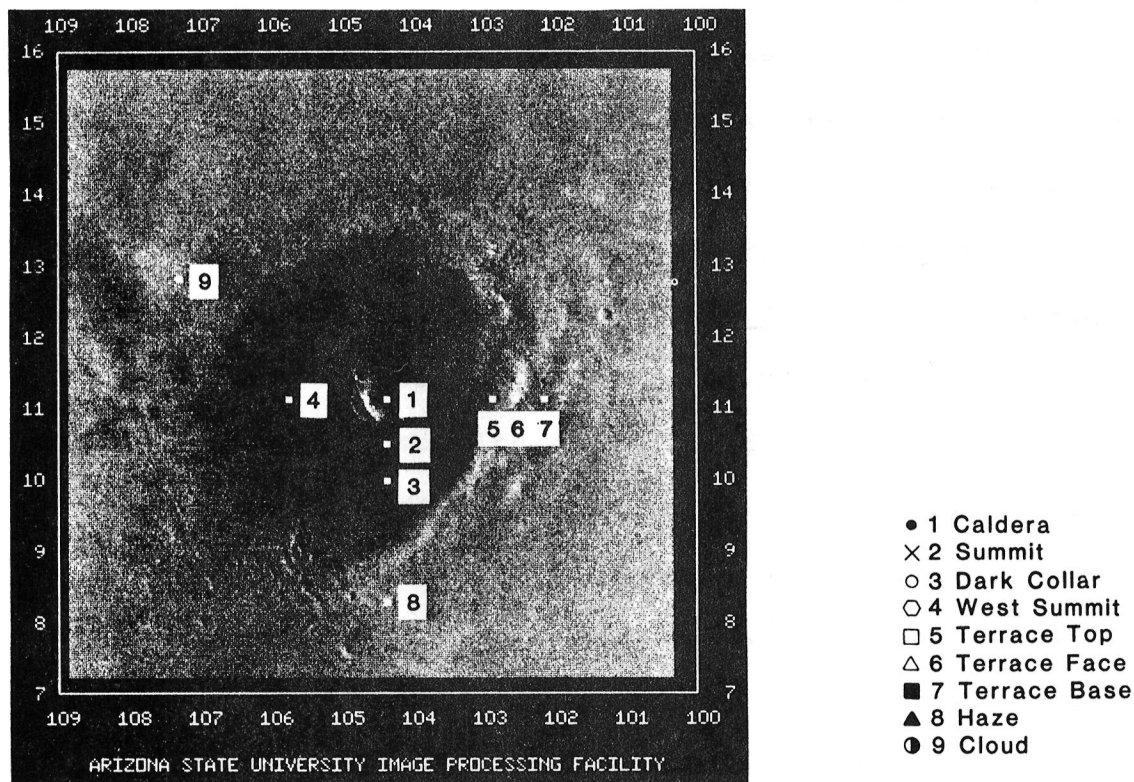


Figure 4.3. Ascræus Mons albedos. a) Shield locations, b) shield locations with incidence angles adjusted to match the caldera red albedo, c) condensate locations, d) comparison of albedos for Ascræus Mons with albedos for Arsia Mons, Syrtis Major, and Arabia (from Soderblom *et al.*, 1978, Fig. 17).

Table 4.1. Albedo values for Ascræus Mons.

	Violet	<u>Filter</u> Green	Red	
Location	<u>Photograph Intensities</u>			
1	.026(1)	.050(1)	.083(2)	
2	.027(1)	.050(1)	.083(2)	
3	.025(1)	.043(1)	.070(2)	
4	.021(1)	.041(1)	.068(2)	
5	.034(1)	.061(2)	.097(2)	
6	.047(1)	.081(2)	.126(3)	
7	.050(1)	.076(2)	.115(2)	
8	.060(1)	.084(1)	.117(1)	
9	.070(1)	.087(1)	.111(1)	
<u>Lambert Albedos</u>				
1	.051	.099	.164	i = 59.5
2	.053	.099	.164	59.5
3	.049	.085	.138	59.5
4	.041	.081	.134	59.5
5	.067	.120	.191	59.5
6	.093	.160	.248	59.5
7	.099	.150	.227	59.5
8	.118	.165	.230	59.5
9	.138	.171	.219	59.5
4	.051	.099	.164	65.5
5	.057	.103	.163	53.5
6	.061	.106	.164	40.0
7	.071	.108	.164	45.5
<u>Minnaert Albedos</u>				
i = 59.5°, e = 8.5°				
k = 1.2      .95      .95				
1	.059	.095	.158	
2	.061	.095	.158	
3	.057	.082	.133	
4	.048	.078	.129	
5	.077	.116	.185	
6	.106	.154	.240	
7	.113	.145	.219	
8	.136	.160	.223	
9	.158	.166	.211	

(Values in parentheses indicate the standard deviation of the third decimal place for nine values of the photograph intensity at each location).

$$A = A_0 \cos i \quad (\text{Eq. 4.1})$$

where  $A$  is the observed reflectance,  $A_0$  is the albedo at zero incidence angle, and  $i$  is the incidence angle of solar illumination measured from the surface normal. Table 4.1 lists the Lambert albedos at each location for the photograph incidence angle ( $59.5^\circ$ ) and at selected locations for other incidence angles.

Natural surfaces often differ significantly from the ideal surface described by the Lambert photometric function. The Minnaert photometric function incorporates the viewing angle, equivalent to the surface emission angle, into the photometric expression (Minnaert, 1941):

$$A = A_0 (\cos i)^k (\cos e)^{k-1} \quad (\text{Eq. 4.2})$$

where  $A$ ,  $A_0$ , and  $i$  are equivalent to the Lambert expressions given above,  $e$  is the emission angle measured from the surface normal, and  $k$  is a coefficient that varies with phase angle and surface material. Phase angle is defined as the angle between the illumination source (Sun) and the detector (spacecraft), measured at the target surface (Saunders and Mutch, 1980). The variation of  $k$  with phase angle produces the "opposition effect", enhanced reflectance near zero phase angle, observed in many different materials (Pleskot, 1981; Thorpe, 1982). At the  $57.5^\circ$  phase angle of the Ascræus Mons color photograph the Minnaert coefficient is 0.95 for the red filter and 1.20 for the violet filter (Thorpe, 1977). Table 4.1

includes Minnaert albedos for the nine locations; these values are quite similar to the Lambert albedos because the Minnaert coefficient is near unity and the emission angle is small. The simpler Lambert photometric function seems adequate for characterizing the surface albedos for Ascræus Mons.

The nine locations on Ascræus Mons show considerable differences between their Lambert albedos (Fig. 4.3). The change in albedo with wavelength is similar for the seven locations on the shield but the absolute values of the albedos vary widely (Fig. 4.3a). The central caldera floor (location 1) is nearly identical to the southern summit (location 2) while the dark collar materials (location 3) are darker than the summit areas at green and red wavelengths. The other four shield locations occur on the west and east flanks of the volcano where topographic effects are most evident for the photometric brightness of the surface. The albedos of locations 4 through 7 were adjusted to match the caldera floor and southern summit values by varying the incidence angle in Eq. 4.1. This procedure provides a new incidence angle for the four locations (Table 4.1). The calculated incidence angle can be related to the topographic slope of the surface, analogous to the computerized technique of Eliason et al. (1981) for obtaining topographic information from multispectral images. A  $6^\circ$  slope to the west causes the

western flank albedos (location 4) to precisely match the caldera floor albedos (Fig. 4.3b); this slope is similar to the  $4^\circ$  slope obtained from photogrammetry. A dark area directly north of the summit caldera (Fig. 4.1) corresponds to the western slope of a topographic peak in this area (Fig. 3.3), consistent with the photometrically darkened western flank. These results suggest that the entire summit area above the dark collar, including the caldera complex, is spectrally similar when corrected for topographic slope.

The adjusted albedos for the terrace (locations 5 through 7) have increasing violet and green albedo with increasing distance down the eastern flank of the volcano (Fig. 4.3b). The clouds and haze have spectra with violet albedos higher than at any shield location (Fig. 4.3c). This suggests that there is an increasing contribution from the haze with decreasing elevation, so that the photometrically inferred surface slopes become more inaccurate down the shield flank. The location above the terrace (5) has a photometrically determined slope of  $6^\circ$  to the east, in good agreement with the  $5.5^\circ$  slope obtained from photogrammetry, while below the terrace (location 7) there is a calculated  $14^\circ$  slope. If this  $8^\circ$  difference is attributed to the haze influence on the albedos, then the terrace front (location 6) can be inferred to have an  $11.5^\circ$  slope, or a  $5.5^\circ$  increase



over the average flank slope. The highlighting of terrace fronts up to  $90^\circ$  from the solar incidence direction suggests that these features could have locally increased albedos (possibly due to condensates) or enhanced scattering from features smaller than the resolution limit of the photograph.

The topography of the surface affects not only the magnitude of the albedos but also albedo ratios (e.g. red/violet; Fig. 4.2). The red/violet ratio has been used to classify reflectance variations on Mars (Soderblom et al., 1978; McCord et al., 1982). The Ascræus Mons results illustrate the potential influence of slopes  $\leq 6^\circ$  on albedo measurements; topographic effects need to be removed from reflectance measurements prior to classification of albedo differences.

The three-color albedos for Ascræus Mons are similar to but distinct from the albedos of Arsia Mons and Earth-based reflectance spectra (Fig. 4.3d). The Arsia Mons albedos (from Soderblom et al., 1978) are consistently less than the Ascræus Mons albedos. Both volcanoes have albedos more comparable to classical dark regions such as Syrtis Major but the wavelength dependence of the Ascræus Mons summit albedos parallels the spectral reflectance of the Arabia bright region (Earth-based data from McCord and Westphal, 1971). These comparisons suggest that the bright material interpreted to be present in the

bright regions (see Singer, 1982) is also present on Ascræus Mons. However, the lower albedo of Ascræus Mons in the visible wavelengths also suggests the bright material coverage is not as complete as in the classical bright regions. The dark collars on the martian volcanoes are interpreted to result from aeolian removal of dust from a darker substrate (Lee et al., 1982; Lee, 1984) so the summit of Ascræus Mons presumably has at least a partial covering of the bright dust. The lower albedos of Arsia Mons could indicate a more thorough removal of bright dust than occurs on Ascræus Mons; this would be consistent with the very extensive dark collar area observed on Arsia Mons (Lee, 1984, p.132). The location of Arsia Mons in the martian southern hemisphere possibly contributes to enhanced dust removal because dust storm activity is usually initiated in the southern hemisphere during maximum solar insolation near the perihelion of Mars (Gierasch and Goody, 1973).

Summary: Visual reflectances at three wavelengths were obtained from three Viking Orbiter photographs of Ascræus Mons. Clouds and a diffuse haze obscured the surface below an elevation of 13 km. Lambert albedos of the caldera complex and summit flanks within 50 km of the caldera rim have uniform values of .05 to .16 at 0.45 and 0.59  $\mu\text{m}$ , respectively, when corrections are made for the topographic slopes on the volcano. Slopes  $\leq 6^\circ$

affect both albedo magnitudes and the ratios between albedos at different wavelengths. The Ascraeus Mons albedos are larger than those of Arsia Mons and comparable in magnitude to earth-based spectra from classical dark regions like Syrtis Major. The wavelength dependence of the albedos at the summit of Ascraeus Mons parallels the spectra from classical bright regions like Arabia, suggesting bright material (dust) is present on the volcano. Aeolian activity removes this dust from the flanks to produce dark collars around the summits of the Tharsis volcanoes (Lee, 1984).

#### Thermal Inertias

Thermal inertia is a measure of the change in temperature of surface materials throughout the day (see Chapter 2). Low thermal inertia materials have large daily temperature variations because they cannot efficiently retain or conduct away heat. Thermal inertia is related to physical conditions such as particle size (Kieffer et al., 1973 and Fig. 2.7), porosity (Kieffer et al., 1977 and Chapter 5), and intergrain bonding (Horai, 1979; Dittion, 1982), all of which affect the surface thermal conductivity. These conditions may vary on terrains with different geologic histories. In this section the thermal inertias for Ascraeus Mons are evaluated in relation to the geologic terrain units.

Four high spatial resolution thermal sequences that cross Ascræus Mons are discussed first. Several corrections must be applied to these data in order to obtain an accurate representation of the thermal inertias on the volcano. All thermal inertias presented here are in units of  $10^{-3} \text{ cal cm}^{-2} \text{ sec}^{-1/2} \text{ K}^{-1}$ . The thermal inertias are then compared to the terrain units (from Chapter 3) in order to examine the geologic implications of the thermal measurements. The combination of nighttime and daytime measurements quantifies the surface temperature extremes throughout the day, which can be related to slope winds on the volcano. Temperature measurements at different wavelengths allow the abundance of spatially unresolved high thermal inertia materials to be determined (Christensen, 1982). Finally, moderate spatial resolution sequences are used to obtain the spatial distribution of thermal inertias over the entire volcano.

High resolution data. Thermal inertias calculated from the observed 20  $\mu\text{m}$  brightness temperatures display considerable disagreement between the four high resolution sequences (Fig. 4.4, uncorrected). These variations are the result of factors not incorporated into the standard thermal inertia calculation. Four such factors are: 1) positional errors along the groundtrack owing to uncertainty in the spacecraft position along the orbit groundtrack, 2) elevation-dependent thermal properties of

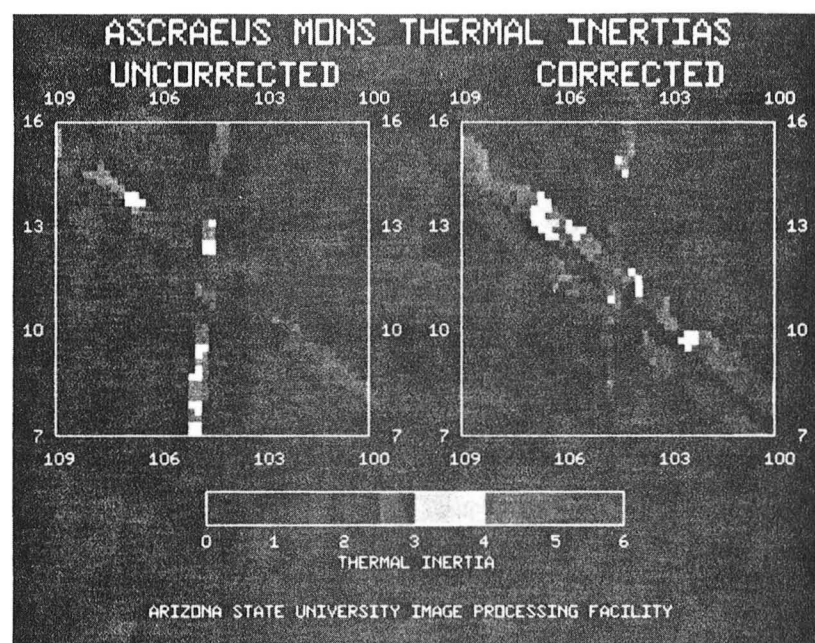


Figure 4.4. High resolution thermal inertias for Ascræus Mons. Left figure shows thermal inertias calculated from  $20\ \mu\text{m}$  brightness temperatures with no corrections. Right figure shows thermal inertias corrected for positional errors, elevation-dependent atmospheric effects, and temperature changes due to atmospheric dust and clouds over the volcano summit. Data were averaged in  $0.2^\circ$  by  $0.2^\circ$  lat/long bins. Note the similar corrected thermal inertias for the shield summit and the plains surrounding the volcano (compare with Fig. 4.1). Appendix 1 provides information about the individual sequences.

the martian atmosphere, 3) atmospheric particulates (dust and condensates), and 4) physical conditions (e.g. sensible heat exchange by winds) affecting the surface temperatures. These effects have been evaluated for the Ascraeus Mons thermal data through the simplifying assumptions described below (Fig. 4.4, corrected).

Positional errors for the high resolution data result from variations in the timing of data collection; the timing errors vary between orbits and are greatest near periapsis when the spacecraft is travelling fastest. The approximate magnitude and direction (up or down the groundtrack) of these errors are known (F. Palluconi, private communication, 1979) but each sequence must be individually manipulated to produce the best fit between ground features and the thermal data. The sequences that cross the summit caldera of Ascraeus Mons can be correlated with surface features to the spatial resolution limit of the data (6 to 8 km along the groundtrack). The one sequence that did not cross the summit caldera had a well-determined orbit and is assumed to be correctly positioned.

The topography of Ascraeus Mons covers a vertical range ( > 14 km) that is greater than the scale height of the martian atmosphere (10 km) (Leovy, 1979) and atmospheric properties vary considerably over this elevation interval. The thermal conductivity of

particulate materials decreases with decreasing atmospheric pressure under martian conditions (Wechsler and Glaser, 1965); however, this effect accounts for about one-third of the lower thermal inertias associated with the Tharsis region (Kieffer et al., 1973, 1977 and Chapter 2).

Jakosky (1979) showed that the thermal radiation from the atmosphere decreases with increasing elevation due to the decreasing atmospheric mass above the surface. This produces greater temperature variations at higher elevations than for the same material properties at low elevation. These elevation-dependent effects on surface temperatures have been removed from the thermal data through assumptions of 1) a uniform atmospheric scale height (10 km) and 2) atmospheric radiation being proportional to the atmospheric mass above a given elevation. Appendix 3 provides a description of this elevation correction procedure.

Jakosky (1979) modelled the thermal contribution from a dusty atmosphere and its effects on surface temperatures. His procedure overemphasized the thermal effects of the dust because scattering processes dominate over radiative processes in the martian atmosphere (Ditteon, personal communication, 1980). The complex optical and thermal properties of the dusty martian atmosphere (Zurek, 1978; Pollack et al., 1979) are not presently incorporated into thermal models that allow dust

corrections to be applied directly to the IRTM data. Moderate to low resolution IRTM data (with  $> 1000 \text{ km}^2$  per resolution element) covering more than a martian year provide evidence of temperature variations at different wavelengths resulting from atmospheric dust (Martin et al., 1979; Hunt, 1979; Christensen, 1982), water ice clouds (Kieffer et al., 1977; Hunt, 1979; Christensen and Zurek, 1984), and carbon dioxide ice clouds (Hunt, 1980), allowing an assessment to be made of the effects of these atmospheric processes on the high resolution thermal data.

The corrected thermal inertias include the addition or subtraction of a constant temperature prior to the elevation corrections in order to produce agreement between the individual sequences at their crossing points near the summit of Ascræus Mons. Sequence A543 (see Appendix 1) was used as the standard for comparison because of its optimum spatial resolution, time of day, and season. The temperature offsets applied to sequences A465, A659, and B484 were -4.5 K, 3 K, and 8 K, respectively. The warmer observed temperatures for sequence A465 are consistent with the increased atmospheric dust opacity at the time these data were acquired (see Table A1.2 in Appendix 1). The A465  $15\mu\text{m}$  atmospheric temperatures (T15) were 15 degrees warmer than the A543 T15 temperatures, consistent with a higher atmospheric dust content and increased



atmospheric thermal radiation to the surface. The lowered temperatures for sequence B484 are due to afternoon water ice clouds over the volcano, as evidenced by a  $-7$  K difference between the  $11$  and  $20$   $\mu\text{m}$  temperatures ( $T_{11}-T_{20}$ ) (after Christensen and Zurek, 1984). Variable cloud opacity over the shield may account for the great variability in the corrected thermal inertias for this daytime sequence.

Ditteon (1982) discussed the thermal effects of physical conditions not included in the Viking thermal model that could affect the calculated thermal inertias. Sensible heat exchange by winds, phase change of volatiles, non-Lambertian surface albedo, temperature dependence of thermal conductivity, and surface roughness all have a relatively small effect on the thermal inertias calculated with the standard Viking model. Vertical inhomogeneity (layering) of low thermal inertia materials ( $I \approx 2$ ) over high thermal inertia materials ( $I \approx 30$ ) is interpreted to be the cause of low temperatures, relative to the standard model, in Tharsis during the late afternoon (Ditteon, 1982). The low temperatures for the early evening sequence (A659) could be a result of layered thermal inertias throughout the Tharsis area.

The corrections described above provide thermal inertias that are better indications of the surface thermal properties. The corrected thermal inertias on Ascræus

Mons increase radially away from the summit area of the volcano. The summit area of the shield has thermal inertias very similar to the values for the Tharsis plains surrounding the volcano. The highest thermal inertias occur within the summit caldera and on the lower flanks of the shield. The thermal inertia change at the shield base correlates closely with the shield-plains geologic contact, discussed in more detail below. The corrected thermal inertias for the shield are still lower than the global average thermal inertia of 6.5 (Kieffer et al., 1977) but the shield materials do not have the exceptionally low thermal inertias proposed early in the Viking mission (Kieffer et al., 1976). This result reduces the need for advocating special materials on the volcano surfaces, such as extremely frothy or vesiculated lavas (Kieffer et al., 1976, 1977). The thermal inertias of Ascraeus Mons are comparable to or larger than the thermal inertias of the vast low thermal inertia regions that cover 20% of the surface area of Mars (Zimbelman and Kieffer, 1979).

Summary: The four high resolution thermal sequences of Ascraeus Mons display considerable disagreement prior to corrections for positional errors and elevation-dependent atmospheric conditions (Fig. 4.4). Atmospheric particulates (dust and condensates) and vertical inhomogeneity (layering of thermal inertias) also

contribute to apparent thermal inertia discrepancies. Corrected thermal inertias for Ascraeus Mons are comparable to or larger than the Tharsis plains thermal inertias; this reduces the need for advocating extremely frothy or vesiculated lavas on the volcano (e.g. Kieffer et al., 1977).

Terrain unit correlations. The high resolution IRTM sequences allow the thermal inertias of individual terrain units to be determined. Correlations between terrain units and thermal inertias have been observed both at a global scale (Kieffer et al., 1977) and with high resolution sequences (Zimbelman and Greeley, 1981, 1982). The thermal inertias (all elevation-corrected) of the terrain units identified on Ascraeus Mons were obtained from the high resolution thermal sequences discussed above.

Three of the high resolution sequences crossed the summit caldera of Ascraeus Mons, where the greatest variability of thermal inertias occurs (Fig. 4.5 and Map 3). The caldera walls have the highest thermal inertias observed in the summit area, with the highest values concentrated along the uppermost walls. The high thermal inertias for the afternoon sequence ( $I > 5$ ) are overestimated because of the lowered temperatures in shadowed areas adjacent to caldera walls. The thermal inertias for the caldera walls ( $I < 4.5$ ) are far below what would be expected for volcanic bedrock on Earth ( $I > 50$ )

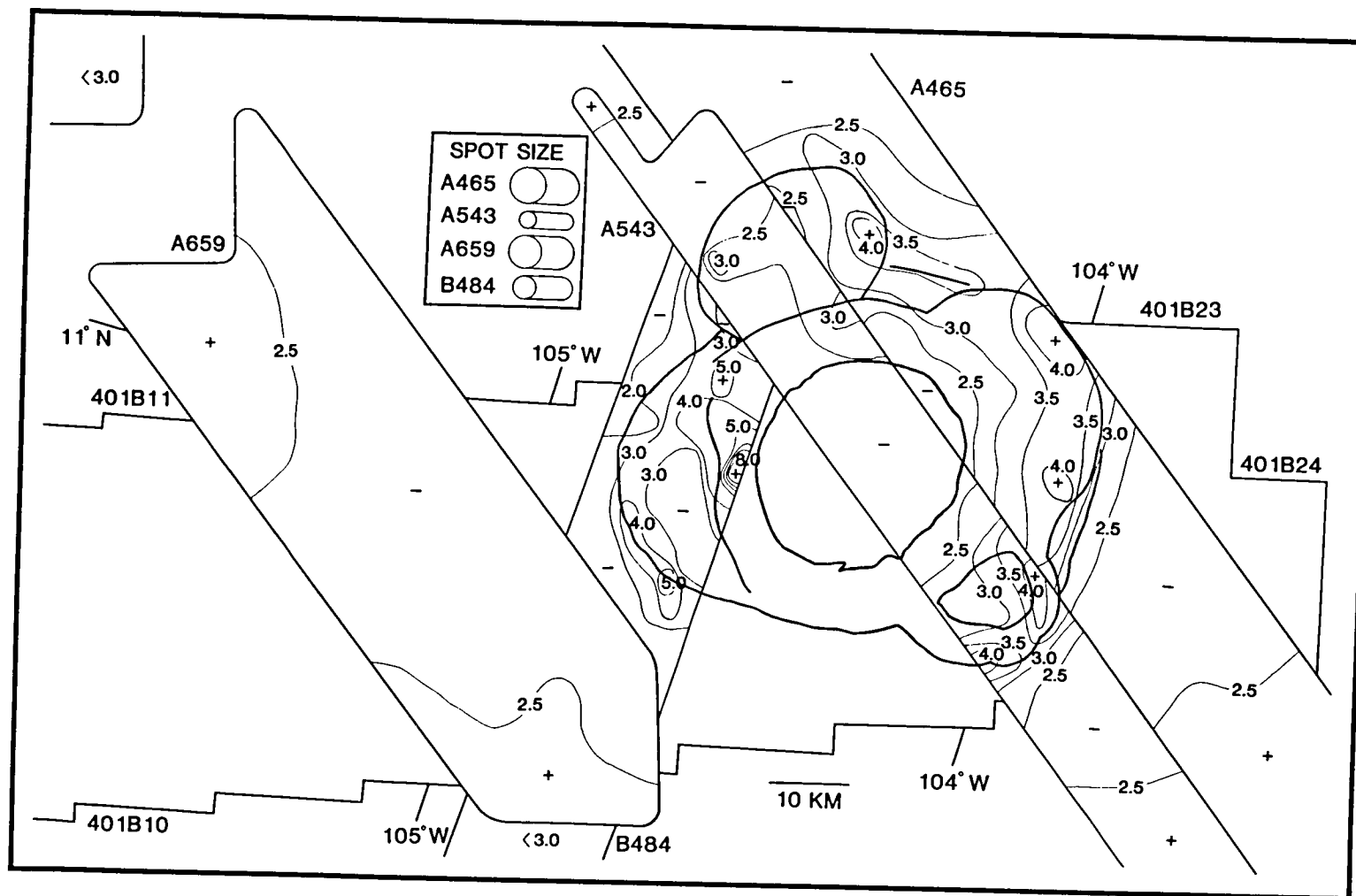


Figure 4.5. Corrected thermal inertias for summit caldera, from Map 3. Photomosaic outline corresponds to eastern portion of Fig. 3.4. Caldera rim and major floor segments are included for reference. Appendix 1 provides information about the individual sequences.

(Kahle, 1980). Atmospheric pressure differences between Earth and Mars suggest that the caldera wall materials would have a thermal inertia approaching 12 if they were on the Earth (see Chapter 5) but even this value does not indicate a dominant proportion of bedrock exposed in the walls. Differences between the IRTM thermal bands, discussed in more detail below, limit the abundance of unresolved high thermal inertia areas (e.g. bedrock) on the caldera walls to < 15%. It is possible that the spacecraft viewing angle reduced the observable thermal flux from near-vertical bedrock exposures within the walls, but this would increase the areal abundance of exposed high thermal inertia materials by less than a factor of two. The grooved caldera wall terrain (cwg, Fig. 3.12) probably has the highest thermal inertias and the most exposed bedrock, consistent with the photogeologic interpretation (Chapter 3). This indicates that mass wasting processes have buried most bedrock exposures produced by the caldera collapse events.

The floor of the central caldera and the summit flanks have similar thermal inertias ( $I = 2.0$  to  $2.5$ ; Fig. 4.5), even though these surfaces show considerable variation in morphology on the scale of 100 to 1000 m (see Chapter 3). The summit flanks covered by the high resolution thermal sequences include individual flows (f), low relief plains (p), and hummocky plains (h), while the central caldera

includes both grooved (cfg) and planar (cf) floor units. None of these terrain units has thermal inertias that are distinguishable from the average summit values.

A uniform thermal inertia for the distinctive terrain units in the summit area could indicate: 1) similar original surfaces or 2) surface modification that results in uniform thermal inertias. Thermal measurements of terrestrial volcanic terrains show temperature differences between pahoehoe and aa flows (Sabins, 1978, p.395 and Chapter 5); this is most likely the result of surface roughness differences on the mm to m scale (Winter et al., 1972). Both pahoehoe and aa flows are interpreted to be present on Ascræus Mons so it is unlikely that all of the summit terrains have identical original surfaces. Surface modification on Ascræus Mons, as discussed in Chapter 3, is probably depositional instead of erosional, which suggests that the summit terrains are all covered by materials of low thermal inertia ( $I \approx 2$ ). Jakosky (1979) has shown that, for planar surfaces, only 3 cm of low thermal inertia material ( $I = 2$ ) is needed to thermally mask underlying higher thermal inertia materials, so that a large quantity of low thermal inertia materials is not required to produce the observed thermal properties of the summit area. The distinct morphology of the summit terrains indicates that the low thermal inertia materials are much thinner than the observable flows ( $< 15$  m).

Both volcanic and aeolian processes may be responsible for the summit area low thermal inertias. Effective particle diameters for  $I = 2$  materials are probably  $< 30 \mu\text{m}$  (Fig. 2.7), consistent with either fine ash or dust. Summit area morphology shows no direct evidence of pyroclastic activity (Mouginis-Mark, 1981). Crater areal abundances have been used to interpret the presence of ash deposits on Hecates Tholus (Mouginis-Mark et al., 1982), however, no analogous deposits can be inferred from the cratering record on Ascraeus Mons. A pyroclastic origin for the fine materials would require great dispersal of the ash in order to cover all summit terrains to depths of at least several cm but not several m. The annual dust storms on Mars provide an aeolian source for the low thermal inertia materials, consistent with the reflectance data discussed above. The available evidence cannot rule out a volcanic origin for the summit area fine materials but an aeolian origin (i.e. dust) is consistent both with the reflectance data for Ascraeus Mons and the present martian climatic conditions.

The thermal inertias for the Ascraeus Mons shield generally increase down the flanks of the volcano and decrease again precisely at the shield-plains contact (Fig. 4.6). The higher thermal inertias at the shield base are associated with the main shield (terrain unit s1 of Map 1)

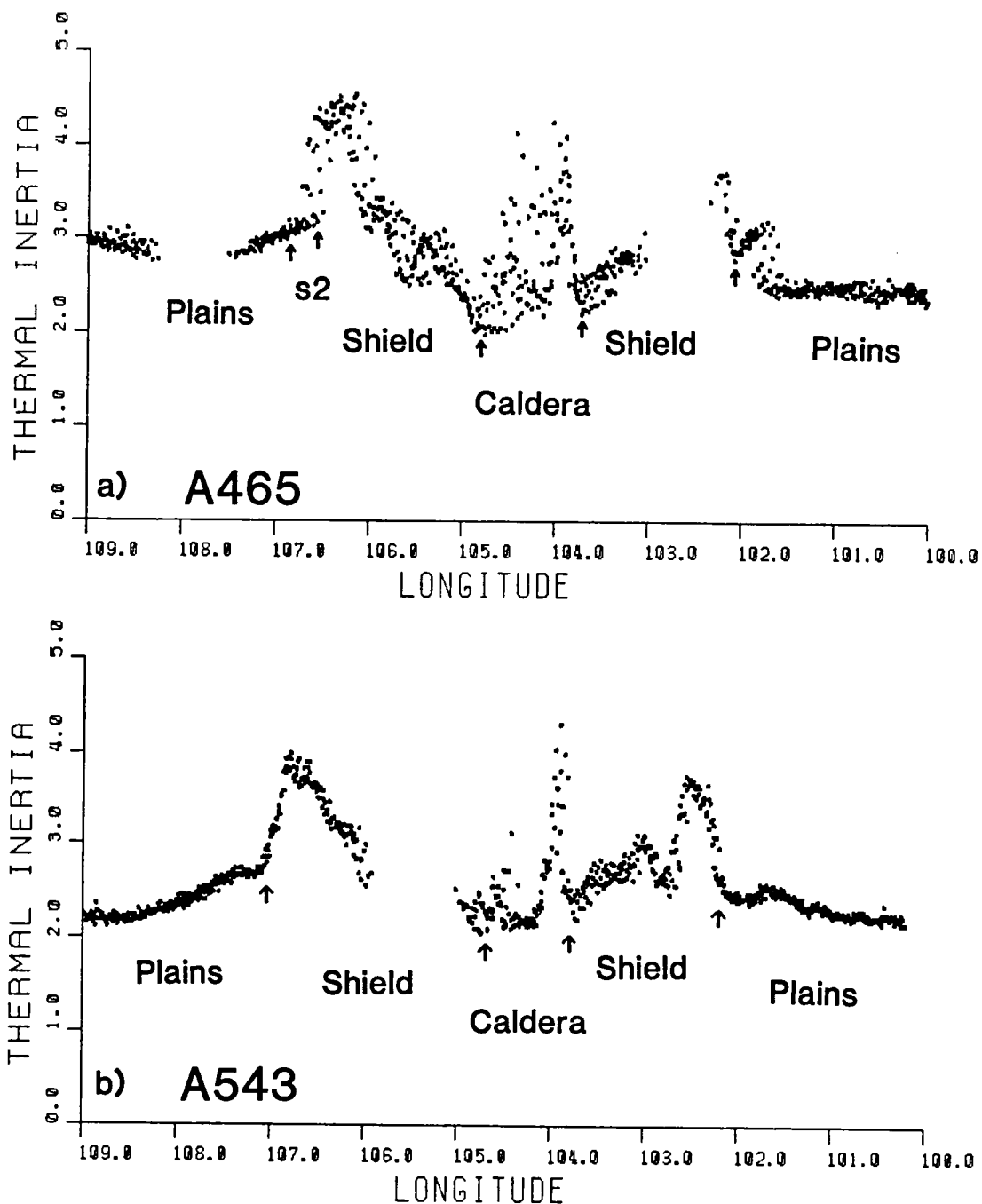


Figure 4.6. Corrected thermal inertias correlated with terrain types from Map 1. a) Sequence A465. Atmospheric dust has slightly increased the apparent thermal inertias at lower elevations (e.g. the plains). b) Sequence A543. Terrain contact locations are indicated by arrows. Caldera correlations are more clearly displayed in Fig. 4.5. Appendix 1 provides information about the individual sequences.



but not with the subdued plains (terrain unit s2) on the northwestern flank of the volcano (Fig. 4.6a). The s2 terrain thermal inertias are consistent with the thermal inertias on the plains, supporting the photogeologic interpretation that flows from Ascræus Mons covered the s2 terrain during emplacement of the p2 plains (Chapter 3).

The shield base has higher thermal inertias than either the Tharsis plains or the summit area, but increased thermal inertias do not appear to be associated with any particular base terrain unit. Numerous irregular depressions were crossed by the thermal sequences on the lower western flank of Ascræus Mons but these features produced no distinguishable thermal inertia signature. The discussion section below includes an evaluation of the flank properties evident in different remote sensing data sets, with the result that downslope sediment transport involving both dust and sand is probably the dominant physical process responsible for the remote sensing properties of the flanks.

Dust or condensate clouds can also result in an apparent increase in thermal inertia due to their insulating effect on surface temperatures (Kieffer et al., 1977; Peterfreund and Kieffer, 1979). Fortunately, clouds produce distinctive differences between temperatures measured in the IRTM thermal bands (Hunt, 1979; Christensen and Zurek, 1984). The temperature

differences in the high resolution thermal sequences are not significantly different between the plains, shield base, and shield summit. A consistent trend of  $T_9 > T_{11} > T_{20}$  (the temperatures at 9, 11, and 20  $\mu\text{m}$ , respectively) over both the shield and the plains for the three nighttime (A spacecraft) sequences indicates at least some atmospheric dust is always present, even above the volcano summit. The daytime sequence (B484) has water ice clouds or haze over both the plains and the shield but the  $T_{11}$ - $T_{20}$  differences discussed earlier indicate the clouds are the thickest over the shield. If clouds were responsible for the increased thermal inertias of the shield base then the clouds would be warmer than the surface during the night, but observed temperature differences are not consistent with either dust clouds or water ice clouds. Hunt (1979) determined that  $T_9$ - $T_{11}$  should always be negative for water ice clouds warmer than the surface. The observed nighttime temperatures all have  $T_9$ - $T_{11} > 0$  so that nighttime water ice clouds should not be present around Ascræus Mons. Clouds do not appear to be the cause of the thermal variations on the volcano flanks.

The only surface features on the flanks of the volcano that have distinguishable thermal inertia signatures are terraces. The subtle variations in thermal inertia (changes of 0.5 to 1.0) on the shield flanks all correspond

to terraces (Fig. 4.6). The higher thermal inertias occur downslope from both the terrace faces and the break in slope at the terrace bases (Fig. 4.7). The gentle ( $6^\circ$ ) slope of the terrace face, relative to the flank slope, inferred from photometry, makes it unlikely that the higher thermal inertias are talus accumulations below the terraces. The terraces probably represent subtle topographic barriers to the downslope transport of sediments, with increased sediment accumulation on the shallower slopes below the terraces.

It is important to note that no thermal inertia changes in the flanks are associated with the presence or absence of the dark collar. The dark collar is interpreted to indicate removal of bright dust from the surface (Lee *et al.*, 1982); the lack of any thermal inertia change associated with the dark collar indicates that the thickness of the mobile dust must be  $\ll 3$  cm. The low thermal inertias of the shield flanks apply to surface materials that do not appear to be greatly influenced by the winds that redistribute the mobile dust. The presence of the dark collar does not indicate that all (or even a significant fraction of the) dust has been removed from that portion of the volcano; this result makes it very unlikely that albedo patterns on the volcano are in any way related to bedrock compositions.

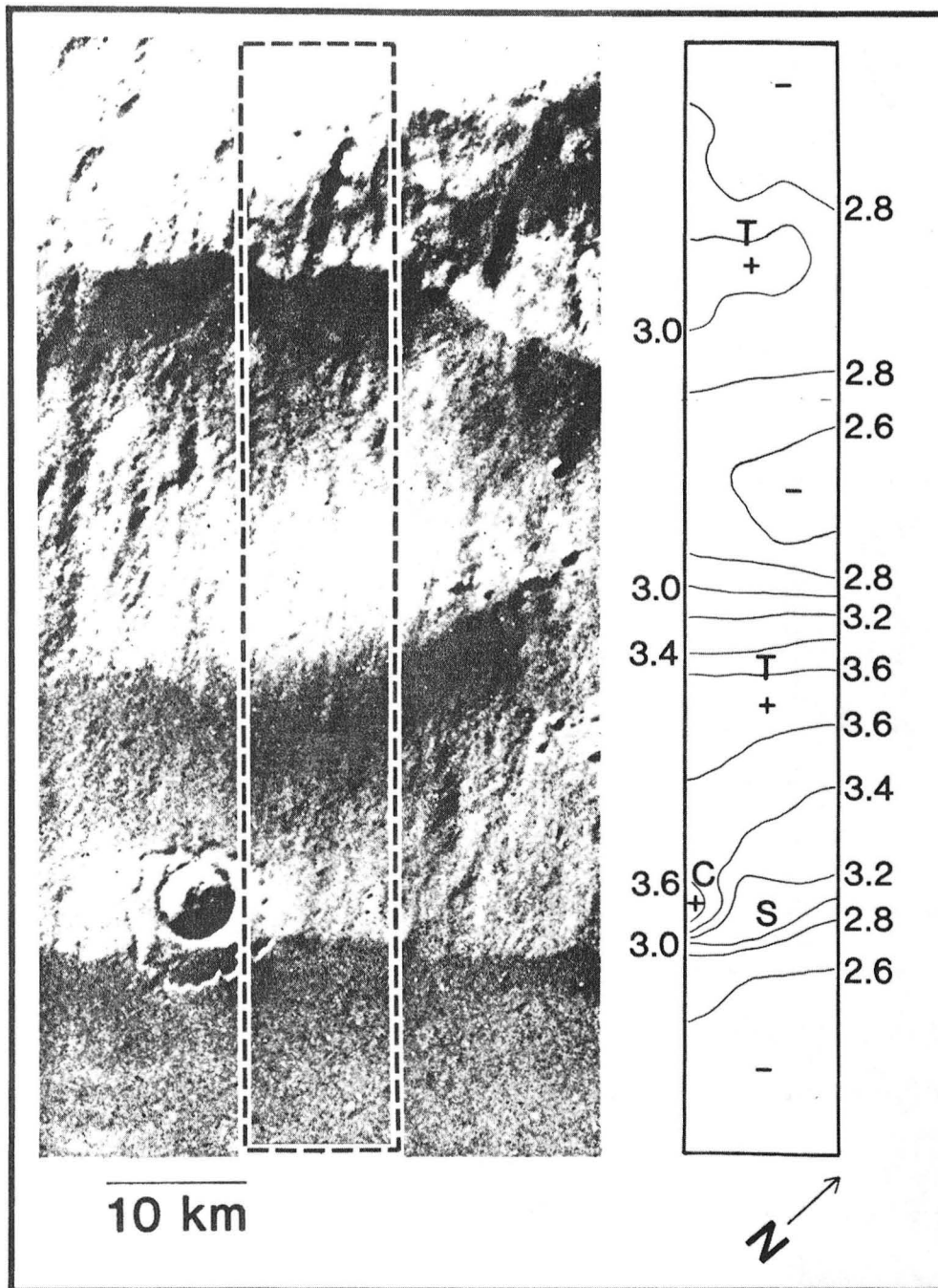


Figure 4.7. Southeast flank of Ascræus Mons. Corrected thermal inertias (right) correspond to dashed area (left) in photograph 892A34 (center:  $9.5^{\circ}\text{N}$ ,  $102.4^{\circ}\text{W}$ ). T indicates the location of the break in slope at the base of flank terraces, S indicates the contact between the s1 shield terrain and the p2 terrain of the plains (from Map 1), and C indicates the location of an impact crater and its ejecta.

The Tharsis plains surrounding Ascræus Mons (unit p2 of Map 2) show no localized thermal inertia variations. Even the well-defined p3 flows west of the volcano (108° to 110°W) are indistinguishable from the p2 plains. As with the summit area terrain units, the Tharsis plains either have uniform intrinsic properties or all terrains have been modified. The p3 flow margins might be expected to be rougher or blockier than either the flow surface or the plains but, as in the summit area, no thermal variations are evident at the margins. The Tharsis plains are only a portion of the immense low thermal inertia region that surrounds Tharsis (see Chapter 2), interpreted to be a site of dust deposition (Kieffer et al., 1977; Zimbelman and Kieffer, 1979; Christensen, 1982, 1984b). It is unlikely that a pyroclastic origin for the fine materials would result in uniform thermal inertias both surrounding the volcano and at its summit. The similarity between the thermal inertias of both the Tharsis plains and the summit of Ascræus Mons favors an aeolian origin for the fine materials at both locations.

Summary: Terrain units on the summit flanks and within the caldera complex do not have distinguishable thermal inertias, except for the uppermost caldera walls. The caldera wall thermal inertias ( $I = 4.5$ ) are far below the value for volcanic bedrock ( $I = 50$ ) and exposed bedrock probably represents < 15% of the caldera wall terrain. The

other summit area terrains, both flank and caldera units, have very similar thermal inertias ( $I = 2.0$  to  $2.5$ ), consistent with an effective particle diameter  $< 30 \mu\text{m}$ . A volcanic (pyroclastic) origin for the fine materials cannot be ruled out but an aeolian origin is favored. The shield flanks increase in thermal inertia with decreasing elevation, consistent with downslope sediment transportation. Terraces are the only flank features with distinguishable thermal inertias; the terraces probably represent subtle topographic barriers to downslope sediment movement. The dark collar has no associated thermal inertia signature, indicating that the albedo patterns on the volcano are probably not related to bedrock compositions. The shield-plains contact correlates with thermal inertia changes from higher values associated with the shield base (sl terrain of Map 1) to values on the plains comparable to the shield summit. Similar thermal inertias on the shield summit and the Tharsis plains support an aeolian origin for the fine materials.

Diurnal temperature amplitude. Thermal inertia can be more precisely constrained by observations of the same surface area at different times of the day. The diurnal temperature amplitude, the difference between the minimum and maximum temperatures throughout the day, provides a measure of thermal inertia independent of the surface albedo (Kieffer et al., 1973) but the

multiple observations needed for this measurement cannot be accomplished by a single spacecraft without averaging data over very large areas. The high resolution data for Ascraeus Mons provide a rare opportunity to measure the diurnal temperature amplitude of a very small surface area on Mars.

Nighttime and daytime temperatures on Ascraeus Mons were obtained only two days apart through the use of both Viking orbiters. The absolute calibration of temperatures for both IRTMs is better than 1 degree (Martin, 1981) so the use of observations from different instruments should not diminish the accuracy of the measurements. The crossing point at 11.5°N, 104.7°W on the northwestern caldera floor had a nighttime temperature of 139 K and a daytime temperature of 271 K. These values correspond to a 25 km<sup>2</sup> area (5 km by 5 km) near the southern margin of the caldera floor well removed from the caldera walls; other locations within the area covered by both sequences may be influenced by the caldera walls and the shadows associated with them. The observed temperatures place a lower limit on the diurnal temperature amplitude of the caldera floor materials of 132 K, corresponding to an upper limit on the thermal inertia of 2.6 (Fig. 4.8).

The diurnal temperature amplitude lower limit can be further raised by considering the conditions under which the data were collected. The afternoon clouds discussed

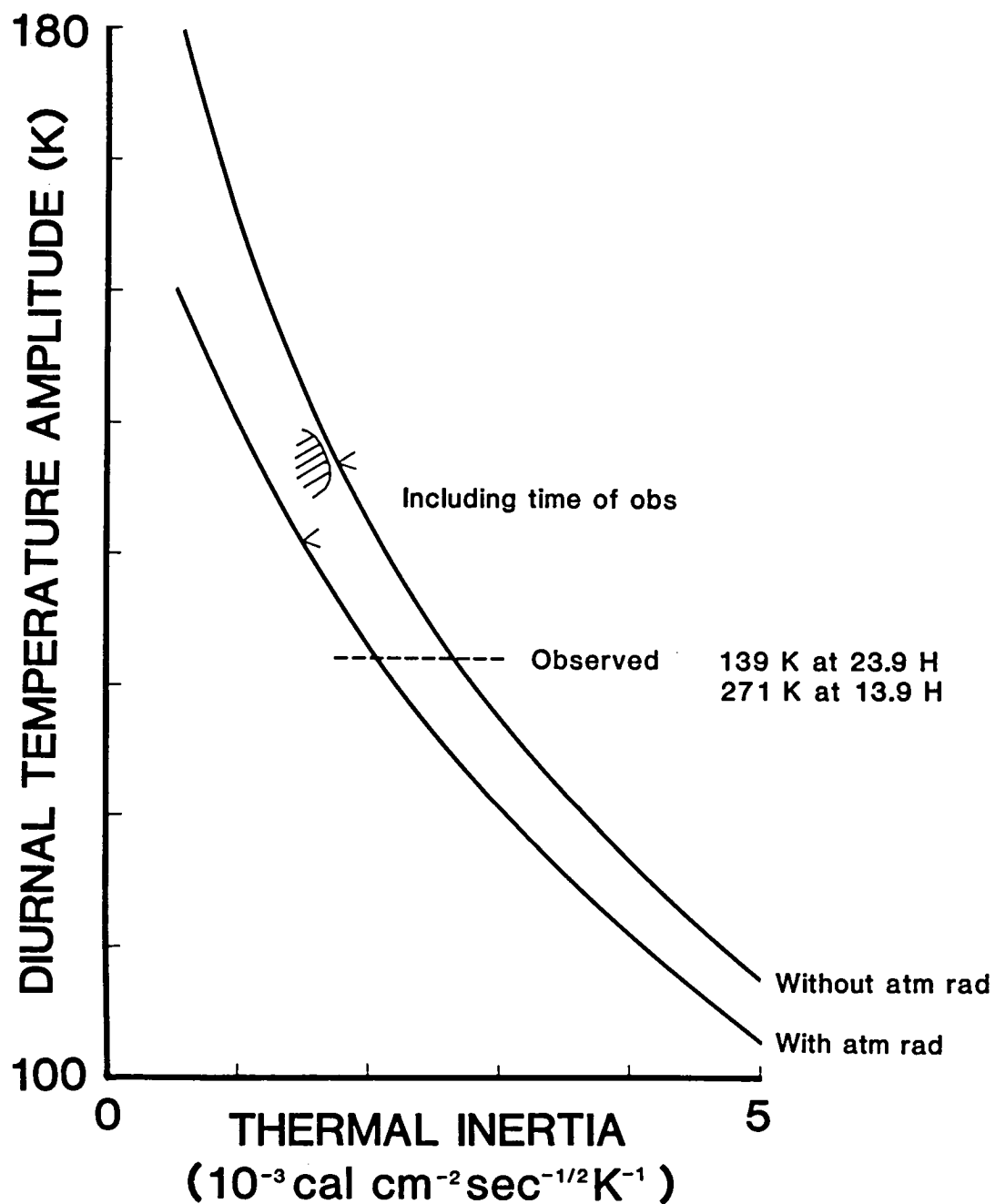


Figure 4.8. Diurnal temperature amplitude for the northeast caldera floor on Ascræus Mons. Dashed line indicates observed temperature difference. Curves indicate diurnal temperature amplitude with (lower) and without (upper) atmospheric radiation. Arrows indicate diurnal temperature amplitude at optimum times of day. Cross-hatched region indicates most likely values.



earlier indicate that the observed daytime temperature is itself only a lower limit. More importantly, the temperatures were not measured at the precise times of maximum and minimum temperature. The 2.6 upper limit to the thermal inertia and the time of day the measurements were made indicate that the actual surface temperature amplitude was 9 to 15 K larger than 132 K. The atmospheric thermal radiation is minimal at the summit of the volcano so that the temperature amplitude there should approach the values corresponding to no atmosphere. The hatched area (Fig. 4.8) represents the range of most likely diurnal temperature amplitude values. These considerations constrain the caldera floor thermal inertia to be less than 1.7. The elevation-dependent correction for thermal conductivity (Appendix 3) results in a corrected thermal inertia upper limit of 2.7. This is in good agreement with the corrected thermal inertia (2.4) determined from temperatures measured at a single time of day for this location, providing support for the accuracy of the thermal inertias calculated from individual high resolution sequences.

The  $> 145$  K diurnal temperature amplitude on Ascræus Mons has significant implications for aeolian activity on the volcano. Magalhães and Gierasch (1982) described the conditions required for slope winds on Mars, but the maximum diurnal temperature amplitude they considered was

120 K. Their results indicated that slope winds could be generated at night over surfaces colder than the atmosphere and the surface shear velocity (related to the surface wind velocity gradient) is directly proportional to the diurnal temperature amplitude. Surface shear velocities in excess of 2 m/sec can be extrapolated from the Ascræus Mons results (from Magalhães and Gierasch, 1982, Fig. 6). This value that could set 100  $\mu$ m sand particles in motion under martian (5 mbar) conditions (Greeley, et al., 1980).

Summary: Two high resolution IRTM sequences measured a 132 K difference between nighttime and daytime temperatures on the northwestern floor of the Ascræus Mons summit caldera. The time of day for the measurements indicates the actual diurnal temperature amplitude is > 145 K, providing an upper limit for the corrected thermal inertia of 2.7. This result increases the likelihood that nighttime slope winds are capable of causing aeolian activity on the flanks of the volcano.

"Block" abundances. Christensen (1982) developed a model for evaluating the relative abundance of spatially unresolved high thermal inertia materials through differences between temperatures obtained at different wavelengths. This model evaluates the temperature difference between two wavelengths (T11-T20 for the low nighttime temperatures on the volcano) as the result of two

thermal inertia components: high thermal inertia "blocks" (defined to have  $I = 30$ , albedo = 0.1, effective particle diameter  $> 10$  cm) and the areally dominant lower thermal inertia soil. The "block" abundance and soil thermal inertias are free parameters but the composite surface thermal flux is constrained to agree with globally determined thermal inertia for the location. The "block" abundance represents all higher thermal inertia materials exposed within the field of view, including rocks, bedrock outcrops, and indurated soils (e.g. the "duricrust" of Dittéon, 1982). Figure 4.9 shows the averaged "block" abundances for the three nighttime high resolution sequences crossing Ascræus Mons. The daytime sequence was not used because the thermal inertia differences of the "blocks" and the soil are not distinguishable during the afternoon.

The "block" abundances on Ascræus Mons (Fig. 4.9) are consistent with the 5 to 20% abundances determined for other locations on Mars (Christensen, 1982). The base portions of the shield have slightly lower "block" abundances than the summit area. The shield "block" abundances are slightly lower than the plains values for sequence A465 but the shield and plains have comparable "block" abundances in sequence A543. Sequence A659 data were collected shortly after local sunset; the westward-facing flank ( $105$  to  $107^\circ\text{W}$ ) may have had higher

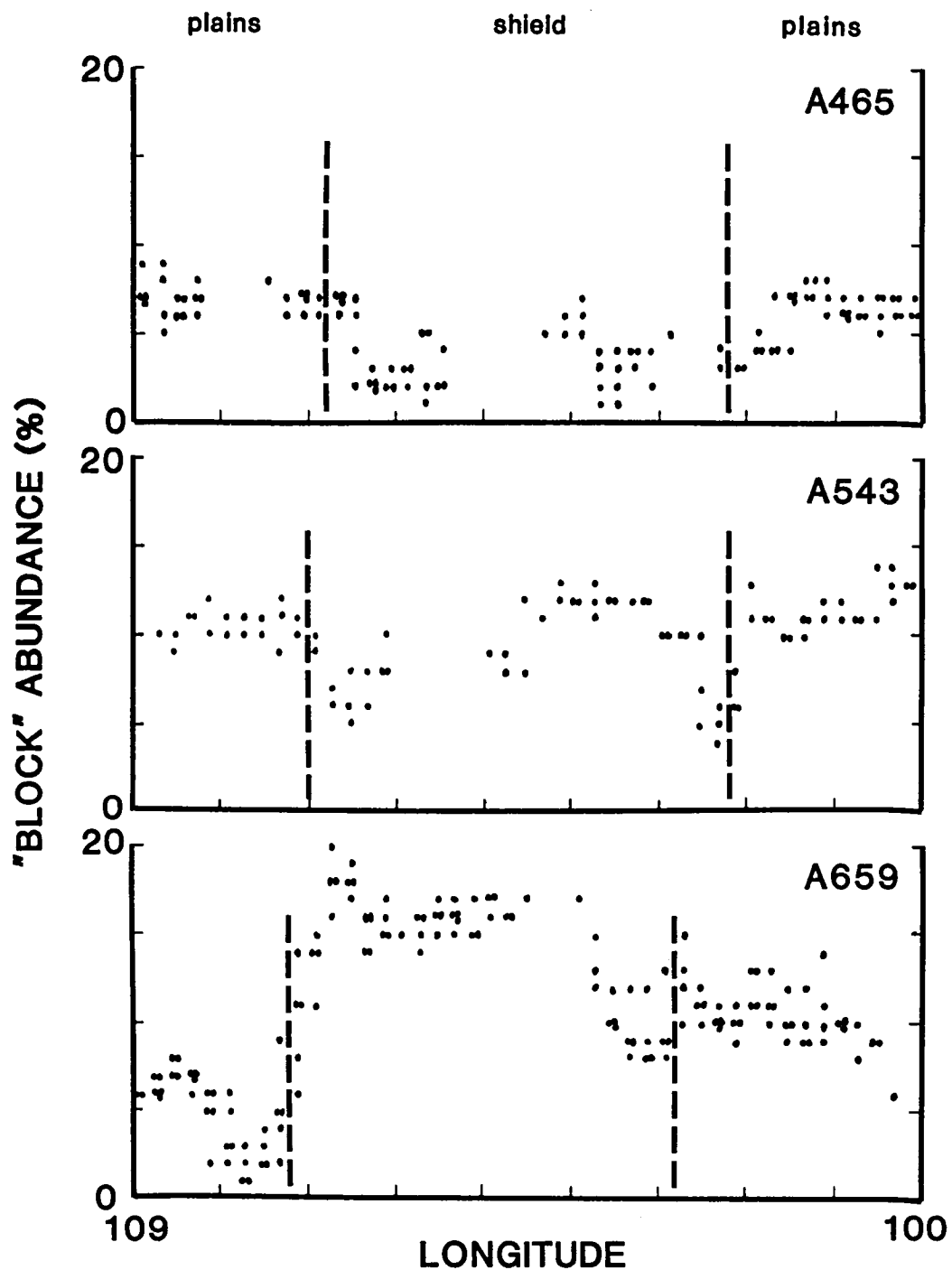


Figure 4.9. "Block" abundances on Ascræus Mons. Values represent the areal abundance of spatially unresolved high thermal inertia materials, after Christensen (1982). Dashed lines indicate contacts between the shield and the plains.

afternoon temperatures because of the 5° shield slope (Christensen, 1981, p.180) that increased the estimate of the shield "block" abundances. The apparent increase in "block" abundances with increasing time after the global dust storm may be due to atmospheric effects since the presence of either dust or water ice clouds tends to decrease the calculated "block" abundance (Christensen, 1981, p.41).

The similarity in "block" abundances between the shield and the plains is reduced by considering elevation-dependent effects (see Appendix 3) on the thermal inertia of the "blocks". Thermal inertia 30 materials at 20 km elevation have surface temperatures equivalent to thermal inertia 50 materials at zero elevation; conversely, thermal inertia 30 materials at 6.1 mbar atmospheric pressure have temperatures comparable to materials of thermal inertia 16 at 20 km elevation. The summit area "block" abundances are therefore underestimated in relation to values from the rest of the planet. Fig. 4.10 compares the predicted T11-T20 values for "block" thermal inertias of 30 and 16; these calculations indicate that the summit area "block" abundances ( $I = 16$ ) are 50 to 60% of the value obtained for equivalent materials at 6.1 mbar atmospheric pressure ( $I = 30$ ), so that summit area "block" abundances are actually 20% or more. The plains surrounding Ascræus Mons have values 85% of the zero elevation "block" values.

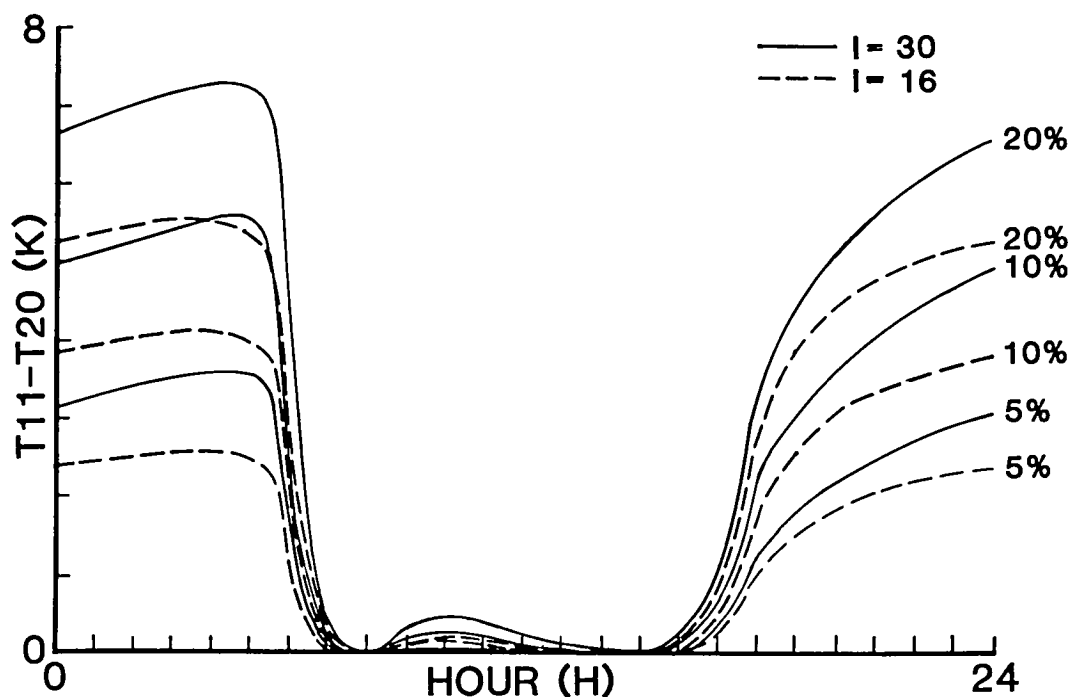


Figure 4.10. Temperature differences for different "block" abundances and thermal inertias. Values represent the areal abundance of spatially unresolved high thermal inertia materials determined from differences between 11 and 20  $\mu\text{m}$  brightness temperatures, after Christensen (1982). Solid lines are for "block" thermal inertias of 30 at zero elevation; dashed lines are for "block" thermal inertias of 16 at 20 km elevation, which has equivalent temperature variations to  $I = 30$  material at zero elevation. Right margin labels are the "block" abundance for each curve. Note that elevation effects cause the "block" abundance at the volcano summit to be underestimated by almost 50% in comparison to zero elevation. Calculations are for sequence A543 at  $10^\circ\text{N}$  latitude, but the values are not strongly affected by season or latitude.

These changes make the shield summit materials "blockier" than the Tharsis plains and the shield base materials, consistent with the trend of morphology degradation down the shield flanks (Chapter 3). The higher "block" abundance in the shield summit area suggests that rock materials there could have their greatest contribution to the remote sensing results. However, fine materials still dominate the observations at visual and infrared wavelengths. Even at the volcano summit, rocks and bedrock are still a minor component in the uppermost several cm of the surface.

The apparent discrepancy between decreasing "block" abundance and increasing thermal inertia with decreasing elevation on the volcano may be related to the sorting of the surface materials (M. Malin, personal communication, 1984). Interpretation of the thermal inertias as effective particle diameters (Fig. 2.7) implies that the average particle size is smaller at the shield summit than at the base. The "block" abundances can similarly be interpreted as the relative abundance of coarse (diameter > 10 cm) materials. Sorting of sediments is related to the dispersion of particle sizes around the average value for the sediments (Pettijohn et al., 1972, p.76). A smaller average particle size and a larger abundance of coarse materials in the summit area indicate that the summit area has poorer sorting than the shield base.

Sediment sorting increases as the duration or number of episodes of mass transport increases (Pettijohn et al., 1972, p.76) so the summit area materials have undergone less sediment transport than the base area materials. This is geologically reasonable since sediment transport should be predominantly downslope. The sediments most easily moved by the atmosphere would probably be transported furthest downslope. The particles most easily moved by the wind on Mars are 100  $\mu\text{m}$  in diameter (Greeley et al., 1980); this particle size corresponds to a thermal inertia of 4 (Fig. 2.7), a typical value for the shield base area (Fig. 4.6). There is no photographic evidence of accumulations of sand on the shield base but the thermal inertia and "block" abundance values suggest that sand-sized particles may be abundant throughout the lower elevations on the volcano.

Summary: "Block" abundances, representing spatially unresolved high thermal inertia materials ( $I = 30$  and effective particle size  $> 10$  cm), can be obtained from temperatures measured at different wavelengths (Christensen, 1982). When elevation-dependent effects are included, "block" abundances of  $> 20\%$ ,  $< 10\%$ , and  $10\%$  are obtained for the shield summit, the shield base, and the Tharsis plains, respectively. Thermal inertias and "block" abundances suggest that the sorting of sediments increases down the flanks of the volcanos, and sand-sized particles



could be abundant throughout the lower flanks.

Moderate resolution data. The high resolution sequences provide good spatial resolution but poor areal coverage on Ascraeus Mons (Fig. 4.4). Moderate resolution thermal data show the spatial distribution of thermal inertias across the entire volcano. Thermal inertias from twelve nighttime sequences and two afternoon sequences were corrected for elevation and binned according to the spatial resolution of each sequence (Figs. 4.11 and 4.12).

Thermal inertias obtained during a time of increased atmospheric dust (A437 and A439 in Fig. 4.11) are comparable to the values determined from high resolution sequence A465 (Fig. 4.6a). The highest thermal inertias associated with the base of the shield occur along the northwestern and southeastern flanks, paralleling the trend of the Tharsis Montes. Thermal inertias at the summit of the shield are lower than the thermal inertias of the Tharsis plains (as in A465), suggesting that atmospheric dust is still significant at the lower elevations. Thermal inertias obtained after the dust opacity decreased to a optical depth of 0.1 (all B spacecraft sequences in Fig. 4.11) are comparable on both the plains and the shield summit, similar to high resolution sequence A543 (Fig. 4.6b). The thermal inertias of the shield base are still highest on the northwest and southeast flanks but the entire shield base has higher thermal inertias than the

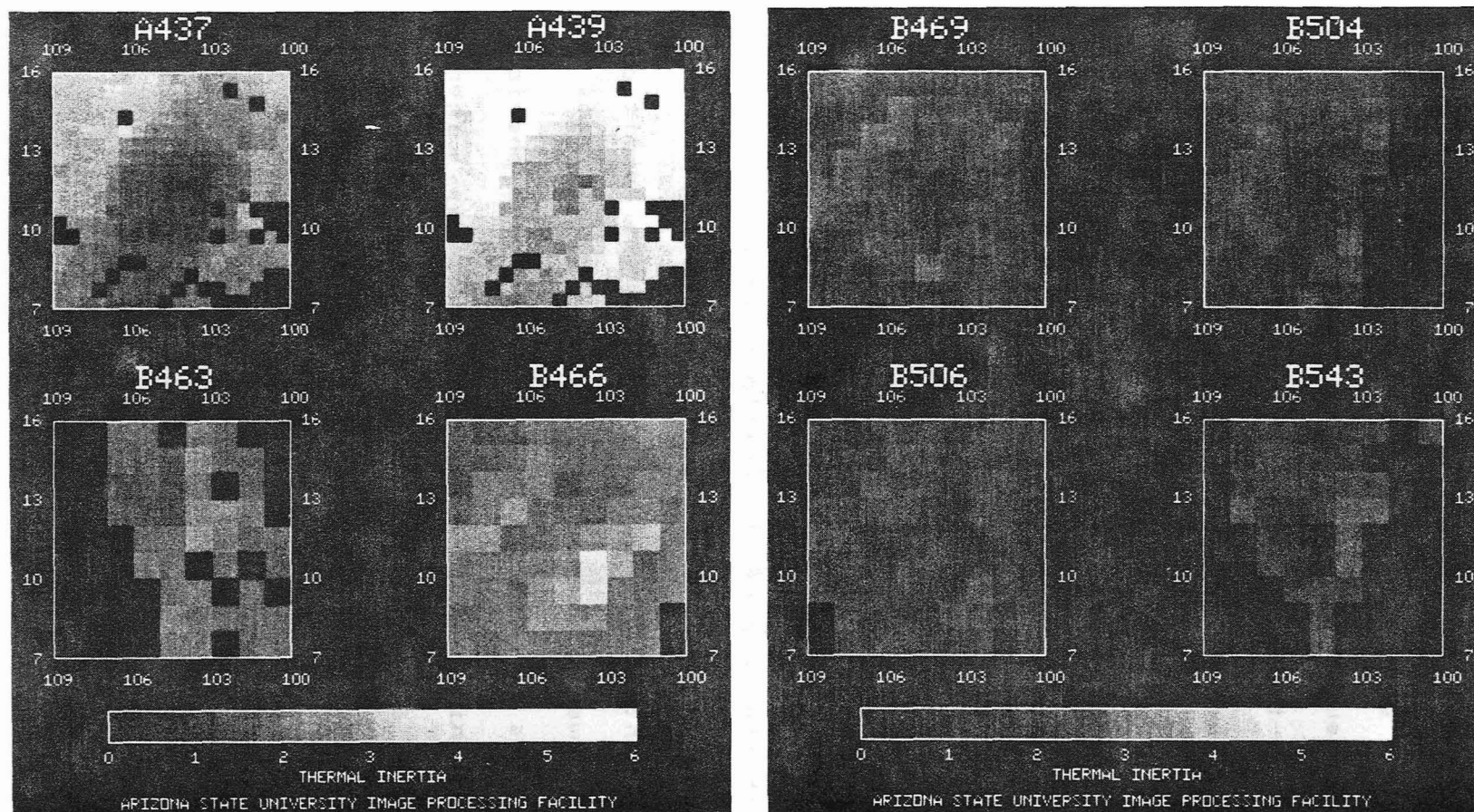


Figure 4.11. Corrected thermal inertias for Ascræus Mons. Thermal inertias are binned according to the spatial resolution of each sequence. Sequences A437 and A439 have higher apparent thermal inertias for the plains around the volcano than the other sequences due to a dusty atmosphere. Note the radial symmetry of thermal inertias around the volcano summit ( $11.5^{\circ}\text{N}$ ,  $104.5^{\circ}\text{W}$ ; compare with Fig. 4.1). Appendix 1 provides information about individual sequences.

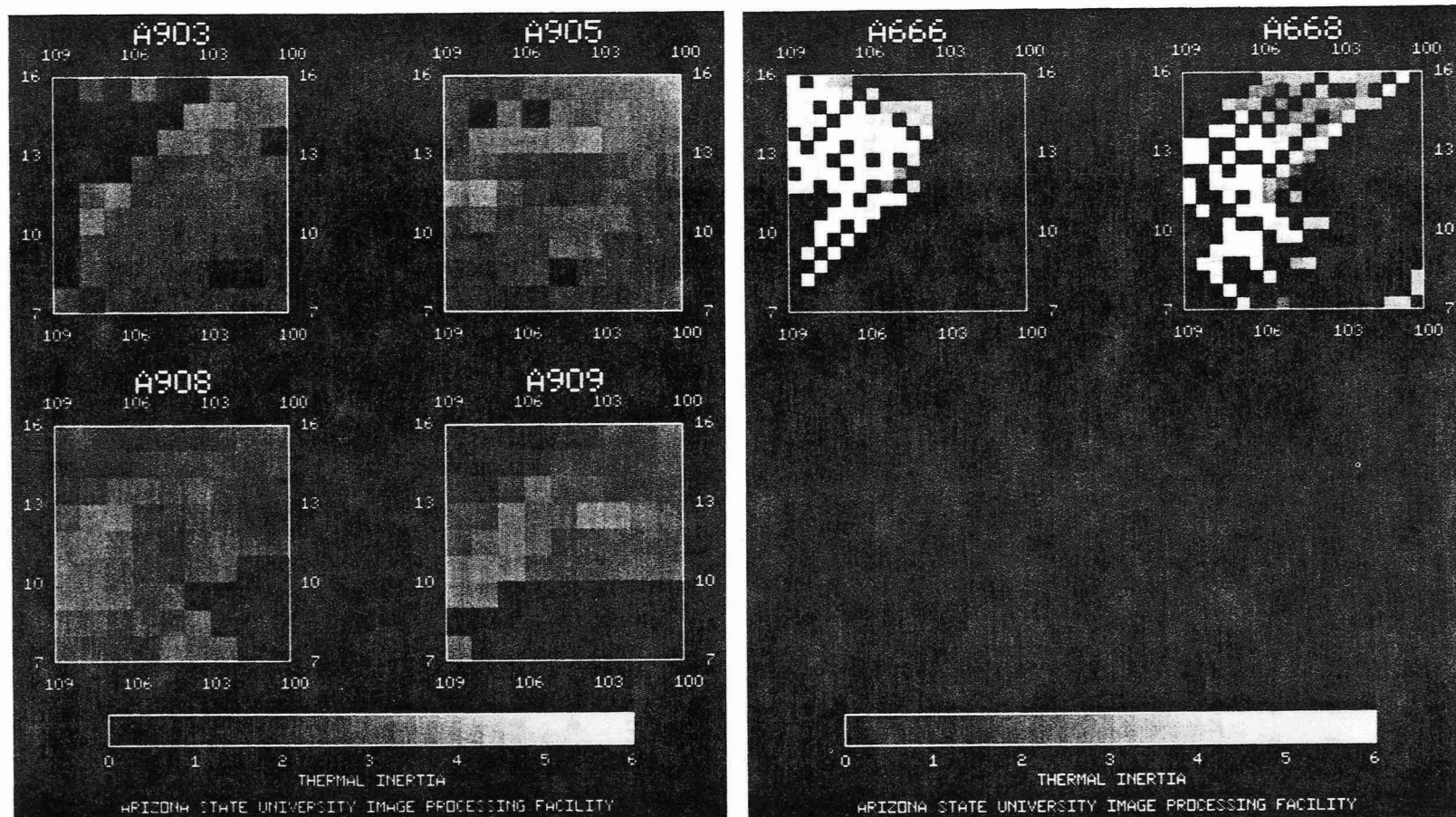


Figure 4.12. Corrected thermal inertias for Ascræus Mons. Thermal inertias are binned according to the spatial resolution of each sequence. Sequences A903 through A909 indicate that the thermal inertias are consistent in location and magnitude on a daily basis and, in comparison with Fig. 4.11, over half of a martian year. Sequences A666 and A668 have high apparent thermal inertias because of afternoon clouds (compare with Fig. 4.1). Appendix 1 provides information about individual sequences.

shield summit, resulting in a radial symmetry of thermal inertias.

Fig. 4.12 shows thermal inertias for Ascraeus Mons on four days during a seven day interval. The summit area thermal inertias are comparable to the thermal inertia of the Tharsis plains and both areas are consistently lower than the values for the base of the shield. The shield base areas of higher thermal inertias are consistent with thermal inertias obtained half a martian year earlier (Fig. 4.11) and vary only slightly in position during the seven day interval, consistent with the low spatial resolution of these data. The thermal inertias on the volcano are consistent both in location and value on a daily basis over at least half of a martian year. This consistency decreases the possibility that clouds are the major contributor to the shield flank thermal inertia variations. The two daytime sequences are dominated by afternoon clouds west and northwest of the volcano (A666 and A668 in Fig. 4.12). The clouds lower the surface temperature and produce anomalously high thermal inertias, similar to the daytime high resolution sequence (B484). The moderate resolution sequences indicate that the properties identified in the high resolution data are representative of the entire shield area.

Summary: Thermal inertias on Ascraeus Mons are radially symmetric around the shield summit. Thermal

inertias are consistent in location and value on a daily basis over half of a martian year. The high resolution sequences are representative of the thermal properties on the entire volcano.

Summary. Elevation dependent corrections (Appendix 3) were applied to four high resolution thermal sequences that crossed the summit of Ascraeus Mons. The corrected thermal inertias for the volcano are comparable to or larger than thermal inertias on the Tharsis plains. Extremely frothy or vesiculated lavas (Kieffer et al., 1977) are not required to explain the thermal inertias on the volcano. The uppermost caldera walls are the only terrain unit in the summit area with distinguishable thermal inertias ( $I = 4.5$ ); exposed bedrock probably represents < 15% of this terrain. All other caldera and summit flank terrains have thermal inertias similar to those of the Tharsis plains ( $I = 2.0$  to  $2.5$ ), suggesting the ubiquitous presence of fine materials (diameter <  $30\ \mu\text{m}$ ). The fine materials are probably aeolian in origin, from global dust storms, but a pyroclastic origin cannot be ruled out. Thermal inertias increase with decreasing elevation but they return to the summit flank value at the shield-plains contact. Nighttime and daytime temperatures indicate the diurnal temperature amplitude is > 145 K, increasing the likelihood that

nighttime slope winds can result in aeolian activity on the volcano. Spatially unresolved high thermal inertia materials ( $I = 30$  and effective particle size  $> 10$  cm) occur on  $> 20\%$  of the summit terrains and  $\leq 10\%$  of the shield base terrains and the Tharsis plains; this information, along with the thermal inertias, suggests that sorting by sediment transport increases down the flanks of the volcano. Sand-sized particles could be present throughout the lower flanks of the shield but there is no photographic evidence of sand accumulations. Thermal inertias from the high resolution sequences are representative of the entire volcano.

#### Surface Roughness

The characteristics of Ascraeus Mons at radar wavelengths (3 to 13 cm) are poorly defined because no quasi-specular radar returns have been received from observation runs that crossed the volcano (Downs et al., 1982). However, the lack of a radar signal from the volcano in itself provides important information about the surface properties. Dual polarization radar results provide additional constraints on the scattering properties of the surface in the Tharsis region (Harmon et al., 1982).

Few radar returns have been received from the Tharsis region for either the continuous-wave (Simpson et

al., 1978a,b) or the delay-Doppler (Downs et al., 1975, 1982) methods of observation. These analyses have concentrated on the quasi-specular radar return that results from specular reflection of the radar signal by the parts of a gently undulating surface oriented perpendicular to the incidence direction (Hagfors, 1964). Use of this scattering law requires that the diffuse radar component, produced by multiple scattering and/or wavelength-scale structures on the surface (Harmon et al., 1982), be small compared to the quasi-specular component. This assumption appears to be reasonable for much of Mars (Downs et al., 1978). However, the Tharsis area is dominated by the diffuse component (averaging 3.2 times the quasi-specular power) so that the quasi-specular return is greatly reduced (Harmon et al., 1982). Ascraeus Mons is one of three possible sources that may be responsible for locally enhanced diffuse scattering (Harmon et al., 1982 and A in Fig. 4.13). Quasi-specular returns from observations that crossed Ascraeus Mons were received west of 101°W, very near the eastern margin of the shield, and east of 109°W at 9.6°N and east of 111°W at 12.1°N (Downs et al., 1982). The western limits are closer to the edge of the mountain materials (Map 1) than the shield margin.

Several factors could contribute to the diminished quasi-specular returns from Ascraeus Mons, including: 1)

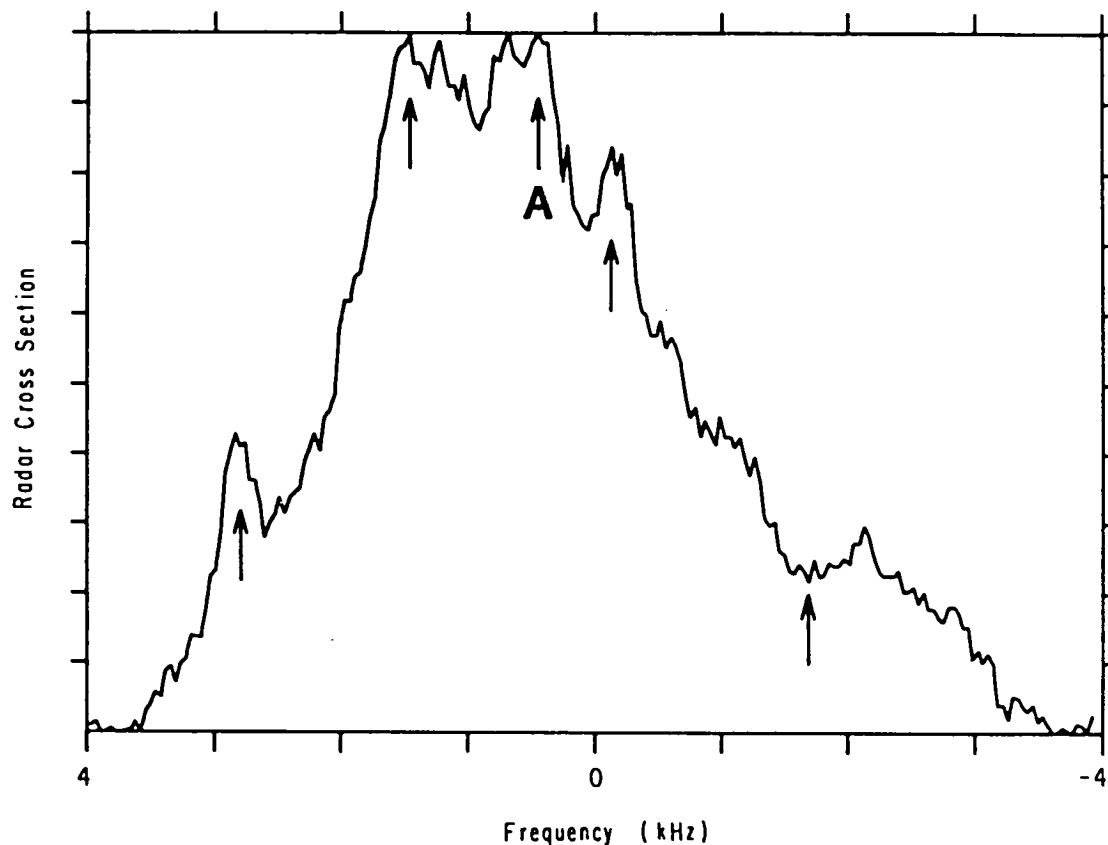


Figure 4.13. Depolarized component of radar data from the Tharsis region (Harmon *et al.*, 1982, Fig. 5a). Data were collected on 9 Feb 1980, centered over 22.0°N, 97.4°W. The broad depolarization enhancement results from scattering of radar signals by the Tharsis Rise. Feature A, with enhanced scattering relative to the Tharsis Rise, was observed on several consecutive runs; Ascraeus Mons, Ceraunius Fossae, and Syria Planum are possible source areas on the planet for this feature. Four additional features (arrows) were also observed on multiple runs, most of which could be related to other Tharsis shield volcanos. Maximum power corresponds to 91 standard deviations of the signal noise.



enhanced roughness due to slopes on the .1-100 m scale (Simpson et al., 1978; Downs et al., 1982),

- 2) large-scale flank slopes (Harmon et al., 1982),
- 3) scattering of the radar signal into the diffuse component (Harmon et al., 1982, and 4) decreased reflectivity and dielectric constant for surface materials (Jakosky and Muhleman, 1981). The present data neither exclude any of these options nor indicate which is most significant. However, the prominent diffuse component from the Tharsis region results in underestimated reflectivity and dielectric constant values obtained from a quasi-specular scattering analysis (Harmon et al., 1982). If Ascraeus Mons is a source of locally enhanced diffuse scattering (Fig. 4.13), it would be reasonable to expect a larger abundance of wavelength-scale rocks on the volcano, consistent with the increased "block" abundances for the summit area obtained from the thermal data. The morphology of the shield surface, even for the subdued base terrains, is much more varied than on the Tharsis plains surrounding the volcano (Chapter 3), consistent with increased roughness < 100 m in scale.

The different radar scattering characteristics of the Ascraeus Mons shield and the Tharsis plains may be related to the different histories of these locations. The shield surface consists of intermixed lava flows typically < 2 km wide and < 10 km long while the plains flows, where they

are visible, are generally  $> 5$  km wide and  $> 50$  km long (Chapter 3). The shield flows and the mass wasting features on the lower flanks may contribute to greater surface variations at the .1 to 100 m scale than on the broad plains. The similar thermal inertias for the shield summit and the plains indicate that fine-grained materials are present throughout the Tharsis region but these materials apparently are not thick enough to mask the surface roughness from the radar signals. Schaber (1980) attributed radar roughness southwest of Arsia Mons to surface variations on lava flows covered by a low thermal inertia aeolian mantle. High thermal inertia "blocks" probably are not the principal cause of radar scattering because other areas on Mars (e.g. Syrtis Major) have "block" abundances comparable to or greater than those in Tharsis (Christensen, 1982) and also have observable radar signals (Simpson et al., 1978).

Summary: No quasi-specular radar returns have been received from Ascraeus Mons (Downs et al., 1982) but strong depolarized radar signals from the Tharsis area indicate that most of the radar power is scattered by surface roughness (Harmon et al., 1982). High thermal inertia "blocks" probably are not the principal radar scatterers; lava flows with surface variations at the .1 to 100 m scale probably contribute to the radar scattering. The Ascraeus Mons shield scatters radar

signals more effectively than the Tharsis plains, suggesting that the intermixed shield flows provide greater roughness than the broad plains flows. The low thermal inertia materials present throughout the Tharsis region do not mask the surface roughness from the radar signals.

#### Atmospheric Water Vapor

The abundance of water vapor in the atmosphere of Mars may be related to volatile transfer through the martian surface materials. Absorbed water is liquidlike even at martian temperatures (Ugolini and Anderson, 1972) and evaporation of this water could deposit evaporites in the martian soil and produce an indurated layer (Binder et al., 1977; Dittéon, 1982). The water vapor abundance over Ascræus Mons aids in evaluating the potential development of indurated soil on the volcano.

The Mars Atmospheric Water Detector (MAWD) instrument provided the first measurements of water vapor abundance on Mars with sufficient spatial resolution to map latitudinal and longitudinal vapor transport (Farmer et al., 1977). During orbit 71 of Viking Orbiter 1 MAWD data were collected across the four shield volcanoes of the Tharsis region, including Ascræus Mons (Farmer et al., 1977 and Fig. 4.14). The water vapor abundance dropped substantially over the volcano, and pressure-dependent corrections for the relief of the volcano did not

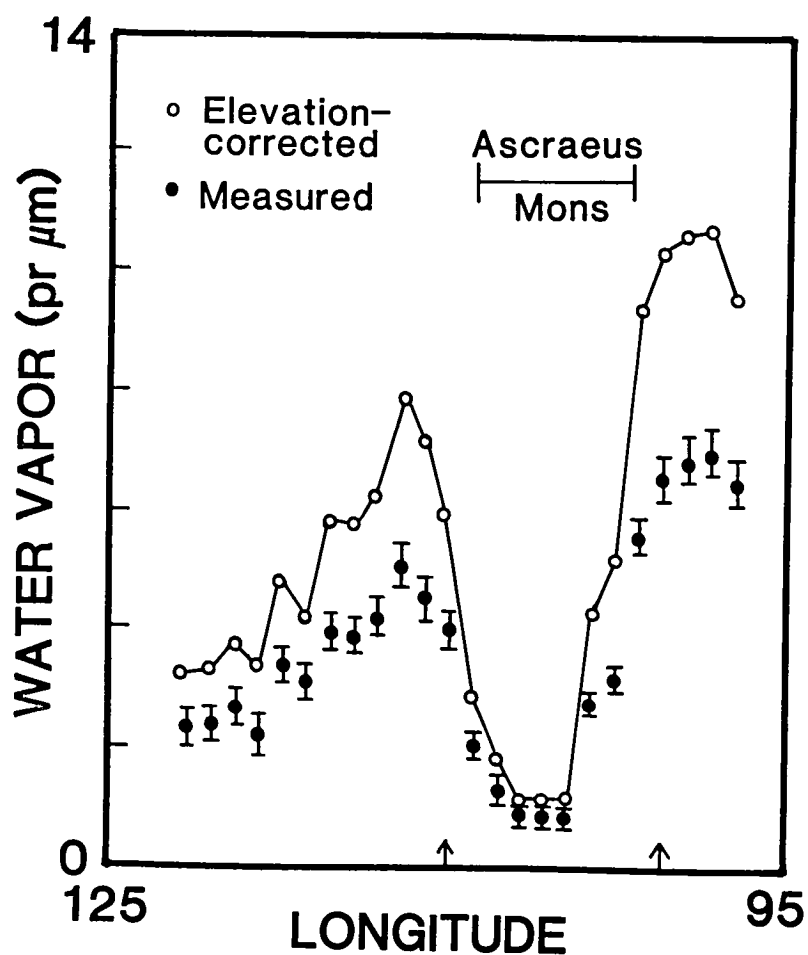


Figure 4.14. Atmospheric water vapor abundance above Ascræus Mons (Farmer *et al.*, 1977, Fig. 14a). Water vapor abundance is expressed as the total amount of precipitable water in the atmosphere. Solid points with error bars represent the average of ten measurements centered on each degree of longitude. Open points are elevation-corrected average values. Arrows indicate longitudes shown in Fig. 4.1.

compensate for the low abundance. The decreased water abundance over the volcano could result from condensation of water vapor into water ice clouds (Christensen and Zurek, 1984). Photographs from this season show clouds and haze around the lower flanks of Ascraeus Mons but not above the summit area (Briggs et al., 1977). The top level of the clouds and haze around Ascraeus Mons occurs at an elevation of approximately 15 km, consistent with other MAWD data that show most of the water vapor on Mars is concentrated in the lower several km of the atmosphere (Davies, 1979).

The MAWD spatial resolution is not sufficient to precisely locate the positions along the shield flanks where the water vapor abundance begins increasing from the low but uniform values over the summit (Fig. 4.14). It is evident that the lower shield flanks have 2 to 6 times more atmospheric water vapor than the summit area. If the increased atmospheric water vapor is associated with evaporation of absorbed water from the soil, induration may be more pronounced at the lower elevations on the volcano. The higher thermal inertias of the shield base, relative to the summit area, could be related to increased induration but then it would not be clear why the Tharsis plains do not also have higher thermal inertias. The lack of correlation between the water vapor abundances and the thermal inertias at low elevations implies that shield base

thermal inertias are probably not related to soil induration.

Summary: The atmospheric water vapor abundance is 2 to 6 times greater over the shield base than it is over the summit area of the volcano. The water vapor abundances were greatest over the Tharsis plains. The lack of correlation between water vapor abundance and thermal inertia implies that the atmospheric water content is probably not directly related to induration of the surface materials.

### Discussion

The various wavelengths used in the remote sensing data described here provide information about different sizes and thicknesses of surface materials that correspond to different segments of the history of Ascraeus Mons. Visual reflectance is sensitive to the topmost microns of the surface and to aeolian activity that can be observed on a timescale of days to years (e.g. Lee, 1984). Thermal infrared measurements are sensitive to the topmost several cm of the surface and changes are not observed in response to visual reflectance features; this material represents the recent history over a period much longer than a year. Radar measurements are sensitive to features at least on the order of the wavelength ( $> 10$  cm) and a timescale that is likely greater than that represented by

the thermal data.

The thermal inertias and visual albedos of the summit area above the dark collar zone on the volcano flank indicate the summit materials have very uniform properties. The lack of correlation between summit morphology and thermal inertias (Maps 2 and 3) suggests the present surface properties are not controlled by the processes responsible for the variety of summit area terrains. The summit thermal inertias are comparable to the plains thermal inertias and indicative of a small effective particle size,  $< 30 \mu\text{m}$  in diameter (Fig. 2.7). The classical high albedo regions of Arabia, Elysium, and Tharsis all have thermal inertias similar to the values obtained here for Ascræus Mons (Palluconi and Kieffer, 1981). The similarity between the reflectance properties of Ascræus Mons and Arabia suggests the fine-grained surface material on the summit is related to the high albedo soils of Mars.

Earth-based reflectance spectra of high albedo regions on Mars are closely matched by laboratory spectra of Hawaiian palagonite, the weathering product of mafic volcanic glass (Singer, 1982). Other palagonites have also been proposed as analogs to martian soil (Soderblom and Wenner, 1978; Allen *et al.*, 1981). The reflectance properties of the Hawaiian palagonites are governed by an amorphous ferric oxide-rich silica gel that coats the

surface (Evans and Adams, 1979, 1980) and these coatings may also be applicable to martian color variations (Evans et al., 1981). The bright martian dust appears to be related to mafic volcanic materials but there is no evidence that the Tharsis volcanoes, or Ascraeus Mons in particular, may be the original source of these materials.

The dark collar surrounding the summit area of Ascraeus Mons covers the transition between the crisp morphology of the summit features and the subdued morphology of the base terrains. The lack of any thermal inertia changes corresponding to the dark collar indicates that the processes responsible for the visual albedo pattern do not significantly change the surface physical properties. The coalesced dark collar streaks are interpreted to be the result of erosion of a thin layer of dust from a darker substrate (Veeverka et al., 1977; Lee, 1984). The thermal inertias indicate that either the darker substrate has physical properties very similar to the bright dust or the bright dust represents such a thin layer that the thermal data are not sensitive to it. Viking lander photographs spanning two martian years have documented the deposition and removal of a thin layer of bright dust, inferred to be only a few microns thick, at both landing sites (Guinness et al., 1982). It is feasible that a similar process occurs on the surface of the volcano. This would imply that the spectral



reflectance data from the volcano primarily documents changes in this mobile dust layer.

The similar low thermal inertias ( $I = 2.0$  to  $2.5$ ) on both the shield summit and the Tharsis plains is potentially related to the aeolian activity observed at visual wavelengths. Lee (1984, p.183) derived dust deposition rates of  $.0009$  and  $.003 \text{ gm cm}^{-2}$  during a martian year at elevations of  $20$  and  $10 \text{ km}$ , respectively. Thermal inertia 3 material must be at least  $2 \text{ cm}$  thick to mask the underlying surface from thermal measurements (Jakosky, 1979). Assuming a  $2 \text{ cm}$  minimum thickness and an average density of  $1.5 \text{ gm cm}^{-3}$  for the dust, the deposition rates given above indicate that at least  $1500$  and  $450$  martian years are required to generate this minimum thickness at  $20$  and  $10 \text{ km}$ , respectively. Erosion along with deposition would cause these times to be lower limits only. These results indicate that an aeolian origin for the low thermal inertias on both the plains and the summit requires at least  $1500$  martian years of average dust deposition. The timescale appropriate to the thermal properties of the surface is at least three orders of magnitude greater than the timescale of the observed variations in albedos.

The shield flanks include features potentially related to the surface history for a timescale greater than that of the summit thermal inertias. Several parameters are

observed to vary systematically with decreasing elevation on the flanks of Ascraeus Mons (Chapters 3 and 4): 1) surface morphology becomes subdued, 2) the abundance of craters < 200 m in diameter decreases, 3) thermal inertia increases, 4) high thermal inertia "block" abundance decreases, and 5) water vapor abundance increases. As noted earlier, the water vapor abundance does not appear to be correlated with surface properties or terrains but the first four conditions are potentially related. In Chapter 3 the morphologic variations on the flanks were attributed to a depositional process and in this chapter the thermal results could be reconciled through sorting associated with downslope sediment transportation. There is no evidence to indicate whether this transportation and deposition of sediments was accomplished through volcanic (pyroclastic) or aeolian processes, but observations of present day aeolian activity on the volcano lends support to an aeolian origin. The sediment thickness at the shield base is probably > 15 m (Chapter 3), which would require more than 300,000 martian years by dust deposition alone. Sand-sized (100  $\mu$ m) particles, the particles most easily moved by the winds on Mars (Greeley et al., 1980), are likely to be associated with aeolian activity; the 100  $\mu$ m effective particle size for the shield base implies that sand may be abundant at lower elevations on the volcano. Electrostatically bound dust aggregate could

produce sand-sized particles (Greeley, 1979) that cause little rock abrasion (Greeley et al., 1982), consistent with the distinct morphology of the summit terrains. Sediment transportation and accumulation on the volcano flanks likely represents hundreds of thousands of years in the surface history of the volcano.

The radar measurements lack the spatial resolution and the signal power to distinguish between terrains on the volcano but the shield produced stronger scattering of the radar signals than the surrounding Tharsis plains. Features > 10 cm in scale result in the radar scattering; these features are more likely to be related to the history of the terrains than the transportable surface sediments observed at visual and infrared wavelengths. As discussed in the surface roughness section above, differences in the flows on the shield and the plains probably contribute to their radar scattering properties. The timescale appropriate to the radar measurements could potentially approach the geologic age of the terrain units.

Summary: Visual reflectance measurements document aeolian activity on the timescale of days to years. Albedo variations on Ascraeus Mons probably involve movement in the topmost several microns of the surface. Thermal measurements are sensitive to the topmost several cm of the surface materials. Thermal inertias for the volcano summit represent a minimum of 1500 martian years of aeolian

deposition at average rates. Flank variations in morphologic and thermal characteristics are consistent with downslope sediment transportation that could represent hundreds of thousands of years. Radar measurements are sensitive to features  $> 10$  cm in scale and may represent timescales that approach the geologic age of the terrain units.

#### Summary: Geologic Implications

Visual reflectance. The reflectance properties of Ascræus Mons obtained from three-color Viking photographs indicate that slopes  $\leq 6^\circ$  affect both albedo magnitudes and the ratios between albedos at different wavelengths. Since these properties are used to distinguish albedo variations for compositional interpretations (e.g. McCord et al., 1982), it is important that photometric variations due to surface slopes are included in the analysis. When slope corrections are made, the summit flanks and caldera complex of Ascræus Mons have uniform albedos of .05 to .16 at 0.45 to 0.59  $\mu\text{m}$ , respectively. The wavelength dependence of the summit area albedos is similar to classical high albedo regions (e.g. Arabia), suggesting bright dust is present on the volcano. Aeolian activity removes at least some of this dust from the flanks to produce a dark collar around the volcano summit (Lee, 1984, p.133). Visual reflectance

on the volcano primarily documents changes in the mobile dust layer and is probably not strongly influenced by bedrock variations.

Thermal inertia. High resolution infrared thermal data across the shield show that the summit area is similar to the Tharsis plains in thermal inertia ( $I = 2.0$  to  $2.5$ ) and effective particle size (diameter  $< 30 \mu\text{m}$ ). Caldera walls are the only terrain unit with distinguishable thermal inertias ( $I = 4.5$ ); exposed bedrock probably represents  $< 15\%$  of this terrain. All other summit area units have similar thermal inertias, suggesting a ubiquitous presence of fine materials on the volcano. This material is probably aeolian in origin, deposited from global dust storms, but a pyroclastic origin cannot be ruled out. The "dark collar" materials are indistinguishable from the summit area thermal properties, indicating the visual albedo differences result from a very thin ( $< 2 \text{ cm}$ ) mobile dust layer. The shield base has higher thermal inertia and fewer spatially unresolved high thermal inertia materials than the summit area; these differences are probably due to downslope aeolian transportation and sorting of sediments. Sand-sized particles, possibly electrostatically bound dust particles (Greeley, 1979), could be present throughout the lower flanks of the volcano but there is no photographic evidence of sand accumulations. Thermal inertias for Ascræus Mons

represent a minimum of 1500 martian years of aeolian dust deposition at average rates.

Surface roughness. Ascraeus Mons strongly scatters radar signals. High thermal inertia materials (e.g. rocks > 10 cm) probably are not the principal radar scatterers; lava flows with surface variations on scales < 100 m but > 10 cm probably contribute the most to the radar scattering. The low thermal inertia materials present throughout the Tharsis region do not mask the surface roughness from the radar signals. The shield of Ascraeus Mons scatters radar signals more effectively than the Tharsis plains, suggesting that the intermixed shield flows produce more roughness than the broad plains flows. Radar scattering characteristics may represent surface variations related to timescales near the geologic age of the terrain unit.

Atmospheric water vapor. Water vapor abundances are as much as 6 times greater over the shield base and the Tharsis plains than over the summit of the volcano. The water vapor abundance is not correlated with thermal inertia changes on the shield-plains contact, which implies that the atmospheric water is not related to particular surface materials or to induration of the shield base soil.

## CHAPTER 5. HAWAII-MARS COMPARISONS

### Introduction

Hawaii has been used as a terrestrial analog for many volcanic features visible on the martian volcanoes (Greeley, 1973; Carr and Greeley, 1980). Some of the results for Ascræus Mons (Chapters 3 and 4) are not easily understood in terms of the spatial distribution or appearance of surface features smaller than the resolution limits of the photographs. Such results include the low thermal inertia and distinct flow morphology observed for the summit area terrains on Ascræus Mons, the high thermal inertia "blocks" on the volcanic terrains, and the similar thermal properties of all of the flow terrains. Several Hawaiian flows (Fig. 5.1) have surface characteristics that are instructive in the interpretation of features on Ascræus Mons.

Differences between the martian and terrestrial environments, particularly with respect to the atmosphere, are likely to influence the remote sensing results obtained for both planets. Laboratory analysis of a suite of Hawaiian rocks (Robertson and Peck, 1974) provides an excellent source of data for quantifying the thermal inertia variations in basalts. This information is also useful in assessing the effects of atmospheric conditions on the thermal inertia of basalt.

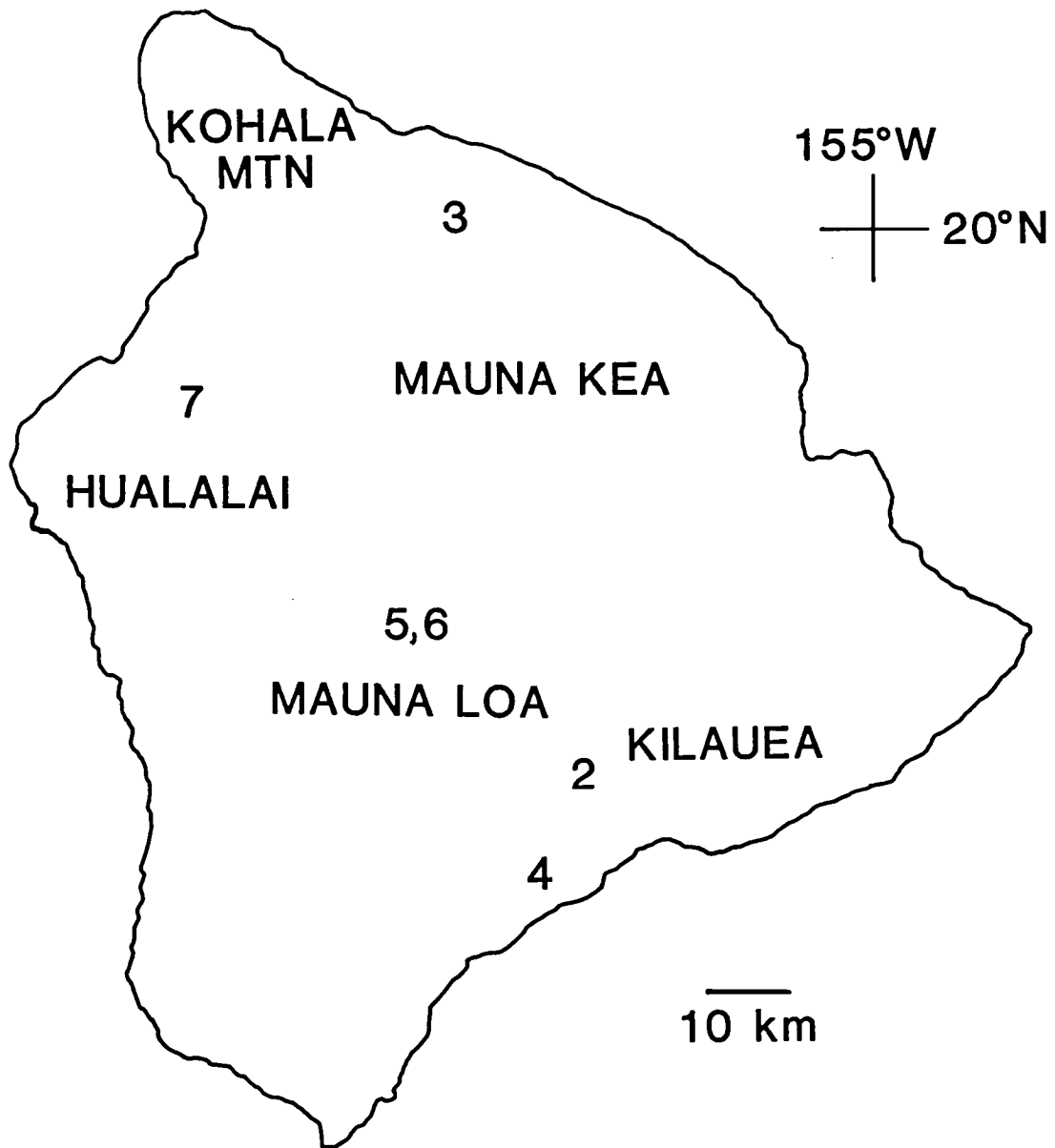


Figure 5.1. Location map for photographs of Hawaiian lava flows. Numbers 2 through 7 show the approximate location of Figs. 5.2 through 5.7, respectively. The five major volcanoes that comprise the island of Hawaii are also identified.



### Hawaiian Lava Flows

Four aspects of Hawaiian flows are considered here for comparison with observations of Ascræus Mons: 1) mantling of flow surfaces by fine-grained materials, 2) surface roughness and its effects on apparent thermal inertias, 3) surface features on hummocky terrain, and 4) ridge dimensions on flows. A summary of all four of these aspects concludes the section.

Mantling. The spectral reflectance and thermal infrared data for Ascræus Mons indicate that fine-grained surface materials are present on much of the volcano. An aa flow near Mauna Iki on Kilauea volcano has been mantled by ash of the Keanakakoi formation associated with relatively recent eruptions of Kilauea (Malin et al., 1983 and Fig. 5.2). This flow appears very subdued on aerial photographs. Both pyroclastic and aeolian sediments are areally abundant in this area, with thicknesses of cm to several m (Sharp and Malin, 1983). This example illustrates both the potential importance of pyroclastics on basaltic shield surfaces and the difficulty of remotely identifying either a volcanic or aeolian origin for the surface fines.

Several knobs of vesicular aa blocks project above the fine-grained surface materials covering this subdued flow (Fig. 5.2). These knobs represent one possible example of

the higher thermal inertia "blocks" identified in the Tharsis area (Chapter 4). Indurated layers presumably would have higher thermal inertias than the particulate surface materials; these features may also contribute to the Mars "block" abundances. The aa blocks and the indurated soil cover roughly 20% of the present surface of the flow (Fig. 5.2) but neither of these materials would likely have a thermal inertia of 30 on Mars (see porosity discussion below). The "block" abundance of this surface under martian conditions would probably be less than the actual areal coverage of the knobs and indurated soil, perhaps < 15%. Such a surface may be similar to the Tharsis plains, which are generally lacking in detailed flow morphology and have "block" abundances of about 10%.

Mantling of flow surfaces does not necessarily limit the visible flow morphology. Flows on the northwest flank of Mauna Kea are part of the grassy rangeland in this area, yet flow margins and leveed channels are clearly distinguishable (Fig. 5.3). These flows are considerably older than the flows of Kilauea (Macdonald and Abbott, 1970, p.290-291), leading to substantial chemical weathering and soil generation. The soil is likely to be at least 10s of cm thick on the flows. The vegetation provides a particularly uniform surface albedo and texture that allows even subtle topographic changes to be visible. Although the environment on Mauna Kea is very different



Figure 5.2. Mantled surface of an aa flow near Mauna Iki on Kilauea volcano. The flow surface is covered by ash of the Keanekaoi formation from Kilauea. Knobs of vesicular aa blocks project above the ash, and indurated layers of ash are exposed at some locations. This surface may be similar to the Tharsis plains around Ascraeus Mons. White card in foreground is 25 cm long.

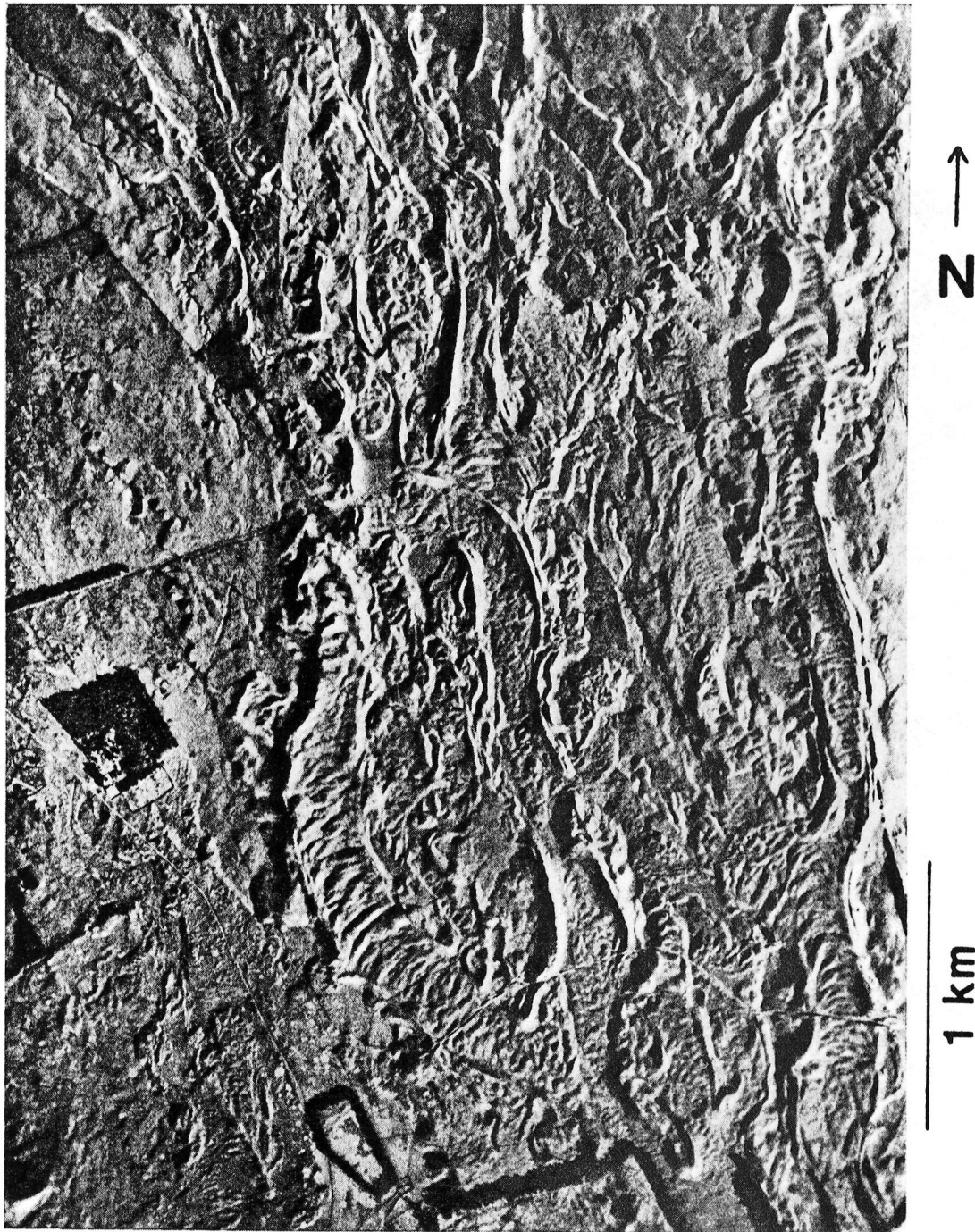


Figure 5.3. Grass-covered flows on the northwest flank of Mauna Kea. Flow margins and leveed channels are clearly visible in spite of ubiquitous soil and vegetation cover. U.S. Department of Agriculture photograph EKL-8CC-77.

from the martian environment, particularly with respect to rainfall and both chemical and physical weathering, the Hawaiian flows illustrate that fine-grained materials could be present on the martian flows without eliminating the large scale ( $> 10$  m) flow morphology. The distinct morphology of flows in the summit area of Ascræus Mons should not be considered a contradiction to the fine particle size inferred from the thermal inertias.

Surface roughness. Surface roughness affects the thermal characteristics of complex surfaces through reradiation to or shadowing of adjacent surfaces (Winter *et al.*, 1972). This process can be observed on lava flows where primary surface features are preserved. Predawn and daytime thermal photographs of the 1823 flow on Kilauea (R. Greeley, personal communication, 1983) show relative temperature differences that are directly associated with surface roughness (Fig. 5.4). The areas warmest at night and coolest during the day (higher apparent thermal inertia) typically have very irregular surfaces on the scale of .001 to 1 m (Fig. 5.4a) while the areas coolest at night and warmest during the day (lower apparent thermal inertia) are comparatively smooth at the sub-meter scale (Fig. 5.4b). The rough locations typically occur within channelized areas of the flow.

The thermal data from Ascræus Mons are of sufficient spatial resolution to distinguish between areas of either





Figure 5.4. Surface roughness on the 1823 flow of Kilauea. a) Irregular surface (higher apparent thermal inertia). b) Smooth surface on the sub-meter scale (lower apparent thermal inertia). Card is 25 cm long.

channelized or unchannelized flows but both terrain types have the same thermal inertias. Thus, these textures either do not influence the martian surface temperatures or, more likely, have no effect on temperatures as a result of surface modification (e.g. deposition of fine-grained materials). The sub-meter scale roughness differences on the martian flows are apparently insufficient within the 2 km by 5.5 km area of the best IRTM sequence to produce distinguishable temperature differences. Radar scattering from Ascraeus Mons indicates that roughness elements  $> 10$  cm are present on the shield surface but the thermal and radar data may be reconciled by fine-grained surface materials that are thicker than several cm but thinner than several m.

Hummocks. The hummocky terrain at the summit of Ascraeus Mons includes areas with 500 m to 1 km spacing of the hummocks (Fig. 3.11, h). The summit area on the northwestern flank of Mauna Loa has a similar hummocky appearance in aerial photographs, and on the ground the entire surface is covered by pahoehoe "toes" that originate from 1 to 3 m high mounds (M. Malin, personal communication, 1983 and Fig. 5.5). Macdonald (1972, p.78-79) used the term "tumuli" for dribble-covered mounds. Individual pahoehoe toes are solid, lacking the gas-filled core often present in near-vent pahoehoe toes; this "degassed" pahoehoe is typical of basaltic lava that is

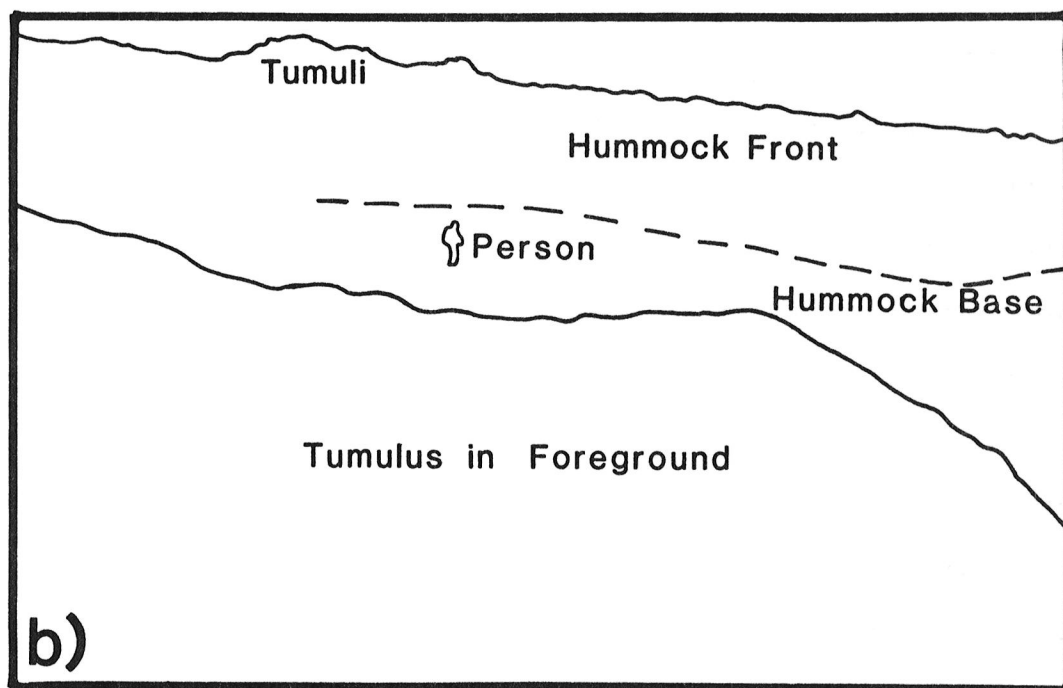


Figure 5.5. Hummocky terrain near the summit of Mauna Loa.  
a) Toey pahoehoe covers the surface, extruded from tumuli 1 to 3 m high. b) Line drawing of photograph.



well removed from the vent area but which has not transformed into clinkery aa (Carr and Greeley, 1980, p.129-130). The positive relief portions of the hummocks (Fig. 5.5, ridge) are spaced hundreds of m apart and rise 10 to 20 m above the relatively planar surfaces at the ridge base. Tumuli are present everywhere but the largest ones typically occur on the crests of individual hummocks. No clear indications remain of the pre-flow topography but at a few locations aa clinkers are only partially covered by the pahoehoe toes (Fig. 5.6), consistent with the observation of isolated flow margins throughout the hummocky terrain on Mars (Chapter 3).

The dominance of toey pahoehoe on the surface of the Hawaiian hummocky terrain suggests that toey pahoehoe could also be present throughout the hummocky terrain on Ascræus Mons. Both aa and pahoehoe flows are interpreted to be present on Ascræus Mons (Chapter 3), and "degassed" toey pahoehoe may represent lavas removed from the vent area but not on slopes steep enough to produce a transition to a clinkery aa (e.g. Williams and McBirney, 1979, p.111). The highest resolution photographs of Ascræus Mons are not capable of resolving features < 50 m in scale, so the presence of tumuli and toey pahoehoe on the martian hummocky terrain cannot be directly substantiated.

Ridges. A trachyte flow on the northwestern flank of Hualalai volcano has ridges of similar height and



Figure 5.6. Pahoehoe toes on a partially covered aa flow. Aa clinkers remained uncovered only near the margin of the flow. Book is 15 cm high.

spacing to ridges on a flow near the summit of Ascræus Mons (Figs. 5.7 and 3.11). The Hawaiian ridges are typically 150 m apart and 15 m high, comparable to the 120 m spacing and 15 m height on the martian flow (Chapter 3). Application of Eqs. 3.4 and 3.5 to the Hawaiian flow results in calculated interior viscosities of  $3.4 \times 10^9$  to  $5.0 \times 10^{11}$  poise for ridge growth times of 1 hour to 1 week, respectively. These values are only a factor of two greater than the calculated viscosities for the martian flow. The trachyte flow on Hualalai is interpreted to be the result of extensive differentiation in a magma chamber isolated from the main magma body of the volcano (Macdonald and Abbot, 1972, pp.305-306) and it is possible that a similar process produced a chemically-evolved magma for the ridged flow on Ascræus Mons.

Summary. 1) Mantling. Fine-grained materials of both volcanic (pyroclastic) and aeolian origin mantle the surfaces of some Hawaiian flows but it would be difficult to determine their origin from remote observations alone. Surface exposures of aa blocks and indurated soil on mantled flows may be comparable to the "block" abundances inferred from thermal measurements of the Tharsis plains. Distinct flow morphology does not automatically rule out the presence of areally abundant fine-grained surface materials, either on Hawaii or Mars. 2) Surface roughness. Thermal photographs of the 1823 flow on Kilauea show areas

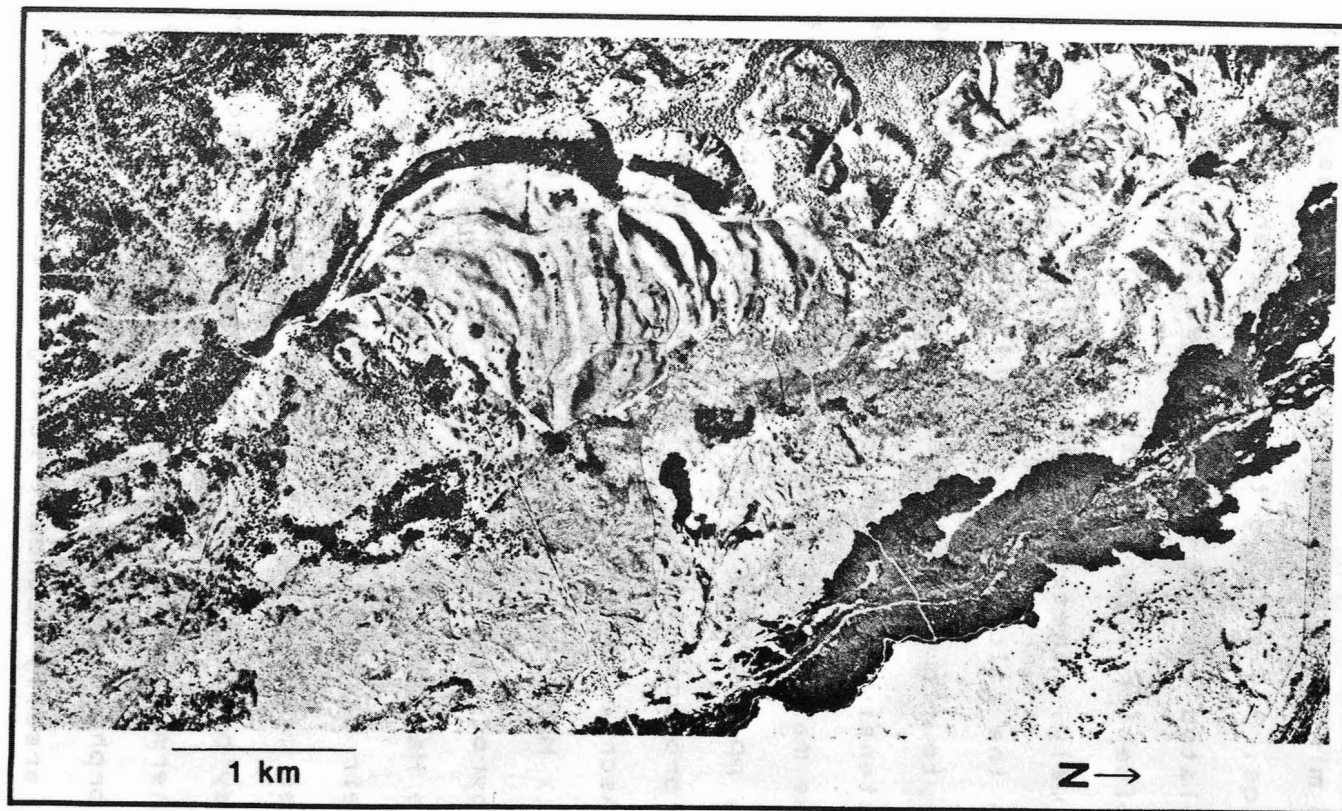


Figure 5.7. Ridges on the Puu Waawaa trachyte flow on Hualalai. The ridges are similar in height and spacing to ridges on an Ascræus Mons flow (Fig. 3.11, large arrow); this results in similar calculated viscosities for both flows. The dark basalt flow is from the 1859 eruption of Mauna Loa. U.S. Department of Agriculture photographs EKL-1CC-22 to 25.

of higher apparent thermal inertia typically have very irregular surfaces on the sub-meter scale while areas of lower apparent thermal inertias are relatively smooth. The lack of thermal inertia variations on the flow terrains of Ascræus Mons suggests that the flow surfaces have all been modified, probably through deposition of fine-grained materials on all terrains. 3) Hummocks. Both Ascræus Mons and Mauna Loa have terrains dominated by irregular undulations with 500 to 1000 m spacing. The Hawaiian terrain is covered by "degassed" toey pahoehoe and tumuli; similar features may also be present on the martian terrain. Toey pahoehoe would be consistent with the pahoehoe and aa flows also interpreted to be present on Ascræus Mons (Chapter 3). 4) Ridges. A trachyte flow on Hualalai has ridges of similar height and spacing to a ridged flow on Ascræus Mons. Viscosity estimates from the ridge dimensions are similar for both flows, and the martian flow could also consist of chemically evolved lava.

#### Porosity and Thermal Inertia

Thermal inertia variations on Mars are interpreted to represent thermal conductivity differences since density and specific heat typically vary much less than thermal conductivity in most rock materials (Kieffer et al., 1973, 1977). Porosity in volcanic materials can also result in considerable density variations in rocks of

the same composition. Laboratory measurements on basalts from Hawaii provide very useful data for evaluating the effects of porosity on thermal inertias.

Robertson and Peck (1974) measured the porosity, thermal conductivity, bulk density, average vesicle diameter, glass content, and modal olivine content for 61 samples that included tholeiite and olivine tholeiite basalts from Kilauea and a few alkali basalts from Mauna Kea and Hualalai. These data were used to relate the various properties to porosity (Fig. 5.8). Statistically, porosity is the best choice as an independent variable for correlation with the other parameters (Table 5.1). Thermal conductivity and density, two of the three physical parameters that determine the thermal inertia (see Eq. 2.1), are strongly correlated with porosity (Fig. 5.8a,b), while the other measured properties show little correlation (Fig. 5.8c,d,e). It is significant that the average vesicle diameter, glass content, and modal olivine content apparently have no strong influence on the physical properties associated with thermal inertia. These three quantities would presumably be the easiest to estimate in the field, but such estimates apparently have little relationship to the thermal behavior of the surface.

The thermal conductivity and density measurements can be used to calculate the thermal inertias for the Hawaiian basalt suite by assuming a value for the specific heat.

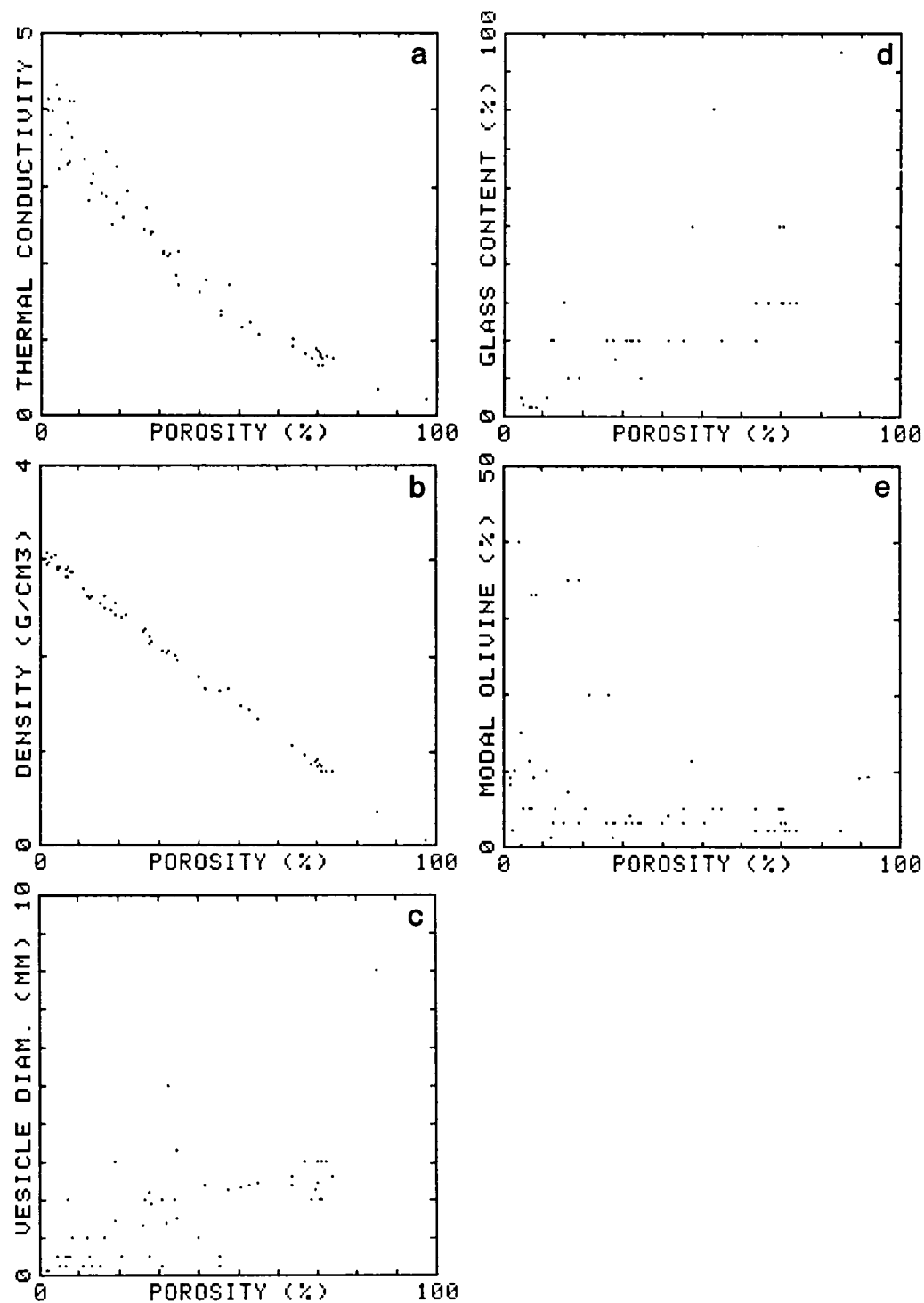


Figure 5.8. Properties of Hawaiian basalts as a function of porosity. Data are from Robertson and Peck (1974). The units of thermal conductivity are cal cm<sup>-1</sup> sec<sup>-1</sup> K<sup>-1</sup>.

Table 5.1. Correlation coefficients for basalt properties.

<u>Porosity</u>		<u>Conductivity</u>	
Conductivity	.965	Porosity	.965
Density	.999	Density	.973
Vesicles	.713	Vesicles	.247
Glass	.760	Glass	.028
Olivine	.347	Olivine	.535
<u>Density</u>		<u>Vesicles</u>	
Porosity	.999	Porosity	.713
Conductivity	.973	Conductivity	.247
Vesicles	.213	Density	.213
Glass	.092	Glass	.726
Olivine	.419	Olivine	.048
<u>Glass</u>		<u>Olivine</u>	
Porosity	.760	Porosity	.347
Conductivity	.028	Conductivity	.535
Density	.092	Density	.419
Vesicles	.726	Vesicles	.048
Olivine	.014	Glass	.014

Underlined parameter is the independent variable in a first order (linear) least squares determination of the correlation coefficient for the parameters listed below it. A second order least squares determination modestly improves some correlations while significantly degrading others.



Basaltic rocks have a consistent value of  $0.20 \pm 0.01$  cal gm<sup>-1</sup> K<sup>-1</sup> for their specific heat (Goranson, 1942; Kahle, 1980) and all types of igneous rocks show a range in specific heat of only 0.16 to 0.23 (Kahle, 1980, p.264). Setting the specific heat to 0.2, the thermal inertias of the Hawaiian basalts are seen to be inversely proportional to porosity (Fig. 5.9a).

The relationship between thermal inertia and porosity can be extended to martian conditions through laboratory measurements of thermal conductivity as a function of atmospheric pressure. Unfortunately, these measurements do not exist for basalts over a wide range of porosities. The best thermal conductivity vs. pressure data at different porosities have been obtained for quartz sands and sandstones and for silica microspheres (Woodside and Messmer, 1961a,b). The change in thermal conductivity associated with a reduction of atmospheric pressure from 1 bar to 6.1 mbar can be related to porosity through these data. This relationship, when applied to the Hawaiian basalt data, provides a comparison of thermal inertias on Earth and Mars for equivalent rock properties (Fig. 5.9b). The martian thermal inertias are consistently lower than the values for Earth due to the lowered gas conductivity at martian atmospheric pressures, attaining a difference of a factor of three for the low thermal inertias typical of much of Mars.

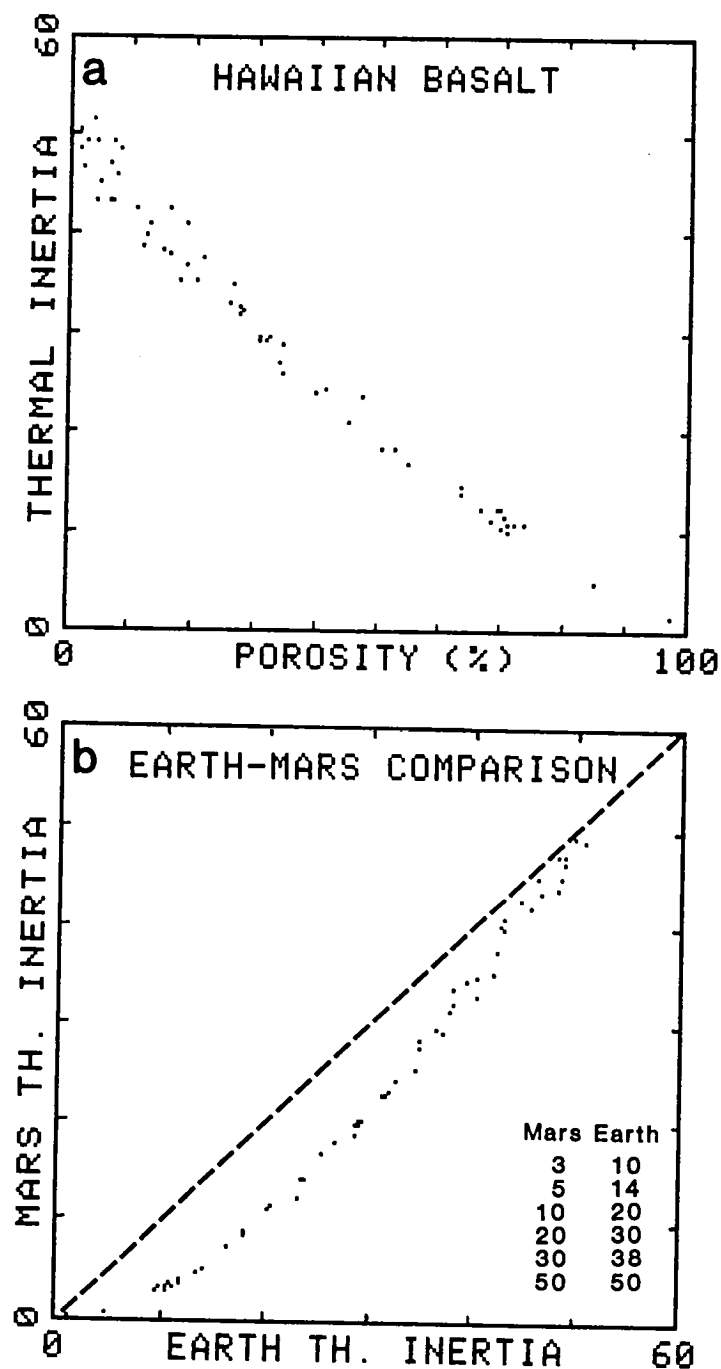


Figure 5.9. Thermal inertias calculated for the Hawaiian basalts. Thermal inertia (units of  $10^{-3} \text{ cal cm}^{-2} \text{ sec}^{-1/2} \text{ K}^{-1}$ ) was calculated from the measured thermal conductivities and densities, with an assumed specific heat of  $0.2 \text{ cal gm}^{-1} \text{ K}^{-1}$ . a) Thermal inertia as inversely correlated with porosity. b) Thermal inertias on Mars and Earth for equivalent rock properties. Martian thermal inertias are consistently lower than terrestrial thermal inertias.

This procedure assumes that the compositional differences between the basalts and the quartz sands do not influence the thermal conductivity measurements. At 1 bar atmospheric pressure both quartz sandstone and basalt have very similar thermal conductivities and thermal inertias (Kahle, 1980, p.264). The thermal conductivities of air and carbon dioxide are slightly different but both gases produce comparable thermal conductivity changes in porous materials as a function of pressure (Kannuluik and Martin, 1933). Therefore, these considerations should not significantly affect the results obtained here.

The difference between the calculated thermal inertias for basalts on Earth and Mars are most pronounced for lower thermal inertias, i.e. large porosities (Fig. 5.9b). For large porosities the composition of the solid particles should not greatly influence the thermal properties, because the size of void spaces governs the total conductivity of the rocks at low gas pressures (Woodside and Messmer, 1961a). The results obtained here for basalts may then be applicable to porous particulates in general, interpreted to be present over most of the surface of Mars (Kieffer et al., 1977). Martian thermal inertias as a whole would then be equivalent to considerably larger thermal inertias on Earth, decreasing the apparent difference between the average martian values ( $I = 2$  to  $20$ , Palluconi and Kieffer, 1981) and thermal inertias

determined on Earth ( $I = 10$  to  $80$ , Kahle et al., 1976; Kahle, 1980). This reduces the need to invoke processes on Mars substantially different from those active on Earth in order to explain the generally low values for martian thermal inertias.

Porosity contributes to the relationship between particle size and thermal inertia in particulate materials (Fig. 2.7) because pore size and volume varies with particle size. The low thermal inertias in nonvolcanic regions such as Arabia are best explained by small particle size (diameter  $< 50 \mu\text{m}$ ). However, the low thermal inertias on volcanic terrains such as Ascraeus Mons could potentially be due to flow surfaces with very high porosity. Lee (1984, p.114) interpreted the dark collars on the Tharsis volcanoes to indicate that dust has a low residence time on the flanks of the volcano and thus the low thermal inertias are the result of highly vesicular lava, as originally proposed by Kieffer et al. (1977). In Chapter 4 the thermal inertia for the summit of Ascraeus Mons was determined to be  $2.0$  to  $2.5$ , comparable to the Tharsis plains. From laboratory measurements on basalt, these values require porosities  $> 85\%$ , which only occur on the glassy surface of recent lava flows (Robertson and Peck, 1974).

It does not seem likely that a pristine flow surface could be preserved over the age of Ascraeus Mons (estimated

to be > 600 million years, Chapter 3) from either chemical or physical weathering. Gooding and Keil (1978) indicate that basaltic glass should weather much more rapidly than crystalline rock in the martian environment and is the likely precursor to clays in the martian dust. If aeolian activity on the volcano involves saltation of sand-sized particles (Chapter 3) then a glassy flow surface should not survive for the age of the volcano. Finally, all of the flow terrains on Ascræus Mons have the same low thermal inertia ( $I \approx 2$ ), both aa and pahoehoe (Chapter 3), while fresh basalt flows on Earth have thermal inertias more representative of bedrock, with higher values on aa flows ( $I = 40$  to  $80$ , Kahle, 1980, p.270). These considerations indicate that a small particle size interpretation of the Ascræus Mons thermal inertias is more likely than a fresh, highly vesiculated volcanic surface.

Summary: Laboratory measurements of thermal and physical properties for Hawaiian basalts (Robertson and Peck, 1974) were used to demonstrate that thermal inertia is inversely proportional to porosity. This result was extended to martian conditions through the gas-pressure dependence of thermal conductivity, as a function of porosity, for silica sands and microspheres. Thermal inertias, for equivalent rock properties, are as much as a factor of three lower under martian atmospheric conditions

than under terrestrial conditions. Porosity contributes to the relationship between particle size and thermal inertia (Fig. 2.7) because a decrease in particle size increases porosity. On volcanic terrain, such as Ascraeus Mons, low thermal inertias could represent highly porous, glassy flow surfaces instead of a small particle size. Physical and chemical weathering make it highly unlikely that pristine, frothy flow surfaces are the cause of the low thermal inertias on Ascraeus Mons.

#### Summary

Hawaiian lava flows. Flows that are substantially degraded in morphology (mantled by fine-grained volcanic and aeolian materials) still have a considerable exposure of rock above the surface mantling materials. Conversely, distinct flow morphology does not indicate that fine-grained materials are absent from the flow surface. Surface roughness on the sub-meter scale influences the thermal behavior of flow surfaces, so the lack of thermal variations between flow terrains on Ascraeus Mons indicates a uniform distribution of sub-meter scale roughness on these flows. Owing to the great variety of surface textures present on basalt lava flows, the uniform thermal properties observed for the martian flow terrains suggest that fine-grained materials, present on all terrains, result in the uniform roughness. Hummocky terrain on

Ascraeus Mons may include toey pahoehoe and tumuli (below the resolution limit of available photographs) if the martian terrain is similar to hummocky terrain near the summit of Mauna Loa. A trachyte flow on Hualalai has ridge geometries similar to a ridged flow on Ascraeus Mons, supporting the possibility of localized eruptions of chemically evolved lavas on Ascraeus Mons.

Porosity and thermal inertia. Hawaiian basalts have calculated thermal inertias that are inversely proportional to porosity. By assuming that the gas pressure dependence of thermal conductivity is the same for both porous basalt and silica particulates, thermal inertias of the same porous basalts would be up to a factor of 3 smaller on Mars than on Earth. Highly porous flow surfaces could cause low thermal inertias on volcanic terrains but it is unlikely that the frothy flow surfaces required to explain the Ascraeus Mons thermal inertias could survive physical and chemical weathering in the martian environment. Small particle size for the surface materials is a more likely explanation for the Ascraeus Mons thermal inertias than a fresh, highly vesiculated flow surface.

## CHAPTER 6. DISCUSSION AND CONCLUSIONS

### Discussion

Ascræus Mons provides an excellent opportunity to examine the relationship between physical properties measured by remote sensing techniques and the surface morphology. Interpretation of spacecraft photographs suggests that Ascræus Mons has had a complex history of endogenic and exogenic events (Chapter 3). Remote sensing data spanning a wide range of wavelengths are spatially coincident with many geologic features of the volcano (Chapter 4). Although no lander photographs are available from the surface of Ascræus Mons, Hawaiian lava flows provide some possible examples of the conditions and types of surface features that may be present on the martian volcano (Chapter 5). In this section the results of these analyses are combined in order to evaluate the processes that have contributed to the geologic history of Ascræus Mons and their implications for other areas of Mars.

Geologic history. This summary of the geologic history of Ascræus Mons is based largely on the photogeologic interpretations presented in Chapter 3. The emplacement and modification of the shield materials are summarized below, followed by a comparison of Ascræus Mons to the stages identified in the history of the Hawaiian shield volcanoes.



Mountainous terrain west of Ascræus Mons is embayed by the plains extending downslope from the volcano. The mountainous terrain was emplaced as lava or debris flows from source vents subsequently buried by flows on the southern margin of the Ascræus Mons shield. Voluminous flows extend down both sides of the Tharsis Rise from a location between Pavonis Mons and Ascræus Mons and northeast of Ascræus Mons; the flows are superimposed on the plains surrounding Ascræus Mons. These major flows indicate that considerable volcanic activity persisted at the northern end of the Tharsis Rise after the centralized eruptions that produced Ascræus Mons. The lack of a localized or consistent source for these eruptions evidently prevented the development of another major shield edifice northeast of Ascræus Mons, possibly because the supply of magma at the Tharsis Montes diminished as a result of volcanism at Olympus Mons.

Modification of the shield surface occurred on Ascræus Mons subsequent to the growth of the shield (Chapter 3). The caldera complex near the summit of the volcano underwent at least nine collapse events, each of which was followed by partial lava flooding of the caldera. The western flank has numerous irregular depressions where mass-wasting processes have excavated into the shield materials. Near the lower margin of the western flank an erosional scarp separates the shield terrain from a

smooth-appearing unit that merges into the Tharsis plains. The smooth unit includes sinuous channels and subtle flows traceable to the shield, indicating that this unit (and the adjacent plains) postdate both the construction of Ascraeus Mons and at least part of the erosional modification of the shield. The channelized embayments into the northeast and southwest flanks of Ascraeus Mons represent more localized disruptions of the shield than occurred on the western flank. Lava erosion, ground ice sublimation, or debris flows (lahars) are the most likely processes associated with the embayment erosion. The embayments are the source of the most recent effusive activity from the volcano (Scott et al., 1981b and Chapter 3).

The events associated with the construction and modification of Ascraeus Mons can be compared to five stages in the history of mid-ocean basaltic shield volcanoes (Macdonald and Abbott, 1970, p.138): 1) the shield-building stage, 2) the caldera stage, 3) the post-caldera stage, 4) the erosional stage, and 5) the rejuvenated stage. Ascraeus Mons has apparently progressed through the first two stages, where fluid lavas enlarge the volcano and repeatedly flood the summit caldera.

The post-caldera stage of the Hawaiian volcanoes involves capping the shield with more chemically evolved lavas and pyroclastic materials, completely hiding the caldera (Macdonald and Abbott, 1970, p.141). This stage

either did not occur or was greatly reduced in intensity on Ascræus Mons. The caldera complex shows no evidence of volcanic activity after the flooding of the central (lowest) caldera. Isolated lava flows on Ascræus Mons could involve chemically evolved magmas but such flows do not appear to be areally significant (Chapter 3). Martian cinder cones should be broader and have less vertical relief than comparable terrestrial cinder cones (McGetchen et al., 1974) but neither photographic nor thermal data for Ascræus Mons shows localized morphologic, albedo, or particle size variations potentially related to cinder deposits. A lack of cinder cones on Ascræus Mons would suggest that Strombolian eruptions, characterized by weak to violent ejection of pyroclasts from lavas slightly more viscous than the fluid basalts of Hawaiian eruptions (Macdonald, 1972, p.219), are not common on the martian volcano. This may indicate that the martian magma is deficient in the volatiles associated with Strombolian eruptions. Alternatively, cinder deposits may be present but mantled by the dust that covers the volcano (Chapter 4). Summit area dust thicknesses ( $> 2$  cm but  $< 15$  m; Chapter 4) probably are not sufficient to obscure all evidence of Strombolian eruptions, so that such eruptions do not appear to represent a major part of the volcanic history of Ascræus Mons. There is no definitive evidence of post-caldera stage volcanic activity on Ascræus Mons.

Post-caldera volcanism on Earth occurs when crystallization in the magma chamber causes chemical differentiation of the magma (Macdonald and Abbott, 1970, p.143). The lack of a post-caldera stage on Ascræus Mons could indicate: 1) continual stirring of the magma chamber to inhibit differentiation, 2) solidification of the magma chamber without further eruptions, 3) withdrawal of magma from the volcano, or 4) progressive lowering of the magma level within the volcano. The first case would require unreasonably prolonged activity within the magma chamber of the volcano (estimated to be > 600 million years old; Table 3.2) unless the stirring was terminated by magma withdrawal (cases 3 and 4). The second case would require very competent rocks surrounding the magma chamber in order to contain the differentiated products generated during the magma solidification time. The third case represents the simplest explanation, but if magma withdrawal were complete, then any subsequent volcanism (i.e. plains-forming eruptions) would require refilling of the magma chamber. The fourth case is a variation of case 3; lowered magma levels could result from removal of hydrostatic support for the magma. The lower elevations for younger caldera floors (Chapter 3) could result from progressively decreased magma levels. The protracted plains-forming effusion from Ascræus Mons suggests that the magma supply was not suddenly removed from the volcano.

Instead, the magma level appears to have progressively dropped during the waning stages of volcanic activity on Ascræus Mons, possibly due to a shift in magma supply either to the northeast, along the Tharsis Rise, or to the west toward Olympus Mons.

Ascræus Mons did not have a rejuvenated stage of volcanism unless it included eruption of fluid lavas at the shield base. The erosion and modification of Ascræus Mons is consistent with the erosional stage of mid-ocean islands but the effusion at the shield base was much more extensive than the isolated eruptions of undersaturated (silica poor) lavas typical of the rejuvenated stage in Hawaii (Macdonald and Abbot, 1970, p.146). The age of the Ascræus Mons shield makes it unlikely that the volcano could still be evolving toward a rejuvenated stage. It appears that volcanic activity ceased at Ascræus Mons during the caldera stage, and the erosion of the shield base may have been associated with the latest effusion on the lower flanks.

Summary: The following sequence of events summarizes the main elements in the geologic history of Ascræus Mons. Volcanism and tectonism produced the Tharsis Rise, which buried the ancient heavily cratered plains (Scott and Carr, 1978). Effusion of fluid lavas centralized at the location of Ascræus Mons, building up a broad shield. The summit area collapsed repeatedly and was partially filled by lava.

Flank erosion (most likely by lava erosion, ground ice sublimation, or debris flows) modified the shield edifice, while lavas flooded the plains surrounding the shield. Eruptions produced voluminous flows SSW and NNE of Ascraeus Mons, along the axis of the Tharsis Rise. Flank erosion localized at the SW and NE margins of the shield, deeply embaying the shield. Volcanic activity on Ascraeus Mons ceased, allowing features to be modified by surface processes. In comparison to the Hawaiian shield volcanoes, Ascraeus Mons did not progress past the caldera stage. Strombolian eruptions do not appear to represent a major part of the volcanic activity recorded on the volcano surface. There is no definitive evidence of post-caldera or rejuvenated stage volcanism on Ascraeus Mons, which could indicate that martian magmas are volatile-poor relative to the Hawaiian lavas.

Surface properties. The remote sensing observations of Ascraeus Mons provide information about the surface at scales below the resolution limit of orbital photographs (Chapter 4). The surface materials (e.g. sediments, soil, rocks) could be related to the processes that have operated on the surface. On Ascraeus Mons the shield flanks show the most variation in the different data sets examined here. The flank properties are summarized below, followed by discussion of their potential implications for the surface history of Ascraeus Mons.

The flanks of Ascraeus Mons have several characteristics that vary with elevation (Chapters 3 and 4). In moving from the shield-plains contact to the summit there is an increase in the number of craters  $< 270$  m, an increase in the relief and tonal contrast of photographs, a decrease in thermal inertia (indicative of a decreasing average particle size), an increase in the areal abundance of high thermal inertia "blocks" (effective particle size  $> 10$  cm), and a decrease in the atmospheric water vapor abundance. The water vapor abundance does not appear to be directly associated with surface terrains (Chapter 4) but the other four characteristics appear to be related to the recent history of the surface materials, subsequent to the emplacement of rock materials within the shield terrains.

The lack of evidence for post-caldera stage eruptive activity (discussed above) lessens the likelihood of substantial pyroclastic activity on Ascraeus Mons. The radially symmetric low thermal inertias on the volcano are also difficult to reconcile with a pyroclastic origin (Chapter 4): 1) the comparatively low thermal inertias for both the volcano and the Tharsis plains would indicate an immense areal coverage ( $> 10^7$  km<sup>2</sup>) by pyroclastic materials of very similar particle size, 2) airfall deposits transported by global winds would not result in the 360° radial symmetry of the thermal inertias, and 3) thermal inertia changes at the shield-plains contact (Fig.

4.6) indicate that the pyroclastics would have had to precede the Tharsis plains surrounding the volcano. Pyroclastics covering the entire shield should affect the surface morphology but the observed elevation-dependent flank characteristics are not consistent with a pyroclastic source at either the summit or the shield base.

The elevation-corrected thermal inertias for the Ascræus Mons summit area and the Tharsis plains are very similar (Chapter 4). This suggests that similar materials are present in the uppermost 3 to 5 cm of both surfaces. If this is so, it weakens the argument that led to the proposal of extremely vesiculated basalt on the Tharsis volcanoes as an explanation of their low thermal inertias (Kieffer et al., 1976). The vesiculated basalt would need to be present throughout much of the Tharsis low thermal inertia region, which covers 15% of the martian surface (Zimbelman and Kieffer, 1979), if it is responsible for the Ascræus Mons surface properties. This situation seems highly improbable. Porosities necessary to produce the low thermal inertias ( $> 85\%$ ; Chapter 5) would make the volcanic rocks very fragile and unlikely to survive either the active aeolian environment observed throughout the Tharsis region or the chemical weathering of mafic volcanic glass (Gooding and Keil, 1978). The thermal inertias for Ascræus Mons are not likely to be governed by rock vesicularity.



Color reflectance values and thermal inertias indicate that the summit area albedos are controlled by a mobile dust layer preferentially removed from the dark collar area (Chapter 4). It is difficult to set dust in motion by the wind without either local roughness to generate turbulent eddies or sand to erode the dust (Bagnold, 1941, p.91). Threshold wind speeds for the initiation of particle motion increase with decreasing atmospheric pressure (Greeley et al., 1980) so that the free stream winds needed to initiate aeolian activity at the summit of the Tharsis volcanoes could approach the speed of sound (Sagan et al., 1974). The presence of m-scale nonerodible roughness elements could reduce the threshold wind speed required for particle motion. At 5 mbar atmospheric pressure, the threshold shear velocity of  $2 \text{ m sec}^{-1}$  corresponds to free stream wind speeds above the boundary layer of either  $100 \text{ m sec}^{-1}$  over a flat surface of erodible grains or  $33 \text{ m sec}^{-1}$  over a surface with m-scale nonerodible features (Greeley et al., 1982). It is not clear that the surface roughness on Ascraeus Mons is sufficient to allow aeolian erosion of dust (without sand) with the 0.5 mbar atmospheric pressure at the volcano summit.

Effective particle sizes inferred from thermal inertias are  $< 30 \text{ }\mu\text{m}$  and  $100 \text{ }\mu\text{m}$  at the shield summit and base, respectively (Chapter 4). The larger

average particle size and smaller areal abundance of high thermal inertia "blocks" (effective size  $> 10$  cm) on the shield base, relative to both the summit area and the Tharsis plains, provide evidence that the shield base materials may be better sorted than either the summit or the plains. Increased sorting results from repeated reworking during transport (Pettijohn et al., 1972, p.76) so the shield base surface materials may have undergone considerable sorting during transportation down the volcano. The particle size of the base materials corresponds to that of fine sand, which is most easily moved by the martian winds (Greeley et al., 1977). Transportation of sand down the volcano flanks would then contribute to the dust removal from the dark collar area. Both the subdued morphology and decreased abundance of "blocks" of the shield base may be the result of burial by mobile sand.

Lee (1984, p.192) indicates that the fresh appearance of surface features on the Tharsis volcanoes argues against significant surface erosion by winds. It is possible that sand-sized particles on Mars are not composed of competent materials such as quartz but rather electrostatically bound dust (Greeley, 1979). Such aggregates could move by saltation but they produce very little abrasion of rock materials (Greeley et al., 1982). Aggregates would also aid in an explanation for a renewable supply of

sand-sized particles at the volcano summit since some of the seasonally deposited dust could form the aggregates.

Differences in volatile transport through the surface could potentially contribute to thermal inertia variations on Ascræus Mons (Chapter 4). The greater abundance of water vapor over the lower elevations of the volcano increases the possibility of alteration of the surface properties with decreasing elevation. The large diurnal temperature amplitude may contribute to a daily transport of water vapor (and dissolved salts) through the topmost several cm of the surface materials. The diffusion of volatiles through the surface fines has been proposed as a mechanism for the production of "duricrust" (Mutch et al., 1977; Dittéon, 1982) or "case-hardened" soil layers (Sharp and Malin, 1984) at the Viking landing sites and such a process could potentially increase the thermal inertia of the surface (Dittéon, 1982). The increased thermal inertias at the base of Ascræus Mons could be consistent with this hypothesis. However, there is no correlation between water vapor abundance and the shield-plains contact, where a distinct thermal inertia change occurs, so there is no direct evidence of enhanced volatile interaction with the shield base materials. Soil induration cannot be ruled out as a possible factor in thermal inertia variations but it is probably less significant than downlope sediment transportation.

The dust, sand, and potentially indurated soils on Ascræus Mons are affected by processes presently active on Mars and do not appear to be directly related to the underlying geomorphic terrains. However, the surface deposits are not thick enough to hide the cm to m-scale features evident in scattered radar signals and exposed high thermal inertia "blocks". These observations indicate that either the surface materials are relatively young on a geologic time scale or the deposition rates are very small. Dust deposition estimates of approximately  $.001 \text{ gm cm}^{-2}$  throughout a martian year (Pollack et al., 1979; Lee, 1984, p.183) support the interpretation of a young age for Tharsis dust deposits (perhaps  $< 10^6$  years old; Christensen, 1984c). The variations in surface morphology on Ascræus Mons suggest that the deposit thicknesses decrease with increasing elevation, consistent both with reduced deposition at higher elevations (Lee, 1984, p.183) and with downslope transport of surface materials.

Summary: The flanks of Ascræus Mons have systematic variations in surface characteristics obtained from various data sets. The areal coverage and spatial distribution of small ( $< 30 \text{ }\mu\text{m}$ ) particles on the volcano and the surrounding plains are difficult to reconcile with a pyroclastic origin for the fine materials. Extremely vesiculated basalt would probably not survive the chemical and physical weathering in the martian environment; thermal

inertias on Ascraeus Mons are not likely to be governed by rock vesicularity. Visual reflectance and thermal inertias indicate that most of the volcano is covered with fine materials, most likely aeolian transported dust.

Sand-sized particles, possibly aggregates of dust, may increase in abundance down the flanks of the volcano. Soil induration probably is less significant than downslope sediment transportation as a possible contributor to thermal inertia variations on the volcano.

Global implications. The surface history of Ascraeus Mons has potential implications for other locations on Mars. The elevation-dependent corrections used for the thermal inertias of Ascraeus Mons were applied to thermal inertias of the equatorial portion of the planet (Figs. 6.1 and 6.2). The moderate thermal inertias for most of the martian surface are generally more uniform in the corrected version, increasing the potential importance of homogenizing surface processes such as aeolian activity.

The elevated Tharsis and Elysium areas show the greatest changes, particularly around the Tharsis Rise (Fig. 6.3). The thermal inertias in the Tharsis region that remain  $< 3$  after the correction (corresponding to particles  $< 50 \mu\text{m}$  in diameter) correlate with some enigmatic surface deposits. The cratered martian plains in these areas have been buried by materials that are proposed to be pyroclastic (Scott, 1982) or paleopolar (Schultz and

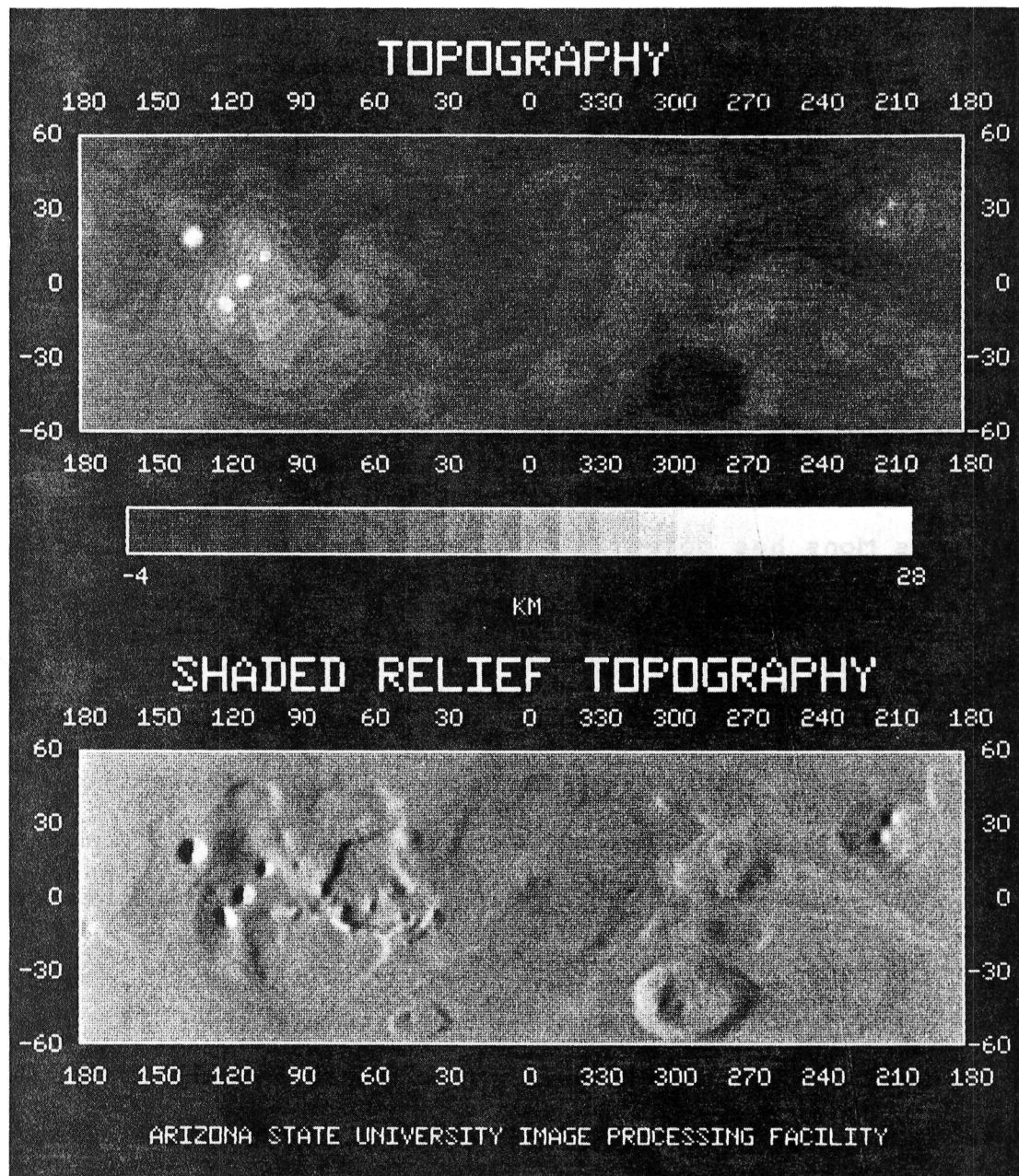


Figure 6.1. Topography of the equatorial region of Mars. Data are from the Mars Consortium (Kieffer *et al.*, 1981). The four Tharsis shield volcanoes are located near  $0^{\circ}\text{N}$ ,  $120^{\circ}\text{W}$ .

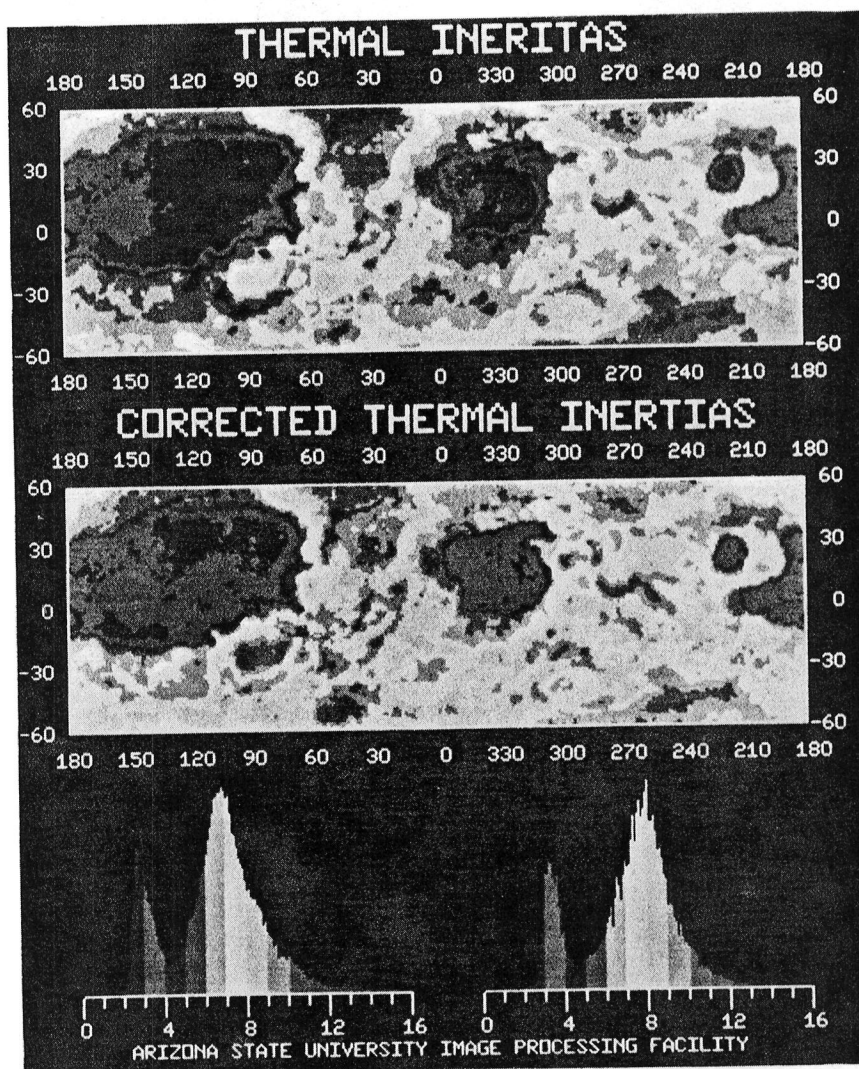


Figure 6.2. Thermal inertias in the equatorial region of Mars. Data are from the Mars Consortium (upper figure and left histogram). Elevation-dependent corrections were applied to the thermal inertias (lower figure and right histogram) using the topography of Figure 6.1. The greatest changes occur in the Tharsis Rise area ( $0^{\circ}\text{N}$ ,  $110^{\circ}\text{W}$ ).



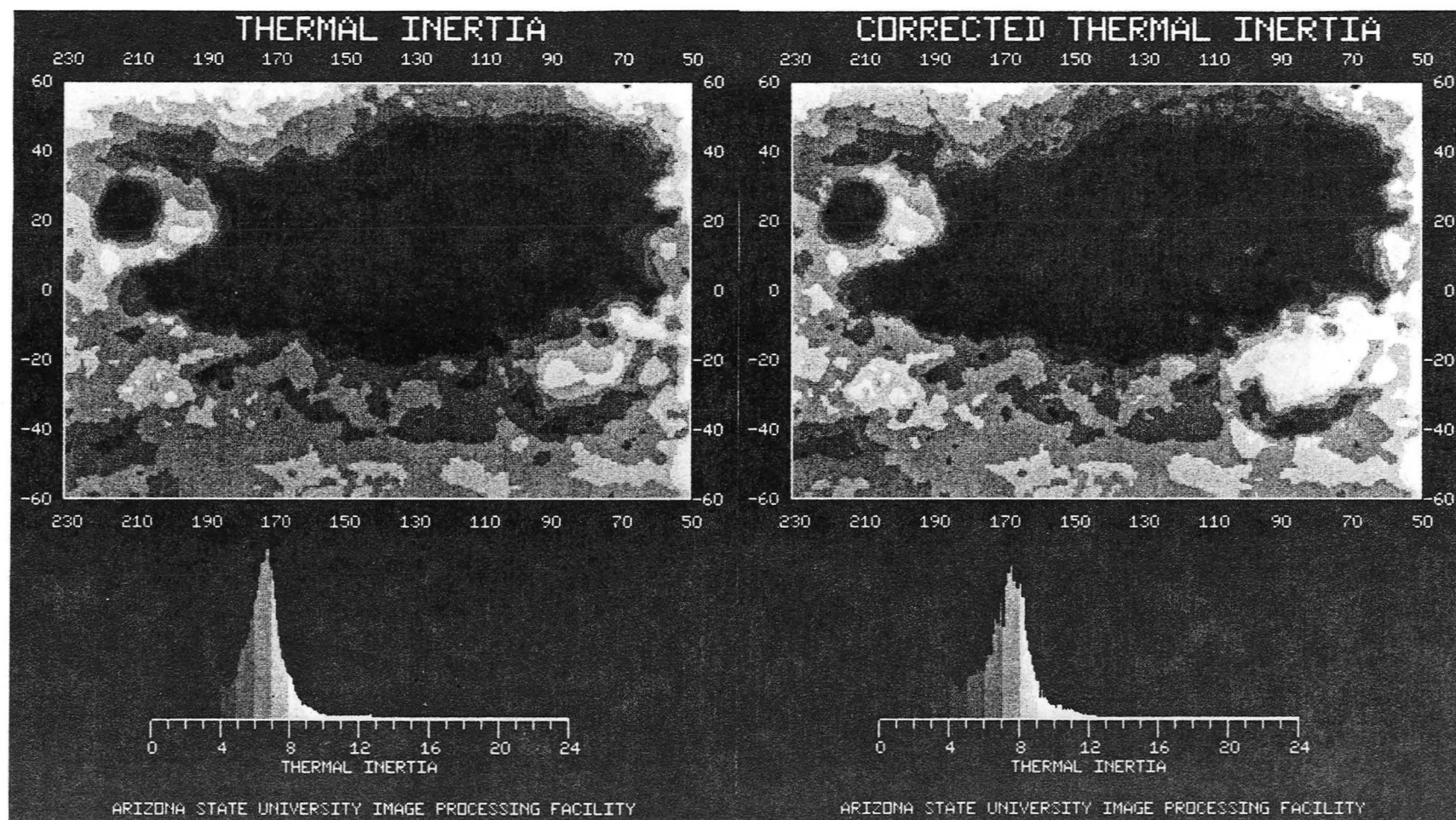


Figure 6.3. Thermal inertias for the Tharsis and Elysium regions. Data at left are from the Mars Consortium. Elevation-dependent corrected thermal inertias are shown at right.



Lutz-Garihan, 1981) in origin; no consensus about these materials has been reached.

The large regions of low thermal inertia in the northern hemisphere, including Ascraeus Mons within the Tharsis region, have been proposed as dust "sinks" for the current major dust storms on Mars (Christensen, 1984c). Global dust storm initiation is related to increased insolation on Mars near perihelion, which currently occurs when the subsolar latitude is in the southern hemisphere (Gierasch and Goody, 1973). Astronomical perturbations produce climate changes on Mars over time periods of  $10^5$  to  $10^7$  years (Toon et al., 1980), and these changes could influence the location of the regions of dust erosion and deposition (Christensen, 1984c). One important consideration for this hypothesis is the probable location of former dust sinks in the southern hemisphere since there is a lack of low thermal inertia regions south of the equator except for a portion of the Tharsis region. The results from Ascraeus Mons suggest that the complex association of dust, sand, and possible indurated soils in the Tharsis area may be related to the history of these global-scale dust deposits.

Ascraeus Mons is old enough to have undergone numerous cycles of dust deposition and erosion on the million-year timescale suggested by Christensen (1984c). The summit area of the volcano bears no clear evidence of these events

while the base area is substantially subdued. If the additional water vapor available at the lower elevations of the volcano does in fact contribute to the induration of the soils, the dust at lower elevations may not be removed but rather incorporated in a growing thickness of indurated materials. Abundant sand in the base area could inhibit the induration process by breaking up the soil. The induration process may also bond the sand-sized particles. In the southern hemisphere Solis Lacus is the current source of global dust storms (Gierasch and Goody, 1973). This broad plain occurs at relatively high elevation (approximately 8 km) which could potentially be an area where dust previously was deposited and has subsequently been indurated. It is interesting to note that an enigmatic high thermal inertia area southeast of Arsia Mons (Kieffer et al., 1976) has a thermal inertia very similar to that of Solis Lacus and may thus be a "window" through the present dust cover of Tharsis to the indurated soil from a previous climatic cycle. Tharsis, possibly including the base of Ascraeus Mons, could be a significant dust source area a million years from now when the initiation of global dust storms takes place in the northern hemisphere.

Summary: The dust deposition and aeolian transportation of sediments on Ascraeus Mons is likely related to climatic conditions that influence the global

transportation of dust. The southern hemisphere, and Solis Lacus in particular, is the current location of global dust storm initiation but low thermal inertias indicative of dust deposits are generally lacking south of the equator. Solis Lacus could potentially be an area where dust previously was deposited and has subsequently been indurated. An area southeast of Arsia Mons has a thermal inertia similar to that of Solis Lacus and could be a "window" through the present dust cover of the Tharsis region.

### Conclusions

Several conclusions can be drawn from this analysis of Ascraeus Mons:

- 1) Ascraeus Mons is similar to terrestrial basaltic shield volcanoes in both surface morphology and estimated rheologic properties. The flows on the flanks of Ascraeus Mons are interpreted to consist of pahoehoe, aa, and toey pahoehoe. Yield strength estimates obtained from flow dimensions are consistent with values for basalt flows in Hawaii.
- 2) The lower flanks of Ascraeus Mons have undergone extensive modification through mass-wasting and sediment burial. Irregularly shaped depressions and channelized embayments have excavated into the shield materials on the lower flanks. The erosional agent

could be lava, sublimation of ground ice, or debris flows. Surface morphology becomes increasingly subdued and the areal abundance of craters < 270 m in diameter decreases with decreasing elevation on the volcano; both conditions are probably due to deposition of fine materials on the surface.

- 3) Surface morphology and albedo provide no direct evidence of pyroclastic activity. The flanks of the volcano have numerous elongate craters interpreted to be endogenic in origin but there is no evidence of pyroclastic deposits around them. The dust present on the volcano (see 5 below) could have buried some pyroclastic deposits. However, the width of a thrust fault on the southern flank suggests that unconsolidated materials (e.g. nonwelded tuff) do not comprise a significant portion of the shield materials.
- 4) Volcanic activity on Ascræus Mons was protracted through time but apparently did not involve significant amounts of chemically evolved magmas. Crater retention ages indicate the shield flanks are probably > 600 million years old, the most recent caldera floor is probably > 400 million years old, and the plains northwest of the shield base are probably > 150 million years old (Table 3.2). Comparison of Ascræus Mons and the Hawaiian shield volcanoes

suggests that no post-caldera or rejuvenated stage volcanic activity (often involving very differentiated lavas) occurred on Ascraeus Mons.

- 5) Dust is abundant everywhere on Ascraeus Mons and the Tharsis plains. Low thermal inertias ( $I = 2$ , or an average particle size  $< 30 \mu\text{m}$ ) characterize both the summit area terrains and the Tharsis plains. The wavelength dependence of albedos on Ascraeus Mons parallels the trend for high albedo regions (e.g. Arabia), interpreted to have bright dust deposits.
- 6) The surface of Ascraeus Mons is neither primarily bedrock exposures nor completely homogenized through burial beneath fine materials. Spatially unresolved high thermal inertias (e.g. rocks, bedrock, and indurated soils) account for  $> 20\%$  of the surface near the summit of Ascraeus Mons. Radar signals are strongly scattered by features  $> 10 \text{ cm}$  in scale on the shield.
- 7) There is no correlation between thermal inertia and geomorphic terrain units except at the shield-plains contact and on caldera walls. The shield base terrains have higher thermal inertias ( $I = 4$ , or an average particle size of  $100 \mu\text{m}$ ) than the Tharsis plains (similar to the shield summit). The caldera walls have the highest thermal inertias in the summit area ( $I = 4.5$ ) but bedrock exposures probably cover  $<$

30% of the unit area. Remote sensing data at visual and infrared wavelengths are not significantly related to the bedrock materials of the shield terrains.

- 8) Sediment variations on the shield flanks probably result from downslope aeolian transportation. The shield base has a larger average particle size but a smaller abundance of unresolved high thermal inertia materials (particle size generally  $> 10$  cm) than the shield summit. This implies that the base materials have become better sorted through downslope transportation. Slope winds should be capable of moving sand-sized particles (possibly aggregates of dust) down the volcano.
- 9) Atmospheric pressure differences result in different thermal inertias on Earth and Mars for equivalent material properties. Laboratory measurements on Hawaiian basalts (Robertson and Peck, 1974) indicate that thermal inertia is inversely proportional to porosity. The low atmospheric pressure on Mars should result in thermal inertias that are up to a factor of 3 smaller than they would be under terrestrial conditions. Porous soils and particulates are probably affected in a similar manner.

Future work. Each of the Tharsis shield volcanoes should receive a thorough photogeologic investigation coincident with analyses of the best available remote sensing data. Arsia Mons should receive the highest priority because of its southern hemisphere location, closer to the region of current dust storm initiation. Flank morphology and surface properties variations can be compared with the results for Ascraeus Mons to assess latitudinal relationships between the surface histories on the volcanoes. The elevation-dependent properties may vary with age due to increased sorting, deposit thickness, or induration on older features (e.g. Arsia Mons). Solis Lacus should also receive a detailed investigation as a possible analog to the Tharsis area during conditions of dust removal. Finally, the Elysium volcanoes appear to provide examples of chemically evolved magmas (Malin, 1974) and deposits identified as pyroclastic airfall (Mouginis-Mark et al., 1982). These volcanoes should receive further investigation for comparison with the results from the Tharsis volcanoes.

## REFERENCES

- Allen, C. C., J. L. Godding, M. Jercinovic, and K. Keil, Altered basaltic glass: A terrestrial analog to the soil of Mars, Icarus, 45, 347 - 369, 1981.
- Arvidson, R. E., E. A. Guinness, and A. P. Zent, Classification of surface units in the equatorial region of Mars based on Viking orbiter color, albedo, and thermal data, J. Geophys. Res., 87, 10149 - 10157, 1982.
- Bagnold, R. A., The physics of blown sand and desert dunes, Chapman and Hall, London, 265p., 1941.
- Banerdt, W. B., R. J. Phillips, N. H. Sleep, and R. S. Saunders, Thick shell tectonics on one-plate planets: Applications to Mars, J. Geophys. Res., 87, 9723 - 9733, 1982.
- Binder, A. B., R. E. Arvidson, E. A. Guinness, K. L. Jones, E. C. Morris, T. A. Mutch, D. C. Pieri, and C. Sagan, The geology of the Viking lander 1 site, J. Geophys. Res., 82, 4439 - 4451, 1977.
- Blasius, K. R., The record of impact cratering on the great volcanic shields of the Tharsis region of Mars, Icarus, 29, 343 - 361, 1976.
- Blasius, K. R., and J. A. Cutts, Topography of martian central volcanoes, Icarus, 45, 87 - 112, 1981.
- Blasius, K. R., J. A. Cutts, J. E. Guest, and H. Masursky, Geology of the Valles Marineris: First analysis of imaging from the Viking 1 orbiter primary mission, J. Geophys. Res., 82, 4067 - 4091, 1977.
- Blunck, J., Mars and its satellites, Exposition Press, Hicksville, N.Y., 200p., 1977.
- Borgia, A., S. Linneman, D. Spencer, L. D. Morales, and J. B. Andre, Dynamics of lava flow fronts, Arenal volcano, Costa Rica, J. Vol. Geoth. Res., 19, 303 - 329, 1983.
- Briggs, G., K. Klaasen, T. Thorpe, J. Wellman, and W. Baum, Martian dynamical phenomena during June-November 1976: Viking orbiter imaging results, J. Geophys. Res., 82, 4121 - 4149, 1977.



- Briggs, G. A., W. A. Baum, and J. Barnes, Viking orbiter imaging observations of dust in the martian atmosphere, J. Geophys. Res., 84, 2795 - 2820, 1979.
- Carr, M. H., Volcanism on Mars, J. Geophys. Res., 78, 4049 - 4062, 1973.
- Carr, M. H., Tectonism and volcanism of the Tharsis region of Mars, J. Geophys. Res., 79, 3943 - 49, 1974a.
- Carr, M. H., The role of lava erosion in the formation of lunar rilles and martian channels, Icarus, 22, 1 - 23, 1974b.
- Carr, M. H., Geologic map of the Tharsis quadrangle of Mars, Map I-893, U. S. Geol. Surv., Washington, D. C., 1975.
- Carr, M. H., Changes in height of martian volcanoes with time, Geologic Romana, 15, 421 - 422, 1976.
- Carr, M. H., The surface of Mars, Yale University Press, New Haven, Mass., 232p., 1981.
- Carr, M. H., and R. Greeley, Volcanic features of Hawaii: A basis for comparison with Mars, NASA SP-403, Washington, D. C., 211p., 1980.
- Carr, M. H., H. Masursky, and R. S. Saunders, A generalized geologic map of Mars, J. Geophys. Res., 78, 4031 - 4036, 1973.
- Carr, M. H., R. Greeley, K. R. Blasius, J. E. Guest, and J. B. Murray, Some martian volcanic features as viewed from the Viking orbiters, J. Geophys. Res., 82, 3985 - 4015, 1977.
- Chase, S. C. Jr., J. L. Engel, H. W. Eyerly, H. H. Kieffer, F. D. Palluconi, and D. Schofield, Viking infrared thermal mapper, Appl. Opt., 17, 1243 - 1251, 1978.
- Christensen, E. J., Martian topography derived from occultation radar, spectral, and optical measurements, J. Geophys. Res., 80, 2909 - 2013, 1975.
- Christensen, P. R., The nature of the martian surface as derived from thermophysical properties, Ph.D. dissertation, Univ. of Calif. at Los Angeles, 229p., 1981.

- Christensen, P. R., Martian mantling and surface composition: interpretation of thermophysical properties, J. Geophys. Res., 87, 9985 - 9998, 1982.
- Christensen, P. R., Thermal emissivity of the martian surface: Evidence for compositional variations (abstract), Lunar Planet. Sci., XV, 150 - 151, 1984a.
- Christensen, P. R., Regional dust deposits on Mars: Physical properties, origin, and age, (submitted to Icarus), 1984b.
- Christensen, P. R., The distribution of rocks on Mars, (paper in progress), 1984c.
- Christensen, P. R., and R. W. Zurek, Martian north polar hazes and surface ice: Results from the Viking survey / completion mission, J. Geophys. Res., 89, 4587 - 4596, 1984.
- Christiansen, E. H., and R. Greeley, Mega-lahars (?) in the Elysium region, Mars (abstract), Lunar Planet. Sci., XII, 138 - 140, 1981.
- Clark, B. C., A. K. Baird, R. J. Weldon, D. M. Tsusaki, L. Schnabel, and M. P. Candelaria, Chemical composition of martian fines, J. Geophys. Res., 87, 10059 - 10067, 1982.
- Collins, S. A., The Mariner 6 and 7 pictures of Mars, NASA SP-263, Washington, D. C., 159p., 1971.
- Cooke, T. I., The works of Hesiod, AMS Press, New York, 203p., 1976.
- Crumpler, L. S., and J. C. Aubele, Structural evolution of Arsia Mons, Pavonis Mons, and Ascraeus Mons: Tharsis region of Mars, Icarus, 34, 496 - 511, 1978.
- Curran, R. J., B. J. Conrath, R. A. Hanel, V. G. Kunde, and J. C. Pearl, Mars: Mariner 9 spectroscopic evidence for H<sub>2</sub>O ice clouds, Science, 182, 381 - 383, 1973.
- Cutts, J. A., and K. R. Blasius, Martian outflow channels: Quantitative comparison of erosive capacities for eolian and fluvial models, Lunar Planet. Sci., X, 257 - 259, 1979.

- Davies, D. W., Effects of dust on the heating of Mars' surface and atmosphere, J. Geophys. Res., 84, 8289 - 8293, 1979.
- DeVaucouleurs, G., J. Blunck, M. Davies, A. Dollfus, I. K. Koval, G. P. Kuiper, H. Masursky, S. Miyamoto, V. I. Moroz, C. Sagan, and B. Smith, The new martian nomenclature of the international astronomical union, Icarus, 26, 85 - 98, 1975.
- Ditteon, R., Daily temperature variations on Mars, J. Geophys. Res., 87, 10197 - 10214, 1982.
- Dollfus, A., Etude polarimetrique de la lumiere reflechie par les nuages et l'atmosphere de la planete Mars, Comptes Rendus Academie des Sciences Paris, 227, 383 - 385, 1948.
- Downs, G. S., R. M. Goldstein, R. R. Green, G. A. Morris, and P. E. Reichley, Martian topography and surface properties as seen by radar: 1971 opposition, Icarus, 18, 8 - 21, 1973.
- Downs, G. S., P. E. Reichley, and R. R. Green, Radar measurements of martian topography and surface properties: The 1971 and 1973 oppositions, Icarus, 26, 273 - 312, 1975.
- Downs, G. S., R. R. Green, and P. E. Reichley, Radar studies of the martian surface at centimeter wavelengths: The 1975 opposition, Icarus, 33, 441 - 453, 1978.
- Downs, G. S., P. J. Mouginis-Mark, S. H. Zisk, and T. W. Thompson, New radar-derived topography for the northern hemisphere of Mars, J. Geophys. Res., 87, 9747 - 9754, 1982.
- Dycus, R. D., The meteorite flux at the surface of Mars, Pub. Astron. Soc. Pac., 81, 399 - 414, 1969.
- Eliason, P. T., L. A. Soderblom, and P. S. Chavez, Extraction of topographic and spectral albedo information from multispectral images, Photogram. Eng. Rem. Sens., 48, 1571 - 1579, 1981.
- Evans, D. L., and J. B. Adams, Comparison of Viking lander multispectral images and laboratory reflectance spectra of terrestrial samples, Proc. Lunar Planet. Sci. Conf., 10th, 1829 - 1834, 1979.

- Evans, D. L., and J. B. Adams, Amorphous gels as possible analogs to martian weathering products, Proc. Lunar Planet. Sci. Conf., 11th, 757 - 763, 1980.
- Evans, D. L., T. G. Farr, and J. B. Adams, Spectral reflectance of weathered terrestrial and martian surfaces, Proc. Lunar Planet. Sci. Conf., 12th, 1473 - 1479, 1981.
- Farmer, C. B., and P. E. Doms, Global seasonal variations of water vapor on Mars and the implications for permafrost, J. Geophys. Res., 84, 2881 - 2888, 1979.
- Farmer, C. B., D. W. Davis, A. L. Holland, D. D. LaPorte, and P. E. Doms, Mars: Water vapor observations from the Viking orbiters, J. Geophys. Res., 82, 4225 - 4248, 1977.
- Fink, J., Surface folding and viscosity of rhyolite flows, Geology, 8, 250 - 254, 1980.
- Flint, R. S., Glacial and quaternary geology, John Wiley and Sons, New York, N.Y., 892p., 1971.
- Frey, H., and M. Jarosewich, Subkilometer martian volcanoes: Properties and possible terrestrial analogs, J. Geophys. Res., 87, 9867 - 9879, 1982.
- Frey, H., B. L. Lowry, and S. A. Chase, Pseudocraters on Mars, J. Geophys. Res., 84, 8075 - 8086, 1979.
- Gierasch, P. J., and R. M. Goody, A model of a martian great dust storm, J. Atm. Sci., 30, 169 - 179, 1973.
- Gooding, J. L., and K. Keil, Alteration of glass as a possible source of clay minerals on Mars, Geophys. Res. Lett., 5, 727 - 730, 1978.
- Goranson, R. W., Heat capacity; Heat of fusion, in Geol. Soc. Am. Sp. Pap., 36, 223 - 242, 1942.
- Greeley, R., Mariner 9 photographs of small volcanic structures on Mars, Geology, 1, 175 - 180, 1973.
- Greeley, R. (ed.), Geologic guide to the island of Hawaii, NASA CR-152416, Washington, D.C., 256p. 1974.

- Greeley, R., Silt-clay aggregates on Mars, J. Geophys. Res., 84, 6248 - 6254, 1979.
- Greeley, R., and D. E. Gault, Endogenic craters interpreted from crater counts on the inner wall of Copernicus, Science, 171, 477 - 479, 1971.
- Greeley R., and P. Spudis, Volcanism in the cratered terrain hemisphere of Mars, Geophys. Res. Lett., 5, 453-455, 1978.
- Greeley, R., and D. E. Gault, Endogenic craters on basaltic lava flows: Size frequency distributions, Proc. Lunar Planet. Sci. Conf. 10th, 2919 - 2933, 1979.
- Greeley, R., and P. D. Spudis, Volcanism on Mars, Rev. Geophys. Sp. Phys., 19, 13 - 41, 1981.
- Greeley, R., B. R. White, J. B. Pollack, J. D. Iverson, and R. N. Leach, Dust storms on Mars: Considerations and simulations, NASA TM-78423, 29p. 1977.
- Greeley, R., R. N. Leach, B. R. White, J. D. Iversen, and J. B. Pollack, Threshold windspeeds for sand on Mars: Wind tunnel simulations, Geophys. Res. Lett., 7, 121 - 124, 1980.
- Greeley, R., R. N. Leach, S. H. Williams, B. R. White, J. B. Pollack, D. H. Krinsley, and J. R. Marshall, Rate of wind abrasion on Mars, J. Geophys. Res., 87, 10009 - 10024, 1982.
- Guinness, E. A., C. E. Leff, and R. A. Arvidson, Two Mars years of surface changes seen at the Viking landing sites, J. Geophys. Res., 87, 10051 - 10058, 1982.
- Hagfors, T., Backscattering from an undulating surface with application to radar returns from the moon, J. Geophys. Res., 69, 3779 - 3784, 1964.
- Handin, J., Strength and ductility, In Handbook of Physical Constants, S. P. Clark, ed., Geol. Soc. Am. Memoir 97, p. 223 - 289, 1966.
- Harmon, J. K., D. B. Campbell, and S. J. Ostro, Dual-polarization radar observations of Mars: Tharsis and environs, Icarus, 52, 171 - 187, 1982.

- Hartmann, W. K., and O. Raper, The new Mars: The discoveries of Mariner 9, NASA SP-337, 179p., 1974.
- Head, J. W., M. Settle, and C. A. Wood, Origin of Olympus Mons escarpment by erosion of pre-volcano substrate, Nature, 263, 667 - 668, 1976.
- Hiller, K. H., P. Janle, G. P. O. Neukum, J. E. Guest, and R. M. C. Lopes, Mars: Stratigraphy and gravimetry of Olympus Mons and its aureole, J. Geophys. Res., 87, 9905 - 9915, 1982.
- Hodges, C. A., Mare ridges and lava lakes, NASA SP-330, 31-12 to 31-21, 1973.
- Hodges, C. A., and H. J. Moore, The subglacial birth of Olympus Mons and its aureoles, J. Geophys. Res., 84, 8061 - 8074, 1979.
- Horai, K. I., Loose and compacted soils: Two basic units composing the martian surface? (abstract), Lunar Planet. Sci., X, 564 - 566, 1979.
- Howard, K. A., and W. R. Muehlberger, Lunar thrust faults in the Taurus-Littrow region, NASA SP-330, 31-22 to 31-25, 1973.
- Hubbert, M. K., and W. W. Rubey, Role of fluid pressure in mechanics of overthrust faulting. I. Mechanics of fluid-filled porous solids and its application to overthrust faulting, Geol. Soc. Am. Bull., 70, 115 - 166, 1959.
- Hulme, G., The interpretation of lava flow morphology, Geophys. J. Roy. Astron. Soc., 39, 361 - 383, 1974.
- Hulme, G., The determination of the rheological properties and effusion rate of an Olympus Mons lava, Icarus, 27, 207 - 213, 1976.
- Hunt, G. E., Thermal infrared properties of the martian atmosphere. 4. Predictions of the presence of dust and ice clouds from Viking IRTM spectral measurements, J. Geophys. Res., 84, 2865 - 2874, 1979.
- Hunt, G. E., On the infrared radiative properties of CO<sub>2</sub> ice clouds: Application to Mars, Geophys. Res. Lett., 7, 481 - 484, 1980.

- King, J. S., and J. R. Riehle, A proposed origin of the Olympus Mons escarpment, Icarus, 23, 300 - 317, 1974.
- Jakosky, B. M., The effects of nonideal surfaces on the derived thermal properties of Mars, J. Geophys. Res., 84, 8252 - 8262, 1979.
- Jakosky, B. M., The role of seasonal reservoirs in the Mars water cycle. I. Seasonal exchange of water with the regolith, Icarus, 55, 1 - 18, 1983a.
- Jakosky, B. M., The role of seasonal reservoirs in the Mars water cycle. II. Coupled models of the regolith, the polar caps, and atmospheric transport, Icarus, 55, 19 - 39, 1983b.
- Jakosky, B. M., and D. O. Muhleman, A comparison of the thermal and radar characteristics of Mars, Icarus, 35, 25 - 38, 1981.
- Kahle, A. B., Surface thermal properties, in Remote sensing in geology, B. S. Siegal and A. R. Gillespie, eds., John Wiley and sons, New York, 257 - 276, 1980.
- Kahle, A. B., A. R. Gillespie, and A. F. H. Goetz, Thermal inertia imaging: A new geologic tool, Geophys. Res. Lett, 3, 26 - 28, 1976.
- Kannuluik, W. G., and L. H. Martin, Conduction of heat in powders, Proc. Roy. Soc. (London), A141, 144 - 158, 1933.
- Kieffer, H. H., S. C. Chase, Jr., E. Miner, G. Munch, and G. Neugebauer, Preliminary report on infrared radiometric measurements from the Mariner 9 spacecraft, J. Geophys. Res., 78, 4291 - 4312, 1973.
- Kieffer, H. H., P. R. Christensen, T. Z. Martin, E. D. Miner, and F. D. Palluconi, Temperatures of the martian surface and atmosphere: Viking observation of diurnal and geometric variations, Science, 194, 1346 - 1351, 1976.
- Kieffer, H. H., T. Z. Martin, A. R. Peterfreund, B.M. Jakosky, E. D. Miner, and F. D. Palluconi, Thermal and albedo mapping of Mars during the Viking primary mission, J. Geophys. Res., 82, 4249 - 4291, 1977.

- Kuiper, G. P., The atmospheres of the earth and planets, U. Of Chicago Press, Chicago, Il., 434p., 1952.
- Lee, S. W., Eolian sediment transport on Mars: Seasonal and topographic effects, Ph.D. thesis, Cornell Univ., 251p., 1984.
- Lee, S. W., P. C. Thomas, and J. Veverka, Wind streaks in Tharsis and Elysium: Implications for sediment transport by slope winds, J. Geophys. Res., 87, 10025 - 10041, 1982.
- Leighton, R. B., N. H. Horowitz, B. C. Murray, R. P. Sharp, A. G. Herriman, A. T. Young, B. A. Smith, M. E. Davies, and C. G. Leovy, Mariner 6 and 7 television pictures: Preliminary analysis, Science, 166, 49 - 67, 1969.
- Leighton, R. B., B. C. Murray, R. P. Sharp, J. D. Allen, and R. K. Sloan, Mariner IV photography of Mars: Initial results, Science, 149, 627 - 630, 1965.
- Leovy, C. B., Martian meteorology, Ann. Rev. Astron. Astrophys., 17, 387 - 413, 1979.
- Leovy, C. B., G. A. Briggs, and B. A. Smith, Mars atmosphere during the Mariner 9 extended mission: Television results, J. Geophys. Res., 78, 4252 - 4266, 1973.
- Lopes, R. M. C., J. E. Guest, and C. J. Wilson, Origin of the Olympus Mons aureole and perimeter scarp, Moon, 22, 221 - 234, 1980.
- Lopes, R., J. E. Guest, K. Hiller, and G. Neukum, Further evidence for a mass movement origin of the Olympus Mons aureole, J. Geophys. Res., 87, 9917 - 9928, 1982.
- Luchitta, B. K., Ice sculpture in the martian outflow channels, J. Geophys. Res., 87, 9951 - 9973, 1982.
- Macdonald, G. A., Volcanoes, Prentice-Hall, Inc., Englewood Cliffs, New Jersey, 510p., 1972.
- Macdonald, G. A., and A. T. Abbott, Volcanoes in the sea, University of Hawaii, Honolulu, 441p., 1970.



- Mackin, J. H., Structural significance of Tertiary volcanic rocks in southwestern Utah, Amer. J. Sci., 258, 81 - 131, 1960.
- Magalhaes, J., and P. Gierasch, A model of martian slope winds: Implications for eolian transport, J. Geophys. Res., 87, 9975 - 9984, 1982.
- Malin, M. C., Comparison of volcanic features of Elysium (Mars) and Tibesti (Earth), Geol. Soc. Am. Bul., 88, 908 - 919, 1977.
- Malin, M. C., Lengths of Hawaiian lava flows, Geology, 8, 306 - 308, 1980.
- Malin, M. C., D. Dzurisin, and R. P. Sharp, Stripping of Keanakakoi tephra on Kilauea volcano, Hawaii, Geol. Soc. Am. Bull., 94, 1148 - 1158, 1983.
- Martin, T. Z., Mean thermal and albedo behavior of the Mars surface and atmosphere over a martian year, Icarus, 45, 427 - 446, 1981.
- Martin, T. Z., A. R. Peterfreund, E. D. Miner, H. H. Kieffer, and G. E. Hunt, Thermal infrared properties of the martian atmosphere: 1. Global behavior at 7, 9, 11, and 20  $\mu$ m, J. Geophys. Res., 84, 2830 - 2842, 1979.
- Masursky, H., R. M. Batson, J. F. McCauley, L. A. Soderblom, R. L. Wilbey, M. H. Carr, D. J. Milton, D. E. Wilhelms, B. A. Smith, T. B. Kirby, J. C. Robinson, C. B. Leovy, G. A. Briggs, T. C. Duxbury, C. H. Acton, Jr., B. C. Murray, J. A. Cutts, R. P. Sharp, S. Smith, R. B. Leighton, C. Sagan, J. Veverka, M. Noland, J. Lederberg, E. Levinthal, J. B. Pollack, J. T. Moore, Jr., W. K. Hartmann, E. N. Shipley, G. DeVaucouleurs, and M. E. Davies, Mariner 9 television reconnaissance of Mars and its satellites: Preliminary results, Science, 175, 294 - 304, 1972.
- McCauley, J. F., M. H. Carr, J. A. Cutts, W. K. Hartmann, H. Masursky, D. J. Milton, R. P. Sharp, and D. E. Wilhelms, Preliminary Mariner 9 report on the geology of Mars, Icarus, 17, 289 - 327, 1972.
- McCord, T. B., and J. A. Westphal, Mars: Narrow band photometry, from 0.3 to 2.5 microns, of surface regions during the 1969 apparition, Astrophys. J., 168, 141 - 153, 1971.

- McCord, T. B., R. B. Singer, B. R. Hawke, J. B. Adams, D. L. Evans, J. W. Head, P. J. Mouginis-Mark, C. M. Pieters, R. L. Huguenin, and S. H. Zisk, Mars: Definition and characterization of global surface units with emphasis on composition, J. Geophys. Res., 87, 10129 - 10148, 1982.
- McGetchin, T. R., and J. W. Head, Lunar cinder cones, Science, 180, 68 - 71, 1973.
- McGetchin, T. R., M. Settle, and B. A. Chouet, Cinder cone growth modeled after northeast crater, Mount Etna, Sicily, J. Geophys. Res., 79, 3257 - 3272, 1974.
- Milton, D. J., Water and processes of degradation in the martian landscape, J. Geophys. Res., 78, 4037 - 4047, 1973.
- Minnaert, M., The reciprocity principle in lunar photometry, Astrophys. J., 93, 403 - 410, 1941.
- Moore, H. J., and G. G. Schaber, An estimate of the yield strength of the Imbrium flows, Proc. Lunar Planet. Sci. Conf. 6th, 101 - 118, 1975.
- Moore, H. J., D. W. G. Arthur, and G. G. Schaber, Yield strengths of flows on the Earth, Mars, and Moon, Proc. Lunar Planet. Sci. Conf. 9th, 3351 - 3378, 1978.
- Moore, H. J., C. R. Spitzer, K. Z. Bradford, P. M. Cates, R. E. Hutton, and R. W. Shorthill, Sample fields of the Viking landers, physical properties, and aeolian processes, J. Geophys. Res., 84, 8365 - 8377, 1979.
- Morris, E. C., Aureole deposits of the martian volcano Olympus Mons, J. Geophys. Res., 87, 1164 - 1178, 1982.
- Mouginis-Mark, P. J., Late-stage summit activity of martian shield volcanoes, Proc. Lunar Sci., 12B, 1431 - 1447, 1981.
- Mouginis-Mark, P. J., S. H. Zisk, and G. S. Down, Ancient and modern slopes in the Tharsis region of Mars, Nature, 297, 546 - 550, 1982a.

- Mouginis-Mark, P. J., L. Wilson, and J. W. Head, Explosive volcanism on Hecates Tholus, Mars: Investigation of eruption conditions, J. Geophys. Res., 87, 9890 - 9904, 1982b.
- Mutch, T. A., and J. W. Head, The geology of Mars: A brief review of some recent results, Rev. Geophys. Space Phys., 13, 411 - 416, 1975.
- Mutch, T. A., R. E. Arvidson, J. W. Head, K. L. Jones, and R. S. Saunders, The geology of Mars, Princeton University Press, Princeton, N.J., 400p., 1976.
- Mutch, T. A., R. E. Arvidson, A. B. Binder, E. A. Guinness, and E. C. Morris, The geology of the Viking lander 2 site, J. Geophys. Res., 82, 4452 - 4467, 1977.
- Neukum, G., and D. U. Wise, Mars: A standard crater curve and possible new time scale, Science, 194, 1381 - 1388, 1977.
- Neukum, G., and K. Hiller, Martian ages, J. Geophys. Res., 86, 3097 - 3121, 1981.
- Palluconi, F. D., and H. H. Kieffer, Thermal inertia mapping of Mars from 60° S to 60° N, Icarus, 45, 415 - 426, 1981.
- Patterson, W. R., F. O. Huck, S. D. Wall, and M. R. Wolf, Calibration and performance of the Viking lander cameras, J. Geophys. Res., 82, 4391 - 4400, 1977.
- Peterfreund, A. R., and H. H. Kieffer, Thermal infrared properties of the martian atmosphere: 3. Local dust clouds, J. Geophys. Res., 84, 2853 - 2863, 1979.
- Pettijohn, F. J., P. E. Potter, and R. Siever, Sand and sandstone, Springer-Verlag, New York, 618p., 1972.
- Phillips, R. J., and R. S. Saunders, The isostatic state of martian topography, J. Geophys. Res., 80, 2893 - 2897, 1975.
- Plescia, J. B., The Tempe volcanic province of Mars and comparisons with the Snake River plains of Idaho, Icarus, 45, 586 - 601, 1981.

- Plescia, J. B., and R. S. Saunders, The chronology of the martian volcanoes, Proc. Lunar Planet. Sci. Conf., 10th, 2841 - 2859, 1979.
- Plescia, J. B., and R. S. Saunders, Tectonic history of the Tharsis region, Mars, J. Geophys. Res., 87, 9775 - 9791, 1982.
- Pleskot, L. K., The opposition effect of particulate mineral surfaces and condensates: Applications to Saturn's rings, Ph.D. dissertation, Univ. of Calif. at Los Angeles, 210p., 1981.
- Pleskot, L. K., and E. D. Miner, Time variability of martian bolometric albedo, Icarus, 45, 427 - 441, 1981.
- Pollack, J. B., D. S. Colburn, F. Michael, R. Kahn, C. E. Carlston, and D. Pidek, Properties and effects of dust particles suspended in the martian atmosphere, J. Geophys. Res., 84, 2929 - 2945, 1979.
- Reimers, C. E., and P. D. Komar, Evidence for explosive volcanic density currents on certain martian volcanoes, Icarus, 39, 88 - 110, 1979.
- Robertson, E. C., and D. L. Peck, Thermal conductivity of vesicular basalt from Hawaii, J. Geophys. Res., 79, 4875 - 4888, 1974.
- Roth, L. E., G. S. Downs, and R. S. Saunders, Radar altimetry of south Tharsis, Mars, Icarus, 42, 287 - 316, 1980.
- Sabins, F. F., Remote sensing principles and interpretation, W. H. Freeman and Co., San Francisco, Ca., 426p., 1978.
- Sagan, C., J. Veverka, R. Steinbacker, L. Quam, R. Tucker, and B. Eross, Variable features on Mars, IV, Pavonis Mons, Icarus, 22, 24 - 47, 1974.
- Sagan, C., D. Pieri, P. Fox, R. E. Arvidson, and E. A. Guinness, Particle motion on Mars inferred from the Viking lander cameras, J. Geophys. Res., 82, 4430 - 4438, 1977.
- Saunders, R. S. and T. A. Mutch, Extraterrestrial geology, in Remote sensing in geology, B. S. Siegal and A. R. Gillespie, eds., John Wiley and sons, New York, 659 - 677, 1980.

- Schaber, G. G., Eratosthenian volcanism in Mare Imbrium: Source of youngest lava flows, NASA SP-330, 30-17 to 30-25, 1973a.
- Schaber, G. G., Lava flows in Mare Imbrium: Geologic evaluation from Apollo orbital photography, Proc. Lunar Sci. Conf. 4th, 73 - 92, 1973b.
- Schaber, G. G., J. M. Boyce, and H. J. Moore, The scarcity of mappable flow lobes on the lunar maria: Unique morphology of the Imbrium flows, Proc. Lunar Sci. Conf. 7th, 2783 - 2800, 1976.
- Schaber, G. G., Radar, visual and thermal characteristics of Mars: Rough planer surfaces, Icarus, 42, 159 - 184, 1980.
- Schultz, P. H., and A. B. Lutz-Garihan, Equatorial paleo-poles on Mars (abstract), Lunar Planet. Sci., XII, 946 - 948, 1981.
- Schumm, S. A., Structural origin of large martian channels, Icarus, 22, 371 - 384, 1974.
- Scott, D. H., Small structures of the Taurus-Littrow region, NASA SP-330, 31-25 to 31-28, 1973.
- Scott, D. H., Volcanoes and volcanic provinces: Martian western hemisphere, J. Geophys. Res., 87, 9839 - 9851, 1982.
- Scott, D. H., and M. H. Carr, Geologic map of Mars, Map I-1083, U. S. Geol. Surv., Washington, D. C., 1978.
- Scott, D. H., and K. L. Tanaka, Mars: Paleostratigraphic restoration of buried surfaces in Tharsis Montes, Icarus, 45, 304 - 319, 1981.
- Scott, D. H., G. G. Schaber, K. C. Horstman, and A. L. Dial, Jr., Map showing lava flows in the northeast part of the Tharsis quadrangle of Mars, Map I-1267, U. S. Geol. Survey, Washington, D.C., 1981a.
- Scott, D. H., G. G. Schaber, and K. L. Tanaka, Map showing lava flows in the southeast part of the Tharsis quadrangle of Mars, Map I-1269, U. S. Geol. Survey, Washington, D.C., 1981b.

- Sharp, R. P., Mars: Troughed terrian, J. Geophys. Res., 78, 4063 - 72, 1973.
- Sharp, R. P., and M. C. Malin, Channels on Mars, Geol. Soc. Am. Bull., 86, 593 - 609, 1975.
- Sharp, R. P., and M. C. Malin, Surface geology from Viking landers on Mars: A second look, Geology, (in press), 1984.
- Short, N. M., Planetary geology, Prentice-Hall, Inc., Englewood Cliffs, New Jersey, 361p., 1975.
- Simpson, R. A., G. L. Tyler, and D. B. Campbell, Arecibo radar observations of martian surface characteristics near the equator, Icarus, 33, 102 - 115, 1978a.
- Simpson, R. A., G. L. Tyler, and D. B. Campbell, Arecibo radar observations of Mars surface characteristics in the northern hemisphere, Icarus, 36, 153 - 173, 1978b.
- Singer, R. B., Spectral evidence for the mineralogy of high-albedo soils and dust on Mars, J. Geophys. Res., 87, 10159 - 10168, 1982.
- Singer, R. B., T. B. McCord, R. N. Clark, J. B. Adams, and R. L. Huguenin, Mars surface composition from reflectance spectroscopy: A summary, J. Geophys. Res., 84, 8415 - 8426, 1979.
- Sjogren, W. L., J. Lorell, L. Wong, and W. Downs, Mars gravity field based on a short arc technique, J. Geophys. Res., 80, 2899 - 2908, 1975.
- Slipher, E. C., The photographic story of Mars, Sky Publishing Corp., Cambridge, Mass., 168p., 1962.
- Snyder, C. W., The missions of the Viking orbiters, J. Geophys. Res., 82, 3971 - 3983, 1977.
- Snyder, C. W., The extended mission of Viking, J. Geophys. Res., 84, 7917 - 7933, 1979.
- Soderblom, L. A., Historical variations in the density and distribution of impacting debris in the inner solar system: Evidence from planetary imaging, in Impact and Explosion Cratering, D. J. Roddy, R. O. Pepin, and R. B. Merrill, eds., Pergamon Press, New York, 629 - 633, 1977.

- Soderblom, L. A., and D. B. Wenner, Possible fossil H<sub>2</sub>O liquid-ice interfaces in the martian crust, Icarus, 34, 622 - 637, 1978.
- Soderblom, L. A., K. Edwards, E. M. Eliason, E. M. Sanchez, and M. P. Charette, Global color variations on the martian surface, Icarus, 34, 446 - 464, 1978.
- Soffen, G. A., The Viking project, J. Geophys. Res., 82, 3959 - 3970, 1977.
- Solomon, S. C., and J. W. Head, Evolution of the Tharsis province of Mars: The importance of heterogeneous lithospheric thickness and volcanic construction, J. Geophys. Res., 87, 9755 - 9774, 1982.
- Sparks, R. S. J., H. Pinkerton, and G. Hulme, Classification and formation of lava levees on Mount Etna, Sicily, Geology, 4, 269 - 271, 1976.
- Tanaka, K. L., Geology of the Olympus Mons region of Mars, Ph.D. dissertation, Univ. of Calif. at Santa Barbara, Calif., 300p., 1984a.
- Tanaka, K. L., Ice-lubricated gravity spreading of the Olympus Mons aureole deposits, (submitted to Icarus), 1984b.
- Thorarinsson, S., The Lakagigar eruption of 1783, Bull. Volcanol., 33, 910 - 929, 1970.
- Thorpe, T. E., Viking Orbiter photometric observations of the Mars phase function July through November 1976, J. Geophys. Res., 82, 4161 - 4165, 1977.
- Thorpe, T. E., Martian surface properties indicated by the opposition effect, Icarus, 49, 398 - 415, 1982.
- Toon, O. B., J. B. Pollack, W. Ward, J. A. Burns, and K. Bilski, The astronomical theory of climatic change on Mars, Icarus, 44, 552 - 607, 1980.
- U. S. Geological Survey, Topographic-bathymetric map of Hawaii, Map NE/NF-4,5, Washington, D. C., 1971.
- U. S. Geological Survey, Topographic map of Mars, Map I-961, Washington, D. C., 1976.

- U. S. Geological Survey, Controlled photomosaic of the Tharsis northeast quadrangle of Mars, Map I-1258, Washington, D. C., 1980a.
- U. S. Geological Survey, Controlled photomosaic of the Tharsis southeast quadrangle of Mars, Map I-1260, Washington, D. C., 1980b.
- U. S. Geological Survey, Special topographic series, MC-9SE, Map M 2M 7/101 T, Washington, D. C., 1981a.
- U. S. Geological Survey, Special topographic series, MC-9NE, Map M 2M 7/102 T, Washington, D. C., 1981b.
- U. S. Geological Survey, Special topographic series, Olympus Mons, Map M 1M 19/134 T, Washington, D. C., 1981c.
- Ugolini, F. C., and D. M. Anderson, Ionic migration in frozen Antarctic soil, Antarc. J., 7, 112 - 113, 1972.
- Veeverka, J., P. Thomas, and R. Greeley, A study of variable features on Mars during the Viking primary mission, J. Geophys. Res., 82, 4167 - 4187, 1977.
- Wallace, P. W., Hesiod and the valley of the Muses, GK. Rom. Byzant. St., 15, 5 - 24, 1974.
- Ward, A. W., Yardangs on Mars: Evidence of recent wind erosion, J. Geophys. Res., 84, 8147 - 8166, 1979.
- Wechsler, A. E., and P. E. Glaser, Pressure effects on postulated lunar materials, Icarus, 4, 335 - 352, 1965.
- Wesselink, A. F., Heat conductivity and the nature of the lunar surface material, Bull. Astron. Inst. Neth., 10, 351 - 363, 1948.
- Whitford-Stark, J. L., Tharsis volcanoes: Separation distances, relative ages, sizes, morphologies, and depths of burial, J. Geophys. Res., 87, 9829 - 9838, 1982.
- Williams, H. and A. R. McBirney, Volcanology, Freeman, Cooper, and Co., San Francisco, 397p., 1979.



- Wilson, L., and J. W. Head, Theoretical analyses of martian explosive eruption mechanisms, in Papers presented at the Third International Colloquium on Mars, Lunar and Planetary Institute, Houston, Texas, 278 - 280, 1981.
- Wilson, L., and J. W. Head, A comparison of volcanic eruption processes on Earth, Moon, Mars, Io and Venus, Nature, 302, 663 - 669, 1983.
- Winter, D. F., J. A. Bastin, and D. A. Allen, Thermal characteristics of lunar surface roughness, in Thermal characteristics of the Moon, J. W. Lucas, ed., MIT Press, Cambridge, Mass., 269 - 299, 1972.
- Woodside, W., and J. H. Messmer, Thermal conductivity of porous media. I. Unconsolidated sands, J. Appl. Phys., 32, 1688 - 1699, 1961a.
- Woodside, W., and J. H. Messmer, Thermal conductivity of porous media. II. Consolidated rocks, J. Appl. Phys., 32, 1699 - 1706, 1961b.
- Yung, Y. L., and J. P. Pinto, Primitive atmosphere and implications for the formation of channels on Mars, Nature, 273, 730 - 732, 1978.
- Zimbelman, J. R., and H. H. Kieffer, Thermal mapping of the northern equatorial and temperate latitudes of Mars, J. Geophys. Res., 84, 8239 - 8251, 1979.
- Zimbelman, J. R., and R. Greeley, High resolution visual, thermal, and radar observations in the northern Syrtis Major region of Mars, Proc. Lunar Planet. Sci., 12B, 1419 - 1429, 1981.
- Zimbelman, J. R., and R. Greeley, Surface properties of ancient cratered terrain in the northern hemisphere of Mars, J. Geophys. Res., 87, 10181 - 10189, 1982.
- Zurek, R. W., Solar heating of the martian dusty atmosphere, Icarus, 35, 196 - 208, 1978.

## APPENDIX 1. DATA DESCRIPTIONS

The location and quality of the data used in this work are summarized below. The photographic data primarily pertain to Chapter 3 and the remote sensing data are discussed in Chapter 4.

### Photographic Data

Viking Orbiter photographs were used for the photogeologic analysis of Ascraeus Mons. Fig. A1.1 shows the outlines of the photographs presented in Chapter 3 and their relative positions on the volcano. Table A1.1 lists the usable photographs of Ascraeus Mons; additional photographs were taken of the volcano but either atmospheric conditions or problems in data transmission degraded the resolution of surface features. During the Viking extended mission the periapses of both orbiters were lowered, reducing the minimum range to the surface from 1500 to 300 km (Snyder, 1979). This improved the best available spatial resolution to 8 m per picture element ("pixel").

Moderate spatial resolution images were combined to produce 1:2,000,000 scale photomosaics throughout the equatorial region of Mars. Fig. 3.2 shows the photomosaics that include Ascraeus Mons (U.S. Geol. Surv., 1980a,b). These photographs were used to map features on a regional

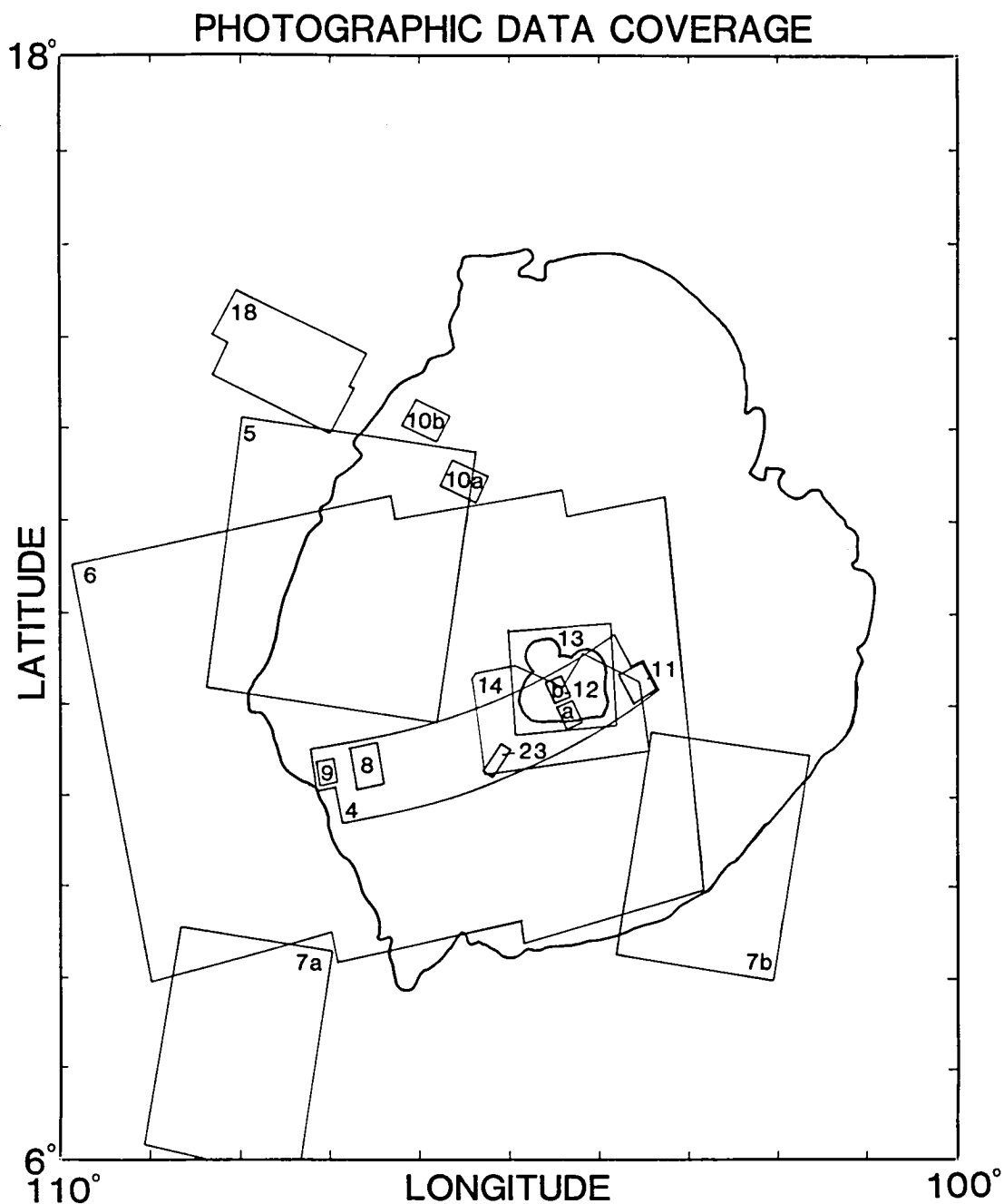


Figure A1.1. Photographic data coverage for Ascræus Mons. Numbers indicate the figure number in Chapter 3 for the corresponding outlined area. The shield-plains contact and the caldera rim (from Map 1) are included for reference. The area shown here corresponds to the areas in Figs. 3.1 through 3.3

Table A1.1. Photographic data for Ascræus Mons.

Frame	Range (km)	Resolution (m/pixel)	Inc. Ang. (deg)	Em. Ang. (deg)	Local Time (H)	Filter	Quality	Ls (deg)
High resolution								
387A01-07	754-786	21.1-22.2	71.1-69.9	12.9-11.1	7.43-7.47	Clear	Hazy	294.77
387A11-17	849-889	21.1-22.2	70.8-69.7	11.4-11.9	7.44-7.48	Clear	Hazy	294.77
697A39-54	1292-1246	32.3-31.2	76.0-80.5	33.7-40.5	17.19-17.33	Clear	Very hazy	86.85
697A61-84	852-707	21.3-17.8	78.2-81.0	11.3-9.7	17.26-17.35	Clear	Very hazy	86.85
698A01-20	1119-982	28.0-24.5	67.5-71.3	2.8-1.6	16.47-17.01	Clear	Hazy	8.29
401B01-24	958-857	24.0-21.5	67.4-71.2	17.7-13.3	16.32-16.55	Minus Blue	Clear	337.86
Moderate/Low resolution								
90A42-56	2525-2545	63.4-63.6	19.2-13.1	19.9-28.4	11.5-12.77	Clear	Clouds	124.76
204A21-32	2850-2906	71.3-72.7	61.4-54.5	18.3-29.5	7.57-8.26	Violet	Hazy	185.06
210A01-20	2669-2740	66.7-68.5	65.7-54.3	14.4-32.0	7.41-8.30	Violet	Hazy	188.60
210A51-70	2373-2304	59.3-57.6	63.9-53.9	26.8-29.7	7.49-8.31	Violet	Hazy	188.60
223A10-16	6355-6370	158.9-159.2	78.5-84.8	17.3-14.4	17.08-17.34	Violet	Clear	196.04
224A84-93	5171-4987	129.3-124.7	51.2-60.1	39.5-27.4	15.14-15.49	Violet	Clear	196.60
643A75-78	11544-11316	288.6-282.9	66.2-69.8	50.4-43.4	7.18-7.10	Red	Clear	63.29
696A41,45,47	32882-32884	822.0-822.1	59.8-59.3	8.1-8.8	7.52-7.55	Vlt,Grn,Red	Some clouds	86.21
892A07-14	5980-5872	149.5-146.8	75.6-67.8	13.2-5.6	6.59-7.33	Red	Clear	182.37
892A28-35	5618-5554	140.4-138.9	75.1-65.8	16.8-16.7	7.01-7.37	Red	Clear	182.37

Numbers correspond to first (left) and last (right) listed frames.

scale around Ascraeus Mons.

The 24 frames from orbit 401 of the B spacecraft (V02) provide the most detailed view of the Ascraeus Mons shield surface (Fig. 3.4a and Map 2). Surface features typically must be resolved into four or more pixels before morphologic identification can be made; for the 401B photographs four pixels correspond to 100 m on the surface. The martian atmosphere was visually clear when these images were taken but, unfortunately, this was not the case for many of the Ascraeus Mons photos. Table A1.1 includes a qualitative indicator of the atmospheric conditions in all of the photographs (column labeled "Quality").  $L_S$  represents the season during which the photographs were taken;  $L_S = 0^\circ$  corresponds to the beginning of spring in the northern hemisphere, with one martian year covering  $360^\circ$ . Clouds around Ascraeus Mons typically were most prevalent during northern spring and summer ( $L_S \approx 30$  to  $150^\circ$ ).

Stereoscopic coverage from some photographs shows topographic relief on the surface which can aid in the interpretation of surface features. When viewed through a stereoscope, Figs. 3.6 and 3.14 show the topographic relationships within the summit caldera and on the western flank of Ascraeus Mons. Fig. A1.2 is the left member of the stereoscopic pair that includes Fig. 3.6. Other photographs listed in Table A1.1 are also useful for



Figure A1.2. Left member of the stereoscopic pair that includes Fig. 3.6. Photographs 224A84-93, nongradient high pass filtered orthographic projection.

viewing the topographic relief on the volcano. Photographs from orbit 387 of Viking Orbiter 1 provide stereoscopic coverage of the summit area south of the caldera but atmospheric haze obscures features < 300 m in scale. The 210A frames provide limited stereoscopic coverage across the shield from the northwest to the southeast, including the summit caldera complex.

#### Remote Sensing Data

The remote sensing data for Ascræus Mons vary greatly in areal coverage, spatial resolution, and quality. The area between 7° to 16°N latitude and 100° to 109°W longitude, centered over the summit caldera of Ascræus Mons, was selected for displaying the coverage of the various data sets (Fig. A1.3).

The Viking Orbiter color photographs of Ascræus Mons (Fig. 4.1) cover most of the area shown in Fig. A1.3. They were taken near apoapsis of the spacecraft orbit in order to maximize the area covered by the photographs taken through different filters and minimize distortion resulting from spacecraft motion. The spatial resolution of the photographs is slightly better than 1 km per pixel. Table A1.1 provides additional geometric information about these photographs.

The thermal infrared data were obtained with the IRTM after the second global dust storm of 1977, which started

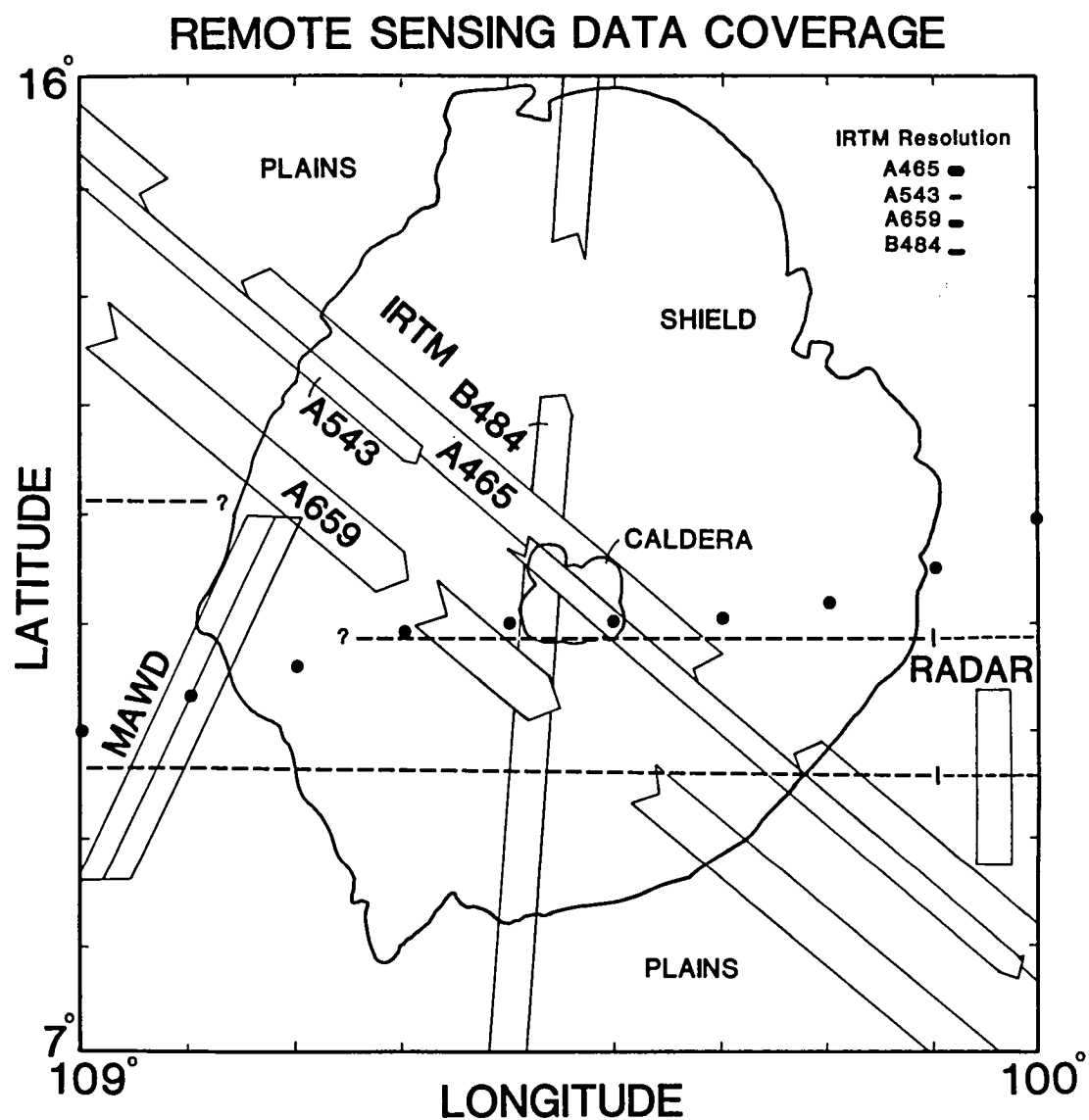


Figure A1.3. Remote sensing data coverage for Ascræus Mons. The areal coverage of the high resolution IRTM sequences (labeled diagonally) are outlined along with the data gaps that resulted from in-flight instrument calibration. The resolution sizes of individual IRTM measurements are shown in the upper right corner. The MAWD resolution is shown for the 108°W spot. The horizontal dashed lines indicate the groundtracks of Earth-based quasi-specular radar data (Downs *et al.*, 1982). Signals were not received from the locations with heavy dashed lines (W of 101°W). The shield-plains contact and the caldera rim (from Map 1) are included for reference.



at  $L_S = 275^\circ$  (Briggs et al., 1979). Table A1.2 lists the geometric information and atmospheric dust content for all of the thermal sequences used in this study. Four high spatial resolution sequences allow the best correlation of the surface thermal properties with geologic features (Fig. A1.3). Instrument calibration during data collection resulted in periodic gaps along each groundtrack. These data were collected near periapsis of the spacecraft orbit in order to obtain the best possible spatial resolution. However, at periapsis the spacecraft was moving fastest relative to the planet so that the "spot size", the area on the surface viewed by each detector, became elongated along the spacecraft groundtrack during the integration time of each measurement. The spatial resolution of these data, including the smearing of the detector sample area along the groundtrack, ranges from 11 to 31 km<sup>2</sup> (Table A1.2), representing an improvement of two orders of magnitude over previously published thermal data for the martian volcanoes (Kieffer et al., 1976, 1977; Zimbelman and Kieffer, 1979). Fourteen moderate to low resolution thermal sequences, including twelve nighttime sequences, provide more uniform areal coverage over the shield for correlation with the higher resolution data.

Individual thermal sequences provide surface brightness temperatures for the local time of day at the

Table A1.2. Thermal infrared data for Ascræus Mons.

Orbit	Seq.	Range (km)	Em. Angle (deg)	Local Time (H)	Dust Opacity ( $\tau$ )	Ls (deg)	Spot Size (km <sup>2</sup> )	Smear (km)	Resolution (km <sup>2</sup> )
<u>High resolution</u>									
A465	2	627-719	56.0-44.3	3.3-3.9	0.3	339	14.4	3.8	30.7 (4.3 by 7.9)
A543	1	359-338	28.1-37.7	23.5-0.2	0.1	18	2.9	4.2	11.0 (1.9 by 5.7)
A659	3	767-575	6.9-17.3	18.6-19.3	<0.1	70	10.4	3.6	23.6 (3.6 by 6.5)
B484	1	424-344	37.9-30.4	13.9-14.0	0.1	19	3.8	4.9	14.8 (2.2 by 6.7)
<u>Low resolution</u>									
A437	1	3421-4691	24.5-46.7	21.4	0.5	323	413	17.4	813 (22.9 by 35.5)
A439	4	3993-4641	16.5-26.6	20.0	0.5	325	409	18.6	833 (22.8 by 36.5)
A666	13	4550-4911	33.6-51.9	13.8	<0.1	72	623	20.3	1195 (28.2 by 42.5)
A668	1	5198-5840	45.2-62.0	12.4	<0.1	73	1049	23.7	1916 (36.5 by 52.4)
A903	1	9369-10169	41.1-53.6	3.8	0.1	189	2878	42.0	5420 (60.5 by 89.5)
A905	1	9193-9956	33.9-49.8	4.1	0.1	190	2514	41.2	4843 (56.6 by 85.6)
A908	1	9046-9705	27.9-43.5	4.4	0.1	192	2211	40.3	4350 (53.1 by 82.0)
A909	1	8901-9485	21.6-37.5	4.6	0.1	193	1985	39.5	3972 (50.3 by 79.0)
B463	3	6671-7165	49.5-63.9	4.1	0.1	10	1781	29.7	3197 (47.6 by 67.1)
B466	11	6880-7791	25.5-38.6	2.3	0.1	11	1297	31.5	2579 (40.6 by 63.5)
B469	2	6289-7254	30.7-49.8	0.9	0.1	12	1227	29.1	2378 (39.5 by 60.2)
B504	8	8299-8886	30.4-44.1	2.0	<0.1	29	1895	36.9	3710 (49.1 by 75.5)
B506	2	6513-7751	31.3-49.5	0.5	<0.1	30	1365	30.7	2643 (41.7 by 63.4)
B543	1	6891-7694	43.1-57.3	0.1	<0.1	46	1697	31.4	3155 (46.5 by 67.9)

Smear indicates the distance traversed on the surface by each IRTM detector during the .98 sec integration time of each measurement. Resolution represents the combination of spot size and smear.

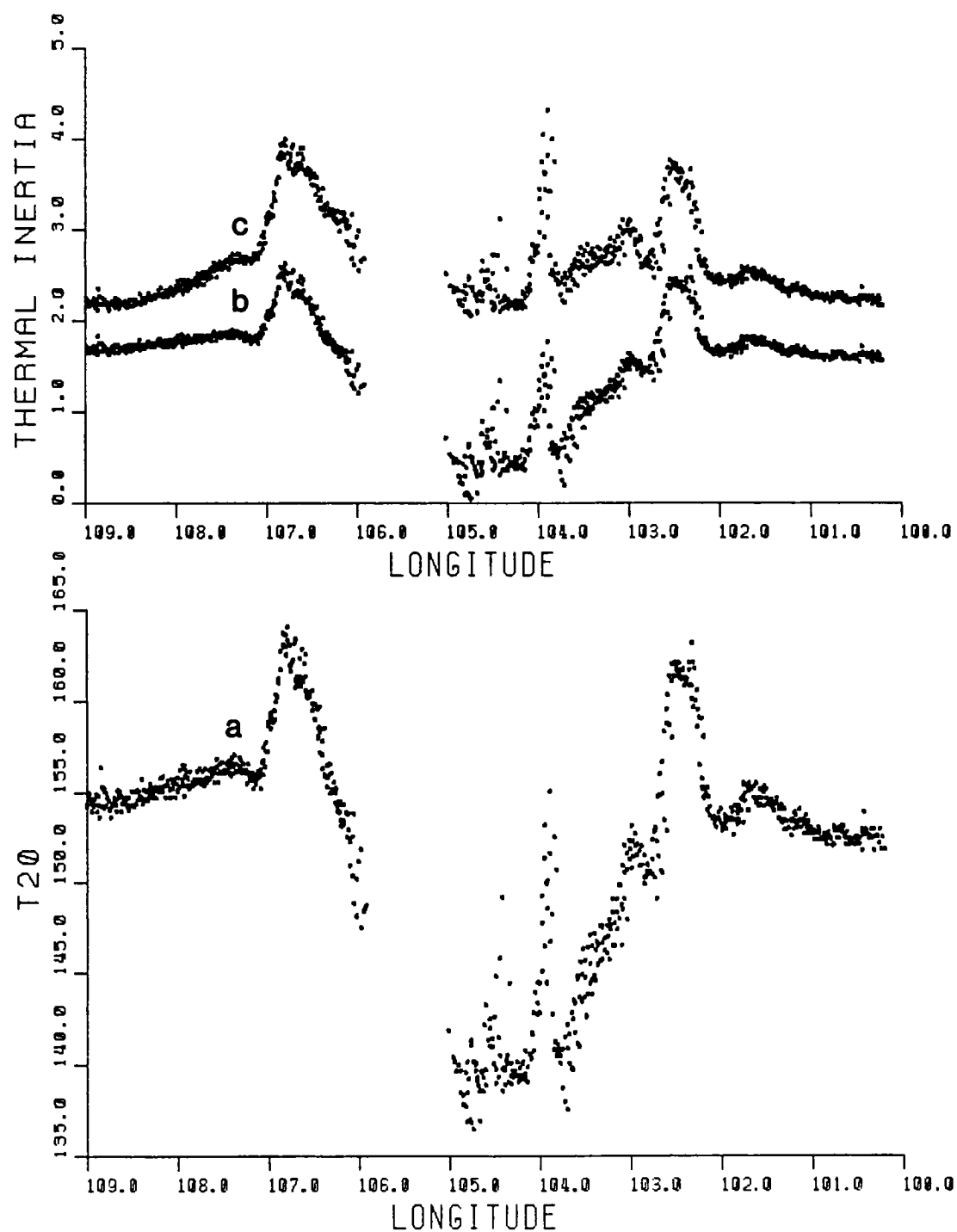


Figure A1.4. High resolution thermal data for Ascræus Mons. Data are from sequence A543. a) 20  $\mu\text{m}$  brightness temperatures, b) thermal inertias calculated from a, c) thermal inertias corrected for elevation-dependent atmospheric effects (see text and Appendix 3).

surface (Fig. A1.4a). These temperatures can be interpreted in terms of model surface thermal inertias (Fig. A1.4b) through comparison with temperatures calculated from the Viking thermal model (Kieffer et al., 1977). The surface albedo is a factor in this thermal inertia determination but it cannot be measured at night. Daytime broadband albedos of 0.24 to 0.28 are found in the vicinity of Ascraeus Mons (Pleskott and Miner, 1981); an albedo value of 0.25 has been assumed for all of the nighttime data used here. The albedo dependence of surface temperatures is small for nighttime data (Kieffer et al., 1977); for the data presented here a  $\pm 0.05$  change in the assumed surface albedo corresponds to a  $\pm 1.5\text{K}$  temperature change or a  $\pm 0.1$  thermal inertia change. The surface albedos represent only minor uncertainties in the calculated thermal inertias. Elevation-dependent corrections must be applied to the thermal inertias determined for the martian shield volcanoes (see Appendix 3). The corrections eliminate the extremely low thermal inertias on the volcanoes (Fig. A1.4c).

Radar data for the Tharsis region is limited in quantity because little of the signal is reflected back to the receiver (Simpson et al., 1976). Earth-based radar determined elevations near Ascraeus Mons that are several km lower, relative to the 6.1 mbar level, than

previously indicated from Mariner 9 data (Downs et al., 1982). Figure A1.3 indicates the location of the radar groundtracks that crossed Ascræus Mons, although no quasi-specular radar returns were received from the shield surface (Downs et al., 1982). Dual polarization radar returns from 22°N provide additional information about the surface roughness in the vicinity of Ascræus Mons but the groundtracks do not directly cross the volcano (Harmon et al., 1982).

The MAWD instrument obtained a profile of the atmospheric water vapor abundance across Ascræus Mons on V01 orbit 71,  $L_S = 120^\circ$  (Farmer et al., 1977). Ten measurements were averaged together for each degree of longitude to increase the signal-to-noise ratio (Fig. A1.3). The resulting spatial resolution of 250 by 100 km is still sufficient to provide several values over the volcano.

## APPENDIX 2. GEOLOGIC TERRAIN UNIT DESCRIPTIONS

### Map 1

Map 1 is a 1:1,770,000 scale geologic map of Ascraeus Mons and the surrounding Tharsis plains (Fig. 3.2). Units associated with Ceraunius Fossae terrain (pf2, pf1, k) are in the Hesperian and Noachian systems (Scott et al., 1981a); all other units are within the Amazonian system (Scott and Carr, 1978; Scott et al., 1981a).

The total area covered by the map is 880,400 km<sup>2</sup>.

### Plains Units.

- p4 - Tharsis plains, from shield embayments. Plains that originate from the embayments on the lower southwest and northeast flanks of Ascraeus Mons. The embayments are aligned with the N40°E trend of the Tharsis Montes. Lineations suggest flow directions were approximately radial from the embayment mouths. No flow margins are visible within 50 km of the shield, but flows are abundant beyond this distance, particularly to the northeast. Channels (similar to those on the shield at the embayments) are very common in the plains south of Ascraeus Mons. Example: 7°N, 107°W. Interpretation: Most recent plains unit associated with Ascraeus Mons. Relatively fluid lavas or debris flows (lahars) were probably involved in the emplacement of these plains.
- p3 - Tharsis plains, well-defined flow margins. Flows with well defined flow margins and flow fronts. Individual flows are 2 to 5 km wide near the volcano and 10 to 40 km wide on the shallow slopes away from the volcano. Flows west of the volcano (108 to 112°W) originate in the saddle area between Ascraeus Mons and Pavonis Mons. Flows at 18°N, 110°W, originate near the Ceraunius Fossae grabens northwest of Ascraeus Mons; flow directions are toward Ascraeus Mons, indicating a topographic depression centered approximately at 17°N, 108°W. Flows northeast of Ascraeus Mons cover an area larger than that of the volcano and they are not traceable to the volcano. Examples: 14°N,

110°W and 17°N, 104°W. Interpretation:  
Voluminous flows that originate at locations not directly associated with Ascræus Mons. These flows postdate all other Tharsis plains around the volcano except the p4 (embayment) plains.

- p2 - Tharsis plains, few flow margins. Plains with relatively few isolated flow margins visible. Very little surface relief is visible on the plains. The p2 plains are superposed on the shield terrain at the shield-plains contact (e.g. southeast shield margin). Two broad mounds 10 to 20 km in diameter are located at 16.2°N, 108.1°W and 14.8°N, 107.3°W; the southernmost mound may have a summit crater. Example: 15°N, 108°W. Interpretation: Fluid lavas that postdate the shield terrain of Ascræus Mons. Few flow directions are evident but most lavas are probably associated with Ascræus Mons volcanic activity. The low mounds may represent small-volume shield volcanoes.
- p1 - Tharsis plains, no flow margins. Flow margins are absent but grabens and channels are typically more abundant than on adjacent plains. Isolated patches of this unit are surrounded by p2 and p4 plains south of Ascræus Mons. Surface relief is generally more variable on this unit than on the p2 plains. Example: 7°N, 104°W. Interpretation: Lavas that predate the p2 plains surrounding Ascræus Mons.
- ppm - Tharsis plains, associated with Pavonis Mons. Plains downslope from the embayment in the lower northeastern flank of Pavonis Mons. The p2 plains are superposed on this unit. Surface morphology is similar to that on the p1 plains around Ascræus Mons. Example: 3°N, 110°W. Interpretation: Lava plains associated with Pavonis Mons volcanism.
- pf2 - Faulted plains, associated with Ceraunius Fossae. Smooth-appearing plains superposed on the intensely faulted Ceraunius Fossae terrains. This unit includes N-S oriented faults associated with the Ceraunius Fossae extensional tectonics but it is much less faulted than unit pf1. The area mapped here represents only the southern margin of terrain that covers an area greater than that of Ascræus Mons (see Scott et al., 1981a). Example: 19°N, 112°W. Interpretation: Lavas associated with volcanic activity in the Ceraunius Fossae region. Crater counts on this terrain indicate that it predates the Tharsis plains (Scott et al., 1981a).

- pf1 - Faulted plains, associated with Ceraunius Fossae. Intensely faulted plains. Grabens 2 to 20 km wide and 50 to > 200 km long have greatly disrupted this unit. The grabens are predominantly oriented N-S. Example: 19°N, 109°W. Interpretation: Plains (most likely volcanic in origin) that predate the Tharsis plains. Intense tectonic activity disrupted this unit prior to the emplacement of the Tharsis plains along their southern margin.

#### Shield Units.

- cf - Caldera floor terrain. Planar surfaces within the caldera complex at the summit of Ascraeus Mons. All caldera floors are partly truncated by subsequent collapse events, except the centermost caldera floor. The caldera rim truncates the summit shield terrains. Example: 11°N, 104°W. Interpretation: Lava infilling of the depressions associated with individual caldera collapse events.
- cw - Caldera wall terrain. Terrain below the rims of individual calderas but above the caldera floors. The uppermost portions of the southern and northern walls of the central caldera have grooves and ridges oriented downslope (also see Map 2). Example: 11°N, 104°W. Interpretation: Shield materials exposed by the collapse events associated with individual calderas.
- s2 - Shield terrain, western flank. Smooth-appearing plains with little visible surface relief on the western and northwestern lower flanks of Ascraeus Mons. This unit is separated from the main shield (s1) terrain by a 400 to 800 m high scarp. Grabens maintain their orientation through both s1 and s2 terrains but they are more subdued on the s2 terrain. Some grabens terminate at the shield-plains contact. Example: 13°N, 107°W. Interpretation: Lavas from Ascraeus Mons that fed the p2 plains flows west and northwest of the volcano. There is a break in slope between the p2 plains and the s2 terrain that parallels the shield flank surface.
- s1 - Shield terrain. Striations generally radial to the summit of the volcano and gentle km-scale undulations cause the flanks of Ascraeus Mons to be readily distinguishable from the uniform appearance of the surrounding Tharsis plains. Terraces, evidenced by breaks in slope approximately concentric to the summit, are spaced 15 to 50 km apart and they are not



present within 50 km of the caldera rim. The northern flanks have numerous 5 to 10 km-diameter craters that are often aligned with nearby grabens or the embayment channels. Example: 13°N, 105°W. Interpretation: Intermixed lava flows, generally much less voluminous than the flows on the Tharsis plains. The craters on the northern flank are predominantly endogenic in origin.

- spm - Shield terrain, Pavonis Mons. Terrain similar to the Ascræus Mons s1 unit. The northern flank of Pavonis Mons lacks the abundant, aligned craters visible on the northern flank of Ascræus Mons. Example: 3°N, 112°W. Interpretation: Intermixed lava flows, as on Ascræus Mons. Crater counts indicate Pavonis Mons is probably older than Ascræus Mons (Plescia and Saunders, 1979).

#### Additional Units.

- r - Ridged terrain. Crescent-shaped unit west of the mountainous terrain by Ascræus Mons. Ridges are present throughout the unit and parallel to the arcuate margin. Average ridge spacing is 1 km. Example: 12°N, 109°W. Interpretation: Landslide deposit from the mountainous terrain (not the Ascræus Mons shield). Similar terrain west of Arsia Mons was interpreted as landslide deposits (Carr et al., 1977).
- m - Mountainous terrain. Very irregular terrain west of Ascræus Mons. Numerous individual knobs and mounds (some as large as 5 km in diameter) occur at the northern portions of this unit. Two channels are visible in the southern portion of this unit but they are truncated at the m-plains contact. Example: 11°N, 108°W. Interpretation: Lava or debris flow material that predates the present shield surface (unit s1) and the Tharsis plains.
- mk - Mountainous terrain, knobby. Km-scale knobs throughout plains adjacent to the mountainous terrain. Example: 12°N, 108°W. Interpretation: Mountainous terrain flooded by the Tharsis plains flows. The knobs are remnants of the mountainous terrain that protrude above the surface of the plains.
- mpm - Mountainous terrain, Pavonis Mons. Terrain similar to unit m but located north of Pavonis Mons. Distinct margins are traceable onto the northern

flank of Pavonis Mons. Example: 5°N, 112°W.  
Interpretation: Lava or debris flow material from Pavonis Mons.

k - Knobby terrain. Irregularly shaped, km-scale knobs. Some lineations are continuous for 20 km through the terrain. All surrounding terrains are superposed on this terrain. Example: 18°N, 112°W.  
Interpretation: The oldest terrain exposed within the area covered by Map 1.

c - Craters. Circular craters > 5 km in diameter with raised rims and, in some cases, lobate ejecta blankets. Example: 18°N, 110°W.  
Interpretation: Impact craters.

## MAP 2

Map 2 is a 1:250,000 scale geologic map of photographs 401B01-24 (Fig. 3.4a). All units are within the Amazonian system of Scott and Carr (1978). The total area covered in the 24 photographs is 10,960 km<sup>2</sup>.

### Caldera Units.

cw - Caldera wall terrain. Smooth-appearing slopes below caldera rim crests. Walls are striated parallel to the slope, visible on surfaces where the solar incidence angle is greater than 80°, with 100 to 300 m spacing. Slopes are generally steeper than 18° since basal contacts are well within shadows cast by rim crests with a 72° incidence angle. Subtle flow-like margins extend from some wall segments onto the adjacent floor material (401B20, E of center). Example: 401B20, center.  
Interpretation: Talus accumulations along the base of wall and rim scarps. Striations are probably the result of downslope mass movement. Outflow onto surrounding floors may be related to landslide events along sections of the wall, or fluid lavas cascading over the wall.

cwg - Caldera wall terrain, grooved. Uppermost terrain on individual wall segments. Alternating ridges and grooves, oriented down slope, give the terrain a fluted appearance. The groove spacing is quite regular, ranging from 150 m on shorter walls to 350 m

at large wall exposures. Deep shadows cast by the ridges separating the grooves indicate relief of  $< 10$  m and  $\leq 30$  m, respectively, for the groove spacing listed above. Some ridges correspond to grabens that intersect the caldera rim but graben are not visible at all fluted wall exposures. The cw terrain is always downslope from the grooved areas. Example: 401B18, NE corner. Interpretation: Shield material exposed by caldera collapse and mass wasting. Joint control of groove orientations may be significant.

- cws - Caldera wall terrain, slumped. Subdued, rounded blocks and mounds at the base of several caldera wall segments. Lineations parallel to the adjacent walls are present at several locations. Shadows indicate up to 300 m of relief along some lineations. Very little surface detail is visible beyond gentle undulations on the scale of hundreds of m. Basal portions of this terrain are buried by caldera floor material. Example: 401B20, N of center. Interpretation: Blocks of shield material that slid into the individual calderas during or after the collapse events but prior to the floor terrain emplacement.
- cf - Caldera floor terrain. Planar surfaces bounded either by steep slopes at the caldera walls or by scarps, with the downdropped side toward the central (lowest) depression. At least nine centers of collapse are indicated by wall segments, only two of which are coincident (Fig. 3.13). The central collapse crosscut all other floors, which are topographically higher than the central floor. Numerous arcuate to linear graben occur on the crosscut floor segments, generally parallel to either nearby walls or the central collapse. Sinuous ridges and broad flow fronts are present on the central floor. Example: 401B19, NE corner. Interpretation: Lava which flooded the calderas subsequent to each collapse.
- cfg - Caldera floor material, grooved. Subparallel to slightly arcuate ridge and valley terrain on the central caldera floor. The ridges and valleys trend  $N20^{\circ}W$  with an average spacing of 200 m; these features are displayed by highlights instead of strong shadows, limiting their relief to  $< 35$  m. This unit is overlain by flows of the central caldera floor terrain. Example: 401B19, center. Interpretation: Modified caldera floor lavas. The

modification could have involved erosion or compression.

- cfs - Caldera floor terrain, slumped. Numerous arcuate blocks on the steep interior slopes of the caldera. Blocks wider than 2 km (between bounding faults) have planar upper surfaces but no resolvable surface detail. Faults are linear to arcuate, parallel to the surrounding caldera rim, and stair-stepped down the interior caldera wall. The most extensive occurrence of this unit is on the eastern side of the caldera complex. Example: 401B21, E of center. Interpretation: Extensively faulted caldera floor material that slumped into the depression caused by the latest collapse event.

#### Summit Units.

- f - Flow terrain. Flows bounded by distinct, lobed margins with a rough visual appearance (abrupt tonal variations over a few pixels, < 100 m in total scale). Leveed central channels are common but not essential. Some flows transition from leveed to planar surfaces near their distal (downslope) margins. One flow (401B24, NE corner; Fig. 3.11) has ridges perpendicular to the flow direction at its distal end; the ridges are 15 m high and spaced 120 m apart. Flow margins are lobate in outline on a scale of 100 to 500 m. Shadow lengths indicate the flow margins are 15 to 45 m high. Caldera collapse truncated some flows on the summit flanks. Contacts with units p and h indicate contemporaneous emplacement of all three terrains but unit f is more commonly on top of the other units. Example: 401B24, center and NE corner. Interpretation: Individual flows of lava less fluid than that of unit p. Leveed central channels, high flow margins, and rough surfaces and margins suggest an aa or block flow texture.
- h - Hummocky plains terrain. Undulatory terrain with a complex assemblage of mounds, flow fronts and isolated leveed channel sections. Individual flow fronts or channel sections are typically not traceable for more than a few km. Relief is variable, up to a maximum of 60 m, over horizontal distances of 200 to 1000 m. East of the caldera the surface undulations occur on a km scale while west of the caldera the dominant scale is 300 to 500 m. Sinuous channels occur within this unit (401B24, E of center) but they are shorter and far less abundant

than in unit p. The unit h sinuous channels are typically associated with distinct sources such as elliptical craters. Contacts with units p and f indicate contemporaneous emplacement of all three terrains. Example: 401B24, N and NE of center. Interpretation: Multiple extrusions, possibly occurring simultaneously, result in an intermixed pattern of flows and surface relief. The increased relief, relative to unit p, and multiple flow features may be associated with less fluid ("degassed") pahoehoe (see Chapter 5, hummocks).

p - Plains terrain. Planar areas with gentle undulations visible by slight tonal variations. Sinuous channels 100 to 200 m wide are very common, some more than 50 km in length. Tonal variations suggest the sinuous channels run along the crests of gently sloping ridges. Elongate toes extend radially from the sinuous channel in 401B24, center (Fig. 3.11). The few flow margins visible within this unit are broad and have low relief (<15 m). Sinuous ridges oriented radial to the caldera are present in this terrain south of the caldera rim. Contacts with units h and f indicate contemporaneous emplacement of all three terrains but unit p is more commonly covered by the other units. Example: 401B24, center. Interpretation: Fluid lavas emplaced along central feeding channels (possibly including collapsed tube segments) or low broad flows. The gentle surface relief and channel morphology suggest a pahoehoe flow texture.

hk - Hummocky plains terrain, knobby. Undulatory terrain consisting predominantly of individual knobs and mounds spaced 200 to 500 m apart. Surface relief is comparable to that of unit h but flow fronts and leveed channel sections are absent. The knobby plains occur west of the summit caldera but this may be due to the limited high resolution photographic coverage available east of the caldera. Mapped outlines are generally elongate radial to the summit area; this is consistent with the h and p contacts that suggest these units moved around and covered the hk terrain. Example: 401B13, N of center. Interpretation: Individual knobs (large tumuli?) generated by localized outpouring of small volumes of lava. This type of emplacement would suggest a toey pahoehoe flow texture.

### Base Units.

Contact relationships for most basal units are difficult to identify due to the subdued tonal and textural variations in the photographs.

- s - Smooth plains terrain. Plains with no visible surface features < 300 m in scale, resulting in a very smooth appearance. Gentle km-scale undulations are evident from tonal variations; many of these appear to be associated with grabens generally parallel to topographic contours and irregularly shaped depressions oriented downslope. Example: 401B01, S and W of center. Interpretation: Heavily mantled surface. The thickness of the mantling material must be 10s of meters in order to obscure all flow relief. This unit overlies all other base terrains.
- fs - Flow terrain, subdued. Flows bounded by lobed margins; tonal contrast across margins and on flow surfaces is reduced compared to that of unit f. Leveed central channels are common but lack dark shadows. The least subdued unit fs flows appear to overlie adjacent units. Example: 401B07, E of center. Interpretation: Individual flows of less fluid lava like unit f but mantled by material that reduces relief and tonal variations.
- hs - Hummocky plains terrain, subdued. Undulatory terrain consisting of mounds and lineations oriented along the slope; tonal contrast is reduced compared to that of unit h. The lineations have a variable texture and tone much like the margins of unit fs flows. Individual flow segments are more common than in unit h but they are not traceable for more than a few km. Irregular depressions 600 to 3000 m across and lacking positive relief rims are scattered throughout this unit at lower elevations. Example: 401B06, center. Interpretation: Numerous individual flows and gentle undulations mantled by material which reduces relief and tonal variations. This terrain is the subdued version of unit h but with a greater abundance of individual flow segments.
- ps - Plains terrain, subdued. Planar areas, typically including sinuous channels, with a subdued surface relief. Sinuous channel relief is also subdued,

relative to unit p sinuous channels, as evidenced by decreased tonal contrast and the lack of dark shadows. Numerous sinuous ridges within this unit (401B10, S and SW of center) coincide with the western end of a large thrust fault south of the summit caldera (see Map 1). Example: 401B10, center and SW corner. Interpretation: Fluid lavas like unit p but mantled by material that reduces relief and tonal variations.

hks - Hummocky plains terrain, knobby, subdued. Undulatory terrain consisting predominantly of individual knobs and mounds spaces 200 to 500 m apart, with little tonal contrast over the entire unit. Individual flow sections are absent. Irregular depressions occur along the upslope unit contact in 401B02. Example: 401B02, W of center. Interpretation: Localized outpouring of small volumes of lava like unit hk but mantled by material that reduces relief and tonal variations.

m - Mound terrain. Rounded mounds 0.5 to 4 km across and < 200 m high. The mounds are common below the 15-km elevation, near the transition from the summit units to the subdued base units. Most mounds lack any prominent surface textures but one of the larger ones has numerous small knobs similar to but smaller and more closely spaced than those of unit hks. Some mounds seem to have deflected plains flows around them while others could be sources of individual flows (401B07, E of center). Example: 401B03, center. Interpretation: Parasitic low shields produced by localized eruptions. Groups of individual mounds oriented along slope may represent fissure-controlled eruption centers.

#### Additional Units.

g - Graben floor terrain. Smooth to knobby surfaces within grabens, oriented perpendicular to the topographic gradient. The graben are linear to slightly arcuate, 500 to 1400 m wide, 30 to 160 m deep, up to 70 km long, and include up to three paired faults on both sides of the depression. The floor areas mapped here do not include materials traceable within or across the graben; such material is included with the unit outside the graben. Example: 401B03, E of center. Interpretation: Material downdropped between graben faults where surface features have been disrupted by the tectonic activity.

- d - Depression floor terrain. Smooth to knobby surfaces within irregular depressions oriented downslope. Some bounding scarps are linear and meet at obtuse angles while other scarps are arcuate. The floor terrain includes no features continuous with surrounding features. The depression are 100 to 220 m deep and 1 to 7.5 km wide. Ejecta from a 1.6 km diameter crater in 401B01 was disrupted by the depression forming process. Large jumbled blocks on the floor area are mapped separately (see unit j below). Example: 401B01, N of center. Interpretation: Disrupted material that collapsed within the irregular depressions. The disruption process involved mass movement through collapse and landslide events, possibly including sapping. Joints or faults may influence some scarp orientations.
- j - Jumbled terrain. Jumbled and rotated blocks within irregularly shaped depressions. Most locations consist of a chaotic accumulation of mounds and elongate blocks 100 to 400 m across. One location (401B03) has parallel, crescentic ridges 50 to 100 m high and spaced 500 m apart. There is no visible surface texture but tonal variations are very abrupt, indicating more surface relief than on unit m. Example: 401B03, center. Interpretation: Disrupted shield material that slumped into the irregular depressions. The crescentic ridges are rotated landslide blocks.
- c - Crater terrain. Crater interior and rim deposits and, where visible, crater ejecta deposits. 10 craters larger than 900 m in diameter were mapped as this unit, where rim and/or ejecta morphology could be identified. Example: 401B01, W of center. Interpretation: Impact craters with circular raised rims and, in some cases, ejecta deposits extending radially from the crater.
- sh - Shadow. Surface features are totally hidden within the shadows adjacent to the caldera walls. Example: 401B17, E side.



### APPENDIX 3. ELEVATION-DEPENDENT CORRECTIONS FOR THERMAL INERTIAS ON MARS.

Thermal inertias on Mars display an inverse correlation with elevation; this effect is most pronounced on the large volcanoes in the Tharsis area (Kieffer et al., 1973, 1977; Jakosky, 1979; Palluconi and Kieffer, 1981). Thermal inertia provides a quantitative measure of surface properties such as particle size, porosity, and intergrain bonding but the martian atmosphere can affect temperatures independent of the surface material properties and alter the apparent thermal inertia. Three atmospheric effects contribute to changes in apparent thermal inertia (Jakosky, 1979; Palluconi and Kieffer, 1981): 1) changes in the thermal conductivity of particulate materials as a function of atmospheric pressure, 2) atmospheric thermal radiation to the surface, and 3) atmospheric dust absorption, scattering, and radiation.

The thermal conductivity of particulate materials varies with atmospheric pressure (Wechsler and Glaser, 1965). At martian atmospheric pressures the thermal conductivity is proportional to the square root of the pressure, so that thermal inertia is proportional to the fourth root of pressure (Kieffer et al., 1973). Mars has no sea level to define an equipotential reference surface for elevation measurements so an atmospheric pressure of 6.1

millibars (the triple point pressure of water) has become the standard zero elevation level (Mutch et al., 1976, p.210). The change in thermal inertia due to atmospheric pressure variations (identified as  $\Delta$ ) can then be related to the standard zero elevation pressure:

$$\Delta = I / I_0 = (P / P_0)^{1/4} \quad (\text{Eq. A3.1})$$

where  $I$  is the thermal inertia at atmospheric pressure  $P$  and  $I_0$  is the thermal inertia of the same materials at zero-elevation pressure ( $P_0$ ) of 6.1 mbar. Assuming a scale height of 10 km (Leovy, 1979), atmospheric pressure can also be directly related to elevation (Fig. A3.1 and Table A3.1). A second order least squares fit to  $\Delta$  as a function of elevation results in the expression:

$$\Delta = 1 / (1.10 - .026 (H + 4) + .00023 (H + 4)^2) \quad (\text{Eq. A3.2})$$

where  $H$  is the surface elevation in km, relative to the 6.1 mbar level. When the surface elevation is known, the measured thermal inertia is divided by  $\Delta$  calculated from Eq. A3.2 to obtain the thermal inertia at 6.1 mbar atmospheric pressure.

Thermal radiation from the atmosphere decreases with increasing elevation as the atmospheric density decreases (Jakosky, 1979). The standard Viking thermal model uses a constant atmospheric radiation flux of .02 of the noontime solar radiation, consistent with the small atmospheric temperature amplitude measured by the IRTM (Kieffer et al., 1977). If it is assumed that the atmospheric

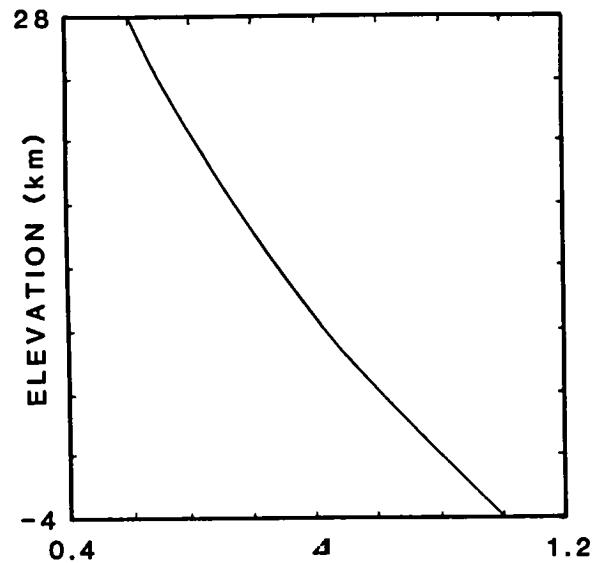


Figure A3.1. Change in apparent thermal inertia due to atmospheric pressure effects on thermal conductivity as a function of elevation.  $\Delta$  is apparent thermal inertia normalized to thermal inertia at zero elevation (Eq. A3.1).

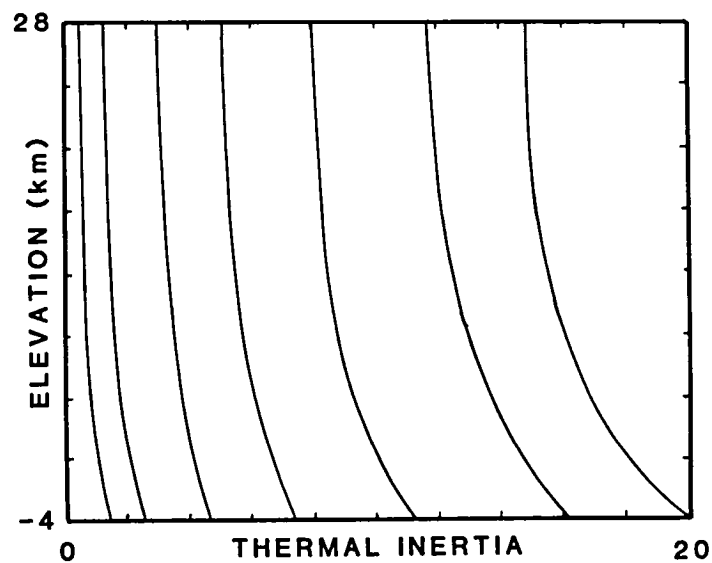


Figure A3.2. Change in apparent thermal inertia due to variations in atmospheric thermal radiation as a function of elevation.

Table A3.1. Change in thermal inertia due to atmospheric pressure effects on thermal conductivity ( $\Delta$ ) and the apparent thermal inertia due to atmospheric radiation at midnight.

El. (km)	P (mbar)	$\Delta$	Apparent Thermal Inertias						
28	0.37	0.50	0.45	1.22	3.00	5.10	7.93	11.66	14.82
26	0.45	0.52	0.45	1.22	3.01	5.12	7.96	11.69	14.85
24	0.55	0.55	0.46	1.23	3.03	5.14	8.00	11.74	14.90
22	0.68	0.58	0.46	1.25	3.06	5.17	8.04	11.80	14.96
20	0.83	0.61	0.47	1.27	3.08	5.21	8.09	11.88	15.04
18	1.01	0.64	0.49	1.29	3.11	5.25	8.15	11.98	15.14
16	1.23	0.67	0.51	1.32	3.14	5.30	8.21	12.09	15.25
14	1.50	0.70	0.53	1.36	3.18	5.36	8.27	12.21	15.38
12	1.84	0.74	0.56	1.40	3.23	5.43	8.39	12.40	15.56
10	2.24	0.78	0.59	1.46	3.31	5.53	8.54	12.63	15.78
8	2.74	0.82	0.63	1.52	3.39	5.64	8.71	12.90	16.04
6	3.35	0.86	0.68	1.60	3.50	5.78	8.93	13.24	16.37
4	4.09	0.90	0.74	1.71	3.63	5.97	9.22	13.66	16.81
2	4.99	0.95	0.81	1.83	3.78	6.20	9.56	14.15	17.33
0	6.10	1.00	0.90	1.97	3.95	6.46	9.95	14.70	17.93
-2	7.45	1.05	1.12	2.19	4.23	6.84	10.51	15.39	18.86
-4	9.10	1.10	1.40	2.46	4.58	7.29	11.17	16.17	19.97

Table A3.2. Apparent thermal inertia due to atmospheric radiation at noon.

El. (km)	Apparent Thermal Inertias						
28	1.48	2.60	4.82	7.75	12.12	17.98	23.72
26	1.48	2.59	4.81	7.74	12.09	17.92	23.63
24	1.47	2.57	4.80	7.72	12.04	17.86	23.52
22	1.46	2.55	4.77	7.69	11.99	17.79	23.39
20	1.44	2.53	4.75	7.65	11.92	17.71	23.24
18	1.43	2.51	4.72	7.61	11.85	17.61	23.07
16	1.41	2.49	4.68	7.55	11.77	17.51	22.88
14	1.38	2.46	4.64	7.49	11.68	17.39	22.68
12	1.35	2.42	4.59	7.41	11.55	17.21	22.38
10	1.30	2.37	4.52	7.31	11.41	17.00	22.04
8	1.25	2.31	4.44	7.21	11.24	16.75	21.64
6	1.19	2.24	4.35	7.08	11.04	16.45	21.18
4	1.11	2.16	4.24	6.92	10.79	16.09	20.63
2	1.01	2.05	4.11	6.73	10.49	15.69	20.02
0	0.91	1.94	3.97	6.52	10.16	15.24	19.34
-2	0.77	1.79	3.78	6.26	9.76	14.68	18.53
-4	0.60	1.61	3.56	5.96	9.31	14.06	17.62

radiation flux is directly proportional to the mass of the atmosphere above the surface (and therefore proportional to pressure), then the thermal models can be rerun for different levels in the atmosphere.

Thermal models with atmospheric radiation constants of .03, .02, .01, .005, .0025, and .00125 were run for seven thermal inertias and related to elevation through a 10 km atmospheric scale height. The surface temperatures corresponding to each level in the atmosphere were used to determine the apparent thermal inertia, and fit by a second order least squares expression (Fig. A3.2). Decreasing the atmospheric radiation tends to decrease the surface temperatures at all times of day, with the result that calculated thermal inertias are too low during the night and too high during the day, relative to the same surface materials at 6.1 mbar pressure. Increased surface albedo could result in lowered temperatures throughout the day but albedo effects on thermal inertia have been included in the two-parameter (albedo and thermal inertia) fits to measured temperatures (Kieffer et al., 1977; Palluconi and Kieffer, 1981). Tables A3.1 and A3.2 list the apparent thermal inertias at several elevations for midnight and noon, respectively. All thermal inertias presented here are in units of  $10^{-3} \text{ cal cm}^{-2} \text{ sec}^{-1/2} \text{ K}^{-1}$ . The values in the two tables are applicable between 18 H (where H represents 1/24th of a martian day) and 5 H local time at night and

between 9 H and 15 H during the day. Apparent thermal inertias are not sensitive to latitudinal or seasonal variations.

A dusty atmosphere can also influence surface temperatures. Jakosky (1979) modelled the thermal contribution to surface temperatures from atmospheric dust but this procedure overemphasized the absorption (relative to scattering) of solar energy (R. Dittion, personal communication, 1980). The complex optical (Pollack et al., 1977, 1979) and thermal (Zurek, 1978) properties of the dusty martian atmosphere are not presently incorporated into models that allow corrections to be applied directly to the IRTM data. Temperatures measured at different wavelengths are calculated to agree within 0.4 K during the night and within 1.9 K during the day for a dust opacity of 0.1 (Christensen, 1982, Table 2); atmospheric dust should not have a significant effect on thermal measurements under these conditions. Most of the IRTM sequences used in this work correspond to seasons where the dust opacity at thermal wavelengths was  $\leq 0.1$  (Table A2.2).

The corrections for elevation-dependent thermal conductivity and atmospheric radiation effects can be combined to obtain thermal inertias more representative of the surface physical properties. The thermal conductivity correction is applied first and this result is used in the atmospheric correction (reversing the order of the

corrections results in thermal inertias typically within 0.2 units of the values obtained by the initial procedure). Application of the atmospheric correction requires specification of night or day for the observations. Thermal inertias obtained from nighttime temperatures (Kieffer et al., 1977; Zimbelman and Kieffer, 1979) are in good agreement with thermal inertias determined from temperatures measured at several times of day (Palluconi and Kieffer, 1981), so that the night correction should be most applicable to global thermal inertia data sets (e.g. Mars Consortium, Kieffer et al., 1981). Thermal inertias calculated from individual temperature measurements should use the correction appropriate for the actual time of data collection.

The following example illustrates the use of the correction tables. A temperature of 149.5 K is measured during the martian night for a location with an elevation of 17 km. The thermal inertia determined from the standard Viking model is 1.4. From Table A3.1 the thermal conductivity correction results in a thermal inertia of 2.1. Table A3.1 also provides the atmospheric radiation corrections for nighttime temperature measurements. At 17 km elevation, the 2.1 value obtained above corresponds to 0.46 of the difference between the nearest listed values; at the 0 km level 0.46 of the difference between the nearest listed values corresponds to a corrected thermal

inertia of 2.9.

The single-point thermal inertias from the high spatial resolution sequences require one or two additional corrections. If the spacecraft pointing geometries contain a timing error, the position of each measurement must be shifted up or down the groundtrack. The magnitude of the shift must be determined by manually matching thermal values with several surface features along the groundtrack. This process is greatly simplified through the use of plots (Fig. A1.4) and maps at a scale sufficient to clearly show individual measurements.

An additional correction results from the method by which model calculations of thermal inertia are performed. The very low nighttime temperatures on Ascræus Mons cause the standard Viking model to greatly underestimate the calculated thermal inertias that are  $< 1$ , at times resulting in physically impossible negative values. This is due to the  $I = 1$  lower limit for calculated temperatures in the standard model data files and the non-linearity between temperature and thermal inertia. The correction involves computing individual thermal models for the date of the sequence at thermal inertias less than 1 and interpolation of the thermal inertias. On Ascræus Mons no thermal inertias calculated in this manner were less than 0.8 (prior to corrections for elevation).










Mercator Projection







## STRATIGRAPHY

- 

## SYMBOLS

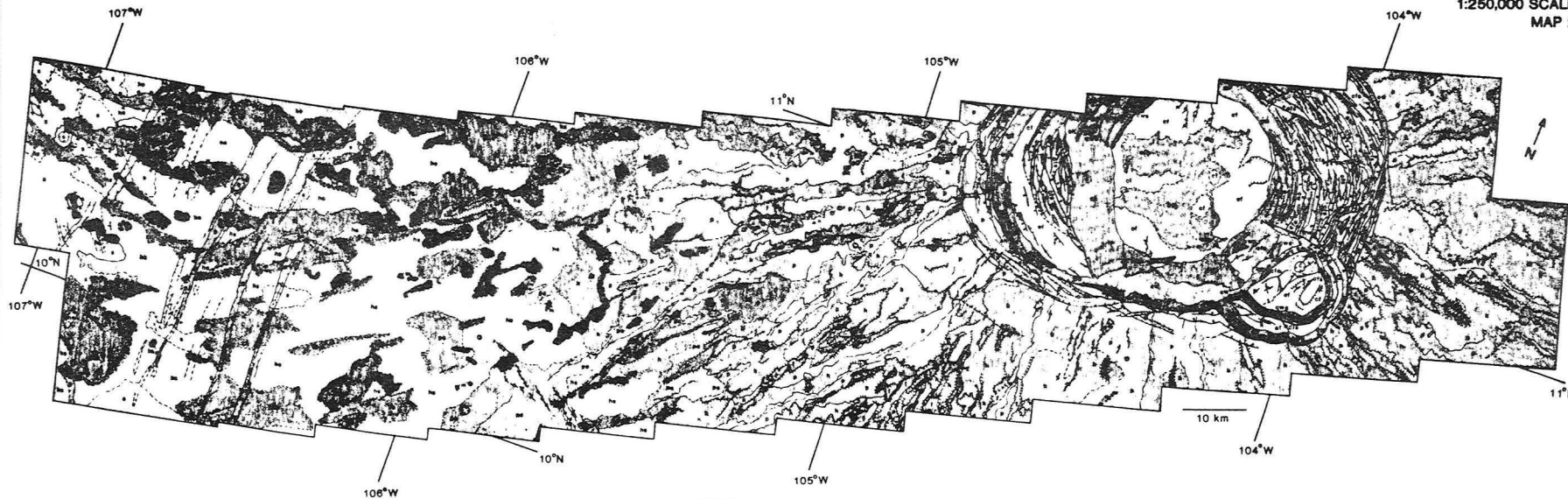
	Shield terrain, western flank
	Caldera floor terrain
	Caldera wall terrain
	Shield terrain
	Shield terrain, Parícuta Monje

--- Contact, queried where explanation uncertain	--- Fault, bar and bar on downward-sloped side
--- Flow margin, hachures extend down front	--- Thrust fault, asymmetrical on upper plate
--- Channel	--- Graben, bar on downward-sloped side
--- Sinuous channel	--- Ridge, following crest
--- Crater / rim	--- Base of terrace
--- Aligned pits	--- Flow direction

- |   |                                 |
|---|---------------------------------|
|  | Rugged terrain                  |
|  | Mountainous terrain             |
|  | Mountainous terrain, knobby     |
|  | Mountainous terrain, Parana Mts |
|  | Knobby terrain                  |
|  | Craters                         |

James R. Zimbelman  
Arizona State University

PHOTOGEOLOGY OF ASCRAEUS MONS  
401B01-24 PHOTOGRAPHS  
1:250,000 SCALE  
MAP 2



TERRAIN UNITS  
See Appendix 2 for descriptions of each unit

#### SYMBOLS

All symbols dashed where inferred

- Contact
- Flow margin, hachures extend down front
- Graben, ball on downdropped side
- Ridge, following crest
- Fault, ball and bar on downdropped side
- Scarp, barb points downslope
- Sinuous channel
- Aligned pits
- Crater rim
- Hill

#### CALDERA UNITS

- ct Caldera floor
- cf Caldera floor, grooved
- cfa Caldera floor, slumped
- cw Caldera wall, grooved
- cwa Caldera wall, slumped

#### SUMMIT UNITS

- f Flows
- h Hummocky plains
- p Plains
- hk Hummocky plains, knobby

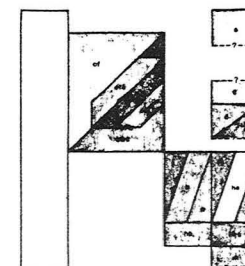
#### BASE UNITS

- s Smooth plains
- fs Flows, subdued
- hs Hummocky plains, subdued
- ps Plains, subdued
- hks Hummocky plains, knobby, subdued
- m Mounds

#### ADDITIONAL UNITS

- g Graben floor
- d Depression floor
- j Jumbled terrain
- c Craters
- sh Shadow (surface not visible)

#### STRATIGRAPHY



See Fig 3.4 for mosaic of photographs

(Map 3 is shown in Fig. 4.5)



1. Report No. NASA TM-88784 volume 1		2. Government Accession No.		3. Recipient's Catalog No.	
4. Title and Subtitle  Advances in Planetary Geology - Volume 1				5. Report Date July 1986	
				6. Performing Organization Code EL	
7. Author(s)				8. Performing Organization Report No.	
9. Performing Organization Name and Address Office of Space Science and Applications Solar System Exploration Division Planetary Geology and Geophysics Program				10. Work Unit No.	
				11. Contract or Grant No.	
12. Sponsoring Agency Name and Address National Aeronautics and Space Administration Washington, DC 20546				13. Type of Report and Period Covered Technical Memorandum	
				14. Sponsoring Agency Code	
15. Supplementary Notes					
16. Abstract  This publication is a compilation of reports focusing on research into the origin and evolution of the solar system with emphasis on planetary geology.					
17. Key Words (Suggested by Author(s))  planetary geology planetology				18. Distribution Statement  Unclassified - Unlimited  Subject Category 91	
19. Security Classif. (of this report) Unclassified		20. Security Classif. (of this page) Unclassified		21. No. of Pages 600	
				22. Price A25	



**National Aeronautics and  
Space Administration  
Code NIT-4**

**Washington, D.C.  
20546-0001**

**Official Business  
Penalty for Private Use, \$300**

**SPECIAL FOURTH-CLASS RATE  
POSTAGE & FEES PAID  
NASA  
Permit No. G-27**

**NASA**

**POSTMASTER: If Undeliverable (Section 158  
Postal Manual) Do Not Return**

---